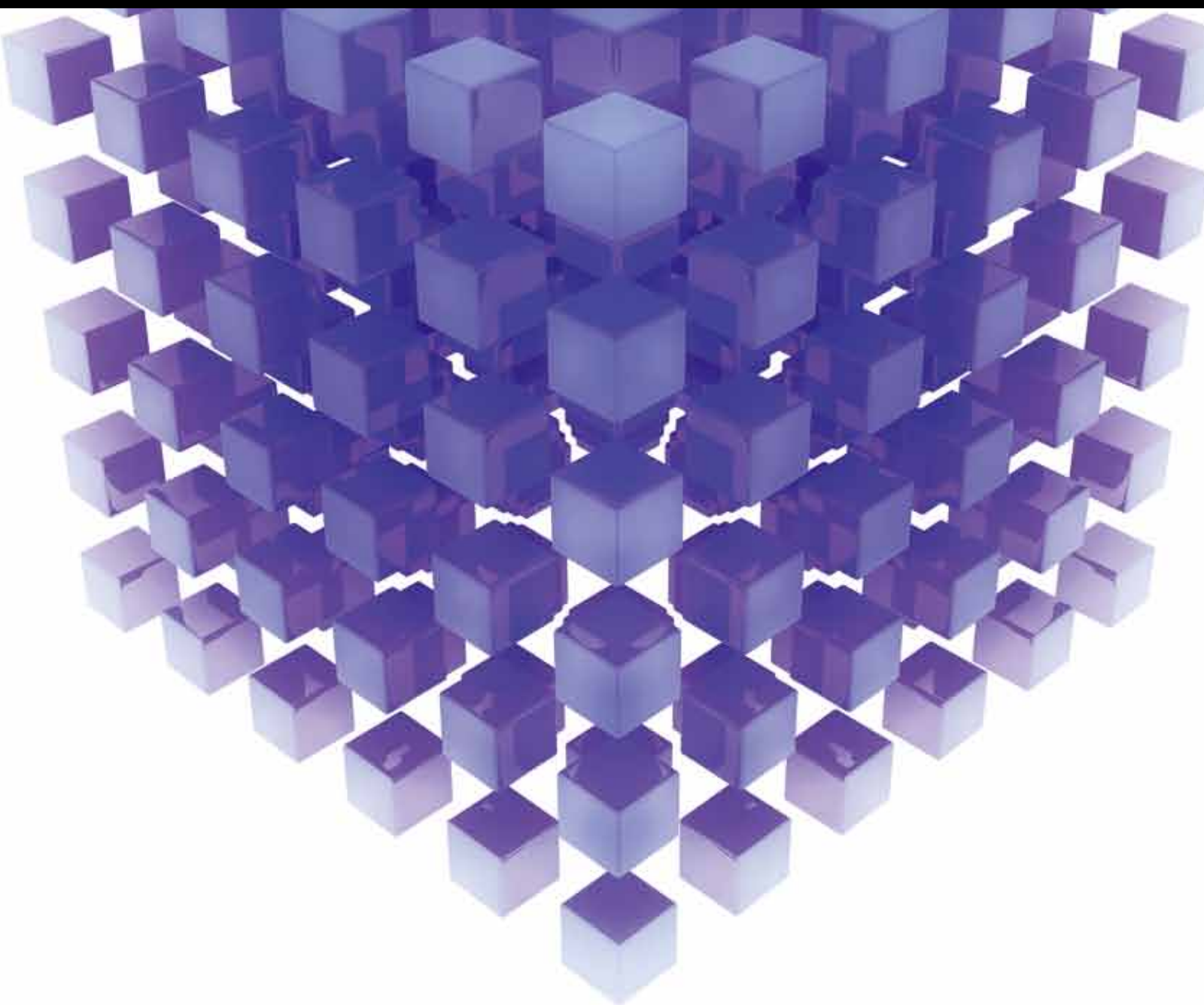


MATHEMATICAL PROBLEMS IN ENGINEERING

# MATHEMATICAL PROBLEMS IN SUSTAINABLE ENERGY AND ENVIRONMENT

GUEST EDITORS: SHENGYONG CHEN, MAURIZIO CARLINI, NATALIYA KRASNOGORSKAYA,  
AND MASSIMO SCALIA





---

# **Mathematical Problems in Sustainable Energy and Environment**

Mathematical Problems in Engineering

---

## **Mathematical Problems in Sustainable Energy and Environment**

Guest Editors: Shengyong Chen, Maurizio Carlini,  
Nataliya Krasnogorskaya, and Massimo Scalia



---

Copyright © 2013 Hindawi Publishing Corporation. All rights reserved.

This is a special issue published in “Mathematical Problems in Engineering.” All articles are open access articles distributed under the Creative Commons Attribution License, which permits unrestricted use, distribution, and reproduction in any medium, provided the original work is properly cited.

## Editorial Board

Mohamed Abd El Aziz, Egypt  
Eihab M. Abdel-Rahman, Canada  
Rashid K. Abu Al-Rub, USA  
Sarp Adali, South Africa  
Salvatore Alfonzetti, Italy  
Igor Andrianov, Germany  
Sebastian Anita, Romania  
W. Assawinchaichote, Thailand  
Erwei Bai, USA  
Ezzat G. Bakhoun, USA  
José Manoel Balthazar, Brazil  
R. K. Bera, India  
Christophe Bérenguer, France  
Jonathan N. Blakely, USA  
Stefano Boccaletti, Spain  
Stephane P. A. Bordas, USA  
Daniela Boso, Italy  
M. Boutayeb, France  
Michael J. Brennan, UK  
Salvatore Caddemi, Italy  
Piermarco Cannarsa, Italy  
Jose E. Capilla, Spain  
Carlo Cattani, Italy  
Marcelo Cavalcanti, Brazil  
Diego J. Celentano, Chile  
Mohammed Chadli, France  
Arindam Chakraborty, USA  
Yong-Kui Chang, China  
Michael J. Chappell, UK  
Xinkai Chen, Japan  
Kui Fu Chen, China  
Kue-Hong Chen, Taiwan  
Jyh-Hong Chou, Taiwan  
Slim Choura, Tunisia  
Cesar Cruz-Hernandez, Mexico  
Swagatam Das, India  
Filippo de Monte, Italy  
Maria de Pinho, Portugal  
Antonio Desimone, Italy  
Yannis Dimakopoulos, Greece  
Baocang Ding, China  
Joao B. R. Do Val, Brazil  
Daoyi Dong, Australia  
B. Dubey, India  
Horst Ecker, Austria  
M. Onder Efe, Turkey  
Elmetwally Elabbasy, Egypt  
Alex Elias-Zuniga, Mexico  
Anders Eriksson, Sweden  
Vedat S. Erturk, Turkey  
Qi Fan, USA  
Moez Feki, Tunisia  
Ricardo Femat, Mexico  
Robertt Fontes Valente, Portugal  
Claudio Fuerte-Esquivel, Mexico  
Zoran Gajic, USA  
Ugo Galvanetto, Italy  
Furong Gao, Hong Kong  
Xin-Lin Gao, USA  
Behrouz Gatmiri, Iran  
Oleg V. Gendelman, Israel  
Didier Georges, France  
Paulo Batista Gonçalves, Brazil  
Oded Gottlieb, Israel  
Fabrizio Greco, Italy  
Quang Phuc Ha, Australia  
M. R. Hajj, USA  
Thomas Hanne, Switzerland  
Katica Hedrih, Serbia  
M. I. Herreros, Spain  
Wei-Chiang Hong, Taiwan  
Jaromir Horacek, Czech Republic  
Gordon Huang, Canada  
Chuangxia Huang, China  
Huabing Huang, China  
Yi Feng Hung, Taiwan  
Hai-Feng Huo, China  
Asier Ibeas, Spain  
Anuar Ishak, Malaysia  
Reza Jazar, Australia  
Zhijian Ji, China  
Jun Jiang, China  
J. J. Judice, Portugal  
Tadeusz Kaczorek, Poland  
Tamas Kalmar-Nagy, USA  
Tomasz Kapitaniak, Poland  
Hamid Reza Karimi, Norway  
Metin O. Kaya, Turkey  
Nikolaos Kazantzis, USA  
Farzad Khani, Iran  
Kristian Krabbenhoft, Australia  
Ren-Jieh Kuo, Taiwan  
Jurgen Kurths, Germany  
Claude Lamarque, France  
Marek Lefik, Poland  
Stefano Lenci, Italy  
Roman Lewandowski, Poland  
Shanling Li, Canada  
Ming Li, China  
Jian Li, China  
Shihua Li, China  
Teh-Lu Liao, Taiwan  
Panos Liatsis, UK  
Jui-Sheng Lin, Taiwan  
Yi-Kuei Lin, Taiwan  
Shueei M. Lin, Taiwan  
Wanquan Liu, Australia  
Bin Liu, Australia  
Yuji Liu, China  
Paolo Lonetti, Italy  
Vassilios C. Loukopoulos, Greece  
Chien-Yu Lu, Taiwan  
Junguo Lu, China  
Alexei Mailybaev, Brazil  
Manoranjan K. Maiti, India  
Oluwole Daniel Makinde, South Africa  
Rafael Martinez-Guerra, Mexico  
Driss Mehdi, France  
Roderick Melnik, Canada  
Xinzhu Meng, China  
Yuri V. Mikhlin, Ukraine  
Gradimir Milovanovic, Serbia  
Ebrahim Momoniat, South Africa  
Trung Nguyen Thoi, Vietnam  
Hung Nguyen-Xuan, Vietnam  
Ben T. Nohara, Japan  
Sotiris Ntouyas, Greece  
Gerard Olivar, Colombia  
Claudio Padra, Argentina  
Bijaya Ketan Panigrahi, India  
Francesco Pellicano, Italy  
Matjaz Perc, Slovenia  
Vu Ngoc Phat, Vietnam  
Alexander Pogromsky, The Netherlands  
Seppo Pohjolainen, Finland

Stanislav Potapenko, Canada

Sergio Preidikman, USA

Carsten Proppe, Germany

Hector Puebla, Mexico

Justo Puerto, Spain

Dane Quinn, USA

Kumbakonam Rajagopal, USA

Gianluca Ranzi, Australia

Sivaguru Ravindran, USA

G. Rega, Italy

Pedro Ribeiro, Portugal

J. Rodellar, Spain

Rosana Rodriguez-Lopez, Spain

Alejandro J. Rodriguez-Luis, Spain

Ignacio Romero, Spain

Hamid Ronagh, Australia

Carla Roque, Portugal

Rubén Ruiz García, Spain

Manouchehr Salehi, Iran

Miguel A. F. Sanjuán, Spain

Ilmar Ferreira Santos, Denmark

Nickolas S. Sapidis, Greece

Evangelos J. Sapountzakis, Greece

Bozidar Sarler, Slovenia

Andrey V. Savkin, Australia

Massimo Scalia, Italy

Mohamed A. Seddeek, Egypt

Alexander P. Seyranian, Russia

Leonid Shaikhet, Ukraine

Cheng Shao, China

Bo Shen, Germany

Daichao Sheng, Australia

Tony Sheu, Taiwan

Jian-Jun Shu, Singapore

Zhan Shu, UK

Dan Simon, USA

Luciano Simoni, Italy

Grigori M. Sisoiev, UK

Christos H. Skiadas, Greece

Davide Spinello, Canada

Sri Sridharan, USA

Rolf Stenberg, Finland

Jitao Sun, China

Xi-Ming Sun, China

Changyin Sun, China

Andrzej Swierniak, Poland

Yang Tang, Germany

Allen Tannenbaum, USA

Cristian Toma, Romania

Irina N. Trendafilova, UK

Alberto Trevisani, Italy

Jung-Fa Tsai, Taiwan

Kuppapalle Vajravelu, USA

Victoria Vampa, Argentina

Josep Vehi, Spain

Stefano Vidoli, Italy

Dan Wang, China

Youqing Wang, China

Yongqi Wang, Germany

Moran Wang, China

Cheng C. Wang, Taiwan

Yijing Wang, China

Xiaojun Wang, China

Gerhard-Wilhelm Weber, Turkey

Jeroen Witteveen, USA

Kwok-Wo Wong, Hong Kong

Zheng-Guang Wu, China

Ligang Wu, China

Wang Xing-yuan, China

X. Frank Xu, USA

Xuping Xu, USA

Xing-Gang Yan, UK

Jun-Juh Yan, Taiwan

Suh-Yuh Yang, Taiwan

Mahmoud T. Yassen, Egypt

Mohammad I. Younis, USA

Huang Yuan, Germany

S. P. Yung, Hong Kong

Ion Zaballa, Spain

Ashraf Zenkour, Saudi Arabia

Jianming Zhan, China

Yingwei Zhang, China

Xu Zhang, China

Lu Zhen, China

Liancun Zheng, China

Jian Guo Zhou, UK

Zexuan Zhu, China

Mustapha Zidi, France

# Contents

**Mathematical Problems in Sustainable Energy and Environment**, Shengyong Chen, Maurizio Carlini, Nataliya Krasnogorskaya, and Massimo Scalia  
Volume 2013, Article ID 919213, 2 pages

**Performance of an Ocean Energy Conversion System with DFIG Sensorless Control**, I. Garrido, Aitor J. Garrido, M. Alberdi, M. Amundarain, and O. Barambones  
Volume 2013, Article ID 260514, 14 pages

**Design and Implementation of a Control Strategy for Microgrid Containing Renewable Energy Generations and Electric Vehicles**, Mingchao Xia, Xuanhu He, and Xiaoqing Zhang  
Volume 2013, Article ID 686508, 15 pages

**Extreme Dynamic Responses of MW-Level Wind Turbine Tower in the Strong Typhoon Considering Wind-Rain Loads**, Zhenyu Wang, Yan Zhao, Fuqiang Li, and Jianqun Jiang  
Volume 2013, Article ID 512530, 13 pages

**Novel Modified Elman Neural Network Control for PMSG System Based on Wind Turbine Emulator**, Chih-Hong Lin  
Volume 2013, Article ID 753756, 15 pages

**Distributed Beacon Drifting Detection for Localization in Unstable Environments**, Ming Xia, Peiliang Sun, Xiaoyan Wang, Yan Jin, and Qingzhang Chen  
Volume 2013, Article ID 865983, 8 pages

**Modeling for Green Supply Chain Evaluation**, Elham Falatoonitoosi, Zulkiflle Leman, and Shahryar Sorooshian  
Volume 2013, Article ID 201208, 9 pages

**Formulation and Implementation of Energy Efficient Ultraviolet Curing for Photosensitive Resin-Bound Diamond Wire Saws**, Chunyan Yao, Wei Peng, and Fuqing Liu  
Volume 2013, Article ID 698360, 6 pages

**Calculation of Lightning Transient Responses on Wind Turbine Towers**, Xiaoqing Zhang and Yongzheng Zhang  
Volume 2013, Article ID 757656, 8 pages

**Nonlinear State Space Modeling and System Identification for Electrohydraulic Control**, Jun Yan, Bo Li, Hai-Feng Ling, Hai-Song Chen, and Mei-Jun Zhang  
Volume 2013, Article ID 973903, 9 pages

**On-Board Computing for Structural Health Monitoring with Smart Wireless Sensors by Modal Identification Using Hilbert-Huang Transform**, Ning Wu, Chengyin Liu, Yukun Guo, and Jianhua Zhang  
Volume 2013, Article ID 509129, 9 pages

**Modeling of an Air Conditioning System with Geothermal Heat Pump for a Residential Building**, Silvia Cocchi, Sonia Castellucci, and Andrea Tucci  
Volume 2013, Article ID 781231, 6 pages

**Determining the Optimum Section of Tunnels Using Ant Colony Optimization**, S. Talatahari

Volume 2013, Article ID 320360, 7 pages

**Wind Speed Forecasting by Wavelet Neural Networks: A Comparative Study**, Chuanan Yao,

Xiankun Gao, and Yongchang Yu

Volume 2013, Article ID 395815, 7 pages

**Bio-Inspired Optimization of Sustainable Energy Systems: A Review**, Yu-Jun Zheng, Sheng-Yong Chen,

Yao Lin, and Wan-Liang Wang

Volume 2013, Article ID 354523, 12 pages

**Cauchy-Matern Model of Sea Surface Wind Speed at the Lake Worth, Florida**, Ming Li, S. C. Lim,

and Wei Zhao

Volume 2012, Article ID 843676, 10 pages

**Hölder Scales of Sea Level**, Ming Li, YangQuan Chen, Jia-Yue Li, and Wei Zhao

Volume 2012, Article ID 863707, 22 pages

**Energy Dependent Divisible Load Theory for Wireless Sensor Network Workload Allocation**,

Haiyan Shi, Wanliang Wang, and Ngaiming Kwok

Volume 2012, Article ID 235289, 16 pages

**The Semitransparent Photovoltaic Films for Mediterranean Greenhouse: A New Sustainable**

**Technology**, Alvaro Marucci, Danilo Monarca, Massimo Cecchini, Andrea Colantoni, Alberto Manzo,

and Andrea Cappuccini

Volume 2012, Article ID 451934, 14 pages

**Modeling Small Scale Solar Powered ORC Unit for Standalone Application**, Enrico Bocci,

Mauro Villarini, Luca Bove, Stefano Esposito, and Valerio Gasperini

Volume 2012, Article ID 124280, 10 pages

**Agent-Based Modeling and Genetic Algorithm Simulation for the Climate Game Problem**,

Zheng Wang and Jingling Zhang

Volume 2012, Article ID 709473, 14 pages

**Photovoltaic Pumps: Technical and Practical Aspects for Applications in Agriculture**, A. Petroselli,

P. Biondi, A. Colantoni, D. Monarca, M. Cecchini, A. Marucci, and Cividino Sirio

Volume 2012, Article ID 343080, 19 pages

**Robust Nash Dynamic Game Strategy for User Cooperation Energy Efficiency in Wireless Cellular**

**Networks**, Shuhuan Wen, Baozhu Hu, Ahmad B. Rad, Xinbin Li, Huibin Lu, and Jianhua Zhang

Volume 2012, Article ID 636159, 10 pages

**Energy Characterization and Gasification of Biomass Derived by Hazelnut Cultivation: Analysis of**

**Produced Syngas by Gas Chromatography**, D. Monarca, A. Colantoni, M. Cecchini, L. Longo,

L. Vecchione, M. Carlini, and A. Manzo

Volume 2012, Article ID 102914, 9 pages

## Editorial

# Mathematical Problems in Sustainable Energy and Environment

**Shengyong Chen,<sup>1</sup> Maurizio Carlini,<sup>2</sup> Nataliya Krasnogorskaya,<sup>3</sup> and Massimo Scalia<sup>4</sup>**

<sup>1</sup> College of Computer Science & Technology, Zhejiang University of Technology, Hangzhou 310023, China

<sup>2</sup> CIRDER, University of Tuscia, Via San Camillo de Lellis s.n.c., 01100 Viterbo, Italy

<sup>3</sup> Department of Production Safety and Industrial Ecology, Ufa State Aviation Technical University, Karl Marx Street 12, 450000 Ufa, Russia

<sup>4</sup> Department of Mathematics, University of Rome "La Sapienza", Piazzale A. Moro 2, 00185 Rome, Italy

Correspondence should be addressed to Shengyong Chen; sy@ieee.org

Received 23 June 2013; Accepted 23 June 2013

Copyright © 2013 Shengyong Chen et al. This is an open access article distributed under the Creative Commons Attribution License, which permits unrestricted use, distribution, and reproduction in any medium, provided the original work is properly cited.

Achieving solutions to energy saving and environment protection problems that we face today requires long-term potential actions for sustainable development. Recent advances in this aspect have contributed to successful solutions to real problems, thus improving the sustainability of energy and environment and the quality of life. The focus of this special issue is on the mathematical models and solution methods to problems in sustainable energy, with modeling, analysis and control problems, communication systems, process control, environmental systems, intelligent manufacturing systems, transportation systems, structural systems, and so forth. A peculiar attention is paid to the related new development in rigorous mathematical physics definitions as well as intelligent methods for effectively solving the problems.

After a rigorous review process on 63 submissions, the special issue selects 23 papers which represent a good panel in the related new development, with the topics being connected with the mathematical problem models, elaborated solution methods, and their applications in real-world energy and environment systems.

In the category of energy production, D. Monarca et al. study the experimentation of innovative plants for electric power production using agroforest biomass and point out a connection among the chemical and physical properties of the outgoing syngas by biomass characterization and gas chromatography analysis. A. Petroselli et al. conduct tests on a PV-DC pump in Viterbo (42°24' North, 12°06' East) from January 2003 to November 2004, involve measurements of solar radiation, and develop a simple method that allows both the assessment of performances of the whole system

and the optimal inclination angle of the panel. E. Bocci et al. simulate the power generation of a generating unit using the Rankine cycle and using refrigerant R245fa as a working fluid and illustrate the modeling of the system using TRNSYS platform, highlighting standard and "ad hoc" developed components as well as the global system efficiency. A. Marucci et al. analyze the radiometric properties of innovative semitransparent flexible photovoltaic materials in order to evaluate their performances in comparison with materials commonly used in the coverage of the greenhouses. M. Li et al. investigate the Hölder multiscales of sea level and reveal that the variations of sea level vary significantly at large time scale, and the dispersion of the Hölder exponents is usually spatial dependent. In another paper, M. Li et al. apply the correlation model to the autocovariance function (ACF) and the PSD of the sea surface wind speed observed in the Lake Worth, FL, USA, over the 1984–2006 period. X. Zhang and Y. Zhang propose a method for calculating lightning transient responses on wind turbine towers. C. Yao et al. present a comparison of three wavelet neural networks for short-term forecasting of wind speed. C. H. Li proposes a novel modified Elman neural network for controlling permanent magnet synchronous generator systems. Z. Wang et al. analyze the dynamic responses of wind turbines under extreme working conditions, considering wind-rain loads. M. Xia et al. present a control strategy for microgrid containing renewable energy generations and electric vehicles.

In the category of energy utilization and saving, I. Garrido et al. investigate the performance of an ocean energy conversion system with DFIG sensorless control. H. Shi et al. adopt the divisible load theory for workload assignment in wireless

sensor networks, which can prolong the energy depletion time of each sensor and make the whole wireless sensor network to operate for an extended duration. In order to increase the energy efficiency of radio access networks, S. Wen et al. propose a dynamic game model based on the control-theoretical approach to study the energy-efficiency issues in cooperative wireless cellular networks and use a predictor to supervise the data of imperfect channel state information. N. Wu et al. present a decentralized data processing approach for structural health monitoring with smart wireless sensors by modal identification. J. Yan et al. build a nonlinear state space model for analyzing the highly nonlinear system and simplify the H-W model into a linear-in-parameters structure. C. Yao et al. develops a novel diamond wire saw for formulation and implementation of energy-efficient ultraviolet curing. S. Cocchi et al. develop a model to simulate an air conditioning system with geothermal heat pump, which leads to optimization design of geothermal heat exchangers. S. Talatahari applies a bioinspired method, Ant Colony Optimization, to determine the optimum section of tunnels. Finally, Y.-J. Zheng et al. summarize the recent advances in bioinspired optimization methods, such as artificial neural networks and evolutionary algorithms, which are applied to the field of sustainable energy development.

In the category of environment protection and sustainability, M. Xia et al. propose a distributed beacon drifting detection algorithm to locate those accidentally moved beacons, which is a fundamental problem in wireless sensor networks, especially in unstable environments. To solve the cooperative game of global temperature lacking automaticity and emotional jamming, Z. Wang and J. Zhang develop an agent-based modelling method, which also uses a genetic algorithm to improve the investment strategy of each agent. E. Falatoonitoosi et al. examine the influential and important main green supply chain management practices, in particular green logistics and environmental protection.

Nevertheless, this special issue is not intended to constitute a complete compendium on the topic, but it does offer the reader an opportunity to appreciate the possibilities and the progress in the research area. It can be seen that although some models and solutions become available, most problems remain open and research is highly active in this field. We are aware of the present and upcoming technologies that will shape the future sustainable energy and environment, and we believe that all of us can contribute to the improvement of sustainability of our life styles.

## Acknowledgments

As guest editors of this special issue, we would like to thank all the authors for their valuable contributions and the referees for their thorough reviews and helpful comments on the papers.

*Shengyong Chen*  
*Maurizio Carlini*  
*Nataliya Krasnogorskaya*  
*Massimo Scalia*

## Research Article

# Performance of an Ocean Energy Conversion System with DFIG Sensorless Control

I. Garrido,<sup>1</sup> Aitor J. Garrido,<sup>1</sup> M. Alberdi,<sup>1</sup> M. Amundarain,<sup>1</sup> and O. Barambones<sup>2</sup>

<sup>1</sup> Department of Automatic Control and Systems Engineering, EUITI de Bilbao, University of the Basque Country (UPV/EHU), Rafael Moreno 3, 48013 Bilbao, Spain

<sup>2</sup> Department of Automatic Control and Systems Engineering, EUI de Vitoria-Gasteiz, University of the Basque Country (UPV/EHU), Nieves Cano 12, 01006 Vitoria-Gasteiz, Spain

Correspondence should be addressed to I. Garrido; [izaskun.garrido@ehu.es](mailto:izaskun.garrido@ehu.es)

Received 24 February 2013; Accepted 21 May 2013

Academic Editor: Massimo Scalia

Copyright © 2013 I. Garrido et al. This is an open access article distributed under the Creative Commons Attribution License, which permits unrestricted use, distribution, and reproduction in any medium, provided the original work is properly cited.

The 2009/28/EC Directive requires Member States of the European Union to adopt a National Action Plan for Renewable Energy. In this context, the Basque Energy Board, EVE, is committed to research activities such as the Mutriku Oscillating Water Column plant, OWC. This is an experimental facility whose concept consists of a turbine located in a pneumatic energy collection chamber and a doubly fed induction generator that converts energy extracted by the turbine into a form that can be returned to the network. The turbo-generator control requires a precise knowledge of system parameters and of the rotor angular velocity in particular. Thus, to remove the rotor speed sensor implies a simplification of the hardware that is always convenient in rough working conditions. In this particular case, a Luenberger based observer is considered and the effectiveness of the proposed control is shown by numerical simulations. Comparing these results with those obtained using a traditional speed sensor, it is shown that the proposed solution provides better performance since it increases power extraction in the sense that it allows a more reliable and robust performance of the plant, which is even more relevant in a hostile environment as the ocean.

## 1. Introduction

There is a current need not only for greater energy accessibility but also to prevent that the energy consumption environmental impact grows to the point that causes irreversible damage to the planet. In this sense, the European Parliament has backed up a climate change package which aims to achieve by 2020 a 20% reduction of greenhouse gas emissions, a 20% increment in energy efficiency, and a 20% of renewable share within European Union (EU) countries. At the same time, recent developments have highlighted that relying so heavily on fossil and fission-based energy poses a security, economic, and human threat. The British Petroleum oil spill in the Gulf of Mexico caused extensive damage on the economy and welfare of the region, the “Arab Spring” has triggered oil-price volatility, and Japan’s Fukushima nuclear catastrophe has brought about doubts over the role of fission-based energy. In recent studies [1, 2], Drs. Jacobson and Delucchi

stated that “barriers to a 100% conversion to wind water and solar power worldwide are primarily social and political, not technological or even economic.” Based on their studies, all the world energy needs might be satisfied from wind, water, and solar power, considering 720,000 0.75 MW wave devices. In any case, the advantages are many since it is a clean, free, readily available, and safe source of energy that, even when it currently requires further research, it is called to play a main roll in a near future.

The Spanish Council of Ministers on 11th November 2011 approved the Renewable Energies Plan for 2011–2020. This plan includes the design of new energy scenarios and incorporating the objectives given in the Directive 2009/28/EC of the European Parliament on the promotion of the use of energy from renewable sources, which sets binding minimum targets for the whole of the European Union and for each of the Member States. In particular, this plan highlights the marine energy potential that Spain possesses with special



FIGURE 1: OWC for the Nereida project by the EVE.

emphasis in wave energy, with the potential to satisfy 15% of EU energy demand, cutting 136 MT/MWh off the CO<sub>2</sub> emissions by 2050. The proposals are directed mainly to the R&D not only of new designs and components aiming to improve equipment fatigue and reduce the cost, but also of demonstration programs for prototypes testing, as well as to develop infrastructure to validate experimental devices. Major efforts are being made in the Basque Country through the Nereida Project, promoted by Basque Energy Board (EVE), which has developed an Oscillating Water Column (OWC) integrated in a breakwater located in Mutriku and involves a €5.7 M investment. The plant consists of 16 turbines, 18.5 kW each, with an estimated overall power of 296 kW (see Figure 1). It was inaugurated in July 2011 [3, 4] and produced 200.000 kWh during the first year while it was estimated 600.000 kWh production per year. Although the difference is mainly due to a storm that damaged the control room and kept the facility closed during the best wave months, an improvement in the power generation could highly benefit the system.

In this power plant, the water surface inside a chamber moves up and down under the wave action causing to inhale and exhale air through the opening at the top. The bidirectional air flow is applied to a special kind of turbine, called Wells turbine, which provides unidirectional rotation despite of the air flow direction [5, 6]. Thus, the Wells turbine transforms the wave potential into mechanical energy that will be transmitted to a double feed induction generator, which feeds AC power to the grid. For that, two pulse-width-modulated three phase converters are connected back to back between the rotor terminal and the utility grid with a DC link. The stator circuit is directly connected to the grid while the rotor winding is connected via slip-rings to the rotor side converter [7].

The OWC system located in Mutriku uses a vector control scheme coupled with cascaded Proportional-Integral-Derivative (PID) controller for current and power loops [8]. This scheme allows power tracking while the Rotor and Grid Side Converters, RSC/GSC, are controlled independently. Besides, it has fault-ride-through (FRT) capabilities and the OWC system also implements a complementary modified antiwind-up PID based valve control for incoming air flow into the turbine [9–11]. The choice of valve control has been

mainly determined by the fact that it is the control used in Mutriku. New Grid Codes oblige distributed power-generation systems to remain connected to the power network during the fault to avoid massive chain disconnections so that the implementation of an adequate FRT capability is indispensable in this kind of systems to ensure its stability and uninterrupted operation [12–17].

All mechanical parts should be designed to withstand the ocean hostile environment and it has to be considered that the turbo-generator control requires a precise knowledge of the system parameters and of the rotor speed in particular. In this context, the most suitable option is to remove the mechanical speed sensor at the rotor shaft so as to simplify the hardware, with the consequent reduction in installation and maintenance costs, increment of disturbance rejection, and plant reliability improvement. However, in order to eliminate the speed sensor from the drive, some of the state variables, such as rotor angular velocity and flux, have to be estimated from measured states. Besides, accuracy, robustness, and sensitivity against parameter deviation can be improved by choosing closed loop observers [18, 19]. Therefore, dynamic performance and steady-state speed accuracy for the lower speed range have been achieved in this particular case considering a closed loop speed observer based in a Luenberger system to estimate the rotor speed from the measured stator voltages and currents [20, 21].

After all these considerations and taking into account the cost effectiveness and improved performance that a speed observer can afford, this paper presents a new sensorless vector control scheme in order to improve the power extraction in the Mutriku OWC, whose results can easily be extended to other wave power plants. The rest of the paper is organized as follows. In Section 2 the OWC is presented, and both its modules, the capture chamber, and the turbine that generates energy are explained. Next, in Section 3, the proposed sensorless control scheme is stated. In Section 4, simulation results for a representative case-study comparing different controlled cases have been obtained. And finally, some concluding remarks are presented in the last section.

## 2. Mutriku OWC Description

*2.1. Mutriku Wave Model and OWC Capture Chamber.* Using data from the Bilbao-Vizcaya exterior buoy of the State Network Ports, the annual average wave height is around 2 m, with period of about 10 s. Statistical study of wave directions reveals the predominance of northeast swell type wave [22, 23]. In order to study regular waves (see also [24]), it is necessary to take into account the spectrum of the wave climate data, that measures the correlation between wave frequency and wave energy, as it may be observed in Figure 2.

This representative spectrum of the wave climate is buoy driven, since it uses a linear wave propagation model to transform measures obtained by an offshore wave rider buoy in deep water to the OWC location in the coast.

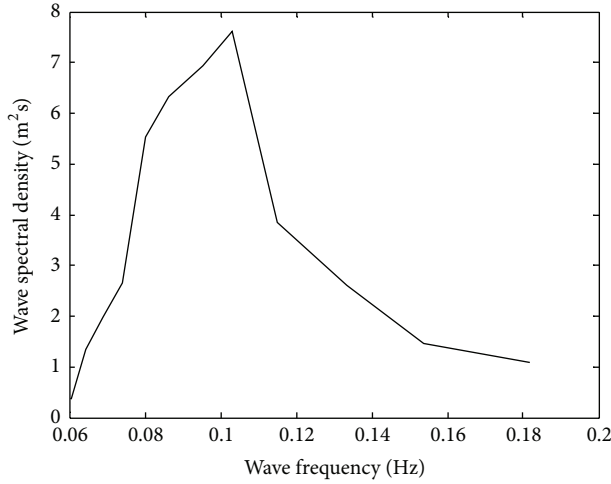


FIGURE 2: Representative spectrum of the wave climate.

Taking these data into consideration, a regular wave may be modelled assuming that its height and frequency correspond to the peak given in Figure 2 so that it can be written as follows:

$$P_{wf} = \frac{\rho_w g A^2 \lambda}{16 T_w} \left[ 1 + \frac{4\pi h / \lambda}{\sinh(4\pi h / \lambda)} \right], \quad (1)$$

$$\lambda = \frac{g T_w^2}{2\pi} \tanh\left(\frac{2\pi h}{\lambda}\right).$$

A thorough overview of wave theory and models may be found in [25].

The breakwater housing the OWC plant is located at a depth of 5 m below MESTLW (Maximum Equinoctial Spring Tide Low Water) with respect to Level 0 at Mutriku port. The opening that transmits the wave oscillations to each air column is 3.20 m high and 4.00 m wide. The lowest point is at  $-3.40$  m, so that the opening is always below sea level [26].

The power available from the air flow in the OWC chamber, which parameters are presented in Figure 3, may be expressed in terms of the air pressure drop and the kinetic energy as follows:

$$P_{in} = \left( dp + \frac{\rho v_x^2}{2} \right) v_x a. \quad (2)$$

For a complete description see [25].

**2.2. Turbo-Generator Module.** In the Mutriku OWC, the turbines are fixed-pitch, which means that they present a robust performance due to the lack of air flow rectifying devices, since they always rotate in the same direction regardless of the air flow and are vertically mounted with a butterfly type valve at the bottom to isolate the chamber if necessary. To minimize the height of the plant room, the length of the turbo-generation assembly has been designed to be relatively small: 2.83 m high by 1.25 m maximum width and approximately 1200 kg (see Figures 1 and 4).

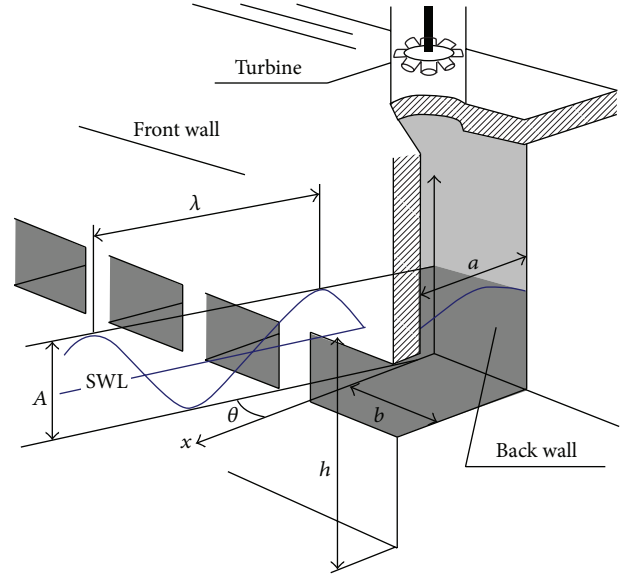


FIGURE 3: OWC capture chamber.

The equations used for modelling the pressure drop across rotor and the torque produced by turbine are (see [27])

$$dp = C_a K \left( \frac{1}{a} \right) [v_x^2 + (r\omega_r)^2], \quad (3)$$

$$T_t = C_t K r [v_x^2 + (r\omega_r)^2], \quad (4)$$

where  $K$  is the turbine constant defined as

$$K = \frac{\rho b n l}{2} \quad (5)$$

so that it may be deduced that the torque

$$T_t = \frac{dp C_t r a}{C_a}. \quad (6)$$

The flow coefficient,  $\phi$ , is usually defined as the nondimensional quantity corresponding to the tangent of the angle of attack at the blade tip. The flow coefficient is

$$\phi = \frac{v_x}{r\omega_r}. \quad (7)$$

Finally, the flow rate and turbine performance can be calculated as

$$q = v_x a, \quad (8)$$

$$\eta_t = \frac{T_t \omega_r}{dp q}.$$

Thus, it may be observed from (3) and (7) that for a given rotational speed, it is possible to establish a linear relationship between the pressure drop and the flow rate. This facilitates an adequate coupling between the turbine and the OWC, which also depends on the pressure drop input. Besides, the developed torque, that is to say the turbine power, depends



FIGURE 4: Turbines for the Mutriku OWC project by the EVE.

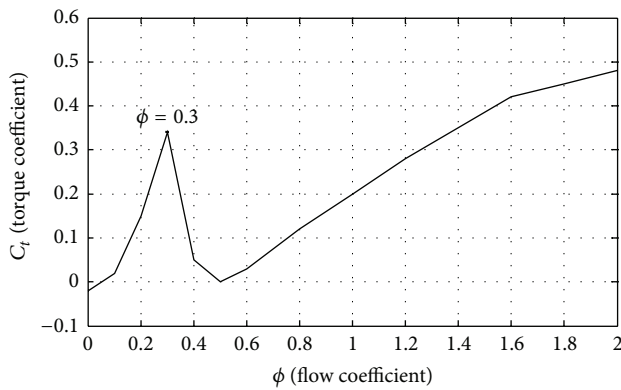


FIGURE 5: Torque coefficient versus flow coefficient from the dataset turbine specifications.

on the pressure drop, the power coefficient, and the torque coefficient (6). It is the relationship of this torque coefficient against the flow coefficient that determines one of the characteristic curves of the Wells turbine under study. It is particularly interesting the behaviour of the torque coefficient  $C_t$ , shown in Figure 5, since it shows that it is negative during the start-up phase, which means that, due to the properties of the turbine, the AC machine acts as a motor until it overcomes the drag forces acting on the blades. Figure 5 also shows that when the flux coefficient reaches a critical value the torque coefficient will drop drastically, which is commonly known as the stalling behaviour of the Wells turbine. On the other hand, when the turbine velocity increases the flow rate decreases (see (7)). Therefore, accelerating the turbine adequately will avoid that the turbine enters into stalling behaviour, drastically dropping its efficiency.

It may be seen in Figure 6 how the performance of the Wells turbine deteriorates when the flow coefficient approaches the corresponding  $C_t$  critical value of Figure 5, 0.3. This behaviour is denoted stalling behaviour and it is the reason why control is particularly relevant in Wells turbines.

In this way, this undesired stalling behaviour can be avoided or delayed if the turbine accelerates fast enough in response to the incoming air flow in order to maintain adequate flow coefficient values (7) (see [8]), so as to maintain the optimal flow coefficient for an efficient conversion of pneumatic power.

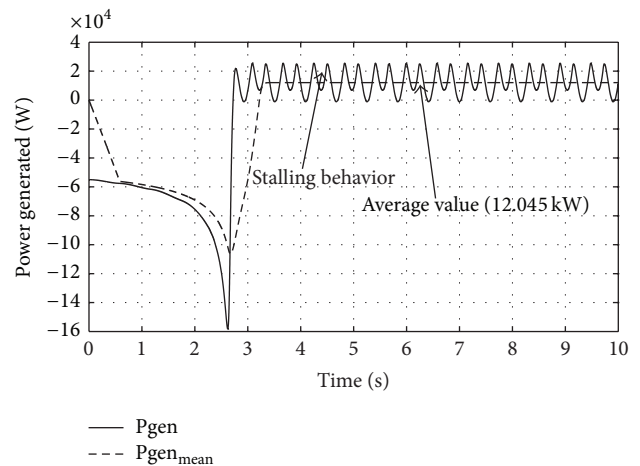


FIGURE 6: Simulated power generated for 7000 Pa maximum pressure drop input under no control (stalling).

The Mutriku OWC consists of 16 chambers, where each chamber has a top opening that is connected to a vertically mounted turbo-generator module. Each module is formed by two five-blade Wells turbines connected to an air cooled DFIG generator. In this kind of induction machines, widely employed in diverse generation applications, the stator circuit is directly connected to the grid while the rotor windings are connected via slip-rings to a three-phase AC-DC-AC source converter that controls both the rotor and the grid currents, so that the rotor frequency is independent of the grid frequency.

The turbine set has fresh water injectors, which regularly clean the blades of any accumulations of encrusted salt, and on the other hand the turbo-generator control requires a precise knowledge of system parameters and of the rotor speed in particular. Thus, to remove the speed sensor rotor is to simplify the hardware, with the consequent reduction in installation and maintenance costs. A detailed description of the OWC numerical model may be found in [28].

### 3. A Sensorless Control Scheme

In this section, a sensorless control scheme with an observer for the induction rotor speed based on a disturbance model

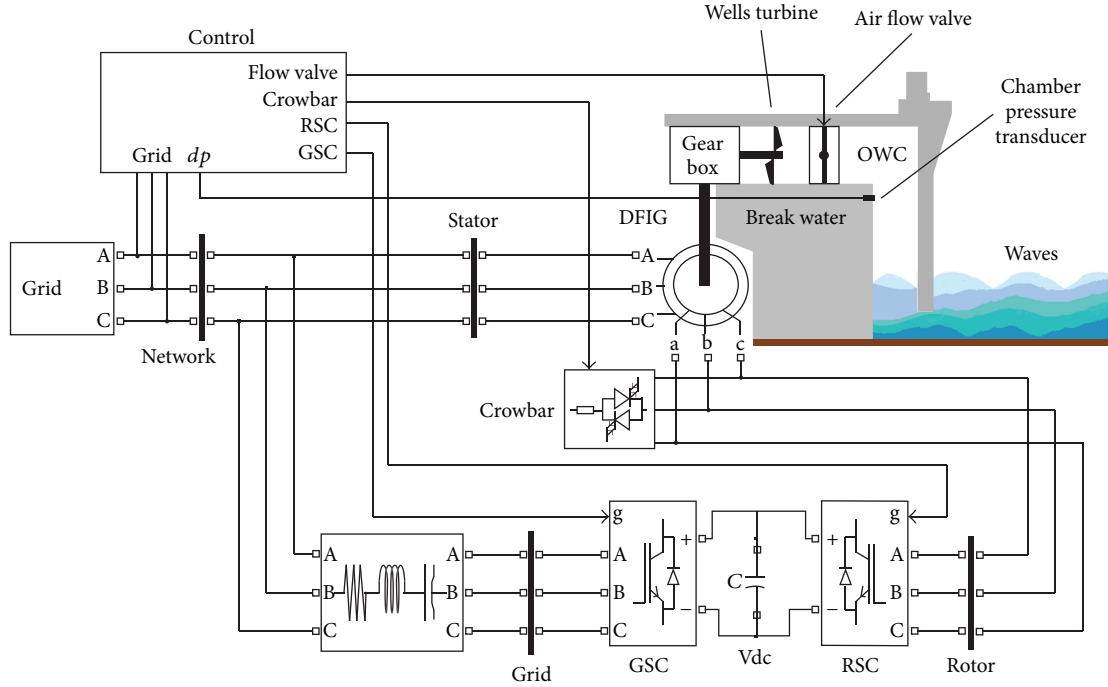


FIGURE 7: OWC control scheme.

is presented. AC drives without speed sensors on the rotor shaft compose a common strategy for cost reduction and robustness, especially in hostile environments (see [29–35]). The proposed observer aims to accurately estimate the rotor angular velocity by employing the stator current and stator voltage as input variables in a closed loop observer structure that was first introduced in [18].

A point tracking technique will be implemented for the control to track a curve that yields the maximum possible power from the sea for any given environmental conditions. This Tracking Characteristic Curve (TCC) is predefined for each turbine, by adjusting the shaft speed of the OWC turbo-generator, so that the flow coefficient  $\phi$  remains bounded, yielding a maximum stalling-free torque coefficient  $C_t$ . Therefore, for a given pressure drop input  $dp$  there is a unique generator slip and a power reference required to satisfy the conditions of maximum wave energy extraction. In our particular case, this TCC is achieved based on a previous study of the Wells turbine at hand using the characteristic curve provided by the manufacturer (see Figure 5), and the required slip values are shown in Table 1.

The control scheme is shown in Figure 7 and its design requires taking into account the dynamics of the turbo-generator module. In particular, in the DFIG-based OWC generation system, the maximum power objective is achieved by regulating the current of the rotor in the RSC. In order to achieve independent control of the stator active power,  $P$ , and reactive power,  $Q$ , the direct and quadrature components of the rotor currents  $i_{qr}$ ,  $i_{dr}$  are used to provide the required voltage signal  $v_{qr}$ ,  $v_{dr}$  by means of PI controllers. Besides, since the OWC air flow control actuator is a throttle-valve subject to saturation, it was necessary to consider an integral wind-up

TABLE 1: Pressure drop input versus slip reference and corresponding flux coefficient variation.

$dP_{AVERAGE}$ (Pa)	$slip_{AVER}$ (%)	Flow Coef. $\phi$
0–5500	–0.56	0–0.2987
5500–5790	–2.34	0–0.2999
5790–5975	–4.13	0–0.2995
5975–6175	–6.00	0–0.2999
6175–6375	–7.90	0–0.2995
6375–6600	–9.86	0–0.2995
6600–6850	–11.94	0–0.2999
6850–7100	–14.06	0–0.2998
7100–7375	–16.28	0–0.2998
7375–7670	–18.60	0–0.2999

effect, in order to avoid this undesired phenomenon. The steps for tuning a PID controller via the closed-loop Ziegler-Nichols method consist of considering all controller gains zero and then increasing the proportional gain  $K_p$  up to a value  $K_p = K_{cr}$  where sustained oscillations occur with period  $P_{cr}$ . Using this procedure, some initial values for the controller parameters were obtained and afterwards refined in an experimental trial-and-error basis. In this way, the obtained throttle valve controller gains are  $K_p = 0.6$ ,  $T_i = 0.5$ , and  $T_d = 0.125$  for initial  $K_{cr} = 0.04$  and  $P_{cr} = 0.008$  values. Then, the output control drives the valve into the demanded position against a counterbalance weight. Once in position, it is hold steady by an electromagnetic brake. In the event of a control failure or in the case that the grid connection is lost or an emergency closure is demanded, the brake supply is interrupted, and the valve closes by means of the influence of

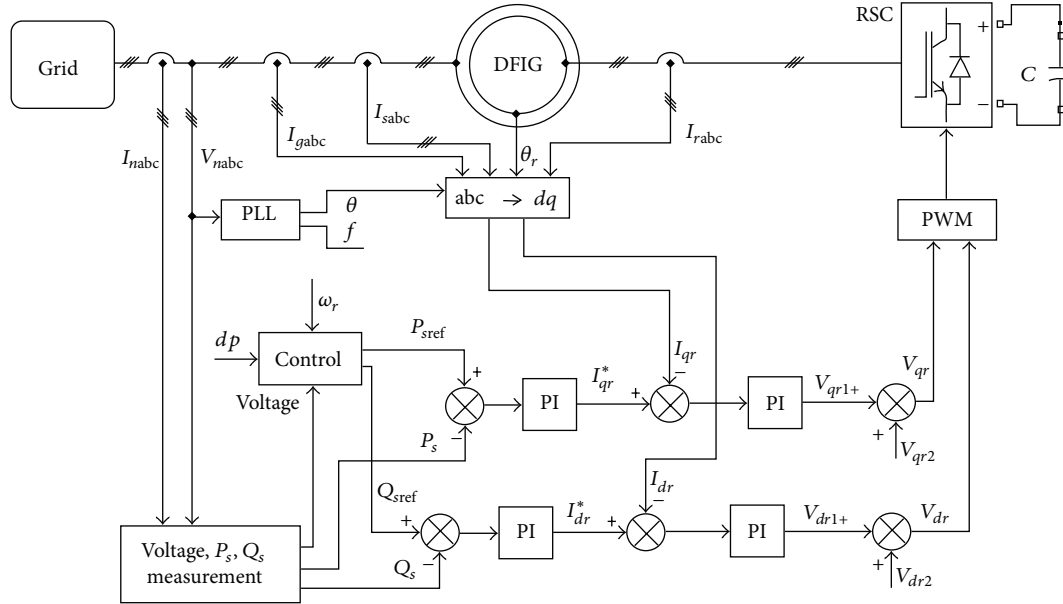


FIGURE 8: Control loop for the RSC.

the weight. In this way, the modulation of the valve aims to adjust the pressure drop across the turbine rotor.

Thus, the proposed sensorless speed controller actively controls the rotor slip by means of the rotor side converter of the DFIG that acts as control actuator so as to avoid the stalling behaviour and to increase the output power. The functioning of the control scheme is detailed as follows. The DFIG is attached to the Wells turbine by means of a gear box. The DFIG stator windings are connected directly to the grid while the rotor windings are connected to the back to back (AC/DC/AC) converter.

The converter is composed of a GSC connected to the grid and a rotor RSC connected to the wound rotor windings. The RSC controls the active ( $P_s$ ) and reactive ( $Q_s$ ) power of the DFIG independently, while the GSC controls the DC voltage and grid side reactive power.

As indicated before, the RSC operates as control actuator and its objective is to regulate the DFIG rotor speed by varying the rotor slip in accordance with the control law signal provided by the rotational speed controller, in such a way that it establishes the maximum power generation allowed at each time instant for the current wave without entering in stalling. In order to achieve this, it is needed an independent regulation of the stator active power (by means of speed control) and reactive power.

The control loop of the RSC is depicted in Figure 8 and the corresponding loop for the GSC would be similar.

This converter controls the active power ( $P_s$ ) and reactive power ( $Q_s$ ) of the DFIG. In order to achieve independent control of them, the instantaneous three-phase rotor currents  $i_{rabc}$  are sampled and transformed into  $d$ - $q$  components  $i_{qr}$  and  $i_{dr}$  in the stator-flux oriented reference frame. In this context,  $P_s$  and  $Q_s$  can be represented as functions of the individual current components. Then, the reference active power

is compared with the power losses and compensated by the stator flux estimator to form the reference  $q$ -current  $i_{qr}^*$ , which is then passed through a standard PI controller. Its output  $v_{qr1}$  is in turn compensated by  $v_{qr2}$  to generate the  $q$  voltage signal  $v_{qr}$ . The RSC reactive power control is also used to maintain a constant stator voltage within the desired range when the DFIG is connected to weak power networks without reactive power compensation. When connected to strong power grids, this control may be set to zero. The reference reactive power is compared with its actual measurement to generate the error signal, which is passed through a PI controller to provide the reference signal  $i_{dr}^*$ . Then, it is compared with its actual signal  $i_{dr}$  to generate an error, which is then used to provide the required  $q$ -voltage signal  $v_{dr1}$  by means of a PI controller. In turn, this voltage is compensated by  $v_{dr2}$  to generate the  $d$  voltage signal  $v_{dr}$  and used by the PWM module to generate the IGBT gate control signals necessary to drive the RSC converter jointly with the  $q$ -component signal  $v_{qr}$  already obtained.

When a grid fault is detected, the primarily objective of the implemented control is the uninterrupted operation feature of the wave energy plant. For this purpose, the rotor is short-circuited by a crowbar and the RSC is blocked to protect it from the rotor high currents, causing the loss of control of active power and reactive power of the DFIG. In order to control the acceleration of the turbo-generator group, the flow is typically reduced accordingly with the modified power reference, regulating the throttle air valve. When the rotor current and DC-link voltage are low enough, the crowbar is turned off and the RSC is restarted. Meanwhile, the GSC keeps the DC-link capacitor voltage constant and the grid side reactive power controllability of the GSC is useful during the process of voltage reestablishment. After voltage recovery, a second crowbar circuit activation may happen if the rotor

currents or the DC-link voltage exceed their maximum allowed values. When the voltage and frequency of the network return to steady-state values, the references are modified again, restoring the normal functioning of the system. For a detailed description of the different parts of the control scheme (see [36]), further information about DFIG control devices by means of RSC and GSC may be found in [37–39].

For this purpose, a simple Luenberger based observer for the rotor flux and angular velocity will be proposed. Field oriented decoupling is applied, giving all expressions in the stator-flux reference frame where the  $d$ -axis is aligned with the stator flux linkage vector  $\Psi_s$ , so that  $\Psi_{ds} = \Psi_s$  and  $\Psi_{qs} = 0$ . This leads to the following relationships (see [38]):

$$\begin{aligned} \frac{d\hat{i}_{qs}}{dt} &= a_1 \hat{i}_{qs} + a_2 \hat{\psi}_{qr} + a_3 \omega_r \hat{\psi}_{dr} + a_4 v_{qs} + k_i (i_{qs} - \hat{i}_{qs}), \\ \frac{d\hat{i}_{ds}}{dt} &= a_1 \hat{i}_{ds} + a_2 \hat{\psi}_{dr} - a_3 \omega_r \hat{\psi}_{qr} + a_4 v_{ds} + k_i (i_{ds} - \hat{i}_{ds}), \\ \frac{d\hat{\psi}_{qr}}{d\tau} &= a_5 \hat{i}_{qs} + a_6 \hat{\psi}_{qr} - \zeta_d - k_2 (\hat{\omega}_r \hat{\psi}_{rd} - \zeta_d), \\ \frac{d\hat{\psi}_{dr}}{d\tau} &= a_5 \hat{i}_{ds} + a_6 \hat{\psi}_{dr} + \zeta_q + k_2 (\hat{\omega}_r \hat{\psi}_{qr} - \zeta_q), \end{aligned} \quad (9)$$

where  $\hat{v}_{ds}$ ,  $\hat{v}_{qs}$ ,  $\hat{i}_{ds}$ ,  $\hat{i}_{qs}$ ,  $\hat{\psi}_{ds}$ ,  $\hat{\psi}_{qs}$  are the estimated components of the stator voltage, current and flux vector of the rotor in the reference frame and

$$\begin{aligned} a_1 &= -\frac{R_s L_r^2 + R_r L_m^2}{\omega L_r}, \\ a_2 &= \frac{R_r L_m}{\omega L_r}, \quad a_3 = \frac{L_m}{\omega}, \\ a_4 &= \frac{L_r}{\omega}, \quad a_5 = \frac{R_r L_m}{L_r}, \\ a_6 &= -\frac{R_r}{L_r}, \quad \omega = L_s L_r - L_m^2. \end{aligned} \quad (10)$$

The structure of this observer is based on treating as disturbances  $\zeta_q$ ,  $\zeta_d$  the corresponding vectors  $\omega_r \hat{\psi}_{qr}$ ,  $\omega_r \hat{\psi}_{dr}$  so as to remove the coupling between cocoordinates as follows:

$$\begin{aligned} \frac{d\zeta_q}{d\tau} &= k_1 (i_{ds} - \hat{i}_{ds}), \\ \frac{d\zeta_d}{d\tau} &= -k_1 (i_{qs} - \hat{i}_{qs}). \end{aligned} \quad (11)$$

The disturbance vector has the same angular velocity as all other vector components. Both disturbance and flux vectors have the same phase and proportional amplitudes so that the velocity may be estimated as

$$\hat{\omega}_r = S \left( \sqrt{\frac{\zeta_q^2 + \zeta_d^2}{\hat{\psi}_{dr}^2 + \hat{\psi}_{qr}^2}} \right) + k_4 (V - V_f), \quad (12)$$

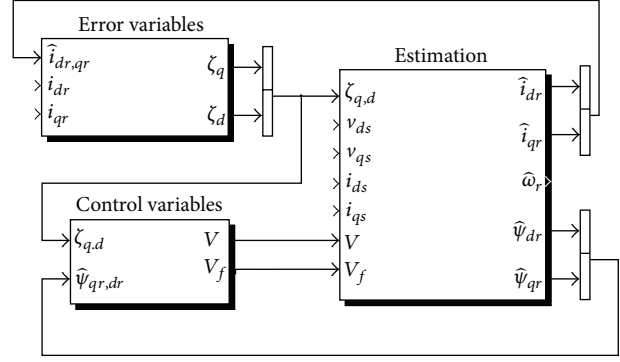


FIGURE 9: Control loop for the state observer.

where  $S$  denotes the sign of the angular velocity. The observer gains  $k_1$ ,  $k_4$  have small values and are selected experimentally while  $k_2$  depends on the rotor speed

$$k_2 = a + b \cdot |\hat{\omega}_{rf}| \quad (13)$$

being  $a$  and  $b$  constants and  $|\hat{\omega}_{rf}|$  the absolute value of the estimated filtered rotor speed.  $V_f$  denotes the filtered signal of the control  $V$ , which is defined as

$$V = \hat{\psi}_{rq} \zeta_d - \hat{\psi}_{rd} \zeta_q, \quad \frac{dV_f}{d\tau} = \frac{1}{T_1} (V - V_f). \quad (14)$$

The control loop for this state observer is depicted in Figure 9. A comprehensive description of Luenberger observers may be found in [40, 41].

As it has been explained before the stator is connected to the grid, so that the influence of the stator resistance is small and the stator magnetizing current  $i_{ms}$  is considered to be constant [42]. For this purpose it is assumed that the machine works away from the magnetic saturation limits. Thus,  $T_e$  may be defined as

$$T_e = -K_T i_{qr}. \quad (15)$$

Therefore, the generator slip may be controlled by regulating the rotor current  $i_{qr}$ , while the stator reactive power  $Q_s$

$$Q_s = \frac{3}{2} \frac{-\omega_s L_m^2 i_{ms} (i_{ms} - i_{dr})}{L_s}, \quad (16)$$

may be controlled by regulating the rotor current  $i_{dr}$ . Consequently, from  $T_e = -K_T i_{qr}$  with  $K_T = L_m i_{ms} / L_s$  being a torque constant and taking into account that  $P = T\omega$ , the sensorless controller that has been designed solves the power tracking problem for DFIG-based OWC power plants in a hostile environment since it allows to achieve maximum power extraction by matching the desired generator slip reference to avoid the stalling behaviour.

#### 4. Simulation Results

As it has been indicated, the Nereida OWC demo project [3] includes 16 Wells turbines in a newly constructed rubble

TABLE 2: System parameters.

Turbine	Generator	Converter
$n = 5$ (2 blade rows)	Rated Power (kW) = 18.5	DC-Link voltage (V) = 800
$K = 0.5$	Width (m) = 1.25 (t-g module)	$P_{\max}$ (p.u.) = 0.4
$r_t = 0.375$	Height (m) = 2.83 (t-g module)	Rated Current (A) = 12
$a_t = 2.3562$	Pole pairs = 2	Max. Transitory Current (A) = 22.8
Hub/Tip Ratio = 0.43	$R_r = 0.0334$	Switching Freq. (kHz) = 14.4
Solidity per row (%) = 40	$R_s = 0.0181$	Cut-off Freq. Current Filters (kHz) = 13.2
Target speed range (rpm) = 1000–3900	$L_{lr} = 0.16$	Cut-off Freq. Grid Voltage Filter (kHz) = 1.32
Tip Mach no = 0.15–0.47	$L_{ls} = 0.13$	
	$L_m = 7.413$	
	Inertia Constant $H = 3.06$	

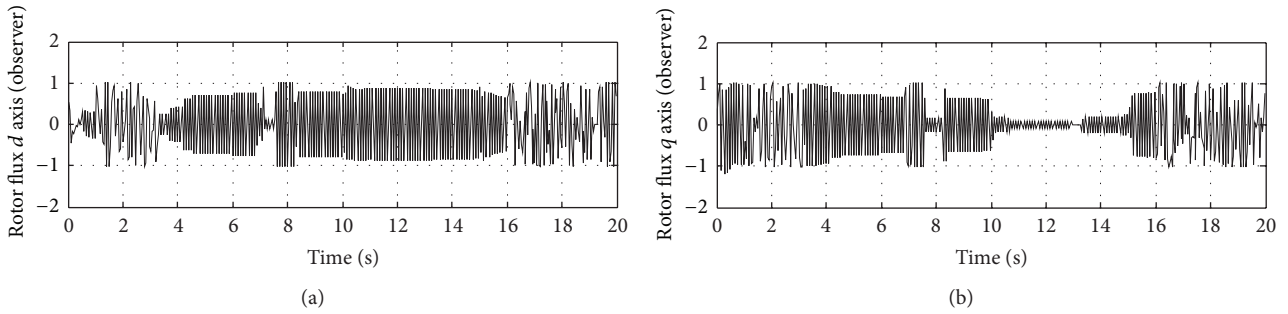


FIGURE 10: Rotor flux for 7000 Pa maximum pressure drop input (observer).

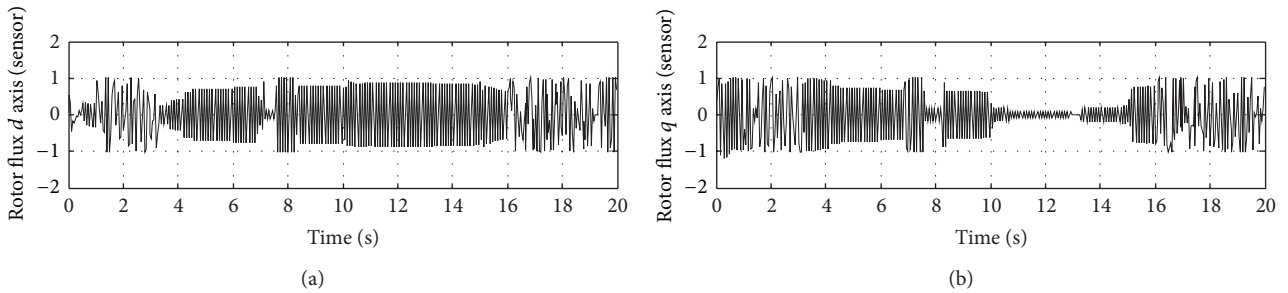


FIGURE 11: Rotor flux for 7000 Pa maximum pressure drop input (sensor).

mound breakwater in the Basque location of Mutriku, in the northern coast of Spain. The main objective of this section is to demonstrate the viability of the proposed rotor angular velocity observer to help develop this OWC technology with Wells turbine power take-off for future commercial plants. For this reason, the simulation data and wave model have been chosen taking into account the spectrum of the wave climate of Mutriku and the OWC system parameters are listed in Table 2.

For this purpose, the maximum power tracking performance of system subject to the proposed speed estimator with stator current based feedback has been tested by means of numerical simulations. The control strategy is composed of a double feed induction generator, DFIG, that is controlled with a vector field oriented strategy, a crowbar, and an air flow control. The crowbar protects the RSC, enforcing short-circuit when overcurrents in the rotor occur while the air valve regulates the incoming air flow so as to avoid stalling.

Finally, the main control loop regulates both active and reactive power of the DFIG using the currents as control variables to match the modified power reference (see Figure 7). See [36] for a detailed explanation of this control and [43] for a summary on fault tolerance control.

**4.1. Balance Faults.** This sensorless control has been applied considering a scenario where waves produce a typical variation for 7000 Pa maximum pressure drop input and a balanced grid fault has been implemented with an 85% reduction of the grid voltage applied at 10 s and cleared at 15 s. For comparison purposes, the same study case has been considered with and without sensor. In particular, in Figure 10 the rotor flux obtained with the proposed sensorless controller is plotted so as to compare it with that obtained using a control where the velocity is computed via a traditional sensor, plotted in Figure 11. As it may be observed there exists no significant difference between them.

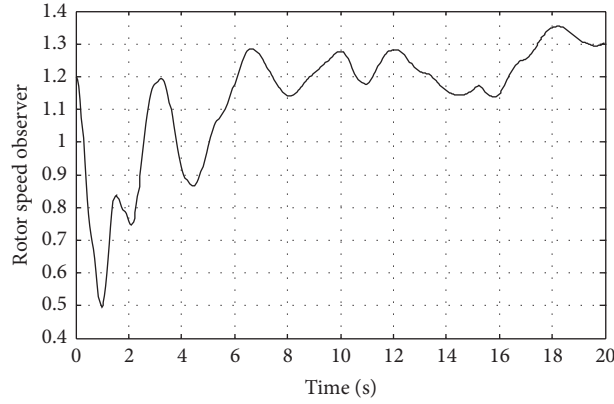


FIGURE 12: Rotor angular velocity for 7000 Pa maximum pressure drop input (observer).

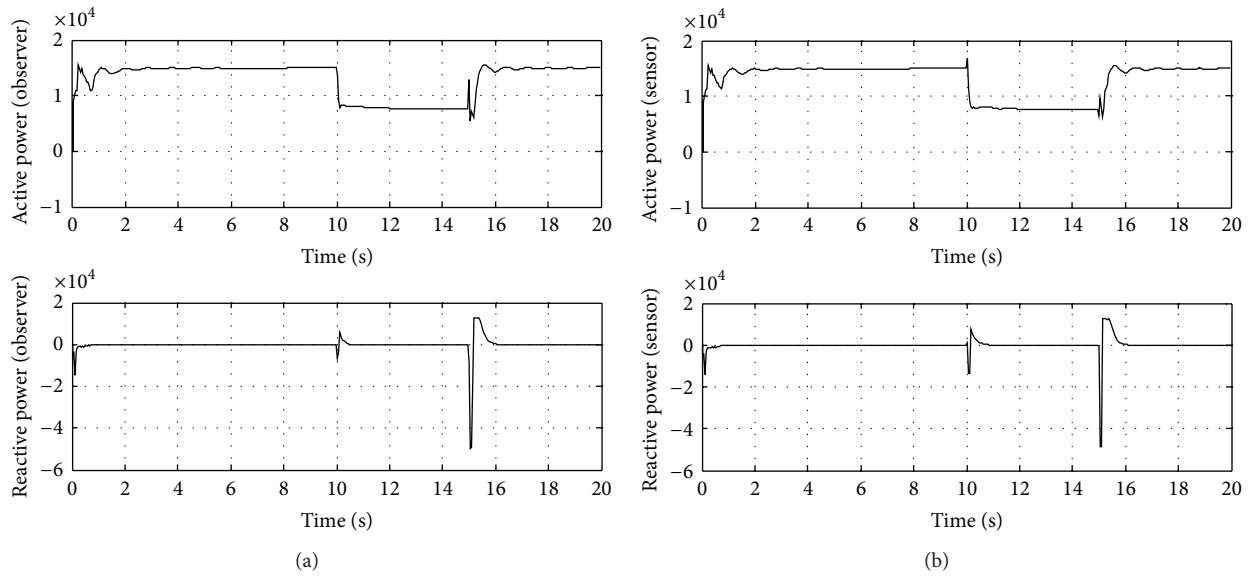


FIGURE 13: Active and reactive power generated using sensorless control (a) versus traditional control (b).

Similarly, due to the FRT capability of the control scheme, it may be seen in Figure 12 that after the transitory,  $\omega_r$  does not increase during the voltage dip, which also affects the flux value. Besides, it should be highlighted that in the Mutriku WOC technical solution, the given reference is the pressure drop whilst the reference for the rotor angular velocity,  $\omega_r^*$ , is not readily accessible, so that the proposed estimator with stator current based feedback suits perfectly the requirements of the system.

Analogously, a comparative study for the power generated has been carried out in order to verify the performance of the proposed observer so as to obtain maximum power extraction capability in the plant, even when it is subject to voltage dips like the one described in the scenario at hand.

Under these conditions it may be seen in Figure 13 the effect of the fault over the active and reactive power at the stator terminals both with sensor and with the proposed observer. In both cases, there is no active power consumption during the fault period and the reactive power overshoot during both the start and clearance of the fault is acceptable.

Besides, the generator oscillatory dynamics have been controlled, while giving reactive power to the grid so that it contributes to the attenuation of the voltage dip. In this context, both figures show that the plant generates active and reactive power during the fault period and, particularly, during the fault recovery, since it is only during 100 ms after the fault recovery that the generator absorbs a little amount of power (less than 60% of the nominal power). These voltage dips are usually caused by remote grid faults in the power system and would normally require disconnecting the generator from the grid until the faults are cleared. However, normative relative to this requirement tends to enforce maintaining active power delivery and reactive power support to the grid, so that grid codes now require ride through voltage dips like the one presented in this paper.

In order to compare the simulation results obtained using the proposed observer with those obtained using a traditional sensor with the controller, a performance evolution function  $J$  is used. This performance function is defined by (16) in terms of the tracking error, where  $e(\tau)$  represents the error

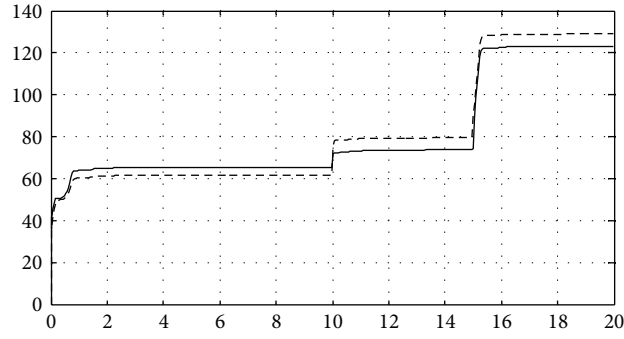


FIGURE 14: Active power performance. Traditional control (—) versus sensorless control (- -).

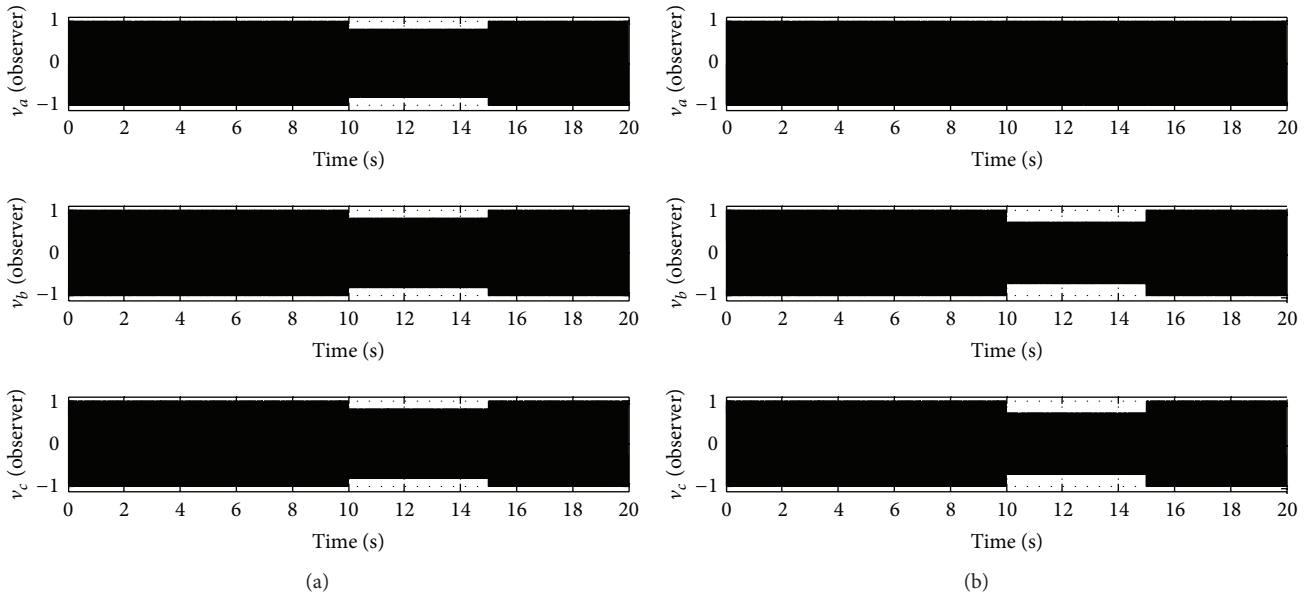


FIGURE 15: Voltages for the balance fault (a) versus negative sequence unbalance fault (b).

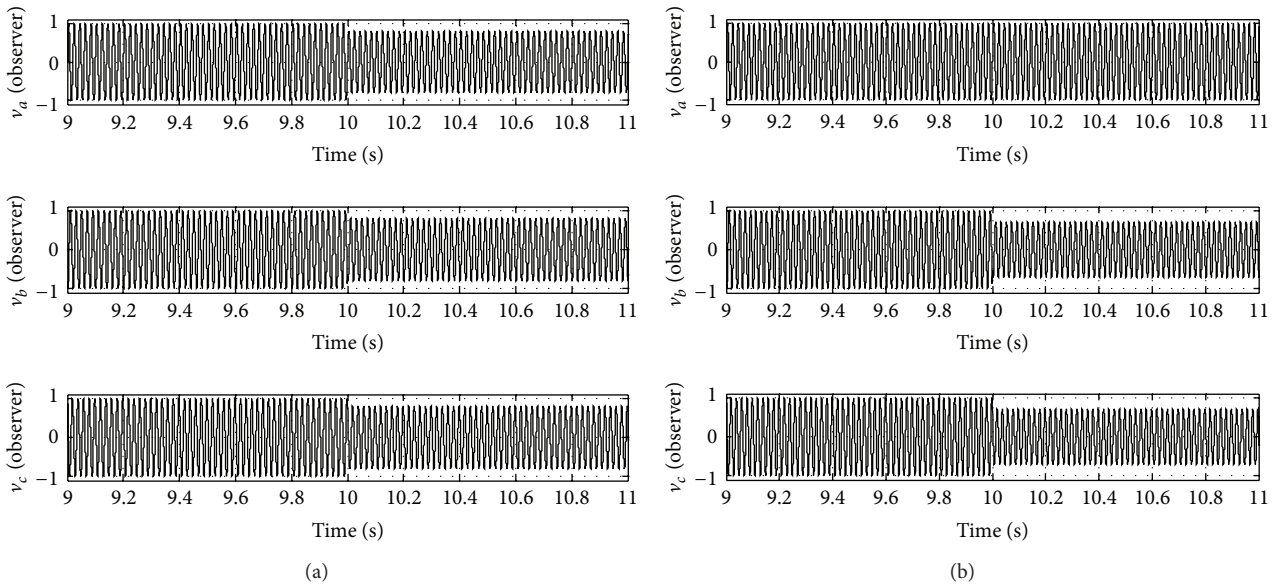


FIGURE 16: Detail of the voltages for the balance fault (a) versus unbalance fault (b).

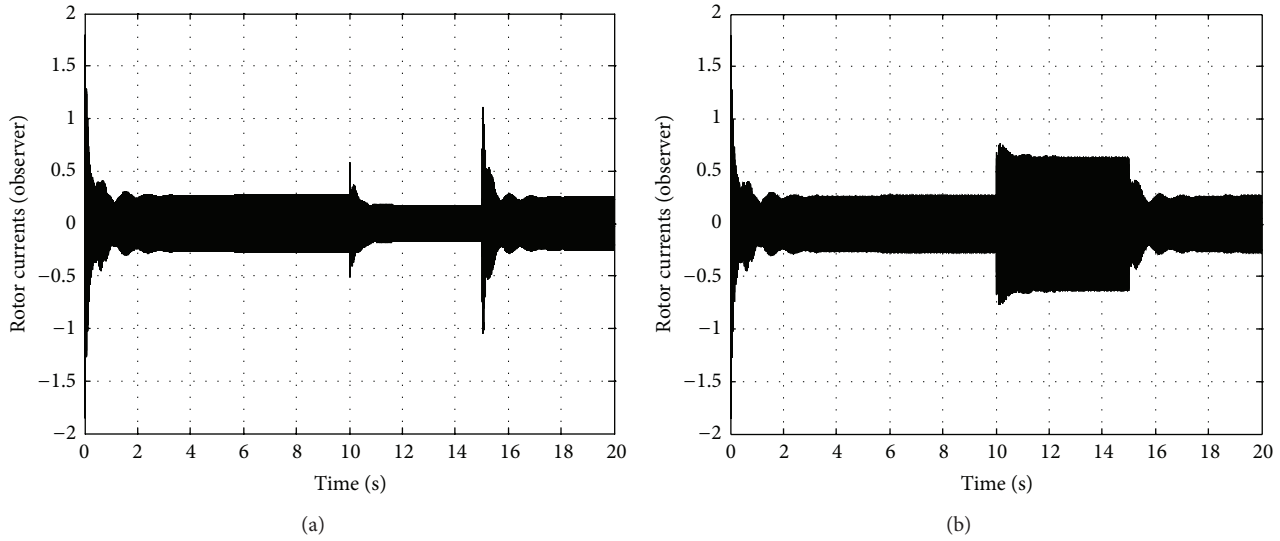


FIGURE 17: Rotor currents for the balance fault (a) versus negative sequence unbalance fault (b).

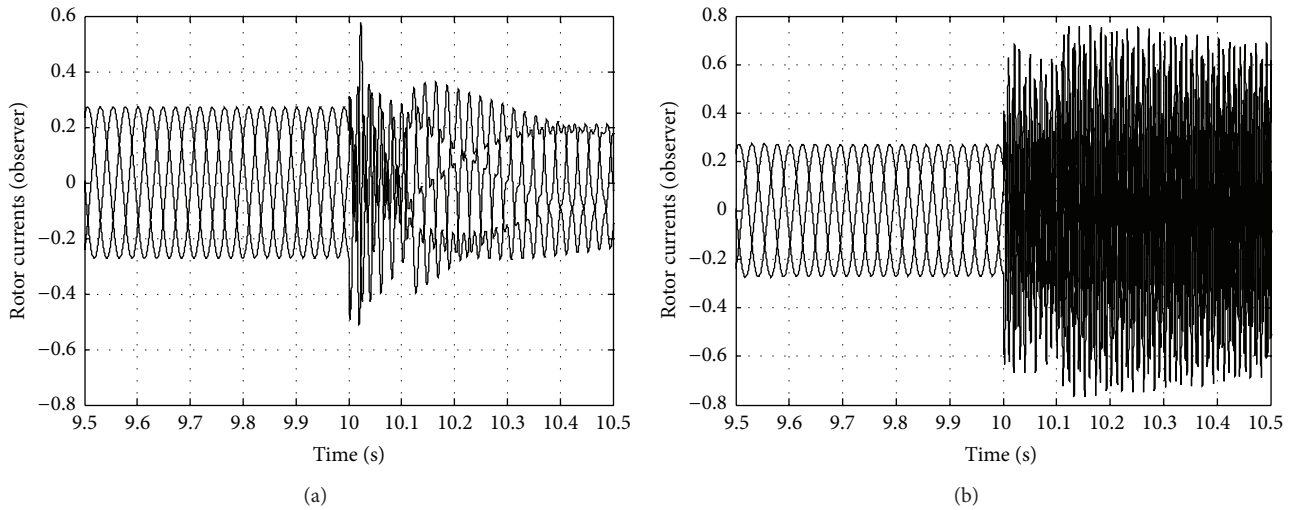


FIGURE 18: Detail of the rotor currents for the balance fault (a) versus unbalance fault (b).

between the desired reference value for the active power and the value obtained from the system output as follows:

$$J(t) = \int e^2(\tau) d\tau. \quad (17)$$

It can be observed in Figure 14 that the values of the performance evolution function for the case of the controller with observer are slightly higher than those obtained with the sensor. It must be taken into account that the control either with sensor or with observer yields similar results, so that the relevance of the results relies on determining the rotor angular velocity without the need of extra hardware from sensors, just observed by means of the stator voltages and currents. For this reason, although in all cases the accumulated error measured with the cost function  $J$  presents a similar increasing behavior, as it should be expected from the  $L_2$ -norm accumulative error defined in (17), it should be noticed that the system

power generated in both cases present a similar rate while the observer provides better performance since it increases power extraction in the sense that the plant is more reliable and independent of external disturbances, which is even more relevant in a hostile environment as the ocean.

**4.2. Unbalance Faults.** Simulation studies on the sensorless control for unbalance faults are carried out over a modification of the balance fault scenario studied in the last section, where a representative example corresponding to the negative sequence is considered as seen in Figures 15 and 16. Previous analyses were performed to confirm the relative significance of the different frequency components present in the current waveforms, corroborating that the negative sequence imposes the most stringent control.

The key problems in the response of a DFIG to an unbalanced fault are illustrated in Figure 17, which shows the rotor

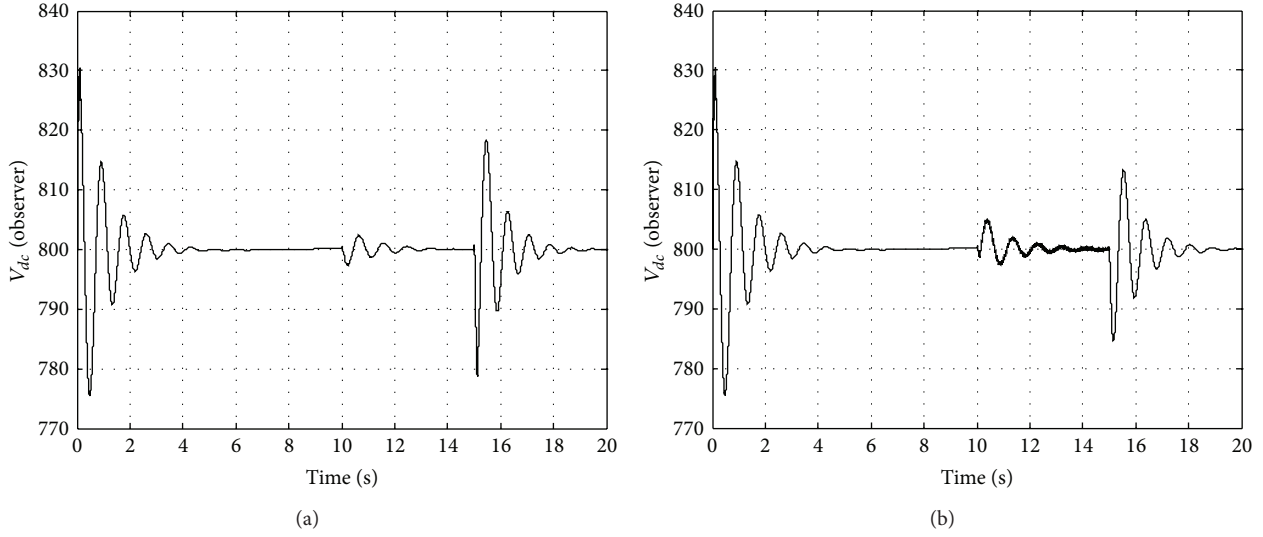


FIGURE 19: DC-link voltage for the balance fault (a) versus negative sequence unbalance fault (b).

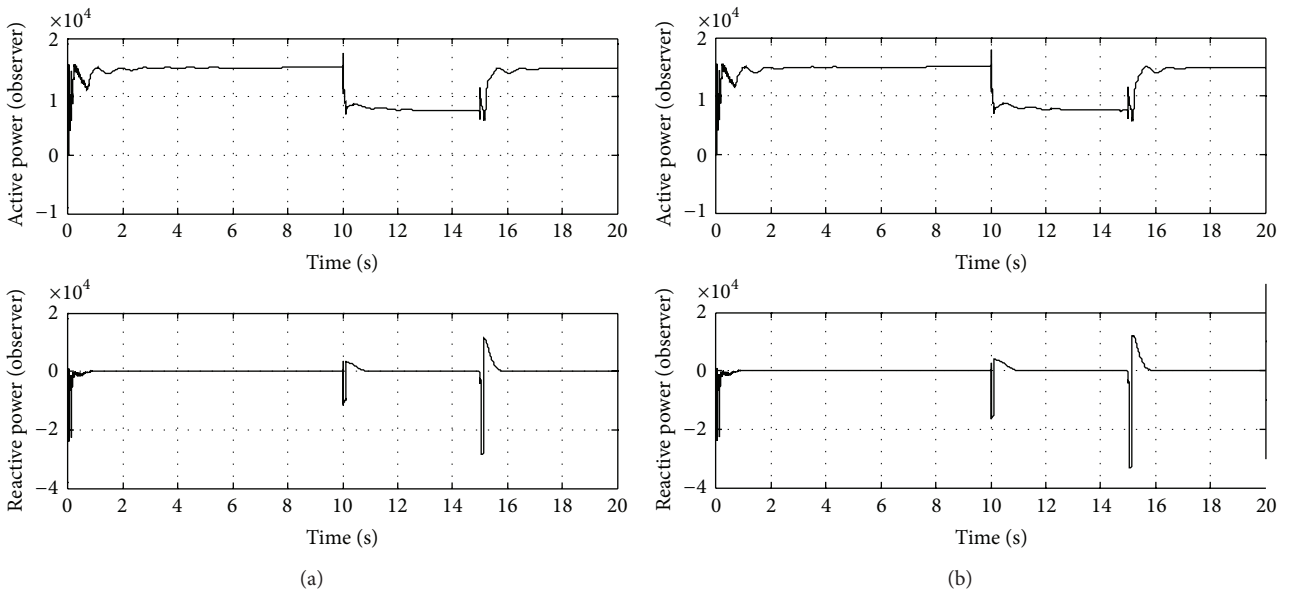


FIGURE 20: Active and reactive power generated using sensorless control (a) versus traditional sensor (b) considering the negative sequence unbalance fault study case.

currents. During the fault, the negative sequence component of the rotor currents is 2.5 times as large as the positive sequence component. This forces the rotor voltage demand close to the limits of the inverter, making control of the DFIG much more difficult. It can be seen from Figures 17 and 18 that the most serious problem is the rotor overcurrent at fault initiation. These overcurrents are alleviated by short-circuiting the rotor windings for a short period (known as a crowbar), removing the power electronics from the rotor circuit to protect them from the high currents.

Despite the value of the currents on the IGBTs, it may be seen in Figures 19 and 20 that both the active and reactive

power supplies as well as the dc-link voltage are successfully controlled. Thus, even when this control scheme does not discern in the treatment of the different sequence current components during faults, it ensures the continuity of supply in compliance with actual requirements [44].

Although stator overcurrents may also occur, they are generally of less concern, because no vulnerable power electronics are involved in the stator connection.

The results obtained for the reference tests, both with observer and with sensor, confirmed that the model behaved as expected, since there are no obvious differences between them. The effect of the unbalance fault over the active

and reactive power at the stator terminals may be seen in Figure 20 for comparison purposes.

## 5. Conclusions

This paper has proposed a new observer to estimate the rotor angular speed for the control of the Mutriku OWC wave power generation demo plant within the Nereida project from the Basque Energy Board (EVE). This closed loop observer is based in a Luenberger system and estimates both rotor angular velocity and fluxes using the measured stator voltages and currents. Due to the nature of this observer, the rotor angular velocity is computed from its flux and a vector of cross-product state variables that is treated as disturbances. In order to verify the performance of the proposed observer to obtain maximum power extraction capability in the plant even when it is subject to voltage dips, a comparative study for the power generated with a traditional sensor and with the proposed observer has been performed. A point tracking technique has been implemented so that the control system tracks a curve that yields the maximum possible power from the sea and no substantial differences between them have been found. As a result, it can be concluded that the proposed observer scheme improves the plant reliability by increasing reliability and disturbance rejection while reducing cost and, therefore, improving the power extraction when applied for maximum power generation purposes.

## Nomenclature

$P_{wf}, P_{in}$ : Incident wave power, power available to turbine  
 $g, v, i$ : Gravitational constant, voltage, current  
 $v_x, dp$ : Air flow speed, pressure-drop across rotor  
 $\rho, \rho_w$ : Air density, seawater density.  
 $a, r, n$ : Area of turbine duct, mean radius of the turbine, number of blades  
 $b, l$ : Blade height, blade chord length  
 $q, \phi$ : Flow rate, flow coefficient  
 $\lambda, T_w$ : Wavelength, wave period  
 $h, A$ : Water depth, wave height  
 $\omega_r, T_t$ : Angular velocity, torque  
 $C_a, C_t$ : Power and torque coefficients  
 $L, R, \Psi$ : Inductance, resistance, flux  
 $P, Q$ : Active and reactive power.

## Subscripts

$d, q, s, r$ : Direct and quadrature components, stator and rotor side  
 $t, g, e, m$ : Turbine, generator, electrical, magnetizing.

## Acknowledgments

This work was supported in part by University of the Basque Country (UPV/EHU) through Research Project GIU11/02 and the Research and Training Unit UF111/07, by the Ministry of Science and Innovation (MICINN) with Research Project ENE2010-18345, and by the EU FP7 EFDA under the task

WP09-DIA-02-01 WP III-2-c. The authors would also like to thank the collaboration of the Basque Energy Board (EVE) through Agreement UPV/EHUEVE23/6/2011 and the Spanish National Fusion Laboratory (CIEMAT) UPV/EHUCIEMAT08/190.

## References

- [1] M. Z. Jacobson and M. A. Delucchi, "Providing all global energy with wind, water, and solar power, part I: technologies, energy resources, quantities and areas of infrastructure, and materials," *Energy Policy*, vol. 39, no. 3, pp. 1154–1169, 2011.
- [2] M. Z. Jacobson and M. A. Delucchi, "Providing all global energy with wind, water, and solar power, part I: technologies, energy resources, quantities and areas of infrastructure, and materials," *Energy Policy*, vol. 39, no. 3, pp. 1154–1169, 2011.
- [3] Basque Energy Board (EVE), <http://www.eve.es/Promocion-de-inversiones/Proyectos-en-desarrollo/Mutriku/Instalaciones.aspx>.
- [4] Y. Torre-Enciso, *Mutriku Wave Power Plant: From Conception to Reality*, European Federation of Regional Energy and Environment Agencies (FEDARENE), 2009, [http://www.fedarene.org/documents/projects/Nereida/Document/01\\_Mutriku-OWC\\_plant.pdf](http://www.fedarene.org/documents/projects/Nereida/Document/01_Mutriku-OWC_plant.pdf).
- [5] A. Thakker and R. Abdulhadi, "Effect of blade profile on the performance of wells turbine under unidirectional sinusoidal and real sea flow conditions," *International Journal of Rotating Machinery*, vol. 2007, Article ID 51598, 8 pages, 2007.
- [6] T. Setoguchi and M. Takao, "Current status of self rectifying air turbines for wave energy conversion," *Energy Conversion and Management*, vol. 47, no. 15-16, pp. 2382–2396, 2006.
- [7] W. Qiao, G. K. Venayagamoorthy, and R. G. Harley, "Real-time implementation of a STATCOM on a wind farm equipped with doubly fed induction generators," *IEEE Transactions on Industry Applications*, vol. 45, no. 1, pp. 98–107, 2009.
- [8] M. Amundarain, M. Alberdi, A. J. Garrido, and I. Garrido, "Modeling and simulation of wave energy generation plants: output power control," *IEEE Transactions on Industrial Electronics*, vol. 58, no. 1, pp. 105–117, 2011.
- [9] Y. Zhou, J. Lian, T. Ma, and W. Wang, "Design for motor controller in hybrid electric vehicle based on vector frequency conversion technology," *Mathematical Problems in Engineering*, vol. 2010, Article ID 627836, 21 pages, 2010.
- [10] K. J. Astrom and T. Hagglund, *Advanced PID Control*, ISA-The Instrumentation, Systems, and Automation Society, 2009.
- [11] R. Vilanova, V. M. Alfaro, O. Arrieta, and C. Pedret, "Analysis of the claimed robustness for PI/PID robust tuning rules," in *Proceedings of the 18th Mediterranean Conference on Control and Automation (MED '10)*, pp. 658–662, June 2010.
- [12] B. C. Rabelo Jr., W. Hofmann, J. L. da Silva, R. G. de Oliveira, and S. R. Silva, "Reactive power control design in doubly fed induction generators for wind turbines," *IEEE Transactions on Industrial Electronics*, vol. 56, no. 10, pp. 4154–4162, 2009.
- [13] ESB National Grid, "Discussion Document for the Review of Requirements for Wind Turbine Generators Under System Fault Conditions," 2003.
- [14] I. Serban, F. Blaabjerg, I. Boldea, and Z. Chen, *A Study of Doubly Fed Wind Power Generator Under Power System Faults*, EPE, Toulouse, France, 2003.
- [15] G. Iwanski and W. Koczara, "DFIG-based power generation system with UPS function for variable-speed applications," *IEEE*

- Transactions on Industrial Electronics*, vol. 55, no. 8, pp. 3047–3054, 2008.
- [16] G. Abad, M. Á. Rodríguez, G. Iwanski, and J. Poza, “Direct power control of doubly-fed-induction-generator-based wind turbines under unbalanced grid voltage,” *IEEE Transactions on Power Electronics*, vol. 25, no. 2, pp. 442–452, 2010.
- [17] A. J. Garrido, I. Garrido, M. Amundarain, and M. Alberdi, “Sliding-mode control of wave power generation plants,” *IEEE Transactions on Industry Applications*, vol. 48, no. 6, pp. 2372–2381, 2012.
- [18] Z. Krzeminski, “New speed observer for control system of induction motor,” in *Proceedings of the 3rd IEEE International Conference on Power Electronics and Drive Systems (PEDS '99)*, pp. 555–560, July 1999.
- [19] Z. Krzemiński, “Observer of induction motor speed based on exact disturbance model,” in *Proceedings of the 13th International Power Electronics and Motion Control Conference (EPE-PEMC '08)*, pp. 2294–2299, September 2008.
- [20] O. Barambones, P. Alkorta, A. J. Garrido, I. Garrido, and F. J. Maseda, “An adaptive sliding mode control scheme for induction motor drives,” *International Journal of Circuits, Systems and Signal Processing*, vol. 1, no. 1, pp. 73–78, 2007.
- [21] O. Barambones and A. J. Garrido, “An adaptive variable structure control law for sensorless induction motors,” *European Journal of Control*, vol. 13, no. 4, pp. 282–392, 2007.
- [22] J. C. Garcia, C. Diego, P. F. de Arróyabe, C. Garmendia, and D. Rasilla, *El Clima Entre el Mar y la Montaña*, The University of Cantabria, Santander, Spain, 2004.
- [23] I. Galparsoro et al., “atlas de energía dek oleaje en la costa Vasca. La planificación espacial marian como herramienta en la selección de zonas adecuadas para la instalacion de captadores,” in *Revista De Investigación Marina*, pp. 1–9, 2008.
- [24] W. K. Tease, J. Lees, and A. Hall, “Advances in oscillating water column air turbine development,” in *Proceedings of the 7th European Wave and Tidal Energy Conference*, Porto, Portugal, 2007.
- [25] M. Alberdi, M. Amundarain, A. J. Garrido, I. Garrido, O. Casquero, and M. De La Sen, “Complementary control of oscillating water column-based wave energy conversion plants to improve the instantaneous power output,” *IEEE Transactions on Energy Conversion*, vol. 26, no. 4, pp. 1021–1032, 2011.
- [26] Y. Torre-Enciso, I. Ortubia, L. I. López de Aguilera, and J. Marqués, “Mutriku wave power plant: from the thinking out to the reality,” in *Proceedings of the 8th European Wave and Tidal Energy Conference*, pp. 319–329, 2009.
- [27] A. El Marjani, F. Castro Ruiz, M. A. Rodriguez, and M. T. Parra Santos, “Numerical modelling in wave energy conversion systems,” *Energy*, vol. 33, no. 8, pp. 1246–1253, 2008.
- [28] M. Amundarain, M. Alberdi, A. J. Garrido, I. Garrido, and J. Maseda, “Wave energy plants: control strategies for avoiding the stalling behaviour in the Wells turbine,” *Renewable Energy*, vol. 35, no. 12, pp. 2639–2648, 2010.
- [29] P. Guglielmi, R. Bojoi, G. Pellegrino, A. Cavagnino, M. Pastorelli, and A. Boglietti, “High speed sensorless control for induction machines in vacuum pump application,” in *Proceedings of the 37th Annual Conference of the IEEE Industrial Electronics Society (IECON '11)*, pp. 1872–1878, November 2011.
- [30] R. Cárdenas, R. Peña, G. Asher, J. Clare, and J. Cartes, “MRAS observer for doubly fed induction machines,” *IEEE Transactions on Energy Conversion*, vol. 19, no. 2, pp. 467–468, 2004.
- [31] R. Cárdenas, R. Peña, J. Clare, G. Asher, and J. Proboste, “MRAS observers for sensorless control of doubly-fed induction generators,” *IEEE Transactions on Power Electronics*, vol. 23, no. 3, pp. 1075–1084, 2008.
- [32] S. Mueller, M. Deicke, and R. W. De Doncker, “Adjustable speed generators for wind turbines based on doubly-fed induction machines and 4-quadrant IGBT converters linked to the rotor,” in *Proceedings of the 35th IAS Annual Meeting and World Conference on Industrial Applications of Electrical Energy*, vol. 4, pp. 2249–2254, October 2000.
- [33] L. Morel, H. Godfroid, A. Mirzaian, and J. M. Kauffmann, “Double-fed induction machine: converter optimisation and field oriented control without position sensor,” *IEE Proceedings of Electric Power Applications*, vol. 145, no. 4, pp. 360–368, 1998.
- [34] H. R. Karimi and M. Chadli, “Robust observer design for Takagi-Sugeno fuzzy systems with mixed neutral and discrete delays and unknown inputs,” *Mathematical Problems in Engineering*, vol. 2012, Article ID 635709, 13 pages, 2012.
- [35] S. Chen, Y. F. Li, J. Zhang, and W. Wang, *Active Sensor Planning for Multiview Vision Tasks*, Springer, 2008.
- [36] M. Alberdi, M. Amundarain, A. J. Garrido, I. Garrido, and F. J. Maseda, “Fault-ride-through capability of oscillating-water-column-based wave-power-generation plants equipped with doubly fed induction generator and airflow control,” *IEEE Transactions on Industrial Electronics*, vol. 58, no. 5, pp. 1501–1517, 2011.
- [37] R. Pena, J. C. Clare, and G. M. Asher, “A doubly fed induction generator using back-to-back PWM converters supplying an isolated load from a variable speed wind turbine,” *IEE Proceedings on Electric Power Applications*, vol. 143, no. 3, pp. 231–241, 1996.
- [38] B. K. Bose, *Modern Power Electronics and AC Drives*, Prentice-Hall, Englewood Cliffs, NJ, USA, 2001.
- [39] I. Sarasola, J. Poza, M. A. Rodriguez, and G. Abad, “Direct torque control design and experimental evaluation for the brushless doubly fed machine,” *Energy Conversion and Management*, vol. 52, no. 2, pp. 1226–1234, 2011.
- [40] A. Lagrioui and H. Mahmoudi, “Speed and current control for the PMSM using a Luenberger observer,” in *Proceedings of the International Conference on Multimedia Computing and Systems (ICMCS '11)*, April 2011.
- [41] M. Trabelsi, M. Jouili, M. Boussak, Y. Koubaa, and M. Gossa, “Robustness and limitations of sensorless technique based on Luenberger state-Observer for induction motor drives under inverter faults,” in *Proceedings of the IEEE International Symposium on Industrial Electronics (ISIE '11)*, pp. 716–721, June 2011.
- [42] Y. Sayed, M. Abdelfatah, M. Abdel-Salam, and S. Abou-Shadi, “Design of robust controller for vector controlled induction motor based on Q-parameterization theory,” *Electric Power Components and Systems*, vol. 30, no. 9, pp. 981–999, 2002.
- [43] M. Benosman, “A survey of some recent results on nonlinear fault tolerant control,” *Mathematical Problems in Engineering*, vol. 2010, Article ID 586169, 25 pages, 2010.
- [44] BOE 254/2006 P.O. 12.3 Response Requirements of Wind Power Generation to Network Voltage Dips.

## Research Article

# Design and Implementation of a Control Strategy for Microgrid Containing Renewable Energy Generations and Electric Vehicles

Mingchao Xia, Xuanhu He, and Xiaoqing Zhang

*School of Electrical Engineering, Beijing Jiaotong University, No. 3 Shang Yuan Cun, Hai Dian District, Beijing 100044, China*

Correspondence should be addressed to Mingchao Xia; [mchxia@bjtu.edu.cn](mailto:mchxia@bjtu.edu.cn)

Received 13 December 2012; Accepted 12 May 2013

Academic Editor: Massimo Scialia

Copyright © 2013 Mingchao Xia et al. This is an open access article distributed under the Creative Commons Attribution License, which permits unrestricted use, distribution, and reproduction in any medium, provided the original work is properly cited.

Large amount of such renewable energy generations as wind/photovoltaic generations directly connected to grid acting as distributed generations will cause control, protection, security, and safety problems. Microgrid, which has advantages in usage and control of distributed generations, is a promising approach to coordinate the conflict between distributed generations and the grid. Regarded as mobile power storages, batteries of electric vehicles can depress the fluctuation of power through the point of common coupling of microgrid. This paper presents a control strategy for microgrid containing renewable energy generations and electric vehicles. The control strategy uses current control for renewable energy generations under parallel-to-grid mode, and uses master-slave control under islanding mode. Simulations and laboratory experiments prove that the control strategy works well for microgrid containing renewable energy generations and electric vehicles and provides maximum power output of renewable energy and a stable and sustainable running under islanding mode.

## 1. Introduction

As long as the growing demands for green, clean, and high-quality energy supplies, renewable energy generations such as solar and wind power acting as distributed generations (DGs) are gaining more and more attentions. Discussions about grid of the future on 2012 International Council on Large Electric Systems (CIGRE2012) pointed that new technologies, new participants, and new market environments are leading the traditional value chain of “fossil energy source-grid transmission end user” to a new value chain adopting renewable energy generations and distributed generations, power storages, and electric vehicles (EVs) [1]. To some extent, DGs can improve power quality, power reliability, economy, and flexibility along with impacts to grid caused by its fluctuant power output. The key factor of using DGs lies on how to coordinate DGs with main grid to stable and reliable running. Concept of microgrid or minigrid—a small grid that integrates DGs and loads to form a controllable grid which can provide power supply both under parallel-to-grid and islanding mode—was proposed and adopted by many countries and power companies.

Control strategies of microgrid containing control of grid and control of DGs must coordinate DGs with main grid under parallel-to-grid mode and coordinate different DGs with loads under islanding mode. Commonly used control methods of microgrid include peel-to-peel control, master-slave control, and multiagent control, while control methods of DGs include current control method, voltage control method, and droop control method. The main concern of control method under parallel-to-grid mode is how to depress the fluctuations of power outputs of DGs while using the maximum amount of DG energy such as wind power or solar power. The main concern of control method under islanding mode is how to coordinate power outputs of different DGs with loads to keep stable voltage and frequency level for constant running.

Electric vehicles regarded as a new traffic method have been paid more common attention. While commonly treated as loads, batteries of electric vehicles can provide power support when necessary—which is called vehicle-to-grid (V2G) mode [2]. V2G mode of electric vehicles can reduce the need of common power storages in microgrid by depressing fluctuation of power and providing emergency power supply.

Compared with common battery storage, batteries of electric vehicles can be regarded as mobile power storage devices: mobility of vehicles cause the capacity change of charging and discharging along with the unpredictability of charging or discharging status; transport demand, charging methods (charge/replace), and charging speed (fast/slow) of vehicles cause differences in control and external characteristics.

To coordinate DGs and grid, considering the instability and unpredictability of DGs and EVs, a control strategy for microgrid containing renewable energy generations and electric vehicles was presented in this paper. Control methods of microgrid were analyzed and studied to propose a comprehensive control strategy for microgrid with DGs and EVs. The control strategy uses MPPT current control for renewable energy generations under parallel-to-grid mode and uses master-slave control which elects battery storages as master while other DGs and EVs as slaves under islanding mode. A common structure microgrid with DGs, battery storage, and EVs was built both in simulation and laboratory experiment. Simulations and laboratory experiments prove that the control strategy works well for microgrid containing renewable energy and EVs and provides maximum power output of renewable energy and a stable and sustainable running under islanding mode.

## 2. Distributed Generations and Microgrid

Generally, distributed generations (DGs) refer to such environment friendly or renewable power generation devices as photovoltaic, wind power, fuel cells or microgas turbine which are located near loads and capacity of tens of kilowatts to several megawatts. DGs can improve power quality and power reliability with the following characteristics [3]. (1) Power Generation near loads without step-up and step-down transformer and load distance transmission will reduce construction and maintenance cost, reduce power loss of transmission and improve efficiency. (2) Immune to faults in transmission, and transformation system which will improve power reliability and power quality. (3) Immune to the interferes of regional voltage and frequency fluctuations, preventing regional failure develop to blackouts.

Commonly adopted DGs are microgas turbine, fuel cell, wind power, photovoltaic, and power storage devices. Microgas turbine burns gas, methane, or gasoline with total efficiency up to 75% under thermoelectricity cogeneration mode which is a promising commercial DG [4]. Fuel cell transforms the fuel chemical energy into the electrical energy through the electrode reaction with little emission, which has higher efficiency than traditional power plant [5]. Nevertheless, gas turbine and fuel cell need primary energy sources such as gas or fuel to produce electric power. On the point of renewable and sustainable energy view, micro gas turbine and fuel cell are not suitable choices while wind power and solar power are more suitable and feasible.

**2.1. Wind Power Generation.** Wind power generation uses wind power to produce electric power which has features of environment friendly and zero emission and now has mature

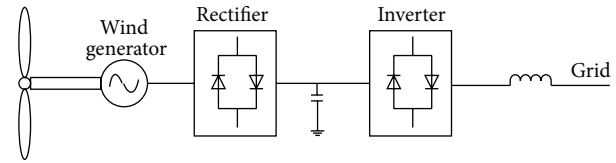


FIGURE 1: Wind power generation system structure.

technology of single generator capacity of 2500 kW. As shown in Figure 1, wind generators are mostly asynchronous generators which produce frequency-varying AC power and need rectifier and inverter to convert to grid frequency and parallel in grid.

Paralleled in through an inverter, wind power generation will consume reactive power while producing active power, and wind power generation is normally combined with power storage, photovoltaic generation, diesel generator, or reactive power generation devices. Operation modes of wind power generation are mainly two types: (1) stand alone operation mode, which uses small wind generators to charge battery storages and through an inverter to support end user or medium wind generators combined with diesel generators or photovoltaics to form hybrid power supply; (2) operation with grid mode, which uses large wind generators capacity range 200 kW to 2500 kW to form wind power farm as power source of grid.

Power output of wind power generation is closely related to the rotating speed of generator under certain wind speed. Figure 2 shows an example relation of torque and rotating speed (a) and relation of power and rotating speed (b) at two wind speeds of  $v_1$  and  $v_2$  [6]. As power output depends on the product of torque  $T$  and rotating speed  $\omega$ , the rotating speed of maximum power output is not the same to that of maximum torque. Commonly, wind power generation uses a speed-varying control system called maximum power point tracking (MPPT) which controls the wind generator works on the speed point of maximum power output [7].

**2.2. Photovoltaic Generation.** Photovoltaic generation (PV), based on the photovoltaic effect of photovoltaic cell to convert solar energy to DC energy, has features of environment friendly, easy maintenance, zero emission, and low cost. Operation modes of PV are mainly two types: (1) islanding mode, that power system with PV is not connected to public power grid, is commonly used for areas far from public power grid such as an island; (2) parallel-in mode, that PV is paralleled to public power grid. This mode can use photovoltaic generations as mass power production and is the most used mode in the world [8–10].

Output voltage and current of photovoltaic cell change with light intensity and temperature. Figure 3 shows an example relation of current and voltage (a) and relation of power and voltage (b) of PV at different light intensities. Figure 4 shows an example relation of current and voltage (a) and relation of power and voltage (b) of PV at different temperatures. At certain light intensity and temperature, photovoltaic cell can work at a different voltage, while

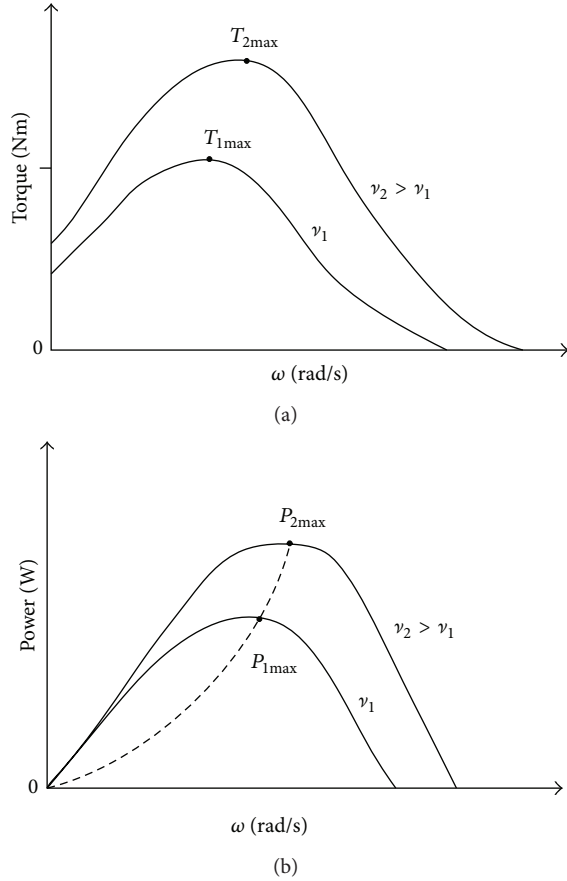


FIGURE 2: Relation of torque/speed and power/speed of wind generator at two wind speeds.

only at a certain voltage, the output power of photovoltaic cell reaches the maximum output. Similar to wind power, photovoltaic generation uses MPPT control of voltage to control the photovoltaic cell works on the voltage point of maximum power output [11].

**2.3. Power Storage Devices and Electric Vehicles.** Acting as a distributed generation, output power is affected by weather conditions (wind/light) wind power generation and photovoltaic generation are intermittent power supply which cannot meet the load demand full time. Thereby, power storage devices are widely used in distributed generation for continuous power supply. Effects of power storage devices in distributed generation are as follows [12]. (1) Power storage devices can depress load wave by charging when load is low and discharging when load is high. (2) Active power and reactive power outputs of power storage devices can change rapidly, which can damp the power and frequency of a system to keep the system stable. (3) Tracking ability of power storage devices can keep distributed power sources working at maximum power point and improve power efficiency. There are many types of power storage devices such as battery storage, super-capacitor storage, flying-wheel storage, and

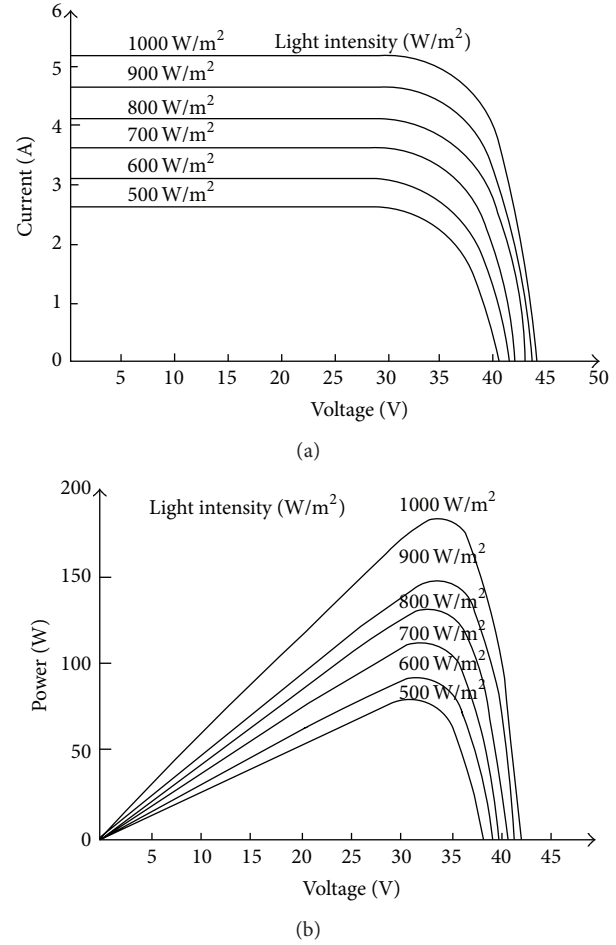


FIGURE 3: Relation of  $I-V/P-V$  of PV cell at different light intensities.

hydroplant, while the most widely used power storage device is battery storage.

As the development and spread of electric vehicles, influence of batteries especially large capacity batteries of EVs connected to grid is gaining more and more attention. Batteries of electric vehicles can provide power support when necessary—which is called vehicle-to-grid (V2G) mode [2, 13]. Compared with common batteries, batteries of EVs can be regarded as mobile power storage devices: the coupling point is mobile; the status and capacity of charging or discharging is indeterminate. When connected to grid, batteries of EVs can act as common battery storages and reduce the demand capacity of common power storages. As the growth of EVs, it is necessary to take full advantage and rational use of batteries of EVs.

**2.4. Microgrid.** Traditional power distribution grid distributes power to end user through a branchy, radialized network which transfers power in single direction. Single DG directly connected to power distribution grid will change the power flow direction and cause analysis, control, and protection problem of power distribution grid. Restrain and isolate methods are commonly adopted by a grid to decrease

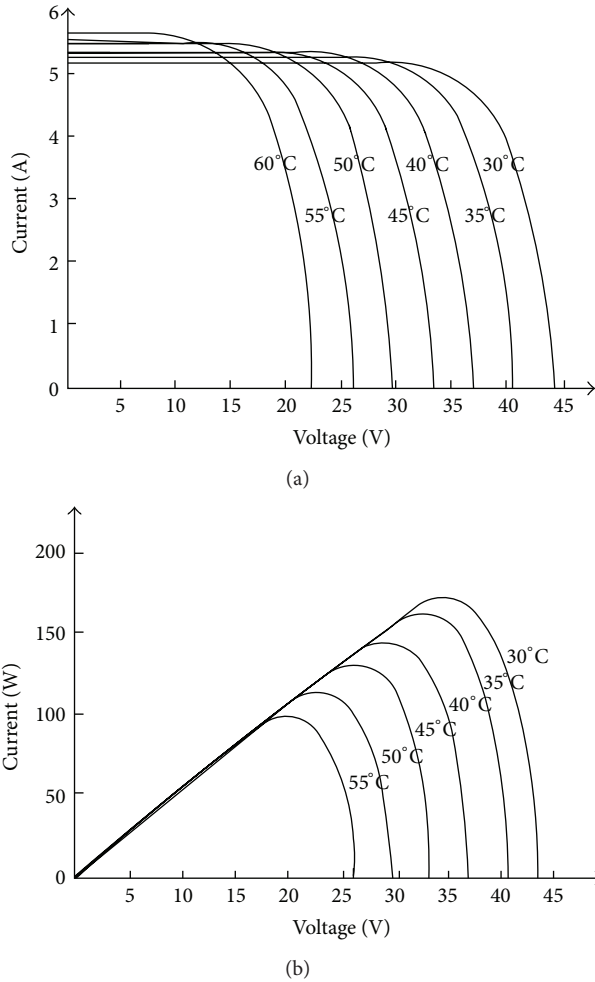


FIGURE 4: Relation of  $I$ - $V$ / $P$ - $V$  of PV cell at different temperatures.

the impact of DGs. A concept of combined DGs with loads to form a so-called microgrid to coordinate grid and DGs was proposed [14, 15]. Although different concepts of microgrid were proposed by different countries according to their own instances, goals and patterns of these concepts are similar, where the concept proposed by Consortium for Electric Reliability Technology Solutions (CERTS) was most widely adopted: “an aggregation of loads and microsourses operating as a single system providing both power and heat. The majority of the microsourses must be power electronic based to provide the required flexibility to insure operation as a single aggregated system. This control flexibility allows the CERTS MicroGrid to present itself to the bulk power system as a single controlled unit that meets local needs for reliability and security.” [15]. Microgrid usually consists of DGs, power storage devices, power electronic devices (such as inverter, solid state switch), and loads. Microgrid has following the characteristics: (1) Microgrid provides an efficient way for DGs to parallel in utility grid, and inherit the advantages of DG; (2) microgrid can switch to island mode on utility grid failure, and does not affect the security and safety of utility grid; (3) plug-and-play

ability of DG connection; (4) improve efficiency of DG by combined heat and power (CHP) or combined cold heat and power (CCHP), (5) damping effect to voltage and frequency fluctuation.

**2.5. Microgrid Containing Renewable Energy and Electric Vehicles.** Single EV has little effect on the utility grid even under V2G mode. But when a certain number of electric vehicles are paralleled in the grid, they will inevitably affect the utility grid. Charging station was adopted in China for individual and public EV charging. A microgrid scheme which combines photovoltaic, power storage, and EV charging station together was proposed by Beijing Jiaotong University (BJTU) and implemented in laboratory where the microgrid with a simplified structure can be regarded as a submicrogrid in the modified structure of CERTS microgrid as shown in Figure 5, where the primary microgrid is connected with the distribution grid through the circuit breaker; the submicrogrid with EVs is connected with the bus through the feeder just as other microsourses.

The submicrogrid with EVs is a simplified microgrid with 1 concentrated busbar as shown in Figure 6 where the busbar can be a DC busbar or AC busbar, while DC busbar will need a large capacity bidirectional power converter at the point of common coupling (PCC), and AC busbar is a more suitable solution for charging station. In Figure 6, DGs and power storage devices are located near charging station, battery storages act as fixed power storage while EVs act as mobile storage.

### 3. Control Methods

**3.1. Control Methods of Microsourses.** Control methods of microgrid consist of microsource control and the grid control. Most DGs are using MPPT control to reach their maximum power output and through a converter/inverter connected to microgrid busbar. As the system in Figure 6, with an AC busbar, microsourses such as wind power and battery storage are connected with inverters. Control methods of microsourses in the simplified system of microgrid with renewable energy and EVs as in Figure 6 focus on control methods of microgrid inverters. The common used control methods of microgrid inverter include current control method, voltage control method, and droop control method [16].

**3.1.1. Current Control Methods.** Current control method of microgrid inverter uses the output current as control signal which produces current of the same frequency and same phase angle with the grid voltage to provide power. Under current control method micro sources can be regarded as controllable current source with large inner impedance. Basic control diagram of current control method is shown as Figure 7 where  $i_0$  is the output current of inverter,  $i_{ref}$  is the setting value of current.

There are two ways of current control method: indirect current control and direct current control. Indirect current control uses the setting current, voltage vector of PWM to

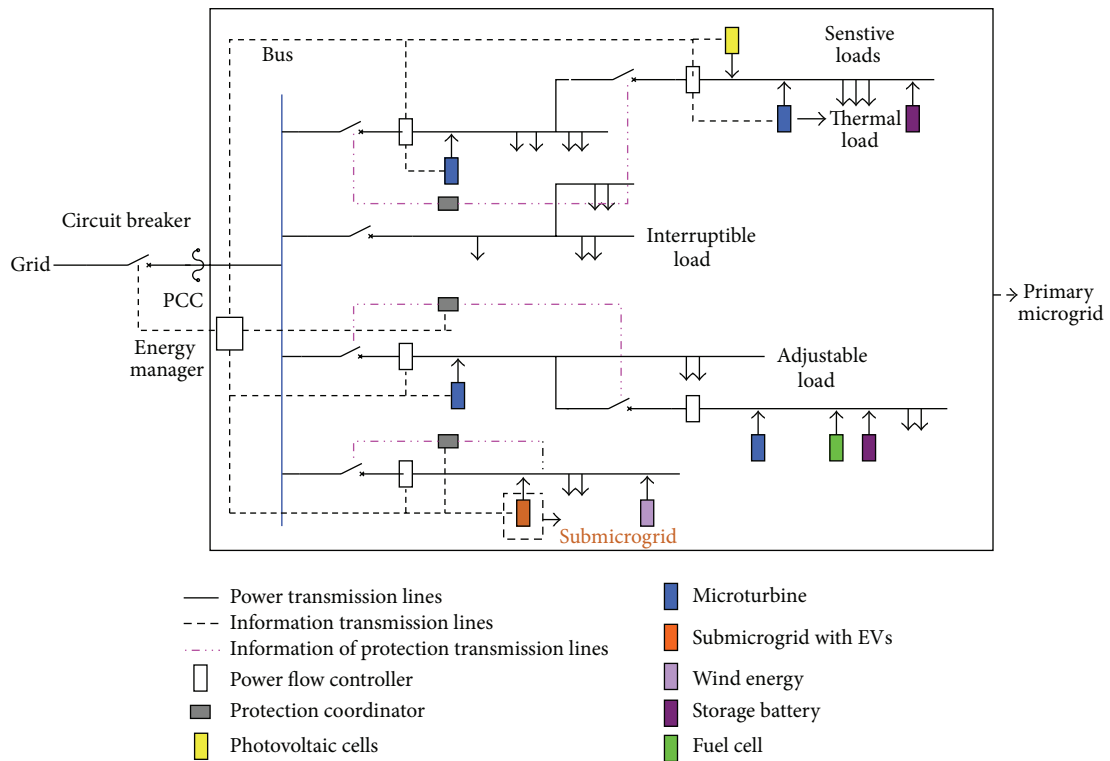


FIGURE 5: Modified structure of CERTS microgrid.

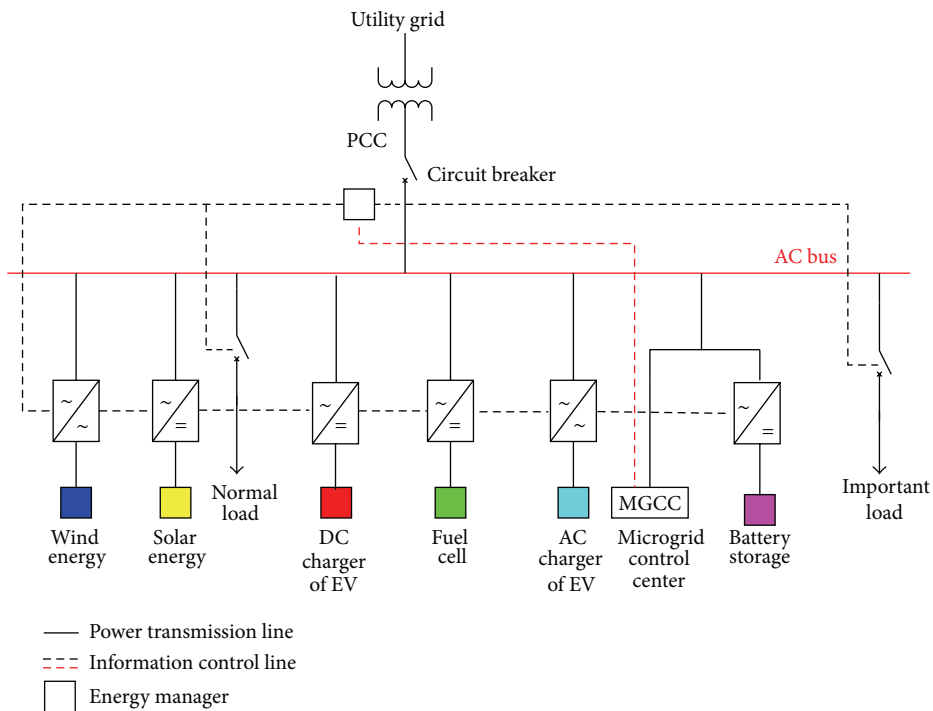


FIGURE 6: Submicrogrid with EV.

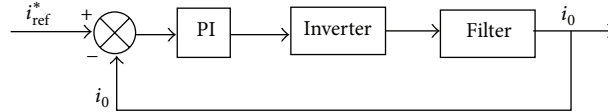


FIGURE 7: Basic diagram of current control method.

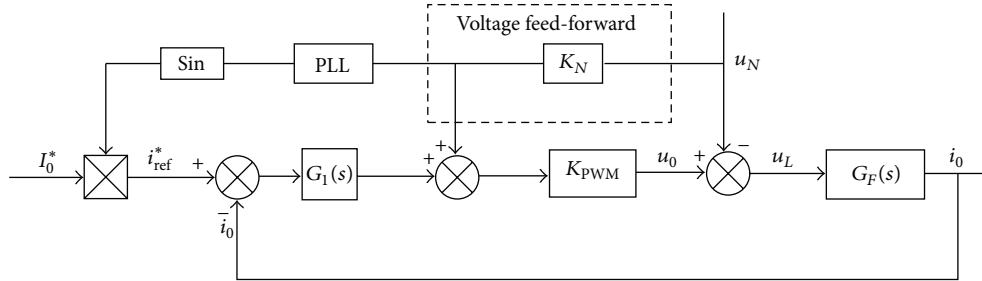


FIGURE 8: Diagram of direct current control with voltage feed-forward.

form closed-loop control which through voltage control to achieve current control. This method is simple and is no need of current detection, but it has disadvantages of slow dynamic response and transient DC-drift and is affected by the quality of grid voltage.

As shown in Figure 8, direct current control directly uses current as feedback to achieve synchronous current with grid voltage, where  $i_0$  is current output of inverter,  $u_N$  is grid voltage,  $K_{PWM}$  is the equivalent gain coefficient of inverter,  $G_1(s)$  is the transfer function of current regulator usually use PI regulation,  $G_F(s)$  is equivalent transfer function of filter, PLL is a phase locked loop module tracking the frequency and phase of grid voltage to keep the frequency and phase of output current same to them. A voltage feed-forward module was introduced to eliminate current fluctuation caused by grid voltage fluctuation [17, 18] where in Figure 8  $K_N$  is the coefficient of voltage feed-forward. The direct current control with voltage feed-forward was adopted in this paper.

**3.1.2. Voltage Control Method.** Voltage control method of microgrid inverter uses the output voltage as the control signal which produces voltage of the same frequency and the same phase angle with the grid voltage to provide power. Under voltage control method, micro sources can be regarded as controllable voltage source with small inner impedance. Basic control diagram of voltage control method is shown as in Figure 9 where  $i_0$  is the output current of inverter,  $V_g$  is the voltage of grid, and  $V_{ref}$  is the setting voltage value of inverter.

Voltage control method as in Figure 9 uses dual control loop—outer loop of voltage to keep voltage stable and inner loop of current to improve dynamic response performance and restrain fluctuation [19]. Compared with current control methods, voltage control method has advantages of good dynamic performances, high steady state accuracy, robust to nonlinear load, and low harmonics. Inverter under voltage control mode provides reference voltage and frequency to microgrid in islanding and is also called a voltage source

converter (VSC); other inverters can use the voltage of VSC as a reference and run in desired mode. While microgrid under parallel-to-grid mode, micro source in VSC mode is a voltage source that must coordinate with the main source of utility grid to keep synchronization. Commonly VSC mode is more suitable for the main micro source in islanding mode microgrid.

**3.1.3. Droop Control Methods.** Micro sources in parallel-to-grid mode microgrid usually work in current control mode, while another mode called droop control method is also used to make a microgrid work more like traditional power grid. Droop control method decouples power and voltage and frequency to form droop style  $P-f$  (active power-frequency) and  $Q-V$  (reactive power-voltage) or  $P-V$  and  $Q-f$  micro source output characteristics like traditional synchronous generator; thus, the traditional grid control methods can be applied in microgrid [20]. Under droop control method, inverter adopts an inner droop curve according to its capacity and type of micro source and produces voltage with amplitude and frequency determined by its active and reactive power output. Control diagram of droop control method is as shown in Figure 10 where  $P_N$ ,  $I_N$ , and  $f_N$  are the rated power, current, and frequency of micro source under droop control mode. Droop control module calculates the voltage amplitude and frequency at input  $P$  and  $Q$  according to its inner droop curve. Voltage combination module provides reference voltage at input  $f$  and  $V$ , and the dual loop control of voltage and current module provide PWM to drive the inverter. Droop control method makes micro sources work like traditional synchronous generators—which are easy to control and dispatch. Nevertheless, it also makes micro sources only work well when voltage and frequency are near rated value; unsuitable droop curves will make system unstable, bad system dynamic performance, and easy to swing because of low damping effects.

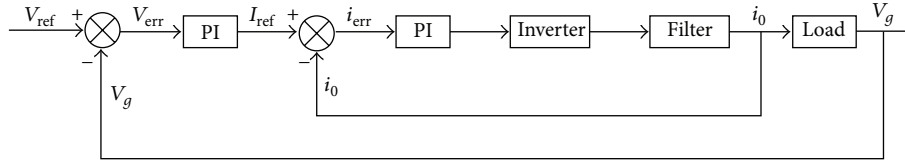


FIGURE 9: Basic diagram of voltage control method.

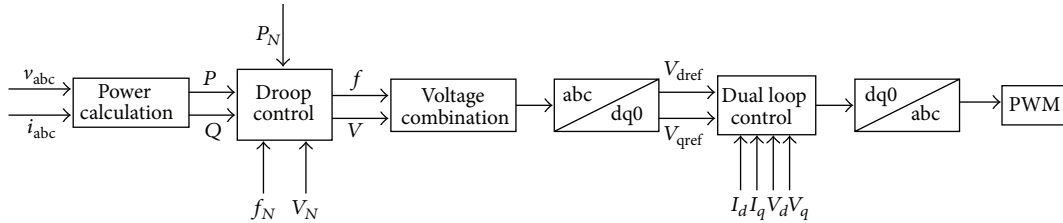


FIGURE 10: Control diagram of droop control method.

### 3.2. Grid Control Methods of Microgrid

3.2.1. *Peer-to-Peer Control.* Under peer-to-peer control method, each micro source acts as a “peer” and equally in microgrid. Each micro source participates in the regulation of voltage and frequency according to their own inner control [21, 22]. Commonly peer-to-peer control is based on the droop control of micro sources which decouple frequency and voltage to active and reactive power. Micro sources are initialized at rated frequency  $f_0$  and inner potential  $E_0$ , while load changes, active power, and reactive power flow in microgrid change accordingly; with that, active power and reactive power outputs of each micro source will change; coordinated by frequency and voltage, system will reach a new balanced point by droop character. This is similar to primary frequency control of synchronous generators. The peer-to-peer grid control method of microgrid has the advantages of simple, easy-to-implement, local controlled (no need of communication), plug-and-play, and easy-to-modify. But this method cannot treat the restoration problem of voltage and frequency caused by severe disturbance of power which is usually regulated by secondary frequency control in traditional synchronous generators [21].

3.2.2. *Master-Slave Control.* Under master-slave control method, one or more micro sources are elected as a master source of microgrid which provides reference voltage and frequency, other micro sources act as a slave source [23]. Master-slave control mode is mostly used for microgrid in islanding mode, while in parallel-to-grid mode the utility grid is master and all micro sources are slaves. Using master-slave control mode in islanded microgrid, the master source elected must have the ability of fast changing to voltage control mode, good voltage and frequency regulation character, and stable and controllable power output. Commonly elected master sources are power storage devices such as battery storage, micro gas turbines, or fuel cells.

The master-slave grid control method of microgrid has the advantages of simple, good voltage, and frequency

regulation character and dynamic response. But the performance of master-slave control method rely on master source: master source needs rapid change to voltage control mode when islanding happens to microgrid; voltage and frequency are regulated by master source where master source failure will cause whole microgrid failure; multimaster sources will cause current loop; fluctuations of power are balanced mainly by main source which require certain power reservation of main source.

3.3. *Control Methods Adopted.* Direct current control method with voltage feed-forward as in Figure 8 was adopted for micro sources (DGs, battery discharging, and V2G) control when microgrid paralleled to utility grid in this paper, where DGs work as current sources. Master-slave grid control method is adopted for microgrid in islanding mode, and battery storage work in voltage control mode was adopted as main source, while other micro sources still work in current control mode.

## 4. Simulations and Laboratory Implementation

Simulations of microgrid with renewable energy and EV were carried out, and a laboratory platform of microgrid was established. Control methods in 3.3 were used both in simulation and laboratory platform. An islanding detection method of over/load voltage and over/low frequency was adopted for control mode change, and a load shedding method was adopted.

4.1. *Simulation Model and Results.* A simulation model as in Figure 11 was built in MATLAB/simulink according to the parameters of the laboratory platform where the utility grid is a 380/220 V system, DG1 is a 25 kW photovoltaic cell (PV), DG2 is a 50kWh lithium battery storage, DG3 is a 18 kW EV, load 1 is a load of 10 kW, load 2 is a load of 10 kW + 1.5 kVar, and load 3 is a 25 kVA fluctuant and interruptible load.

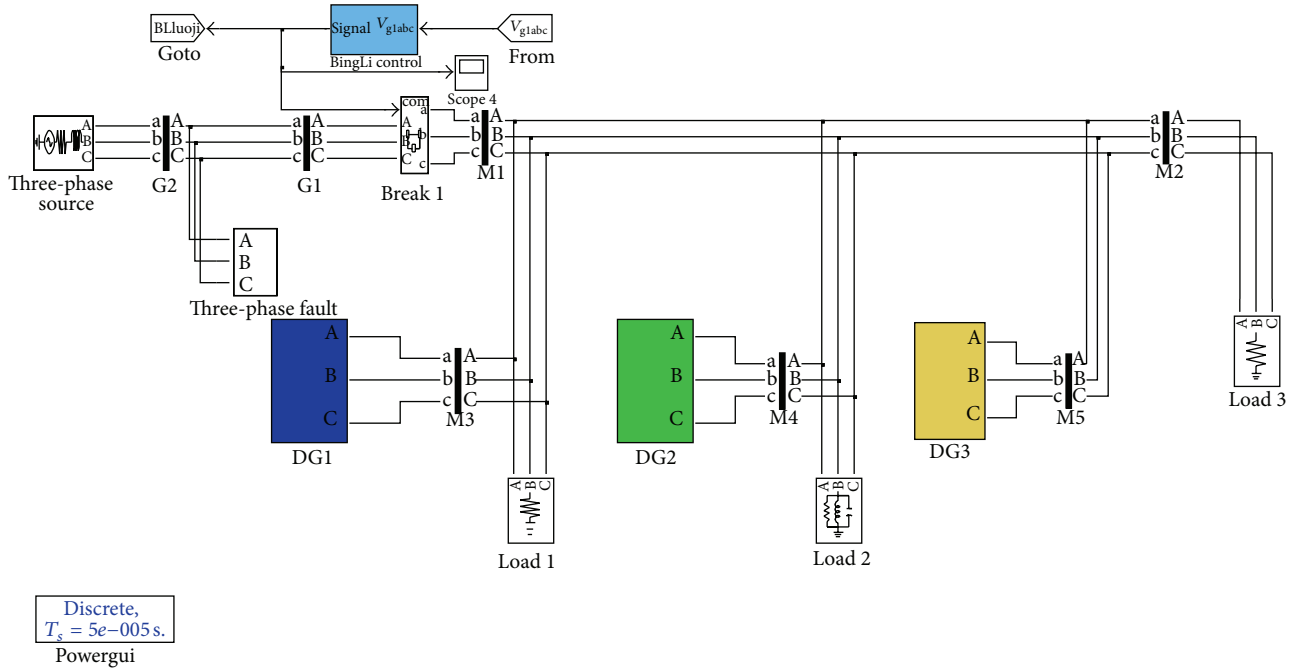


FIGURE 11: Simulation mode of microgrid with PV and EV.

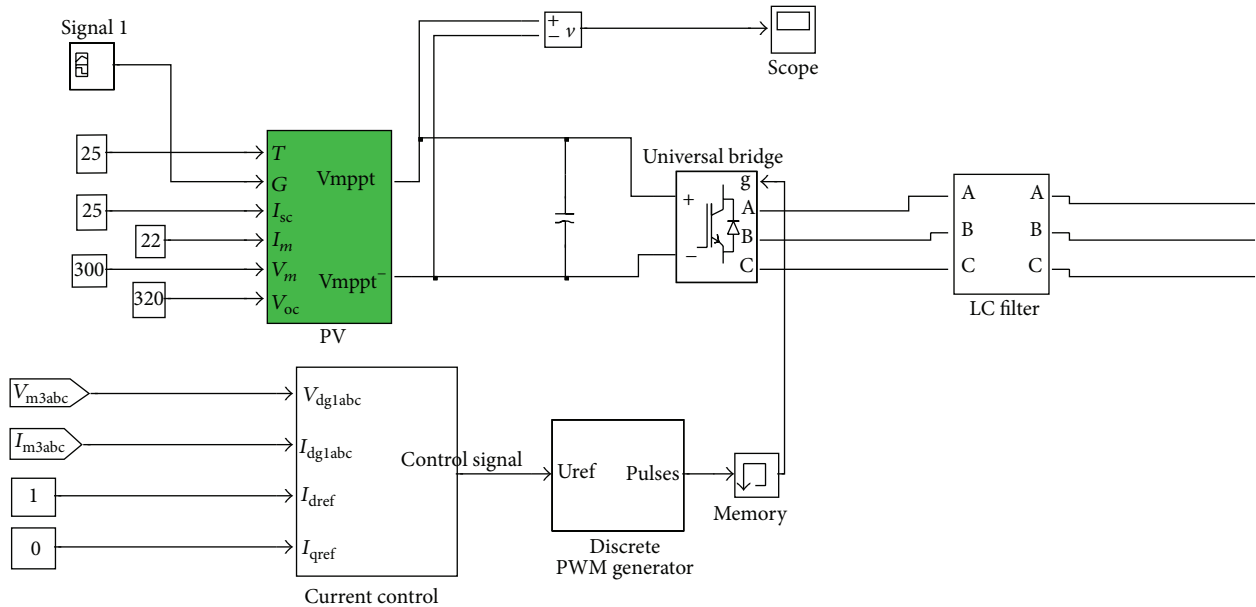


FIGURE 12: Simulation model of PV (DG1).

DG1 in Figure 11 is the simulation model of PV as shown in Figure 12 which adopts the PV array model used in [24] and MPPT control in [25]. Inverter of DG1 works in current control mode. DG2 in Figure 11 is the simulation model of battery storage as shown in Figure 13 which uses battery module in MATLAB /simulink. Converter of DG2 works in current control mode when microgrid paralleled to grid and

works in voltage control mode as main power source when microgrid is islanded.

Figure 14 shows the simulation model of EV (DG3) in Figure 11. SOC and capacity of battery was adopted with 10% fluctuation normal distributed. A uncontrolled rectifier was adopted for battery charging, and a current control mode was adopted for battery discharging.



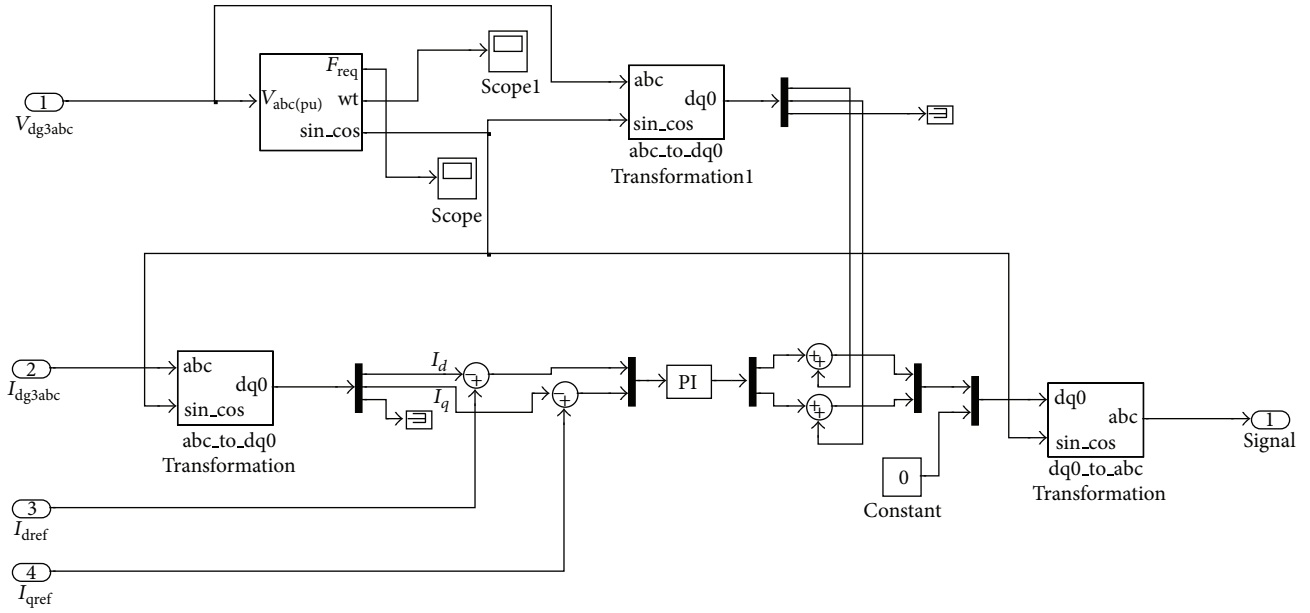


FIGURE 15: Diagram of current control in simulation.

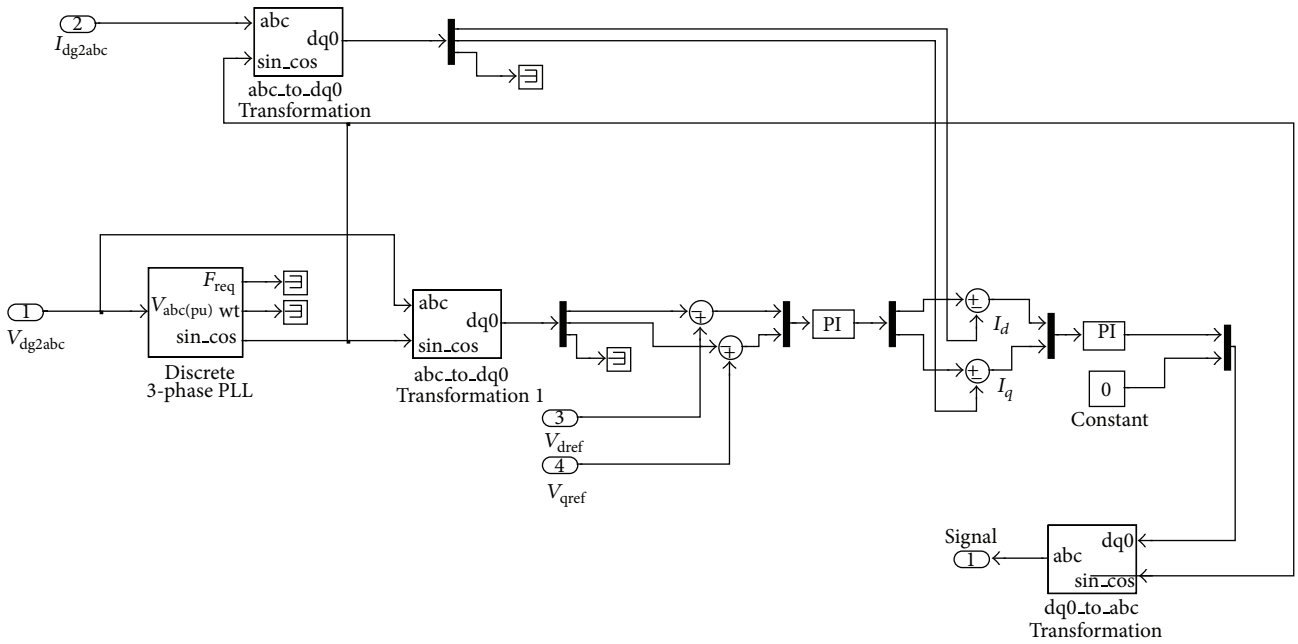


FIGURE 16: Diagram of voltage control in simulation.

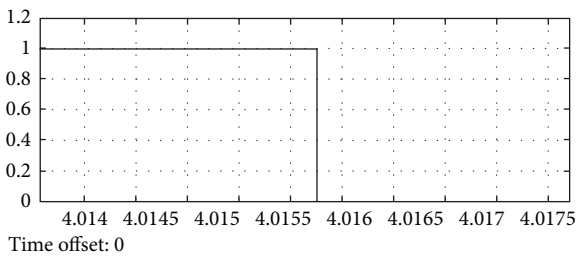


FIGURE 17: Output signal of microgrid island detection.

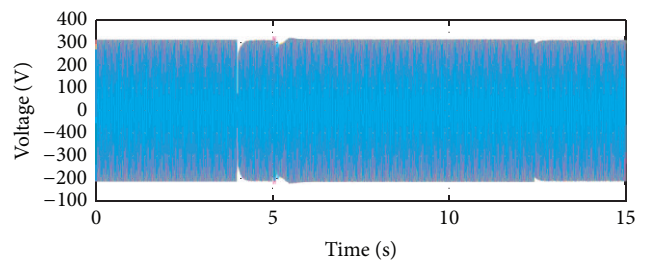


FIGURE 18: Voltage wave of microgrid busbar.

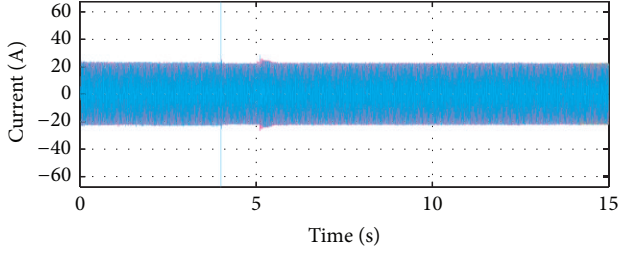


FIGURE 19: Current wave of DG1 (PV).

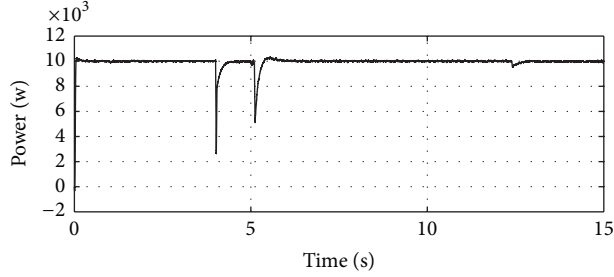


FIGURE 20: Active power output of DG1.

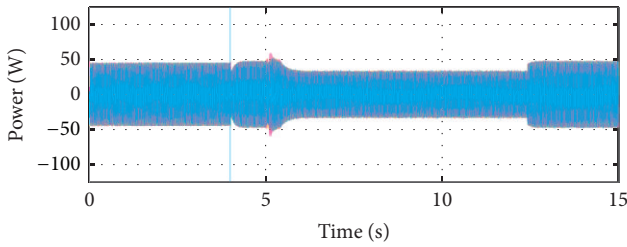


FIGURE 21: Current wave of DG2 (battery).

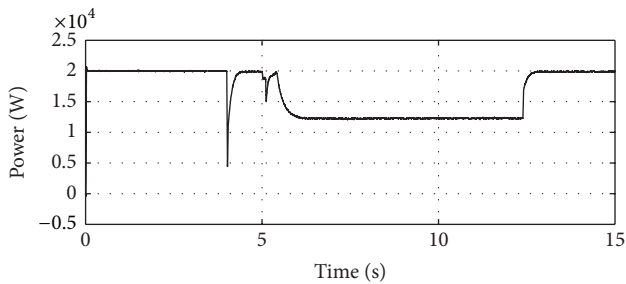


FIGURE 22: Active power output of DG2 (battery).

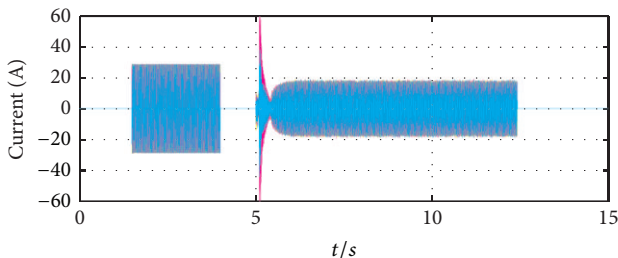


FIGURE 23: Current wave of DG3 (EV).

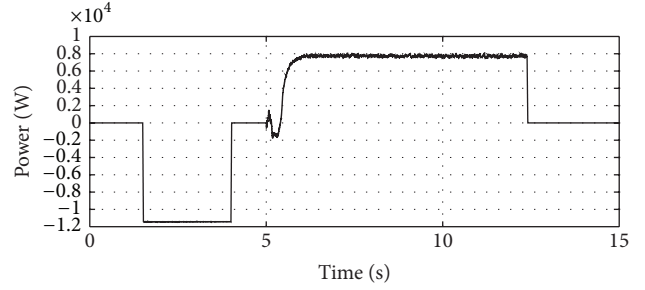


FIGURE 24: Active power output of DG3 (EV).

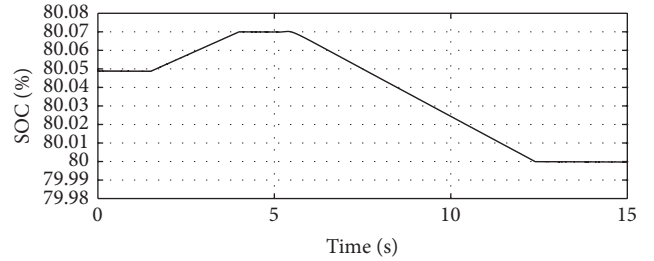


FIGURE 25: Real-time capacity of EV.

TABLE I: Time list of simulation events.

Time (s)	Event
1.5	EV connected to grid as load
4	Utility grid failure
5	EV change to V2G mode
12.5	EV exit

at 4 s and 5 s that utility grid failure and EV change to V2G mode. Figures 21, 22, 23, and 24 show that EV as current source provides power in islanding mode and decreases power output of main source. Figure 25 shows that EV will exit V2G mode when SOC reach lower limit (which is set to 80% in simulation).

**4.2. Laboratory Platform of Microgrid with Photovoltaic and EV.** A laboratory platform of microgrid with 25 kW photovoltaic, 50 kWh/25 kW lithium battery packs, 15 kWh/18 kW EV, 25 kW load simulator and 24 kW lighting loads was formed in BJTU as shown in Figure 26. The EV is a Tong Yue EV manufactured by Jianghuai Automobile China (JAC) with 50 Ah battery, 7 hours of charging time, rated power 18 kW and maximum power 42 kW. Structure of the microgrid is shown in Figure 27, where battery inverter works in VSC mode when microgrid islanded,  $I_g$ ,  $I_{m1}$ ,  $I_{m2}$ ,  $I_P$ ,  $I_B$  as directions shown in Figure 27 are currents of PCC, converter 1, converter 2, PV, and battery. Control methods are adopted as in Section 3.3.

Experiments of parallel/islanding were carried out in different load status. Figures 28, 29, 30, 31, 32, 33, and 34 show the voltage/current wave, frequency wave, voltage amplitude wave, and power wave of one example experiment where in microgrid parallel status load power is  $P_l = 4.0$  kW,  $Q_l =$



FIGURE 26: Laboratory platform of microgrid with photovoltaic and EV.

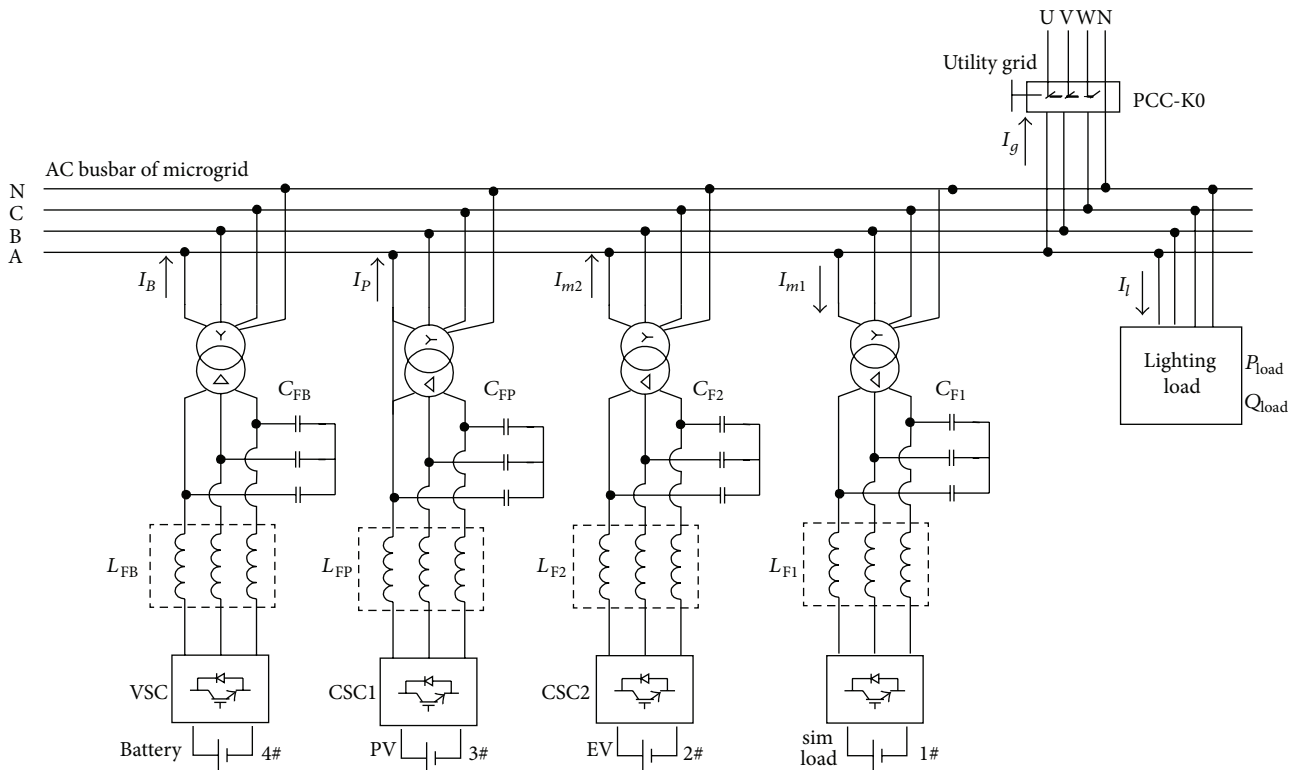


FIGURE 27: Structure of the Laboratory platform.

2 kVar, sim-load power(1) is  $P_1 = 8.0 \text{ kW}$ ,  $Q_1 = 0 \text{ kVar}$ , EV (2) power is  $P_2 = -2.0 \text{ kW}$ ,  $Q_2 = 0 \text{ kVar}$  (charging), PV (3) output power is  $P_{P3} = 5.1 \text{ kW}$ ,  $Q_{P3} = 0 \text{ kVar}$ , and battery charging power is  $P_{B4} = -4.0 \text{ kW}$ ,  $Q_{B4} = 0 \text{ kVar}$  (charging). In islanding mode, load power is  $P_l = 4.0 \text{ kW}$ ,  $Q_l = 2 \text{ kVar}$ , sim-load power (1) is  $P_1 = 8.0 \text{ kW}$ ,  $Q_1 = 0 \text{ kVar}$ , EV (2) power

is  $P_2 = 11.0 \text{ kW}$ ,  $Q_2 = 1.5 \text{ kVar}$  (discharging), PV (3) output power is  $P_{P3} = 5.1 \text{ kW}$ ,  $Q_{P3} = 0 \text{ kVar}$ , and battery storage power is  $P_{B4} = 1.0 \text{ kW}$ ,  $Q_{B4} = 0.5 \text{ kVar}$  (discharging). At the “second regulation” point, EV output power decrease as the SOC of EV has dropped to the point of low power output point; battery output power increases to balance the power.

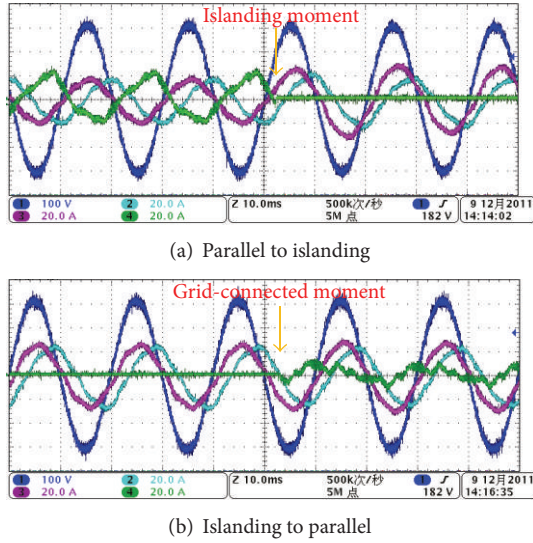


FIGURE 28: Voltage/current wave of parallel/islanding transfer (CH1: phase A voltage, CH2: phase A current of  $I_{m1}$ , CH3: phase A current of  $I_p$ , and CH4: phase A current at PCC ( $I_g$ )).

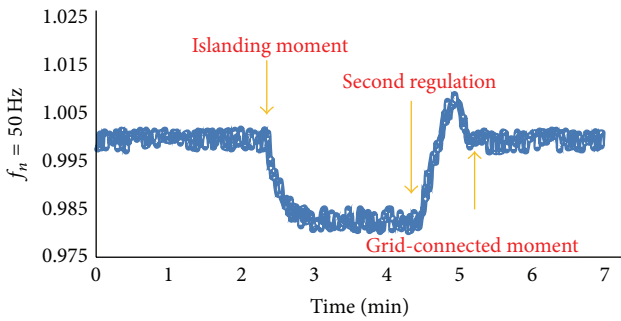


FIGURE 29: Frequency wave.

As we can see that using the control strategy proposed in this paper, maximum power output of renewable energy was utilized both under parallel-to-grid and islanding mode, and the stably operation time of microgrid under islanding was prolonged as a result of the participant of EV as power source.

### 5. Conclusions

This paper presented a control strategy for microgrid containing renewable energy and electric vehicles. The strategy uses current control mode for renewable energy generations under parallel-to-grid mode and uses master-slave grid control which elects battery storages as main power sources DGs and EVs as slave power source under islanding mode. Compared with other strategies, this strategy does not need to change working mode of DGs while transferring between parallel-to-grid and islanding and can fully use the power of DGs, immune to output power fluctuation of DGs, and prolong the stable running time of microgrid under islanding mode. According to simulation results and laboratory experiments, the proposed control strategy works

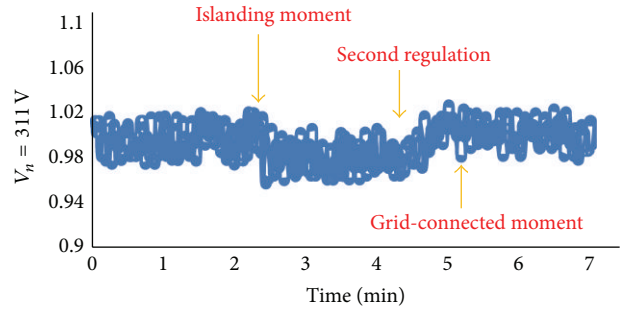


FIGURE 30: Voltage amplitude wave.

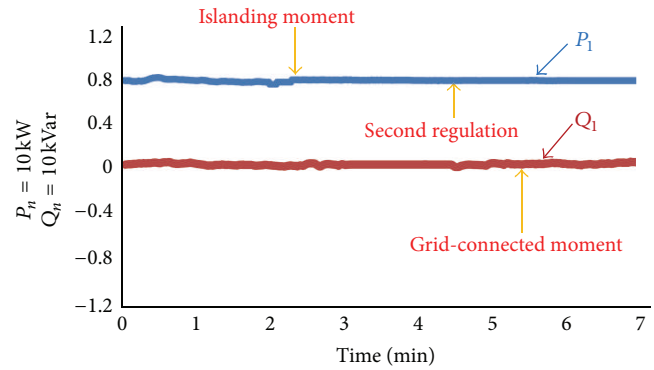


FIGURE 31: Power wave of converter 1.

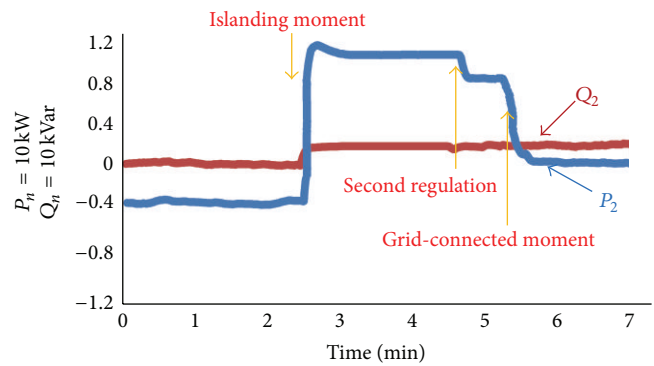


FIGURE 32: Power wave of converter 2.

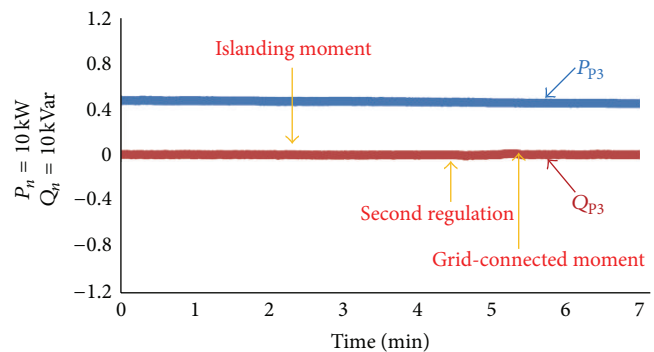


FIGURE 33: Power wave of converter 3.

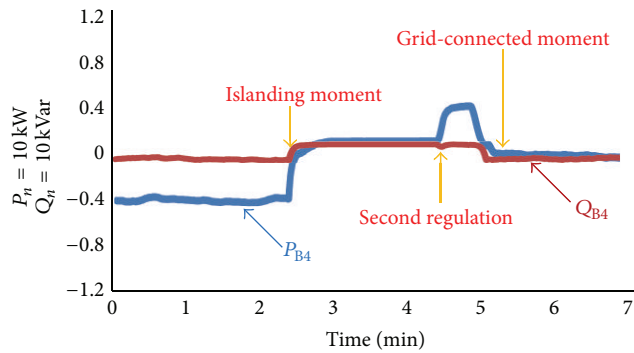


FIGURE 34: Power wave of converter 4.

well and provides maximum power output of renewable energy and stable and sustainable microgrid running under islanding mode. We hope that the strategy will be adopted for industrial applications.

## Acknowledgment

The authors gratefully acknowledge the support of the National Natural Science Foundation of China, for financial support under Grant no. 51277009.

## References

- [1] C. W. Gellings, "The grid of the future: the need for technology and intelligence in the future power system," in *Proceedings of the Technical Exhibition, Grid of the Future Symposium (CIGRE '12)*, Kansas City, Mo, USA, October 2012.
- [2] W. Kempton and J. Tomić, "Vehicle-to-grid power implementation: from stabilizing the grid to supporting large-scale renewable energy," *Journal of Power Sources*, vol. 144, no. 1, pp. 280–294, 2005.
- [3] F. Blaabjerg, R. Teodorescu, M. Liserre, and A. V. Timbus, "Overview of control and grid synchronization for distributed power generation systems," *IEEE Transactions on Industrial Electronics*, vol. 53, no. 5, pp. 1398–1409, 2006.
- [4] Z. Xue-Mei, G. Jia-Sheng, C. Zhi-Gang, S. Cen, Q. Chao-Kui, and F. Jian-Ping, "Thermodynamic model study of micro-turbine with MATLAB/Simulink," in *Proceedings of the International Conference on Consumer Electronics, Communications and Networks (CECNet '11)*, pp. 913–918, Ningbo, China, April 2011.
- [5] B. Chen, "Research and development of fuel cell technology in China," in *Proceedings of the Asia-Pacific Power and Energy Engineering Conference (APPEEC '11)*, pp. 1–4, Wuhan, China, March 2011.
- [6] E. Denny and M. O'Malley, "Wind generation, power system operation, and emissions reduction," *IEEE Transactions on Power Systems*, vol. 21, no. 1, pp. 341–347, 2006.
- [7] H. Valderrama-Blavi, J. M. Bosque, F. Guinjoan et al., "Power adaptor device for domestic DC microgrids based on commercial MPPT inverters," *IEEE Transactions on Industrial Electronics*, vol. 60, no. 3, pp. 1191–1203, 2013.
- [8] H. Yan, Z. Zhou, and H. Lu, "Photovoltaic industry and market investigation," in *Proceedings of the 1st International Conference on Sustainable Power Generation and Supply (SUPERGEN '09)*, pp. 1–4, Nanjing, China, April 2009.
- [9] S. M. Moosavian, N. A. Rahim, and J. Selvaraj, "Photovoltaic power generation: a review," in *Proceedings of the IEEE 1st Conference on Clean Energy and Technology (CET '11)*, pp. 359–363, Kuala Lumpur, Malaysia, June 2011.
- [10] E. J. Simburger, "Is a residential photovoltaic system a cost effective investment for the homeowner?" in *Proceedings of the 34th IEEE Photovoltaic Specialists Conference (PVSC '09)*, pp. 2336–2339, Philadelphia, Pa, USA, June 2009.
- [11] B. Subudhi, R. Pradhan, B. Subudhi et al., "A comparative study on maximum power point tracking techniques for photovoltaic power systems," *IEEE Transactions on Sustainable Energy*, vol. 4, no. 1, pp. 89–98, 2013.
- [12] G. Coppez, S. Chowdhury, and S. P. Chowdhury, "Impacts of energy storage in distributed power generation: a review," in *Proceedings of the International Conference on Power System Technology: Technological Innovations Making Power Grid Smarter (POWERCON '10)*, pp. 1–7, Hangzhou, China, October 2010.
- [13] C. Battistelli, L. Baringob, and A. J. Conejob, "Optimal energy management of small electric energy systems including V2G facilities and renewable energy sources," *Electric Power Systems Research*, vol. 92, no. 1, pp. 50–59, 2012.
- [14] R. H. Lasseter and P. Paigi, "Microgrid: a conceptual solution," in *Proceedings of the IEEE 35th Annual Power Electronics Specialists Conference (PESC '04)*, pp. 4285–4290, Aachen, Germany, June 2004.
- [15] R. H. Lasseter, "CERTS microgrid," in *Proceedings of the IEEE International Conference on System of Systems Engineering (SOSE '07)*, pp. 1–5, San Antonio, Tex, USA, April 2007.
- [16] R. Joan, L. Alvaro, and B. Frede, "Control of power converters in AC microgrids," *IEEE Transactions on Power Electronics*, vol. 27, no. 11, pp. 4734–4749, 2012.
- [17] R. Lin, P. Yeh, and C. Liu, "Positive feed-forward control scheme for distributed power conversion system with multiple voltage sources," *IEEE Transactions on Power Electronics*, vol. 27, no. 7, pp. 3186–3194, 2012.
- [18] M. A. Herran, J. R. Fischer, S. A. Gonzalez et al., "Adaptive dead-time compensation for grid-connected PWM inverters of single-stage PV systems," *IEEE Transactions on Power Electronics*, vol. 28, no. 6, pp. 2816–2825, 2013.
- [19] A. E. Leon, J. A. Solsona, and M. I. Valla, "Control strategy for hardware simplification of voltage source converter-based power applications," *IET Power Electronics*, vol. 4, no. 1, pp. 39–50, 2011.
- [20] J. Kim, J. M. Guerrero, P. Rodriguez, R. Teodorescu, and K. Nam, "Mode adaptive droop control with virtual output impedances for an inverter-based flexible AC microgrid," *IEEE Transactions on Power Electronics*, vol. 26, no. 3, pp. 689–701, 2011.
- [21] L. Guo, C. Wang, L. Guo, and J. Cao, "Dynamical characteristic of MicroGrid with peer to peer control," in *Proceedings of the China International Conference on Electricity Distribution (CICED '08)*, pp. 1–7, Guangzhou, China, December 2008.
- [22] P. Yuan, L. Pei-Qiang, L. Xin-Ran et al., "Strategy of research and application for the microgrid coordinated control," in *Proceedings of the International Conference on Advanced Power System Automation and Protection*, pp. 873–878, Beijing, China, 2011.

- [23] B. Zhao, X. Zhang, and J. Chen, "Integrated microgrid laboratory system," *IEEE Transactions on Power Systems*, vol. 27, no. 4, pp. 2175–2185, 2012.
- [24] V. Badescu, "Dynamic model of a complex system including PV cells, electric battery, electrical motor and water pump," *Energy*, vol. 28, no. 12, pp. 1165–1181, 2003.
- [25] S. Jiang, D. Cao, Y. Li, and F. Zheng Peng, "Grid-connected boost-half-bridge photovoltaic microinverter system using repetitive current control and maximum power point tracking," *IEEE Transactions on Power Electronics*, vol. 27, no. 11, pp. 4711–4722, 2012.

## Research Article

# Extreme Dynamic Responses of MW-Level Wind Turbine Tower in the Strong Typhoon Considering Wind-Rain Loads

Zhenyu Wang, Yan Zhao, Fuqiang Li, and Jianqun Jiang

*College of Civil Engineering and Architecture, Zhejiang University, Hangzhou 310058, China*

Correspondence should be addressed to Zhenyu Wang; [wzyu@zju.edu.cn](mailto:wzyu@zju.edu.cn)

Received 22 January 2013; Accepted 25 April 2013

Academic Editor: Massimo Scalia

Copyright © 2013 Zhenyu Wang et al. This is an open access article distributed under the Creative Commons Attribution License, which permits unrestricted use, distribution, and reproduction in any medium, provided the original work is properly cited.

The damage and collapse accidents of wind turbines during violent typhoons and rainstorms have increased in recent years. To determine the dynamic response characteristics of high-power wind turbines under extreme conditions, wind load and rain load are simulated. The typhoon average wind velocity and fluctuating wind velocity are simulated by the unstable wind profile and harmony superposition method. The raindrop size distribution is simulated by the M-P spectrum, and the rain load is calculated according to the momentum theorem. A finite element model is established to study the aerodynamic responses of a wind turbine under random typhoon load and typhoon-rain loads. The maximum displacements and accelerations at the tower top and the maximum von Mises stresses at the tower bottom are calculated and compared after considering various combinations of wind direction deflections and rainfall intensities. The results indicate that instantaneous wind direction deflection has a substantial impact on the dynamic responses of wind turbines, and after introducing the effect of rain, the dynamic responses increase up to 13.7% with increasing rainfall intensities. This study has significant implications for analysing collapse accidents of wind turbines and for optimising the design of wind turbines under extreme typhoon conditions.

## 1. Introduction

Worldwide wind power has rapidly developed with the increased demand for renewable energy [1]. It can be expected that wind power will continue its fast development in the coming years. By the end of 2010, the total installed capacity of wind turbines in China had achieved 41.827 GW, ranked first in the world [2]. In wind turbine design, wind is the main external load. Because of their large ratio of height to horizontal dimension, wind turbines are more slender and more sensitive to aerodynamic loads than other structures [3]. Lavassas et al. [4] studied the static and dynamic behaviour of a 1 MW wind turbine tower using both detailed and simplified finite element models. Murtagh et al. [5] modelled the tower and rotating blades as discretised multiple-degree-of-freedom entities and used the mode acceleration method to investigate the along-wind responses of a wind turbine. Li et al. [6] analysed the aerodynamic responses of wind turbines under random wind load using the finite element method, and the results showed that the tower top displacement increased with an increase of the blades'

rotational speed. Generally, current studies mostly focus on the aerodynamic responses of wind turbine towers under normal wind regimes.

In recent years, structural damage and collapse accidents related to typhoons have increased. The typhoon is different from normal wind (nontyphoon) in velocity profile, gradient height, extreme wind speed, surface roughness length, and gust factor [7]. Increasing attention has been given to the wind-induced responses of flexible structures in typhoons. Xu and Zhu [8] studied the buffeting analysis of long-span cable-supported bridges under skew winds during typhoons using a finite-element-based framework and compared those data with field measurements. Zhao et al. [9] compared the wind-excited responses of long-span bridges under normal and typhoon climate modes with time-domain FEM computations. Li et al. [10–12] conducted full-scale measurements of wind-induced responses of super-tall buildings during the passages of typhoons.

With more and more wind turbines built from land to offshore, they are at risk of damage from typhoons or hurricanes. Although few analyses are available regarding

the aerodynamic responses of wind turbines in typhoons, visible damage to wind turbines during typhoons is reported frequently. In 2003, all six wind turbines on Miyakojima Island were extensively damaged by Typhoon Maemi [13]. On September 28, 2008, Typhoon Jangmi struck Taiwan, and one wind turbine tower located on the shore of Taichung Harbor collapsed due to strong wind and heavy rainfall [14]. When Typhoon Dujan landed at Shanwei on September 3, 2003, the observed instantaneous extreme wind velocity in the Red Cove wind farm was 57 m/s, and 13 of 25 wind turbines ceased to operate due to serious damage [15]. Super Typhoon Saomai passed through Hedingshan wind farm of Zhejiang province in 2006, and the observed wind speed was as high as 70–90 m/s. Four units out of 28 wind turbines collapsed, and 20 units were damaged to various degrees [16]. All of these accidents seem to indicate that the practical wind profile on wind turbines may be different from the supposed ultimate limit state in the design [13]. The wind turbine is usually designed with the function that the yaw system should be locked with disk-brake when the wind speed exceeds the cut-out speed. However, the yaw system of a wind turbine could also be moved when the wind speed exceeds the cut-out speed. For example, in Typhoon Maemi, the nacelles of wind turbines no. 3, 4, and 5 at the Karimata wind power plant were moved clockwise from 94° to 156° when the wind speed exceeded 25 m/s [14]. As a result, they suffered larger wind load than when the blades were feathering during the typhoon. Another unfavourable wind regime occurs when the wind direction of a typhoon has sudden changes during its approach because of strong turbulent movement or local topographic effects. When Typhoon Maemi passed Miyakojima Island, the observed wind direction suddenly changed by 120 degrees [14]. In short, because of the complex factors related to wind turbine control as well as sudden changes in wind direction and wind velocity in extreme typhoon conditions, the loads on wind turbines are significantly larger than conventional design loads.

Furthermore, when a typhoon lands, it always brings a heavy rainstorm. The rain is given a horizontal velocity component by the wind, striking the wind turbines' surface along with the wind load, aggravating the vibration of the wind turbines. Some scholars have begun to consider the impact of rainfall on structures. Choi [17] observed the relationship between wind speed and rainfall intensities in thunderstorms and nonthunderstorms, which showed that under a well-conditioned model, there was little difference between wind effects on structures and simultaneous wind and rain effects. However, under an extreme climate mode, such as a thunderstorm or a typhoon, the effects of the rain load will be very great. The coupling of wind and rain is complex, but some simplified methods to calculate the simultaneous action of wind and rain loads are still valuable. Chen and Wu [18] used numerical simulation techniques to investigate the wind-driven rain distribution on a low-rise building. Xin et al. [19] analysed the wind-rain-induced static forces of long-span bridge decks for the simultaneous actions of wind and rain, and the results showed that rainfall can increase the wind-induced drag force on the bridge deck. Li et al. [20–22] analysed the dynamic responses of

transmission line systems under strong wind-rain loads using finite element software and discovered that under the same wind speed, the effects of rainfall on structures increased with an increase of rainfall intensity. However, to the best of authors' knowledge, research on the dynamic responses and damage mechanisms of large wind turbines during strong typhoons and rainstorms is still lacking in the literature. Even though extreme typhoon and heavy rainstorm events rarely occur, their influence may be catastrophic. Thus, the dynamic responses of wind turbines under such extreme working conditions should be given more attention. After the influence of extreme conditions on wind turbines is studied and understood, design and vulnerability analyses of wind turbine tower can be developed further.

This paper mainly focuses on analysing the dynamic responses of wind turbines under extreme working conditions, especially strong typhoons, considering wind-rain loads. The unstable wind profile is used to calculate the average wind velocity of a typhoon. The typhoon fluctuating time histories are calculated by the harmony superposition method based on the Shinozuka theory, and the calculated spectrum result is in line with the trend of the target spectrum. Then, according to the M-P spectrum and the characteristics of rainfall, the rain load time histories are calculated based on the momentum theorem. In order to explore the dynamic responses on the occasion of a sudden change of wind direction, the wind-rain loads profile on the wind turbine is simulated with the blades feathering and with sudden wind direction deflections of 90° and 180°. The effects of various rainfall intensities are also studied in the dynamic response analysis. The research results help elucidate the dynamic characteristics and failure mechanisms of wind turbines under typhoon conditions and promote a safety evaluation of wind turbines.

## 2. Typhoon Wind Velocity Simulation

*2.1. Average Wind Velocity of a Typhoon.* The IEC 61400-1 wind turbine design/safety standard gives the calculation method for wind velocity variation with height under normal wind [23]. The logarithmic wind profile  $\bar{U}(z)$  can be described as follows:

$$U(z) = \bar{U}(z_r) \frac{\ln(z/z_0)}{\ln(z_r/z_0)}, \quad (1)$$

where  $U(z)$  is the wind speed at height  $z$ ;  $z$  is the height above ground;  $z_0$  is the roughness length;  $z_r$  is a reference height above ground used for fitting the profile.

The calculation method for typhoon wind velocity is different from that for normal wind velocity. The existing research on various characteristics of typhoons with rough surfaces is insufficient. The Australian/New Zealand Standard [24] classifies Australia into four regions and gives each region an extreme typhoon wind velocity. According to the coefficient of wind pressure, which varies with altitude, the wind velocities at various heights can be calculated, and then the dynamic amplification factor based on the turbulence intensity can be obtained. Pang [25] believed that the range

of typhoons should be determined first when studying the average typhoon velocity problem. He also suggested that the region within 300 km of a typhoon-centre be treated as a typhoon region and that the region beyond that radius be treated as a generally strong wind region. Xu and Mu [26] used the Air Pollution Model (TAPM) and exponential law to calculate the wind profile and considered the suitable power exponent to be 0.09–0.10 if the wind speed at different heights was calculated using an exponential formula. At present, many scholars consider typhoon wind to be a steady flow; that is, the average velocity of typhoon wind does not change with time within a certain period. Chen and Xu [27, 28] analysed typhoon characteristics using empirical mode decomposition and considered that the nonstationary wind speed can be decomposed into a deterministic time-varying mean wind speed component and a Gaussian distribution stationary random process for the fluctuating wind speed component.

In this paper, the unstable wind profile [29] is used to simulate the average wind velocity of a typhoon. The formula is as follows:

$$\bar{U} = \left( \frac{u_*}{K} \right) \left[ \ln \left( \frac{z-d}{z_0} \right) + \psi_M \left( \frac{z}{l_0} \right) \right], \quad (2)$$

with

$$\psi_M \left( \frac{z}{l_0} \right) = -2 \ln \left[ \frac{(1+x_M)}{2} \right] - \ln \left[ \frac{(1+x_M^2)}{2} \right] + 2 \tan^{-1}(x_M) - \frac{\pi}{2}, \quad (3)$$

$$x_M = \left[ 1 - 15 \left( \frac{z}{l_0} \right) \right]^{1/4}.$$

Here,  $l_0$  is the Obukhov length;  $u_*$  is the friction velocity;  $K = 0.4$  is the Karman constant.

**2.2. Fluctuating Wind Velocity Simulation of a Typhoon.** The fluctuating wind is assumed to be a multivariable uniform Gaussian random process with zero-mean and composed of along-wind, across-wind, and vertical-wind components. According to the typhoon characteristics in a certain area, the proper wind spectral model can be obtained, which is the key to simulating fluctuating wind. Shi et al. [30] proposed an empirical formula for the horizontal wind velocity spectrum that does not change with altitude, according to the observed data in Shanghai from 1956. Taking into account the characteristics of the typhoon turbulence scale, which vary with altitude, at the surface boundary layer for the Shanghai district, Tian et al. [31] presented an empirical formula of horizontal wind velocity spectrum that varies with height. In this paper, the fluctuating wind velocity spectrum proposed by Hojstrup [32] is used, as shown in the following equation:

$$\frac{f S_u(f)}{u_*^2} = 0.5 n_\delta (1 + 2.2 n_\delta^{5/3})^{-1} \left( \frac{-\delta}{l_0} \right) \frac{2}{3} + 105 n (1 + 33 n)^{-5/3}. \quad (4)$$

Here,  $n = fz/\bar{U}$  is the reduced frequency;  $n_\delta = f\delta/\bar{U}$  is the reduced frequency with respect to the boundary layer thickness  $\delta$ ;  $f$  is the fluctuating wind frequency. Sharma and Richards [33] considered that when  $l_0 = -100$  m and  $\delta = 500$  m, the simulation of a typhoon is well described.

The harmonic superposition method is a standard algorithm to simulate the steady Gaussian process. Because the horizontal size of the tower is far less than the vertical size, only the vertical correlations between the calculation points are considered in this paper. Therefore, the power spectrum density function matrix of fluctuating wind can be expressed as follows:

$$S(\omega) = \begin{bmatrix} S_{11}(\omega) & & & \\ S_{21}(\omega) & S_{22}(\omega) & \text{Sym} & \\ \vdots & \vdots & \ddots & \\ S_{m1}(\omega) & S_{m2}(\omega) & \cdots & S_{mm}(\omega) \end{bmatrix}, \quad (5)$$

where  $S_{ii}(\omega)$  is the auto-power spectrum, and  $S_{ij}(\omega)$  is the cross-power spectrum, which can be calculated as follows:

$$S_{ij}(\omega) = \sqrt{S_{ii}(\omega) S_{jj}(\omega)} \rho_{ij}, \quad (6)$$

where  $\rho_{ij}$  is the coherent coefficient, and it uses the simplified expression proposed by Shiotani and Avai [34] as follows:

$$\rho_{ij} = \exp \left( -\frac{|z_i - z_j|}{L_z} \right). \quad (7)$$

Here,  $|z - z'|$  is the spatial distance between two points in the vertical direction, and  $L_z$  is usually 60 [35].

According to the theory presented by Shinozuka [36], the fluctuating wind velocity time histories  $f_j(t)$  can be simulated as follows:

$$f_j(t) = \sqrt{2(\Delta\omega)} \sum_{m=1}^j \sum_{l=1}^N |H_{jm}(\omega_{ml})| \cos[\omega_{ml}t - \theta_{jm}(\omega_{ml}) + \Phi_{ml}], \quad (8)$$

$j = 1, 2, \dots, n.$

Here,  $N$  is the division number of the fluctuating wind frequency;  $j$  is the number of points that are considered;  $\omega = (\omega_u - \omega_0)/N$  is the frequency step, with  $\omega_u$  and  $\omega_0$  as the upper limit and lower limit frequencies of fluctuating wind, respectively;  $\omega_{ml} = (l-1) \times \Delta\omega + (m/j) \times \Delta\omega$ ;  $\Phi_{ml}$  represents the uniformly distributed random numbers in  $[0, 2\pi]$ . In addition,  $H(\omega)$  is the Cholesky decomposition of the matrix of power spectrum  $S(\omega)$ , and  $\theta_{jm}(\omega)$  is the argument of  $H(\omega)$  as

$$S_{n \times n}(\omega) = H_{n \times n}(\omega) H_{n \times n}^T(\omega), \quad (9)$$

$$\theta_{jm}(\omega) = \arctan \left\{ \frac{\text{Im}[H_{jm}(\omega)]}{\text{Re}[H_{jm}(\omega)]} \right\}.$$

Here,  $H^T(\omega)$  is the transposed matrix of  $H(\omega)$ , and  $\theta_{jm}(\omega)$  is the ratio of the imaginary and real parts.

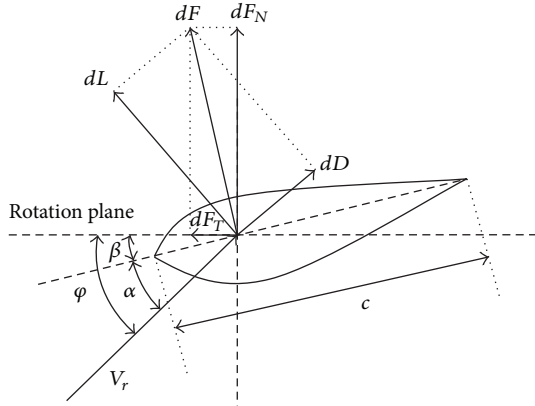


FIGURE 1: The forces on a blade element.

### 3. Calculation Methods of the Wind Load

**3.1. Blade Element Theory.** The wind turbine rotor is a complex aerodynamic system that extracts energy from the wind and converts it into mechanical power. To calculate the wind load acting on the blades, the blade element theory is widely used in the design and aerodynamic performance evaluation of wind turbine blades. The blade element theory assumes that the different spanwise elements are independent of each other and that the forces on blade elements are only determined by the lift-drag characteristic of the airfoil shape. The blade element theory simplifies the blade into a finite number of blade elements along the length of the blade. Therefore, the dynamic characteristics of the three-dimensional blade can be obtained by integration along the blade direction. Figure 1 shows a cross-section of a wind turbine blade [37].

The lift force  $dL$  per unit length is perpendicular to the relative speed  $V_r$  of the wind as follows:

$$dL = \frac{\rho c}{2} V_r^2 C_L. \quad (10)$$

The drag force  $dD$  per unit length, which is parallel to  $V_r$ , is given by

$$dD = \frac{\rho c}{2} V_r^2 C_D. \quad (11)$$

Here,  $\rho = 1.25 \text{ kg/m}^3$  is the air density;  $C_L$  and  $C_D$  are the lift and drag coefficients of the blade, respectively;  $c$  is the blade chord length. Because the forces normal to and tangential to the rotation plane are of greater concern, the lift force and drag force are projected onto these two directions, which are described by

$$\begin{aligned} dF_N &= dD \sin \varphi + dL \cos \varphi, \\ dF_T &= dL \sin \varphi - dD \cos \varphi, \\ \varphi &= \alpha + \beta, \end{aligned} \quad (12)$$

where  $\alpha$  and  $\beta$  are the attack angle and the pitch angle, respectively.

The axial thrust acts on the tower top of the wind turbine, and the rotary moment produced by the rotary tangential

force accelerates the blades. The force and moment acting on the blade can be integrated by the force and moment acting on the blade elements. The axial thrust of a blade  $F_N$  and its moment  $M_N$  can be calculated as follows:

$$\begin{aligned} F_N &= \int_0^R dF_N, \\ M_N &= \int_0^R r dF_N. \end{aligned} \quad (13)$$

The rotary tangential force of a blade  $F_T$  and its moment  $M_T$  can be calculated as follows:

$$\begin{aligned} F_T &= \int_0^R dF_T, \\ M_T &= \int_0^R r dF_T. \end{aligned} \quad (14)$$

Here,  $R$  is the length of the blade, and  $r$  is the length from the specific blade element to the root of the blade.

**3.2. Calculation Methods of the Wind Load on Tower, Nacelle, and Hub.** The relationship between the wind velocity and wind pressure under standard atmospheric pressure, normal temperature, and dry conditions can be obtained by the Bernoulli equation:

$$w = \frac{1\gamma}{2g} v^2 \approx \frac{v^2}{1630}. \quad (15)$$

Here,  $w$  is the wind pressure;  $\gamma$  is the unit weight of air;  $g = 10 \text{ m/s}^2$  is the acceleration of gravity;  $v$  is wind velocity. The wind load acting on the tower, nacelle, and hub can be calculated by the following equation:

$$F = \mu_s \cdot A \cdot w. \quad (16)$$

Here,  $A$  is the projection area of the tower, nacelle, and hub surfaces perpendicular to the wind direction, and  $\mu_s$  is the shape coefficient of the wind load.

### 4. Rain Load Simulation

There is always heavy rain associated with typhoons. The raindrops impact against the wind turbine structures with great energy, which aggravates the vibration of the wind turbines. The energy of a raindrop impact on the wind turbine structure is related to the diameter and impact speed of the raindrop [38]. Rainfall intensity is an important feature of rain, and the quantity of rainfall in one hour is taken as the rain grading standard [18], as shown in Table 1. In this paper, the dynamic results are presented only for the rainfall intensity larger than 32 mm/h.

**4.1. The Distribution of the Raindrop Size.** Throughout the descent process of rain, the large raindrops absorb the small raindrops, the volumes of the raindrops increase, and the shapes of the raindrops become ellipsoid. When the raindrop

TABLE 1: The classification of rain intensity.

Classification	Light rain	Moderate rain	Heavy rain	Rainstorm	Heavy rainstorm (weak)	Heavy rainstorm (moderate)	Heavy rainstorm (strong)	Heavy rainstorm (extreme)
Rain intensity (mm/h)	2.5	8	16	32	64	100	200	709.2

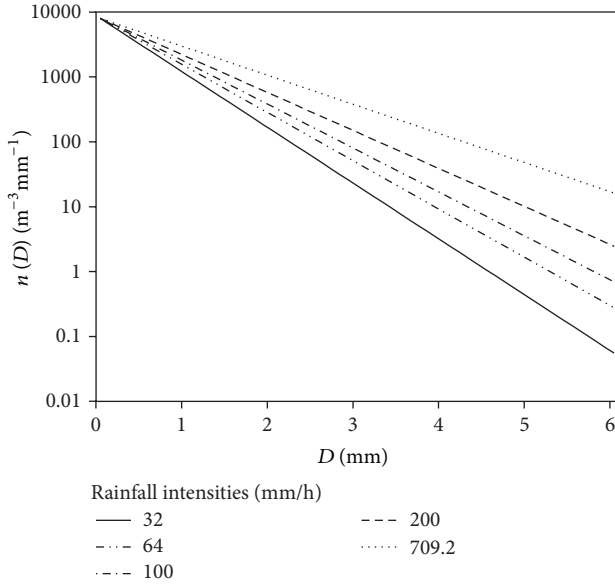


FIGURE 2: Raindrops size distribution for various rainfall intensities.

diameter increases to a certain degree, the air friction exceeds the molecular cohesion that keeps the raindrop as a whole. Then, the large raindrops split into smaller raindrops. The diameters of raindrops generally vary from 0.1 mm to 6 mm [39].

Usually the equivalent diameter (the diameter of a ball with the same volume as the raindrop) is used to describe the size of the raindrop. A large number of observations show that the raindrop size obeys a negative exponential distribution. The Marshall-Palmer exponential size distribution (referred to as M-P spectrum) is widely used [40, 41] as follows:

$$n(D) = n_0 \exp(-\Lambda D). \quad (17)$$

Here,  $D$  is the diameter of the raindrop;  $n_0 = 0.08 \text{ cm}^{-4}$  for any rainfall intensity;  $\Lambda = 4.1I^{-0.21} \text{ cm}^{-1}$  is the slope factor;  $I$  is the rainfall intensity. Figure 2 shows that the raindrop size distributions for various rainfall intensities are monotonically decreasing function of the size.

**4.2. The Occupancy of the Rainfall in the Air.** According to the raindrop size, the number of raindrops with diameters between  $[d_1, d_2]$  in a unit volume of air can be calculated as follows:

$$N(D) = \int_{d_1}^{d_2} n(D) dD, \quad (18)$$

where  $d_1 = 0.1 \text{ mm}$  and  $d_2 = 6 \text{ mm}$ .

The volume occupancy of each category of raindrops in the rain is

$$\alpha = \frac{1}{6} \pi d^3 N(D). \quad (19)$$

**4.3. The Calculation of the Rain Load.** The raindrop's velocity becomes zero very quickly when the raindrop impacts on the structure. The interaction process between the raindrops and the wind turbine structure obeys Newton's second law [22, 42]. According to the momentum theorem,

$$\int_0^\tau \vec{f}(t) dt + \int_{V_t}^0 m d\vec{v} = 0. \quad (20)$$

Here,  $\vec{f}(t)$  is the impact force vector of a raindrop;  $\vec{v}$  is the raindrop velocity vector;  $m$  is the mass of the raindrop;  $V_t$  is the raindrop velocity before acting on the structure;  $V_t$  is the value of the along-wind velocity at the corresponding height;  $\tau$  is the time interval for the raindrop speed change from  $V_t$  to zero.

The shape of the raindrop is assumed to be spherical in the descent process. The mass of a raindrop is  $m = (1/6)\rho\pi d^3$ , and  $\tau = d/2V_t$  is the actuation duration. The impact force of a single raindrop on the wind turbine in a very short time interval  $\tau$  can be calculated by the following equation:

$$F(\tau) = \frac{1}{\tau} \int_0^\tau f(t) dt = \frac{mV_t}{\tau} = \frac{1}{6\tau} \rho\pi d^3 V_t. \quad (21)$$

Here,  $\rho$  is the raindrop density, and  $d$  is the raindrop diameter.

The impact force of a raindrop, shown earlier, can be converted into a uniformly distributed load as follows:

$$F_d = \frac{F(\tau) b \alpha}{A}. \quad (22)$$

Here,  $A = \pi d^2/4$  is the action area of a raindrop;  $b$  is the width of the structure against the rain;  $\alpha$  is the volume occupancy of each category of raindrops. Substituting  $A, \alpha$  into (22) yields the following equation:

$$F(d) = \frac{2}{9} n \rho \pi d^3 V_t^2 b. \quad (23)$$

The impact force of rainfall on the structure can be expressed as forces in two directions: vertical and along-wind directions. In the vertical direction,  $V_t$  is the free-fall velocity without wind. In the along-wind direction,  $V_t$  is the wind velocity along the wind direction.

The typhoon and rainstorm sometimes occur separately and sometimes simultaneously. Similarly, the strength of the wind load and the rain load are also random. Sometimes the

strength of the wind load is very large, but the strength of the rain is not significant, and vice versa. The distribution of the frequency and intensity of the wind and rainfall have regional meteorology characteristics whose complex mechanism is beyond the scope of this study. For a feasible and simplified structural analysis, in this paper, the wind load is the main design load of the wind turbine, and the rain load only acts as an additional load. That is, only the effect of wind and rain together is considered, and the rain load is assumed to be a uniform load. This simulation method not only can address the nature of the problem but also simplifies the calculation.

## 5. Vibration Equations of Wind Turbines

*5.1. Free Vibration Analysis.* The free vibration equation of the wind turbine for eigenvalue analysis can be written as

$$M\ddot{x} + Kx = 0, \quad (24)$$

and assuming the general form of the solutions is

$$x = \varphi \sin(\omega t + \alpha), \quad (25)$$

then the eigenvalue equation of the wind turbine can be expressed as

$$|K - \omega^2 M| = 0, \quad (26)$$

where  $[M]$  and  $[K]$  are the mass matrix and stiffness matrix of a wind turbine, respectively;  $\omega$  is the frequency;  $\varphi$  is the mode shape of the wind turbine.

*5.2. Dynamic Analysis of Wind Turbines.* The vibration equation of a wind turbine under wind and rain loads can be obtained by the D'Alembert principle [43]:

$$[M] \{\ddot{u}(t)\} + [C] \{\dot{u}(t)\} + [K] \{u(t)\} = \{F_T(z, t)\} + \{F_B(z, t)\}, \quad (27)$$

where  $[M]$ ,  $[C]$ , and  $[K]$  are the mass matrix, damping matrix, and stiffness matrix of a wind turbine, respectively;  $\{\ddot{u}(t)\}$ ,  $\{\dot{u}(t)\}$ , and  $\{u(t)\}$  are the time-dependent acceleration, velocity, and displacement vectors, respectively;  $\{F_T(z, t)\}$  and  $\{F_B(z, t)\}$  are the wind load and rain load on the wind turbine tower and blades. This paper employs the Newmark method, and the dynamic analysis is performed using the finite element software ABAQUS.

## 6. Numerical Simulation Examples

The wind turbine chosen as an example in this paper is located at a coastal wind farm in Zhejiang province, China, which uses 1.5 MW wind turbines. According to the data observed by an anemometer tower, the maximum average wind speed over a 50-year return period for a 10-minute time period is 23.48 m/s, the average turbulence intensity is approximately 0.173~0.128 at the height of 10~70 m, and the surface roughness length is 0.1432. During the period 1949–2008, 41 typhoons struck the Zhejiang province [44].

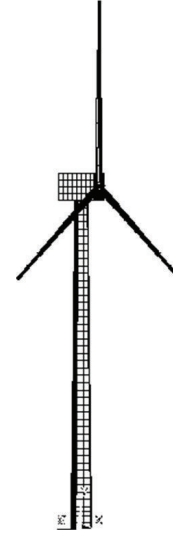


FIGURE 3: Finite element model of a wind turbine.

Therefore, the wind turbines will be at risk of damage from typhoons and rainstorms. The mean velocity at 10 m is taken as 32.7 m/s, which is the approximate wind speed of 12 typhoons.

The elastic-plastic model is established in ABAQUS to analyse the dynamic responses of the wind turbine, as shown in Figure 3. The model consists of three rotating blades connected to a nacelle, which is rigidly connected to the top of the tower [5]. The tower is modeled using shell elements while the nacelle and hub are modeled with solid elements. The connection of the nacelle and tower top is accomplished using the shell-to-solid coupling option, which allows the connection between nonconforming shell and solid models. The tower is composed of three variable cross-section steel towers for transportation and erection purposes that are bolted together by heavy flanges and bolts. The tower bottom is fully fixed at the base with no consideration of the foundation-soil interaction [45]. The main parameters of the 1.5 MW wind turbine are as follows. The tubular tower has a total height of 63 m and is formed as a truncated cone with an external diameter of 4 m at the base and 2.7 m at the top and a shell thickness of 0.022 m. The tower material is Q345E steel, and its yield stress is 325 MPa. The elastic modulus and density of the tower steel are taken as 200 GPa and 7850 kg/m<sup>3</sup>, respectively. Poisson's ratio is 0.3, and the structural damping ratio is 0.05. The masses of the nacelle and rotor system are 55.6 t and 35.6 t, respectively. Furthermore, at the bottom of the tower, a substantial door opening is considered. To clearly express the entrance door direction, a coordinate system is established. The coordinate origin is taken at the centre of the tower bottom, and 0 degrees is the direction perpendicular to the rotation plain of the blades. The direction of the entrance door is shown in Figure 4. The negative influence of this opening on the wind turbine is partly counterbalanced by heavy reinforcement along its perimeter [46].

TABLE 2: Natural frequencies of the wind turbine tower (Hz).

Modal number	Natural frequency
1	0.431
2	0.432
3	3.446
4	3.514
5	5.371
6	5.627
7	5.627
8	7.377
9	7.377
10	9.030

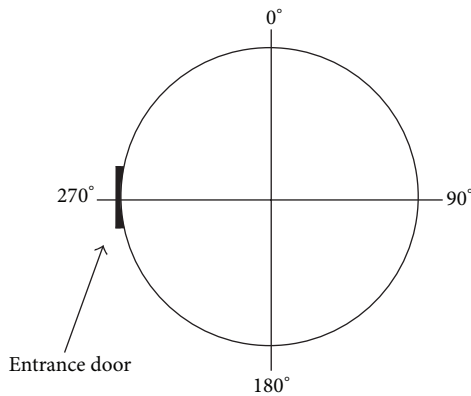


FIGURE 4: The location of the entrance door.

The blades are made of reinforced fibreglass polyester material, and the lift and drag forces are determined by the lift-drag characteristic of the airfoil shape based on the blade element theory. In the dynamic analysis using ABAQUS, the airfoil shape is simplified as equivalent rectangular cantilever beam [47], and the stiffnesses of the rectangular beam in two directions are equal to the flatwise stiffness and edgewise stiffness of the blade, respectively. The blades are attached to the hub using tie constraint where a “master” and “slave” surface is defined with all degrees of freedom for the nodes on the “slave” surface being eliminated, allowing for the two parts bonded together and no longer separate in the process of analysis. The length of each blade is 35.5 m. The mass per unit length is assumed to vary linearly from 173.89 kg/m at the base to 11.35 kg/m at the tip, and the elastic modulus along the blade and chord wise are all 17.5 GPa. Table 2 presents the natural frequencies of the wind turbine tower/nacelle model. The whole model consists of 6923 elements and 8938 nodes.

6.1. *The Random Wind Velocity Time Histories of a Typhoon.* The unstable wind profile method put forward by Stull and the logarithm law are used to calculate the variation of the average typhoon wind velocity with altitude, as shown in Figure 5. The comparison of the two wind profiles shows that the average wind velocity calculated by the unstable wind profile method is smaller than that calculated by the logarithm law at the same height, which corresponds with

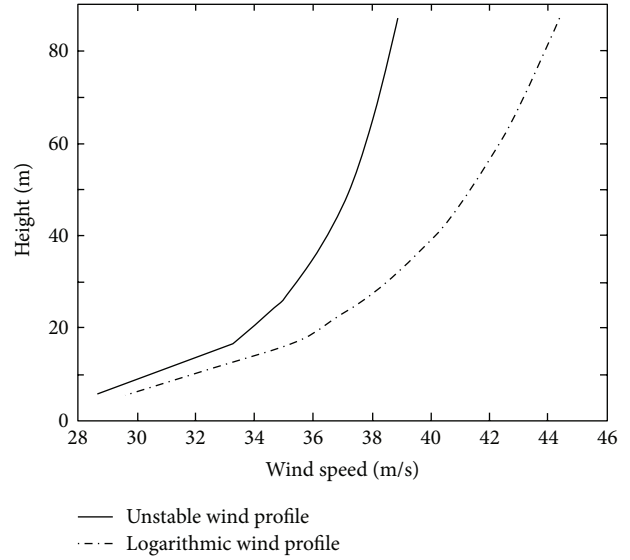


FIGURE 5: Average wind profile of a typhoon.

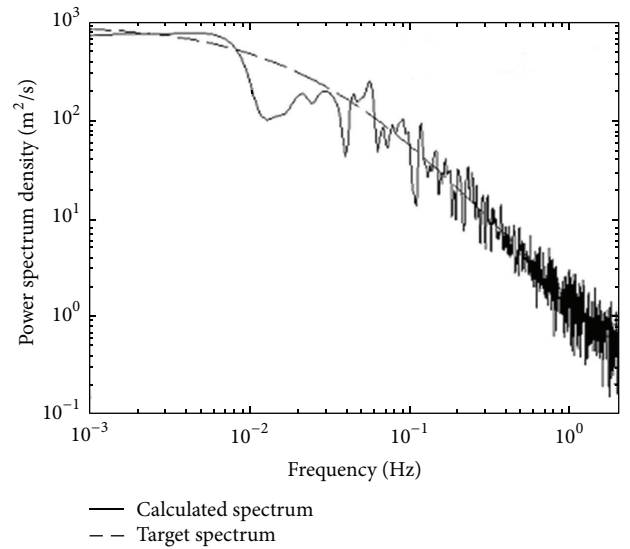


FIGURE 6: Comparison of calculated spectrum and target spectrum of typhoon fluctuating wind.

the rule that a typhoon’s strong convective motion makes the upper and lower wind velocities reach unanimity.

The typhoon spectrum proposed by Hojstrup is applied to simulate fluctuating wind. To verify the simulation results, a comparison of the calculated power spectrum and the target spectrum at a height of 65 m is illustrated in Figure 6. Comparison of the results shows that the calculated spectrum is in agreement with the trend of the target spectrum, which verifies that the simulation is accurate. The total wind velocity time histories of each point along the height direction of the wind turbine can be attained by adding the typhoon fluctuating wind and the average wind time histories. The total typhoon velocity time histories at the tower height of

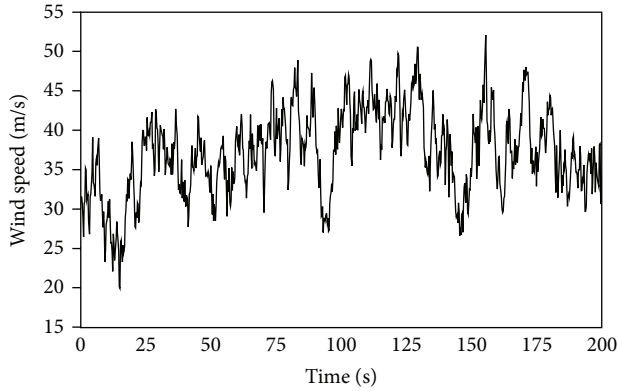


FIGURE 7: Wind velocity time history of hub on the tower.

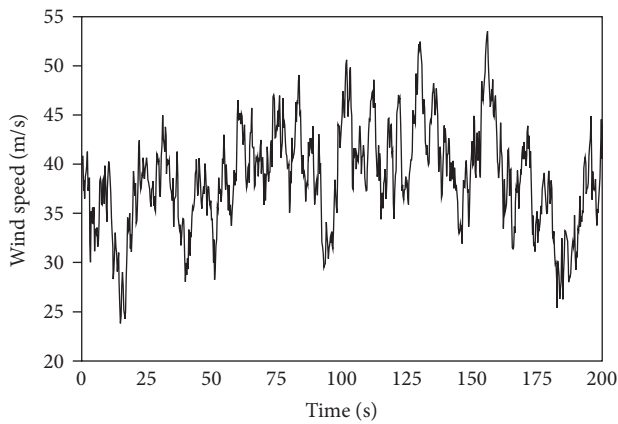


FIGURE 8: Wind velocity time history at the height of 95 m.

65 m (at the hub) and at the blade height of 95 m are shown in Figures 7 and 8, respectively.

**6.2. Dynamic Responses of the Wind Turbine under a Typhoon Alone.** In this section, the wind load on the wind turbine is calculated first. Then, the dynamic responses of the wind turbine under different conditions with the typhoon alone are calculated and compared. When the wind speed is greater than the cut-out speed of the wind turbine, the wind turbine blades stop rotating and feather. The wind direction is assumed as 0 degrees in this scenario, as shown in Figure 9(a). When the wind direction suddenly changes in a typhoon, if the nacelle cannot deflect as fast as the wind or the yaw is locked successfully, then the working conditions may appear to be different from the conventional conditions. Taking the wind direction deflections of  $90^\circ$  and  $180^\circ$  as examples, the relative position of the blades and the wind direction are shown in Figures 9(b) and 9(c).

**6.2.1. Calculation of the Wind Load.** To simplify the calculation, the tower is divided into several sections, and each blade is divided into a number of independent elements along the length. The wind load is calculated on each tower section and each blade element and then applied to the wind turbine

TABLE 3: The maximum dynamic response of the wind turbine under typhoon conditions alone.

Working conditions as shown in Figure 9	(a)	(b)	(c)
Tower top response			
Displacement (m)	-0.11	1.05	0.37
Acceleration ( $\text{m/s}^2$ )	0.52	-2.49	1.58
Tower bottom von Mises stress (MPa)	48.4	233	91.7

structure. Then, the dynamic responses of wind turbine can be calculated.

When the blades are feathering, the drag coefficient of the blade is 0.013. When the wind direction has a sudden deflection of  $90^\circ$  in a typhoon, a greater portion of the surface of the blades and nacelle will face the wind. In such a case, the drag coefficient of the blades is 1.2, and the lift force is much smaller compared to the drag force and thus can be neglected. When the wind direction has a sudden deflection of  $180^\circ$ , the drag coefficient of the blades is 0.5. The load on each blade element is calculated according to the previously described load calculation method and then is integrated to obtain the load on the entire blades. The total wind load time histories of the three blades with the same wind velocity profile, when the blades are feathering and the wind direction has a sudden deflection of  $90^\circ$  and  $180^\circ$ , are shown in Figures 10, 11, and 12. It can be observed that the sudden wind direction deflection has a significant effect on the load of the blades. The total wind load on the blades with a wind direction deflection of  $90^\circ$  is several tens times greater than the wind load with a wind direction of  $0^\circ$ , although the blades are feathering nominally.

**6.2.2. Dynamic Response Analysis of the Wind Turbine under Typhoon Conditions Alone.** With the wind load on the wind turbine, the dynamic responses can be calculated using ABAQUS software. For comparison, the maximum tower top displacement, acceleration, and tower bottom von Mises stress are presented in Table 3 when the blades are feathering and when the wind direction has a sudden deflection of  $90^\circ$  or  $180^\circ$ . Figures 13, 14, and 15 show the displacement, the acceleration responses at the tower top, and the von Mises stress at the tower bottom when the wind direction has a sudden deflection of  $90^\circ$ , as shown in Figure 9(b). The maximum displacement and acceleration at the tower top are 1.05 m and  $2.49 \text{ m/s}^2$ , and the maximum von Mises stress at the tower bottom is 233 MPa.

The calculation results also show that when the blades are feathering successfully, the wind direction is perpendicular to the rotation plane of the blades, and the windward face of the wind turbine blades is greatly reduced. In this case, the dynamic responses are relatively small. When the blades are feathering successfully, if the wind direction suddenly deflects  $90^\circ$  in a typhoon, a larger surface of the blades will face the wind and suffer greater wind load. The dynamic response is the largest in this situation. If the wind direction has a sudden deflection of  $180^\circ$  in a typhoon, the wind load on the blades only increases slightly, but the moment generated

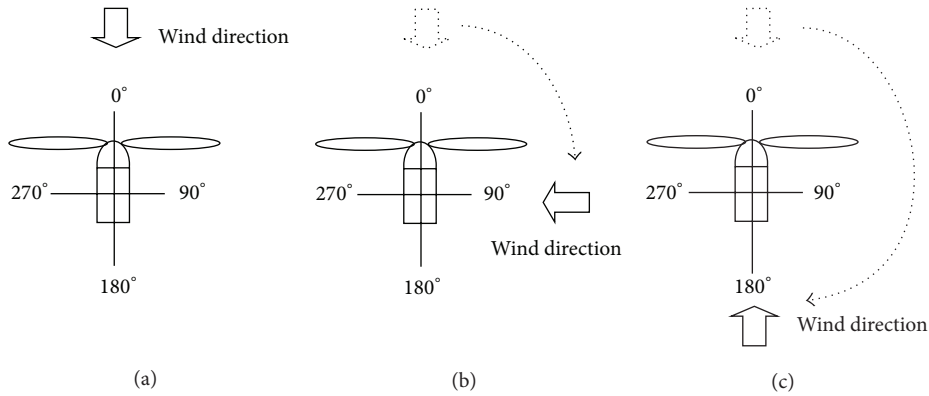


FIGURE 9: The relative position of the blades and wind direction. (a) wind direction of  $0^\circ$  with blades feathering, (b) Wind direction deflection of  $90^\circ$ , and (c) wind direction deflection of  $180^\circ$ .

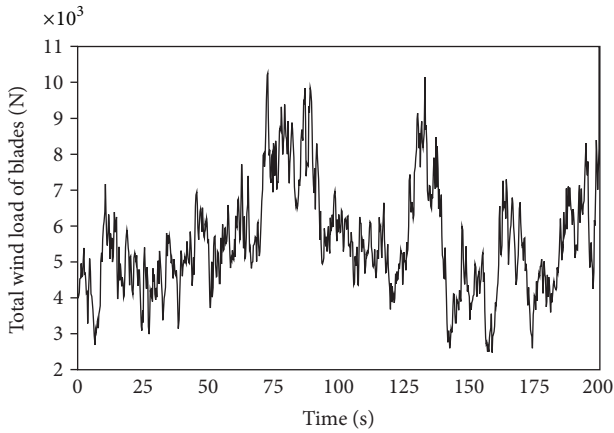


FIGURE 10: The total wind load time history of the blades with the wind turbine feathering.

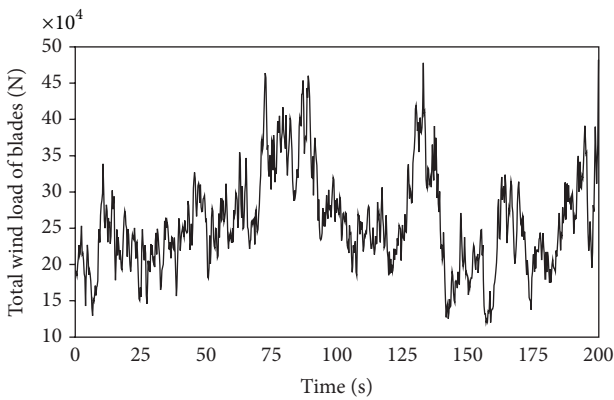


FIGURE 11: The total wind load time history of the blades with a wind direction deflection of  $90^\circ$ .

by the gravity load of the nacelle and blades will be added to that generated by the wind load in the same direction. The dynamic response of this condition is also more violent than the case in Figure 9(a).

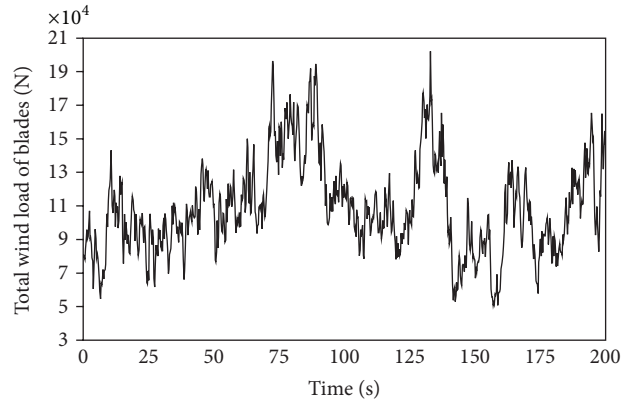


FIGURE 12: The total wind load time history of the blades with a wind direction deflection of  $180^\circ$ .

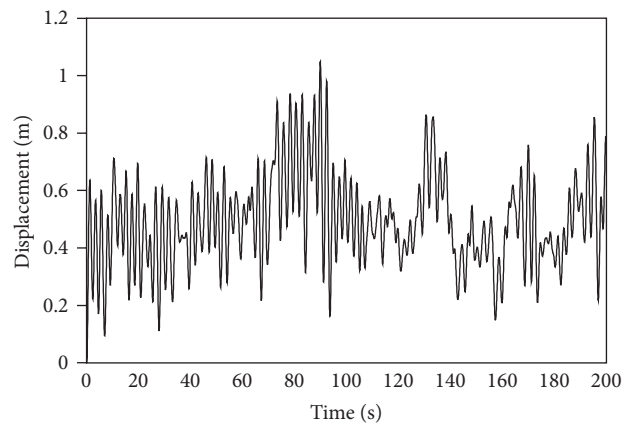


FIGURE 13: Displacement response at the tower top with a wind direction deflection of  $90^\circ$ .

### 6.3. Dynamic Responses of the Wind Turbine under Typhoon and Rain Together

6.3.1. Calculation of the Rain Load. Because the condition in which the wind direction suddenly deflects  $90^\circ$  is the most

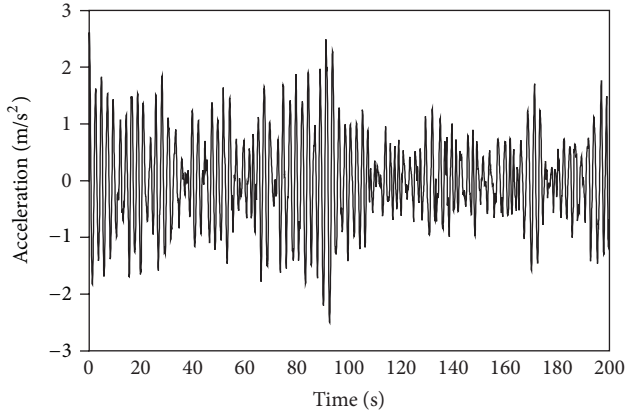


FIGURE 14: Acceleration response at the tower top with a wind direction deflection of 90°.

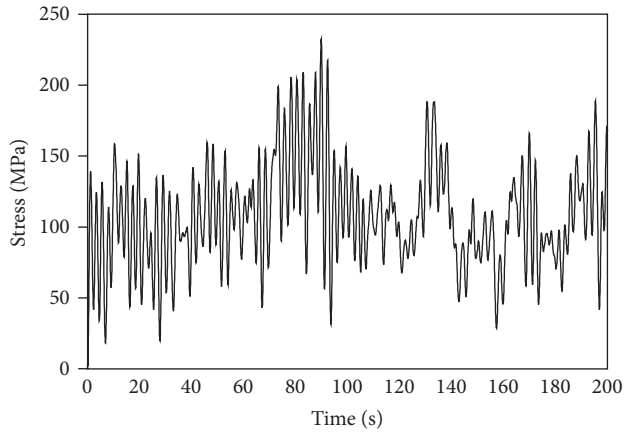


FIGURE 15: The stress at the tower bottom with a wind direction deflection of 90°.

unfavourable when the wind turbine is under the effect of a typhoon alone, only the responses with the combinations of various rainfall intensities and the wind direction deflection of 90° are computed and compared. The time histories of the rain load per unit area of the wind turbine can be calculated by (23), and Figures 16, 17, and 18 show the total rain load time histories of the wind turbine blades under the rainfall intensities of 32 mm/h, 100 mm/h, and 709.2 mm/h, respectively.

**6.3.2. Dynamic Response Analysis of the Wind Turbine under Typhoon and Rain Together.** To analyse the effect of rainfall intensities on the structural dynamic responses, dynamic analyses of the wind turbine are conducted for the working conditions shown in Table 4, in which working conditions 1, 2, 3, 4, and 5 represent the combinations of a wind direction deflection of 90° and rainfall intensities of 32 mm/h, 64 mm/h, 100 mm/h, 200 mm/h, and 709.2 mm/h, respectively. The maximum dynamic responses are presented in Table 5. The results in Table 5 are compared with the dynamic results when the wind turbine is under typhoon

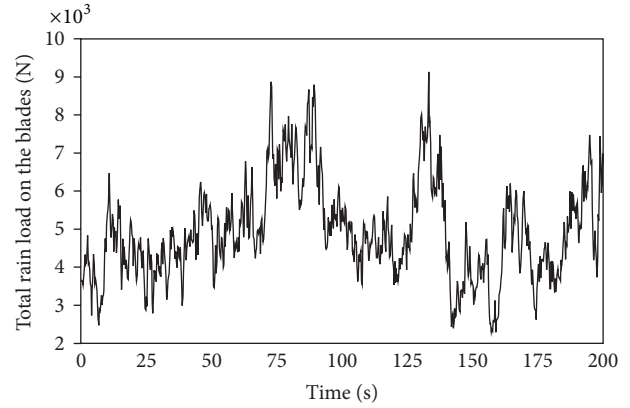


FIGURE 16: The total rain load of blades under the rainfall intensity of 32 mm/h.

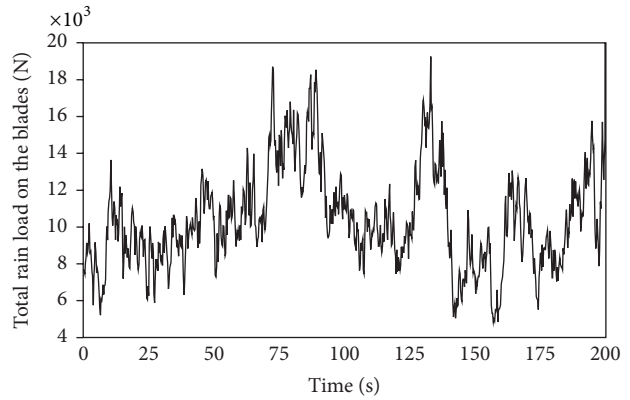


FIGURE 17: The total rain load of blades under the rainfall intensity of 100 mm/h.

TABLE 4: The combinations of a typhoon with various rainfall intensities.

Working conditions	Wind direction deflection	Average wind speed at 10 m (m/s)	Rain intensity (mm/h)
1	90°	32.7	32
2	90°	32.7	64
3	90°	32.7	100
4	90°	32.7	200
5	90°	32.7	709.2

conditions alone with a wind direction deflection of 90°, and the percentage increase is shown in Table 6.

Figures 19, 20, and 21 show the displacement, the acceleration responses at the tower top, and the von Mises stress at the tower bottom when the wind turbine is under typhoon conditions with a wind direction deflection of 90° and a rainfall intensity of 709.2 mm/h. The maximum displacement and acceleration at the tower top are 1.19 m and 2.82 m/s<sup>2</sup>, respectively, and the maximum von Mises stress at the tower bottom is 265 MPa, which have increases of 13.3%, 13.25%, and 13.7%, respectively, compared to the case with the typhoon load alone. It can be seen that the effect of the rain

TABLE 5: The maximum dynamic responses of the wind turbine under combinations of a typhoon with a wind direction deflection of 90° and various rainfall intensities.

Working conditions	1	2	3	4	5
Tower top response					
Displacement (m)	1.07	1.08	1.09	1.12	1.19
Acceleration (m/s <sup>2</sup> )	-2.54	-2.57	-2.59	-2.65	-2.82
Tower bottom von Mises stress (MPa)	237	240	242.7	248.6	265

TABLE 6: The percentage increase of the dynamic responses under typhoon and rain together compared to typhoon alone with a wind direction deflection of 90°.

Working conditions	1	2	3	4	5
Tower top response					
Displacement (m)	1.9%	3.0%	3.8%	6.3%	13.3%
Acceleration (m/s <sup>2</sup> )	2.0%	3.2%	4.0%	6.4%	13.25%
Tower bottom von Mises stress (MPa)	1.7%	3.0%	4.2%	6.7%	13.7%

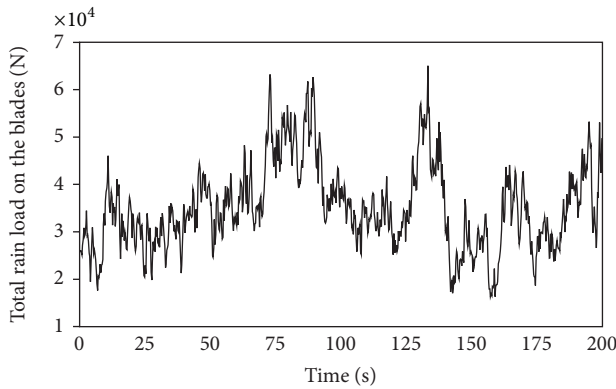


FIGURE 18: The total rain load of blades under the rainfall intensity of 709.2 mm/h.

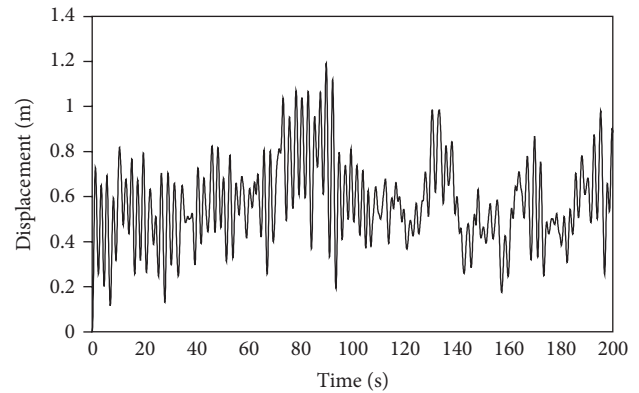


FIGURE 19: Displacement response at the tower top under the action of the typhoon and rain together.

load on the structural dynamic responses cannot be ignored and merits attention in the wind turbine design. The average wind speed of a typhoon at the height of 10 m is taken as 32.7 m/s in this numerical example, and the maximum von Mises stress at the tower bottom is less than the steel yield stress. However, the instantaneous wind speed in a practical project may be higher than that adopted in this example. We can deduce that the maximum von Mises stress at the tower bottom can exceed the steel yield stress if the wind speed further increases, which most likely contributes to the collapse of wind turbines in typhoons.

### 7. Conclusions

With the development of wind power as well as the increase of extremely violent typhoon events, wind turbines are prone to be damaged due to wind-rain loads. In this paper, a dynamic analysis method for wind turbines under typhoon and rainstorm conditions is proposed. Additionally, finite element models of the blade and the wind turbine are established. The main conclusions are as follows.

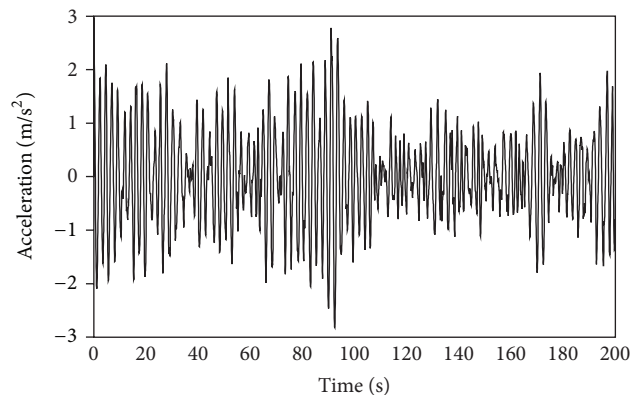


FIGURE 20: Acceleration response at the tower top under the action of the typhoon and rain together.

- (1) The average wind velocity of a typhoon is calculated by the unstable wind profile, and the fluctuating wind is simulated by the harmony superposition method. The dynamic responses of the wind turbine are

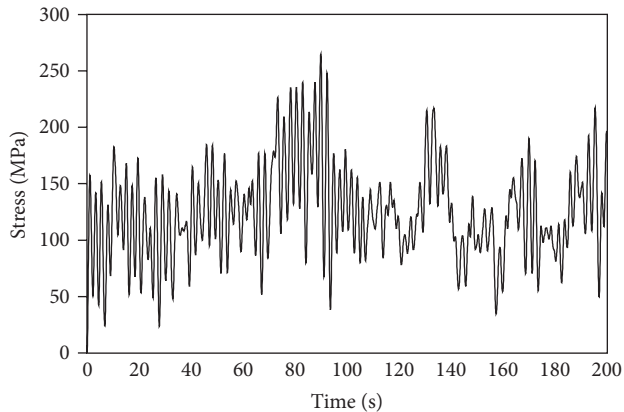


FIGURE 21: The stress at the tower bottom under the action of the typhoon and rain together.

calculated when blades are feathering as well as when the wind direction has a sudden deflection of  $90^\circ$  or  $180^\circ$  when the wind turbine blades are feathering successfully. The results show that a sudden deflection of wind direction can greatly increase both the windward area and the load on the wind turbine in a strong typhoon environment.

- (2) This paper is the first to explore the rain load on a wind turbine. The raindrop size distribution is simulated by the M-P spectrum, and the rain load time history is calculated according to the momentum theorem. The calculation method of the rain load on the blades is proposed based on the blade element theory, and the combinations of a typhoon and rain with various rainfall intensities are also presented.
- (3) The dynamic responses of the wind turbines increase after considering the effect of the rain load. Under the same wind velocity, the effect of the rain load on the dynamic responses of the wind turbine increases with increasing rainfall intensity. The maximum von Mises stress increased by 13.86% under the extreme condition, with a rainfall intensity of 709.2 mm/h. Therefore, the effect of the rain load on structural dynamic responses should also receive attention in wind turbine design.
- (4) The feathering of wind turbine blades plays a significant role in reducing the load on wind turbines in normal wind regimes. However, under the typhoon conditions, the conventional control strategies for wind turbines may need to be improved to withstand special situations, such as sudden changes of wind direction.

## Conflict of Interests

The authors declare no possible conflict of interests.

## Acknowledgment

The authors gratefully acknowledge financial support from the Chinese National Nature Science Foundation (nos. 51079127, 51179171, and 51279180).

## References

- [1] B. K. Sahu, M. Hiloidhari, and D. C. Baruah, "Global trend in wind power with special focus on the top five wind power producing countries," *Renewable and Sustainable Energy Reviews*, vol. 19, pp. 348–359, 2012.
- [2] J. F. Li, P. F. Shi, and H. Gao, *China Wind Power Outlook 2010*, Hainan Publishing House, Haikou, China, 2010, (in Chinese).
- [3] O. Kiyomiya, T. Rikiji, and P. H. A. J. M. van Gelder, "Dynamic response analysis of onshore wind energy power units during earthquakes and wind," in *Proceedings of the 12th International Offshore and Polar Engineering Conference*, pp. 520–526, Kitakyushu, Japan, May 2002.
- [4] I. Lavassas, G. Nikolaidis, P. Zervas, E. Efthimiou, I. N. Doudoumis, and C. C. Baniotopoulos, "Analysis and design of the prototype of a steel 1-MW wind turbine tower," *Engineering Structures*, vol. 25, no. 8, pp. 1097–1106, 2003.
- [5] P. J. Murtagh, B. Basu, and B. M. Broderick, "Along-wind response of a wind turbine tower with blade coupling subjected to rotationally sampled wind loading," *Engineering Structures*, vol. 27, no. 8, pp. 1209–1219, 2005.
- [6] J. Li, J. Chen, and X. Chen, "Aerodynamic response analysis of wind turbines," *Journal of Mechanical Science and Technology*, vol. 25, no. 1, pp. 89–95, 2011.
- [7] E. C. C. Choi, "Gradient height and velocity profile during typhoons," *Journal of Wind Engineering and Industrial Aerodynamics*, vol. 13, no. 1–3, pp. 31–41, 1983.
- [8] Y. L. Xu and L. D. Zhu, "Buffeting response of long-span cable-supported bridges under skew winds. Part 2: case study," *Journal of Sound and Vibration*, vol. 281, no. 3–5, pp. 675–697, 2005.
- [9] L. Zhao, Y. J. Ge, and L. D. Zhu, "Investigation of wind-induced performance about long-span bridges under typhoon climate," *Zhendong Gongcheng Xuebao/Journal of Vibration Engineering*, vol. 22, no. 3, pp. 237–245, 2009 (Chinese).
- [10] J. R. Wu, P. F. Liu, and Q. S. Li, "Effects of amplitude-dependent damping and time constant on wind-induced responses of super tall building," *Computers and Structures*, vol. 85, no. 15–16, pp. 1165–1176, 2007.
- [11] Q. S. Li and J. R. Wu, "Time-frequency analysis of typhoon effects on a 79-storey tall building," *Journal of Wind Engineering and Industrial Aerodynamics*, vol. 95, no. 12, pp. 1648–1666, 2007.
- [12] Q. S. Li, Y. Q. Xiao, J. R. Wu, J. Y. Fu, and Z. N. Li, "Typhoon effects on super-tall buildings," *Journal of Sound and Vibration*, vol. 313, no. 3–5, pp. 581–602, 2008.
- [13] S. Rose, P. Jaramillo, M. J. Small, I. Grossmann, and J. Apt, "Quantifying the hurricane risk to offshore wind turbines," *Proceedings of the National Academy of Sciences of the United States of America*, vol. 109, no. 9, pp. 3247–3252, 2012.
- [14] T. Ishihara, A. Yamaguchi, K. Takahara, T. Mekar, and S. Matsuura, "An analysis of damaged wind turbines by typhoon maemi in 2003," in *Proceedings of the 6th Asia-Pacific Conference on Wind Engineering*, pp. 1413–1428, Seoul, Korea, 2005.
- [15] L. X. Hong and B. Moller, "An economic assessment of tropical cyclone risk on offshore wind farms," *Renewable Energy*, vol. 44, pp. 180–192, 2012.

- [16] Z. Q. Li, S. J. Chen, H. Ma, and T. Feng, "Design defect of wind turbine operating in typhoon activity zone," *Engineering Failure Analysis*, vol. 27, pp. 165–172, 2012.
- [17] E. C. C. Choi, "Wind-driven rain and driving rain coefficient during thunderstorms and non-thunderstorms," *Journal of Wind Engineering and Industrial Aerodynamics*, vol. 89, no. 3–4, pp. 293–308, 2001.
- [18] S. F. Chen and X. P. Wu, "Numerical study of wind-driven rain distribution on low-rise buildings with different roof styles," in *Proceedings of the International Conference on Electric Technology and Civil Engineering (ICETCE '11)*, pp. 3282–3285, April 2011.
- [19] D. B. Xin, H. Li, L. Wang, and J. P. Ou, "Experimental study on static characteristics of the bridge deck section under simultaneous actions of wind and rain," *Journal of Wind Engineering and Industrial Aerodynamics*, vol. 107–108, pp. 17–27, 2012.
- [20] H. N. Li and H. F. Bai, "High-voltage transmission tower-line system subjected to disaster loads," *Progress in Natural Science*, vol. 16, no. 9, pp. 899–911, 2006.
- [21] H. N. Li and H. F. Bai, "Dynamic behavior and stability of transmission tower-line system under wind (rain) forces," *Tumu Gongcheng Xuebao/China Civil Engineering Journal*, vol. 41, no. 11, pp. 31–38, 2008 (Chinese).
- [22] H. N. Li, Y. M. Ren, and H. F. Bai, "Rain-wind-induced dynamic model for transmission tower system," *Proceedings of the CSEE*, vol. 27, no. 30, pp. 43–48, 2007.
- [23] IEC 61400-1 Ed.3, "International electro-technical commission," Wind turbines-Part 1: Design requirements, 2005.
- [24] AS/NZS 1170.2, "Australian/New Zealand Standard," Structural design actions-Part 2: Wind actions, 2002.
- [25] J. B. Pang, *Field investigation and wind tunnel simulation of strong wind characteristics in coastal and mountainous regions [Ph.D. thesis]*, Tongji University, 2006, (in Chinese).
- [26] J. L. Xu and H. Z. Mu, "Numerical simulation and analysis of offshore wind field features in shanghai under the influence of typhoon," *Journal of Tropical Meteorology*, vol. 25, no. 3, pp. 281–286, 2009.
- [27] J. Chen and Y. L. Xu, "On modelling of Typhoon-induced non-stationary wind speed for tall buildings," *The Structural Design of Tall and Special Buildings*, vol. 13, no. 2, pp. 145–163, 2004.
- [28] Y. L. Xu and J. Chen, "Characterizing nonstationary wind speed using empirical mode decomposition," *Journal of Structural Engineering*, vol. 130, no. 6, pp. 912–920, 2004.
- [29] R. B. Stull, *An Introduction to Boundary Layer Meteorology*, Kluwer Academic, Boston, Mass, USA, 1988.
- [30] Y. Shi, W. Lu, and Y. Zhong, "The study of typhoon characteristics in the Shanghai region," in *Proceedings of the second National Conference on Wind Effect*, 1988, (in Chinese).
- [31] P. Tian, L. Feng, and Q. Ye, "The study of typhoon wind spectrum," in *Proceedings of the 2nd National Conference on Wind Effect*, 1988, (in Chinese).
- [32] J. Hojstrup, "Velocity spectra in the unstable planetary boundary layer (Kansas, Minnesota)," *Journal of the Atmospheric Sciences*, vol. 39, no. 10, pp. 2239–2248, 1982.
- [33] R. N. Sharma and P. J. Richards, "A re-examination of the characteristics of tropical cyclone winds," *Journal of Wind Engineering and Industrial Aerodynamics*, vol. 83, pp. 21–33, 1999.
- [34] M. Shiotani and H. Avai, "Lateral structures of gusts in high winds," in *International Conference on Wind Effects on Buildings and Structures*, 1967.
- [35] X. T. Zhang, "The spatial correlations and conversion factor of wind -excited random vibration for towers and tall buildings," *Journal of Tongji University*, vol. 2, 1982 (Chinese).
- [36] M. Shinozuka, "Simulation of multivariate and multidimensional random process," *Journal of the Acoustical Society of America*, vol. 49, no. 1, pp. 357–367, 1971.
- [37] A. Ahlström, *Aeroelastic simulation of wind turbine dynamics [Ph.D. thesis]*, Royal Institute of Technology, Stockholm, Sweden, 2005.
- [38] M. Abuku, H. Janssen, J. Poesen, and S. Roels, "Impact, absorption and evaporation of raindrops on building facades," *Building and Environment*, vol. 44, no. 1, pp. 113–124, 2009.
- [39] W. L. Chen and Z. L. Wang, "The trial research on the behaviours of artificial rainfall by simulation," *Bulletin of Soil and Water Conservation*, vol. 11, no. 2, pp. 55–62, 1991.
- [40] J. Marshall and W. Palmer, "The distribution of raindrops with size," *Journal of Meteorology*, vol. 5, pp. 165–166, 1948.
- [41] E. Villermaux and B. Bossa, "Single-drop fragmentation determines size distribution of raindrops," *Nature Physics*, vol. 5, no. 9, pp. 697–702, 2009.
- [42] L. Gong, "Erosion calculation of raindrops' Kinetic energy of loess plateau's rainfall," *Journal of Lanzhou Jiaotong University (Nature Sciences)*, vol. 24, no. 4, pp. 43–45, 2005 (Chinese).
- [43] P. J. Murtagh, B. Basu, and B. M. Broderick, "Along-wind response of a wind turbine tower with blade coupling subjected to rotationally sampled wind loading," *Engineering Structures*, vol. 27, no. 8, pp. 1209–1219, 2005.
- [44] W. H. Fang, X. C. Zhong, Y. Qiao, W. Lin, H. Xu, and Y. Li, "Estimation of rural residential building vulnerability to tropical cyclone hazards by insurance claim data: case study in Zhejiang province of China," *Journal of Beijing Normal University (Nature Science)*, vol. 47, no. 4, pp. 409–414, 2011.
- [45] J. Li, J. Chen, and X. Chen, "Aerodynamic response analysis of wind turbines," *Journal of Mechanical Science and Technology*, vol. 25, no. 1, pp. 89–95, 2011.
- [46] N. Bazeos, G. D. Hatzigeorgiou, I. D. Hondros, H. Karamaneas, D. L. Karabalis, and D. E. Beskos, "Static, seismic and stability analyses of a prototype wind turbine steel tower," *Engineering Structures*, vol. 24, no. 8, pp. 1015–1025, 2002.
- [47] J. Li, J. Chen, and X. Chen, "Dynamic characteristics analysis of the offshore wind turbine blades," *Journal of Marine Science and Application*, vol. 10, no. 1, pp. 82–87, 2011.

## Research Article

# Novel Modified Elman Neural Network Control for PMSG System Based on Wind Turbine Emulator

**Chih-Hong Lin**

*Department of Electrical Engineering, National United University, Miao Li 360, Taiwan*

Correspondence should be addressed to Chih-Hong Lin; [jhlin@nuu.edu.tw](mailto:jhlin@nuu.edu.tw)

Received 24 December 2012; Accepted 22 March 2013

Academic Editor: Shengyong Chen

Copyright © 2013 Chih-Hong Lin. This is an open access article distributed under the Creative Commons Attribution License, which permits unrestricted use, distribution, and reproduction in any medium, provided the original work is properly cited.

The novel modified Elman neural network (NN) controlled permanent magnet synchronous generator (PMSG) system, which is directly driven by a permanent magnet synchronous motor (PMSM) based on wind turbine emulator, is proposed to control output of rectifier (AC/DC power converter) and inverter (DC/AC power converter) in this study. First, a closed loop PMSM drive control based on wind turbine emulator is designed to generate power for the PMSG system according to different wind speeds. Then, the rotor speed of the PMSG, the voltage, and current of the power converter are detected simultaneously to yield better power output of the converter. Because the PMSG system is the nonlinear and time-varying system, two sets online trained modified Elman NN controllers are developed for the tracking controllers of DC bus power and AC power to improve output performance of rectifier and inverter. Finally, experimental results are verified to show the effectiveness of the proposed control scheme.

## 1. Introduction

Since the petroleum is gradually exhausting and environmental protection is progressively rising, the usage of the clean energy sources such as wind, photovoltaic, and fuel cells has become very important and quite popular in electric power industries. Clean energy sources such as wind, photovoltaic, and fuel cells can be interfaced to a multilevel converter system for a high power application [1–3].

Wind turbine which acted as sources of energy has progressively increased in the whole earth. The various control methods and convert technologies of wind energy conversion systems are fast developed in energy conversion application. The PM synchronous generator system has been used for wind power generating system due to many advantages such as simpler structure, better reliability, lower maintenance, and higher efficiency [4–8]. Therefore, the PM synchronous generator generation system stands for a significant trend in progress of wind power applications [4–8]. The output power behavior of wind turbine is nonlinear. The provided power of vertical-axis turbines is very sensitive to the load variation due to different structure effect [4–8]. Thus, the control of operating point is indispensable for maximum output power. The controllable rectifier is used to convert

varied AC voltage generated by PM synchronous generator into DC bus voltage. Then, the controllable inverter is used to convert DC bus voltage into AC at a fixed frequency in order to provide for the stand alone or grid applications of electrical utilizations. The major purposes of utilizing wind turbines are to extract maximum power of turbine and deliver appropriate energy to stand alone power or grid power. According to these purposes, the better structure of the power conversion in wind turbines is the AC to DC to AC power converter [9–12]. Reference [11] proposes the intelligent control of a wind-turbine emulator and an induction-generator (IG) system with an AC/DC power converter using a radial basis function network (RBFN). An on-line trained RBFN is developed for the tracking controller of DC-link power to improve the control performance. Reference [12] proposes a radial basis function network (RBFN) controlled three-phase IG system using AC/DC and DC/AC power converters. Two online trained RBFNs using backpropagation learning algorithm with improved particle swarm optimization (IPSO) are used as the regulating controllers for both the DC-link voltage and the AC line voltage of the DC/AC power inverter. The IPSO is adopted in this study to adapt the learning rates in the backpropagation process of the RBFNs to improve the learning capability.

The Elman neural network (NN) is a partial recurrent network model that was first proposed by Elman [13]. Typical Elman NN has one hidden layer with delayed feedback. The Elman NN is capable of providing the standard state-space representation for dynamic systems. The Elman NN can be considered to be a special type of recurrent neural network with feedback connections from the hidden layer to the context layer. The context layer is an additional layer that is used as an extra memory to memorize previous activations of the hidden neurons and to feed all the hidden neurons after the one-step time delay. Therefore, compared with the general recurrent neural networks, Elman NN has a special explicit memory to store the temporal information. Due to the context neurons, it has certain dynamical advantages over static neural network [14–16] and it also has been widely applied in dynamical systems identification and control [17–20]. Generally, Elman NN can be considered to be a special kind of feed-forward neural network with additional memory neurons [13]. Furthermore, the Elman NN can approximate high-order systems with high precision, and its converge speed is fast. Reference [20] proposes a field-programmable gate array (FPGA)-based Elman NN control system to control the mover position of a linear ultrasonic motor (LUSM). A piecewise continuous function is adopted to replace the sigmoid function in the hidden layer of the ENN to facilitate implementation of the FPGA chip hardware in order to reduce cost and raise high performance.

The recurrent neural network has received increasing attention due to its structural advantage in nonlinear system modeling and dynamic system control [21–25]. The most important characteristic of the recurrent neural network is its self-connection to memorize feedback information of the historical influence in the same neuron. Moreover, in the general recurrent neural networks, the specific self-connection feedback of the hidden neuron or output neuron is responsible for memorizing the specific previous activation of the hidden neuron or output neuron and feeding itself only. Therefore, the outputs of the other neurons have no ability to affect the specific neuron. However, in the complicated nonlinear dynamic system such as PMSG system direct-driven by PMSM, the friction torque, various wind, and external nonlinear interference are always a factor. Hence, if each neuron in the recurrent neural networks is considered as a state in the nonlinear dynamic systems, the self-connection feedback type is unable to approximate the dynamic systems efficiently. On the other hand, the feedbacks in Elman NN not only are self-connecting but they also store in the context neurons and feed all the hidden neurons. Thus, the structure of Elman NN is more powerful than the general recurrent neural networks for dealing with time varying, and nonlinear dynamic systems can be approximated efficiently with the additional context layer. In order to improve the ability of identifying high-order systems, some modified Elman NN [26–28] have been proposed recently, which proved to have more advantages than the basic Elman NNs, including a better performance, higher accuracy, dynamic robustness, and a fast transient performance. The modified Elman neural network adopted in this paper has not only the feedback connection from the context layer in the hidden layer but also

the delay feedback connection from the output layer in the input layer to raise control and transient performance.

Since the PMSGs have robust construction, lower initial and lower maintenance cost, PMSG are suitable for stand alone or grid power sources in small wind energy application. Therefore a PMSM direct-drive PMSG system using the two sets of the same modified Elman NN controllers is introduced as the adjusting controllers for both the DC bus voltage of the rectifier and the AC 60 Hz line voltage of the inverter in this study. Two online trained modified Elman NNs are introduced as the adjusting controllers for both the DC bus voltage of the controllable rectifier and the AC 60 Hz line voltage of the controllable inverter. Moreover, the training algorithms of two sets of the same online trained modified Elman NNs based on backpropagation are derived to train the recurrent weights, connective weights, translations, and dilations. Additionally, for the comparison of the control performance, the proportional integral (PI) controller can be also executed in the PMSG system. However, the control gains of the PI controller are obtained by trial and error method which is very time-consuming in practical applications. Due to the PMSG system with many uncertainties, adjusted capacity and tracking capacity of output voltage controlled by using the PI controller is less improved. To raise the desired robustness and overcome the above problem, the modified Elman NN controller is proposed to control output DC bus voltage of the rectifier produced by PMSM direct-driven PMSG system and control output voltage of the inverter provided by DC bus power. In the proposed modified Elman NN controller, the recurrent weights, connective weights, translations, and dilations are trained online via learning algorithm. Meanwhile, to demonstrate better dynamic characteristics of the proposed controller, comparative studies with the PI controller and the conventional NN controller are demonstrated by experimental results. Therefore, the control performance of the proposed modified Elman NN control system is much improved and can be verified by some experimental results.

This paper is organized as follows. The configuration of PMSG system is reviewed in Section 2. The novel modified Elman NN control system design is presented in Section 3. Experimental results are illustrated in Section 4. Some conclusions are given in Section 5.

## 2. Configuration of PMSG System

The variable speed wind turbine of the PMSG system direct-driven by PMSM is a complex electromechanical system, which includes the mechanical components and the PMSG. The description of these components is presented as follows.

*2.1. Model of Wind Turbine.* The characteristic curve of the wind power versus rotor speed for model of wind turbine at different wind speeds in steady state shown in Figure 1 is very important for PMSG system direct-driven by PMSM. The power specification of the adopted wind turbine is the 1.5 kW in this paper. Its diameter is 2 m. It is the three-blade horizontal axis type. It is capable of obtaining the working point of the wind turbine that used the intersection point of the load characteristic curve and the turbine characteristic

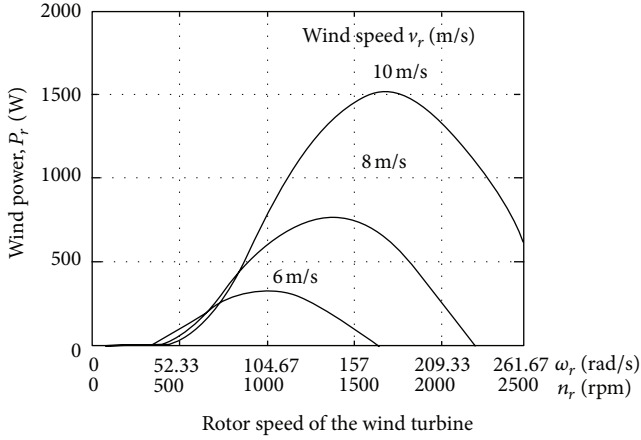


FIGURE 1: Characteristic curves of wind power versus rotor speed for wind turbine model at different wind speeds.

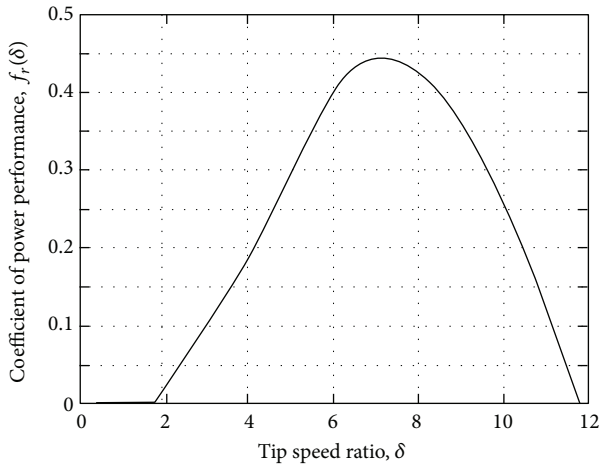


FIGURE 2: Characteristic curve of coefficient  $f_r(\delta)$  of power performance versus tip ratio  $\delta$  for wind turbine.

curve at a designated wind speed. It is a very important characteristic curve that the shaft power of the wind turbine relates to the wind speed  $v_1$  and rotor speed  $\omega_r$  to the maximum power tracking in Figure 1. For convenient usage and application, the characteristic curve shown in Figure 2 can also be expressed as the characteristic curve of the wind turbine model. It represents relationship curve between coefficient  $f_r(\delta)$  of power performance and tip speed ratio  $\delta$ . According to aerodynamic principle [1, 4–7], the tip speed ratio  $\delta$  of the wind turbine can be represented as

$$\delta = \frac{d_r \omega_r}{v_r}, \quad (1)$$

where  $\delta$  is the tip speed ratio of the wind turbine,  $d_r$  is the rotor radius of the wind turbine in meter,  $\omega_r$  is the rotor speed of the wind turbine in rad/s, and  $v_r$  is the wind speed in m/s. The output mechanical power  $P_r$  of the wind turbine can be expressed as [1, 4–7]

$$P_r = \frac{\rho_r A_r f_r(\delta) v_r^3}{2} = \frac{\rho_r A_r f_r(\delta) d_r^3 \omega_r^3}{(2\delta^3)}, \quad (2)$$

where  $\rho_r$  is the density of air in  $\text{kg/m}^3$ , and  $A_r$  is the undraped area in  $\text{m}^2$ . The generated torque of the wind turbine for different wind speeds can be obtained from the  $f_r(\delta) - \delta$  curve in modeling usage. It is a very important case that the aerodynamic efficiency is maximum at the optimum tip speed ratio. The produced torque of the wind turbine can be indicated as follows [1, 4–7]:

$$T_r = \frac{P_r}{\omega_r} = \frac{\rho_r A_r f_r(\delta) v_r^3}{(2\omega_r)} = \frac{\rho_r A_r d_r^3 f_r(\delta) \omega_r^2}{(2\delta^3)}, \quad (3)$$

where  $T_r$  is the produced torque of the wind turbine in N-m. A block diagram for the wind turbine model is shown in Figure 3. The block diagram shown in Figure 3 is to clearly describe the function between the input variable and output variable of the model.

Since the rotor of the wind turbine and the rotor of the PMSG are directly coupled through iron coupler, the mechanical angular speed of the rotor of the wind turbine is the same as the mechanical angular speed of the rotor of the PMSG for neglecting the stiffness of the wind turbine and the PMSG. From [29], the mechanical dynamic equation of torque, which the produced torque  $T_r$  of the wind turbine subtract to the electromagnetic torque  $T_{er}$  of the PMSG, can be represented as

$$T_r - T_{er} = J_r \frac{d\omega_r}{dt} + B_r \omega_r, \quad (4)$$

$$\omega_{er} = \frac{P\omega_r}{2},$$

where  $J_r$  is the total moment of inertia in the direct-decoupled system of the wind turbine and the PMSG;  $B_r$  is the total viscous friction coefficient in the direct-decoupled system of the wind turbine and the PMSG,  $\omega_{er}$  is the electrical angular speed of rotor, and  $P$  is the number of poles of the PMSG.

**2.2. Wind Turbine Emulator Based on PMSM.** The wind turbine emulator, which is proposed in [4–10], is adopted in this study in order to emulate the wind turbine. Additionally, the adopted field-oriented controlled PMSM can be emulated the power speed characteristic curve of a wind turbine in this paper. In addition, a closed-loop robust speed controller, which can fight the intrinsic nonlinear and time-varying characteristic of the PMSM drive, is adopted to adjust the rotor speed with the relevant wind speed in order to emulate the wind variation.

**2.3. Field-Oriented Controlled PMSG System.** The voltage equations for the PMSG in the rotating reference frame can be indicated as follows [1, 7–10]:

$$v_{q1} = -R_{s1} i_{q1} - L_{q1} \dot{i}_{q1} - \omega_{er} L_{d1} i_{d1} + \omega_{er} \lambda_{pm} \quad (5)$$

$$v_{d1} = -R_{s1} i_{d1} - L_{d1} \dot{i}_{d1} + \omega_{er} L_{q1} i_{q1},$$

where  $v_{d1}$  is the  $d$ -axis stator voltage,  $v_{q1}$  is the  $q$ -axis stator voltage,  $i_{d1}$  is the  $d$ -axis stator current,  $i_{q1}$  is the  $q$ -axis stator current,  $L_{d1}$  is the  $d$ -axis stator inductance,  $L_{q1}$  is the  $q$ -axis

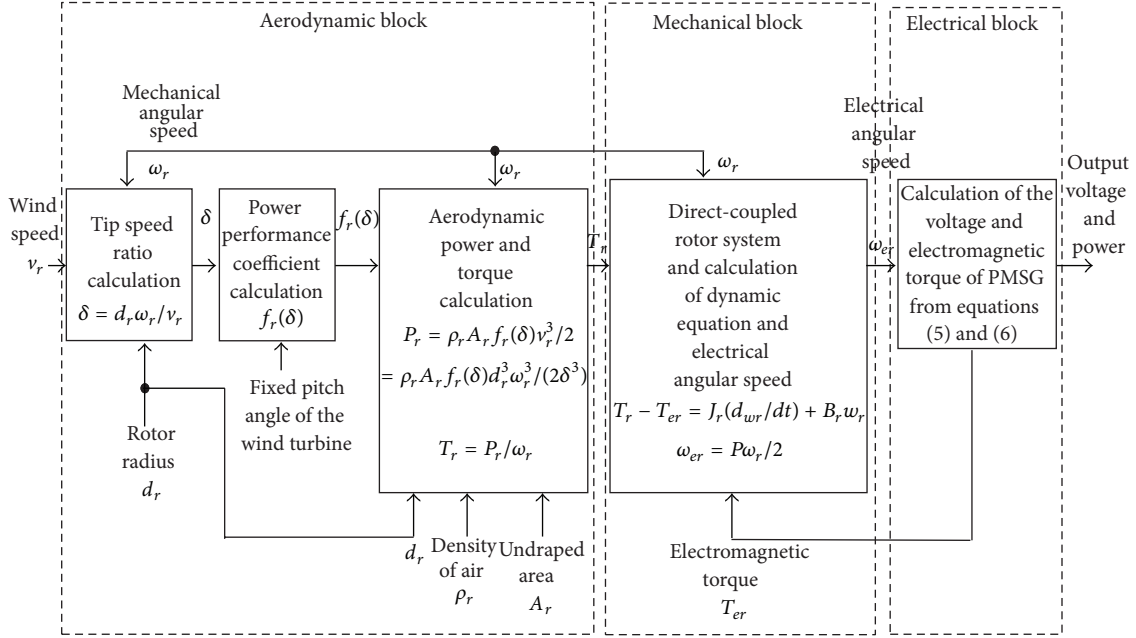


FIGURE 3: Block diagram for the wind turbine model.

stator inductance, and  $R_{s1}$  is the stator resistance. A field-oriented control is adopted in [7–10]. By using the field-oriented control, the  $d$ -axis stator current can be set zero, that is,  $i_d = 0$ . Moreover, the electromagnetic torque of the PMSG can be expressed as

$$T_{er} = \frac{3P}{2} \left[ \lambda_{pm} i_{q1} - (L_{d1} - L_{q1}) i_{d1} i_{q1} \right] = \frac{3}{4} \lambda_{pm} i_{q1} = K_t i_{q1}, \quad (6)$$

where  $\lambda_{pm}$  is the permanent magnet flux linkage, and  $K_t = 3P\lambda_{pm}/4$  is the torque constant. For convenient analysis, the field-oriented controlled PMSG system is adopted. To emulate the operation of the wind turbine, the primary machine has adopted PM synchronous motor which directly mounted to PMSG. The control principle of the PMSG system is based on field orientation. Due to  $L_{d1} = L_{q1}$  and  $i_{d1} = 0$  in PMSG system, the second term of (6) is zero. Moreover,  $\lambda_{pm}$  is constant for a field orientation control of PMSG system. The electromagnetic torque  $T_{er}$  is a function of  $i_{q1}$ . The electromagnetic torque  $T_{er}$  is linearly proportional to  $q$ -axis current  $i_{q1}$ . When the  $d$ -axis rotor flux is constant, the maximum electromagnetic torque per ampere can be reached for the field-oriented control at the  $T_{er}$  proportional to the  $i_{q1}$ .

**2.4. PMSG System.** The control block diagram of the two sets of the same four-layer modified Elman NNs controlled PMSG direct-driven PMSG system is shown in Figure 4. The wind pattern can be acquired by appropriately programming the PMSG speed. The AC power of variable frequency and voltage generated by the PMSG system is rectified to DC power by controllable rectifier. The power converts of the PMSG system direct-driven by a PMSG consist of two field-oriented institutions, two current control loops, two sine pulse-width-modulation (SPWM) control circuits, two

interlock and isolated circuits, and two IGBT power modules for rectifier and inverter. The DC bus voltage of the PMSG system directly driven by a PMSG via controllable rectifier can be controlled by using the first of modified Elman NN controller. Then, the inverter, which is controlled by using the second of modified Elman NN controller based on field-oriented control, can convert the DC bus voltage into the AC 60 Hz line voltage to provide for the stand-alone load. The specification of PMSG is a three-phase four-pole 1.5 kW 220 V 10 A 2000 rpm type for experimental test in this study. The electric parameters of the PMSG are  $R_{s1} = 0.2 \Omega$ ,  $L_{d1} = L_{q1} = 6$  mH, and  $L_m = 6.2$  mH. The specification of three-phase PMSG which acted as prime machine is a 1 kW 220 V 7 A 2000 rpm type. In practical applications, the pure differentiator may amplify the high-frequency noise, so the stability of the closed-loop PMSG drive system will be greatly affected. Thus, a filter is implemented as an alternative for the pure differentiators shown in Figure 4. It is designed to behave as a pure differentiator for the main low-frequency dynamic signal and become a low-pass filter for the high-frequency signals.

The output voltages of rectifier and inverter controlled by two sets of the same modified Elman NN controllers were implemented by using two independent sets TMS320C32 DSP control system in Figure 4, where  $\theta_r$  is the rotor position of the PMSG;  $i_{dr}^*$  is the  $d$  axis control current of the rectifier;  $i_{qr}^*$  is the  $q$  axis control current of the rectifier;  $i_{ar}^*$ ,  $i_{br}^*$  and  $i_{cr}^*$  are the desired phase currents of the PMSG in phases  $ar$ ,  $br$ , and  $cr$ , respectively;  $i_{ar}$ ,  $i_{br}$ , and  $i_{cr}$  are the actual measured phase currents of the PMSG in phases  $ar$ ,  $br$ , and  $cr$ , respectively;  $T_{ar}$ ,  $T_{br}$ , and  $T_{cr}$  are the SPWM control signals of the rectifier in phases  $ar$ ,  $br$ , and  $cr$ , respectively;  $V_d$  is the actual measured magnitude of the DC bus voltage in output end of the rectifier;  $V_d^*$  is the desired magnitude of the DC

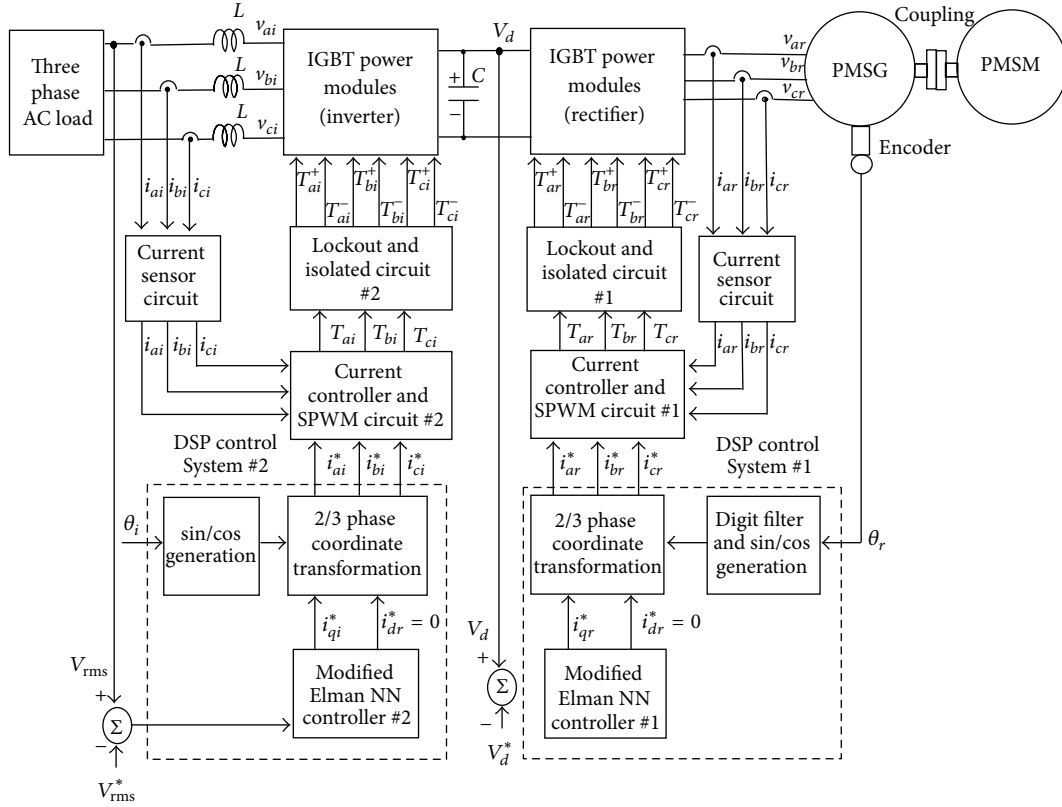


FIGURE 4: System configuration of the two sets of the same modified Elman NNs controlled PMSG system direct-driven by PMSM with rectifier and inverter.

bus voltage in output end of the rectifier;  $i_{di}^*$  is the  $d$  axis control current of the inverter;  $i_{qi}^*$  is the  $q$  axis control current of the inverter;  $\theta_i$  is the electric angular angle of the inverter which integrates the command electric angular frequency with respect to  $t$ ;  $i_{ai}^*$ ,  $i_{bi}^*$  and  $i_{ci}^*$  are the desired phase currents of the inverter in phases  $ai$ ,  $bi$ , and  $ci$ , respectively;  $i_{ai}$ ,  $i_{bi}$ , and  $i_{ci}$  are the actual measured phase currents of the inverter in phases  $ai$ ,  $bi$ , and  $ci$ , respectively;  $v_{ai}$ ,  $v_{bi}$ , and  $v_{ci}$  are the actual measured phase voltages of the inverter in phases  $ai$ ,  $bi$ , and  $ci$ , respectively;  $T_{ai}$ ,  $T_{bi}$ , and  $T_{ci}$  are the SPWM control signals of the inverter in phases  $ai$ ,  $bi$ , and  $ci$ , respectively;  $V_{rms}$  is the actual root-mean-square magnitude of the AC 60 Hz line voltage in output end of the inverter;  $V_{rms}^*$  is the desired root-mean-square magnitude of the AC 60 Hz line voltage in output end of the inverter.

### 3. Novel Modified Elman NN Controller

3.1. Description of Modified Elman NN. In the proposed two sets of the same four-layer modified Elman NNs with input layer using feedback signals from output layer are taken into account to result in better learning efficiency. The architecture of the two sets of the same four-layer modified Elman NNs, which consists of the first layer (the input layer), the second layer (the hidden layer), the third layer (the context layer), and the fourth layer (the output layer), is shown in Figure 5. The exciting functions and signal propagations of nodes in

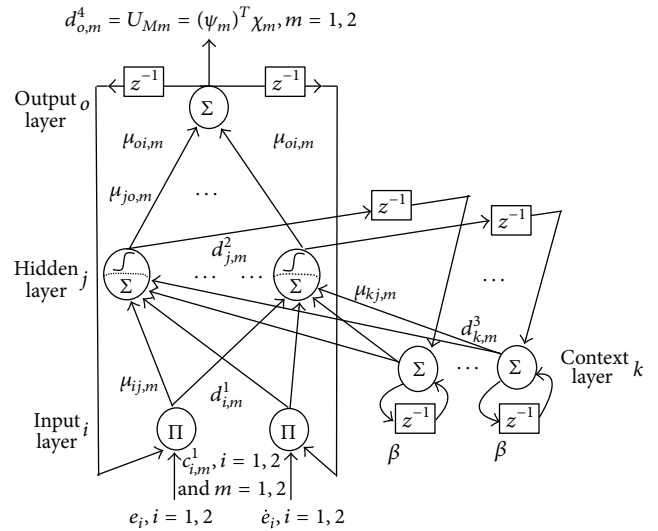


FIGURE 5: Structure of the two sets of the same four-layer novel modified Elman NNs.

each layer of the modified Elman NN can be described as follows.

3.1.1. First Layer: Input Layer. Each node  $i$  in this layer is indicated by using,  $\Pi$  which multiplies by each other between each other for input signals. Then outputs signals are

the results of product. The input and the output for each node  $i$  in this layer are expressed as

$$\begin{aligned} \text{nod}_{i,m}^1(N) &= \prod_{o,m} c_{o,m}^1(N) \cdot \mu_{oi,m} \cdot d_{o,m}^4(N-1), \\ d_{i,m}^1(N) &= g_{i,m}^1(\text{nod}_{i,m}^1(N)) \\ &= \text{nod}_{i,m}^1(N), \quad i = 1, 2, \quad m = 1, 2, \end{aligned} \quad (7)$$

where  $c_{i,m}^1$  is the input of the  $i$ th nod in the  $m$ th modified Elman NN, and  $d_{i,m}^1$  is the output of the  $i$ th nod in the  $m$ th modified Elman NN. The different inputs of the two sets of modified Elman NNs are  $c_{1,1}^1 = e_1 = V_d^* - V_d$ ,  $c_{2,1}^1 = \dot{e}_1$  for the rectifier end of the PMSG system in the first modified Elman NN, and  $c_{1,2}^1 = e_2 = V_{\text{rms}}^* - V_{\text{rms}}$ ,  $c_{2,2}^1 = \dot{e}_2$  for the inverter end of the PMSG system in the second modified Elman NN, respectively. The  $N$  indicates the number of iterations. The connecting weights  $\mu_{oi,m}$  are the recurrent weights between the output layer and the input layer in the  $m$ th modified Elman NN.  $d_{o,m}^4$  is the output value of the output layer in the  $m$ th modified Elman NN.

**3.1.2. Second Layer: Hidden Layer.** The single node  $j$ th in this layer is labeled with  $\Sigma$ . It computes outputs of the input layer and the context layer as the summation of all input signals. The net input and the net output for node  $j$ th in this layer are expressed as

$$\begin{aligned} \text{nod}_{j,m}^2(N) &= \sum_k \mu_{kj,m} d_{k,m}^3(N) + \sum_i \mu_{ij,m} d_{i,m}^1(N), \\ d_{j,m}^2(N) &= g_{j,m}^2(\text{nod}_{j,m}^2(N)) \\ &= \frac{1}{1 + e^{-\text{nod}_{j,m}^2(N)}}, \quad j = 1, \dots, n, \quad m = 1, 2, \end{aligned} \quad (8)$$

where  $\mu_{kj,m}$  are the connective weights between the context layer and the hidden layer in the  $m$ th modified Elman NN,  $\mu_{ij,m}$  are the connective weights between the input layer and the hidden layer in the  $m$ th modified Elman NN, and  $n$  is the number of neurons in the hidden layer;  $g_{j,m}^2$  is the activation function in the  $m$ th modified Elman NN, which is also a sigmoid function;  $d_{i,m}^1(N) = c_{i,m}^1(N)$  represents the  $i$ th output node of input layer in the  $m$ th modified Elman NN, and  $d_{k,m}^3(N) = c_{k,m}^3(N)$  represents the  $k$ th input to the node of context layer in the  $m$ th modified Elman NN.

**3.1.3. Third Layer 3: Context Layer.** In the context layer, the node input and the node output are represented as

$$\begin{aligned} \text{nod}_{k,m}^3(N) &= d_{j,m}^2(N-1) + \beta d_{k,m}^3(N-1), \\ d_k^3(N) &= g_k^3(\text{nod}_k^3(N)) = \text{nod}_k^3(N), \quad k = 1, \dots, l, \end{aligned} \quad (9)$$

where  $d_{j,m}^2(N) = c_{j,m}^4(N)$  represents the  $j$ th output node of hidden layer in the  $m$ th modified Elman NN;  $d_{k,m}^3(N)$  represents the  $k$ th output to the node of context layer in the  $m$ th modified Elman NN;  $l$  is the number of neurons in the context layer;  $0 \leq \beta < 1$  is the self-connecting feedback gain of context layer.

**3.1.4. Fourth Layer: Output Layer.** The single node  $o$ th in this layer is labeled with  $\Sigma$ . It computes the overall output as the summation of all input signals. The net input and the net output for node  $o$ th in this layer are expressed as

$$\text{nod}_{o,m}^4(N) = \sum_j \mu_{jo,m} c_{j,m}^4(N),$$

$$d_{o,m}^4(N) = g_{o,m}^4(\text{nod}_{o,m}^4(N)) = \text{nod}_{o,m}^4, \quad o = 1, \quad m = 1, 2, \quad (10)$$

where  $\mu_{jo,m}$  are the connective weights between the hidden layer and the output layer in the  $m$ th modified Elman NN;  $g_{o,m}^4$  is the activation function in the  $m$ th modified Elman NN, which is set to be unit;  $d_{j,m}^2(N) = c_{j,m}^4(N)$  represents the  $j$ th input to the node of output layer in the  $m$ th modified Elman NN. The outputs in the  $m$ th recurrent wavelet NN can be represented as  $d_{o,m}^4$

$$d_{o,m}^4 = (\psi_m)^T \chi_m, \quad m = 1, 2. \quad (11)$$

The output values of the two sets of the same four-layer modified Elman NNs can be rewritten as  $U_{M1} = (\psi_1)^T \chi_1 = i_{qr}^*$  for rectifier and  $U_{M2} = (\psi_2)^T \chi_2 = i_{qi}^*$  for inverter. Two vectors  $\psi_1 = [\mu_{11,1}^4 \mu_{21,1}^4 \cdots \mu_{l1,1}^4]^T$  and  $\psi_2 = [\mu_{11,2}^4 \mu_{21,2}^4 \cdots \mu_{l1,2}^4]^T$  are to be adjusted parameters between the mother layer and the output layer of the two sets of the same four-layer modified Elman NNs.

The  $\chi_m = [c_{1,m}^4 \ c_{2,m}^4 \cdots \ c_{l,m}^4]^T$ ,  $m = 1, 2$  are the inputs vectors in the output layer of the two sets of the same four-layer modified Elman NNs, in which  $c_{j,m}^4$  are determined by the selected sigmoid function and  $0 \leq c_{j,m}^4 \leq 1$ .

**3.2. Online Learning Algorithm of Modified Elman NN.** To explain the online learning algorithm of the modified Elman NN using supervised gradient decent method, firstly the energy function  $V_{c,m}$  is defined as

$$V_{c,m} = \frac{1}{2} e_m^2, \quad m = 1, 2, \quad (12)$$

where  $e_1$  equals to  $V_d^* - V_d$  in rectifier end of the PMSG system;  $e_2$  equals to  $V_{\text{rms}}^* - V_{\text{rms}}$  in the inverter end of the PMSG system. Then, the learning algorithm is described as follows.

**3.2.1. Fourth Layer.** The propagated error term in the  $m$ th modified Elman NN is

$$v_m^4 = -\frac{\partial V_{c,m}}{\partial d_{o,m}^4} \frac{\partial d_{o,m}^4}{\partial \text{nod}_{o,m}^4}, \quad m = 1, 2. \quad (13)$$

Then variation  $\Delta \mu_{jo,m}$  of connective weights in the  $m$ th modified Elman NN can be calculated as

$$\begin{aligned} \Delta \mu_{jo,m} &= -\gamma_{1,m} \frac{\partial V_{c,m}}{\partial d_{o,m}^4} \frac{\partial d_{o,m}^4}{\partial \text{nod}_{o,m}^4} \frac{\partial \text{nod}_{o,m}^4}{\partial \mu_{jo,m}} \\ &= \gamma_{1,m} \cdot v_m^4 \cdot c_{j,m}^4, \quad m = 1, 2, \end{aligned} \quad (14)$$

where  $\gamma_{1,m}$  is the learning rate between hidden layer and output layer in the  $m$ th modified Elman NN. The connective weights  $\mu_{jo,m}$  between hidden layer and output layer in the  $m$ th modified Elman NN can be renewed according to the following equation:

$$\mu_{jo,m}(N+1) = \mu_{jo,m}(N) + \Delta\mu_{jo,m}, \quad m = 1, 2. \quad (15)$$

3.2.2. *Second Layer.* The propagated error term in the  $m$ th modified Elman NN is

$$\begin{aligned} v_{j,m}^2 &\triangleq -\frac{\partial V_{c,m}}{\partial d_{o,m}^4} \frac{\partial d_{o,m}^4}{\partial \text{nod}_{o,m}^4} \frac{\partial \text{nod}_{o,m}^4}{\partial d_{j,m}^2} \frac{\partial d_{j,m}^2}{\partial \text{nod}_{j,m}^2} \\ &= v_m^4 P_{j,m}(N), \quad m = 1, 2, \end{aligned} \quad (16)$$

where  $P_{j,m} \equiv \partial d_{j,m}^2 / \partial \text{nod}_{j,m}^2$  can be calculated from (8).

Then variation  $\Delta\mu_{kj,m}$  of connective weights in the  $m$ th modified Elman NN can be calculated as

$$\begin{aligned} \Delta\mu_{kj,m} &= -\frac{\partial V_{c,m}}{\partial d_{o,m}^4} \frac{\partial d_{o,m}^4}{\partial \text{nod}_{o,m}^4} \frac{\partial \text{nod}_{o,m}^4}{\partial d_{j,m}^2} \frac{\partial d_{j,m}^2}{\partial \text{nod}_{j,m}^2} \frac{\partial \text{nod}_{j,m}^2}{\partial \mu_{kj,m}} \\ &= v_{j,m}^2 \cdot d_{k,m}^3, \quad m = 1, 2, \end{aligned} \quad (17)$$

where connective weights  $\mu_{kj,m}$  between context layer and hidden layer in the  $m$ th modified Elman NN can be renewed according to the following equation:

$$\mu_{kj,m}(N+1) = \mu_{kj,m}(N) + \Delta\mu_{kj,m}, \quad m = 1, 2. \quad (18)$$

Then variation  $\Delta\mu_{ij,m}$  of connective weights in the  $m$ th modified Elman NN can be calculated as

$$\begin{aligned} \Delta\mu_{ij,m} &= -\frac{\partial V_{c,m}}{\partial \text{nod}_{o,m}^4} \frac{\partial d_{o,m}^4}{\partial \text{nod}_{o,m}^4} \frac{\partial \text{nod}_{o,m}^4}{\partial d_{j,m}^2} \frac{\partial d_{j,m}^2}{\partial \text{nod}_{j,m}^2} \\ &\quad \times \frac{\partial \text{nod}_{j,m}^2}{\partial \mu_{ij,m}} = v_{j,m}^2 \cdot d_{i,m}^1, \quad m = 1, 2, \end{aligned} \quad (19)$$

where connective weights  $\mu_{ij,m}$  between hidden layer and input layer in the  $m$ th modified Elman NN can be updated as

$$\mu_{ij,m}(N+1) = \mu_{ij,m}(N) + \Delta\mu_{ij,m}, \quad m = 1, 2. \quad (20)$$

Then variation  $\Delta\mu_{oi,m}$  of connective weights in the  $m$ th modified Elman NN by using the chain rule and the gradient descent method can be calculated as

$$\begin{aligned} \Delta\mu_{oi,m} &= -\frac{\partial V_{c,m}}{\partial \text{nod}_{j,m}^2} \frac{\partial \text{nod}_{j,m}^2}{\partial d_{i,m}^1} \frac{\partial d_{i,m}^1}{\partial \text{nod}_{i,m}^1} \frac{\partial \text{nod}_{i,m}^1}{\partial \mu_{oi,m}} \\ &= v_{j,m}^2 \cdot Q_{j,m}, \end{aligned} \quad (21)$$

where  $Q_{j,m} \equiv \partial d_{j,m}^2 / \mu_{oi,m}$  can be calculated from (7). The recurrent weights  $\mu_{oi,m}$  between output layer and input layer

in  $m$ th modified Elman NN can be renewed according to the following equation:

$$\mu_{oi,m}(N+1) = \mu_{oi,m}(N) + \Delta\mu_{oi,m}, \quad m = 1, 2. \quad (22)$$

Due to the uncertainty effect of the system dynamics, the accurate computation of the Jacobian  $\partial V_{c,m} / \partial d_{o,m}^4$ ,  $m = 1, 2$  in the PMSG system cannot be determined. To dispel the difficulty and endure the above matter, using the delta adaptation law [20] can raise the online learning capacity of the connective weights. Therefore, the delta adaptation law can be calculated as [20]

$$v_m^4 = e_m + \dot{e}_m, \quad m = 1, 2. \quad (23)$$

3.3. *Convergence Analysis.* Selection of the values for the learning-rate parameters has a significant effect on the network performance. In order to train the modified Elman NN effectively, the varied learning rate, which guarantee convergence of the output error based on the analyses of a discrete-type Lyapunov function, is derived in this section. The convergence analysis is to derive specific learning-rate parameter for specific types of network parameter to assure convergence of the output error [30].

**Theorem 1.** Let  $\gamma_m$  be the learning-rate parameter of the  $m$ th modified Elman NN and let  $p_{\max,m}$  be defined as  $p_{\max,m} \equiv \max_N \|p_m(N)\|$ , where  $p_m(N) = \partial d_{o,m}^4 / \partial \mu_{jo,m}$  in the  $m$ th modified Elman NN and  $\|\cdot\|$  is the Euclidean norm in  $\mathfrak{R}^n$ . The convergence is guaranteed if  $\gamma_{1,m}$  is chosen as  $\gamma_{1,m} = \lambda_1 / (p_{\max,m}^2) = \lambda_1 / R_{u,m}$ , in which  $\lambda_1$  is a positive constant gain;  $R_{u,m}$  is the number of nodes in hidden layer of the  $m$ th modified Elman NN.

*Proof.* Since

$$p_m(N) = \frac{\partial d_{o,m}^4}{\partial \mu_{jo,m}} = c_{j,m}^4. \quad (24)$$

Thus

$$\|p_m(N)\| < \sqrt{R_{u,m}}. \quad (25)$$

Then, a discrete-type Lyapunov function is selected as

$$V_m(N) = \frac{1}{2} e_m^2(N). \quad (26)$$

The change in the Lyapunov function is obtained by

$$\begin{aligned} \Delta V_m(N) &= V_m(N+1) - V_m(N) \\ &= \frac{1}{2} [e_m^2(N+1) - e_m^2(N)]. \end{aligned} \quad (27)$$

The error difference can be represented by [30]

$$\begin{aligned} e_m(N+1) &= e_m(N) + \Delta e_m(N) \\ &= e_m(N) + \left[ \frac{\partial e_m(N)}{\partial \mu_{jo,m}} \right]^T \Delta \mu_{jo,m}, \end{aligned} \quad (28)$$

where  $\Delta\mu_{j_o,m}$  represents a weight change between hidden layer and output layer in the  $m$ th modified Elman NN. Using (11), (12), (13), and (28), then

$$\frac{\partial e_m(N)}{\partial \mu_{j_o,m}} = \frac{\partial e_m(N)}{\partial d_{o,m}^4} \frac{\partial d_{o,m}^4}{\partial \mu_{j_o,m}} = -\frac{v_m^4}{e_m(N)} P_m(N),$$

$$e_m(N+1) = e_m(N) - \left[ \frac{v_m^4}{e_m(N)} P_m(N) \right]^T \gamma_{1,m} v_m^4 P_m(N). \quad (29)$$

Then

$$\begin{aligned} & \|e_m(N+1)\| \\ &= \left\| e_m(N) \left[ 1 - \gamma_{1,m} \left( \frac{v_m^4}{e_m(N)} \right)^2 P_m^T(N) P_m(N) \right] \right\| \\ &\leq \|e(N)\| \left\| 1 - \gamma_{1,m} \left( \frac{v_m^4}{e_m(N)} \right)^2 P_m^T(N) P_m(N) \right\|. \end{aligned} \quad (30)$$

If  $\gamma_{1,m}$  is chosen as  $\gamma_{1,m} = \lambda_1 / (P_{\max,m}^2) = \lambda_1 / R_{u,m}$ , the term  $\|1 - \gamma_{1,m} (v_m^4 / e_m(N))^2 P_m^T(N) P_m(N)\|$  in (30) is less than 1. Therefore, the Lyapunov stability of  $V_m > 0$  and  $\Delta V_m < 0$  is guaranteed. The output error between the reference model and the actual system will converge to zero as  $t \rightarrow \infty$ . This completes the proof of the theorem.  $\square$

*Remark 2.* The values of the learning-rate parameter  $\gamma_{1,m}$  is dependent on the selection of the value  $\lambda_1$ .

#### 4. Experimental Results

The two sets of the same modified Elman NNs controlled PMSG system are realized in two sets TMS320C32 DSP control system. A photo of the experimental setup is shown in Figure 6. To implement current controlled PWM rectifier and inverter by field-oriented control, the two sets IGBT power modules are adopted BSM 100 GB-120DLC manufactured by Eupec Co. The switching frequency of both IGBT power modules is all 15 kHz. The two programs of the two sets TMS320C32 DSP control system used for executing the two sets of the same modified Elman NNs and online training of the two sets of the same modified Elman NNs need 2 ms sampling interval. The proposed methodology for the real-time control implementation consists of the two main programs and two interrupt service routines (ISRs) in the two sets of DSP control system as shown in Figure 7. In the main program #1, parameters and input/output (I/O) initialization are processed first. Then, the interrupt interval for the ISR #1 is set. After enabling the interrupt, the main program #1 is used to monitor control data. The ISR #1 with 2 ms sampling interval is used for reading the rotor position of the PM synchronous generator from encoder, reading mechanic torque from torque transducer, reading measured DC bus voltage and current from analog/digital (A/D) converters, calculating maximum DC bus power of the PM synchronous generator and DC bus power, and executing the modified Elman NN control system #1. On the other

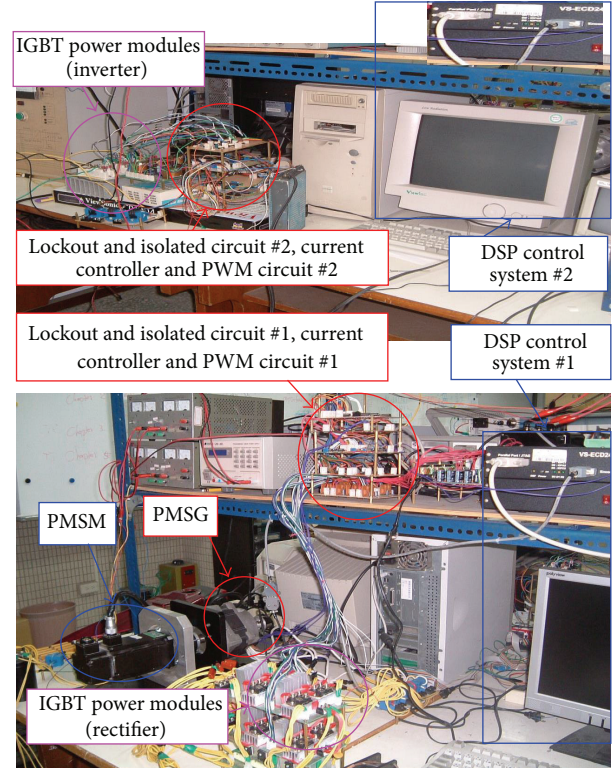


FIGURE 6: A photo of the experimental setup.

hand, in the main program #2, parameters and input/output (I/O) initialization are processed first. Then, the interrupt interval for the ISR #2 is set. After enabling the interrupt, the main program is used to monitor control data. The ISR #2 with 2 ms sampling interval is used for reading the command angular frequency of sinusoidal wave to match demand of grid system, reading command root-mean-square AC line voltage and measured root-mean-square AC line voltage from analog/digital (A/D) converters, and executing the modified Elman NN control system #2. Furthermore, to show the effectiveness of the control system, comparative studies with the PI controller and the conventional NN controller are demonstrated by experimental results. The conventional NN has 2, 5, and 1 nodes in the input layer, the hidden layer with sigmoid function, and the output layer, respectively. The modified Elman NN has 2, 5, 5, and 1 nodes in layer 1, layer 2, layer 3, and layer 4, respectively. The parameter adjustment process remains continually active for the duration of the experimentation. To verify the control performance of the proposed two sets of the same modified Elman NNs controlled PMSG system direct-driven by PMSM based on wind turbine emulator, three cases with the field-oriented control current  $i_{di}^* = 0$  A and  $i_{dr}^* = 0$  A are tested. To show the adjusting and tracking responses for the stand alone power application, three cases are selected. Firstly, case 1 is the  $\Delta$  connection three-phase load 100  $\Omega$ , and the rotor speed  $\omega_r(n_r)$ , the step desired magnitude  $V_d^*$  of DC bus voltage, and the step desired root-mean-square magnitude  $V_{\text{rms}}^*$  of AC 60 Hz line voltage are set as 78.5 rad/s (750 rpm), 220 V, and 110 V, respectively. Secondly, case 2 is the  $\Delta$  connection three-phase load 50  $\Omega$  and the rotor speed  $\omega_{r1}$ , the desired

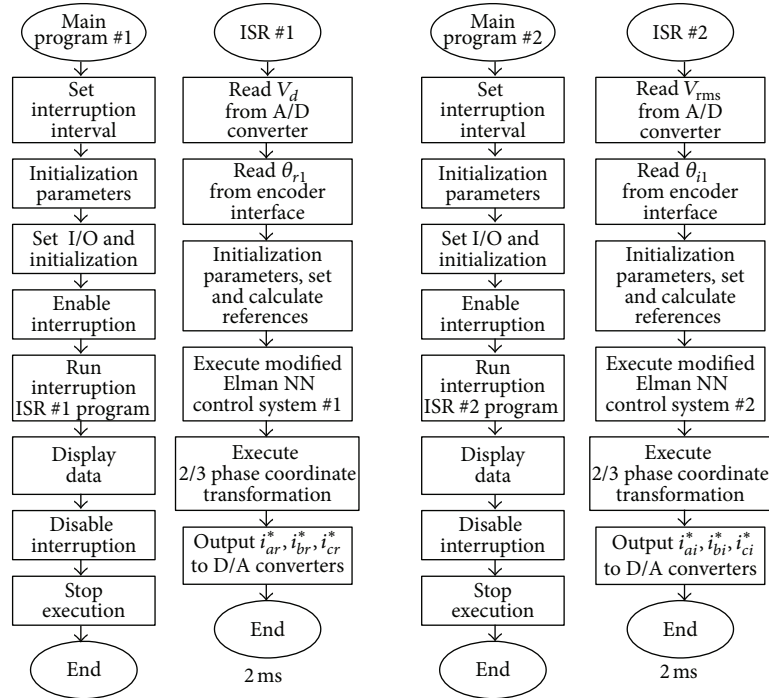


FIGURE 7: Flowcharts of two sets of the same modified Elman NN control systems controlled PMSG system.

magnitude  $V_d^*$  of DC bus voltage, the desired root-mean-square magnitude  $V_{rms}^*$  of AC 60 Hz line voltage are set as 157 rad/s (1500 rpm), 220 V, and 110 V, respectively. Thirdly, case 3 is the  $\Delta$  connection three-phase load 18  $\Omega$  and the rotor speed  $\omega_r$ , the desired magnitude  $V_d^*$  of DC bus voltage, the desired root-mean-square magnitude  $V_{rms}^*$  of AC 60 Hz line voltage are set as 209.3 rad/s (2000 rpm), 220 V, and 110 V, respectively. The  $\Delta$  connection three-phase loads of 100  $\Omega$ , 50  $\Omega$ , and 18  $\Omega$  dispatched powers as 121 W, 242 W, and 672 W, respectively. The  $\Delta$  connection three-phase loads of 100  $\Omega$  and 50  $\Omega$ , and 18  $\Omega$  dispatched powers as 121 W, 242 W, and 672 W, respectively. Some experimental results of the PI controlled PMSG system direct-driven by PMSM are demonstrated for the comparison of the control performance. Since the PMSG system is a nonlinear time-varying system, the gains of the PI controllers for both the DC bus voltage adjustment and AC 60 Hz line voltage adjustment are obtained by trial and error to achieve steady state control performance. The control gains are  $K_p = 5.2$ ,  $K_i = 10.2$  for the DC bus voltage adjustment and  $K_p = 4.8$ ,  $K_i = 10.8$  for the AC 60 Hz line voltage adjustment in the two sets PI controllers. The experimental results of the PI controlled PMSG system direct-driven by PMSM for the  $\Delta$  connection three-phase loads of 100  $\Omega$  with  $\omega_r = 78.5$  rad/s ( $n_r = 750$  rpm) at case 1, the  $\Delta$  connection three-phase loads of 50  $\Omega$  with  $\omega_r = 150$  rad/s ( $n_r = 1500$  rpm) at case 2, and the  $\Delta$  connection three-phase loads of 18  $\Omega$  with  $\omega_r = 209.3$  rad/s ( $n_r = 2000$  rpm) at case 3 are shown in Figures 8, 9 and 10, respectively; where rotor speed  $\omega_r(n_r)$  is shown in Figures 8(a), 9(a) and 10(a); adjusting response of step desired magnitude  $V_d^*$  of the DC bus voltage and actual measured magnitude  $V_d$  of the DC bus voltage in output end of the rectifier is shown in Figures

8(b), 9(b), and 10(b); adjusting response of step desired root-mean-square magnitude  $V_{rms}^*$  of the AC 60 Hz line voltage and actual measured root-mean-square magnitude  $V_{rms}$  of the AC 60 Hz line voltage in output end of the inverter is shown in Figures 8(c), 9(c), and 10(c); tracking response of the desired phase current  $i_{ai}^*$  and actual measured phase current  $i_{ai}$  in phase  $ai$  of the inverter is shown in Figures 8(d), 9(d), and 10(d) respectively. From the experimental results, sluggish DC bus voltage and AC 60 Hz line voltage adjusting responses are obtained for the PI controlled PMSG system direct-driven by PMSM because of the weak robustness of the linear controller.

Some experimental results of the conventional NN controlled PMSG system direct-driven by PMSM for the  $\Delta$  connection three-phase loads of 100  $\Omega$  with  $\omega_r = 78.5$  rad/s ( $n_r = 750$  rpm) at case 1, the  $\Delta$  connection three-phase loads of 50  $\Omega$  with  $\omega_r = 150$  rad/s ( $n_r = 1500$  rpm) at case 2, and the  $\Delta$  connection three-phase loads of 18  $\Omega$  with  $\omega_r = 209.3$  rad/s ( $n_r = 2000$  rpm) at case 3 are shown in Figures 11, 12, and 13, respectively, where rotor speed  $\omega_r(n_r)$  is shown in Figures 11(a), 12(a), and 13(a); adjusting response of step desired magnitude  $V_d^*$  of the DC bus voltage and actual measured magnitude  $V_d$  of the DC bus voltage in output end of the rectifier is shown in Figures 11(b), 12(b), and 13(b); adjusting response of step desired root-mean-square magnitude  $V_{rms}^*$  of the AC 60 Hz line voltage and actual measured root-mean-square magnitude  $V_{rms}$  of the AC 60 Hz line voltage in output end of the inverter is shown in Figures 11(c), 12(c), and 13(c); tracking response of the desired phase current  $i_{ai}^*$  and actual measured phase current  $i_{ai}$  in phase  $ai$  of the inverter is shown in Figures 11(d), 12(d), and 13(d) respectively. From the experimental

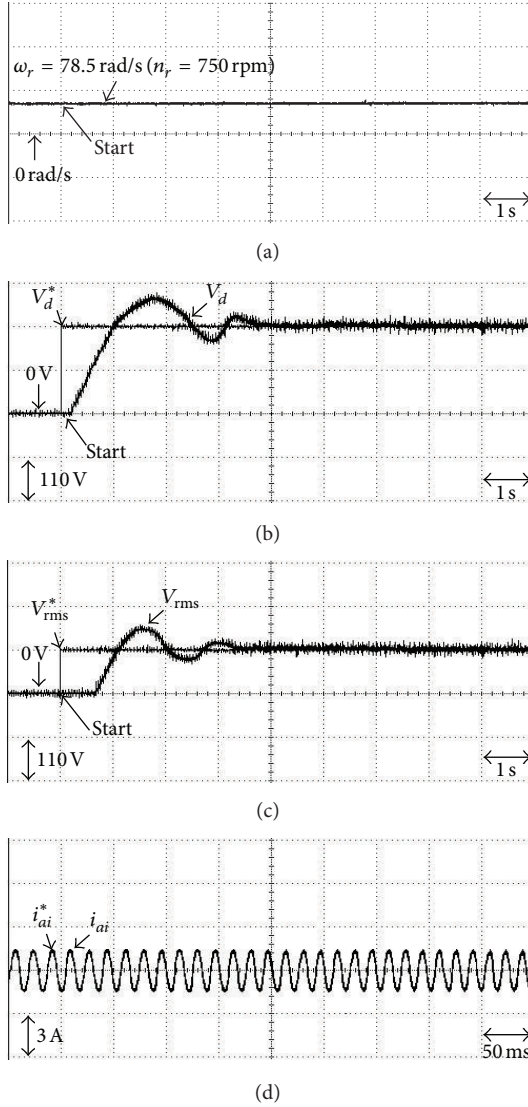


FIGURE 8: Experimental results of PMSM direct-driven PMSG system using the PI controller for the  $\Delta$  connection three-phase loads of  $100 \Omega$  with  $\omega_r = 78.5 \text{ rad/s}$  ( $n_r = 750 \text{ rpm}$ ) at case 1: (a) rotor speed  $\omega_r(n_r)$ ; (b) adjusting response of step desired magnitude  $V_d^*$  of the DC bus voltage and actual measured magnitude  $V_d$  of the DC bus voltage in output end of the rectifier; (c) adjusting response of step desired root-mean-square magnitude  $V_{rms}^*$  of the AC 60 Hz line voltage and actual measured root-mean-square magnitude  $V_{rms}$  of the AC 60 Hz line voltage in output end of the inverter  $V_{rms}$ ; (d) tracking response of the desired phase current  $i_{ai}^*$  and actual measured phase current  $i_{ai}$  in phase  $ai$  of the inverter.

results, few sluggish DC bus voltage and AC 60 Hz line voltage adjusting responses are obtained for the conventional NN controlled PM synchronous motor direct-drive PM synchronous generator system because the conventional NN is static input/output mapping schemes that can approximate a continuous function to an arbitrary degree of accuracy.

Some experimental results of the modified Elman NN controlled PMSG system direct-driven by PMSM for the  $\Delta$  connection three-phase loads of  $100 \Omega$  with  $\omega_r = 78.5 \text{ rad/s}$

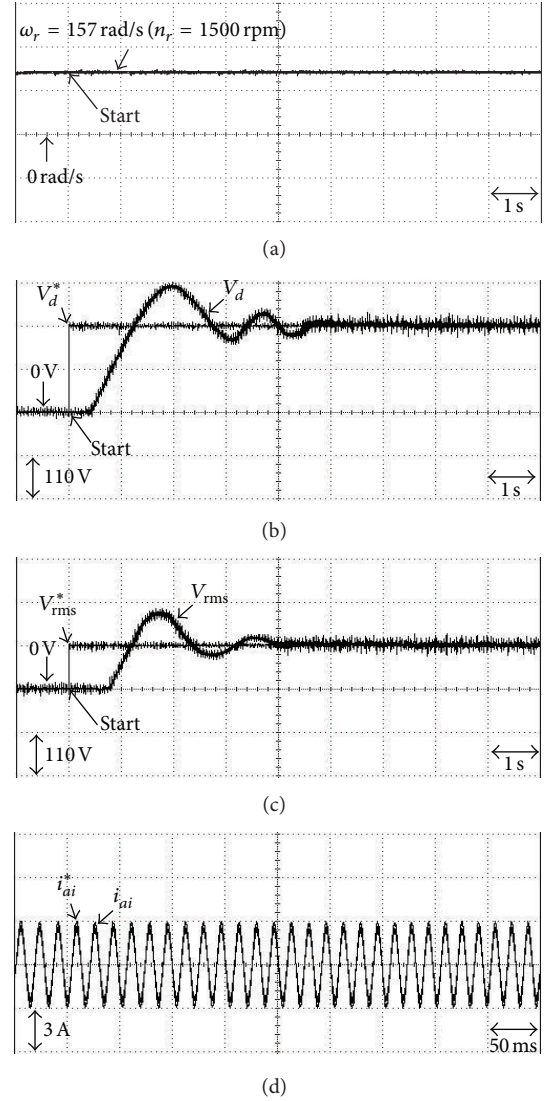


FIGURE 9: Experimental results of PMSM direct-driven PMSG system using the PI controller for the  $\Delta$  connection three-phase loads of  $50 \Omega$  with  $\omega_r = 150 \text{ rad/s}$  ( $n_r = 1500 \text{ rpm}$ ) at case 2: (a) rotor speed  $\omega_r(n_r)$ ; (b) adjusting response of step desired magnitude  $V_d^*$  of the DC bus voltage and actual measured magnitude  $V_d$  of the DC bus voltage in output end of the rectifier; (c) adjusting response of step desired root-mean-square magnitude  $V_{rms}^*$  of the AC 60 Hz line voltage and actual measured root-mean-square magnitude  $V_{rms}$  of the AC 60 Hz line voltage in output end of the inverter  $V_{rms}$ ; (d) tracking response of the desired phase current  $i_{ai}^*$  and actual measured phase current  $i_{ai}$  in phase  $ai$  of the inverter.

( $n_r = 750 \text{ rpm}$ ) at case 1, the  $\Delta$  connection three-phase loads of  $50 \Omega$  with  $\omega_r = 150 \text{ rad/s}$  ( $n_r = 1500 \text{ rpm}$ ) at case 2, and the  $\Delta$  connection three-phase loads of  $18 \Omega$  with  $\omega_r = 209.3 \text{ rad/s}$  ( $n_r = 2000 \text{ rpm}$ ) at case 3 are shown in Figures 14, 15, and 16, respectively; where rotor speed  $\omega_r(n_r)$  is shown in Figures 14(a), 15(a), and 16(a); adjusting response of step desired magnitude  $V_d^*$  of the DC bus voltage and actual measured magnitude  $V_d$  of the DC bus voltage in output end of the rectifier is shown in Figures 14(b), 15(b), and 16(b); adjusting

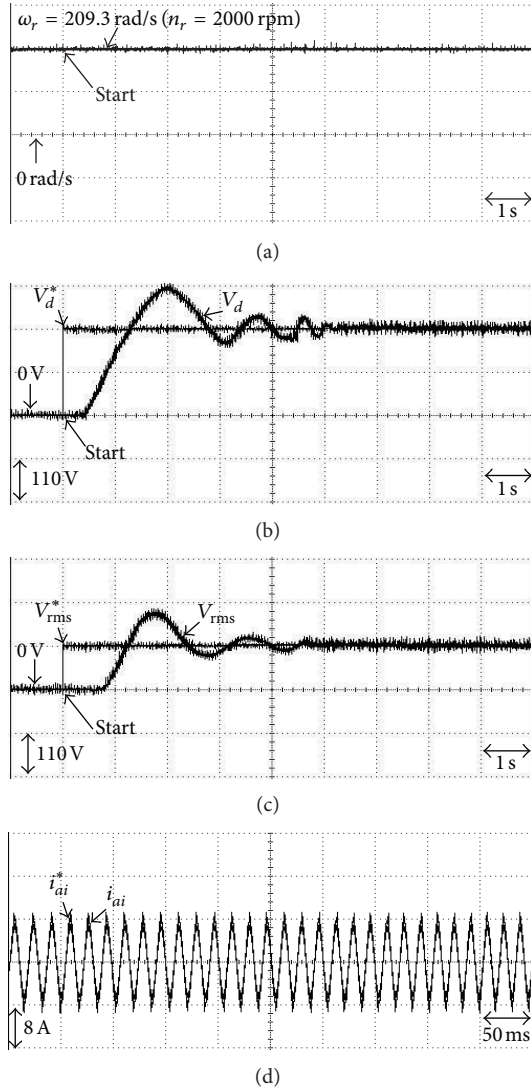


FIGURE 10: Experimental results of PMSM direct-driven PMSG system using the PI controller for the  $\Delta$  connection three-phase loads of  $18 \Omega$  with  $\omega_r = 209.3 \text{ rad/s}$  ( $n_r = 2000 \text{ rpm}$ ) at case 3: (a) rotor speed  $\omega_r(n_r)$ ; (b) adjusting response of step desired magnitude  $V_d^*$  of the DC bus voltage and actual measured magnitude  $V_d$  of the DC bus voltage in output end of the rectifier; (c) adjusting response of step desired root-mean-square magnitude  $V_{rms}^*$  of the AC 60 Hz line voltage and actual measured root-mean-square magnitude  $V_{rms}$  of the AC 60 Hz line voltage in output end of the inverter  $V_{rms}$ ; (d) tracking response of the desired phase current  $i_{ai}^*$  and actual measured phase current  $i_{ai}$  in phase  $ai$  of the inverter.

response of step desired root-mean-square magnitude  $V_{rms}^*$  of the AC 60 Hz line voltage and actual measured root-mean-square magnitude  $V_{rms}$  of the AC 60 Hz line voltage in output end of the inverter is shown in Figures 14(c), 15(c), and 16(c); tracking response of the desired phase current  $i_{ai}^*$  and actual measured phase current  $i_{ai}$  in phase  $ai$  of the inverter is shown in Figures 14(d), 15(d), and 16(d), respectively. The overshoot and undershoot in DC bus voltage and AC 60 Hz line voltage at different rotor speeds by using modified Elman

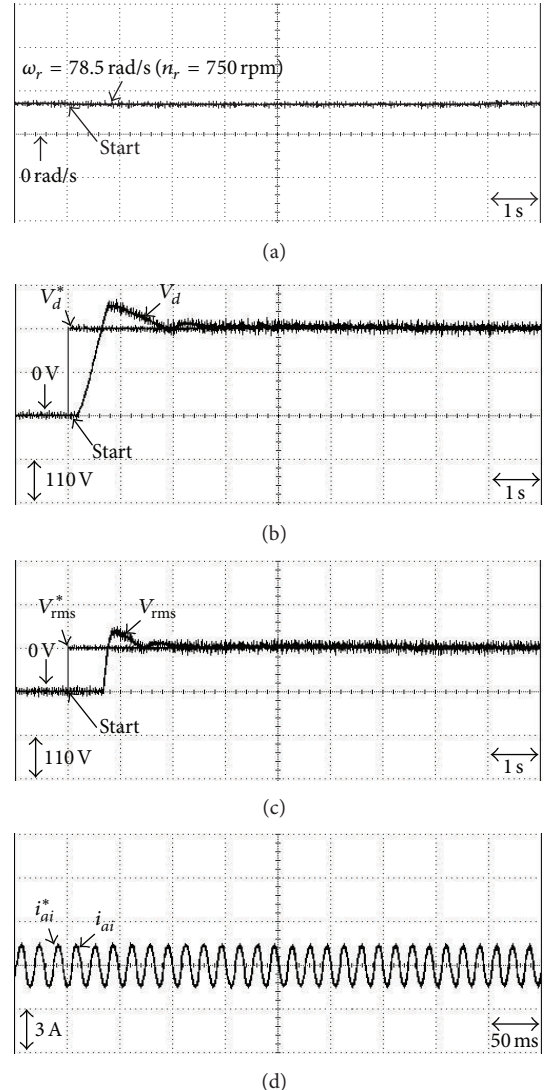


FIGURE 11: Experimental results of PMSM direct-driven PMSG system using the conventional NN controller for the  $\Delta$  connection three-phase loads of  $100 \Omega$  with  $\omega_r = 78.5 \text{ rad/s}$  ( $n_r = 750 \text{ rpm}$ ) at case 1: (a) rotor speed  $\omega_r(n_r)$ ; (b) adjusting response of step desired magnitude  $V_d^*$  of the DC bus voltage and actual measured magnitude  $V_d$  of the DC bus voltage in output end of the rectifier; (c) adjusting response of step desired root-mean-square magnitude  $V_{rms}^*$  of the AC 60 Hz line voltage and actual measured root-mean-square magnitude  $V_{rms}$  of the AC 60 Hz line voltage in output end of the inverter  $V_{rms}$ ; (d) tracking response of the desired phase current  $i_{ai}^*$  and actual measured phase current  $i_{ai}$  in phase  $ai$  of the inverter.

NN controllers as shown in Figures 14(b), 14(c), 15(b), 15(c), 16(b), and 16(c) are less magnitude and much improved by using the PI controller shown in Figures 8(b), 8(c), 9(b), 9(c), 10(b), and 10(c) and by using the conventional NN controller shown in Figures 11(b), 11(c), 12(b), 12(c), 13(b), and 13(c). Moreover, compared with the PI control and the conventional NN control, the proposed modified Elman NN control has much improved for the tracking ability and obviously reduced the oscillations in steady state.

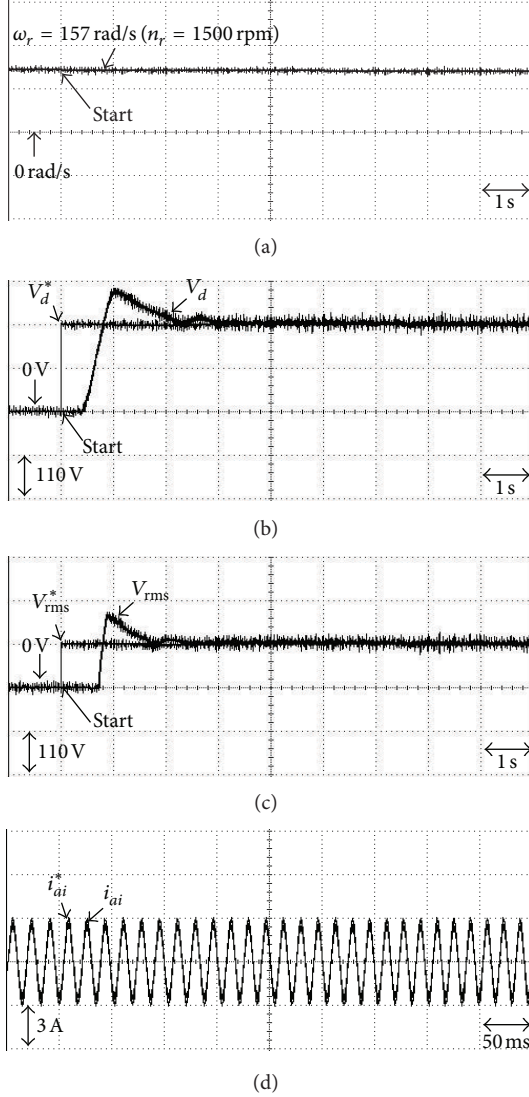


FIGURE 12: Experimental results of PMSG direct-driven PMSG system using the conventional NN controller for the  $\Delta$  connection three-phase loads of  $50 \Omega$  with  $\omega_r = 150 \text{ rad/s}$  ( $n_r = 1500 \text{ rpm}$ ) at case 2: (a) rotor speed  $\omega_r(n_r)$ ; (b) adjusting response of step desired magnitude  $V_d^*$  of the DC bus voltage and actual measured magnitude  $V_d$  of the DC bus voltage in output end of the rectifier; (c) adjusting response of step desired root-mean-square magnitude  $V_{rms}^*$  of the AC 60 Hz line voltage and actual measured root-mean-square magnitude  $V_{rms}$  of the AC 60 Hz line voltage in output end of the inverter  $V_{rms}$ ; (d) tracking response of the desired phase current  $i_{ai}^*$  and actual measured phase current  $i_{ai}$  in phase  $ai$  of the inverter.

## 5. Conclusions

This study demonstrated the implementation of both the DC bus voltage and AC 60 Hz line voltage adjustment of the PMSG system direct-driven by PMSG based on wind turbine emulator by using the two sets of the same modified Elman NN controllers for stand alone power applications. Firstly, the field-oriented control was implemented for the control of the PMSG system direct-driven by PMSG based on wind turbine emulator. Then, the proposed two sets of the same

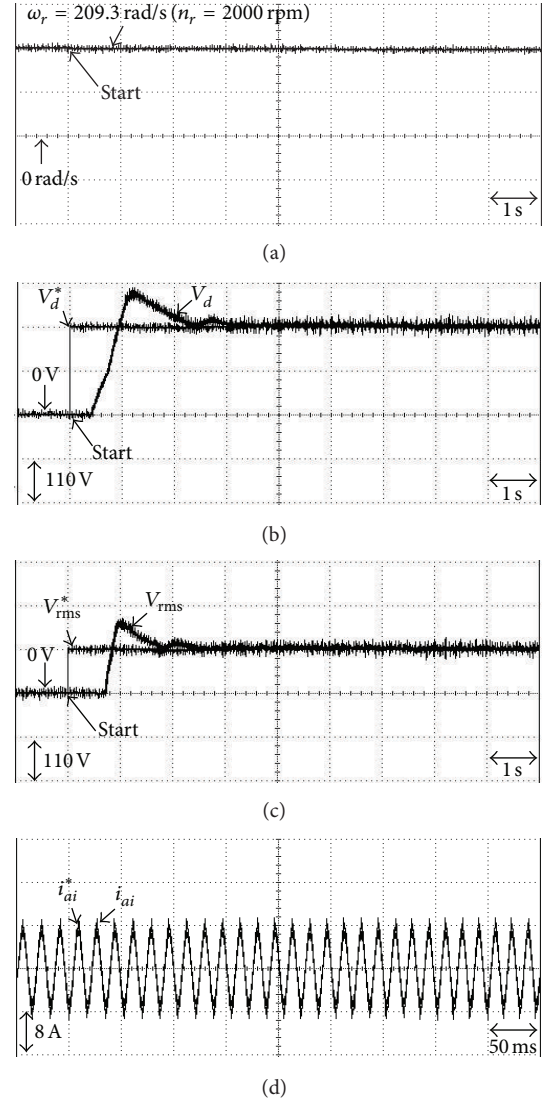


FIGURE 13: Experimental results of PMSG direct-driven PMSG system using the conventional NN controller for the  $\Delta$  connection three-phase loads of  $18 \Omega$  with  $\omega_r = 209.3 \text{ rad/s}$  ( $n_r = 2000 \text{ rpm}$ ) at case 3: (a) rotor speed  $\omega_r(n_r)$ ; (b) adjusting response of step desired magnitude  $V_d^*$  of the DC bus voltage and actual measured magnitude  $V_d$  of the DC bus voltage in output end of the rectifier; (c) adjusting response of step desired root-mean-square magnitude  $V_{rms}^*$  of the AC 60 Hz line voltage and actual measured root-mean-square magnitude  $V_{rms}$  of the AC 60 Hz line voltage in output end of the inverter  $V_{rms}$ ; (d) tracking response of the desired phase current  $i_{ai}^*$  and actual measured phase current  $i_{ai}$  in phase  $ai$  of the inverter.

modified Elman NN controllers were proposed to adjust the DC bus voltage of the rectifier and the AC 60 Hz line voltage of the inverter. In addition, the control performance of the proposed modified Elman NN controlled PMSG system direct-driven by PMSG is robust with regard to two operating conditions of the PMSG. Because of the weak robustness of the linear controller for the PI controlled PMSG system direct-driven by PMSG, dull DC bus voltage and AC 60 Hz line voltage adjusting responses are obviously obtained from

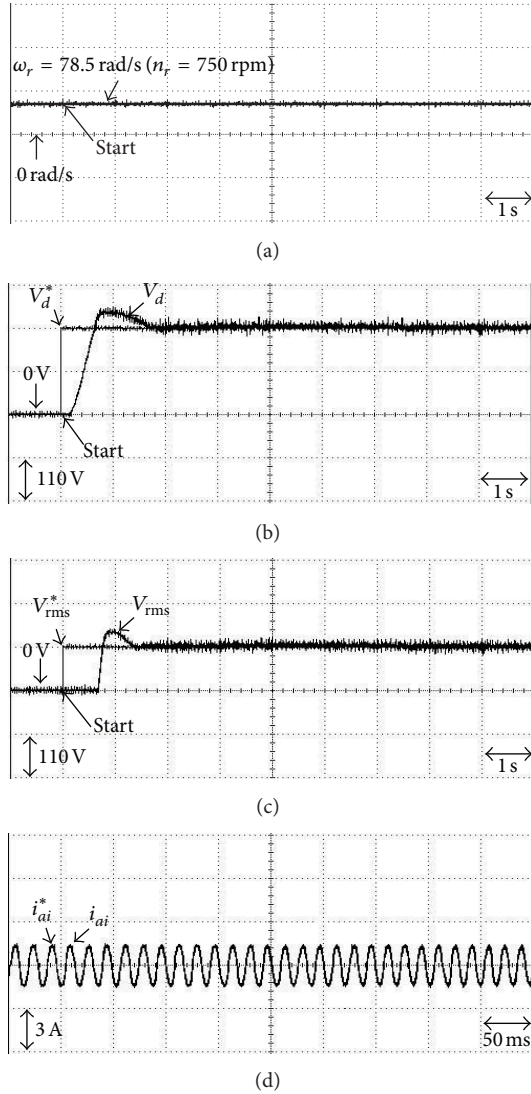


FIGURE 14: Experimental results of PMSM direct-driven PMSG system using the modified Elman NN controller for the  $\Delta$  connection three-phase loads of  $100 \Omega$  with  $\omega_r = 78.5 \text{ rad/s}$  ( $n_r = 750 \text{ rpm}$ ) at case 1: (a) rotor speed  $\omega_r(n_r)$ ; (b) adjusting response of step desired magnitude  $V_d^*$  of the DC bus voltage and actual measured magnitude  $V_d$  of the DC bus voltage in output end of the rectifier; (c) adjusting response of step desired root-mean-square magnitude  $V_{rms}^*$  of the AC 60 Hz line voltage and actual measured root-mean-square magnitude  $V_{rms}$  of the AC 60 Hz line voltage in output end of the inverter  $V_{rms}$ ; (d) tracking response of the desired phase current  $i_{ai}^*$  and actual measured phase current  $i_{ai}$  in phase  $ai$  of the inverter.

the experimental results. The important contribution of this study is successful application of the two sets of the same recurrent wavelet NN controllers on the PM synchronous motor direct-driven PM synchronous generator system to adjust the DC bus voltage of the rectifier and the AC 60 Hz line voltage of the inverter with robust control performance. Finally, control performance of the proposed modified Elman NN controller shown in experimental results is superior to the PI controller and the conventional NN controller for the

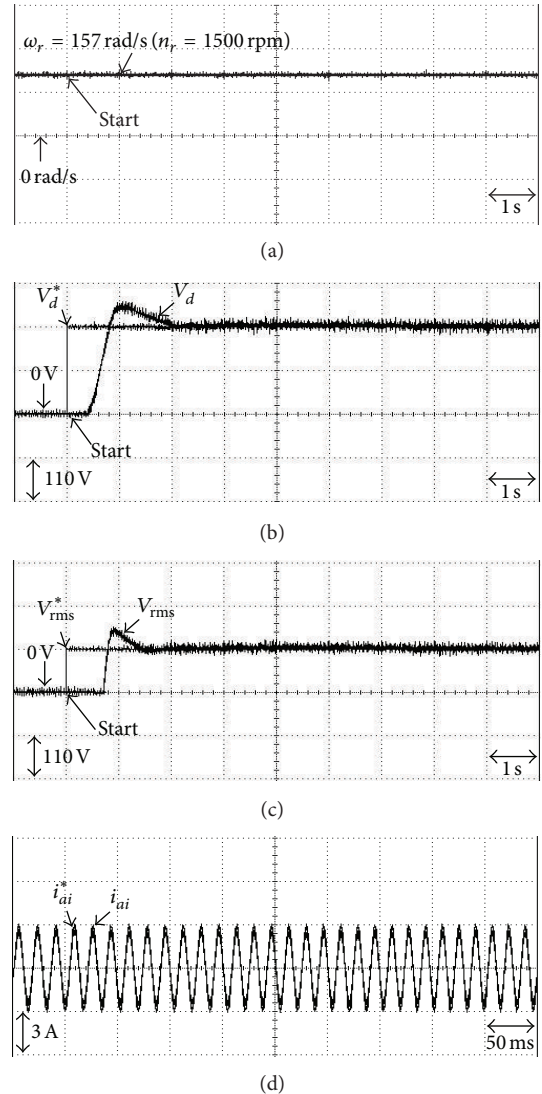


FIGURE 15: Experimental results of PMSM direct-driven PMSG system using the modified Elman NN controller for the  $\Delta$  connection three-phase loads of  $50 \Omega$  with  $\omega_r = 150 \text{ rad/s}$  ( $n_r = 1500 \text{ rpm}$ ) at case 2: (a) rotor speed  $\omega_r(n_r)$ ; (b) adjusting response of step desired magnitude  $V_d^*$  of the DC bus voltage and actual measured magnitude  $V_d$  of the DC bus voltage in output end of the rectifier; (c) adjusting response of step desired root-mean-square magnitude  $V_{rms}^*$  of the AC 60 Hz line voltage and actual measured root-mean-square magnitude  $V_{rms}$  of the AC 60 Hz line voltage in output end of the inverter  $V_{rms}$ ; (d) tracking response of the desired phase current  $i_{ai}^*$  and actual measured phase current  $i_{ai}$  in phase  $ai$  of the inverter.

PMSG system direct-driven by PMSM based on wind turbine emulator with a rectifier and an inverter for stand alone power applications.

### Acknowledgment

The author would like to acknowledge the financial support of the National Science Council in Taiwan, through its Grant NSC 99-2221-E-239-040-MY3.

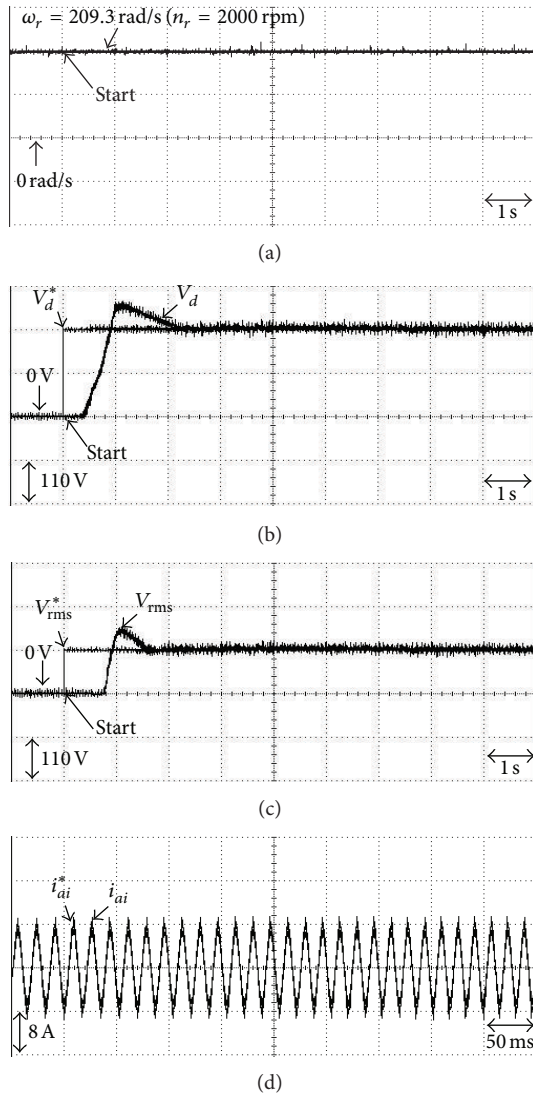


FIGURE 16: Experimental results of PMSM direct-driven PMSG system using the modified Elman NN controller for the  $\Delta$  connection three-phase loads of  $18 \Omega$  with  $\omega_r = 209.3 \text{ rad/s}$  ( $n_r = 2000 \text{ rpm}$ ) at case 3: (a) rotor speed  $\omega_r(n_r)$ ; (b) adjusting response of step desired magnitude  $V_d^*$  of the DC bus voltage and actual measured magnitude  $V_d$  of the DC bus voltage in output end of the rectifier; (c) adjusting response of step desired root-mean-square magnitude  $V_{rms}^*$  of the AC 60 Hz line voltage and actual measured root-mean-square magnitude  $V_{rms}$  of the AC 60 Hz line voltage in output end of the inverter  $V_{rms}$ ; (d) tracking response of the desired phase current  $i_{ai}^*$  and actual measured phase current  $i_{ai}$  in phase  $ai$  of the inverter.

## References

- [1] K. Tan and S. Islam, "Optimum control strategies in energy conversion of PMSG wind turbine system without mechanical sensors," *IEEE Transactions on Energy Conversion*, vol. 19, no. 2, pp. 392–399, 2004.
- [2] M. Kolhe, J. C. Joshi, and D. P. Kothari, "Performance analysis of a directly coupled photovoltaic water-pumping system," *IEEE Transactions on Energy Conversion*, vol. 19, no. 3, pp. 613–618, 2004.
- [3] G. K. Andersen, C. Klumpner, S. B. Kjaer, and F. Blaabjerg, "A new green power inverter for fuel cells," in *Proceedings of the IEEE 33rd Annual Power Electronics Specialists Conference (PESC '02)*, pp. 727–733, June 2002.
- [4] Z. Lubosny, *Wind Turbine Operation in Electric Power Systems*, Springer, Berlin, Germany, 2003.
- [5] T. Ackermann, *Wind Power in Power Systems*, John Wiley & Sons, New York, NY, USA, 2005.
- [6] M. Karrari, W. Rosehart, and O. P. Malik, "Comprehensive control strategy for a variable speed cage machine wind generation unit," *IEEE Transactions on Energy Conversion*, vol. 20, no. 2, pp. 415–423, 2005.
- [7] I. Boldea, *Synchronous Generators*, Taylor & Francis, Boca Raton, Fla, USA, 2006.
- [8] M. Chinchilla, S. Arnaltes, and J. C. Burgos, "Control of permanent-magnet generators applied to variable-speed wind-energy systems connected to the grid," *IEEE Transactions on Energy Conversion*, vol. 21, no. 1, pp. 130–135, 2006.
- [9] S. Sajedi, F. Kahlifeh, T. Karimi, and Z. Khalifeh, "Maximum power point tracking of variable speed wind energy conversion system," *International Journal of Physical Sciences*, vol. 6, no. 30, pp. 6843–6851, 2011.
- [10] F. Gharedaghi, H. Jamali, M. Deysi, and A. Khalili, "Maximum power point tracking of variable speed wind generation system connected to permanent magnet synchronous generator," *International Review of Electrical Engineering*, vol. 4, no. 4, pp. 1044–1049, 2011.
- [11] F. J. Lin, L. T. Teng, P. H. Shieh, and Y. F. Li, "Intelligent controlled-wind-turbine emulator and induction-generator system using RBFN," *IEE Proceedings Electric Power Applications*, vol. 153, no. 4, pp. 608–618, 2006.
- [12] F. J. Lin, L. T. Teng, and M. H. Yu, "Radial basis function network control with improved particle swarm optimization for induction generator system," *IEEE Transactions on Power Electronics*, vol. 23, no. 4, pp. 2157–2169, 2008.
- [13] J. L. Elman, "Finding structure in time," *Cognitive Science*, vol. 2, no. 14, pp. 179–211, 1990.
- [14] M. N. Eskander, "Minimization of losses in permanent magnet synchronous motors using neural network," *Journal of Power Electron*, vol. 2, no. 3, pp. 220–229, 2002.
- [15] M. Ghariani, I. B. Salah, M. Ayadi, and R. Neji, "Neural induction machine observer for electric vehicle applications," *International Review on Modelling and Simulations*, vol. 3, no. 3, pp. 314–324, 2010.
- [16] P. Brandstetter, M. Kuchar, and I. Neborak, "Selected applications of artificial neural networks in the control of AC induction motor drives," *International Review of Electrical Engineering*, vol. 4, no. 3, pp. 1084–1093, 2011.
- [17] R. Koker, "Design and performance of an intelligent predictive controller for a six-degree-of-freedom robot using the Elman network," *Information Sciences*, vol. 176, no. 12, pp. 1781–1799, 2006.
- [18] A. Kalinli and S. Sagioglu, "Elman network with embedded memory for system identification," *Journal of Information Science and Engineering*, vol. 22, no. 6, pp. 1555–1568, 2006.
- [19] D. Samek, "Elman neural networks in model predictive control," in *Proceedings of the 23rd European Conference on Modelling and Simulation*, pp. 577–584, June 2009.
- [20] F. J. Lin and Y. C. Hung, "FPGA-based elman neural network control system for linear ultrasonic motor," *IEEE Transactions on Ultrasonics, Ferroelectrics, and Frequency Control*, vol. 56, no. 1, pp. 101–113, 2009.

- [21] T. W. S. Chow and Y. Fang, "A recurrent neural-network-based real-time learning control strategy applying to nonlinear systems with unknown dynamics," *IEEE Transactions on Industrial Electronics*, vol. 45, no. 1, pp. 151–161, 1998.
- [22] M. A. Brdys and G. J. Kulawski, "Dynamic neural controllers for induction motor," *IEEE Transactions on Neural Networks*, vol. 10, no. 2, pp. 340–355, 1999.
- [23] X. D. Li, J. K. L. Ho, and T. W. S. Chow, "Approximation of dynamical time-variant systems by continuous-time recurrent neural networks," *IEEE Transactions on Industrial Electronics*, vol. 52, no. 10, pp. 656–660, 2005.
- [24] C. H. Lu and C. C. Tsai, "Adaptive predictive control with recurrent neural network for industrial processes: an application to temperature control of a variable-frequency oil-cooling machine," *IEEE Transactions on Industrial Electronics*, vol. 53, no. 3, pp. 1366–1375, 2008.
- [25] A. F. Payam, M. N. Hashemnia, and J. Faiz, "Robust DTC control of doubly-fed induction machines based on input-output feedback linearization using recurrent neural networks," *Journal of Power Electron*, vol. 11, no. 5, pp. 719–725, 2011.
- [26] X. Z. Gao, X. M. Gao, and S. J. Ovaska, "Modified Elman neural network model with application to dynamical systems identification," in *Proceedings of the IEEE International Conference on Systems, Man and Cybernetics*, pp. 1376–1381, November 1996.
- [27] X. Y. Yang, D. P. Xu, X. J. Han, and H. N. Zhou, "Predictive functional control with modified Elman neural network for reheated steam temperature," in *Proceedings of the International Conference on Machine Learning and Cybernetics (ICMLC '05)*, pp. 4699–4703, June 2005.
- [28] J. Li, H. Wu, and J. Pian, "The application of the equipment fault diagnosis based on modified Elman neural network," in *Proceedings of the International Conference on Electronic and Mechanical Engineering and Information Technology*, pp. 4135–4137, November 2011.
- [29] M. Singh and S. Santoso, "Dynamic models for wind turbines and wind power plants," Subcontract Report NREL/SR-5500-52780, 2011.
- [30] C. M. Lin, K. N. Hung, and C. F. Hsu, "Adaptive neuro-wavelet control for switching power supplies," *IEEE Transactions on Industrial Electronics*, vol. 54, no. 1, pp. 87–95, 2007.

## Research Article

# Distributed Beacon Drifting Detection for Localization in Unstable Environments

Ming Xia,<sup>1</sup> Peiliang Sun,<sup>2</sup> Xiaoyan Wang,<sup>1</sup> Yan Jin,<sup>1</sup> and Qingzhang Chen<sup>1</sup>

<sup>1</sup> College of Computer Science and Technology, Zhejiang University of Technology, 288 Liuhe Road, Hangzhou 310023, China

<sup>2</sup> Department of IT and Management, Zhejiang Police Vocational Academy, No. 2 Street, Hangzhou 310018, China

Correspondence should be addressed to Ming Xia; xiaming@zjut.edu.cn

Received 14 January 2013; Accepted 23 February 2013

Academic Editor: Shengyong Chen

Copyright © 2013 Ming Xia et al. This is an open access article distributed under the Creative Commons Attribution License, which permits unrestricted use, distribution, and reproduction in any medium, provided the original work is properly cited.

Localization is a fundamental research issue in wireless sensor networks (WSNs). In most existing localization schemes, several beacons are used to determine the locations of sensor nodes. These localization mechanisms are frequently based on an assumption that the locations of beacons are known. Nevertheless, for many WSN systems deployed in unstable environments, beacons may be moved unexpectedly; that is, beacons are drifting, and their location information will no longer be reliable. As a result, the accuracy of localization will be greatly affected. In this paper, we propose a distributed beacon drifting detection algorithm to locate those accidentally moved beacons. In the proposed algorithm, we designed both beacon self-scoring and beacon-to-beacon negotiation mechanisms to improve detection accuracy while keeping the algorithm lightweight. Experimental results show that the algorithm achieves its designed goals.

## 1. Introduction

A wireless sensor network (WSN) [1, 2], which consists of a large number of sensor nodes to sense, process, and transmit monitored information in an environment cooperatively, has changed the way people interact with the physical world. Currently, WSN technologies have been widely adopted in environmental monitoring systems [3] and are foreseen to be used in more application fields, such as civil engineering [4] and sustainable energy systems [5]. Localization [6] is one of the most essential research issues in WSNs because the position of the monitored information is frequently one of our major concerns. Currently available localization algorithms typically use a small set of beacon nodes (or simply beacons) which are aware of their positions to deduce sensor nodes' positions through trilateration [7] or other techniques such as maximum likelihood estimation [8]. To mark the positions of beacons, we can either equip beacons with GPS receivers to let them calculate their locations automatically or mark beacons' positions manually in deployment. Because of relatively high price and power consumption, GPS receivers may not be available for many low-power WSN systems, and the second method is frequently used. As a result, these

algorithms are frequently based on an assumption that the beacons should be immobile and their position information is accurate. Nevertheless, this assumption does not hold in unstable environments. Because nodes in WSNs are typically battery powered [9], we frequently deploy WSN systems in unstable environments to perform monitoring tasks, and beacons' positions may be changed unexpectedly in this case. For instance, topographic change can move one or more beacons to other positions without being noticed. We denote these unexpected movements of beacons as that the beacons are drifting. The beacon drifting problem we discuss here is different from the well-investigated mobile beacon problem [10]. In the mobile beacon problem, beacons are moving along specific tracks in the monitored area to reduce the number of beacons required or to increase localization accuracy. Therefore, the position information of beacons is still accurate. But in the beacon drifting problem, beacons are unaware of the accidental movements, and the preset position information might be totally incorrect. In this occasion, the localization result will be seriously affected if we use inaccurate beacon position information.

In this paper, we focus on the beacon drifting detection problem, in which we have to determine: (1) whether all

beacons are still at their original deployed positions; (2) if not, which beacons have moved unexpectedly. With this information, we can, for example, avoid using moved beacons in localization to ensure localization accuracy. In this paper, we introduce a distributed beacon drifting detection algorithm. We chose to let each beacon keep monitoring the variance of RSSI (received signal strength indication) measurement value between itself and its neighboring beacons and the beacon can use the monitored RSSI information to determine if itself has moved. We based our detection algorithm on RSSI measurement because it is available in almost all RF receivers on the market. However, the unreliable nature of RSSI measurement will cause serious fault detection problem. As a result, we first analyzed different types of fault detections and then designed beacon self-scoring and beacon-to-beacon negotiation mechanisms to reduce the possibility of fault detection while keeping low operating overhead.

The rest of the paper is organized as follows. Section 2 introduces the state of the art. Section 3 proposes the design of the distributed beacon drifting detection algorithm. Section 4 provides evaluation results, and Section 5 concludes the paper.

## 2. Related Work

Localization algorithms can be roughly categorized into range-based and range-free algorithms. Range-based algorithms require the distance information between beacons and sensor nodes in deducing the sensor nodes' positions. Currently available range-based algorithms frequently use RSSI [11] or TOA/TDOA (time of arrival/time difference of arrival) [12, 13] to estimate the distance. Range-free algorithms do not need distance information and alternatively use network connectivity information, such as hop counts [14] from beacons to sensor nodes, to estimate the locations of sensor nodes. Most currently available range-based and range-free algorithms are based on one essential assumption: beacons are immobile, and their position information is known and accurate.

Some researchers have proposed a different solution called "mobile beacon" for localization, in which one or more beacons are travelling along specific tracks in the monitored area [10, 15]. We can estimate one sensor node's position according to the distance measurement from the sensor node to the beacons, and the position information of beacons at that time. Through this "mobile beacon" method, it is possible for us to improve the accuracy of localization and reduce the number of beacons in the network. In these algorithms, the position information and moving tracks of beacons must be known and accurate. In this paper, we will focus on those WSNs whose beacons are designed to be immobile because the mobile beacon solution frequently requires additional localization and driving components on beacons, which may not be available for many low-cost, low-power WSN systems.

The "beacons are reliable" assumption frequently does not hold for many WSN systems deployed in unstable environments because beacons may be moved unexpectedly to other positions. In this occasion, the beacons will

no longer be reliable and the localization result will be seriously affected. Srirangarajan et al. considered the effect of inaccurate beacon positions and proposed a distributed localization algorithm based on second-order cone programming (SOCP) relaxation [16]. The proposed algorithm tries to refine beacons' positions by using the relative distance information exchanged with their neighbors. Fan et al. presented a centralized localization algorithm to deal with both inaccurate TOA estimation and positioned beacons [17]. Vemula et al. developed a distributed localization mechanism that incorporates beacon position uncertainty using iterative and Monte Carlo sampling-based methods [18]. Lui et al. devised a semidefinite programming (SDP) algorithm for TOA-based localization in the presence of beacon positions and signal propagation speed uncertainties [19]. The authors also presented a simplified form of the devised algorithm based on the assumption that beacon position errors are independently and identically distributed. Feng et al. designed a robust multihop localization scheme based on trust evaluation to alleviate the effect of inaccurate beacon positions on localization accuracy [20]. In the proposed algorithm, sensor nodes use the trust degrees of beacons as weights in localization to achieve robust estimation of their positions. In the above works, researchers tried to optimize the performance of a specific localization method in case that beacons' positions are no longer reliable. As a comparison, we focus on the beacon drifting detection problem in this paper and try to investigate a distributed detection algorithm that can be applied to existing localization mechanisms to improve localization accuracy.

The most related work to ours is by Kuo et al. [21, 22], who proposed beacon movement detection (BMD) algorithm to detect the unexpected movements of beacons. The basic idea of BMD algorithm is to let the beacons record the variance of RSSI measurement results between each other and report to a calculation center to determine the moved beacons. Like all other centralized algorithms, BMD algorithm will bring a heavy communication burden in collecting detection information from beacons. At the same time, it is also difficult to ensure the completeness of the detection information collected along a long routing path. In order to alleviate the problem, we propose a distributed algorithm to determine the moved beacons in this paper.

## 3. Algorithm Design

We frequently use RSSI measurement value to estimate the distance between nodes. Typically, greater variance of RSSI measurement value over time indicates greater possibility of relative movement between nodes. Thus, we can judge if there is a beacon drifting event through monitoring the variance of RSSI measurement value between beacons. In this section, we will try to investigate a distributed beacon drifting detection algorithm, in which the beacon itself will determine if it has moved. This distributed algorithm does not require a calculation center and, thus, will not bring heavy communication burden in a large-scale network.

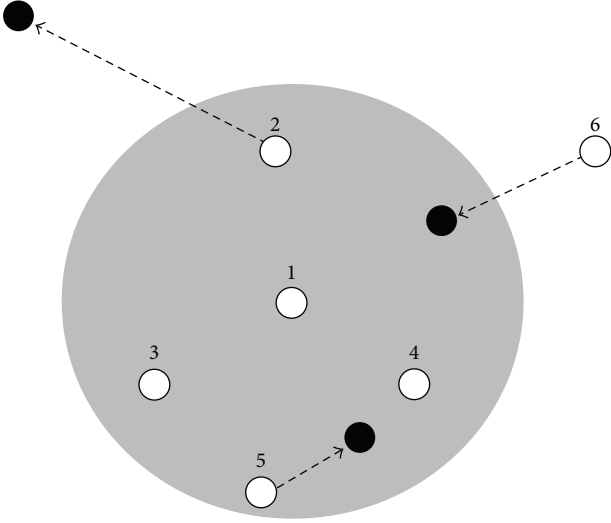


FIGURE 1: An example of fault detection.

Nevertheless, using RSSI measurement value to distributedly deduce the beacon drifting event may cause serious fault detection problem, which can be described as below:

- (i) RSSI measurement value is not always trustable; it may vary even if there is no relative movement between two beacons.
- (ii) Even if the variance of RSSI measurement value can precisely describe the relative movement between beacons, it is also difficult for us to determine exactly which one moves or both of them move. Figure 1 gives an example. In the figure, white dots indicate the original positions of beacons, and the black dots indicate the new positions of beacons after movement. The shadowed area indicates the communication range of beacon 1. We can see that no movement occurred on beacons 1, 3, and 4. Beacon 5 has moved, but is still within the communication range of beacon 1. Beacon 2 moved outside the communication range of beacon 1. Beacon 6 moved into the communication range of beacon 1 and became a new neighboring beacon of beacon 1. Even if the RSSI measurement is accurate (i.e., beacons can accurately detect that if there is a relative movement between each other), different beacons may have different conclusions on movement detection. For instance, the relative distances between beacon 1 and beacons 2, 5, and 6 have changed due to the movements of beacons 2, 5, and 6. For beacon 1, it will find that beacons 2, 5 and 6 have moved. But for beacons 2, 5, and 6, they may find that beacon 1 has moved, but not themselves. This conflicting conclusion will make it difficult for a distributed algorithm to find the correct set of moved beacons.

In order to alleviate the fault detection problem, we designed a cooperative algorithm for beacons including the self-scoring phase and negotiation phase. Generally, the algorithm works as follows:

- (1) each beacon calculates an initial score for itself. This score indicates the movement possibility of the beacon based on the RSSI monitoring results between itself and neighboring beacons.
- (2) Each beacon negotiates with neighboring beacons by telling them its score and adjusts its score based on the received neighboring beacons' scores. This score exchanging process can let beacons share their monitoring results and determine who have moved cooperatively.
- (3) After several rounds of negotiation, each beacon gets a final score. The beacon will determine if itself has moved based on its final score.

**3.1. Beacon Self-Scoring Algorithm.** The beacon self-scoring algorithm is designed based on the monitoring results of RSSI measurement value variance over a period of time. The basic principle of the designed algorithm is for a certain beacon, if there is a large variance of the RSSI measurement value between itself and its neighboring beacons, its position information tends to be unreliable.

Given a network with  $N$  beacons, beacon  $b_i$  can record its RSSI measurement value between itself and its neighboring beacons in a RSSI vector  $O_{i(t)}$  at time  $t$ , as shown in (1), in which  $M_i$  is the number of neighboring beacons of the beacon  $b_i$ ,  $\text{RSSI}_{ij(t)}$  is the RSSI measurement value between the beacons  $b_i$  and  $b_j$  at time  $t$ ,  $s$  is RF receiver sensitivity of beacons, and  $o_{ij(t)}$  is the  $j$ th element in the RSSI vector  $O_{i(t)}$ .  $o_{ij(t)}$  indicates the monitoring result between the beacon  $b_i$  and beacon  $b_j$  at time  $t$ :

$$o_{ij(t)} = \begin{cases} \text{RSSI}_{ij(t)}, & \text{if } b_i \text{ can hear } b_j \\ s, & \text{otherwise} \end{cases} \quad (0 < i \leq N, 0 < j \leq M_i). \quad (1)$$

Beacons update their RSSI vectors periodically, and calculate changed RSSI vectors and unchanged RSSI vectors, as shown in (2), in which  $P_{i(t)}$  and  $Q_{i(t)}$  are the changed RSSI vector and unchanged RSSI vector of beacon  $b_i$  at time  $t$ , respectively.  $p_{ij(t)}$  and  $q_{ij(t)}$  are the  $j$ th elements of  $P_{i(t)}$  and  $Q_{i(t)}$ , respectively.  $\delta$  is a threshold:

$$p_{ij(t)} = \begin{cases} 1, & \text{if } |o_{ij(t)} - o_{ij(0)}| > \delta, \\ 0, & \text{otherwise,} \end{cases}$$

$$q_{ij(t)} = \begin{cases} 1, & \text{if } |o_{ij(t)} - o_{ij(0)}| \leq \delta \quad (o_{ij(t)} \neq s \text{ or } o_{ij(0)} \neq s) \\ 0, & \text{otherwise} \end{cases} \quad (0 < i \leq N, 0 < j \leq M_i). \quad (2)$$

We denote the number of "1" in  $P_{i(t)}$  by  $C_{P_{i(t)}}$ , and the number of "1" in  $Q_{i(t)}$  by  $C_{Q_{i(t)}}$ .

Then, the score can be calculated according to (3), in which the notation  $|\cdot|$  means calculating the absolute value of each element in the vector,  $Sr_{i(t)}$  is the score of beacon  $b_i$  at time  $t$ , and  $k$  is the weight of unmoved neighboring beacons:

$$Sr_{i(t)} = |O_{i(0)} - O_{i(t)}| P_{i(t)}^T - kC_{Q_{i(t)}} \quad (0 < i \leq N). \quad (3)$$

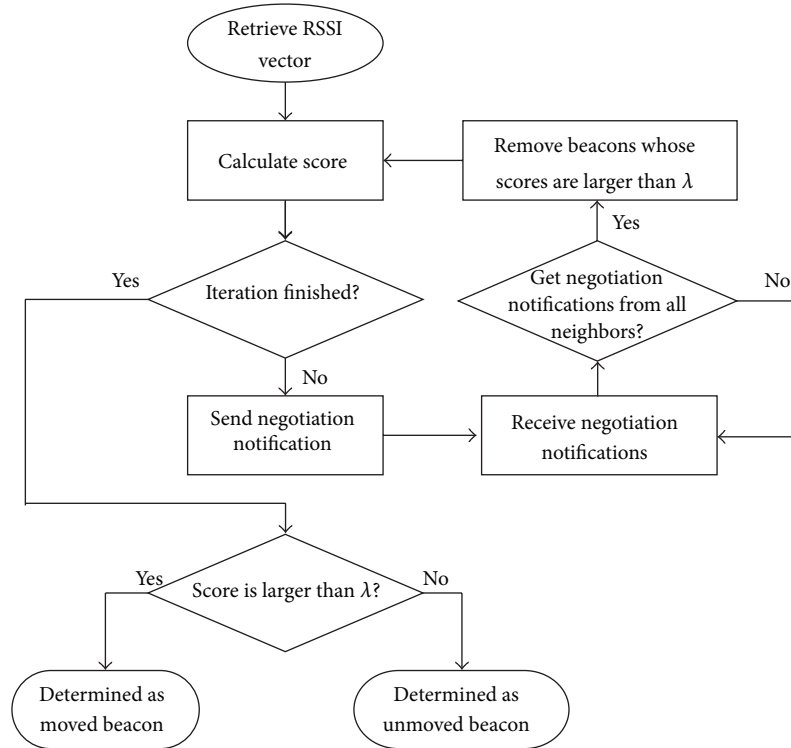


FIGURE 2: Beacon-to-beacon negotiation mechanism.

According to (3), for a certain beacon, if there is a larger change in RSSI measurement value, or the number of its neighboring beacons that are detected to have a large change in RSSI measurement value increases, the score will be higher. As a result, the score reflects the possibility of drifting from the beacon's point of view. A high score indicates that the beacon has a high possibility of drifting.

**3.2. Beacon-to-Beacon Negotiation Mechanism.** The beacon self-scoring algorithm calculates the possibility of drifting by the beacon itself. Obviously, if there are more neighboring beacons are drifting, the self-scoring result is more unreliable. Thus, we designed a negotiation mechanism to alleviate the problem, which can be described as below:

- (1) each beacon broadcasts a negotiation notification which contains its self-scoring result to its neighboring beacons.
- (2) Each beacon that received negotiation notifications from all its neighboring beacons repeats the self-scoring process but excludes those beacons whose scores are larger than a threshold  $\lambda$ . Through this operation, a beacon can use the RSSI monitoring results between itself and those neighboring beacons which are more likely to be unmoved in calculating score, and thus the detection accuracy can be increased.
- (3) The above two steps can be repeated for several times. If the iteration finished and the score of one beacon is still above  $\lambda$ , the beacon will determine itself as

a moved beacon, or it will determine itself as an unmoved beacon.

Figure 2 describes the negotiation process. Higher iteration times may further increase detection accuracy, but will also bring a heavier communication and calculation burden. We will discuss the iteration times selection in Section 4.

**3.3. Determining Algorithm Parameters.** The number of drifting beacons and their moving patterns (e.g., distance) might be different in different networks. Figure 3 shows the simulation results of RSSI measurement value variances in different networks, in which plus signs are the original positions of beacons, circles are the positions of beacons after movement, dotted lines are the directions of movements, and a solid line indicates that there is a relative movement detected between two beacons. It can be seen that when the number of moved beacons is small and the number of all beacons is large, moved beacons have much more connected solid lines than unmoved beacons, and thus we can easily distinguish these two sets of beacons. However, when the number of moved beacons and the number of all beacons are close, it will be difficult to distinguish moved and unmoved beacons. In the discussion below, we will discuss how to choose parameters in the proposed detection algorithm.

**RSSI Variance Threshold ( $\delta$ ).** Through adjusting the RSSI variance threshold  $\delta$ , we aim to realize the following: (1) if the distance between beacons does not change, minimize the possibility of fault detection of beacon drifting; (2) if the distance between beacons does change, minimize the

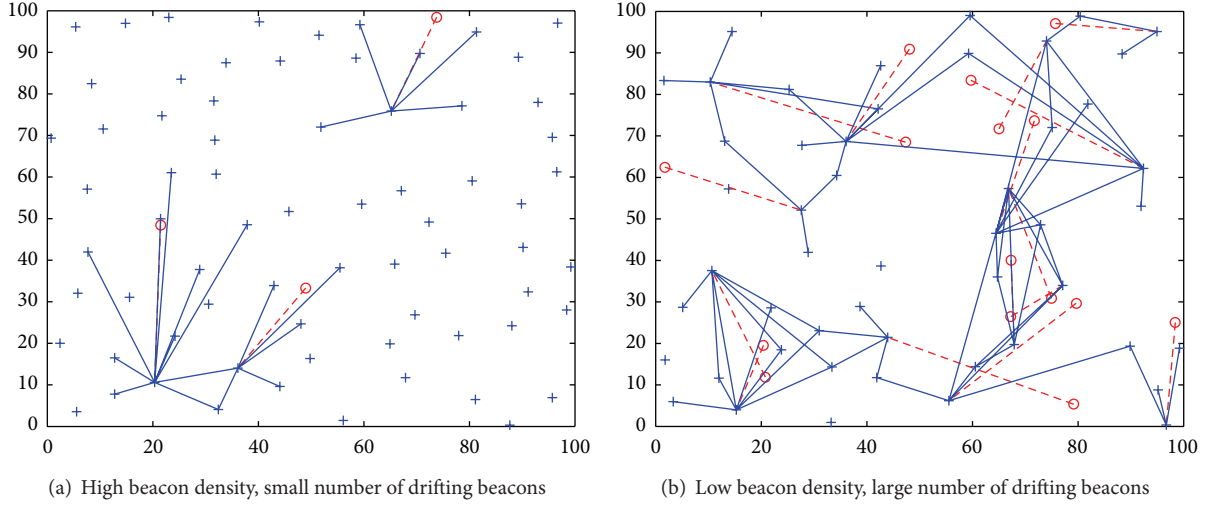


FIGURE 3: The variances of RSSI measurement value in different networks.

possibility of failure to detect beacon drifting. According to previous research results, RSSI measurement value follows the distribution of  $E \sim N(E_0 - 10n_p \lg(d/d_0), \sigma^2)$ , in which  $E$  and  $E_0$  are the RSSI measurement values in case that the distances between two beacons are respectively  $d$  and a short reference distance  $d_0$ , and  $n_p$  is the path loss exponent [23]. We chose the confidence interval as 95.4% and set the RSSI variance threshold  $\delta = 2\sigma$ . In this case, if there is no beacon drifting event, the possibility of RSSI measurement value variance caused by RSSI noise exceeding the threshold is only about 5%.

*Weight of Unmoved Neighboring Beacons ( $k$ ).* Through adjusting the weight of unmoved neighboring beacons  $k$ , we aim to be able to keep the score around threshold  $\lambda$  if it is difficult to judge whether there is a beacon drifting event occurs. For example, if half the neighboring beacons are moved and the rest neighboring beacons are unmoved, it will be difficult to judge if one beacon is moved. Considering (3), when the number of moved beacons and unmoved beacons are equal, the score should be around the threshold  $\lambda$ . For instance, if we use 0 as the threshold  $\lambda$ , then  $k$  should be equal to the mathematical expectation of all elements of  $|O_{i(0)} - O_{i(t)}|$ . However, it is almost impossible to estimate the above mathematical expectation in every deployment. Because the change of RSSI vector over time largely depends on the beacons' receiver sensitivity, we can set  $k$  to the absolute value of  $\alpha s$  in deployment, in which  $s$  is the RF receiver sensitivity. Our experimental exploration shows that  $1/4$  is an appropriate value for  $\alpha$ .

## 4. Evaluation Results

In evaluation, we assume that  $N$  beacons are deployed randomly in a  $L \times L$  square region, and  $N_d$  beacons are drifting randomly within circular areas with radii of  $D$ . The maximum communication distance between beacons is 20 m;  $\lambda$  is set to 0.

We use success rate  $R_s$  and error rate  $R_e$  to evaluate the detection performance. The calculation of  $R_s$  and  $R_e$  is given in (4), in which  $B_d$  is the set of actually moved beacons,  $B_{dg}$  is the set of moved beacons generated by the proposed algorithm, and  $B$  is the set of all beacons:

$$R_s = \frac{\text{card}(B_{dg} \cap B_d)}{\text{card}(B_d)}, \quad (4)$$

$$R_e = \frac{\text{card}(B_{dg} \cap (B - B_d))}{\text{card}(B_d)}.$$

In the discussion below, we will base our evaluation on simulation because it is frequently difficult to build an accurate analytical model for a complex networked system due to its traffic and topology dynamics [24].

*4.1. Selection of the Iteration Times of Negotiation.* In this subsection, we will study the impact of different iteration times of negotiation on the performance of the proposed algorithm. In simulation,  $L$  is set to 100 m,  $N$  is set to 50, and  $D$  is set to 40 m, and we tested the algorithm performance in case that  $N_d$  varies from 1 to 25. Figure 4 gives the test results.

From the figure, we can observe that the noniterative version of the proposed algorithm (i.e., no negotiation is executed in calculating score) gets a high success rate, and at the same time, a relatively high error rate. The success rate almost always keeps at 100%, but maximum error rate also reaches about 60%. This is because that the self-scoring algorithm actually tries to search for as many suspected moved beacons as possible, and thus one beacon has a high possibility of mistakenly judging itself as a moved beacon. We will then check the performance of the proposed algorithm with negotiation. We can see that if the negotiation process iterates once, we can get a much lower error rate (although at this time the success rate drops a little). When we increase the iteration times, it does not bring any obvious performance improvement, but causes a high communication burden. As

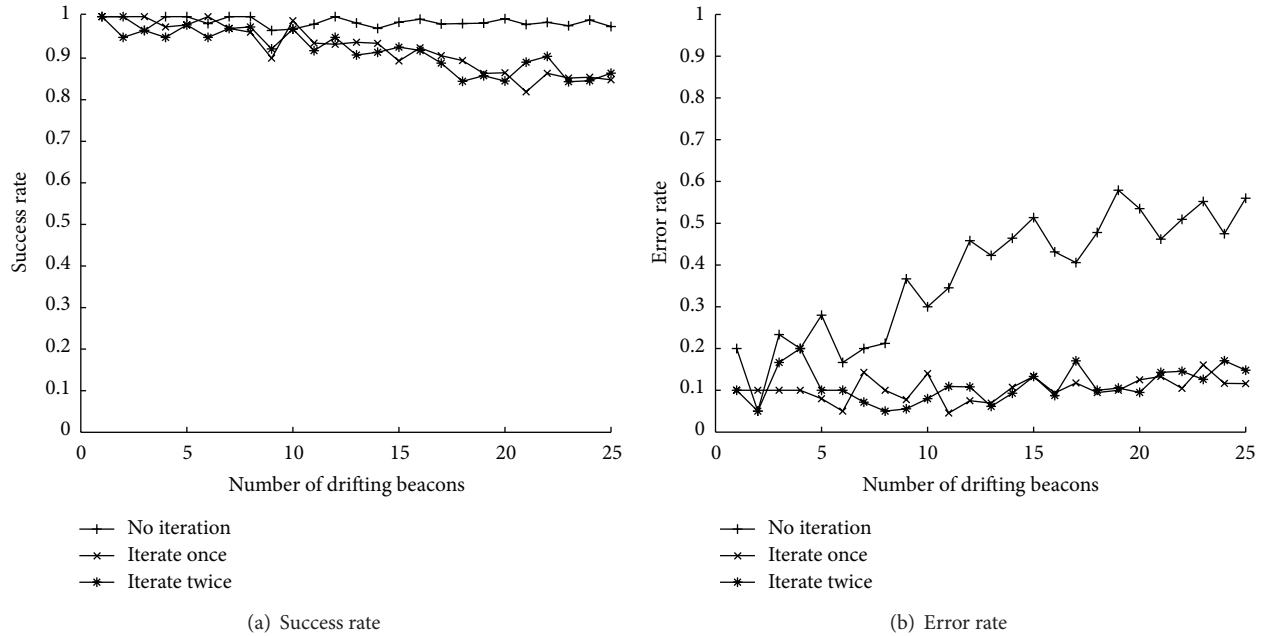


FIGURE 4: Impact of iteration times of negotiation on the proposed algorithm.

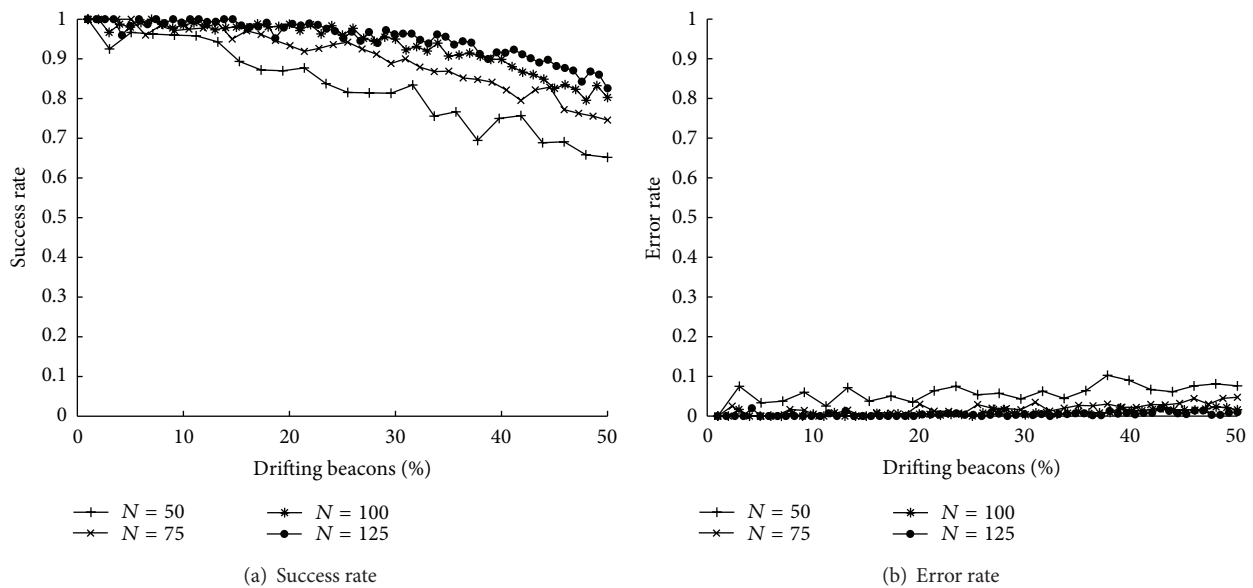


FIGURE 5: Performance of the proposed algorithm in different networking scenarios.

shown in the figure, when we iterate the negotiation process twice, the algorithm performs almost the same as that whose iteration times is set to 1.

As a result, we typically choose to execute the negotiation process once in detecting drifting beacons and will use this setting in later discussions.

#### 4.2. Algorithm Performance in Different Networking Scenarios.

In this subsection, we will study the performance of the proposed algorithm in different networking scenarios. The different networking scenarios we discuss here include (1)

different percentages of drifting beacons out of all beacons in the network; (2) different beacon densities (the number of beacons in a given size network coverage area). In the simulation,  $L$  is set to 100 m,  $D$  is set to 40 m, and we compare the algorithm performance in case that the percentage of drifting beacons varies from 1% to 50%, and  $N$  is respectively set to 50, 75, 100, and 125. Figure 5 shows the simulation results. It can be observed that if the percentage of drifting beacons is low, we can get an ideal detection success rate and error rate. With the increase of the percentage of drifting beacons, both the success rate and error rate degenerate. However, if there are no more than 30% beacons are drifting,

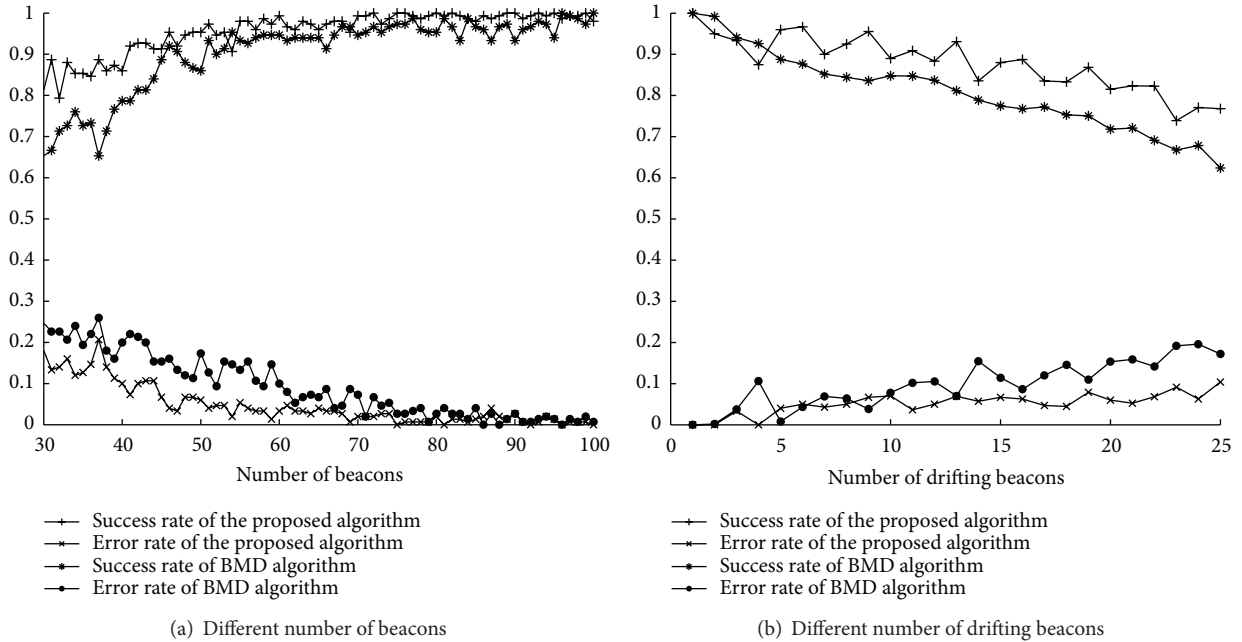


FIGURE 6: Detection performance comparison.

the worst detection success rate is still higher than 0.8. At the same time, the worst detection error rate is always within 0.1 even if there are 50% beacons are drifting. The simulation results also show that the proposed algorithm performs better in high-density networks. For instance, when 50% of beacons are drifting, the success rate and error rate of the proposed algorithm are about 0.65 and 0.08 if there are 50 beacons in total in the network. As a comparison, if there are 125 beacons in the network, the success rate and error rate of the proposed algorithm can be improved to about 0.83 and 0.01, respectively.

**4.3. Algorithm Comparison.** In this subsection, we compare the detection performance and communication overhead between the proposed algorithm and BMD algorithm.

Figure 6 provides the detection performance comparison results, in which  $L$  is set to 100 m, and  $D$  is set to 40 m. In Figure 6(a),  $N_d$  is set to 15, and  $N$  varies from 30 to 100. In Figure 6(b),  $N$  is set to 50, and  $N_d$  varies from 1 to 25. It can be seen that the proposed algorithm performs better than BMD algorithm in both cases.

Figure 7 shows the communication overhead comparison results, in which  $L$  varies from 100 m to 200 m,  $N$  is proportional to  $L^2$  to keep the beacon density constant,  $D$  is set to 40 m, and  $N_d$  is set to 5. Here, the communication overhead indicates the total number of delivered data packets in performing drifting beacon detection. It can be seen that the communication overhead of the proposed algorithm is almost the same as that of BMD algorithm when the network scale is small. With the increase of the network scale, the communication overhead of BMD algorithm increases much faster than that of the proposed algorithm. This is because

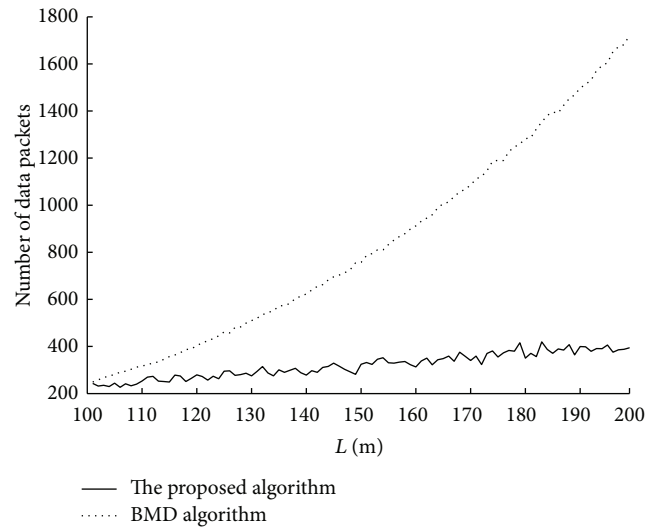


FIGURE 7: Communication overhead comparison.

BMD algorithm is a centralized algorithm, and beacons have to report monitored information to a calculation center to perform detection. As a result, when the network scale increases, the hop counts from beacons to the calculation center increase, and the number of delivered data packets increases fast. As a comparison, the proposed algorithm performs detection in a distributed manner, one beacon only needs to communicate with neighboring beacons to determine if it has moved, and thus the communication overhead increases much slower than centralized algorithms.

## 5. Concluding Remarks

Beacon drifting (the unexpected movement of beacon) greatly affects localization accuracy. In this paper, we proposed a distributed beacon drifting detection algorithm. The proposed algorithm can be applied to existing localization algorithms to avoid using moved beacons in calculating the positions of sensor nodes, and thus the localization accuracy can be improved. Both beacon self-scoring and beacon-to-beacon negotiation mechanisms were designed to achieve high detection accuracy, and at the same time, low operating overhead. Evaluation results show that the proposed algorithm works well in different networking scenarios and outperforms the existing centralized algorithm in both detection accuracy and communication overhead.

## Acknowledgments

This work is supported by the Natural Science Foundation of Zhejiang Province (no. Y1110649), Research Program of Department of Science and Technology of Zhejiang Province (no. 2012C33073), and the Collaborative Industry-University Research Project of Hangzhou (no. 20112731E54).

## References

- [1] I. F. Akyildiz, W. Su, Y. Sankarasubramaniam, and E. Cayirci, "A survey on sensor networks," *IEEE Communications Magazine*, vol. 40, no. 8, pp. 102–114, 2002.
- [2] H. Shi, W. Wang, N. Kwok, and S. Chen, "Game theory for wireless sensor networks: a survey," *Sensors*, vol. 12, no. 7, pp. 9055–9097, 2012.
- [3] J. Polastre, R. Szewczyk, A. Mainwaring, D. Culler, and J. Anderson, "Analysis of wireless sensor networks for habitat monitoring," *Wireless Sensor Networks*, pp. 399–423, 2004.
- [4] P. Lu, S. Chen, and Y. Zheng, "Artificial intelligence in civil engineering," *Mathematical Problems in Engineering*, vol. 2012, Article ID 145974, 22 pages, 2012.
- [5] Y. Zheng, S. Chen, Y. Lin, and W. Wang, "Bio-inspired optimization of sustainable energy systems: a review," *Mathematical Problems in Engineering*, vol. 2013, Article ID 354523, 12 pages, 2013.
- [6] G. Mao, B. Fidan, and B. D. O. Anderson, "Wireless sensor network localization techniques," *Computer Networks*, vol. 51, no. 10, pp. 2529–2553, 2007.
- [7] P. Bahl and V. Padmanabhan, "Radar: an in-building rf-based user location and tracking system," in *Proceedings of the IEEE 19th Annual Joint Conference of the IEEE Computer and Communications Societies (INFOCOM '00)*, pp. 775–784, March 2000.
- [8] A. Savvides, C. C. Han, and M. B. Strivastava, "Dynamic fine-grained localization in ad-hoc networks of sensors," in *Proceedings of the 7th Annual International Conference on Mobile Computing and Networking (MOBICOM '01)*, pp. 166–179, July 2001.
- [9] H. Shi, W. Wang, N. Kwok, and S. Chen, "Adaptive-indexed divisible load theory for wireless sensor network workload allocation," *International Journal of Distributed Sensor Networks*, vol. 2013, Article ID 484796, 18 pages, 2013.
- [10] M. L. Sichitiu and V. Ramadurai, "Localization of wireless sensor networks with a mobile beacon," in *Proceedings of the IEEE International Conference on Mobile Ad-Hoc and Sensor Systems (MASS '04)*, pp. 174–183, October 2004.
- [11] E. Goldoni, A. Savioli, M. Risi, and P. Gamba, "Experimental analysis of RSSI-based indoor localization with IEEE 802.15.4," in *Proceedings of the IEEE European Wireless Conference (EW '10)*, pp. 71–77, April 2010.
- [12] L. Girod and D. Estrin, "Robust range estimation using acoustic and multimodal sensing," in *Proceedings of the IEEE/RSJ International Conference on Intelligent Robots and Systems (IROS '01)*, pp. 1312–1320, November 2001.
- [13] N. B. Priyantha, A. Chakraborty, and H. Balakrishnan, "The cricket location-support system," in *Proceedings of the 6th Annual International Conference on Mobile Computing and Networking (MOBICOM '00)*, pp. 32–43, August 2000.
- [14] D. Niculescu and B. Nath, "DV based positioning in ad hoc networks," *Telecommunication Systems*, vol. 22, no. 1–4, pp. 267–280, 2003.
- [15] S. Li, D. Lowe, X. Kong, and R. Braun, "Wireless sensor network localization algorithm using dynamic path of mobile beacon," in *Proceedings of the 17th IEEE Asia-Pacific Conference on Communications (APCC '11)*, pp. 344–349, October 2011.
- [16] S. Srirangarajan, A. Tewfik, and Z. Q. Luo, "Distributed sensor network localization using SOCP relaxation," *IEEE Transactions on Wireless Communications*, vol. 7, no. 12, pp. 4886–4895, 2008.
- [17] R. Fan, H. Jiang, S. Wu, and N. Zhang, "Ranging error-tolerable localization in wireless sensor networks with inaccurately positioned anchor nodes," *Wireless Communications and Mobile Computing*, vol. 9, no. 5, pp. 705–717, 2009.
- [18] M. Vemula, M. F. Bugallo, and P. M. Djurić, "Sensor self-localization with beacon position uncertainty," *Signal Processing*, vol. 89, no. 6, pp. 1144–1154, 2009.
- [19] K. W. K. Lui, W. K. Ma, H. C. So, and F. K. W. Chan, "Semi-definite programming algorithms for sensor network node localization with uncertainties in anchor positions and/or propagation speed," *IEEE Transactions on Signal Processing*, vol. 57, no. 2, pp. 752–763, 2009.
- [20] R. Feng, X. Guo, N. Yu, and J. Wan, "Robust multihop localization for wireless sensor networks with unreliable beacons," *International Journal of Distributed Sensor Networks*, vol. 2012, Article ID 972101, 13 pages, 2012.
- [21] S. P. Kuo, H. J. Kuo, Y. C. Tseng, and Y. F. Lee, "Detecting movement of beacons in location-tracking wireless sensor networks," in *Proceedings of the IEEE 66th Vehicular Technology Conference (VTC-Fall '07)*, pp. 362–366, October 2007.
- [22] S. P. Kuo, H. J. Kuo, and Y. C. Tseng, "The beacon movement detection problem in wireless sensor networks for localization applications," *IEEE Transactions on Mobile Computing*, vol. 8, no. 10, pp. 1326–1338, 2009.
- [23] N. Patwari, J. N. Ash, S. Kyperountas, A. O. Hero, R. L. Moses, and N. S. Correal, "Locating the nodes: cooperative localization in wireless sensor networks," *IEEE Signal Processing Magazine*, vol. 22, no. 4, pp. 54–69, 2005.
- [24] S. Chen, W. Huang, C. Cattani, and G. Altieri, "Traffic dynamics on complex networks: a survey," *Mathematical Problems in Engineering*, vol. 2012, Article ID 732698, 23 pages, 2012.

## Research Article

# Modeling for Green Supply Chain Evaluation

Elham Falatoonitoosi,<sup>1</sup> Zulkiflle Leman,<sup>1</sup> and Shahryar Sorooshian<sup>2</sup>

<sup>1</sup> Department of Mechanical and Manufacturing Engineering, Universiti Putra Malaysia (UPM), 43300 Serdang, Selangor, Malaysia

<sup>2</sup> Faculty of Technology, University Malaysia Pahang (UMP), Malaysia

Correspondence should be addressed to Shahryar Sorooshian; sorooshian@gmail.com

Received 13 January 2013; Revised 17 March 2013; Accepted 18 March 2013

Academic Editor: Shengyong Chen

Copyright © 2013 Elham Falatoonitoosi et al. This is an open access article distributed under the Creative Commons Attribution License, which permits unrestricted use, distribution, and reproduction in any medium, provided the original work is properly cited.

Green supply chain management (GSCM) has become a practical approach to develop environmental performance. Under strict regulations and stakeholder pressures, enterprises need to enhance and improve GSCM practices, which are influenced by both traditional and green factors. This study developed a causal evaluation model to guide selection of qualified suppliers by prioritizing various criteria and mapping causal relationships to find effective criteria to improve green supply chain. The aim of the case study was to model and examine the influential and important main GSCM practices, namely, green logistics, organizational performance, green organizational activities, environmental protection, and green supplier evaluation. In the case study, decision-making trial and evaluation laboratory technique is applied to test the developed model. The result of the case study shows only “green supplier evaluation” and “green organizational activities” criteria of the model are in the cause group and the other criteria are in the effect group.

## 1. Introduction

Environmental protection is becoming more and more important for enterprises because of stronger public awareness, competitors and communities, and government regulations. For this purpose, some programs become more popular for environmentally aware performing including total quality environmental management, ISO 14000 standards, and green supply chain management. Reducing the environmental pollution from upstream to downstream during procuring raw materials, producing, distribution, selling products, and products depreciation is the most important goal of green supply chain management (GSCM).

Indeed, there is no research that determines main factors in a whole green supply chain system or specify their power of influence on each other to find their role in a system. This study fills this gap by presenting a model that consists of five main practices to improve GSCM by selecting green supplier.

Supplier selection is a fundamental issue of supply chain area which heavily contributes to the overall supply chain performance [1]. Suppliers' development is a critical function within supply chain management. Green supplier

improvement is also essential for effective green supply chain management.

Supply Chain managers could minimize the products' environmental impact based on some related environmental criteria. It harmonizes the economic, customer value, manufacturability, and other factors that may also be evaluated. Additionally, buyer-supplier relations play an increasingly important role in addressing environmental issues. The third concern is that firms should change their environmental performance methods in order to incorporate environmental concerns of external sources. Therefore, a system analysis is needed to integrate environmental management with the greening of the supply chain. Supply chain managers must consider the complete environmental impact of a product during its entire life cycle, including raw material, manufacturing/assembly processes, distribution, use, and disposal. The environmental effects include material, energy, air, water, and solid waste pollution [2].

The main and basic challenges in the green supply chain are modeling a strategy to manage the resources and meet the demands [3]. Select the green suppliers that will deliver the goods and services that are required to manufacture the

product, deliver the product to the customers environmentally, and arrange for return of the product for servicing through customers, if there is any fault in the product. This study concentrates mainly on the supplier selection problem. Selecting suitable suppliers for purchasing the raw materials is an important part of the operation [4, 5].

The decision of selecting the right supplier is prone to errors. The right supplier is the one who will meet and complement the organization's needs from its corporate culture to long-term future requirements [6, 7]. Today, buyers are willing to purchase products and services from suppliers that manage to provide them with high quality, low cost, and short lead time with environmental responsibility at the same time because of increasing environmental attentiveness. On the contrary, a number of criteria are quantitative such as "price of the product," "lead time for delivery," "transportation cost," and so forth [8]; whereas some, like "pollution control," "reducing the waste," "quality of service," and so forth, are qualitative [9]. No single methodology appears to be dominant in solving the supplier selection problem [10].

In the last century, the most important challenge for enterprises has been integrating of social, environment, and economic performance to obtain sustainable improvement [11]; in other words, if firms want to survive in the global market they cannot disregard environmental issues. In spite of traditional supplier selection that focused on price, quality, and delivery on time [12] or concentrated only on the requirements of single organizations and lose to consider the whole supply chain [13], green supplier selection processes have to focus on improving environmental factors in whole supply chain through organizational performance and activities, consumption, logistics, customer service, and financial performance concurrently [14, 15].

One of the most obvious gaps by considering to previous studies is the large number of mathematical and quantitative models that have been applied for selecting green suppliers such as AHP (Analytic Hierarchy Process) technique [16, 17], fuzzy comprehensive evaluation [10], comprehensive grade model [18], grey widespread evaluation [9], and so forth. In fact, the nature of supplier selection is both quantitative and qualitative; therefore, the quantitative models could not be reliable enough. On the other hand, some of these quantitative methods have complicated calculation, while others cannot avoid subjective presumption [8]. As well, there is not any consideration to complex causal relationship between criteria of the system along dependences and feedbacks among criteria and alternatives simultaneously [13]. Therefore, the DEMATEL technique is applied in this study to examine both direct and indirect effects among green practices and visualize the causal relationships among them.

## 2. Literature Review

*2.1. Supply Chain and Green Supply Chain Management.* The concepts of supply chain management (SCM) and supply chain have been remarked as one major trend of the management. The Supply chain has been known to comprise of suppliers, manufacturers, retailers, transporters, warehouses,

and customers; these are all directly or indirectly helped in customer request fulfillment [19]. Moreover, coordination benefits were revealed by the partners of supply chain [20], thus making SCM to become organizations critical strategy to formulate competitive benefits [21].

The supply chain includes not only suppliers and manufacturers, but also warehouses, retailer's transporters, and consumers themselves. A supply chain is a distribution and facility network that carries out the activities of material procurement and its reformation into finished and intermediary products as well as the finished products distribution to customers [22, 23]. The monitoring of environmental management programs of GSCM is reactive, proactive practices including reverse logistics, recycling, and remanufacturing. However, [24] believed that it is an innovative chain supply management from green purchase, green packaging, green manufacturing, and reverse logistics.

For the companies transfer to the "green" of their supply chain, motivators should be different. Although some of the motivators are unclear, according to, some of the organizations do this due to the fact that it is the right thing for the environment. Although some are more radical for the change of the environment while others may not [25], researchers have reported that reduction in the cost and profitability are some of the major business motivators to become "green" in the supply chain [26, 27]

*2.2. Importance of Supplier Selection.* Suppliers are the sellers that provide the raw material, services, or components which an organization may not be able to provide for it. In the present manufacturing environment for supply chain, the supplier is the major part of an organization. A suitable supplier is capable of offering the company the correct quality products and quantity at affordable prices at the best time [28]. The emergence of supply relationship has shown that suppliers are needed for a set of competences that form part of the supply system, which is capable of facing market competition [29].

## 3. Material and Methods

This study proposes an evaluation framework based on the DEMATEL methodologies to assist in GSCM strategic decisions. Firstly, we identify the green supplier evaluation criteria and present the proposed evaluation model in the following subsections, and then we mention the proposed techniques. According to previous researches, five main concepts for improving green supply chain management have been identified.

*3.1. Green Supplier Evaluation Framework.* The general view of the proposed green supplier evaluation framework is shown in Figure 1. Green supplier selection problem is a sort of complex multiple criteria decision making problem including both quantitative and qualitative factors, which may be inconsistent and may also be uncertain. Due to the nature of supplier selection, Multicriteria decision making

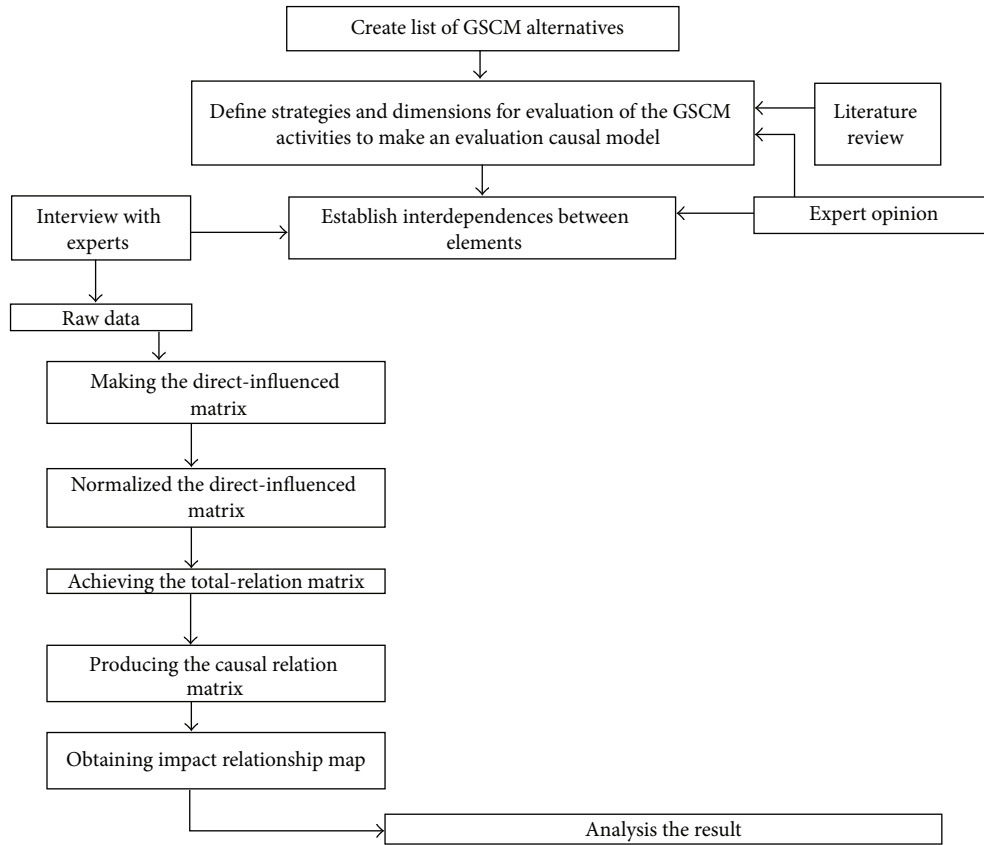


FIGURE 1: Green supplier evaluation framework.

(MCDM) methods are required to handle and solve the problem effectively. The techniques of MCDM are comprehensibly derived to manage this kind of problems [30].

3.2. *Criteria for Green Supplier Evaluation.* According to review of previous researches, five main concepts for improving green supply chain management have been identified: organizational performance (OP), green logistics (GL), green organizational activities (GOA), environmental protection (EP) and green supplier evaluation (GSE).

3.2.1. *Organizational Performance.* The requirements for strategic performance may not be environmentally based and are important to assist in identifying how well different alternative factors can be performed. They are essential because the selected alternative should not only support the green supply chain, it is also sensible of the area of business [31]. The adoption of OP measures was supported by many thinkers [32, 33]. One characteristic about the performance measure is that they are static. They are dynamic over time and are influenced by the product lifecycle.

3.2.2. *Green Logistics.* GL is the management activities to pursue customer satisfaction and social development goals, connecting the main body of green supply and demand, overcoming space and time obstacles to achieve efficient

and rapid movement of goods and services. It inhibited the damage to environment to achieve the purification of the logistics environment and the best use of logistics resources. GL is a multilevel concept which includes both the green logistics business activities and social activities for green logistics management, standardization, and control [34].

3.2.3. *Environmental Protection.* Protection of the environment is a major area of green supply chain which compares the system of environmental protection like controlling all kinds of pollution and designs products according to green image, ISO 14001, and so forth. Major indicators are engaged in the recovery of resources conservation and resource utilization and resource type, environmental governance, environmental pollution, and reinvented ability. Moreover, it is made up of packaging materials, transport, emissions, garbage, and emissions [35, 36]. In the US Air pollution Control Act and Water Pollution Control Act 1955 and 1948 were introduced by the Environmental Protection Agency (EPA).

3.2.4. *Green Organizational Activities.* GOA consists of different subjects such as recycling, reducing all kind of waste, reusing abilities, and so forth. In other words, managing of recovered products has become an important business for many firms. Used products from variable sources carried out the covering process to gain sustainable effect in the supply

chain for lower cost [7]. According to Theyel [37], collection of schemes is classified according to material to sort and reuse products to reduce manufacturing costs. The products are obtained from the end users and returned to the factory for disposal.

**3.2.5. Green Supplier Evaluation Criteria.** It includes several concepts such as quality of services, new technologies, organization levels, and so forth that is, the level of relationship cooperation and attitudes are the major factors for GSC supplier suitability. The organizational cultural agreement and level of fitness are the sum of the attributes desires [38]. Moreover, one major part of GSE has been green consumption, its services and related products use which responds to the basic needs with better quality of life while natural resources and toxic material are maximized preventing future generation exposure to pollutants [39].

**3.3. Green Supplier Evaluation Model.** Based on criteria identification phase, direct and indirect effects and interactions between criteria are detected and evaluation model for green supplier selection is provided in Figure 2, a causal evaluation model (CEM).

For determining the relation and concepts, in this phase, five researchers from University Putra Malaysia (UPM), who work on SCM, are consulted. As a result the CEM has been proposed at the end of this phase.

In Figure 2 a straight line or an arc indicates the interactions between two criteria. For instance, when the factors of a cluster “green logistics” depend on factors of another “criteria”, this relation is represented by an arrow from component “green logistics” to “Criteria.”

From a mathematical view, the CEM says:

$$\text{CEM} = f(\text{GSE}, \text{EP}, \text{GOA}, \text{GL}, \text{OP}) \quad (1)$$

subject to

$$\begin{aligned} \text{GSE} &= f(\text{EP}, \text{GOA}, \text{GL}, \text{OP}), \\ \text{EP} &= f(\text{GSE}, \text{GOA}, \text{GL}, \text{OP}), \\ \text{GOA} &= f(\text{GSE}, \text{EP}, \text{GL}, \text{OP}), \\ \text{GL} &= f(\text{GSE}, \text{EP}, \text{GOA}, \text{OP}), \\ \text{OP} &= f(\text{GSE}, \text{EP}, \text{GOA}, \text{GL}). \end{aligned} \quad (2)$$

#### 4. Application and Testing of the Model

For testing the model, a case study with expert interview technique is applied for this research. The objects were 10 professional experts who are working in supply chain departments of Iran Khodro Co. (SAPCO). Each interview has been done individually by each expert and took time between minimum 45 minutes to maximum 60 minutes for each of them. During the interviews, questions did not follow. First, the evaluation model along with all components and interactions between criteria was described for each of them. Next step in interview is determining relations

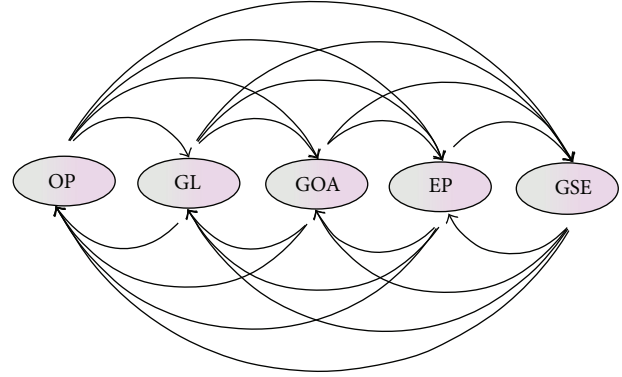


FIGURE 2: Causal evaluation model (CEM).

between concepts according to loops and arcs. In this step, consultation committee with experts determines the relations among influential factors in evaluation model. Each expert performs pairwise comparisons between each to factors and gives the score from 0 to 4 according to their experiences and believes that factor  $i$  affects factor  $j$ . For this purpose, a group of engineers is selected from SAPCO (Supplying Automotive Parts Co.), the most important supplier and the main subset for Khorasan Iran Khodro Company. In fact, to apply DEMATEL technique, using expert’s opinion among and within the elements to to paired comparison analysis is required.

#### 5. Case Analysis Method

Green supplier selection problem is a sort of complex multiple criteria decision making problem including both quantitative and qualitative factors, which may be inconsistent and may be uncertain. Due to the nature of supplier selection, MCDM methods are required to handle and solve the problem effectively [40]. Multiple criteria decision making (MCDM) using the decision making trial and evaluation laboratory (DEMATEL) was proposed in this case analysis. The method of DEMATEL was chosen to assess the inner dependence level existence of green supply chain management, for selected practice indicators, and to build a network relationship map (NRM) as well as structural complex causal relationship visualization between the system criteria which acquires the criteria influence levels. In DEMATEL structure, each factor or part may exert on and obtain other higher or lower level factors. One of excellence of this technique rather than others decision making method in applying feedback application. The entire factors establish worth and importance of factors instead of considering only specific factors [41–43].

For applying DEMATEL, there are 6 main steps:

- (1) making the direct-influenced matrix,
- (2) calculating the direct-influenced matrix normalization,
- (3) achieving the total-relation matrix,
- (4) producing a causal diagram,

- (5) obtaining the inner dependence matrix and impact relationship map,
- (6) obtaining the inner dependence matrix. In this step, the sum of each column in total-relation  $n \times n$  matrix is equal to 1 by the normalization method, and then the inner dependence matrix can be acquired.

5.1. *The Procedures of the DEMATEL Technique.* The procedures of the DEMATEL method can be expressed as follow.

*Step 1* (finding the direct-relation (average) matrix). Four scales determine the values of relationships among different factors according to the experts' opinion:

0 = no influence, 1 = low influence, 2 = high influence, 3 = very high influence.

In DEMATEL technique,  $H$  experts and  $n$  factor (criteria) have to be considered. Each expert answers the certain questions to demonstrate the degree of a criterion  $i$  effect criterion  $j$  based on her or his beliefs. For now,  $a_{ij}$  donates pair wise comparisons between any two criteria and it is assigned integer score ranging from 0, 1, 2, 3, 4. The scores are given by each expert and  $X^1 X^2 \dots X^H$  are answers to each of them that make the  $n \times n$  nonnegative matrix  $X^k = [x_{ij}^k]_{n \times n}$ , with  $1 < k < H$ . A high score indicates a belief that greater improvement in  $i$  is required to improve  $j$ . Then it is possible to calculate the  $n \times n$  average matrix  $A$  on account of all expert's opinions by averaging the  $H$  their scores as follows:

$$[a_{ij}]_{n \times n} = \frac{1}{H} \sum_{k=1}^H [x_{ij}^k]_{n \times n}. \quad (3)$$

The initial direct effects that each criterion exerts on and receives from other criteria are exposed in the average matrix  $[a_{ij}]_{n \times n}$ , which is also called the initial direct influenced. Moreover, in this level, gaining the causal effect between each pair of criteria in a system by drawing an influence map will be possible, also as follows:

- (1) If  $a_{ij} \leq 1$  (independent is identified among all criteria; otherwise, nonindependent will be identified).
- (2) The structural relations between the criteria of a system are converted to intelligible and logical map of the system. Figure 1 shows an example of such a network influence map which helps to explain the structure of the factors.  $C_i$  represents a criterion in the system. As an instance the arrow from  $C_1$  to  $C_2$  indicates the effect that  $C_1$  has on  $C_2$  and the power of its effect is 3.

*Step 2* (normalize the initial direct-relation matrix). Normalized initial direct relation matrix  $D$  is obtained by normalizing the average matrix  $A$ , in the following formulas:

$$S = \max \left\{ \max_{j=1}^n \sum_{i=1}^n a_{ij}, \max_{i=1}^n \sum_{j=1}^n a_{ij} \right\}, \quad (4)$$

$$D = \frac{A}{S}.$$

TABLE 1

	OP	GL	GOA	EP	GSE
Organizational performance	0	3.5	0	0	0
Green logistics	3.7	0	0	3.4	0
Green organizational activities	0	3.1	0	3.2	0
Environmental protection	0	3	2.8	0	0
Green supplier evaluation	3.8	3.4	3.1	3.3	0

TABLE 2: Direct-relation matrix  $D$ .

	Main criteria				
	OP	GL	GOA	EP	GSE
Organizational performance (OP)	0.000	0.257	0.000	0.000	0.000
Green logistics (GL)	0.272	0.000	0.000	0.250	0.000
Green organizational activities (GOA)	0.000	0.228	0.000	0.235	0.000
Environmental protection (EP)	0.000	0.221	0.206	0.000	0.000
Green supplier evaluation (GSE)	0.279	0.250	0.228	0.243	0.000

As a result total direct influences that criterion  $i$  gives to the other criteria are gained by sum of each row  $i$  of matrix  $A$  as well as the sum of each column  $j$  represent most direct effects on others by total direct effects of the criterion. Likewise, since the sum of each column  $j$  of matrix  $A$  represents the total direct effects received to other criteria by criterion  $i$ ,  $\max \sum_{i=1}^n a_{ij}$  represents the total direct effects that the criterion  $j$  receives the most direct effects from other criteria and the positive numerical  $s$  takes the smaller of the two as the upper bound, and the matrix  $D$  is obtained by dividing each element of  $A$  by the scalar  $s$ . Each element  $d_{ij}$  of matrix  $D$  is between zero and less than 1:  $0 < d_{ij} < 1$ .

*Step 3* (calculate the total-relation matrix). A continuous reducing of the indirect effects of problems beside the powers of matrix  $D$ , like to an engrossing Markov chain matrix, guarantees convergent solutions to the matrix inversion.

Note that

$$D^2, D^3, \dots, D^\infty,$$

$$\lim_{m \rightarrow \infty} D^m = [0]_{n \times n}, \quad (5)$$

$[0]_{n \times n}$  is a  $(n \times n)$  null matrix.

The total relation matrix  $T_{n \times n}$  is achieved as follow:

$$\begin{aligned} \sum_{m=1}^{\infty} D_i &= D + D^2 + D^3 \dots D^m \\ &= D(I + D + D^2 + \dots + D^{m-1}) \\ &= D(I - D)^{-1} (I - D) (I + D + D^2 + \dots + D^{m-1}) \\ &= D(1 - D)^{-1} (I - D^m) = D(I - D)^{-1}. \end{aligned} \quad (6)$$

$I$ : identity matrix,  $T$ : total-relation matrix ( $[T]_{n \times n}$ ).

TABLE 3: Total-relation matrix.

	Main criteria							
	OP	GL	GOA	EP	GSE	R	R + C	R - C
Organizational performance (OP)	0.081	0.299	0.016	0.079	0.000	0.475	1.477	-0.527
Green logistics (GL)	0.316	0.163	0.063	0.306	0.000	0.848	2.511	-0.815
Green organizational activity (GOA)	0.093	0.342	0.069	0.337	0.000	0.841	1.544	0.138
Environmental protection (EP)	0.089	0.327	0.234	0.137	0.000	0.787	2.098	-0.524
Green supplier evaluation (GSE)	0.423	0.532	0.321	0.452	0.000	1.728	1.728	1.728
C	1.002	1.663	0.703	1.311	0.000			

The sum of rows and sum of columns of the total relation matrix  $T$  are computed as an  $r$  and  $c_{n \times 1}$  vectors, one has

$$[r_i]_{n \times 1} = \left( \sum_{j=1}^n t_{ij} \right)_{n \times 1}, \quad (7)$$

$$[c_j]_{1 \times n} = \left( \sum_{i=1}^n t_{ij} \right)_{1 \times n}.$$

$[r_i]_{n \times 1}$  demonstrates the total effects, both direct and indirect, given by criterion  $i$  to the other criteria  $j = 1, 2, \dots, n$ ; similarly  $[c_j]_{1 \times n}$  represents total effects, direct and indirect, received by criterion  $j$  from the other criteria  $i = 1, 2, \dots, n$ . As a result, while  $i = j$  the sum  $(r_i + c_i)$  that is called "prominence" proves the degree of importance role of criterion  $i$  in system and also gives an index that shows the total effects both given and received by criterion  $i$ . likewise, the  $(r_i - c_i)$  that in called "Relation" shows the net effect that criterion  $i$  donates to the system. When  $(r_i - c_i)$  is positive, criterion  $i$  will be to the cause group, and when  $(r_i - c_i)$  is negative, criterion  $i$  is a net receiver.

## 6. Case Analysis, Result, and Discussion

In this phase, both direct and indirect influences will be achieved by applying DEMATEL technique and finally criterions will be divided to cause and effect groups.

*Step 1.* At first, a committee was formed including the ten experts from Supply Chain Department in an automotive company named Iran Khordo, the biggest automotive company in the middle east.

*Step 2.* Finding the initial direct-relation (Average) matrix: Table 2 illustrates the values of relationships between criteria that are determined by pair wise comparisons between any two criteria according to the experts' opinion and they are assigned integer score ranging from 0 to 4. The values in Table 1 are calculated according to (3).

In addition, Figure 3 demonstrates the relations among the influential main criteria. The numbers show the direct effect that each cluster gives to other clusters or receives from them.

*Step 3.* Normalized initial direct relation matrix  $D$  is obtained by normalizing the initial matrix  $A$  according to (4); matrix  $D$  is indicated in Table 2.

TABLE 4: Cause and effect group of environmental protection.

Cause group	Green supplier evaluation
	Green organizational activities
Effect group	Green logistics
	Organizational performance
	Environmental protection

TABLE 5: The inner dependence of environmental protection.

	OP	GL	GOA	EP	GSE
Organizational performance (OP)	0.171	0.629	0.034	0.166	0.000
Green logistics (GL)	0.373	0.192	0.074	0.361	0.000
Green organizational activity (GOA)	0.111	0.407	0.082	0.401	0.000
Environmental protection (EP)	0.113	0.416	0.297	0.174	0.000
Green supplier evaluation (GSE)	0.245	0.308	0.186	0.262	0.000

*Step 4.* Calculating the total-relationships matrix  $T$  for causal relation by achieving the  $D(I - D)^{-1}$  according (6). Table 3, indicates the total-relation matrix  $T$ .

By considering proposed evaluation framework, green supplier evaluation (GSE) has significant effect on other four clusters and receives effects from none of them. In other words, all criteria have been affected by GSE. Besides, green organizational activities (GOA) receive and give influences equally in spite of other three main criteria. It is clear that GSE belongs to the cause group and also GOA can be part of the cause group. Eventually, results show GSE by the greatest  $(R - C)$  score with 1.728 is part of the cause group and GOA are located in the second place of cause group with 0.138. In addition green logistics (GL) has the maximum  $(R + C)$  score that is showing it is the most important criteria for the GSC improvement, but the  $(D - R)$  value of GL (-0.815) is the smallest score among effect factor. Indeed, the degree of influential impact  $D$  and degree of influenced impact  $C$  which are 0.848 and 1.663, respectively, are the highest scores of all factors. It means that GL is an effect factor; it noticeably affects other aspects and on the entire system.

Unconformably with Table 4, all five criteria are divided into the cause and effect groups. And with Figure 4, Impact Relation Map for main criteria is shown.

TABLE 6: Ranking dimensions evaluation model.

	Ranking of important factors	Ranking of affected factors	Ranking of influential factors
1	Green logistics	Green logistics	Green supplier evaluation
2	Environmental protection	Environmental protection	Green logistics
3	Green supplier evaluation	Organizational performance	Environmental protection
4	Green organizational activity	Green organizational activity	Green organizational activity
5	Organizational performance	Green supplier evaluation	Organizational performance

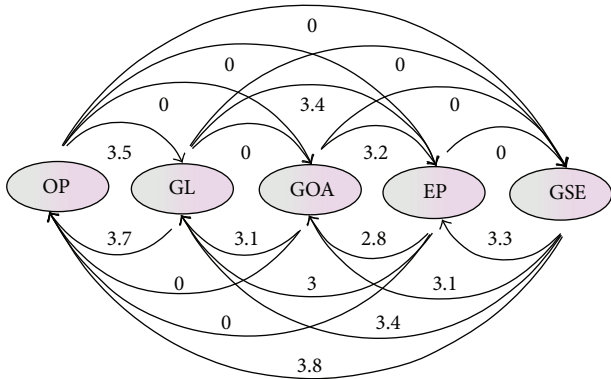


FIGURE 3: Graphical causal relation criteria.

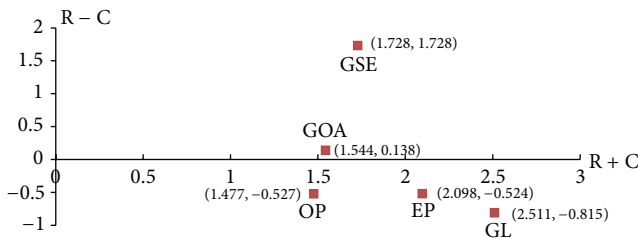


FIGURE 4: Impact Relation Map for main criteria.

By considering Table 4, GSE and GOA belong to the case group. It means that both of these criteria have significant impacts on other criteria in the causal model. In other words by improving GSE and GOA, a noticeable development will be happened on other criteria and in a whole system.

According to Figure 4, GSE is the most influential factor and GL is the most important factor in the whole system.

As in Table 5, by the normalization method, the sum of each column in total-relation matrix is equal to 1 and then the inner dependence matrix can be acquired. By considering Table 5, the comparison between criteria becomes easier because of the same scale.

By considering the result, all five factors of evaluation model can be prioritized based on the most important, most influential, and the most affected. Table 6 demonstrates ranking of criteria on framework.

### 7. Conclusion

This study proposes the evaluation framework to improve green supply chain by applying the DEMATEL method to analyze and prioritize essential factors in green supplier

selection on automotive industries. As a conclusion, green Logistics, organizational performance, green organizational activities, environmental performance and green supplier evaluation are ranked according to power of influence and degree of importance in a whole green supply chain system; therefore, manufacturers and suppliers will be able to develop their activities according to the green image by adopting the results of this study. In addition, there is not any research in this area that presents the same result, so there is no way to compare outcomes.

On one hand, the results of this research enable enterprises to find out which suppliers are suitable by considering environmental and traditional practices in proposed model. The proposed model can be applied in two purposes: first, it would help enterprises to find out which factors are more effective and important to select the best possible green supplier with regard to both direct and indirect relations between elements. On the other hand, if a company is a supplier for other companies and wants to implement environmental practices in own manufacturing system, it can provide the model the whole system.

In fact, the case study of this research finds criteria that influence green supplier selection and set up the strategy map among these criteria by using DEMATEL technique. The direct relationship map indicates interdependencies among all criteria and their strengths in model. The current study finds that both green supplier evaluation and green organizational activities have a considerable impact on the other criteria; so by improving these 2 criterions, other criteria will be improved automatically.

For further studies we suggest more case studies to valid CEM in different industries and also to gain more understanding of interrelationship effects of GSE, EP, GOA, GL, and OP. The CEM can be modified by using hybrid fuzzy DEMATEL.

### Conflict of Interests

The authors declare no possible conflict of interests.

### References

- [1] A. Sanayei, S. F. Mousavi, and A. Yazdankhah, "Group decision making process for supplier selection with VIKOR under fuzzy environment," *Expert Systems with Applications*, vol. 37, no. 1, pp. 24–30, 2010.
- [2] P. Ramin, "Modeling for green management," in *Proceedings of the Conference on Management*, pp. 23–26, Kerman, Iran, October 2009.

- [3] J. Sarkis, "A strategic decision framework for green supply chain management," *Journal of Cleaner Production*, vol. 11, no. 4, pp. 397–409, 2003.
- [4] A. H. I. Lee, H. Y. Kang, C. F. Hsu, and H. C. Hung, "A green supplier selection model for high-tech industry," *Expert Systems with Applications*, vol. 36, no. 4, pp. 7917–7927, 2009.
- [5] W.-N. Pi and C. Low, "Supplier evaluation and selection via Taguchi loss functions and an AHP," *International Journal of Advanced Manufacturing Technology*, vol. 27, no. 5-6, pp. 625–630, 2006.
- [6] A. Karunaratne, L. M. Chi, H. S. Min, and S. Sorooshian, "Supply chain strategy," *International Journal of Innovative Ideas*, vol. 12, no. 4, pp. 7–8, 2012.
- [7] W. F. Oh, I. Resty, X. Y. Yang, and S. Sorooshian, "Strategy for supply chains," *Journal of Science*, vol. 2, no. 1, p. 90, 2012.
- [8] R. Handfield, R. Sroufe, and S. Walton, "Integrating environmental management and supply chain strategies," *Business Strategy and the Environment*, vol. 14, no. 1, pp. 1–19, 2005.
- [9] J. D. Linton, R. Klassen, and V. Jayaraman, "Sustainable supply chains: an introduction," *Journal of Operations Management*, vol. 25, no. 6, pp. 1075–1082, 2007.
- [10] A. Amid, S. H. Ghodsypour, and C. O'Brien, "Fuzzy multiobjective linear model for supplier selection in a supply chain," *International Journal of Production Economics*, vol. 104, no. 2, pp. 394–407, 2006.
- [11] H. J. Wu and S. Dunn, "Environmentally responsible logistics systems," *International Journal of Physical Distribution & Logistics Management*, vol. 25, pp. 20–38, 1995.
- [12] S. J. Lin, I. J. Lu, and C. Lewis, "Grey relation performance correlations among economics, energy use and carbon dioxide emission in Taiwan," *Energy Policy*, vol. 35, no. 3, pp. 1948–1955, 2007.
- [13] Y.-J. Chen, "Structured methodology for supplier selection and evaluation in a supply chain," *Journal of Information Sciences*, vol. 19, pp. 1651–1670, 2011.
- [14] J. D. Linton, R. Klassen, and V. Jayaraman, "Sustainable supply chains: an introduction," *Journal of Operations Management*, vol. 25, no. 6, pp. 1075–1082, 2007.
- [15] J. Sarkis, "A strategic decision framework for green supply chain management," *Journal of Cleaner Production*, vol. 11, no. 4, pp. 397–409, 2003.
- [16] W.-N. Pi and C. Low, "Supplier evaluation and selection via Taguchi loss functions and an AHP," *International Journal of Advanced Manufacturing Technology*, vol. 27, no. 5-6, pp. 625–630, 2006.
- [17] U. P. Wen and J. M. Chi, "Developing green supplier selection procedure: a DEA approach," in *Proceedings of the 17th International Conference on Industrial Engineering and Engineering Management (IE & EM '10)*, pp. 70–74, Xiamen, China, October 2010.
- [18] K. L. Choy, W. B. Lee, H. C. W. Lau, S. C. K. So, and V. Lo, "An enterprise collaborative management system: a case study of supplier selection in new product development," *International Journal of Technology Management*, vol. 28, no. 2, pp. 206–226, 2004.
- [19] S. Chopra and P. Meindl, *Supply Chain Management: Strategy, Planning, and Operations*, Prentice-Hall, Upper Saddle River, NJ, USA, 2001.
- [20] Q. Su, J. H. Shi, and S. J. Lai, "Study on supply chain management of Chinese firms from the institutional view," *International Journal of Production Economics*, vol. 115, no. 2, pp. 362–373, 2008.
- [21] J. D. Linton, R. Klassen, and V. Jayaraman, "Sustainable supply chains: an introduction," *Journal of Operations Management*, vol. 25, no. 6, pp. 1075–1082, 2007.
- [22] R. Ganeshan and T. P. Harrison, *An Introduction to Supply Chain Management*, Department of Management Sciences and Information Systems, Pennsylvania State University, PA, USA, 1995.
- [23] J. T. Mentzer, W. DeWitt, J. S. Keebler et al., "Defining supply chain management," *Journal of Business Logistics*, vol. 22, no. 2, p. 18, 2001.
- [24] P. Rao and D. Holt, "Do green supply chains lead to competitiveness and economic performance?" *International Journal of Operations and Production Management*, vol. 25, no. 9, pp. 898–916, 2005.
- [25] H. J. Wu and S. Dunn, "Environmentally responsible logistics systems," *International Journal of Physical Distribution & Logistics Management*, vol. 25, pp. 20–238, 1995.
- [26] N. Darnall, G. J. Jolley, and R. Handfield, "Environmental management systems and green supply chain management: complements for sustainability?" *Business Strategy and the Environment*, vol. 17, no. 1, pp. 30–45, 2008.
- [27] S. K. Srivastava and R. K. Srivastava, "Managing product returns for reverse logistics," *International Journal of Physical Distribution and Logistics Management*, vol. 36, no. 7, pp. 524–546, 2006.
- [28] L. De Boer, E. Labro, and P. Morlacchi, "A review of methods supporting supplier selection," *European Journal of Purchasing and Supply Management*, vol. 7, no. 2, pp. 75–89, 2001.
- [29] E. Esposito and R. Passaro, "The evolution of supply chain relationships: an interpretative framework based on the Italian inter-industry experience," *Journal of Purchasing and Supply Management*, vol. 15, no. 2, pp. 114–126, 2009.
- [30] N. Aissaoui, M. Haouari, and E. Hassini, "Supplier selection and order lot sizing modeling: a review," *Computers and Operations Research*, vol. 34, no. 12, pp. 3516–3540, 2007.
- [31] Y. Yang and L. Wu, "Grey entropy method for green supplier selection," in *Proceedings of the International Conference on Wireless Communications, Networking and Mobile Computing (WiCOM '07)*, pp. 4677–4680, Shanghai, China, September 2007.
- [32] R. Handfield, R. Sroufe, and S. Walton, "Integrating environmental management and supply chain strategies," *Business Strategy and the Environment*, vol. 14, no. 1, pp. 1–19, 2005.
- [33] D. J. Ketchen and G. T. M. Hult, "Bridging organization theory and supply chain management: the case of best value supply chains," *Journal of Operations Management*, vol. 25, no. 2, pp. 573–580, 2007.
- [34] L. Zheng and J. Zhang, "Research on green logistics system based on circular economy," *Asian Social Science*, vol. 6, pp. 116–119, 2010.
- [35] P. K. Humphreys, Y. K. Wong, and F. T. S. Chan, "Integrating environmental criteria into the supplier selection process," *Journal of Materials Processing Technology*, vol. 138, no. 1–3, pp. 349–356, 2003.
- [36] X. Ma and T. Liu, "Supplier selection analysis under the green supply chain," in *Proceedings of the International conference on Automotive and Logistics*, vol. 5, pp. 205–209, 2011.
- [37] G. Theyel, "Customer and supplier relations for environmental performance," *Greener Management International*, no. 35, pp. 61–69, 2001.
- [38] S. K. Srivastava, "Green supply-chain management: a state-of-the-art literature review," *International Journal of Management Reviews*, vol. 9, no. 1, pp. 53–80, 2007.

- [39] E. Fontela and A. Gabus, "The DEMATEL observer," DEMATEL Report, Battelle Geneva Research Center, Geneva, Switzerland, 1976.
- [40] J. L. Yang and G.-H. Tzeng, "An integrated MCDM technique combined with DEMATEL for a novel cluster-weighted with ANP method," *Expert Systems with Applications*, vol. 38, no. 3, pp. 1417–1424, 2011.
- [41] M. Amiri, J. S. Sadaghiyani, N. Payani, and M. Shafieezadeh, "Developing a DEMATEL method to prioritize distribution centers in supply chain," *Journal of Management Science Letters*, vol. 1, no. 3, p. 307, 2011.
- [42] S. Sorooshian, A. Anvari, M. Salimi, and E. Falatoonitoosi, "Interrelation study of entrepreneur's capability," *World Applied Sciences Journal*, vol. 17, no. 7, pp. 818–820, 2012.
- [43] E. Falatoonitoosi, Z. Leman, S. Sorooshian, and M. Salimi, "Decision making trial and evaluation laboratory," *Research Journal of Applied Sciences, Engineering, and Technology*, vol. 5, no. 13, pp. 3475–3480, 2013.

## Research Article

# Formulation and Implementation of Energy Efficient Ultraviolet Curing for Photosensitive Resin-Bound Diamond Wire Saws

Chunyan Yao, Wei Peng, and Fuqing Liu

Key Laboratory of E&M Zhejiang University of Technology, Ministry of Education & Zhejiang Province, Hangzhou 310023, China

Correspondence should be addressed to Wei Peng; pengwei@zjut.edu.cn

Received 3 January 2013; Revised 10 March 2013; Accepted 2 April 2013

Academic Editor: Shengyong Chen

Copyright © 2013 Chunyan Yao et al. This is an open access article distributed under the Creative Commons Attribution License, which permits unrestricted use, distribution, and reproduction in any medium, provided the original work is properly cited.

It is a currently dominant method to use wire saws for cutting silicon material because of its production efficiency and energy efficiency. Diamond wire saws, or fixed abrasive wire saws, have attracted much attention to researchers and engineers due to many advantages, including high cutting efficiency and low environmental pollution. This paper develops a novel diamond wire saw using ultraviolet curing technology. High-strength piano wires and polyethylene wires are selected as wire cores, and photosensitive resin is used as the binder. The problem of wire saw strength is mathematically formulated, and the effective parameters are analyzed. The surface morphology is analyzed for the developed diamond wire saw. A series of cutting experiments with different saws of varying manufacturing parameters are carried out. The slicing performance of such diamond wire saws is evaluated and compared. The experimental results show that the developed saw using the photosensitive resin has a very good performance in slicing silicon ingots. By the comparison between the developed diamond wire saw and the electroplated diamond wire saw, the surface smoothness of the workpiece is better than that by the latter.

## 1. Introduction

For cutting silicon material, diamond wire saws or fixed abrasive wire saws have been attracting much attention in the community due to their many advantages [1–3]. For example, their kerf loss is small, which can improve the utilization of materials, and they are particularly attractive for machining expensive, hard, and brittle materials. The key technical challenge for diamond wire saw slicing of hard and brittle materials is the machined material's surface integrity, including roughness and subsurface damage [4]. Further study is very necessary in this area. In the past decade, several major technical developments in diamond wire saw machining have emerged. Recently, some researchers, for example, Clark, Sugawara, Peng, and Furutani, have investigated diamond wire saws [5–9]. Three basic categories of diamond wire saw can be distinguished according to the kind of bonding material employed: metallic bonding materials, organic bonding materials, and resin bonding materials.

This paper proposes a technology for developing diamond wire saw with photosensitive resin, based on our

previous research results [8, 9]. According to the characteristics of the photosensitive resin, we develop different bonding agents for a diamond wire saw. High-strength piano wires and polyethylene wires are selected as the core wire. According to the manufacturing process of this new diamond wire saw, a manufacturing machine has been designed. Some diamond wire saws are produced using different raw materials. A series of cutting experiments with different wire saws are carried out. A novel diamond wire saw is developed by using ultraviolet curing technology. High-strength piano wires and polyethylene wires are selected as wire cores, and photosensitive resin is used as the binder. The problem of wire saw strength is mathematically formulated, and the effective parameters are analyzed. Mathematical analysis and optimization method are necessary in this issue [10, 11]. The surface morphology is analyzed for the developed diamond wire saw. A series of cutting experiments with different saws of varying manufacturing parameters are carried out. The slicing performance of such diamond wire saws is evaluated and compared in this paper.

## 2. Ultraviolet Curing Process

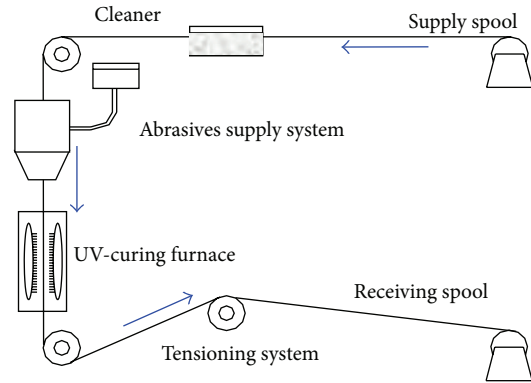
**2.1. Composition Materials.** The main composition materials for the manufacture of the new diamond wire saw are photosensitive resin, core wire, and abrasive [12–23]. The photosensitive resin plays a vital role in the performance of the diamond wire saw. It is used as the binder of the diamond wire saw and is composed of epoxy acrylate resin, an appropriate quantity of preformed polymer, active diluent, photoinitiator, and other additives. After referring to the vast domestic and foreign technical literature on the manufacture of wire saws, a lot of resin-modified experiments have been done in order to improve its bond strength. Based on performance testing of several resins, their softness, tensile strength, and their film properties, two kinds of homemade photosensitive resin, epoxy acrylate and modified epoxy acrylate, were selected as the binder for the manufacture of the new diamond wire saw.

Diamond is the best abrasive for grinding hard brittle materials in general, for example, optical glass, ceramics, gems, stones, and so forth. Nickel-plated diamond surfaces have more roughness, and this can improve the bonding strength with the resin. The reason is that the material wetting performance between the diamond and the resin is changed [24]. Basic adhesion experiments between the resin and three types of diamonds were made. The diamonds are ordinary RVG diamond without nickel plating and RVG diamond with nickel plating, of weight gains 30% and 50%. The results show that RVG diamond with nickel plating weight gain 50% has a higher bonding strength with the resin [25, 26].

During the cutting process, the wire saw is always maintained in a tension state, which is generally controlled in 20~30 N [5]. In order to meet the cutting conditions, the tensile strength and toughness of the wire saw should be higher. In the experiment, the piano wire and polyethylene wire are selected as the core wire [27, 28].

**2.2. Formulation of Diamond Wire Saws.** For the experiments, the core wire diameter of the new diamond wire saw is  $\Phi = 0.2$  mm. According to preliminary findings [25–28], the abrasive layer theoretical thickness is approximately 0.04 mm, and thus the abrasive particle size is in the range 50~40  $\mu\text{m}$ . Relative to the curing level and the height of the abrasive protrusion, the abrasive concentration in the abrasive layer was set at 100%, which means that if the abrasive is ordinary RVG diamond, the diamond content per unit volume is 0.88  $\text{g}/\text{cm}^3$ .

**2.3. Manufacturing Process.** Automatic control is applied in the manufacturing process of the fixed-abrasive diamond wire saw, which is designed in a coating machine. The coating machine is made up of a supply spool, a cleaning system, a tensioning system, an abrasive supply system, a UV-curing furnace, and a receiving spool. The manufacturing process consists of the following steps. Firstly, an ultrafine diamond abrasive plated with nickel, and the ultraviolet-curing resin should be mixed and churned up well. Then, it is injected into a coating cup by air pressure. Secondly, the core wire is



(a)



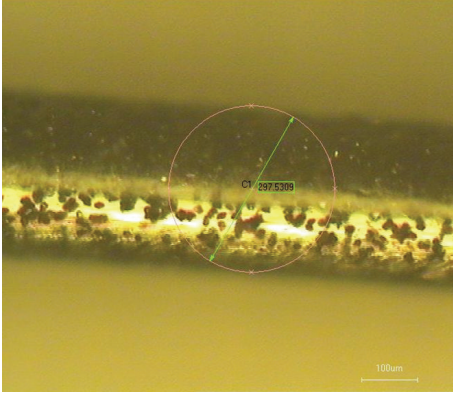
(b)

FIGURE 1: The wire saw manufacturing process and curing oven.

pretreated in our home-made solution. Then the core wire is installed on the coating machine. It goes through the supply spool, tensioning system, abrasive supply system, UV-curing furnace, and receiving spool. Thirdly, the core wire is coated with the abrasive solution in the coating cup. In succession, the abrasive layer is cured by ultraviolet light in a UV-curing furnace. Finally, the diamond wire saw is executed in the coating machine. Figure 1(a) shows the basic manufacturing process of the coating technique. In order to ensure the stability of the diamond wire saw production process, the diamond wire saw manufacturing machine was designed and manufactured according to the appropriate characteristics and technical requirements of the wire saw manufacturing process. Figure 1(b) is the curing oven for the new diamond wire saw manufacturing. Figure 2 shows a photo of the new diamond wire saw, with image contrast enhancement by histogram smoothing [29].

## 3. Evaluation Parameters

Usually, to evaluate wire saw cutting performance, the parameters are its cutting efficiency, service life, and workpiece machining quality. In certain conditions, the cutting efficiency and service life are the main factors that determine the machining performance of wire saw. For the sake of evaluating the machining properties of the new diamond

FIGURE 2: Microvision of a diamond wire saw ( $\times 500$ ).

wire saw, the material removal rate  $M$  (MRR) and wearing resistance rate  $W$  (WRR) are redefined in this paper. The material removal rate  $M$  is defined as the average volume of material removed from the workpiece per unit time and reflects the efficiency of wire saw machining:

$$M = \frac{V}{t}, \quad (1)$$

where  $V$  is the total volume ( $\text{mm}^3$ ) of material removed in the cutting process and  $t$  is the cutting time (minute). The wearing resistance rate  $W$  is defined as the ratio of the material removal volume to the weight loss of the wire saw. It reflects the durability of the saw. A greater value of  $W$  reflects better wearing resistance of the wire saw and vice versa:

$$W = \frac{V}{\Delta M} = \frac{V}{m_i - m_f}, \quad (2)$$

where  $V$  is the total volume of workpiece material removed ( $\text{mm}^3$ ) in the cutting process,  $\Delta M$  is the weight loss of wire saw (g),  $m_i$  is the initial weight (g) of the wire saw, which is weighed before the cutting process, and  $m_f$  is the final weight (g) of the wire saw which is weighed after the cutting process.

## 4. Impact of Ingredients

**4.1. Experimental Conditions.** The processing performance of the wire saw is the ultimate test of whether the choice of material is reasonable. For estimating the processing performance of the newly developed diamond wire saw, some slicing experiments were done. The slicing technology conditions are showed in Table 1. The slicing experiment for slicing workpiece, poly-silicon ingot, was carried out on the WXD170 reciprocating cutting machine by using various new diamond wire saws.

**4.2. Photosensitive Resin.** The properties of the photosensitive resin depend on the performance of the oligomers and its composition. Adding a monomer can modify the photosensitive resin, which can affect the performance of the new diamond wire saw to a certain extent. In this

TABLE 1: Experimental conditions in the slicing process.

Item	Value
Wire sawing machine	WXD170
Workpiece	$\Phi 44$ mm silicon ingot
Wire saw diameter (mm)	$\Phi 0.28$
Wire saw line speed (m/min)	2.5
Wire saw feed speed (mm/min)	0.375
Workpiece rotate speed (rpm)	3.5
Wire tension (MPa)	0.2
Coolant	tap water

TABLE 2: The experimental results.

Wire saw type	Material removal rate $M$ [ $\text{mm}^3/\text{min}$ ]	Wearing resistance rate $W$ [ $\text{mm}^3/\text{g}$ ]
Photosensitive resin		
OOP	395	6.89
MOP	538	7.19
Diamond abrasives		
MOP	535	7.12
MNP	551	7.24
Core wire		
MNP	540	7.20
MNL	376	7.32

experiment, epoxy acrylate and epoxy acrylate blended with 5% SR351 monomer were selected as the binder for the manufacture of diamond wire saw the by with OOP and MOP, respectively. Under the technological conditions described above, the slicing experiments were carried out to investigate the material removal rate  $M$  and wearing resistance rate  $W$  of the new diamond wire saw. The experimental results are shown in Table 2.

It can be seen that the wearing resistance rate of wire saw sample 2 is increased about 36%. Analyzed from the perspective of materials science, the hardness of the resin layer increases when the monomer is added. This improves the wear resistance of the resin layer and then improves the WRR of the diamond wire saw. When the resin layer hardness increases, the abrasive inlaid in the resin layer does not come off easily. From Table 2, we can see that the material removal rate of workpiece cutting by MOP increases about 4.3%.

**4.3. Diamond Abrasives.** The cutting process of a wire saw is a micropolishing process by the diamond abrasive which is embedded in the resin layer. The bonding strength between the diamond grit and the resin layer determines the cutting performance of a diamond wire saw. Based on these experimental results, two kinds of diamond, that is, ordinary RVG diamond without nickel plating and RVG diamond with nickel plating weight gain 50%, are adopted for manufacturing the developed diamond wire saw and labeled by MOP and MNP, respectively. Similarly, the slicing experiments are carried out under the described above technological conditions. The experimental results are shown in Table 2. It

is seen that nickel plating on the diamond can increase the bonding strength of the diamond and resin. Therefore, the higher the bond strength of the resin and diamond, the higher the cutting ability of the diamond wire saw gained during cutting process.

The wear failure form of a diamond wire saw is that the abrasive resin layer is broken and off the core wire. Figure 3 shows a typical microscope surface topography of a worn diamond wire saw. It can be seen that the diamond abrasive is broken (Figure 3(a)) and worn away from the resin layer (Figure 3(b)).

**4.4. Core Wire.** During the cutting process, the wire saw is always maintained in a state of tension. It will be bended due to the workpiece feed force. So the strength of the wire saw includes tensile strength and bending strength. The wire tensile force can be calculated as follows:

$$F_1 = F_0 + \Delta F, \quad (3)$$

where  $F_1$  is the wire tensile force,  $F_0$  is the wire initial tensile force, and  $\Delta F$  is the change amount of the wire tensile force, which is calculated based on the following formula (4):

$$\Delta F = EA\varepsilon, \quad (4)$$

where  $A$  is the cross-sectional area of wire,  $E$  is the modulus of elasticity,  $\varepsilon$  is the axial strain of wire.

The tensile stress of wire saw is defined as:

$$\sigma_1 = \frac{F_1}{A} = \frac{F_0}{A} + E \left( \sqrt{1 + tg^2\alpha} - 1 \right), \quad (5)$$

where  $\alpha$  is the angle of wire saw during the cutting process.

The bending stress of wire saw is defined as

$$\sigma_2 = E \frac{d}{D}, \quad (6)$$

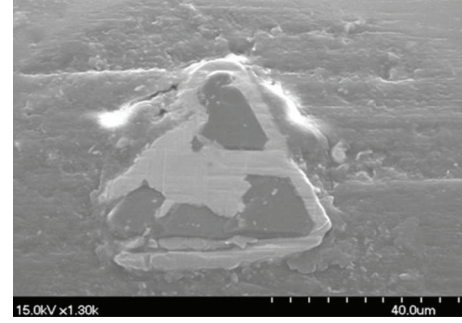
where  $d$  is the diameter of wire and  $D$  is the diameter of guide pulley during the cutting process.

If we use comprehensive tensile stress to describe the strength of the wire saw and take a safety factor in order to ensure that the wire saw during the cutting process is not pulled off, the comprehensive tensile stress is required to meet the following relationship:

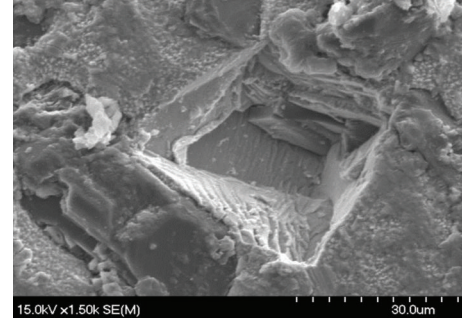
$$\sigma > k(\sigma_1 + \sigma_2) = kE \left( \frac{F_0}{EA} + \sqrt{1 + tg^2\alpha} + \frac{d}{D} - 1 \right), \quad (7)$$

where  $\sigma$  is the comprehensive tensile stress,  $\sigma_1$  is the tensile stress,  $\sigma_2$  is the bending stress,  $k$  is the safety factor, here 1.1,  $F_0$  is the initial tension, here 35 N,  $E$  is the modulus of elasticity, here about 200 GP,  $d$  is the diameter of the wire, here 0.2 mm, and  $D$  is the diameter of the guide pulley, here 250 mm.

The comprehensive tensile stress of wire is about 1230 Mpa by a calculation. As long as the material can meet the strength requirements of the core wire, it can be theoretically used to make the wire saw. The material for a wire saw is metal, generally. Beyond the conventional, we not only chose metal materials but also selected nonmetallic materials to



(a)



(b)

FIGURE 3: The typical micrographs of worn wire saws.

TABLE 3: Choices of the core wire.

Core wire	Diameter (mm)	Tensile stress (MPa)	Manufacturer
Piano wire	Φ 0.2	2820 ± 100	Korea Steel Ltd.
Polyethylene wire	Φ 0.2	3440 ± 100	Ningbo Dacheng Advanced Material Co., Ltd.

make the core wire in the experiment. The core wire material is illustrated in Table 3.

We manufacture the new diamond wire saw using piano wire and polyethylene wire and label these two types by MNP and MNL, respectively. Similarly, the slicing experiments are carried out under the technological conditions described above. The experimental results are shown in Table 2. The results show that the wearing resistance rate of wire labeled MNL is lower. The reason is that the elongation of polyethylene wire is higher than that of piano wire, which makes the abrasive resin layer flake off the core wire easily. Since the abrasive resin layer is so easy to flake off and its wearing resistance rate is lower, the material removal rate of it is higher. The reason may be that some of the abrasives flaked from resin layer are involved in the cutting.

## 5. Comparative Experiments on Surface Roughness

On the basis of these studies of the raw materials and manufacturing processes of the diamond wire saw and the

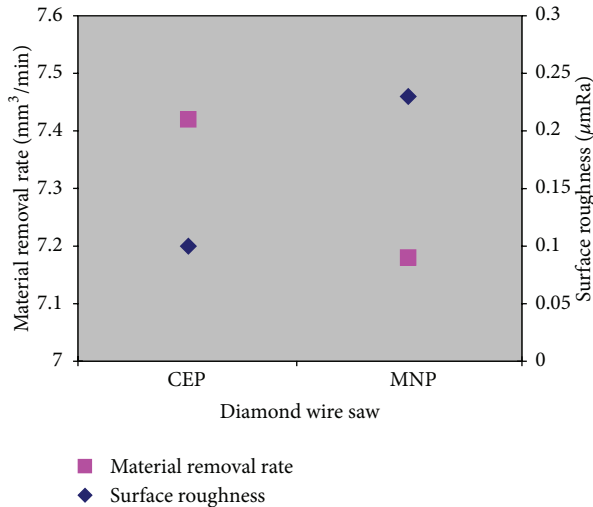


FIGURE 4: The MRR and average surface roughness Ra of work-piece.

new diamond wire saw was manufactured with piano wire, diamond with nickel plating, and modified epoxy acrylate. In order to compare the cutting performance of the new diamond wire saw with other diamond wire saws, cutting experiments were carried out under the conditions listed in Table 1. The commercial electroplated diamond wire saw was selected as the reference wire saw, labeled by CEP. Figure 4 shows the material removal rate and average surface roughness Ra. The surface roughness was measured by the Mahr Perthometer S2 surface roughness measuring instrument. It was measured along the radial direction of the workpiece. The average surface roughness and the material removal rate of the new diamond wire saw are lower than that of the commercial diamond wire saw. In the slicing process, due to the characteristics of the resin itself, its consolidation capacity with the abrasive grit is weaker than that obtained by electroplating, so the abrasive resin layer was broken to pieces easily, which makes the slicing performance of the new diamond wire saw lower. But on the other hand, this small broken abrasive resin layer works as a microblade, cutting on the surface of the workpiece because of the vibration of the wire. It assists the polishing of the surface and makes the surface roughness lower.

## 6. Conclusion

This paper has exploited the techniques of a diamond wire saw based on an ultraviolet curing method. A wire saw manufacturing machine was designed and manufactured according to the characteristics and technical requirements of the manufacturing process. We found that the characteristics of the photosensitive resin and abrasive grit affect the performance of the new diamond wire saw. A modified epoxy acrylate and diamond with nickel were applied for the manufacture of this new wire saw. The cutting performance is evaluated and compared. The experimental results show that the diamond wire saw made with the photosensitive

resin has a good performance in cutting poly-silicon ingots. It demonstrates that the new method is feasible. For the sake of evaluating the machining properties of the developed diamond wire saw, the material removal rate and wearing resistance rate were redefined. Surface roughness obtained by the new diamond wire saw is better than that by the usual electroplated wire saw.

## Acknowledgments

The work was supported by the National Natural Science Foundation of China (51075367) and Natural Science Foundation of Zhejiang Province (Y1090931).

## References

- [1] C. Chung, C. S. Korach, and I. Kao, "Experimental study and modeling of lapping using abrasive grits with mixed sizes," *Journal of Manufacturing Science and Engineering*, vol. 133, no. 3, Article ID 031006, 2011.
- [2] M. Fathi, A. Mefoued, A. Messaoud, and A. Boukennou, "Cost-effective photovoltaics with silicon material," *Physics Procedia*, vol. 2, pp. 751–757, 2009.
- [3] E. Teomete, "Investigation of long waviness induced by the wire saw process," *Proceedings of the Institution of Mechanical Engineers B*, vol. 225, no. B7, pp. 1153–1162, 2011.
- [4] J. Sugawara, H. Hara, and A. Mizoguchi, "Development of fixed-abrasive-grain wire saw with less cutting loss," *SEI Technical Review*, vol. 58, no. 6, pp. 7–11, 2004.
- [5] W. I. Clark, A. J. Shih, C. W. Hardin, R. L. Lemaster, and S. B. McSpadden, "Fixed abrasive diamond wire machining—part I: process monitoring and wire tension force," *International Journal of Machine Tools and Manufacture*, vol. 43, no. 5, pp. 523–532, 2003.
- [6] P. Q. Ge, L. Zhang, W. Gao, and Z. C. Liu, "Development of endless diamond wire saw and sawing experiments," *Materials Science Forum*, vol. 471–472, pp. 481–484, 2004.
- [7] K. Furutani and Y. Murase, "Fabrication of Wire Saw with Patterned Hard Bumps by Electrical Discharge Machining with Powder Suspended in Working Oil," in *Proceedings of the 41st CIRP Conference on Manufacturing Systems*, pp. 361–364, Tokyo, Japan, 2008.
- [8] W. Peng, F. Q. Liu, and C. Y. Yao, "Research on the ultraviolet-curing resin wire saw," in *Proceedings of the International Technology and Innovation Conference (ITIC '06)*, vol. 524, pp. 2347–2350, Hangzhou, China, November 2006.
- [9] W. Peng, C. Y. Yao, X. Lv, F. Q. Liu, T. Gao, and J. L. Yuan, "Experimental study on new bonding materials for developing nano-grinding plates," *Key Engineering Materials*, vol. 329, pp. 489–494, 2007.
- [10] Y. Zheng, S. Chen, Y. Lin, and W. Wang, "Bio-inspired optimization of sustainable energy systems: a review," *Mathematical Problems in Engineering*, vol. 2013, Article ID 354523, 12 pages, 2013.
- [11] Y. Zheng, H. Shi, J. Xue, and S. Chen, "Formal calculation and invariant-based validation establish dependable algorithmic programs," *China Communications*, vol. 8, no. 4, pp. 58–64, 2011.
- [12] H. Wu and S. N. Melkote, "Study of ductile-to-brittle transition in single grit diamond scribing of silicon: application to wire sawing of silicon wafers," *Journal of Engineering Materials and Technology*, vol. 134, no. 4, 2012.

- [13] E. Teomete, "Roughness damage evolution due to wire saw process," *International Journal of Precision Engineering and Manufacturing*, vol. 12, no. 6, pp. 941–947, 2011.
- [14] G. Skomedal, E. Ovreid, S. Armada, and N. Espallargas, "Effect of slurry parameters on material removal rate in multi-wire sawing of silicon wafers: a tribological approach," *Proceedings of the Institution of Mechanical Engineers J*, vol. 225, no. J10, pp. 1023–1035, 2011.
- [15] T. Liedke and M. Kuna, "A macroscopic mechanical model of the wire sawing process," *International Journal of Machine Tools and Manufacture*, vol. 51, no. 9, pp. 711–720, 2011.
- [16] Z. Li, Z. Pei, and P. Funkenbusch, "Machining processes for sapphire wafers: a literature review," *Proceedings of the Institution of Mechanical Engineers B*, vol. 225, no. B7, pp. 975–989, 2011.
- [17] A. Bidiville, K. Wasmer, J. Michler, P. M. Nasch, M. Van Der Meer, and C. Ballif, "Mechanisms of wafer sawing and impact on wafer properties," *Progress in Photovoltaics*, vol. 18, no. 8, pp. 563–572, 2010.
- [18] S. Bhagavat, J. C. Liberato, C. Chung, and I. Kao, "Effects of mixed abrasive grits in slurries on free abrasive machining (FAM) processes," *International Journal of Machine Tools and Manufacture*, vol. 50, no. 9, pp. 843–847, 2010.
- [19] Z. J. Pei, G. R. Fisher, and J. Liu, "Grinding of silicon wafers: a review from historical perspectives," *International Journal of Machine Tools and Manufacture*, vol. 48, no. 12-13, pp. 1297–1307, 2008.
- [20] S. Bhagavat and I. Kao, "A finite element analysis of temperature variation in silicon wafers during wiresaw slicing," *International Journal of Machine Tools and Manufacture*, vol. 48, no. 1, pp. 95–106, 2008.
- [21] S. Bhagavat and I. Kao, "Ultra-low load multiple indentation response of materials: in purview of wiresaw slicing and other free abrasive machining (FAM) processes," *International Journal of Machine Tools and Manufacture*, vol. 47, no. 3-4, pp. 666–672, 2007.
- [22] M. Mizuno, T. Iyama, S. Kikuchi, and B. Zhang, "Development of a device for measuring the transverse motion of a saw-wire," *Journal of Manufacturing Science and Engineering*, vol. 128, no. 3, pp. 826–834, 2006.
- [23] S. Bhagavat and I. Kao, "Theoretical analysis on the effects of crystal anisotropy on wiresawing process and application to wafer slicing," *International Journal of Machine Tools and Manufacture*, vol. 46, no. 5, pp. 531–541, 2006.
- [24] J. Y. Gu, *Adhesive Bonding Theory and Basic*, Science Press, Beijing, China, 2003.
- [25] F. Liu, *Research on manufacturing technology of ultraviolet-curing diamond wire saw [Ph.D. thesis]*, Zhejiang University of Technology, 2009.
- [26] W. Peng, F. Q. Liu, and C. Y. Yao, "Surface modification of diamond to improve machining properties of ultraviolet-curing wire saw," *Advanced Materials Research*, vol. 69-70, pp. 24–28, 2009.
- [27] F. Liu, C. Yao, and W. Peng, "Key factors in ultraviolet-curing wire saw," in *Proceedings of the International Conference on Integration and Commercialization of Micro and Nanosystems*, pp. 1283–1288, January 2007.
- [28] C. Y. Yao, W. Peng, M. H. Wang, and F. Q. Liu, "The diamond wire saw with a nonmetallic core," *Advanced Materials Research*, vol. 69-70, pp. 328–332, 2009.
- [29] N. M. Kwok, X. Jia, D. Wang, S. Y. Chen, Q. P. Ha, and G. Fang, "Image contrast enhancement based on histogram smoothing and continuous intensity relocation," in *Proceedings of the 3rd International Congress on Image and Signal Processing (CISP '10)*, pp. 1–5, Yantai, China, October 2010.

## Research Article

# Calculation of Lightning Transient Responses on Wind Turbine Towers

**Xiaoqing Zhang and Yongzheng Zhang**

*School of Electrical Engineering, Beijing Jiaotong University, Beijing 100044, China*

Correspondence should be addressed to Yongzheng Zhang; zhangyz2@126.com

Received 12 December 2012; Revised 16 March 2013; Accepted 16 March 2013

Academic Editor: Massimo Scalia

Copyright © 2013 X. Zhang and Y. Zhang. This is an open access article distributed under the Creative Commons Attribution License, which permits unrestricted use, distribution, and reproduction in any medium, provided the original work is properly cited.

An efficient method is proposed in this paper for calculating lightning transient responses on wind turbine towers. In the proposed method, the actual tower body is simplified as a multiconductor grid in the shape of cylinder. A set of formulas are given for evaluating the circuit parameters of the branches in the multiconductor grid. On the basis of the circuit parameters, the multiconductor grid is further converted into an equivalent circuit. The circuit equation is built in frequency-domain to take into account the effect of the frequency-dependent characteristic of the resistances and inductances on lightning transients. The lightning transient responses can be obtained by using the discrete Fourier transform with exponential sampling to take the inverse transform of the frequency-domain solution of the circuit equation. A numerical example has been given for examining the applicability of the proposed method.

## 1. Introduction

Lightning is a complex atmospheric discharge phenomenon. The recorded lightning current has a highest peak value of around 300 kA and a duration of a few hundred microseconds [1]. In fact, this peak value rarely occurs in China. The median peak value is 26 kA occurring with 50% probability according to Chinese measured data [2]. With respect to wind turbines (WTs), the lightning strokes can be classified into two main types, downward flash and upward flash. The WTs with the height exceeding 100 m are mostly struck by upward flash. The impacts of lightning on WTs range from disturbances on control electronics, damages to single components, such as generator and sensor, to fires resulting in a complete loss of the installation. The control system frequently suffering from lightning transient overvoltages is typically the electrical control cabinet in the bottom of the WT tower. Its damage accounts for about 40% of all lightning damage events of WTs in the west of China. Furthermore, offshore WTs are often equipped with relatively advanced equipment such as communication antenna, transponder, GPS receiver, sea marking light, air traffic warning light,

fog-horns, and meteorological instrument, all of which are especially susceptible to lightning damage. Since accessing WTs offshore is not as easy as on land, lightning damage to WTs offshore can result in significantly higher costs of repair and maintenance. In view of the seriousness of lightning stroke to WTs, the lightning protection design has been regarded with more and more attention. In the lightning protection design of WTs, the need exists for determining the lightning transient responses on the WT tower since the tower body is the longest conducting path of lightning current in the WT structure. The previous methods usually modeled the WT tower as a transmission line [3, 4] or a capacitance chain [5]. Although the previous methods are simple, they cannot give the lightning transient responses in different parts on the tower body owing to their neglecting the structural feature of the tower body. For an improvement in the lightning transient calculation of WTs, a novel method is proposed in this paper. The proposed method represents the actual WT tower in the shape of the circular truncated cone as an equivalent cylindrical shell. The cylindrical shell is further subdivided into a discrete multiconductor grid. A set of analytic formulas are deduced for evaluating

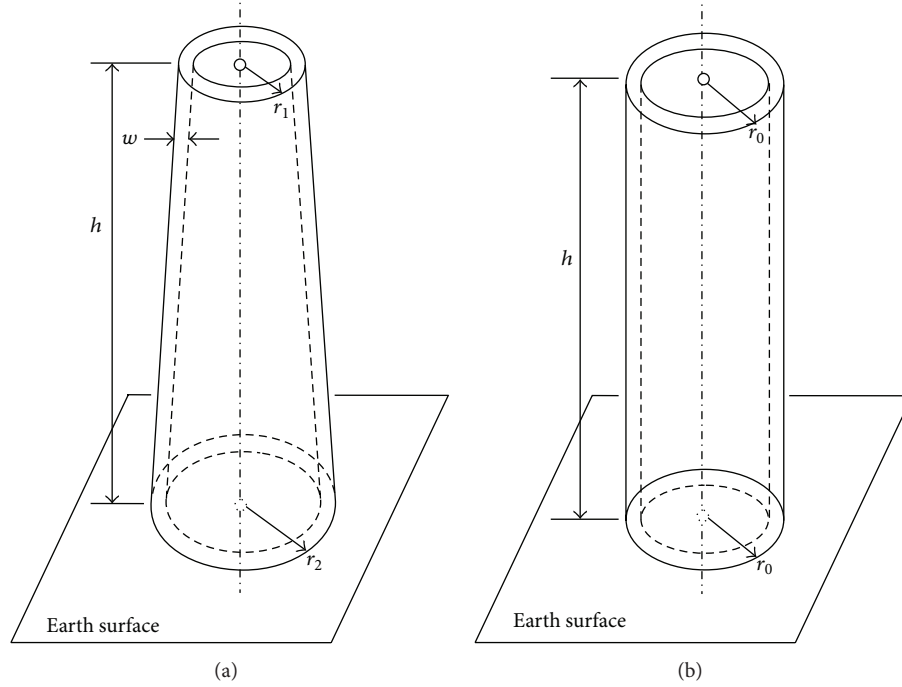


FIGURE 1: Geometric simplification of WT tower: (a) hollow circular truncated cone; (b) cylindrical shell.

the circuit parameters of the branches in the multiconductor grid. Based on the circuit parameters, the multiconductor grid is converted into an equivalent circuit. The hybrid equation is built in the frequency-domain for the equivalent circuit, and then the discrete Fourier transform with exponential sampling is used to obtain the lightning transient responses in different parts on the tower body. As compared to the traditional time-domain method [6], the proposed method can give due consideration to the frequency-dependent characteristic of the branch impedance directly in the frequency-domain and present better applicability to the lightning transient calculation. A numerical example has also been given for checking the validity of the proposed method.

## 2. Discretization Treatment of WT Tower

An actual WT tower is usually a hollow circular truncated cone, as shown in Figure 1(a). Since  $h \gg r_1$  and  $r_2$ , and  $r_2$  is not much larger than  $r_1$ , the actual tower body may be simplified as a cylindrical shell, as shown in Figure 1(b). For the purpose of transient calculation, the continuous cylindrical shell can be subdivided into a multiconductor grid constituted by longitudinal and transverse branches [6, 7], as shown in Figure 2(a). As the lightning current flowing through the WT tower presents significant harmonic components not exceeding a few MHz, the lightning transient responses should be calculated by the distribution parameter circuit model. However, if the branch length is taken as significantly small, an approximate calculation can be conducted referring to lumped parameter circuit model. For

this reason, the branch length  $l$  has to respect the following condition:

$$l < \frac{\xi_{\min}}{10}, \quad (1)$$

where  $\xi_{\min}$  is the minimum wavelength associated to the maximum frequency of the spectrum [8]. The circuit parameters of the branches in the multiconductor grid are represented by the impedances and capacitances. For convenience of the parameter calculation, each transverse arc is approximately replaced by its corresponding chord, as shown in Figure 2(b), and all the branches are taken as cylindrical conductors whose radii are estimated from their respective average cross-sections.

## 3. Derivation of Impedance and Capacitance Formulas

In view of the electromagnetic couplings between the branches, the impedances and capacitances are expressed as the matrices  $\mathbf{Z}$  and  $\mathbf{C}$ , respectively.  $\mathbf{Z}$  and  $\mathbf{C}$  are symmetric matrices according to the reciprocity principle [9]. The formulas for evaluating  $\mathbf{Z}$  and  $\mathbf{C}$  are derived later.

**3.1. Impedance.** Consider two transverse branches in the multiconductor grid shown in Figure 2(b). The earth is not perfectly conducting in reality, and its resistivity  $\rho$  has to be taken into account in the impedance calculation. For this purpose, a complex depth  $d$  is introduced into the image

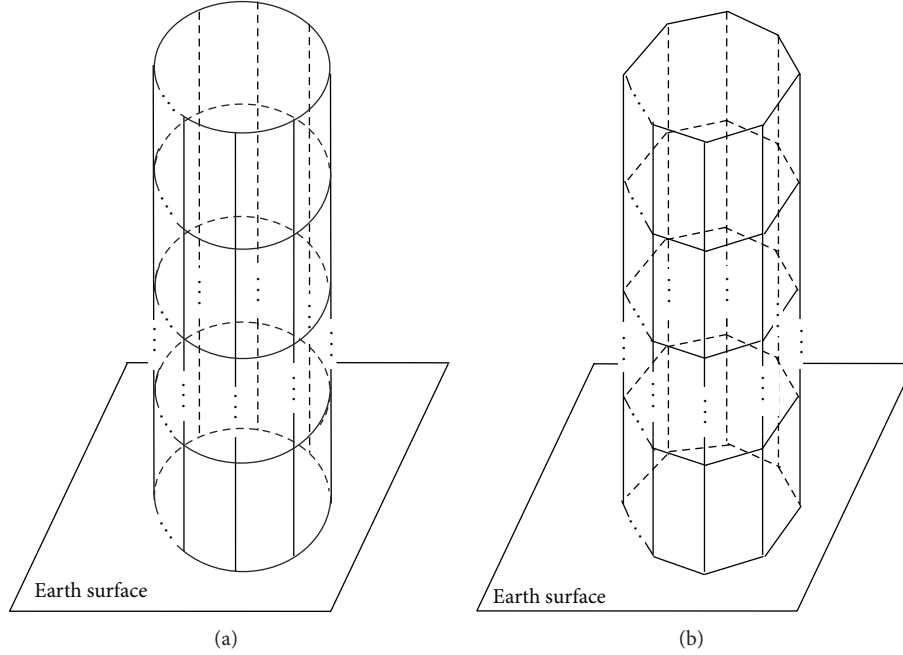


FIGURE 2: Multiconductor grid: (a) cylinder; (b) prism.

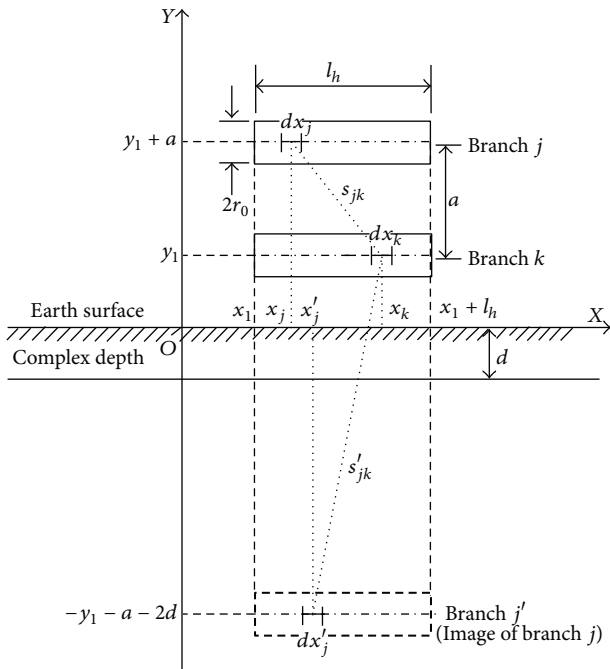


FIGURE 3: Two parallel transverse branches.

installation [10], as shown in Figure 3. The complex depth is defined by

$$d = \sqrt{\frac{\rho}{j\omega\mu_0}}, \quad (2)$$

where  $\mathbf{j} = \sqrt{-1}$ ,  $\omega$  is the angular frequency,  $\rho$  the earth resistivity, and  $\mu_0$  the space permeability ( $4\pi \times 10^{-7}$  H/m).

The real branch  $j$  and its image branch  $j'$  are considered to be symmetric about a plane which is located at a distance  $d$  below the earth surface. In terms of the Neumann's integral formula [10, 11], the mutual impedance between the branches  $j$  and  $k$  is expressed by

$$\begin{aligned} z_{jk}(\omega) &= R_{jk}(\omega) + j\omega L_{jk}(\omega) \\ &= j\omega \frac{\mu_0}{4\pi} \left[ \int_{x_1}^{x_1+l_h} \int_{x_1}^{x_1+l_h} \frac{dx_j dx_k}{s_{jk}} - \int_{x_1}^{x_1+l_h} \int_{x_1}^{x_1+l_h} \frac{dx'_j dx_k}{s'_{jk}} \right], \end{aligned} \quad (3)$$

where

$$\begin{aligned} s_{jk} &= \sqrt{(x_j - x_k)^2 + a^2}, \\ s'_{jk} &= \sqrt{(x_k - x'_j)^2 + (2y_1 + a + 2d)^2}. \end{aligned} \quad (4)$$

Evaluating the double integrals in (3) leads to

$$\begin{aligned} z_{jk}(\omega) &= j\omega \frac{\mu_0}{2\pi} \\ &\times \left[ l_h \sinh^{-1} \frac{l_h}{a} - \sqrt{a^2 + l_h^2} z \right. \\ &\quad \left. + a - l_h \sinh^{-1} \frac{l_h}{2y_1 + a + 2d} \right. \\ &\quad \left. + \sqrt{l_h^2 + (2y_1 + a + 2d)^2} - (2y_1 + a + 2d) \right]. \end{aligned} \quad (5)$$

The self-impedance  $Z_{jj}(\omega)$  of the transverse branch  $j$  is obtained by substituting  $a = r_0$  into (5). In a similar way, the mutual impedance between two longitudinal branches, as shown in Figure 4, is given by

$$\begin{aligned}
 Z_{mm}(\omega) &= \mathbf{j}\omega \frac{\mu_0}{2\pi} \\
 &\times \left[ (2y_1 + l_v + 2d) \sinh^{-1} \frac{2y_1 + l_v + 2d}{b} \right. \\
 &\quad + \sqrt{(2y_1 + l_v + 2d)^2 + b^2} - (y_1 + l_v + d) \\
 &\quad \times \sinh^{-1} \frac{2(y_1 + l_v + d)}{b} - \frac{1}{2} \sqrt{4(y_1 + l_v + d)^2 + b^2} \\
 &\quad - (y_1 + d) \sinh^{-1} \frac{2(y_1 + d)}{b} \\
 &\quad \left. + \frac{1}{2} \sqrt{4(y_1 + d)^2 + b^2} + l_v \sinh^{-1} \frac{l_v}{b} - \sqrt{b^2 + l_v^2} + b \right]. \quad (6)
 \end{aligned}$$

In (6), letting  $b = r_0$  gives the self-impedance  $Z_{mmm}(\omega)$  of the longitudinal branch  $m$ .

After the self and mutual impedances are calculated for a coupled branch unit with  $N$  transverse or longitudinal branches by using (5) or (6), the impedance matrix  $\mathbf{Z}$  can be formed as

$$\mathbf{Z} = [\mathbf{R}_{jk}(\omega)]_{N \times N} + \mathbf{j}\omega [\mathbf{L}_{jk}(\omega)]_{N \times N} = [\mathbf{z}_{jk}(\omega)]_{N \times N} \quad (7)$$

or

$$\mathbf{Z} = [\mathbf{R}_{mn}(\omega)]_{N \times N} + \mathbf{j}\omega [\mathbf{L}_{mn}(\omega)]_{N \times N} = [\mathbf{z}_{mn}(\omega)]_{N \times N}. \quad (8)$$

It is clear from (7) and (8) that the resistance and inductance in the impedance exhibit a pronounced frequency-dependent characteristic owing to introducing the complex depth  $d$ . If the earth is assumed to be perfectly conducting ( $\rho = 0$ ), the complex depth  $d$  is zero according to (2). Substitution of  $d = 0$  into (5) or (6) shows that the real part of the impedance is also zero. As a result, the impedance matrix  $\mathbf{Z}$  is further simplified as

$$\mathbf{Z}_0 = \mathbf{j}\omega \mathbf{L}_0, \quad (9)$$

where  $\mathbf{L}_0$  is the constant inductance matrix which is independent on the angular frequency  $\omega$ .

**3.2. Capacitance.** In the calculation of capacitances, the frequency effect on the charge density distribution can be significantly neglected since the charge attenuation constant  $\tau = \varepsilon\rho$  ( $\varepsilon$  is the permittivity) is rather small in the frequency range of lightning transient for both the branch conductor and the earth [12]. Therefore, the capacitances of the branches can still be calculated on the assumption that the earth is perfectly conducting. On the basis of the electromagnetic

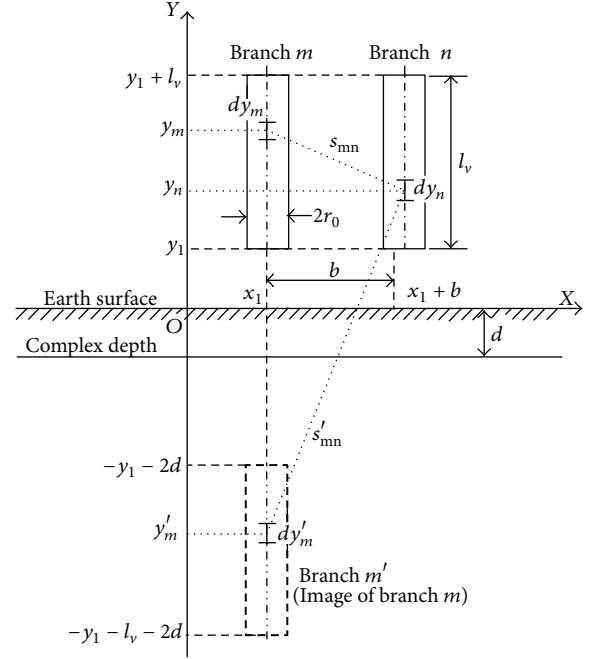


FIGURE 4: Two parallel longitudinal branches.

analogy [9], the product of the impedance matrix  $\mathbf{Z}_0 = \mathbf{j}\omega \mathbf{L}_0$  and the admittance matrix  $\mathbf{Y} = \mathbf{j}\omega \mathbf{C}$  of the coupled branches becomes diagonal with negative elements determined from space permeability  $\mu_0$  and permittivity  $\varepsilon_0$  [10] as

$$\mathbf{Z}_0 \cdot \mathbf{Y} = (\mathbf{j}\omega \mathbf{L}_0) \cdot (\mathbf{j}\omega \mathbf{C}) = -(\omega^2 \varepsilon_0 \mu_0) \mathbf{E}, \quad (10)$$

where  $\mathbf{C}$  is capacitance matrix of the coupled branches and  $\mathbf{E}$  is the unit matrix. Consequently, the capacitance matrix can be obtained as

$$\mathbf{C} = \varepsilon_0 \mu_0 \mathbf{Z}_0. \quad (11)$$

## 4. Equivalent Circuit Model

During a lightning stroke, the lightning current is usually injected to the tower body from its top and then dissipated in the earth by the earthing system. This process can be illustrated in Figure 5, where the earthing system is simply represented as the earthing resistances ( $R_g$ ). Once the impedance and capacitance parameters are obtained using the formulas given earlier, each coupled branch unit in the multiconductor grid can equivalently be represented by a  $\pi$ -circuit consisting of the series impedance and shunt capacitance [6, 13]. Figures 6(a) and 6(b) show the  $\pi$ -circuit representing three coupled branches. If the circuit parameters are expressed in matrix form, Figure 6(b) can be further depicted as a compact  $\pi$ -circuit, as shown in Figure 6(c).

With all the coupled branch units in the multiconductor grid replaced by the  $\pi$ -circuits, Figure 5 is converted into an equivalent circuit consisting of resistances, inductances, and capacitances. The lightning current is modeled as a current source and applied to the top node of the equivalent

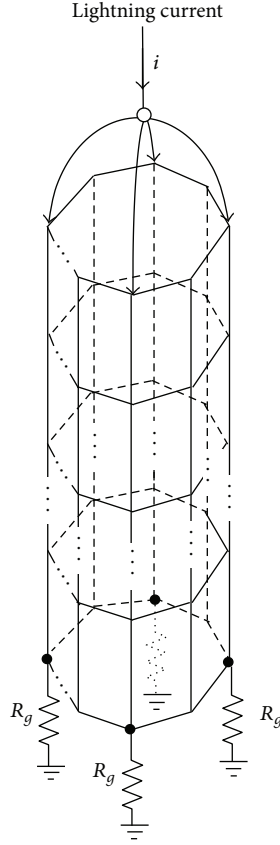


FIGURE 5: Injection of lightning current to tower body.

circuit. The lightning transient responses in different parts on the tower body can be obtained by performing a transient calculation for the equivalent circuit.

## 5. Circuit Equation and Its Numerical Solution

In order to take into account the frequency-dependent characteristic of the resistances and inductances in series impedances on lightning transients, the circuit equation is built in frequency-domain. The circuit components of the equivalent circuit are numbered in the sequence of shunt capacitance, series impedance, and lightning current source. In accordance with the component number, the incidence matrix of the equivalent circuit is written as

$$A = [A_C, A_{im}, A_S], \quad (12)$$

and the relevant current vector is

$$\mathbf{I}(\omega) = [\mathbf{I}_C(\omega), \mathbf{I}_{im}(\omega), I_S(\omega)]^T, \quad (13)$$

where the subscripts C, im, and S denote shunt capacitance, series impedance, and lightning current source, respectively. From Kirchhoff's current law, the node current equation is derived from (12) and (13) as

$$A\mathbf{I}(\omega) = A_C\mathbf{I}_C(\omega) + A_{im}\mathbf{I}_{im}(\omega) + A_S I_S(\omega) = \mathbf{0}. \quad (14)$$

Substituting  $A_C\mathbf{Y}_C A_C^T \mathbf{U}_n(\omega)$  for  $A_C\mathbf{I}_C(\omega)$  in (14) gives

$$A_C\mathbf{Y}_C A_C^T \mathbf{U}_n(\omega) + A_{im}\mathbf{I}_{im}(\omega) + A_S I_S(\omega) = \mathbf{0}, \quad (15)$$

where  $\mathbf{Y}_C$  is the shunt capacitive admittance matrix. Let  $\mathbf{U}_n(\omega)$  and  $\mathbf{Z}_{im}$  be the node voltage vector and series impedance matrix, respectively. The branch equation of the series impedance is given by

$$A_{im}^T \mathbf{U}_n(\omega) - \mathbf{Z}_{im}\mathbf{I}_{im}(\omega) = \mathbf{0}. \quad (16)$$

Hence, the hybrid equation of the equivalent circuit can be built by merging (15) and (16) as

$$\begin{bmatrix} A_C\mathbf{Y}_C A_C^T & A_{im} \\ A_{im}^T & -\mathbf{Z}_{im} \end{bmatrix} \begin{bmatrix} \mathbf{U}_n(\omega) \\ \mathbf{I}_{im}(\omega) \end{bmatrix} = \begin{bmatrix} -A_S I_S(\omega) \\ \mathbf{0} \end{bmatrix}. \quad (17)$$

On the right hand of (17), lightning current source  $I_S(\omega)$  is the Fourier transform of the injected lightning current  $i$  (see Figure 5).  $i$  is usually expressed by the double exponential function [14]

$$i = I(e^{-\alpha t} - e^{-\beta t}). \quad (18)$$

In accordance with the Chinese national standard [2], the waveform parameter of  $i$  is  $2.6/50 \mu\text{s}$ . This gives  $\alpha = 1.5 \times 10^{-2} \mu\text{s}^{-1}$  and  $\beta = 1.86 \mu\text{s}^{-1}$  by using the least square fitting method [15]. The peak current  $I$  takes the value of 100 kA in light of the severe lightning stroke condition. Thus, finding the Fourier transform of (18) gives

$$I_S(\omega) = \frac{(\beta - \alpha) I}{(\alpha + j\omega)(\beta + j\omega)}. \quad (19)$$

By taking the  $I_S(\omega)$  as the excitation, the frequency responses  $\mathbf{U}_n(\omega)$  and  $\mathbf{I}_{im}(\omega)$  can be obtained by solving (17). For each given angular frequency  $\omega$ , (17) is a system of complex linear algebraic equations and can be generally written as

$$\Lambda \mathbf{X}(\omega) = \mathbf{b}, \quad (20)$$

where

$$\Lambda = [\Lambda_{jk}]_{M \times M} = \begin{bmatrix} A_C\mathbf{Y}_C A_C^T & A_{im} \\ A_{im}^T & -\mathbf{Z}_{im} \end{bmatrix}_{M \times M},$$

$$\mathbf{X}(\omega) = [X_j(\omega)]_{M \times 1} = \begin{bmatrix} \mathbf{U}_n(\omega) \\ \mathbf{I}_{im}(\omega) \end{bmatrix}_{M \times 1}, \quad (21)$$

$$\mathbf{b} = [b_j]_{M \times 1} = \begin{bmatrix} -A_S I_S(\omega) \\ \mathbf{0} \end{bmatrix}_{M \times 1},$$

where  $M$  is the order of the coefficient matrix in (17). The Gauss elimination with column pivoting is employed

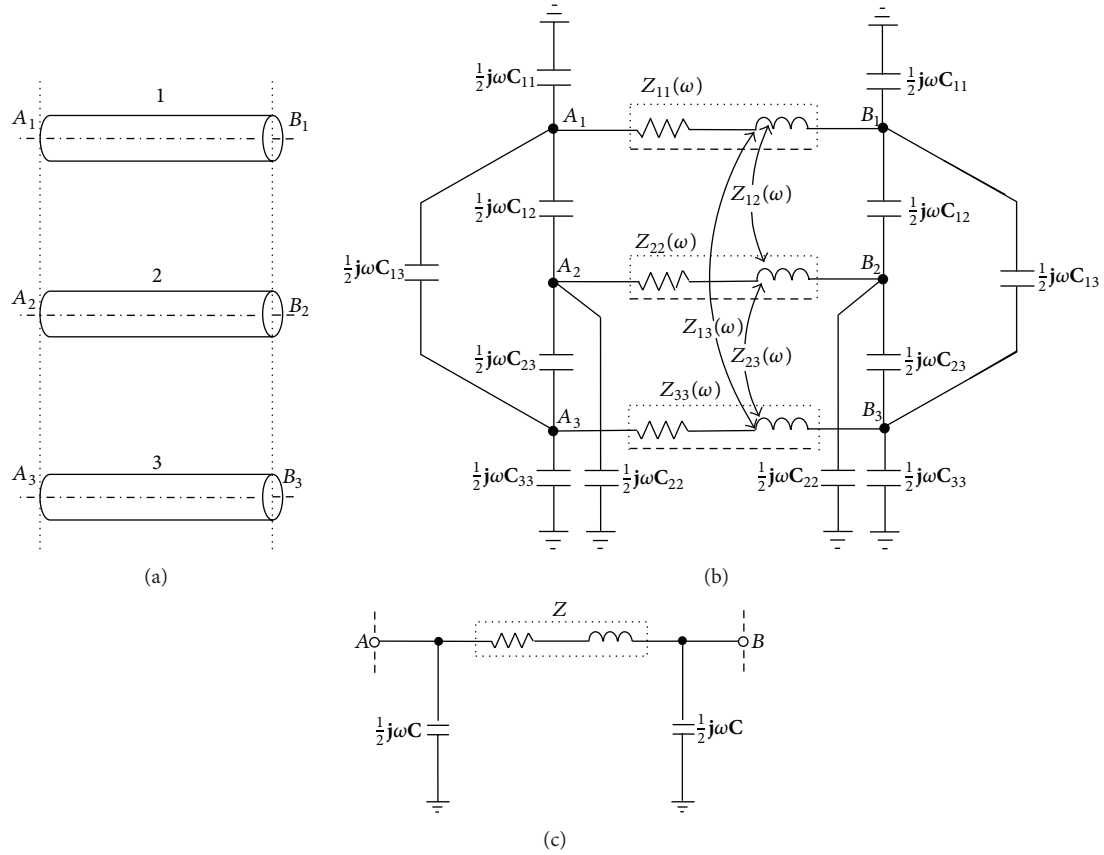


FIGURE 6:  $\pi$ -circuit of three branches: (a) three coupled branches, (b) coupled  $\pi$ -circuit, and (c) compact  $\pi$ -circuit expressed in matrix.

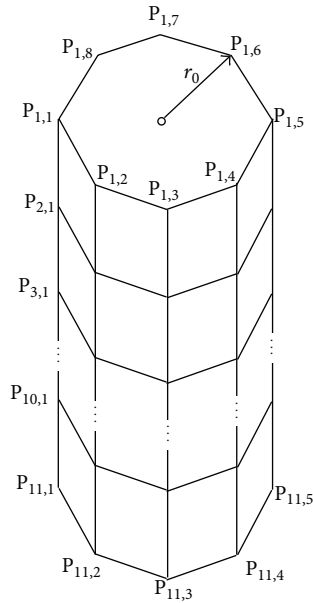


FIGURE 7: Multiconductor grid of a 1.5 MW WT tower.

$$\begin{bmatrix} \Lambda_{11}^{(1)} & \Lambda_{12}^{(1)} & \cdots & \Lambda_{1k}^{(1)} & \cdots & \Lambda_{1M}^{(1)} \\ 0 & \Lambda_{22}^{(2)} & \cdots & \Lambda_{2k}^{(2)} & \cdots & \Lambda_{2M}^{(2)} \\ \vdots & \vdots & \cdots & \vdots & \cdots & \vdots \\ 0 & 0 & \cdots & 0 & \Lambda_{kk}^{(k)} & \cdots & \Lambda_{kM}^{(k)} \\ \vdots & \vdots & \cdots & \vdots & \cdots & \vdots \\ 0 & 0 & \cdots & 0 & \cdots & 0 & \Lambda_{MM}^{(M)} \end{bmatrix} \begin{bmatrix} X_1(\omega) \\ X_2(\omega) \\ \vdots \\ X_k(\omega) \\ \vdots \\ X_M(\omega) \end{bmatrix} = \begin{bmatrix} b_1^{(1)} \\ b_2^{(2)} \\ \vdots \\ b_k^{(k)} \\ \vdots \\ b_M^{(M)} \end{bmatrix} \quad (22)$$

The detailed elimination procedure has been stated in [16, 17]. Subsequently, the solution of vector  $\mathbf{X}(\omega)$  is obtained by the back substitution operations

$$X_M(\omega) = \frac{b_M^{(M)}}{\Lambda_{MM}^{(M)}},$$

$$X_k(\omega) = \frac{\left( b_k^{(k)} - \sum_{j=k+1}^M \Lambda_{jk}^{(k)} X_j(\omega) \right)}{\Lambda_{kk}^{(k)}} \quad (23)$$

$$(k = M - 1, M - 2, \dots, 2, 1).$$

to solve (20). It consists of two main phases: the forward elimination and the back substitution. After performing  $M-1$  step elimination operations, the original matrix  $\Lambda$  in (20) is converted into an upper triangular matrix

An element of vector  $\mathbf{X}(\omega)$ ,  $X_j(\omega)$  ( $j = 1, 2, \dots, M$ ), is the frequency response and needs to be transformed into time-domain to give the corresponding time response. The inverse

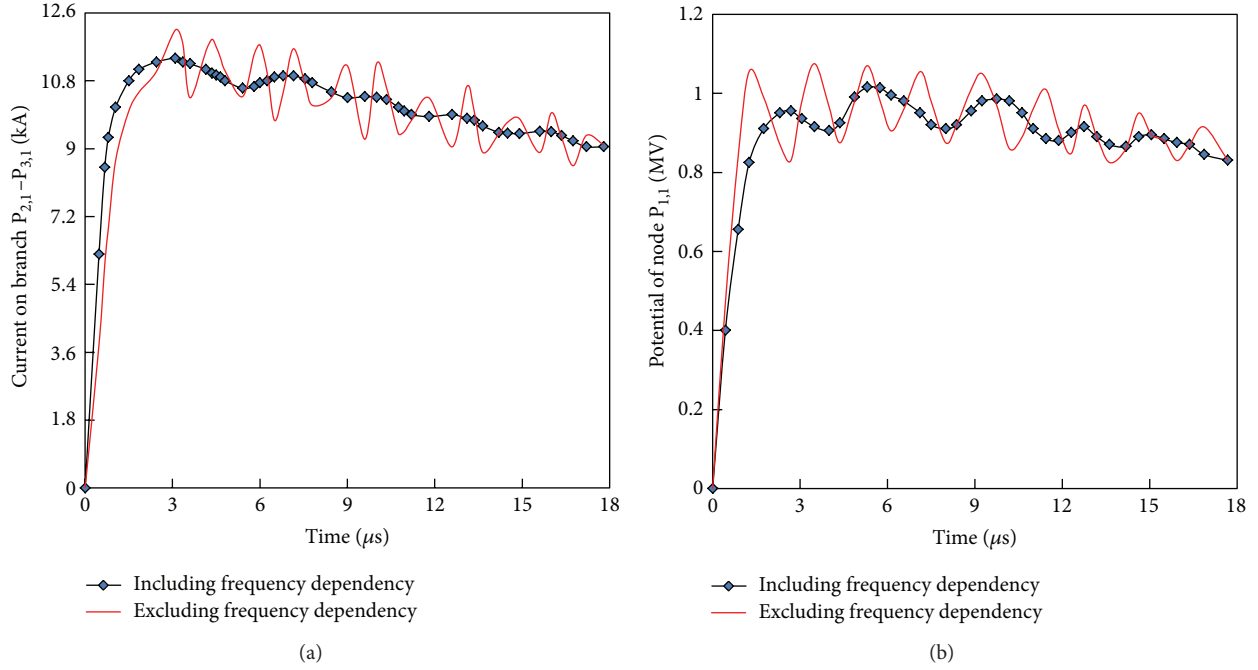


FIGURE 8: Current and potential waveforms: (a) current waveform on branch  $P_{2,1} - P_{3,1}$  and (b) potential waveform of node  $P_{1,1}$ .

Fourier transform with exponential sampling is chosen for this purpose [18, 19]. The inverse transform method takes the sampling frequency in an exponential manner, that is,

$$\gamma\Delta\omega, \gamma^2\Delta\omega, \gamma^3\Delta\omega, \dots, \gamma^j\Delta\omega, \dots, \gamma^{\lambda_m}\Delta\omega, \quad (24)$$

where  $\Delta\omega (= 2\pi\Delta f)$  is the angular frequency step,  $\lambda_m$  the total number of frequency samples, and  $\gamma$  the frequency ratio between two neighbor sampling points. The value of  $\gamma$  is experientially chosen in range of 1.03 to 1.05 for solution of the fast electrical transients [20]. In (24), the maximum sampling frequency  $f_m (= \gamma^{\lambda_m}\Delta\omega/2\pi)$  is determined from the frequency spectrum of lightning current and may be of the order (0.5~5) MHz [19], depending on the waveform of lightning current. The total number of frequency samples  $\lambda_m$  is evaluated by

$$\lambda_m = \frac{\ln(f_m/\Delta f)}{\ln \gamma}. \quad (25)$$

Therefore, for a frequency response  $X_j(\omega)$ , its time response  $x_j(t)$  can be obtained by

$$x_j(t) = \frac{1}{\pi} \sum_{k=1}^{\lambda_m} X_j \left[ (\gamma^{2k-1} - 1) \Delta\omega \right] \times \exp \left[ \mathbf{j} (\gamma^{2k-1} - 1) \Delta\omega t \right] \sigma \gamma^{2(k-1)} (\gamma^2 - 1) \Delta\omega, \quad (26)$$

where  $\sigma$  is the standard smoothing factor

$$\sigma = \frac{\sin \left[ (\lambda^{2k-1} - 1) \pi / (\gamma^{2\lambda_m} - 1) \right]}{(\gamma^{2k-1} - 1) \pi / (\gamma^{2\lambda_m} - 1)}. \quad (27)$$

Owing to a high accuracy and long observation time with a small number of sampling steps, (26) is suitable for the lightning transient calculation.

## 6. A Numerical Example

A typical Chinese-built WT with 1.5 MW is considered here for practical application purpose. The dimensions of the WT tower are and  $h = 82$  m,  $r_1 = 2.7$  m,  $r_2 = 4.3$  m, and  $w = 0.025$  m (see Figure 1(a)). The relevant discrete multiconductor grid is shown in Figure 7, where  $r_0 = 3.5$  m. The earthing resistance  $R_g$  is  $3.5\Omega$ . The transient responses on the tower body are calculated by using the proposed method. The waveforms of current on branch  $P_{2,1} - P_{3,1}$  and potential at node  $P_{1,1}$  are shown in Figure 8, where the corresponding waveforms excluding the frequency-dependent characteristic of the resistances and inductances (see (9)) are also given for comparison. As seen from Figure 8 that the waveforms excluding the frequency-dependency contain the obvious numerical oscillations, while the waveforms including frequency-dependency are relatively smooth. This indicates that inclusion of the frequency-dependency can give a higher accuracy for the lightning transient calculation. In order to check the validity of the proposed method, the peak potentials at different nodes on the tower body are calculated by the PSCAD/EMTDC software, the time-domain method [6], and the proposed method, respectively. The calculated results are shown in Figure 9. The PSCAD/EMTDC software used here has been specifically developed by Manitoba HVDC.

Research Centre for electromagnetic transient simulation and widely applied in electric power systems. It is clear from

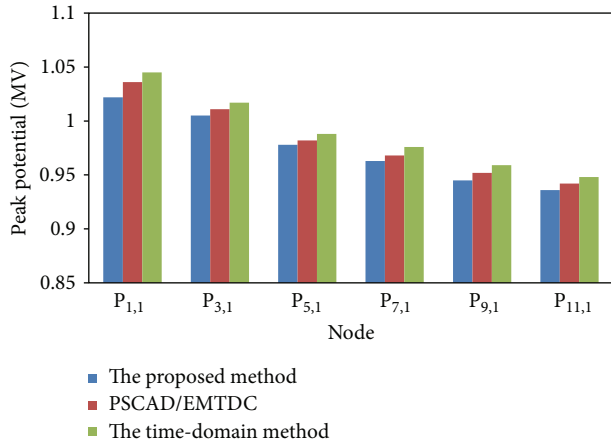


FIGURE 9: Peak potentials at different nodes on the tower body.

Figure 9 that a close agreement appears between the potential values obtained from the proposed method and those from the PSCAD/EMTDC software and the time-domain method.

## 7. Conclusions

The lightning transient calculation has been performed in this paper for obtaining the transient responses on WT towers. Discretization representation of the actual tower body in the shape of circular truncated cone as a cylindrical multiconductor grid makes a significant simplification to the transient calculation. A set of analytical formulas have been given for evaluation of the circuit parameters of the coupled branches in the multiconductor grid, and the discrete Fourier transform with exponential sampling has been employed to calculate the transient responses on the WT tower. This calculation procedure can take into account the effect of frequency-dependent characteristic of resistances and inductances on lightning transients. The practical applicability of the proposed method has been examined by a numerical example of 1.5 MW WT tower, which shows that proposed method is useful in lightning transient calculation of WT towers.

## Acknowledgment

This work was financially supported by the National Natural Science Foundation of China under Award no. 509770926. The authors express their thanks to the foundation committee.

## References

- [1] V. A. Rakov and M. A. Uman, *Lightning-Physics and Effects*, Cambridge University Press, Cambridge, UK, 2000.
- [2] *Chinese National Standard GB50064, Code for Design of Overvoltage Protection and Insulation Coordination for AC Electrical Installations*, Standard Press of China, Beijing, China, 2011.
- [3] Y. Méndez-Hernández, A. Claudi, B. Hahn, and M. Happe-Kilpper, "A first approach in modeling lightning effects on

megawatt-class onshore and offshore wind turbines by means of EMTP and models," in *Proceedings of the European Wind Energy Conference & Exhibition*, London, UK, November 2004.

- [4] R. B. Rodrigues, V. M. F. Mendes, and J. P. S. Catalão, "Protection of wind energy systems against the indirect effects of lightning," *Renewable Energy*, vol. 36, no. 11, pp. 2888–2896, 2011.
- [5] Z. Haixiang and W. Xiaorong, "Overvoltage analysis of wind turbines," *Power System Technology*, vol. 24, no. 3, pp. 27–29, 2009.
- [6] X. Q. Zhang, "Lightning transient simulation of wind turbine towers," *International Review of Electrical Engineering*, vol. 7, no. 1, pp. 3505–3511, 2012.
- [7] C. Buccella and A. Orlandi, "An efficient technique for the evaluation of lightning-induced voltage in a cylindrical vessel containing charged oil," *IEEE Transactions on Industry Applications*, vol. 39, no. 2, pp. 368–373, 2003.
- [8] G. Celli and F. Pilo, "EMTP models for current distribution evaluation in LPS for high and low buildings," in *Proceedings of the 24th International Conference on Lightning Protection*, Rhodes, Greece, September 2000.
- [9] C. Z. Feng, *Electromagnetic Field Theory*, Higher Education Press, Beijing, China, 2002.
- [10] A. Ametani, Y. Kasai, J. Sawada, A. Mochizuki, and T. Yamada, "Frequency-dependent impedance of vertical conductors and a multiconductor tower model," *IEE Proceedings: Generation, Transmission and Distribution*, vol. 141, no. 4, pp. 339–345, 1994.
- [11] C. R. Paul, *Inductance-Loop and Partial*, John Wiley & Sons, Hoboken, NJ, USA, 2010.
- [12] W. H. Wu and F. L. Zhang, *Numerical Computation of Transient Overvoltages in Power Systems*, Science Press, Beijing, China, 2001.
- [13] H. W. Dommel, *EMTP Theory Book*, Microtran Power System Analysis Corporation, Vancouver, Canada, 2nd edition, 1992.
- [14] E. A. Feilat, "Prony analysis technique for estimation of the mean curve of lightning impulses," *IEEE Transactions on Power Delivery*, vol. 21, no. 4, pp. 2088–2090, 2006.
- [15] X. H. Wang and X. Q. Zhang, "Lightning transients of wind turbine towers involving frequency-dependent characteristics," *High Voltage Engineering*, vol. 35, no. 6, pp. 1344–1349, 2009.
- [16] J. D. Hoffman, *Numerical Methods for Engineers and Scientists*, Marcel Dekker, New York, NY, USA, 2001.
- [17] J. Kiusalaas, *Numerical Methods in Engineering with MATLAB*, Cambridge University Press, New York, NY, USA, 2005.
- [18] F. S. Li, *Calculation of Overvoltages in Electric Power Networks*, Electric Power Press, Beijing, China, 2000.
- [19] X. Zhang, "A circuit approach to the calculation of lightning transients in cage-like multiconductor systems," *International Journal of Electrical Engineering Education*, vol. 47, no. 2, pp. 213–222, 2010.
- [20] A. Ametani and K. Imanishi, "Development of exponential Fourier transform and its application to electrical transients," *Proceedings IEEE*, vol. 126, no. 1, pp. 51–56, 1979.

## Research Article

# Nonlinear State Space Modeling and System Identification for Electrohydraulic Control

**Jun Yan, Bo Li, Hai-Feng Ling, Hai-Song Chen, and Mei-Jun Zhang**

*College of Field Engineering, PLA University of Science and Technology, Nanjing 210007, China*

Correspondence should be addressed to Hai-Feng Ling; [hf.ling@ymail.com](mailto:hf.ling@ymail.com)

Received 6 January 2013; Accepted 29 January 2013

Academic Editor: Shengyong Chen

Copyright © 2013 Jun Yan et al. This is an open access article distributed under the Creative Commons Attribution License, which permits unrestricted use, distribution, and reproduction in any medium, provided the original work is properly cited.

The paper deals with nonlinear modeling and identification of an electrohydraulic control system for improving its tracking performance. We build the nonlinear state space model for analyzing the highly nonlinear system and then develop a Hammerstein-Wiener (H-W) model which consists of a static input nonlinear block with two-segment polynomial nonlinearities, a linear time-invariant dynamic block, and a static output nonlinear block with single polynomial nonlinearity to describe it. We simplify the H-W model into a linear-in-parameters structure by using the key term separation principle and then use a modified recursive least square method with iterative estimation of internal variables to identify all the unknown parameters simultaneously. It is found that the proposed H-W model approximates the actual system better than the independent Hammerstein, Wiener, and ARX models. The prediction error of the H-W model is about 13%, 54%, and 58% less than the Hammerstein, Wiener, and ARX models, respectively.

## 1. Introduction

Electrohydraulic control systems are widely used in industry, due to their unique features of small size to power ratio, high nature frequency, high position stiffness, and low position error [1]. However, the dynamics of hydraulic systems is highly nonlinear in nature. The systems may be subjected to nonsmooth nonlinearities due to control input saturation, friction, valve overlapping, and directional changes of valve opening. A number of robust and adaptive control strategies have been proposed to deal with such problems [2–4], but modeling and identification of control systems remain an important and difficult issue in most real-world applications.

Linear models of electrohydraulic control systems are simple and widely used, but they assume that the hydraulic actuator always moves around an operating point [5, 6], which does not accord with most real-world cases where the actuator moves in a wide range with hard nonlinearities. In the literature, Wang et al. [7] analyzed the nonlinear dynamic characteristics of hydraulic cylinder, such as nonlinear gain, nonlinear spring, and nonlinear friction force. Jelali and Schwarz [8] identified the nonlinear models in observer canonical form of hydraulic servodrives. Kleinstueber and Sepehri [9] used a polynomial abductive network modeling

technique to describe a class of hydraulic actuation systems which were used in heavy-duty mobile machines. Yousefi et al. [10] proposed the Differential Evolution algorithm to identify the nonlinear model of a servohydraulic system with flexible load. Yao et al. [2] also pointed out that there were many considerable model uncertainties, such as parametric uncertainties and uncertain nonlinearities. As we can see, modeling and identifying the electrohydraulic control system as a flexible nonlinear black-box or grey-box are more appropriate for real-world applications.

In the field of nonlinear system identification, the Hammerstein and Wiener (H-W) models are widely used [11]. Kwak et al. [12] proposed two Hammerstein-type models to identify hydraulic actuator friction dynamics. The Hammerstein-type models are built by linear time-invariant (LTI) dynamic subsystems and static nonlinear (SN) elements in a cascade structure; they are able to approximate most of the nonlinear dynamics with an arbitrarily high accuracy, and can generate both physical insights and flexible structures. Generally, the Wiener model is supposed to represent the output nonlinearities and sensor nonlinearities, while the Hammerstein model is supposed to represent the input nonlinearities and actuator nonlinearities. The Hammerstein-Wiener (H-W) model, which is defined as a static nonlinear

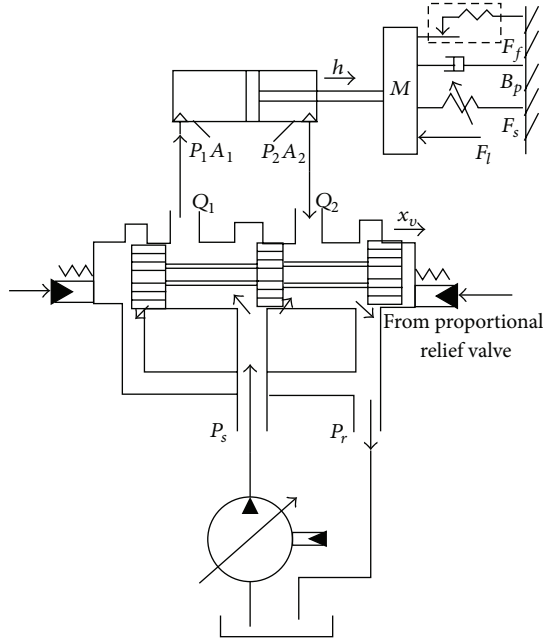


FIGURE 1: Valve controlled asymmetric cylinder system.

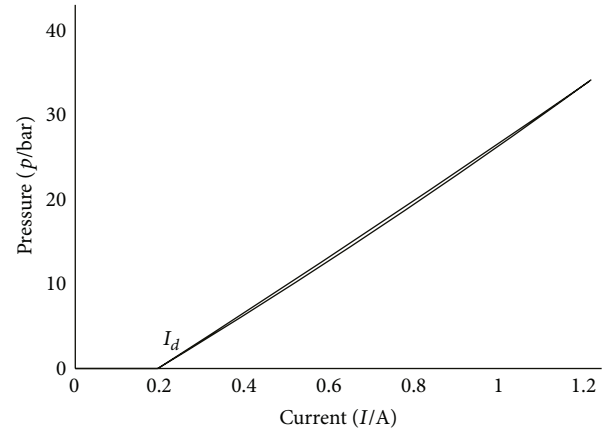
element in cascade with a linear dynamic system followed by another static nonlinear element, is adopted in this paper.

The H-W model is a parameterized nonlinear model in black-box term. There are two advantages of the H-W model. The first one is that only the input and output signals are used for identification of all the unknown parameters; that is, no information on the internal states is needed, which can simplify the identification process and improve the prediction accuracy by less sensors and noise. The second one is that it has a physical insight into the nonlinear characteristics of the actual system, which is important in system analyzing, monitoring, diagnosis, and controller design.

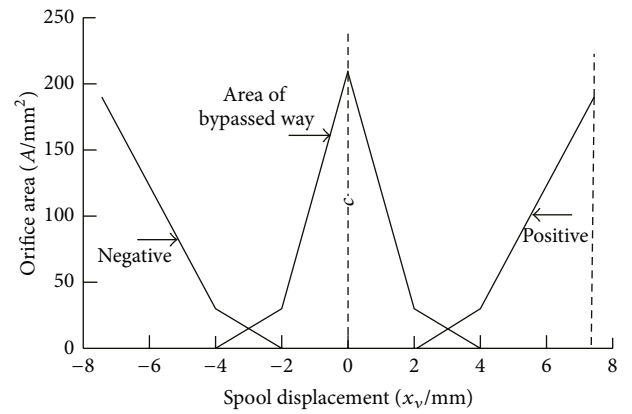
The rest of this paper is organized as follows. Section 2 presents the theoretic modeling of an electrohydraulic control system. Section 3 describes our H-W model in detail. Section 4 proposes the iterative identification algorithm for the H-W model. Section 5 presents the experimental tests as well as the identification results. Finally, Section 6 concludes the paper.

## 2. Theoretic Modeling

A general electrohydraulic control system is mainly comprised of an electrohydraulic proportional valve and a valve controlled asymmetric cylinder. In this paper, we study a proportional relief valve controlled valve-cylinder system as shown in Figure 1, where  $h$  is the displacement of piston,  $M$  is the equivalent load mass,  $A_1$  and  $A_2$  are the areas of piston in the head and rod sides of cylinder,  $P_1$  and  $P_2$  are the pressures inside the two chambers of the cylinder,  $P_s$  is the supply pressure,  $P_r$  is the pressure of return oil,  $Q_1$  and  $Q_2$  are the flows in and out of the cylinder,  $x_v$  is displacement of the spool valve,  $B_p$  is the viscous damping coefficient,  $F_f$  represents nonlinear friction,  $F_s$  represents nonlinear spring



(a) Dead band of the pilot relief valve



(b) Dead band of the main valve

FIGURE 2: Dead band of the electrohydraulic proportional system.

force,  $F_c$  represents viscous force, and  $F_l$  represents uncertain load.

Modeling the system by physical laws gives us a particular insight into the system's properties, which allows us to seek the parameterized models that are flexible enough to capture all dynamic behavior of the system [13, 14]. The electrohydraulic proportional valve is controlled directly by the digital controller. It can be modeled as a first order transfer function [9]:

$$G_I = \frac{x_v(s)}{I_v(s)} = \frac{k_v}{1 + \tau_v s}, \quad (1)$$

where  $k_v$  is the gain of the electrohydraulic proportional valve,  $\tau_v$  is the time constant of the first order system,  $I_v = I - I_d$  is the effective current,  $I$  and  $I_d$  are the practical input current of the proportional relief valve and the current to overcome dead band of the valve, respectively. The dead bands mainly due to the pilot relief valve and the main valve are depicted in Figure 2.

The valve controlled asymmetric cylinder is shown in Figure 1. Generally, its model is constructed by combining the flow equation of spool valve, the continuity equation

of hydraulic cylinder, and the force equilibrium equation of hydraulic cylinder [2]. Define the state variables as

$$[x_1 \ x_2 \ x_3 \ x_4 \ x_5]^T \triangleq [h \ \dot{h} \ p_1 \ p_2 \ x_v]^T. \quad (2)$$

The entire system can be modeled as the following nonlinear state space model [15]:

$$\begin{aligned} \dot{x}_1 &= x_2, \\ \dot{x}_2 &= \frac{A_1 x_3}{M} - \frac{A_2 x_4}{M} - \frac{F_f(x_2)}{M} \\ &\quad - \frac{F_s(x_1)}{M} - \frac{F_c(x_2)}{M} - \frac{F_l}{M}, \\ \dot{x}_3 &= -\frac{\beta_e A_1 x_2}{V_1} - \frac{\beta_e (C_i + C_e) x_3}{V_1} + \frac{\beta_e C_i x_4}{V_1} + \frac{\beta_e g_1(x)}{V_1} x_5, \\ \dot{x}_4 &= \frac{\beta_e A_2 x_2}{V_2} + \frac{\beta_e C_i x_3}{V_2} - \frac{\beta_e (C_i + C_e) x_4}{V_2} - \frac{\beta_e g_2(x)}{V_2} x_5, \\ \dot{x}_5 &= \frac{k_v}{\tau_v} I_v - \frac{x_5}{\tau_v}, \end{aligned} \quad (3)$$

$$\begin{aligned} g_1(x) &= \operatorname{sgn} \left( (1 + \operatorname{sgn}(x_5)) \frac{P_s}{2} - \operatorname{sgn}(x_5) x_3 \right) \\ &\quad \times C_{d1} W \sqrt{\frac{2}{\rho} \left( (1 + \operatorname{sgn}(x_5)) \frac{P_s}{2} - \operatorname{sgn}(x_5) x_3 \right)}, \\ g_2(x) &= \operatorname{sgn} \left( (1 - \operatorname{sgn}(x_5)) \frac{P_s}{2} + \operatorname{sgn}(x_5) x_4 \right) \\ &\quad \times C_{d2} W \sqrt{\frac{2}{\rho} \left( (1 - \operatorname{sgn}(x_5)) \frac{P_s}{2} + \operatorname{sgn}(x_5) x_4 \right)}, \end{aligned} \quad (4)$$

where  $\beta_e$  is the effective bulk modulus,  $V_1$  and  $V_2$  are effective volumes of the two chambers,  $C_i$  and  $C_e$  are internal and external leakage coefficients,  $W$  is the area gradient of the valve orifice, and  $C_{d1}$  and  $C_{d2}$  are flow discharge coefficients of the spool valve.

Several physical phenomena have been taken into consideration in the above model, for example, nonlinear friction  $F_f$ , nonlinear spring force  $F_s$ , viscous force  $F_c$ , uncertain load  $F_l$ , discontinuous flow discharge  $g_i$ , oil compliance, internal leakage, and external leakage. From the theoretic modeling of the electrohydraulic control system, we can see that the system is a highly nonlinear system containing complex features, such as the dead band nonlinearity, saturation, squared pressure drop, and asymmetric response property.

There are also some hard-to-model nonlinearities in (3), such as nonlinear friction, nonlinear spring force, and uncertain external disturbances. So, modeling this system just by physical laws fails to approximate the actual system. Furthermore, identification of the unknown parameters in (3) is hard due to its demand on internal states measurement. In the following, we adopt an H-W model to model this highly

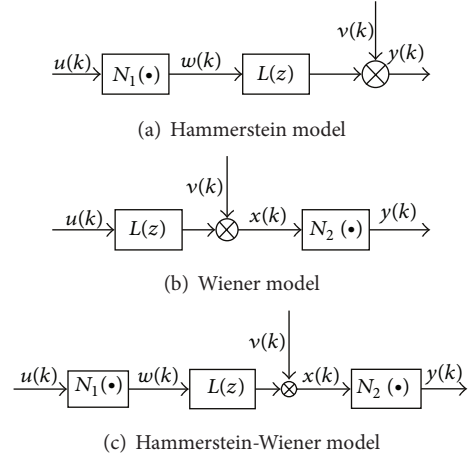


FIGURE 3: Hammerstein and Wiener models.

nonlinear dynamic system. The H-W model is a flexible black-box model based on the physical insight into the actual system. We identify the parameters of the H-W model using the input and output signals, which can simplify the identification process and improve the prediction accuracy by less sensors and noise.

### 3. Hammerstein-Wiener Model

The “universal” nonlinear black-box methods, such as neural networks, Volterra series, and fuzzy models, are widely used to model complex nonlinear systems. Most of these methods can avoid unmodeled dynamics in the aforementioned mathematical model [16, 17]. However, these models do not provide deep insight into the nonlinear characteristics of the actual system, which is important in system analyzing, monitoring, diagnosis, and controller design. In comparison, the Hammerstein-Wiener (H-W) model possesses the flexibility to capture all relevant nonlinear phenomena as well as the physical insight into the actual system. In this section, we develop an H-W model to describe the electrohydraulic control system.

The H-W model is composed of an internal linear dynamic block and two static nonlinear blocks; it is the combination of Hammerstein and Wiener model. The Hammerstein model is a nonlinear model with a static nonlinear block followed by a linear dynamic block, as shown in Figure 3(a), and this N-L type of model may account for actuator nonlinearities and other input nonlinear effects. The Wiener model has linear dynamic block followed by a nonlinear block, as shown in Figure 3(b), and this L-N type of model mainly accounts for sensor nonlinearities and output nonlinear effects. A series combination of a Hammerstein and a Wiener model yields the H-W model, as shown in Figure 3(c), and this N-L-N type of model has both characteristics of the Hammerstein and Wiener models. Moreover, all of the three models have proved to be able to accurately describe a wide variety of nonlinear systems in [9].

According to the nonlinearities of the abovementioned electrohydraulic control system, for example, dead band,

saturation, nonlinear friction, nonlinear spring force, and asymmetric dynamics of the cylinder, we describe the input nonlinearity ( $N_1$ ) block of the models in Figure 3 by a two-segment polynomial nonlinearities. The two-segment polynomial nonlinearities have the advantage of describing a system whose dynamic properties differ significantly at the positive and negative directions [18]; it has less parameters to be estimated than a single polynomial and piecewise linear models [19]. It can be written as

$$w(k) = \begin{cases} f(u(k)) = \sum_{l=0}^{r_1} f_l u^l(k), & u(k) \geq 0, \\ g(u(k)) = \sum_{l=0}^{r_1} g_l u^l(k), & u(k) < 0, \end{cases} \quad (5)$$

where  $f_l$  and  $g_l$  are parameters of the polynomial function,  $u(k)$  is the input,  $w(k)$  is the output of static nonlinear function  $N_1$ , and  $r_1$  is the degree of the polynomial function.

Define the switching function as

$$h(u) = \begin{cases} 0, & u \geq 0, \\ 1, & u < 0. \end{cases} \quad (6)$$

Then the relation between inputs  $\{u(k)\}$  and outputs  $\{w(k)\}$  of the input nonlinear block can be written as

$$\begin{aligned} w(k) &= f(u(k)) + (g(u(k)) - f(u(k)))h(u(k)) \\ &= \sum_{l=0}^{r_1} f_l u^l(k) + \sum_{l=0}^{r_1} p_l u^l(k)h(u(k)), \end{aligned} \quad (7)$$

where  $p_l = g_l - f_l$ .

The difference equation model  $L(z)$  of the linear dynamic block is described by an extended autoregressive (ARX) model as

$$A(z^{-1})x(k) = z^{-n_k}B(z^{-1})w(k) + v(k), \quad (8)$$

where  $w(k)$  and  $x(k)$  are the input and output of the linear dynamic block, respectively,  $v(k)$  is white noise,  $n_k$  represents the pure delay of the system, and  $A(z^{-1})$  and  $B(z^{-1})$  are scalar polynomials in the unit delay operator  $z^{-1}$ :

$$\begin{aligned} A(z^{-1}) &= 1 + a_1 z^{-1} + \dots + a_{n_a} z^{-n_a}, \\ B(z^{-1}) &= b_0 + b_1 z^{-1} + \dots + b_{n_b} z^{-n_b}. \end{aligned} \quad (9)$$

The output nonlinear block  $N_2$  is described by a single polynomials:

$$y(k) = q(x(k)) = \sum_{m=1}^{r_2} q_m x^m(k), \quad (10)$$

where  $q_m$  is unknown parameter,  $r_2$  is the degree of the polynomial function  $N_2$ , and  $y(k)$  is output of the entire system, and in this paper, it represents the output velocity.

The H-W model of the system is depicted in Figure 4.

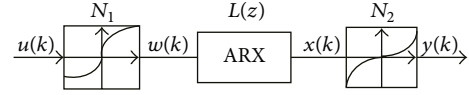


FIGURE 4: Schematic diagram of the H-W model.

## 4. Iterative Identification Algorithm

As we know, the cascade mode of the models depicted in Figure 3 leads to composite mappings, for example, Hammerstein model:  $L(N_1(u(k)))$ , Wiener model:  $N_2(L(u(k)))$ , H-W model:  $N_2(L(N_1(u(k))))$ . Substituting the mathematic models of each block (i.e., (7), (8), and (10)) into the composite mappings directly leads to complex models which are strongly nonlinear in both of the variables and the unknown parameters. It is not appropriate for parameter estimation [20]. In the following, we apply the so-called key term separation principle to simplify the H-W model into a linear-in-parameters structure and then adopt a modified recursive least square algorithm with internal variable estimation to estimate both of the linear and nonlinear block parameters simultaneously.

**4.1. Key Term Separation Principle.** Let  $f$ ,  $g$ , and  $h$  be one-to-one mappings defined on nonempty sets  $U$ ,  $X$ , and  $Y$  as

$$\begin{aligned} f &: U \longrightarrow X, \\ g &: X \longrightarrow Y, \\ h &= g \circ f : U \longrightarrow Y. \end{aligned} \quad (11)$$

Then the composite mapping  $h$  can be given by

$$y(t) = g[x(t)] = g[f[u(t)]] = h[u(t)]. \quad (12)$$

The basic idea of key term separation principle is a form of half-substitution suggested in [21]. Suppose  $g$  be an analytic nonlinear mapping which can be rewritten into the following additive form:

$$y(t) = x(t) + G[x(t)], \quad (13)$$

Which consists of the key term  $x(t)$ , plus the remainder of the original mapping assigned as  $G(\cdot)$ . Rewrite the one-to-one mapping  $f$

$$x(t) = f[u(t)]. \quad (14)$$

We substitute (13) only into the first term in the right side of (14) and then obtain the following mapping:

$$y(t) = f[u(t)] + G[x(t)]. \quad (15)$$

Equations (14) and (15) describe the mapping function  $h$  in a compositional way. This makes the inner mapping appears both explicitly and implicitly in the outer one, which may be helpful for parameter identification. Note that, this decomposition technique can easily be extended to a more multilayer composite mapping.

**4.2. Modified Least Square Algorithm.** In this section, we decompose the H-W model into a linear-in-parameters structure by the key term separation principle and develop a modified iterative least square algorithm with internal variables estimation to identify all the unknown parameters of the H-W model. We also apply this method to the Hammerstein and Wiener models.

According to the key term separation principle, we rewrite the output nonlinear block  $N_2$ , that is, (10) as

$$y(k) = q_1 x(k) + \sum_{m=2}^{r_2} q_m x^m(k), \quad (16)$$

where the internal variable  $x(k)$  is separated. The dynamic linear block  $L(z)$ , that is, (8) can be rewritten as

$$x(k) = b_0 w(k) z^{-n_k} + z^{-n_k} [B(z^{-1}) - b_0] w(k) + [1 - A(z^{-1})] x(k), \quad (17)$$

where the internal variable  $w(k)$  is separated. Now, to complete the sequential decomposition, first, we substitute (7) into (17) only for  $w(k)$  in the first term and then substitute the new equation (17) into (16) only for  $x(k)$  in the first term again. The final output equation of the H-W model will be

$$y(k) = q_1 \left\{ b_0 (f(u(k)) + p(u(k)) h(u(k))) z^{-n_k} + z^{-n_k} [B(z^{-1}) - b_0] w(k) + [1 - A(z^{-1})] x(k) \right\} + \sum_{m=2}^{r_2} q_m x^m(k). \quad (18)$$

As the H-W model depicted in Figure 4 consists of three subsystems in series, the parameterization of the model is not unique because many combinations of parameters can be found [22]. Therefore, one parameter in at least two blocks has to be fixed in (18). Evidently, the choices  $q_1 = 1$  and  $b_0 = 1$  will simplify the model description. Then, the H-W model can be written as

$$y(k) = \sum_{l=0}^{r_1} f_l u^l(k - n_k) + \sum_{l=0}^{r_1} p_l u^l(k - n_k) h(u(k - n_k)) + \sum_{i=1}^{n_b} b_i w(k - n_k - i) + \sum_{j=1}^{n_a} a_j x(k - j) + \sum_{m=2}^{r_2} q_m x^m(k). \quad (19)$$

Equation (19) is linear-in-parameters for given  $u(k)$ ,  $x(k)$ , and  $w(k)$ ; it can be written in the following least square format:

$$y(k) = \Phi^T(k, \theta) \theta, \quad (20)$$

where the internal variables  $w(k)$  and  $x(k)$  are estimated by (7) and (17) using the preceding estimated parameters during each iterative process and

$$\Phi^T = \left[ 1, u(k - n_k), \dots, u^{r_1}(k - n_k), h(u(k - n_k)), u(k - n_k) h(u(k - n_k)), \dots, u^{r_1}(k - n_k) h(u(k - n_k)), w(k - n_k - 1), \dots, w(k - n_k - i), -x(k - 1), \dots, -x(k - j), x^2(k), \dots, x^{r_2}(k) \right], \quad (21)$$

$$\theta = \left[ f_0, f_1, \dots, f_{r_1}, p_0, p_1, \dots, p_{r_1}, b_1, \dots, b_{n_b}, a_1, \dots, a_{n_a}, q_2, \dots, q_{r_2} \right]^T.$$

Now, we apply the modified recursive least square method with iterative estimation of the internal variable to (20) [17]. Minimizing the following least square criterion [12]:

$$\hat{\theta} = \arg \min_{\theta} \sum_{k=1}^n \lambda^{n-k} \left[ y(k) - \hat{\Phi}^T(k) \theta \right]^2, \quad (22)$$

where  $\lambda \leq 1$  is the forgetting factor, the formulas of the recursive identification algorithm supplemented with internal variable estimation are as follows:

$$\hat{\theta}(k) = \hat{\theta}(k - 1) + \frac{\mathbf{P}(k - 1) \hat{\Phi}(k) \left[ y(k) - \hat{\Phi}^T(k) \hat{\theta}(k - 1) \right]}{\lambda + \hat{\Phi}^T(k) \mathbf{P}(k - 1) \hat{\Phi}(k)}, \quad (23)$$

$$\mathbf{P}(k) = \frac{\mathbf{P}(k - 1)}{\lambda} - \frac{\mathbf{P}(k - 1) \hat{\Phi}(k) \hat{\Phi}^T(k) \mathbf{P}(k - 1)}{1 + \hat{\Phi}^T(k) \mathbf{P}(k - 1) \hat{\Phi}(k) / \lambda}, \quad (24)$$

$$\hat{w}(k) = \sum_{l=0}^{r_1} \hat{f}_l(k - 1) u^l(k) + \sum_{l=0}^{r_1} \hat{p}_l(k - 1) u^l(k) h(u(k)), \quad (25)$$

$$\hat{x}(k) = \hat{w}(k - n_k) + \sum_{i=1}^{n_b} \hat{b}_i(k - 1) \hat{w}(k - n_k - i) - \sum_{j=1}^{n_a} \hat{a}_j(k - 1) x(k - j), \quad (26)$$

$$\hat{\Phi}(k) = \left[ 1, u(k - n_k), \dots, u^{r_1}(k - n_k), h(u(k - n_k)), u(k - n_k) h(u(k - n_k)), \dots, u^{r_1}(k - n_k) h(u(k - n_k)), \hat{w}(k - n_k - 1), \dots, \hat{w}(k - n_k - i), -\hat{x}(k - 1), \dots, -\hat{x}(k - j), \hat{x}^2(k), \dots, \hat{x}^{r_2}(k) \right]^T, \quad (27)$$

where  $\mathbf{P}(0) = \mu \mathbf{I}$ ,  $\mathbf{I}$  is unit matrix, and  $0 < \mu < \infty$ .

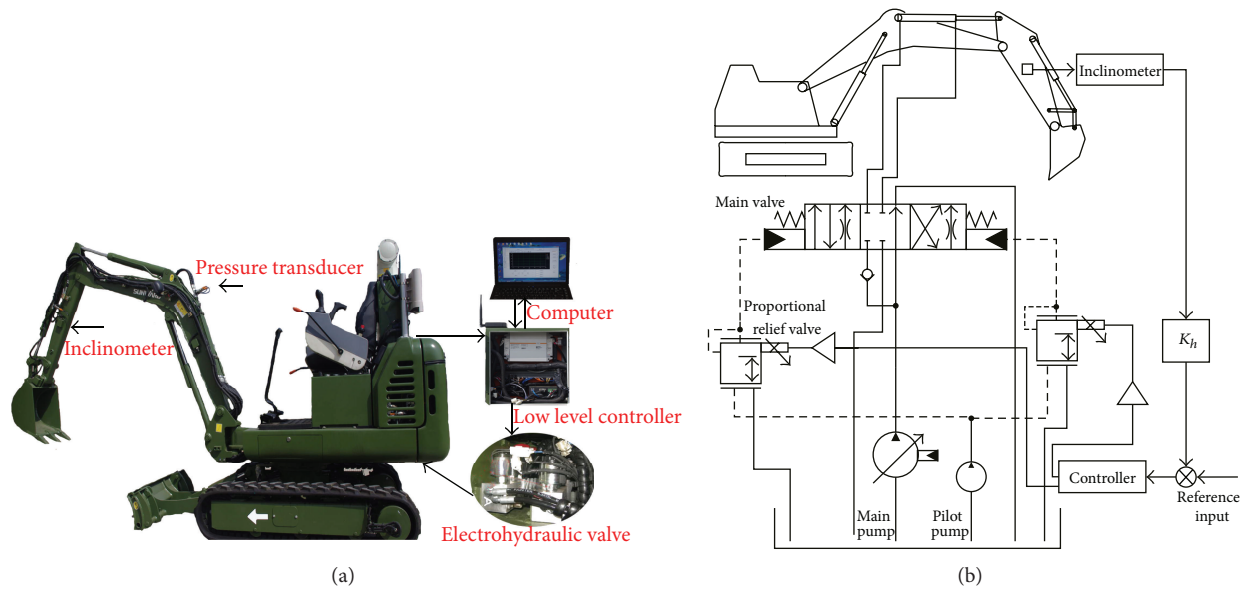


FIGURE 5: Experimental prototype machine.

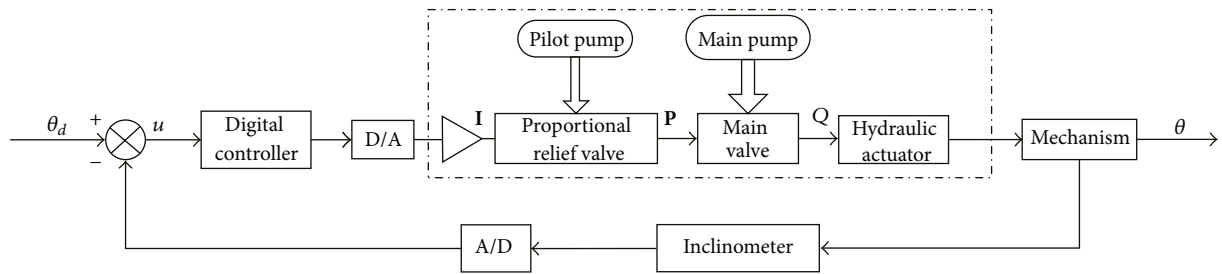


FIGURE 6: Electrohydraulic position servocontrol system.

In conclusion, the iterative identification algorithm can be presented as follows.

*Step 1.* Set the initial values of  $x(0)$ ,  $w(0)$ ,  $u(0)$ , and  $\mathbf{P}(0)$ .

*Step 2.* Estimate the parameter  $\hat{\theta}(k)$  by algorithm (23) and calculate  $\mathbf{P}(k)$  by (24).

*Step 3.* Estimate the internal variables  $\hat{w}(k)$  and  $\hat{x}(k)$  by (25) and (26) using the recent estimates of model parameters  $\hat{\theta}(k)$ .

*Step 4.* Update the values of  $\hat{\Phi}(k)$  by (27).

*Step 5.* Return to Step 2 until the parameter estimates converge to constant values.

## 5. Experiment

*5.1. Experimental Environment.* A hydraulic excavator was retrofitted to be controlled by computer in our laboratory [23]. Figure 5 shows the prototype machine, whose manual pilot hydraulic control system was replaced by electrohydraulic proportional control system; inclinometers and pressure transducers were also installed on the excavator arms

for position and force servocontrol. Schematic diagram of the electrohydraulic servosystem is shown in Figure 6.

*5.2. Experimental Results.* In order to obtain the nonlinear characteristics of the system when changing the directions and to obtain sufficient excitation, we adopted a multisine input signal which contained the frequency of 0.05 Hz, 0.1 Hz, 0.2 Hz, 0.4 Hz, and 0.5 Hz to the identification experiments. The sample rate was chosen to be 20 Hz on the machine. The input signal and angle output were obtained from the computer of the experiment machine. Ten groups of input and output signals with time duration of 55 seconds were sampled in the repeated experiments; the averaged measurement results are shown in Figure 7. Finally, we calculate the output angle velocity by numerical differentiation.

We set the parameters  $n_a = 3$ ,  $n_b = 2$ ,  $n_k = 8$ ,  $r_1 = r_2 = 3$ ,  $x(0) = 0$ ,  $w(0) = 0$ ,  $u(0) = 0$ , and  $\mathbf{P}(0) = 10^6 \mathbf{I}$ . Note that lower forgetting factor  $\lambda$  is useful for reducing the influences of old data, while a value of  $\lambda$  close to 1 is less sensitive to disturbance. Therefore, we chose the forgetting factor to be  $\lambda = 0.98$  during the first 200 samples, and  $\lambda = 1$  otherwise. Compiling the developed iterative least square algorithm in MATLAB to identify the ARX model containing only the  $L(z)$

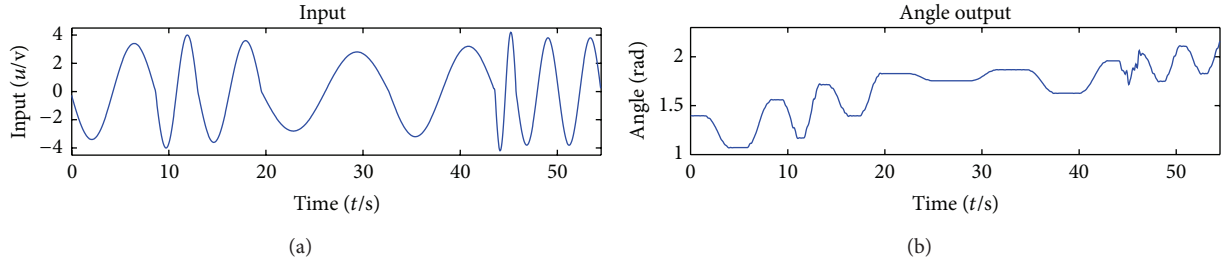


FIGURE 7: Input and output signals of the identification experiment.

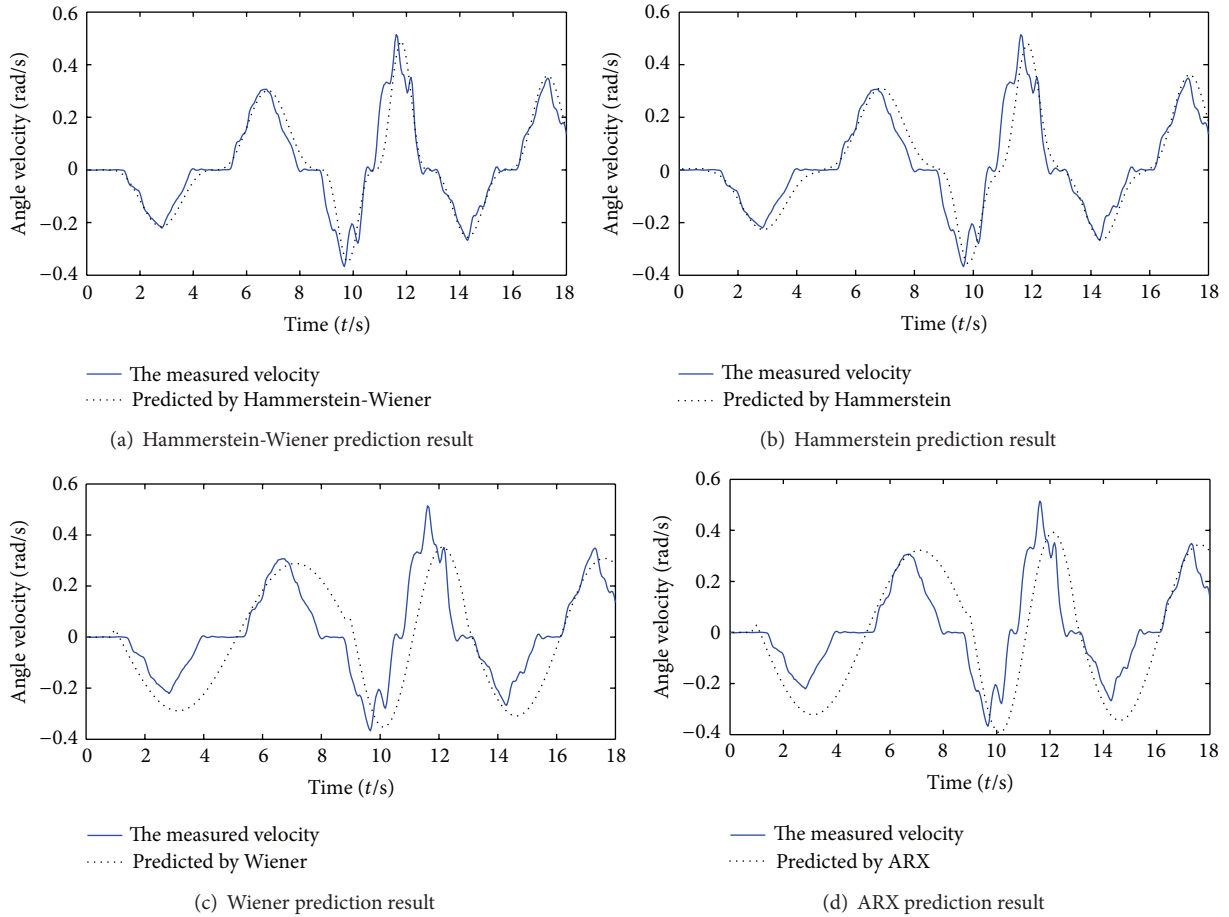


FIGURE 8: Comparison results of the identified models.

block, Hammerstein model consisting of  $N_1$  and  $L(z)$ , Wiener model consisting of  $L(z)$  and  $N_2$ , and H-W model consisting of  $N_1$ ,  $L(z)$ , and  $N_2$ , respectively, we obtain the identification results shown in Table 1.

We use the identified models to predict the tracking velocity of a general trajectory. The comparative results are shown in Figures 8 and 9. They demonstrate that the H-W and Hammerstein models which contain the input nonlinear block with two-segment polynomial nonlinearities capture the actual system well, while the Wiener and ARX models cannot approximate the actual system well. The mean-square errors (MSE) of the identified models in Table 2 show that the

prediction error of the H-W model is about 13%, 54%, and 58% less than the Hammerstein, Wiener, and ARX models, respectively.

## 6. Conclusion

This paper investigates the nonlinear modeling and identification of an electrohydraulic control system. We develop a theoretic state space model for system analysis, propose an H-W model for the highly nonlinear system based on a deeply physical insight into the actual system, and apply a modified

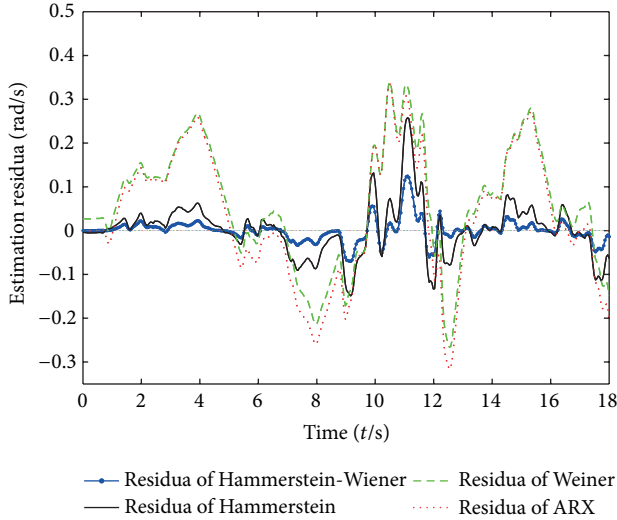


FIGURE 9: Comparison of the estimation residua.

TABLE 1: The identification results.

Parameters	Model type			
	H-W	Hammerstein	Wiener	ARX
$b_0$	1	1	-0.0358	-0.0276
$b_1$	0.0349	0.0105	0.0151	0.0124
$b_2$	0.0617	0.0147	-0.0069	0.0514
$a_1$	-0.0309	-0.0596	0.0069	-0.0661
$a_2$	-0.0598	-0.0613	-0.0075	-0.0653
$a_3$	-0.0897	-0.0610	-0.0081	-0.0619
$f_0$	0.0109	0.0027	—	—
$f_1$	$-1.4619 \times 10^{-5}$	0.0012	—	—
$f_2$	-0.0050	-0.0012	—	—
$f_3$	0.0052	0.0045	—	—
$p_0$	-0.0165	-0.0055	—	—
$p_1$	0.0033	0.0013	—	—
$p_2$	0.0104	0.0036	—	—
$p_3$	-0.0010	$-8.6858 \times 10^{-4}$	—	—
$q_1$	1	—	1	—
$q_2$	0.0050	—	0.0013	—
$q_3$	$6.3562 \times 10^{-4}$	—	$2.6895 \times 10^{-4}$	—

TABLE 2: MSE of the identified models.

Errors	Model type			
	H-W	Hammerstein	Wiener	ARX
$\delta/r \cdot s^{-1}$	0.0321	0.0417	0.1081	0.1218

recursive least square method with internal variables estimation to identify its parameters. The main findings of the paper include the following: (1) the proposed H-W model simplifies the identification procedure because it only uses the input and output signals to identify all the parameters. (2) The H-W model containing the input nonlinear block with two-segment polynomial nonlinearities captures the actual system very well. As shown by the comparative results, the prediction

error of the H-W model is about 13%, 54%, and 58% less than the Hammerstein, Wiener, and ARX models, respectively. The results provide a physical insight into the nonlinear characteristics of the actual system, which is important for system analyzing, monitoring, and diagnosis. Future work includes addressing uncertain and fuzzy properties of the system [24, 25] and extending the model for a wider range of equipment [26].

## Acknowledgment

This work was supported in part by grants from National Natural Science Foundation (Grant nos. 51175511 and 61105073) of China.

## References

- [1] H. E. Merritt, *Hydraulic Control System*, John Wiley & Sons, New York, USA, 1967.
- [2] B. Yao, F. Bu, J. Reedy, and G. T. C. Chiu, "Adaptive robust motion control of single-rod hydraulic actuators: theory and experiments," *IEEE/ASME Transactions on Mechatronics*, vol. 5, no. 1, pp. 79–91, 2000.
- [3] S. Wen, W. Zheng, J. Zhu, X. Li, and S. Chen, "Elman fuzzy adaptive control for obstacle avoidance of mobile robots using hybrid force/position incorporation," *IEEE Transactions on Systems, Man and Cybernetics C*, vol. 42, no. 4, pp. 603–608, 2012.
- [4] S. Y. Chen, J. Zhang, H. Zhang, N. M. Kwok, and Y. F. Li, "Intelligent lighting control for vision-based robotic manipulation," *IEEE Transactions on Industrial Electronics*, vol. 59, no. 8, pp. 3254–3263, 2012.
- [5] Q. H. He, P. Hao, and D. Q. Zhang, "Modeling and parameter estimation for hydraulic system of excavator's arm," *Journal of Central South University of Technology*, vol. 15, no. 3, pp. 382–386, 2008.
- [6] K. Ziaei and N. Sepehri, "Modeling and identification of electrohydraulic servos," *Mechatronics*, vol. 10, no. 7, pp. 761–772, 2000.
- [7] L. Wang, B. Wu, R. Du, and S. Yang, "Nonlinear dynamic characteristics of moving hydraulic cylinder," *Chinese Journal of Mechanical Engineering*, vol. 43, no. 12, pp. 12–19, 2007.
- [8] M. Jelali and H. Schwarz, "Nonlinear identification of hydraulic servo-drive systems," *IEEE Control Systems Magazine*, vol. 15, no. 5, pp. 17–22, 1995.
- [9] S. Kleinstueber and N. Sepehri, "A polynomial network modeling approach to a class of large-scale hydraulic systems," *Computers and Electrical Engineering*, vol. 22, no. 2, pp. 151–168, 1996.
- [10] H. Yousefi, H. Handroos, and A. Soleymani, "Application of differential evolution in system identification of a servo-hydraulic system with a flexible load," *Mechatronics*, vol. 18, no. 9, pp. 513–528, 2008.
- [11] F. Giri and E. W. Bai, *Block-Oriented Nonlinear System Identification*, vol. 404 of *Lecture Notes in Control and Information Sciences*, Springer, Berlin, Germany, 2010.
- [12] B. -J. Kwak, A. E. Yagle, and J. A. Levitt, "Nonlinear system identification of hydraulic actuator friction dynamics using a Hammerstein model," in *Proceedings of the IEEE International Conference on Acoustics, Speech and Signal Processing*, vol. 4, pp. 1933–1936, Seattle, Wash, USA, 1998.

- [13] Y. J. Zheng, S. Y. Chen, Y. Lin, and W. L. Wang, "Bio-Inspired optimization of sustainable energy systems: a review," *Mathematical Problems in Engineering*, vol. 2013, Article ID 354523, 12 pages, 2013.
- [14] C. Cattani, R. Badea, S. Chen, and M. Crisan, "Biomedical signal processing and modeling complexity of living systems," *Computational and Mathematical Methods in Medicine*, vol. 2012, Article ID 298634, 2 pages, 2012.
- [15] B. Li, J. Yan, A. X. Liu, Y. H. Zeng, and G. Guo, "Nonlinear identification of excavator's electro-hydraulic servo system," *Transactions of the Chinese Society For Agricultural Machinery*, vol. 43, no. 4, pp. 20–25, 2012.
- [16] J. Ljung, *System Identification, Theory for the User*, Prentice Hall Press, New York, NY, USA, 1999.
- [17] S. Chen, W. Huang, C. Cattani, and G. Altieri, "Traffic dynamics on complex networks: a survey," *Mathematical Problems in Engineering*, vol. 2012, Article ID 732698, 23 pages, 2012.
- [18] J. Vörös, "Iterative algorithm for parameter identification of Hammerstein systems with two-segment nonlinearities," *IEEE Transactions on Automatic Control*, vol. 44, no. 11, pp. 2145–2149, 1999.
- [19] J. Vörös, "Recursive identification of Hammerstein systems with discontinuous nonlinearities containing dead-zones," *IEEE Transactions on Automatic Control*, vol. 48, no. 12, pp. 2203–2206, 2003.
- [20] J. Vörös, "An iterative method for Hammerstein-Wiener systems parameter identification," *Journal of Electrical Engineering*, vol. 55, no. 11-12, pp. 328–331, 2004.
- [21] J. Vörös, "Identification of nonlinear dynamic systems using extended Hammerstein and Wiener models," *Control Theory and Advanced Technology*, vol. 10, no. 4, part 2, pp. 1203–1212, 1995.
- [22] E.-W. Bai, "A blind approach to the Hammerstein-Wiener model identification," *Automatica*, vol. 38, no. 6, pp. 967–979, 2002.
- [23] J. Yan, B. Li, Q. Z. Tu, G. Gang, and Y. H. Zeng, "Automatization of excavator and study of its auto-control," in *Proceedings of the 3rd International Conference on Measuring Technology and Mechatronics Automation*, pp. 604–609, Shanghai, China, 2011.
- [24] Y. J. Zheng and H. F. Ling, "Emergency transportation planning in disaster relief supply chain management: a cooperative fuzzy optimization approach," *Soft Computing*, 2013.
- [25] Y. J. Zheng and S. Y. Chen, "Cooperative particle swarm optimization for multiobjective transportation planning," *Applied Intelligence*, 2013.
- [26] Y. Zheng, S. Chen, and H. Ling, "Efficient multi-objective tabu search for emergency equipment maintenance scheduling in disaster rescue," *Optimization Letters*, vol. 7, no. 1, pp. 89–100, 2013.

## Research Article

# On-Board Computing for Structural Health Monitoring with Smart Wireless Sensors by Modal Identification Using Hilbert-Huang Transform

Ning Wu,<sup>1</sup> Chengyin Liu,<sup>1</sup> Yukun Guo,<sup>1</sup> and Jianhua Zhang<sup>2</sup>

<sup>1</sup> Harbin Institute of Technology Shenzhen Graduate School, Shenzhen 518055, China

<sup>2</sup> College of Computer Science and Technology, Zhejiang University of Technology, Hangzhou 310023, China

Correspondence should be addressed to Chengyin Liu; [chengyin.liu08@gmail.com](mailto:chengyin.liu08@gmail.com)

Received 14 December 2012; Accepted 6 February 2013

Academic Editor: Shengyong Chen

Copyright © 2013 Ning Wu et al. This is an open access article distributed under the Creative Commons Attribution License, which permits unrestricted use, distribution, and reproduction in any medium, provided the original work is properly cited.

Smart wireless sensors have been recognized as a promising technology to overcome many inherent difficulties and limitations associated with traditional wired structural health monitoring (SHM) systems. Despite the advances in smart sensor technologies, on-board computing capability of smart sensors has been considered as one of the most difficult challenges in the application of the smart sensors in SHM. Taking the advantage of recent developments in microprocessor which provides powerful on-board computing functionality for smart sensors, this paper presents a new decentralized data processing approach for modal identification using the Hilbert-Huang transform (HHT) algorithm, which is based on signal decomposition technique. It is shown that this method is suitable for implementation in the intrinsically distributed computing environment found in wireless smart sensor networks (WSSNs). The HHT-based decentralized data processing is, then, programmed and implemented on the Crossbow IRIS mote sensor platform. The effectiveness of the proposed techniques is demonstrated through a set of numerical studies and experimental validations on an in-house cable-stayed bridge model in terms of the accuracy of identified dynamic properties.

## 1. Introduction

Vibration-based structural health monitoring (SHM) provides valuable information regarding the dynamic characteristics of structures. The identification process consists of measuring vibration responses from structures and analyzing the measured data to build a numerical model of the structure. Traditionally, the vibration responses are obtained using centralized data acquisition systems with wired sensors. However, wired sensors have proven to be difficult to implement, particularly for dense deployment of sensors on large-scale civil infrastructures due to the long setup time, the difficulties in cabling, and the high cost in equipments.

Smart wireless sensors are more flexible than traditional wired sensors in communication, and their performance in data processing is also better [1–3]. A smart sensor is equipped with an independent on-board microprocessor that can be used for digital signal processing, self-diagnosis,

self-identification, and self-adaptation, and the smart sensor platform is battery powered with reliable wireless communication technology.

Smart sensors provide a promising alternative to the traditional wired sensor systems, and there have been many successful applications. Spencer et al. [4] defined smart sensors with mainly four features: (i) on-board computing capability, (ii) small size, (iii) wireless communication, and (iv) low cost. Lynch and Loh [5] reviewed over 150 papers on wireless sensors for SHM with research conducted at more than 50 institutes worldwide. SHM applications with smart sensors have been studied using both scale models and full-scale structures, respectively. Recent studies [6–11] have demonstrated the potential of applying smart sensors to monitor large-scale civil infrastructure using a dense array of sensors. However, the power consumption and long-term reliability of smart sensors are still expected to be improved. Many different methods have been proposed for power harvesting

TABLE 1: IRIS features.

Processor	Clock speed (MHz)	Memory (KB)	SRAM (KB)	Program flash (KB)	Radio (Hz)	Data rate (kbp/sec)	ADC (bit)
ATMega1281V	8	128	8	512	2.4 G	250	10

of sensors, for example, solar power and vibration power [6, 12–14], but the system development is too complicated. One way to alleviate this problem is to reduce the number of communication cycles, since, in statistics, communication consumes most of the battery energy.

The performance of data communication in wireless smart sensor networks (WSSNs) is based on the data acquisition and processing schemes within the WSSNs. A single-sensor node which generates 16-bit vibration data along three axes at 500 samples per second can easily consume one-fourth of the nominal data rate of the IEEE 802.15.4 low-power radio. A large structure typically comprises hundreds of members and will require at least two triaxial sensors measuring accelerations at each end of every member, so that the damaged members can be detected. Clearly, transferring raw sensor data in a continuous mode for a traditional central data repository is not an efficient way for the WSSNs. Therefore, decentralized approaches have been introduced to process the sensor data within the network before transmitting it to a central computer [15]. The key challenge here is how to adapt the existing SHM signal-processing techniques to perform as much data reduction within the network as possible.

The extraction of the modal information, such as modal frequencies and mode shapes from sensor data is very important for the assessment of the structural performance and the calibration of the analytical design model [16]. In an attempt to merge the modal identification methods into a state-of-the-art wireless sensing paradigm, the Peak Picking (PP) method and the Frequency Domain Decomposition (FDD) technique [17] are modified for use within a distributed (i.e., decentralized) wireless sensing network [18]. While the amount of data wirelessly transferred in the network is significantly reduced when using these independent processing approach, modal identification methods have been addressed with some drawbacks in terms of their sensitivity to environmental effects such as temperature and moisture and nonlinearities [19].

A time-series analysis, known as the Hilbert-Huang transform (HHT), is recently introduced by Huang et al. [20] and has received considerable attention in structural health monitoring applications. The HHT is an adaptive signal-processing technique that produces signal decomposition in both time and frequency domains, providing instantaneous frequencies, phase, and damping for extracting damage sensitive features from the processed and decomposed data [21–24].

In order to realize data aggregation and modal identification based on HHT, this paper proposes a new distributed SHM scheme for the implementation in the intrinsically decentralized computing environment in WSSNs. In this

study, a laboratory bridge model is built and tested on a commercial off-the-shelf WSN platform. The identification of the modal properties for vibration signals using the embedded HHT method on smart sensors is examined. The results from both simulation and experiments show that the proposed method achieves higher accuracy for identifying modal characteristics. The on-board computing features of the proposed system are also proven to be tolerant to environmental fluctuations in temperature and noise levels.

In the next section of this paper, the distributed SHM scheme will be introduced, and the simulation and experimental results will be shown in Sections 3 and 4. Finally, a conclusion will be made.

## 2. Background

*2.1. Wireless Smart Sensor Node.* As it is shown in Figure 1, the IRIS mote wireless sensor was developed by the researchers at the University of California, Berkeley [25], and it is a smart sensor platform designed for data intensive applications. The IRIS is an open hardware and software platform for smart sensing, and it consists of a plug-in sensor boards, a processor, a transceiver, and an AA battery pack. The specifications are shown in Table 1. The processor speed may be scaled based on the application requirement, and thereby maintaining its power usage efficiency.

A variety of sensor boards for the mote are available in the market. MTS400 sensor board from Crossbow Technology is one of the most popular sensors used in research [26], and it is implemented with acceleration, light, pressure, and temperature sensors, as shown in Table 2. In this paper, an IRIS with an MTS400 sensor board will be used in the decentralized SHM system.

The operating system used on the IRIS for this research is TinyOS, which is a distributed, open-source operating system [27]. TinyOS supports large-scale, self-configuring sensor networks, and its functions include radio messaging, message hopping from mote to mote, low-power modes, sensor measurements, and signal processing. NesC is used as the programming language for TinyOS. This operating system has a small memory footprint and is, therefore, suitable for smart sensors with limited resource. TinyOS also has a large user community and many successful smart sensor applications.

*2.2. Hilbert-Huang Transform Algorithm.* In 1998, Huang et al. [20] introduced a new adaptive signal-processing method, referred to as the Hilbert-Huang transform (HHT), suitable for the requirements for processing linear, nonlinear, stationary, and nonstationary signals. The HHT consists of

TABLE 2: Sensors on MTS400.

Sensor	Type	Measurement range	Resolution
Acceleration	Analog devices ADXL202JE	$\pm 2$ (g)	2 mg (60 Hz)
Pressure	Intersema MS5534AM	300–1100 mbar	0.1 mbar
Light	TAOSTSL2550D	400–1000 nm	None
Temperature	Sensirion SHT11	0–100% RH;	0.03% RH

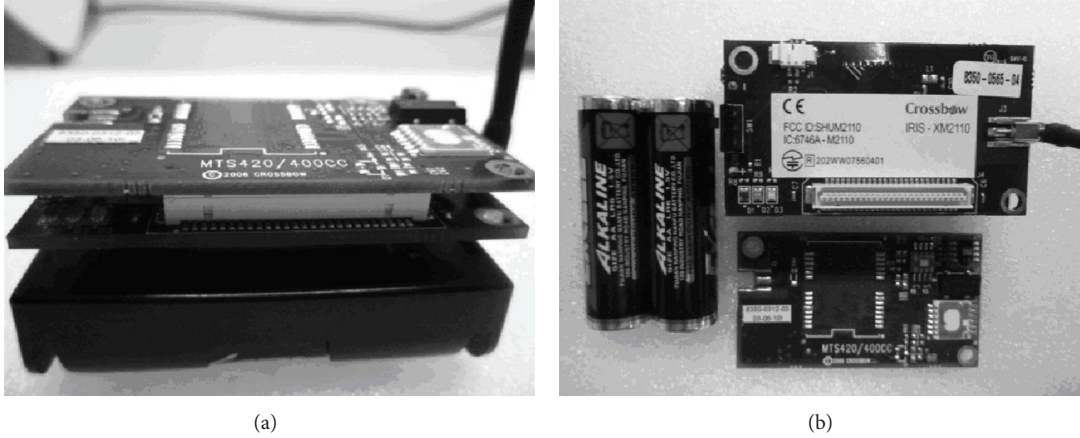


FIGURE 1: IRIS mote with MTS400 board (a) and its components (b).

two main parts: (i) EMD and (ii) Hilbert transform. The EMD method decomposes a real signal into a collection of simpler modes or intrinsic mode functions (IMFs), which are basically associated with the energy of the signal at different timescales and contain important data characteristics [20]. The Hilbert transform, when applied to IMFs, will produce an energy-frequency-time distribution of the data, known as a Hilbert spectrum. In general, the decomposition resulting from HHT is well localized in the time-frequency domain and reveals important information within data.

The EMD extracts the IMFs by applying a sifting process to a given time signal, and two cubic splines are fitted through the signal's local maxima and minima in order to produce an upper and lower envelope, respectively. The average of these two splines is then subtracted from the original signal. The resultant signal is subsequently treated and repeated as the original time signal. The first IMF component contains the shortest period component of the signal. In order to derive other IMFs, the first IMF is removed from the signal, the residue is considered as the new signal, and the sifting process is performed to obtain the second IMF component. This procedure is repeated for all subsequent residues to derive the longer period components. After extracting all IMFs, the original signal is decomposed into  $n$  empirical modes,  $c_i$ , and a residue,  $r_n$ , which can either be the mean trend or a constant. This can be represented by the following equation:

$$x(t) = \sum_{i=1}^n C_i(t) + r_n(t). \quad (1)$$

After extraction of IMFs through the sifting process, the Hilbert transform can be applied to each IMF in order to obtain the amplitude, phase, and frequency information,

respectively. For a given IMF  $C_i(t) \equiv x(t)$ , the Hilbert transform  $y(t)$  is defined as the convolution of  $x(t)$  and  $1/(\pi t)$ . The mathematical form of Hilbert transform is expressed as

$$H[x(t)] = y(t) = \frac{1}{\pi} P \int_{-\infty}^{+\infty} \frac{x(\tau)}{t - \tau} d\tau, \quad (2)$$

where  $P$  indicates that the integral is to be considered as a Cauchy principal value, which prevents a possible singularity at  $t = \tau$  and  $\pm\infty$ . When the Hilbert transform is applied to  $x(t)$ , the magnitude is kept unchanged but the phase of all frequency components is shifted by  $\pi/2$ . Using the Hilbert transform, an analytic signal  $z(t)$  can be defined as the complex conjugate of  $x(t)$  and its Hilbert transform  $y(t)$  [20],

$$\begin{aligned} z(t) &= x(t) + iy(t) = a(t) e^{i\theta(t)}, \\ a(t) &= \sqrt{x^2(t) + y^2(t)}, \\ \theta(t) &= \arctan\left(\frac{y(t)}{x(t)}\right), \end{aligned} \quad (3)$$

where  $a(t)$  and  $\theta(t)$  are called the amplitude and the instantaneous phase function of  $x(t)$ , respectively. Mathematically, the above polar expression provides the best local fit for any signal  $x(t)$  with varying amplitude and phase [20]. Because the IMFs are symmetric with respect to zero mean, the instantaneous phase increases monotonically as a function of time.

In summary, the processing of vibration signals by EMD coupled with the Hilbert transform reveals significant fundamental information hidden in the signals for detecting damage sensitive features in structural health monitoring.

TABLE 3: Modal frequencies obtained from on-board and offline computing in numerical example.

Mode	Frequency of on-board result	Frequency of offline result	Error
First order	1.91 Hz	1.98 Hz	3.60%
Second order	3.82 Hz	3.76 Hz	1.50%

TABLE 4: Experimental cable-stayed bridge model mechanical characteristics.

Element	Cross section	Material	Density (kg/m <sup>3</sup> )	Modulus (GP)	Poisson ratio	Dimension (m)
Middle tower	Box □	Aluminum alloy	2700	68.6	0.34	3.1 × 0.1375 × 0.095
Side tower	Box □	Aluminum alloy	2700	68.6	0.34	1.9 × 0.12 × 0.075
Deck	Separate box	Aluminum alloy	2700	68.6	0.34	15.2 × 0.82 × 0.07
Cable	Circle ○	High-strength steel wire	7850	200	0.30	varies

Depending on the structure being studied, there are various types of data extracted from the HHT and EMD. This data include intrinsic mode functions, instantaneous frequency, phase, amplitude, and damping. The next section discusses the implementation of this strategy on smart sensor platform.

**2.3. Smart Sensor System Realization.** The implementation of the decentralized approach is composed of a modal identification algorithm and middleware services. Major numerical routines utilized in this approach include empirical modal decomposition (EMD), quick sort, and Hilbert transform. These functions are either developed from scratch or adapted from functions previously written in C language. The performance of these functions is examined on the IRIS system. Middleware services for the SHM include data aggregation, reliable communication, and synchronized sensing. These techniques are coded as C functions and compatible with TinyOS.

The time synchronization and reliable data delivery mechanisms in the framework can be implemented, respectively, by using suitable existing techniques; however, this issue is beyond the scope of this paper. The main focus of this paper is on the design of distributed algorithms for WSN-based SHM. When the synchronized sensing is completed, the data acquired will be processed immediately. The measured acceleration time histories and the intermediate processed results, such as the structural modal parameters, are sent back to the back-end server, where damage alarm or other applications will be executed.

### 3. Numerical Studies

The objective of the numerical studies in this section is to investigate the performance of the proposed distributed modal identification method for structural health monitoring based on the embedded processing capability of smart sensors. An original sine function signal,  $y = 100 * \sin(24 * t) + 100 * \sin(12 * t)$ , for simulation is selected in order to identify its dominant frequencies.

Cheraghi et al. [28, 29] suggested a band-pass filtering scheme in order to retain the interested frequencies only. In the present study, the signal is filtered with various bands according to the former Fourier transformation results. The

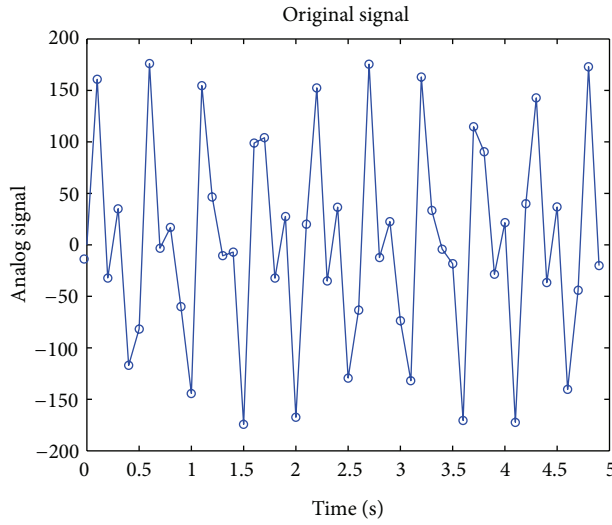
first range is from 1 to 1.5 Hz, and the second range is from 3.5 to 5 Hz. The amplitudes at other frequency ranges are much lower than the bands mentioned before.

Figure 2 illustrates the IMF and phase angle obtained from on-board computing and offline computing, respectively, for the first frequency case. From Figure 2 it can be seen that for all frequency cases, the IMF and phase calculated on IRIS sensor have very good agreement with those obtained by offline calculation method. After resolving the phase by the least square method, the frequencies in this example as listed in Table 3 can be obtained. The first and second frequencies measured from the on-board computing are 1.91 Hz and 3.82 Hz, respectively. In contrast to 1.98 Hz and 3.76 Hz from the offline computing, the errors are 3.6% and 1.5% for the first and second frequency, respectively. The major influencing factors resulting in these errors may be due to the limited CPU power, accumulated errors, and data package lagging in numerical processing. However, these errors are small and ignorable in engineering applications. In general, it can be concluded that the on-board computing technique of smart sensor based on HHT algorithm is reliable, and the smart characteristics of wireless sensor could be used for the SHM purpose.

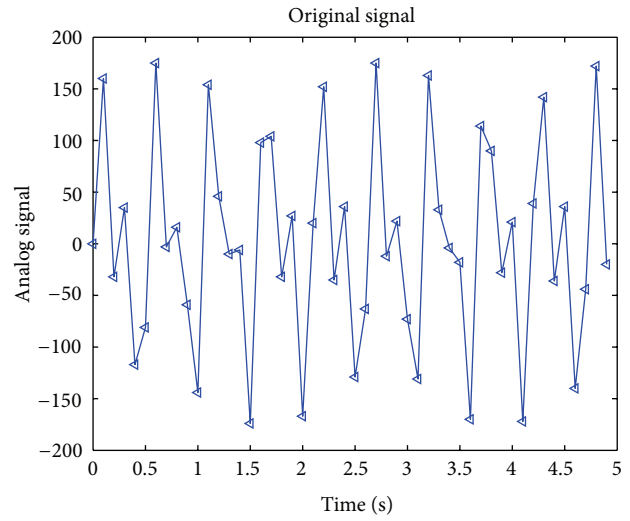
### 4. Validation Test and Result Analysis

In an attempt to further investigate the onboard computing capabilities in smart sensors, the same methodology is applied to examine an in-house cable-stayed bridge model built in a laboratory. The vertical vibration signals of the bridge model in the tests is measured by the IRIS installed along the bridge deck. White noise loads are applied through two magnetic vibration generators underneath the bridge deck. The same test is carried out for 15 times with the sampling frequency of 50 Hz, and the duration of each record is about 1 sec.

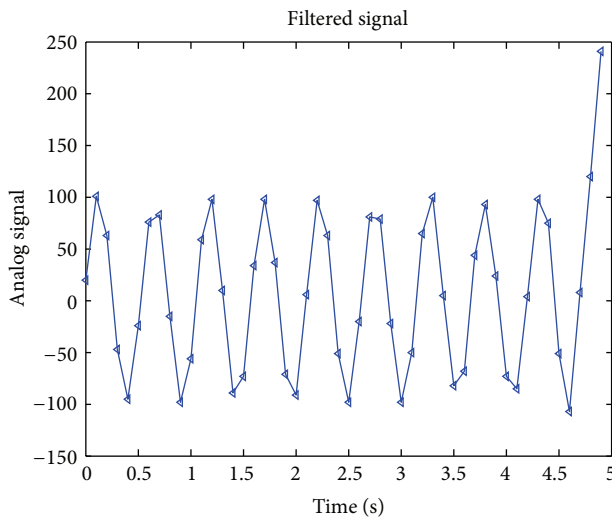
**4.1. Test Structure.** The test structure represents a reduced-scale model of Shandong Binzhou Yellow River cable-stayed Bridge (see Figure 3). The two-span bridge model is mainly made of aluminum. Effective stiffness criterion is utilized in the reduced-scale dynamic-elastic bridge model design. Additional masses are added so the bridge model which gives



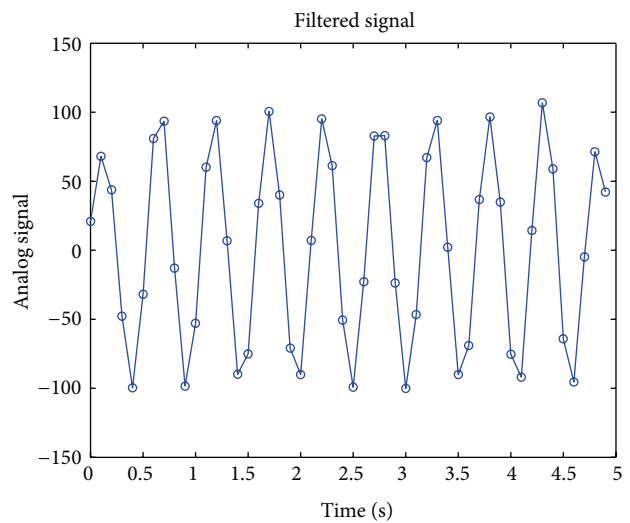
(a) On-board original signal



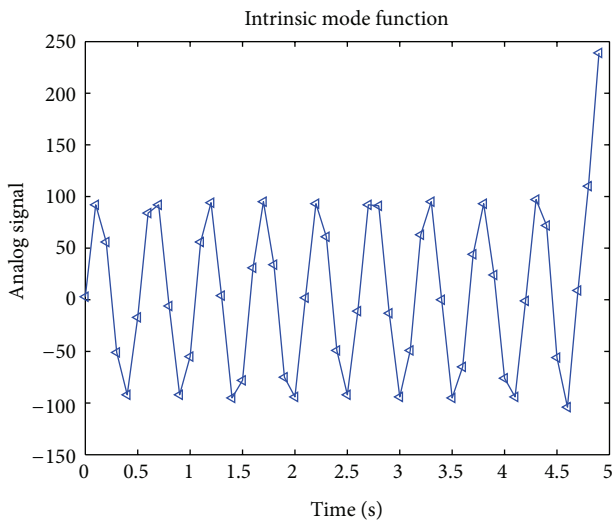
(b) Offline original signal



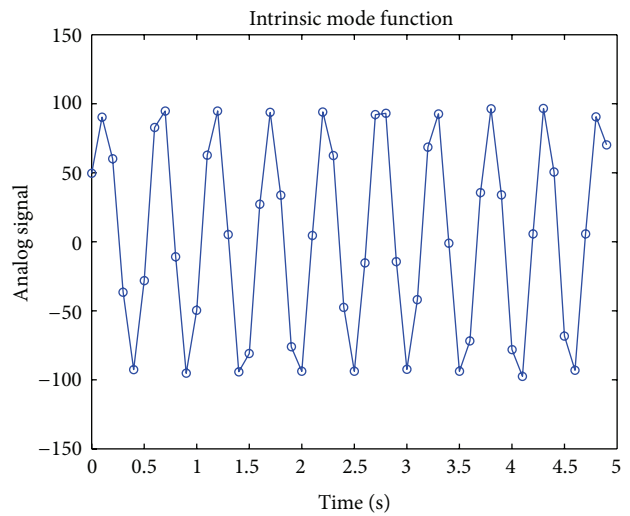
(c) On-board band-pass filtered signal



(d) Offline band-pass filtered signal



(e) On-board IMF



(f) Offline IMF

FIGURE 2: Continued.

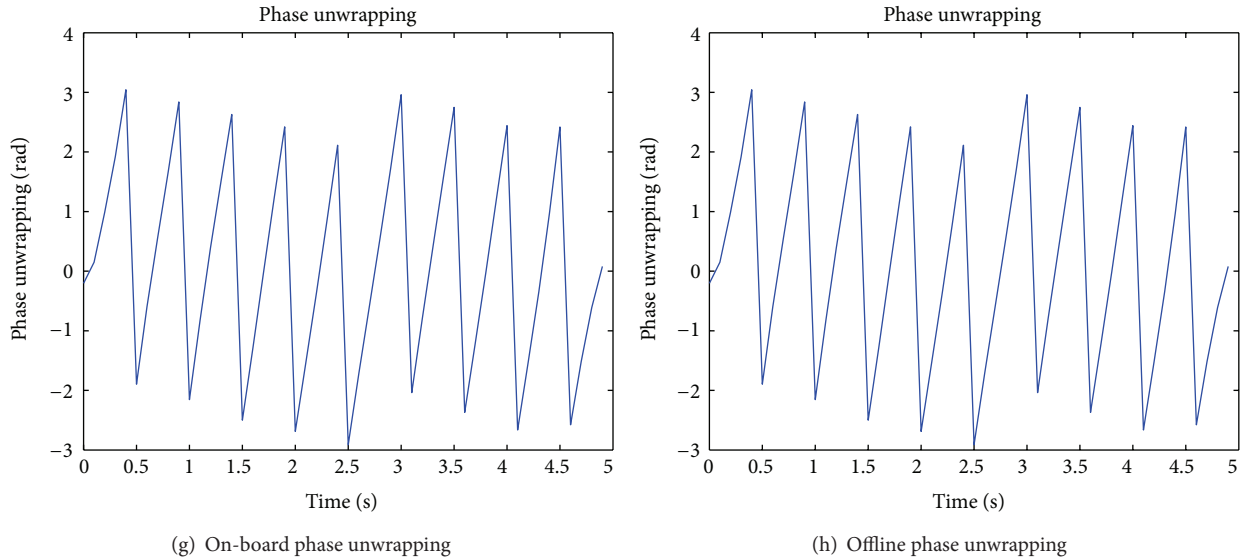


FIGURE 2: Numerical HHT algorithm evaluated from on-board computing and offline computing for the first frequency case.



FIGURE 3: Photo of Binzhou Yellow River cable-stayed bridge.



FIGURE 4: Photo of the reduced-scale laboratory bridge model.

similar dynamic characteristics within the range of the prototype bridge. The bridge model is eventually built in a ratio of 1:40 to the prototype bridge considering lab conditions and costs (see Figure 4). Table 4 lists the specific mechanical parameters of the bridge model. Several experiments have been previously done with various configurations of this structure [30] based on the similarity theory, in order to show that the reduced-scale bridge model with added masses has a good degree of similarity with the prototype bridge.

**4.2. Finite Element Analysis.** In order to verify the accuracy of testing results and provide dominant frequency ranges, a full three-dimensional finite element model is developed using ANSYS. The geometry and member details of the model are based on the design data of the laboratory test bridge model. The main structural members are composed of stay cables, floor beams, and towers, all of which are discretized by different finite element types.

The modeling of stay cable can be realized in ANSYS by employing the 3D tension-only truss elements (LINK8) and utilizing its stress-stiffening capability. Each stay cable

is modeled by one element, which results in 60 tension-only truss elements in the model. Two steel main girders are modeled as the 3D elastic beam elements (BEAM4) for simplicity, since they are the structural members possibly subjected to tension, compression, bending, and torsion. There are in total 508 elements of this type. Towers consist of both equivalent and variable sections so that they are discretized by BEAM188 elements with a total number of 140. All piers and platforms are modeled by the solid elements (SOLID45), of which there are 852 elements. The diaphragms are modeled by 80 beam elements (BEAM44). In addition, 210 concentrated mass elements (MASS21) are used to include the mass of equilibrium blocks, parapet, and anchors that are non-structural members.

The complete model consists of 1371 nodes and 1500 elements resulting in 8202 active degrees of freedom (DOFs). The model represents the bridge in its current as-built configuration and structural properties. The first three vertical bending modal shapes of bridge model from FEA are shown

TABLE 5: On-board computing, offline computing, and FE results.

Mode	Frequency from on-board computing	Frequency from offline computing	Errors	FE result
First order	4.64 Hz	4.52 Hz	2.6%	4.23 Hz
Second order	8.69 Hz	8.66 Hz	0.27%	10.92 Hz
Third order	10.47 Hz	10.52 Hz	0.49%	12.16 Hz

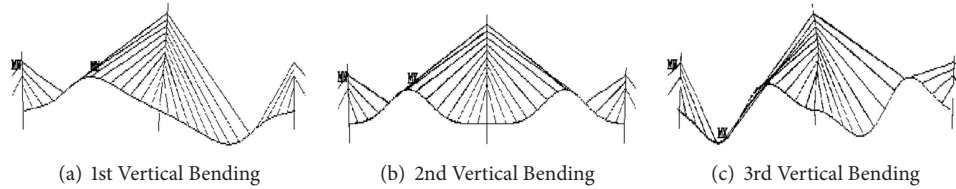


FIGURE 5: The operational deflection shapes for the first three fundamental modes of vibration.

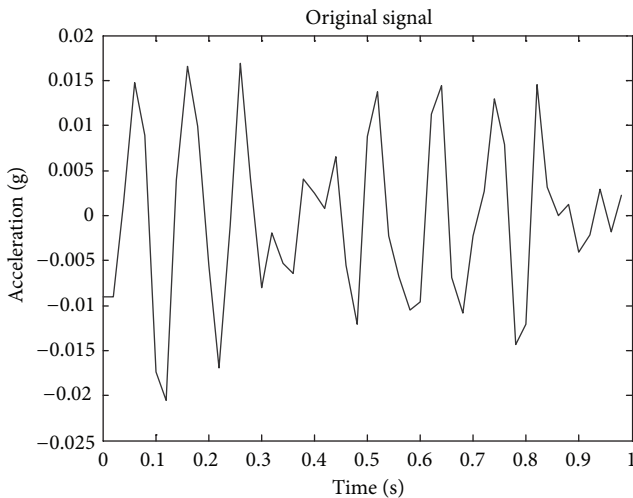


FIGURE 6: Typical acceleration signal of wireless sensor from testing.

in Figure 5, and their corresponding natural frequencies are listed in Table 5.

**4.3. Testing Results.** After obtaining the encouraging results from FE analysis, the application of the proposed approach is examined experimentally on the cable-stayed bridge model. The band-pass filtering used in this experimental test should be carefully implemented in order to take into account the frequency components that are only sensitive to the bridge model. According to the afore mentioned FE analysis, it is concluded that band-pass filters with the band-pass frequency of 3.5–5.0 Hz, 8.0–9.5 Hz, and 10.0–11.0 Hz (corresponding to the first three bridge vibration modes), respectively, can give rise to the best resolution for modal parameter identification.

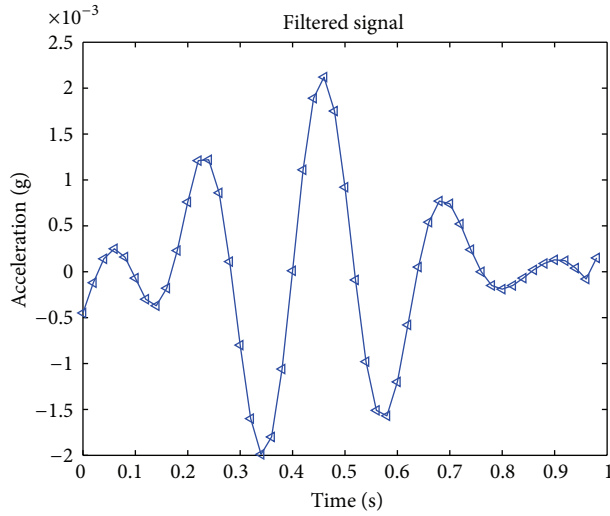
Typical experimental results of this investigation are presented in Figures 6 and 7 for the first natural frequency case, respectively. Figure 6 shows the original experimental acceleration signal from a typical wireless sensor node. Figure 7 shows the band-pass filtered signal and the IMF along with phase obtained both by on-board computing and offline

computing for the first natural frequency case. It can be found that the estimated IMF obtained by the on-board computing method is in excellent agreement with the offline computing counterpart. Based on the IMF and phase values, we can calculate the natural frequency based on the least square method. Similar to the first natural frequency, the second and third natural frequency can be obtained using the same procedure. The natural frequencies obtained from the on-board computing are shown in Table 5, and they are compared with the results from the offline computation and FE analysis. For all three cases, the largest relative error of natural frequency obtained from the on-board computing to that from the offline computing is only 2.6% (in the first case). It can be seen that the proposed embedded method has achieved the modal parameters comparable with those obtained using the traditional method, but the energy consumption has greatly been reduced.

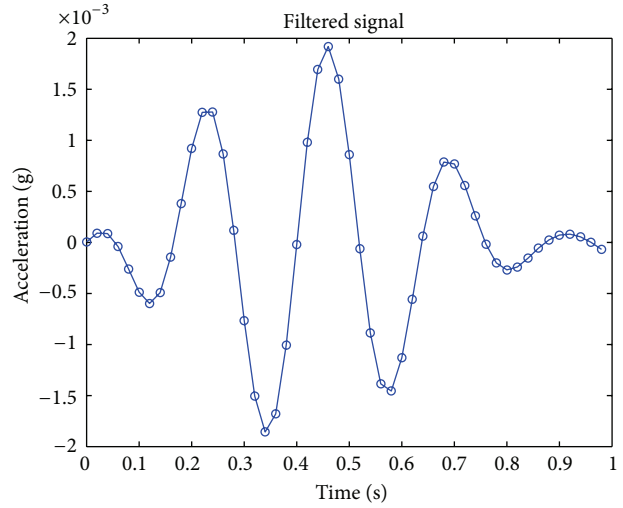
### 5. Conclusions

In this study, an application of the HHT-based decentralized data processing approach is proposed based on smart wireless sensors, and it has been verified with both simulation and experiment. The basic concept is to analyze the structural vibration signals through the EMD and HHT, taking advantage of on-board computing capability of smart sensor. The proposed approach is programmed and embedded into the data processing module of a smart sensor. The performance of decentralized HHT is assessed in terms of accuracy of the identified modal properties of the test structure.

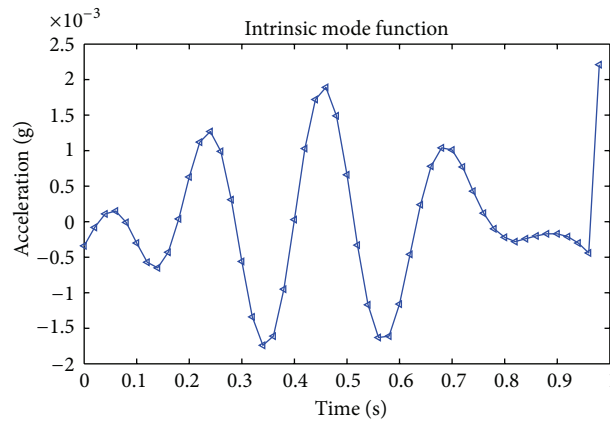
A laboratory cable-stayed bridge model is employed to investigate the performance of decentralized HHT on the IRIS wireless sensor platform. The offline data processing approach is selected as a reference for numerical comparison, and finite element analysis has been introduced to provide necessary modal information of the structure. Results from both simulation and experiment show that in all dominant frequency cases the smart sensor implemented with on-board HHT algorithm can identify the modal parameters such as the natural frequency at the same resolution as the traditional offline approach. More importantly, the proposed method



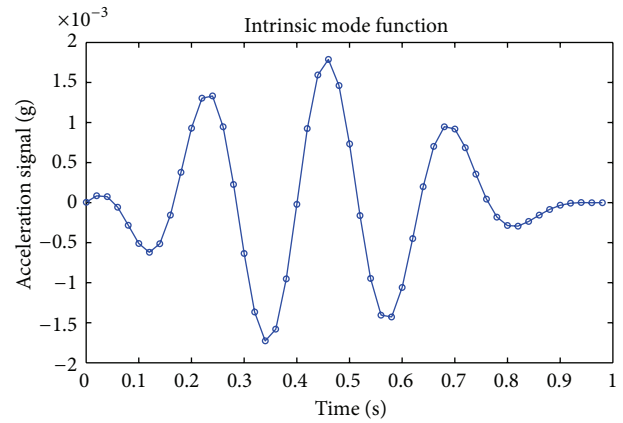
(a) On-board band-pass filtered signal



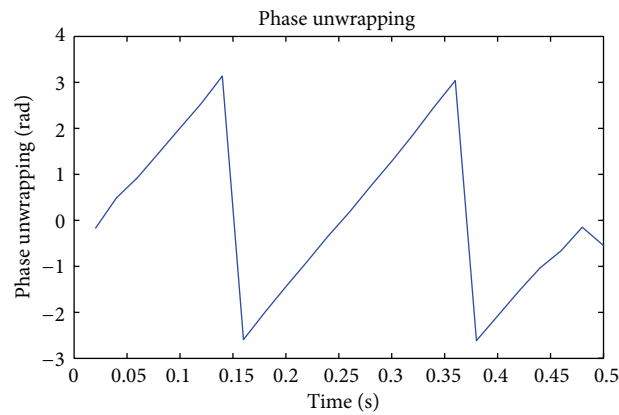
(b) Offline band-pass filtered signal



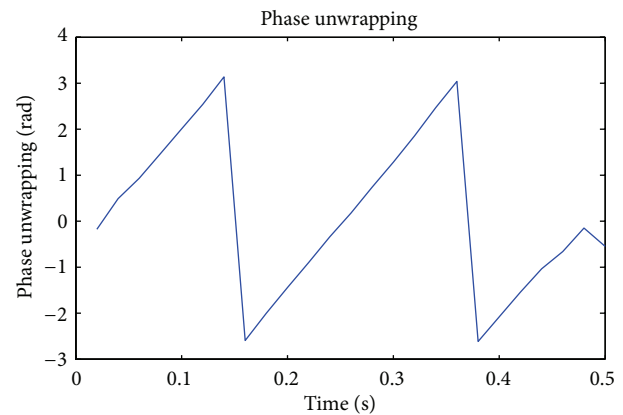
(c) On-board IMF



(d) Offline IMF



(e) On-board Phase-unwrapping



(f) Offline Phase-unwrapping

FIGURE 7: Experimental HHT algorithm evaluated from on-board computing and offline computing for the first frequency case.

could locally compute these coefficients and transmit them to the central location, instead of transmitting the entire data. Therefore, this method increases the efficiency in wireless communication for real applications of SHM.

Overall, the proposed modal identification technique in this study is a low cost and effective tool for SHM. Based

on the experimental results, we can see that there is a great potential to develop a practical and reliable modal identification procedure for WSN-based structural health monitoring. Despite the successful implementation of the HHT and EMD methods on the laboratory scale, some issues must yet be taken into account when considering real-world

applications, where a large number of sensors will be densely deployed over a large structure.

## Acknowledgments

Financial supports from the National Science Foundation of China (no. 51108129) and Guangdong Science and Technology Major Project (no. 2012A080104014) to initiate this research project are greatly acknowledged.

## References

- [1] H. Shi, W. Wang, N. M. Kwok, and S. Y. Chen, "Game theory for wireless sensor networks: a survey," *Sensors*, vol. 12, no. 7, pp. 9055–9097, 2012.
- [2] C. Cattani, S. Chen, and G. Aldashev, "Information and modeling in complexity," *Mathematical Problems in Engineering*, vol. 2012, Article ID 868413, 4 pages, 2012.
- [3] S. Chen, W. Huang, C. Cattani, and G. Altieri, "Traffic dynamics on complex networks: a survey," *Mathematical Problems in Engineering*, vol. 2012, Article ID 732698, 23 pages, 2012.
- [4] B. F. Spencer Jr., M. E. Ruiz-Sandoval, and N. Kurata, "Smart sensing technology: opportunities and challenges," *Journal of Structural Control and Health Monitoring*, vol. 11, no. 4, pp. 349–368, 2004.
- [5] J. P. Lynch and K. J. Loh, "A summary review of wireless sensors and sensor networks for structural health monitoring," *The Shock and Vibration Digest*, vol. 38, no. 2, pp. 91–128.
- [6] S. Jang, H. Jo, S. Cho et al., "Structural health monitoring of a cable-stayed bridge using smart sensor technology: deployment and evaluation," *Smart Structures and Systems*, vol. 6, no. 5–6, pp. 439–459, 2010.
- [7] S. Cho, H. Jo, S. Jang et al., "Structural health monitoring of a cable-stayed bridge using wireless smart sensor technology: data analyses," *Smart Structures and Systems*, vol. 6, no. 5–6, pp. 461–480, 2010.
- [8] Y. Nitta, T. Nagayama, B. F. Spencer Jr., and A. Nishitani, "Rapid damage assessment for the structures utilizing smart sensor MICA2 MOTE," in *Proceedings of the 5th International Workshop on Structural Health Monitoring*, pp. 283–290, Stanford, Calif, USA, 2005.
- [9] Y. Gao, B. F. Spencer Jr., and M. Ruiz-Sandoval, "Distributed computing strategy for structural health monitoring," *Structural Control and Health Monitoring*, vol. 13, no. 1, pp. 488–507, 2006.
- [10] J. A. Rice and B. F. Spencer Jr., "Flexible smart sensor framework for autonomous full-scale structural health monitoring. Newmark Structural Engineering Laboratory (NSEL)," Report Series no. 18, University of Illinois at Urbana-Champaign, Urbana, Ill, USA, 2009, <http://hdl.handle.net/2142/13635>.
- [11] N. A. Tanner, J. R. Wait, C. R. Farrar, and H. Sohn, "Structural health monitoring using modular wireless sensors," *Journal of Intelligent Material Systems and Structures*, vol. 14, no. 1, pp. 43–56, 2003.
- [12] S. Castellucci, M. Carlini, M. Guerrieri, and T. Honorati, "Stability and control for energy production parametric dependence," *Mathematical Problems in Engineering*, vol. 2010, Article ID 842380, 21 pages, 2010.
- [13] M. Li, W. Zhao, and S. Chen, "mBm-based scalings of traffic propagated in internet," *Mathematical Problems in Engineering*, vol. 2011, Article ID 389803, 21 pages, 2011.
- [14] M. Rahimi, H. Shah, G. S. Sukhatme, J. Heideman, and D. Estrin, "Studying the feasibility of energy harvesting in a mobile sensor network," in *Proceedings of the IEEE International Conference on Robotics and Automation (ICRA '03)*, pp. 19–24, September 2003.
- [15] T. Nagayama, S. H. Sim, Y. Miyamori, and B. F. Spencer, "Issues in structural health monitoring employing smart sensors," *Smart Structures and Systems*, vol. 3, no. 3, pp. 299–329, 2007.
- [16] S. Cho, C. -B. Yun, J. P. Lynch, A. Zimmerman, B. Spencer Jr., and T. Nagayama, "Smart wireless sensor technology for structural health monitoring of civil structures," *Journal of Steel Structures*, vol. 81, pp. 267–275, 2004.
- [17] R. Brincker, L. Zhang, and P. Andersen, "Modal identification of output-only systems using frequency domain decomposition," *Smart Materials and Structures*, vol. 10, no. 3, pp. 441–445, 2001.
- [18] A. T. Zimmerman, M. Shiraishi, R. A. Swartz, and J. P. Lynch, "Automated modal parameter estimation by parallel processing within wireless monitoring systems," *Journal of Infrastructure Systems*, vol. 14, no. 1, pp. 102–113, 2008.
- [19] D. Pines and L. Salvino, "Structural health monitoring using empirical mode decomposition and the Hilbert phase," *Journal of Sound and Vibration*, vol. 294, no. 1-2, pp. 97–124, 2006.
- [20] N. E. Huang, Z. Shen, S. R. Long et al., "The empirical mode decomposition and the Hilbert spectrum for nonlinear and non-stationary time series analysis," *The Royal Society of London Series A*, vol. 454, no. 1971, pp. 903–995, 1998.
- [21] S. Y. Chen, H. Tong, Z. Wang, S. Liu, M. Li, and B. Zhang, "Improved generalized belief propagation for vision processing," *Mathematical Problems in Engineering*, vol. 2011, Article ID 416963, 12 pages, 2011.
- [22] X.-H. Yang, B. Wang, S.-Y. Chen, and W.-L. Wang, "Epidemic dynamics behavior in some bus transport networks," *Physica A*, vol. 391, no. 3, pp. 917–924, 2012.
- [23] S. Chen, Y. Wang, and C. Cattani, "Key issues in modeling of complex 3D structures from video sequences," *Mathematical Problems in Engineering*, vol. 2012, Article ID 856523, 17 pages, 2012.
- [24] M. Li, S. C. Lim, and S. Chen, "Exact solution of impulse response to a class of fractional oscillators and its stability," *Mathematical Problems in Engineering*, vol. 2011, Article ID 657839, 9 pages, 2011.
- [25] K. S. J. Pister, J. M. Kahn, and B. E. Boser, "Smart Dust: wireless networks of millimeter-scale sensor nodes," Electronics Research Laboratory Research Summary, 1999.
- [26] Crossbow Technology, <http://www.xbow.com/>.
- [27] TinyOS, <http://webs.cs.berkeley.edu/tos/>.
- [28] N. Cheraghi, M. J. Riley, and F. Taheri, "A novel approach for detection of damage in adhesivelybonded joints in plastic pipes based on vibration method using piezoelectric sensors," in *Proceedings of the International Conference on Systems, Man and Cybernetics*, pp. 3472–3478, October 2005.
- [29] N. Cheraghi and F. Taheri, "A damage index for structural health monitoring based on the empirical mode decomposition," *Journal of Mechanics of Materials and Structures*, vol. 2, no. 1, pp. 43–62, 2007.
- [30] L. Zhou, O. Yang, and J. Ou, "Design and analysis of laboratory health monitoring model of a long-span cable-stayed bridge," in *Proceedings of the 20th National Compilation of Vibration and Noise of High Technology and Application Conference*, pp. 57–66, 2007.

## Research Article

# Modeling of an Air Conditioning System with Geothermal Heat Pump for a Residential Building

Silvia Cocchi,<sup>1</sup> Sonia Castellucci,<sup>2</sup> and Andrea Tucci<sup>1</sup>

<sup>1</sup> DAFNE, Università degli Studi della Tuscia, via San Camillo de Lellis, 01100 Viterbo, Italy

<sup>2</sup> CIRDER, Università degli Studi della Tuscia, via San Camillo de Lellis, 01100 Viterbo, Italy

Correspondence should be addressed to Sonia Castellucci; [sonia.castellucci@unitus.it](mailto:sonia.castellucci@unitus.it)

Received 14 December 2012; Accepted 10 January 2013

Academic Editor: Massimo Scalia

Copyright © 2013 Silvia Cocchi et al. This is an open access article distributed under the Creative Commons Attribution License, which permits unrestricted use, distribution, and reproduction in any medium, provided the original work is properly cited.

The need to address climate change caused by greenhouse gas emissions attaches great importance to research aimed at using renewable energy. Geothermal energy is an interesting alternative concerning the production of energy for air conditioning of buildings (heating and cooling), through the use of geothermal heat pumps. In this work a model has been developed in order to simulate an air conditioning system with geothermal heat pump. A ground source heat pump (GSHP) uses the shallow ground as a source of heat, thus taking advantage of its seasonally moderate temperatures. GSHP must be coupled with geothermal exchangers. The model leads to design optimization of geothermal heat exchangers and to verify the operation of the geothermal plant.

## 1. Introduction

The increasing energy demands the fact that fossil fuels are finite resources and the problem of pollutant emissions has allowed renewable energy sources (RES) to be considered and developed, including geothermal [1].

Geothermal energy is used in order to generate electricity or for direct uses, especially for heating [2]. Direct use of geothermal energy is the oldest and the most common utilization of this energy source.

There are many possibilities for these uses: geothermal heat pumps or ground source heat pumps (GSHPs), space heating, greenhouse and covered ground heating, aquaculture pond and raceway heating, agricultural crops drying, industrial process heat, snow melting and space cooling, bathing, and swimming [3].

The GSHP systems for heating and cooling are considered one of the most energy-efficient and cost-effective renewable energy technology [4]. Moreover these systems allow to reduce the greenhouse gases (GHGs) emissions [5].

Geothermal heat pumps systems use the subsoil (the interior of the earth) as a source and extract heat at low deep [6].

Heat pumps are devices that allow to transfer heat from a lower temperature system to a higher temperature system.

Geothermal heat pump or ground source heat pump (GSHP) is a heating and/or cooling system that pumps heat to or from the ground. The GSHP uses earth as a heat source (during winter time) or a heat sink (during summer time). This design takes advantage of the moderate temperatures in the ground to boost efficiency and reduce the operational costs of heating and cooling systems [7]. The major advantage of GSHPs derives from their better performance if compared with traditional system because they take advantage of a more stable temperature of the heat source during the whole year, thus the coefficient of performance (COP) is increased, and the operational costs of heating and cooling are reduced [8].

The GSHPs systems can be classified as follows:

- (i) open systems: if groundwater is used as heat transfer fluid,
- (ii) closed systems: if there are some heat exchangers in the underground, and the groundwater is not the heat transfer fluid [9].

Among the closer systems there are many different configurations: horizontal, spiral, and vertical loop [10].

An air conditioning system with geothermal heat pumps consists of three parts [11]:

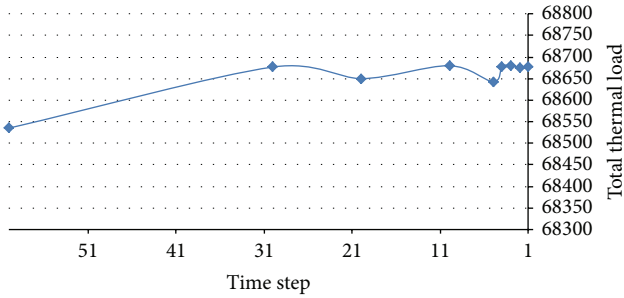


FIGURE 1: Thermal load as a function of time step.

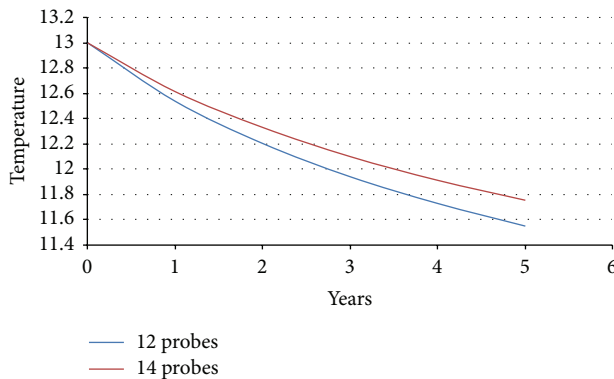


FIGURE 2: Ground temperature variations with exchanger numbers.

- (i) geothermal heat exchangers,
- (ii) heat pump,
- (iii) heat distribution system (radiant floors are particularly suitable because they have the great advantage of working with lower temperature gradients if compared to conventional systems [12]).

The operating mechanism for heating is as follows:

- (i) the fluid (antifreeze added water), flowing in geothermal heat exchangers, exchanges heat with the ground and comes back heated to surface;
- (ii) fluid transmits its heat to the heat pump and back in the heat exchangers with lower temperature;
- (iii) heat pump transmits its heat to the fluid flowing in radiant floors;
- (iv) radiant floors heat the building.

GSHP must have a heat exchanger in contact with the ground or groundwater in order to extract or dissipate heat. Several major design options are available for these, which are classified according to layout and fluid: direct exchange systems circulate refrigerant underground, closed loop systems use a mixture of antifreeze and water, and open loop systems use natural groundwater. Direct exchange geothermal heat pump is the oldest type of geothermal heat pump technology.

In this work a GSHP system with vertical heat exchangers has been studied.

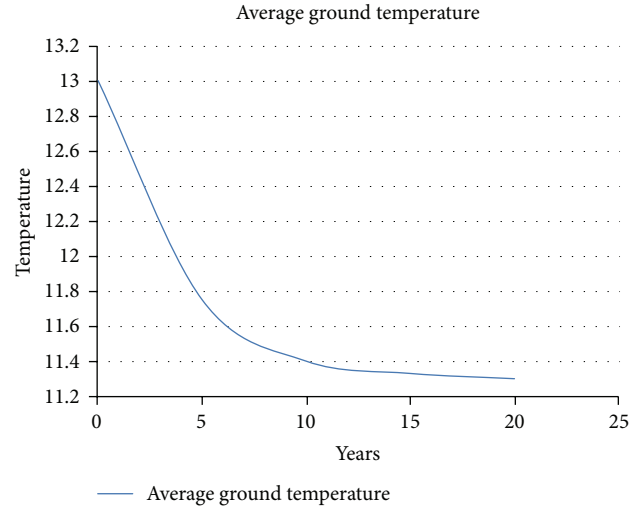


FIGURE 3: Average ground temperature for 14 exchangers in 20 years.

The growth of GSHPs technology was slower than other RES or conventional technologies due to many factors: nonstandardized system designs, significant capital costs if compared with other systems, and limited individuals knowledgeable in the installation of GSHP systems. Nevertheless these problems have been resolved on an ongoing basis, and the acceptance of the GSHP technology is increasing [1].

GSHP systems COP is higher than COP of other heat pump systems: it usually varies from 3 to 6, depending on the earth connection setups, system sized earth characteristics, installation depths, and climate of the area. Instead, for example, for an air source heat pump system the COP range is from 2,3 to 3,5 [1].

GSHP systems have higher initial costs than conventional ones because of the costs of the heat pump unit and the connection with the ground, specially drilling, but the operating costs are lower than conventional systems because of their high efficiency. Therefore the economic feasibility of GSHP systems depends on location, due to the price of electricity, natural gas, and other heating fuel. If these are not expensive, GSHP system may not be the cheapest option. On the contrary when there are low electricity costs, the GSHP systems are economically advantageous [1].

In particular, for example, if electricity is produced by a photovoltaic system the operating costs and the GHG emissions become remarkably low.

Therefore in order to increase the efficiency of the GSHP system and to reduce the costs, the optimal sizing of the plant is needful. The TRNSYS17 software can be used for the system simulation in order to refine the sizing.

## 2. Methods

**2.1. Presizing.** The studied building is part of a building complex and consists of 14 apartments located over 4 floors.

The building was planned to include a central heating system, for heating and domestic hot water, that uses one heat pump and vertical geothermal heat exchangers. During

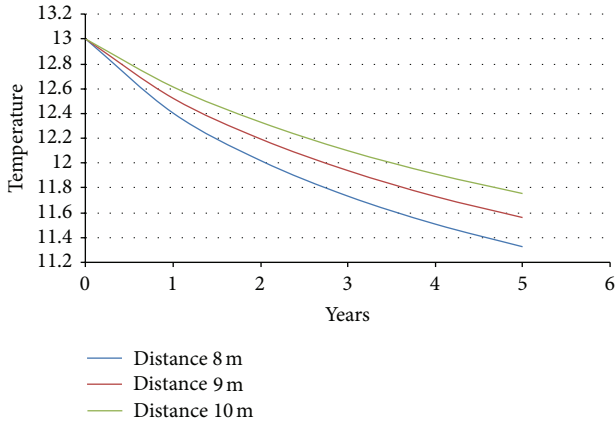


FIGURE 4: Average ground temperature varying number of exchangers.

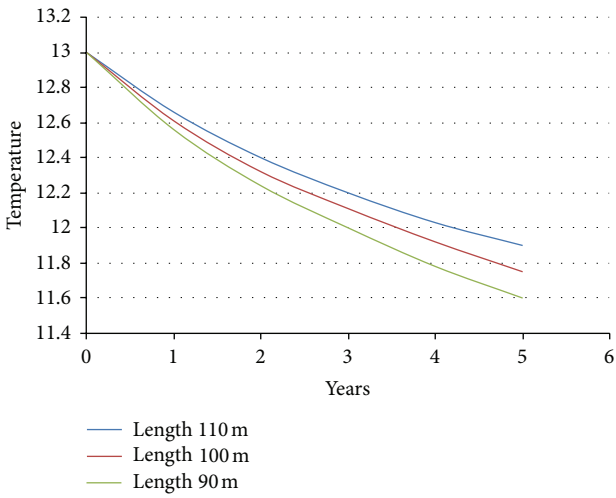


FIGURE 5: Average ground temperature varying exchangers length.

TABLE 1: Data for calculation of thermal load.

Building data		
Thermal zone		D
Number of heating days		167
Daily hours of heating		12
Heated surface (gross)	m <sup>2</sup>	3510,61
Outer surface that bounds the volume	m <sup>2</sup>	2101,73
Usable area	m <sup>2</sup>	930
Climatic data project		
Value of internal project temperature	°C	20

summer time, the system works in natural cooling operative mode.

The thermal load of the building is 43,2kW for heating (Table 1).

We choose one geothermal heat pump with a power of 47,2kW, whose fluid consists of water and ethylene glycol (25%), with freezing temperature of -13°C.

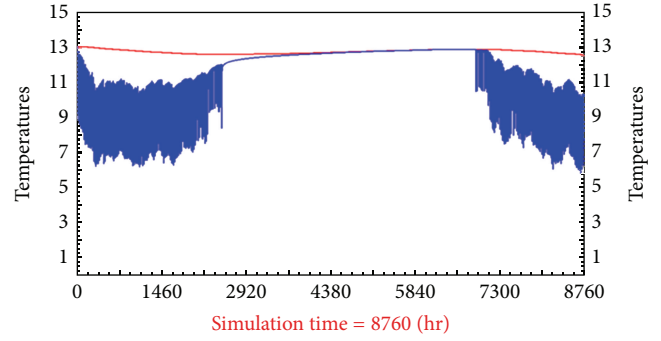


FIGURE 6: Fluid temperature in output from exchangers during the first year.

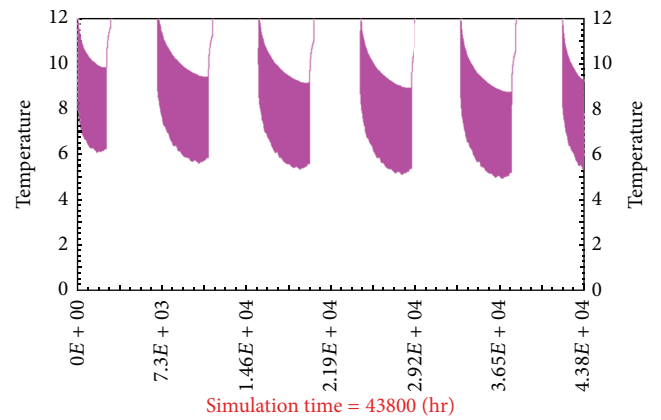


FIGURE 7: Fluid temperature in output from exchangers during 5 years.

TABLE 2: Features of vertical heat exchangers.

Features of vertical exchangers	
Number	12
Length	100 m
Distance	8 m
Type	single U
External diameter U	32 mm
Internal diameter U	29 mm
Bore diameter	12 cm
Distance by centers of U	5 cm

Geothermal heat exchangers have been presized according to the procedure described in VDI4640 German law [9]. The procedure of VDI4640 is strictly applied for small sized systems (<30 kW), but we used this procedure for an approximate sizing only. Then the final size has been obtained by the approximate one, by simulation with software TRNSYS 17.

The presizing procedure of VDI4640 is the following [13]:

- (1) calculation of heating load  $P_t$  (= 43, 2 kW);
- (2) definition of temperature of radiant floor (= 35°C);

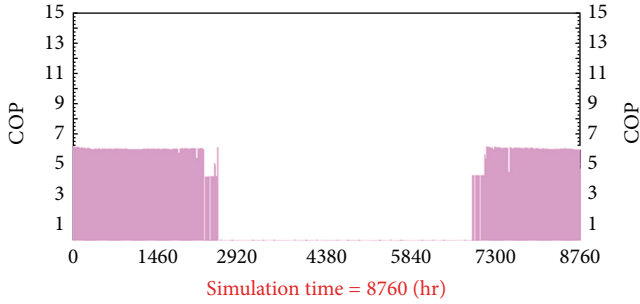


FIGURE 8: COP of heat pump in the first year (during winter time).

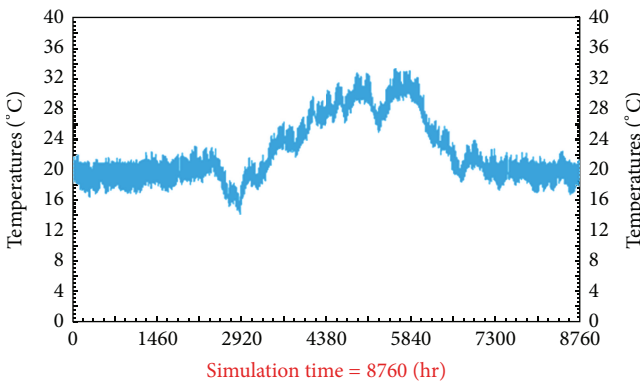


FIGURE 9: Air temperature in the apartment.

- (3) choice of heat pump and definition of the COP (coefficient of performance) with the operating condition B0/W35,  $COP = 4,33$ ;
- (4) calculation of the power exchanged with the ground  $P_{ev} [= (COP - 1)P_i/COP = 33, 22 \text{ kW}]$ ;
- (5) extraction from VDI4640 of the specific power extraction  $P_{ter} (= 30 \text{ W/m})$ ;
- (6) calculation of total length of vertical geothermal heat exchangers  $L (= P_{ev}/P_{ter} = 1107 \text{ m})$ ;
- (7) oversized (15%)  $L = 1273 \text{ m}$ ;
- (8) assumption of 12 vertical heat exchangers (each one 100 m long) (Table 2).

2.2. *Simulation.* The software TRNSYS 17 has been used in order to simulate the operations system.

TRNSYS is a complete and extensible simulation environment for the transient simulation of systems, including multizone buildings.

TRNSYS consists of a suite of programs: the TRNSYS Simulation Studio, the Simulation Engine (TRNDll.dll) with its executable (TRNExe.exe), the Building input data visual interface (TRNBuild.exe), and the Editor used to create stand-alone redistributable programs, known as TRNSED applications (TRNEdit.exe) [14].

The main visual interface is the TRNSYS Simulation Studio. Here, we can create projects by drag-and-dropping components to the workspace, connecting them together and

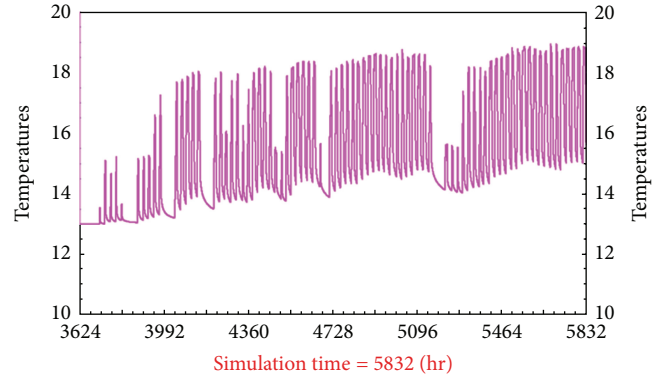


FIGURE 10: Fluid temperature in input in radiant floor in summer (natural cooling).

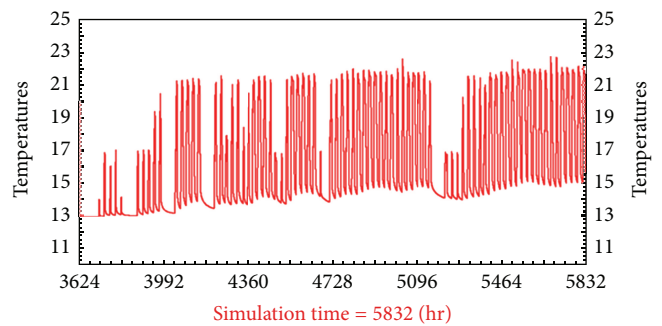


FIGURE 11: Fluid temperature in output from radiant floor in summer (natural cooling).

setting the global simulation parameters. When you run a simulation, the Studio also creates a TRNSYS input file (a text file, that contains all simulation information but no graphical information).

The Simulation Studio also includes an output manager, by which you control which variables are integrated, printed, and/or plotted, and a log/error manager that allows you to study in detail what happened during the simulation [15].

The system has been represented in TRNSYS Simulation Studio and the Building has been created in TRNBuild.

The Building has been modeled in TRNBuild by dividing it into 16 thermal zones (14 apartments, 1 zone of stairs, and 1 garage) [16].

The simulation with TRNSYS 17 allows the calculation and displays one or more variables on interval of time. Most of variables are studied within annual simulation, but average ground temperature is studied in five-year simulation.

We studied the following variables:

- (1) thermal loads;
- (2) air temperature in thermal zones;
- (3) fluid temperature in input and output from radiant floors;
- (4) fluid temperature in input and output from geothermal heat exchanger;
- (5) average ground temperature;

- (6) COP of heat pump;
- (7) optimal time step for simulations.

Optimal time step has been studied observing building thermal loads varying with time steps.

### 3. Results

The results of the simulation are represented in Table 3 and in Figure 1.

The optimal time step for simulation is 1 minute.

The study of average ground temperature is very important because this variable must not change more than 2°C over long period. Simulations are carried out for more conditions (12, 13, and 14 exchangers; distance between exchangers of 8, 9, and 10 m; arrangement of exchangers in series and parallel; length of exchanger of 90, 100, and 110 m).

We have chosen the following as target for the average ground temperature:

- (1) ensure no overexploitation of the ground;
- (2) achieve a new balance for the ground average temperature.

Changes in ground temperature varying with number of exchangers are shown in Figure 2.

The average ground temperature change after 20 years is shown in Figure 3, and it is equal to 1,7°C, below the threshold of 2°C, necessary not to have an overexploitation.

Changes in average ground temperature as a function of distance between exchanger are shown in Figure 4.

Changes in average ground temperature varying with exchangers length are shown in Figure 5.

We obtained that the configuration which gives the best performance has the following characteristics: 14 vertical exchangers in series with distance of 10 m and length of 100 m (Table 4).

The temperature of fluid in output from exchangers is represented in Figure 6.

It can be seen in Figure 6 that during the first year the minimum temperature of the fluid in output from the exchangers is 6°C. In Figure 7 we can see that the same temperature at five years is 5°C.

The temperature of fluid in input in the heat pump is in the allowable range (-5, +25°C).

The COP of the heat pump is represented in Figure 8. Note that the performance is good because COP is always more than 4.

Moreover, it resulted that the minimum temperature of the fluid in output from the heat pump is 1,5°C. The heating due to the ground is 4,5°C.

Air temperature in the apartments (represented in Figure 9) ensure comfort conditions.

The fluid temperature in input in the radiant floors resulted 19°C at the end of the summer, while fluid temperature in output at the end of the summer was 22°C as shown in Figures 10 and 11.

TABLE 3: Thermal load varying time step simulation.

Time-step	Total thermal load [kWh]
1 hour	68535,845218584532
30 minutes	68677,478548530451
20 minutes	68469,790308356302
10 minutes	65833,167347961783
5 minutes	68533,186713158425
4 minutes	68678,316559261531
3 minutes	68680,138881754820
2 minutes	68676,275556369017
1 minute	68677,942675267512

TABLE 4: Configuration of exchangers that gives the best performance.

Number of vertical exchangers	14
Distance	10 m
Length	100 m
Configuration	14 exchangers in series

### 4. Conclusion

In order to refine the sizing of the system, the TRNSYS 17 software is used.

The simulation of the system over a period of 5 years shows the best configuration for the exchangers: 14 vertical heat exchangers in series with distance of 10 m and length of 100 m.

The results show that the system works properly, because

- (1) the temperature in the apartments ensures comfort conditions;
- (2) the ground is not subject to overexploiting;
- (3) high heat pump efficiency.

Simulation with software TRNSYS allows to refine the sizing of the system and accordingly to reduce the initial costs for the ground connection—in particular for drilling and probes that are about the 35% of the total costs—and the operating costs.

### Conflict of Interests

The authors certify that there is no conflict of interests with any financial organization regarding the material discussed in the paper.

### References

- [1] S. J. Self, B. V. Reddy, and M. A. Rosen, "Geothermal heat pump systems: status review and comparison with other heating options," *Applied Energy*, vol. 101, pp. 341–348, 2013.
- [2] E. Barbier, "Geothermal energy technology and current status: an overview," *Renewable and Sustainable Energy Reviews*, vol. 6, no. 1-2, pp. 3–65, 2002.
- [3] M. Carlini and S. Castellucci, "Efficient energy supply from ground coupled heat transfer source," in *Proceedings of the International Conference on Computational Science and Applications*

- (ICCSA '10), vol. 6017 of *Lecture Notes in Computer Science*, part 2, pp. 177–190, Springer, Fukuoka, Japan, 2010.
- [4] J. W. Lund, D. H. Freeston, and T. L. Boyd, “Direct application of geothermal energy: 2005 worldwide review,” *Geothermics*, vol. 34, no. 6, pp. 691–727, 2005.
- [5] A. M. Omer, “Ground-source heat pumps systems and applications,” *Renewable and Sustainable Energy Reviews*, vol. 12, no. 2, pp. 344–371, 2008.
- [6] P. Bayer, D. Saner, S. Balay, L. Rybach, and P. Blum, “Greenhouse gas emission savings of ground source heat pump systems in Europe: a review,” *Renewable and Sustainable Energy Reviews*, vol. 16, no. 2, pp. 1256–1267, 2012.
- [7] M. Carlini and S. Castellucci, “Modelling the vertical heat exchanger in thermal basin,” in *Proceedings of the International Conference on Computational Science and Applications (ICCSA '11)*, vol. 6785 of *Lecture Notes in Computer Science*, part 4, pp. 277–286, Springer, Santander, Spain, 2011.
- [8] M. Carlini and S. Castellucci, “Modelling and simulation for energy production parametric dependence in greenhouses,” *Mathematical Problems in Engineering*, vol. 2010, Article ID 590943, 28 pages, 2010.
- [9] Y. Bi, X. Wang, Y. Liu, H. Zhang, and L. Chen, “Comprehensive exergy analysis of a ground-source heat pump system for both building heating and cooling modes,” *Applied Energy*, vol. 86, no. 12, pp. 2560–2565, 2009.
- [10] J. Mazo, M. Delgado, J. M. Marin, and B. Zalba, “Modeling a radiant floor system with Phase Change Material (PCM) integrated into a building simulation tool: analysis of a case study of a floor heating system coupled to a heat pump,” *Energy and Buildings*, vol. 47, pp. 458–466, 2012.
- [11] C. Cattani, S. Chen, and G. Aldashev, “Information and modeling in complexity,” *Mathematical Problems in Engineering*, vol. 2012, Article ID 868413, 4 pages, 2012.
- [12] S. Y. Chen, H. Tong, and C. Cattani, “Markov models for image labeling,” *Mathematical Problems in Engineering*, vol. 2012, Article ID 814356, 18 pages, 2012.
- [13] VDI Technical Division Energy Conversion and Application, *Thermal Use of the Underground—Ground Source Heat Pump Systems*, 2001.
- [14] M. Carlini, T. Honorati, and S. Castellucci, “Photovoltaic greenhouses: comparison of optical and thermal behaviour for energy savings,” *Mathematical Problems in Engineering*, vol. 2012, Article ID 743764, 10 pages, 2012.
- [15] M. Carlini, S. Castellucci, M. Guerrieri, and T. Honorati, “Stability and control for energy production parametric dependence,” *Mathematical Problems in Engineering*, vol. 2010, Article ID 842380, 21 pages, 2010.
- [16] Solar Energy Laboratory, University of Wisconsin, TRNSYS 17 Documentation.

## Research Article

# Determining the Optimum Section of Tunnels Using Ant Colony Optimization

**S. Talatahari**

*Marand Faculty of Engineering, University of Tabriz, Tabriz 51666-14766, Iran*

Correspondence should be addressed to S. Talatahari; [talatahari@tabrizu.ac.ir](mailto:talatahari@tabrizu.ac.ir)

Received 16 November 2012; Accepted 30 December 2012

Academic Editor: Maurizio Carlini

Copyright © 2013 S. Talatahari. This is an open access article distributed under the Creative Commons Attribution License, which permits unrestricted use, distribution, and reproduction in any medium, provided the original work is properly cited.

Ant colony optimization is developed to determine optimum cross sections of tunnel structures. Tunnel structures are expensive infrastructures in terms of material, construction, and maintenance and the application of optimization methods has a great role in minimizing their costs. This paper presents the formulation of objective function and constraints of the problem for the first time, and the ant colony optimization, as a developed metaheuristic approach, has been used to solve the problem. The results and comparisons based on numerical examples show the efficiency of the algorithm.

## 1. Introduction

In general, the optimization techniques can be categorized into classical and metaheuristic search methods. Classical optimization methods often require substantial gradient information, the final results depend on the initially selected points, and many engineering problems are too complex to be handled with classical methods [1–3]. However, metaheuristic methods do not require the gradient data and perform better global search abilities [4–8].

Among many exiting metaheuristics, there are few algorithms that present many results (instead of only one best result). The ant colony optimization (ACO) was one of them. In the design of tunnel, engineers need to have many different designs to combine/select/improve them as the final result. Therefore, we select ACO in this paper. Previously, ACO has been applied to water distribution system optimization [9], optimal design of open channels [10], optimization of soil hydraulic parameters [11], identifying optimal sampling networks that minimize the number of monitoring locations in groundwater design optimization [12], and deterring the optimum design of skeletal structures with optimum weight [2], among many others. The advantages of applying ACO to engineering problems are similar to those of other evolutionary algorithms. It is a multiagent randomized search

technique in which in each cycle a number of search space points are selected and tested. The random selection and the information obtained in each cycle are used to choose new design vectors in subsequent cycles.

On the other hand, the necessity for tunnels and the benefits they bring cannot be overestimated. Tunnels improve connections and shorten lifelines. The utilization of underground space for storage, power and water treatment plants civil defense, and other activities is often a must in view of limited space, safe operation, environmental protection, and energy saving [13]. Of course, the construction of tunnels is risky and expensive and requires a high level of technical skill [13]. There are many methods proposed in the community for the modeling of the complex problem and geometrical structures [14–16]. For the first time, this paper presents the formulation of tunnel cross-sectional design problems and utilizes ant colony optimization to determine the optimum section of tunnels.

## 2. Formulation of the Optimization Problem

**2.1. Problem Statement.** There are different shapes or profiles for a tunnel cross section. The choice of the profile aims at accommodating the performance requirements of the tunnel.

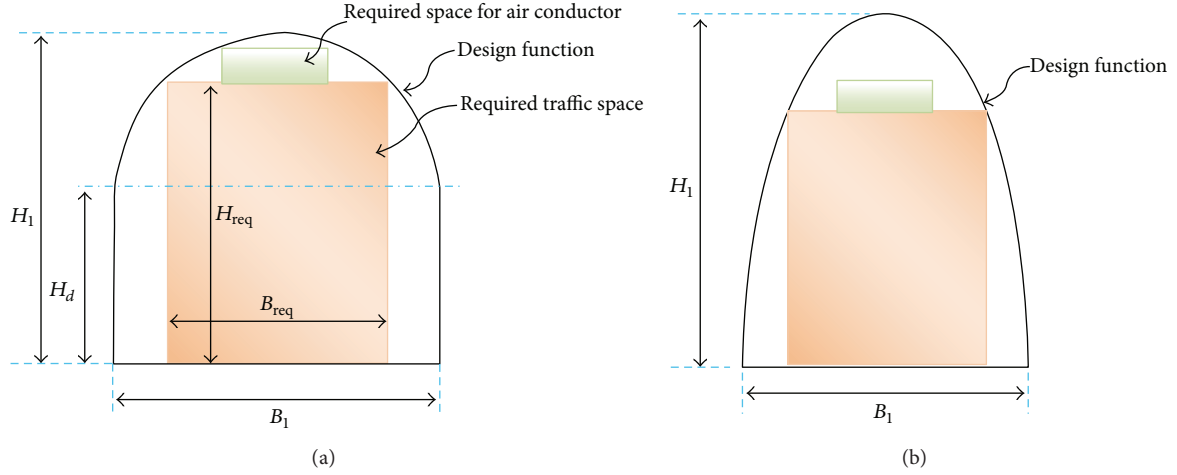


FIGURE 1: The different profiles of tunnel cross sections.

Moreover, it tries to minimize bending moments in the lining (or displacements) as well as costs for excavation and lining [13]. Therefore, the objective function can be defined as

$$\text{minimize } A + \varphi d, \quad (1)$$

where  $A$  is the area of the profile, and  $d$  is the maximum value of displacements. Also,  $\varphi$  is a constant parameter.

A typical problem of tunnel design is to fit two rectangles (one is required as a traffic space, and the other is required as air conductor space) into a mouth profile as shown in Figure 1. The figure shows two types of cross sections: in Figure 1(a), for a determined height ( $H_d$ ), a vertical wall is considered, while in Figure 1(b), the vertical wall is not utilized. For both types, the design functions of crown should be determined. Based on the kind of the selected function for crown, different shapes of profiles will be achieved. Here, we utilized the polynomial functions. As a result, the aim of optimization problem is to determine the parameters of the crown polynomial functions. The value of  $H_d$  for profile type I should be also considered as a variable. The geometry constraints of a such problem can be summarized as follows.

For the profile with vertical wall (type I):

$$\begin{aligned} H_{d\min} &\leq H_d \leq H_{d\max}, \\ H_{\text{req}} &\leq H_1, \\ B_{\text{req}} &\leq B_1, \\ A_s + B_{\text{req}} \times H_{\text{req}} &\leq A. \end{aligned} \quad (2)$$

For the profile without vertical wall (type II):

$$\begin{aligned} B_{\text{req}} &\leq B_1, \\ A_s + B_{\text{req}} \times H_{\text{req}} &\leq A, \end{aligned} \quad (3)$$

where  $H_{\text{req}}$  and  $B_{\text{req}}$  are the required height and width of traffic space, respectively. min and max denote lower and upper bounds, respectively.  $A_s$  is the required space for the air conductor.

**2.2. Constraint Handling Approach.** There are different methods to handle the constraints [16–18]. One of well known approaches to handle constraints is to employ a penalty function. In utilizing penalty functions, if the constraints are between the allowable limits, the penalty is zero; otherwise, the amount of penalty is obtained by dividing the violation of allowable limit to the limit itself, as

$$H_{\text{req}} \leq H_1 \implies \Phi_H = 0,$$

$$H_{\text{req}} > H_1 \implies \Phi_H = \frac{H_1 - H_{\text{req}}}{H_{\text{req}}},$$

$$B_{\text{req}} \leq B_1 \implies \Phi_B = 0,$$

$$B_{\text{req}} > B_1 \implies \Phi_B = \frac{B_1 - B_{\text{req}}}{B_{\text{req}}},$$

$$A_s + B_{\text{req}} \times H_{\text{req}} \leq A \implies \Phi_A = 0,$$

$$A_s + B_{\text{req}} \times H_{\text{req}} > A \implies \Phi_A = \frac{A - (A_s + B_{\text{req}} \times H_{\text{req}})}{A_s + B_{\text{req}} \times H_{\text{req}}}, \quad (4)$$

and the total value of the penalty functions equals

$$\Phi = \Phi_H + \Phi_B + \Phi_A. \quad (5)$$

### 3. Ant Colony Optimization

**3.1. General Aspects.** Ant colony optimization (ACO) is a cooperative search technique that mimics the foraging behavior of real life ant colonies [19]. The ant algorithms mimic the techniques employed by real ants to rapidly establish the shortest route from food source to their nest and vice versa. Ethologists observed that ants can construct the shortest path from their colony to the feeding source and back through the use of pheromone trails [19]. When an isolated ant comes across some food source in its random sojourn, it deposits a quantity of pheromone on that location. Other randomly

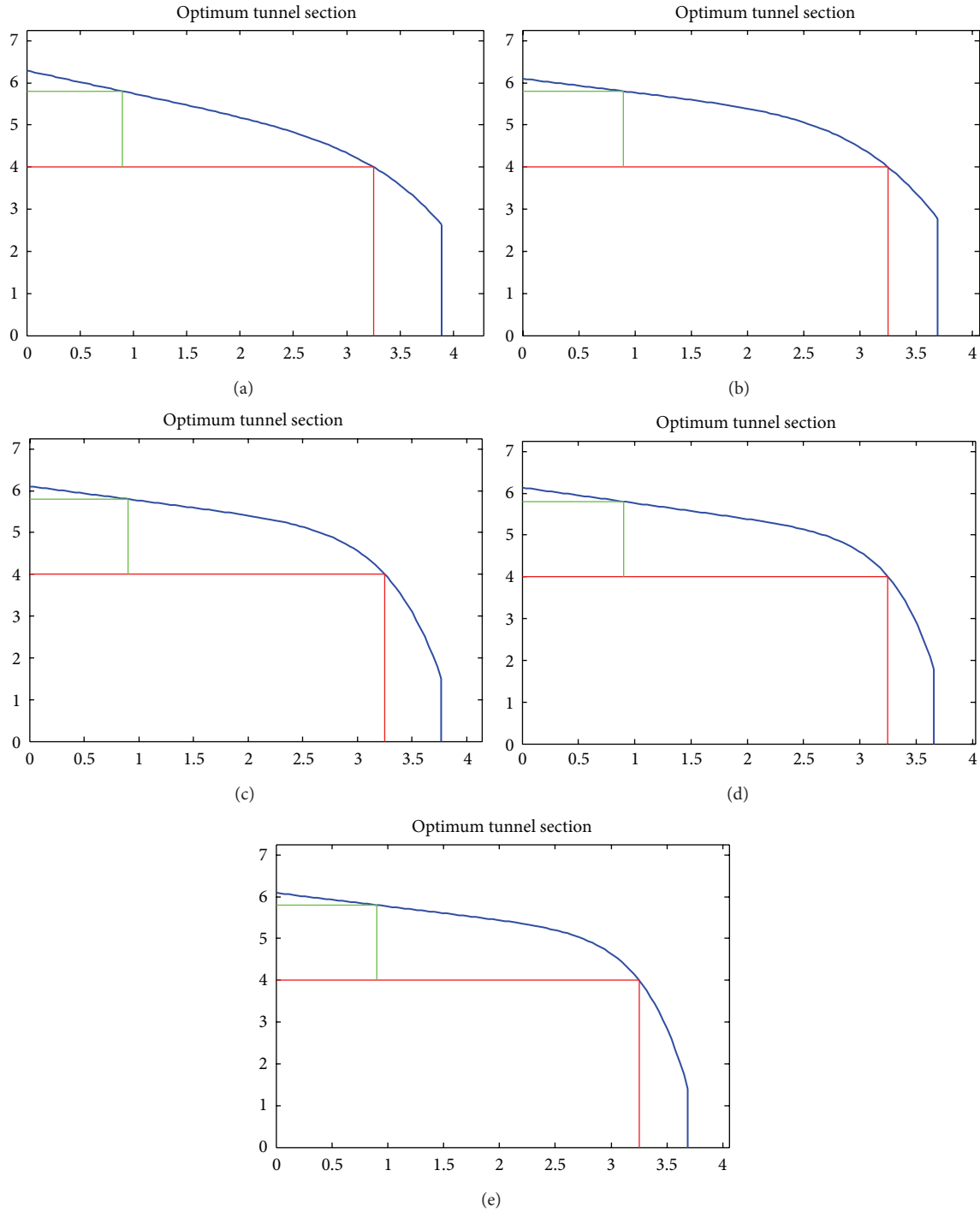


FIGURE 2: The optimum profiles of tunnel cross sections (type I); the order of functions is as follows: (a) 7, (b) 8, (c) 9, (d) 10, and (e) 20.

moving ants in the neighborhood can detect this marked pheromone trail. Further, they follow this trail with a very high degree of probability and simultaneously enhance the trail by depositing their own pheromone. More and more ants follow the pheromone-rich trail, and the probability of the trail being followed by other ants is further enhanced by the increased trail deposition. This is an autocatalytic

(positive feedback) process which favors the path along which more ants previously traversed [19]. The ant algorithms were based on the indirect communication capabilities of the ants. Artificial ants in ACO algorithms are deputed to generate rules by using heuristic information or visibility and by using the principle of indirect pheromone communication capabilities for iterative improvement of rules [2].

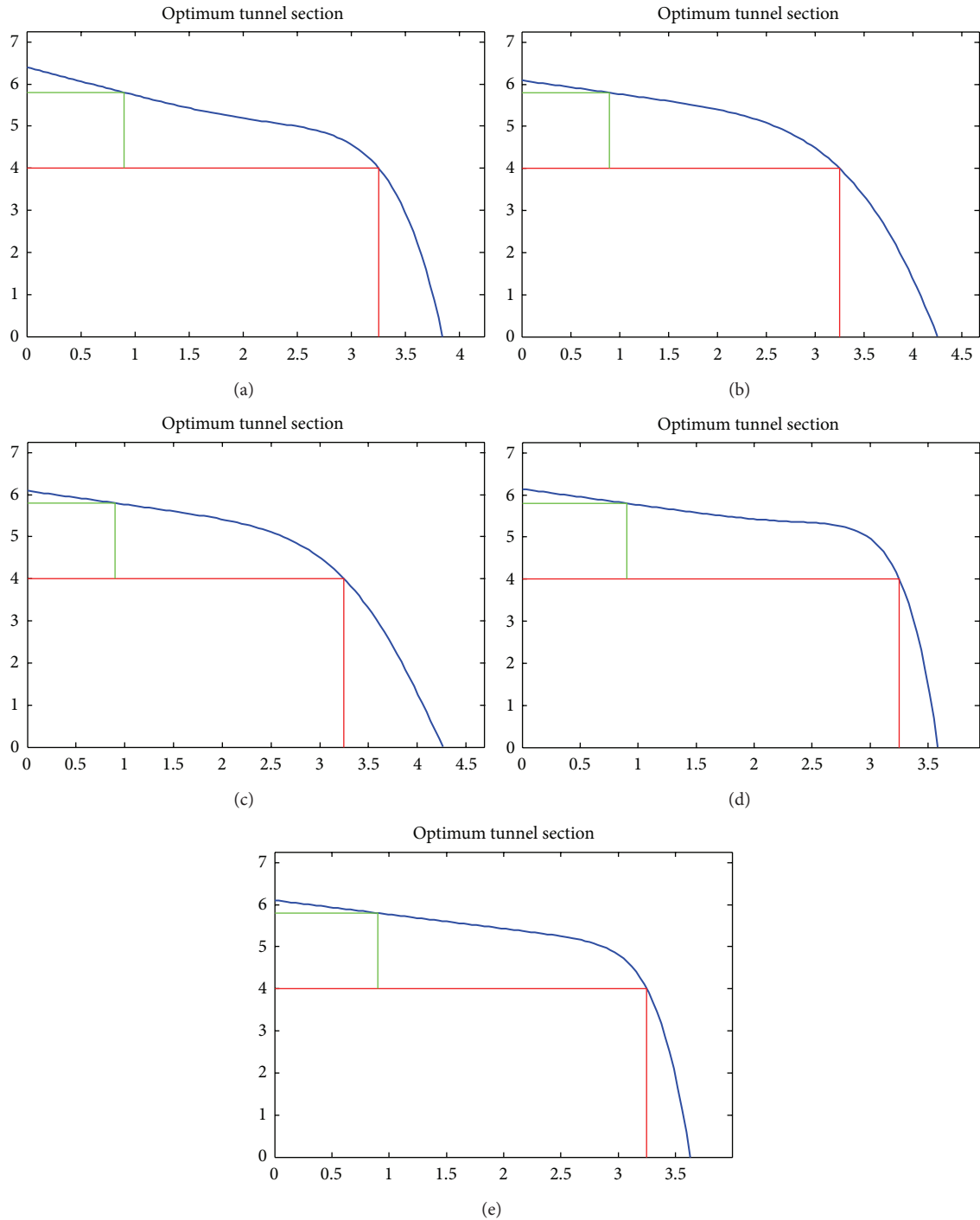


FIGURE 3: The optimum profiles of tunnel cross sections (type II); the order of functions is as follows: (a) 7, (b) 8, (c) 9, (d) 10, and (e) 20.

**3.2. Pseudocode.** The general procedure of the ACO algorithm manages the scheduling of four activities [2].

**Step 1 (initialization).** The initialization of the ACO consists of the initialization of the pheromone trail, the number of ants randomly and the required constant parameters.

**Step 2 (solution construction).** In the iteration step, each ant constructs a complete solution to the problem according to a state transition rule. The state transition rule depends mainly on the state of the pheromone and visibility of ant. Visibility is an additional ability used to make this method more efficient. In engineering problems, the visibility for allowable value

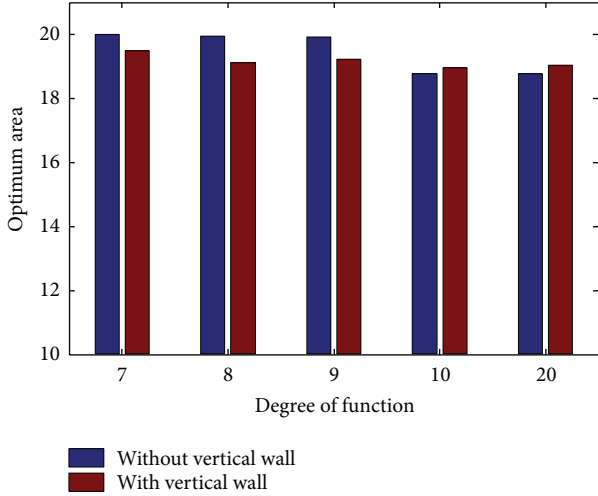


FIGURE 4: Comparison of final optimum results of types I and II.

number  $j$ , in variable  $i$ , equals the reverse of its real value, as

$$\eta_{ij} = \frac{1}{x_{ij}}. \quad (6)$$

For the  $k$ th ant, the selection of allowable value  $j$  of variable  $i$  is according to the transition probability function as

$$P_{ij}^k(t) = \frac{[\tau_{ij}(t)]^\alpha \cdot [\eta_{ij}]^\beta}{\sum_{l \in N_i} [\tau_{il}(t)]^\alpha \cdot [\eta_{il}]^\beta}, \quad \forall j \in N_i, \quad (7)$$

where  $\tau_{ij}(t)$  is the intensity of pheromone on variable  $i$  and allowable value  $j$ ,  $N_i$  is the list of allowable values that are available to variable  $i$ , and the  $\alpha$  and  $\beta$  are control parameters. The intensity of pheromone reflecting the previous experiences of the ants is a shared memory which provides an indirect communication between ants. Pheromone information stored in the trail matrix provides a global view about the selection of the edge based on a quality measure of the solution constructed afterward. On the other hand, the value of visibility is determined by a greedy heuristic for the original problem which considers only the local information on allowable values.

*Step 3* (pheromone updating rule). When every ant has constructed a solution, the intensity of pheromone trails on selected values is updated by the pheromone updating rule (global pheromone updating rule). The global pheromone updating rule is applied in two phases: first, an evaporation phase where a fraction of the pheromone evaporates, second, a reinforcement phase where the elitist ant, which has constructed the best solution in that iteration, deposits an amount of pheromone

$$\tau_{ij}(t + ng) = (1 - \rho) \cdot \tau_{ij}(t) + \rho \cdot \Delta\tau_{ij}^+, \quad (8)$$

where  $\rho$  ( $0 < \rho < 1$ ) represents the persistence of pheromone trails ( $(1 - \rho)$  is the evaporation rate),  $ng$  is the number of

variables, and  $\Delta\tau_{ij}^+$ , the amount of pheromone increase for the elitist ant, equals

$$\Delta\tau_{ij}^+ = \frac{1}{L^+}, \quad (9)$$

where  $L^+$  is the length of the solution found by the elitist ant.

At the end of each movement, local trail updating rule reduces the level of trail on values selected by the ant colony during the preceding iteration. When an ant selects the value  $j$  for variable  $i$ , the local update rule adjusts the intensity of trail by

$$\tau_{ij}(t + 1) = \xi \cdot \tau_{ij}(t), \quad (10)$$

where  $\xi$  is the adjustable parameter between 0 and 1 representing the persistence of the trail.

*Step 4* (stopping control level). This process is repeated until a stopping criterion is fulfilled.

**3.3. Improved Ant Colony Optimization.** Kaveh and Talatahari [2] suggested an improved ACO, using sub-optimization mechanism which divides the search space into smaller parts and deletes the infeasible parts, and then the remaining space is divided into smaller parts again for more investigation in the next stage. So, the algorithm can be summarized as follows.

*Step 1.* Calculating cross-sectional area boundaries for each variable.

*Step 2.* Creating the series of the allowable cross-sectional areas.

*Step 3.* Determining the optimum solution of the stage by using ACO algorithm.

*Step 4.* Repeating Steps 1–3 for definite times.

## 4. Numerical Examples

A numerical investigation is performed in this section. The required height and width are 4 and 6.5 meters, respectively.  $A_s$  is set to  $1.8 \times 1.8$  meters. The proposed algorithm is coded in MATLAB and structures are analyzed using a finite element method. In fact, by using the constant properties for the utilized materials, a detailed model of tunnel sections is provided.

The values of constants  $\alpha$  and  $\beta$  are set to 1.0 and 0.4, respectively. The local update coefficient,  $\xi$ , is taken as 0.25, and the global update coefficient,  $\rho$ , is set to 0.2, [2]. Our research results show that the number of 20 ants is sufficient to reach the desirable solution.

Figure 2 shows the obtained optimum profiles of tunnel cross sections (type I) when the order of polynomial functions is changed from 7 to 20. For type II, Figure 3. Presents the obtained results of tunnel cross sections. Due to the symmetry of the section, only one half of the tunnel is shown in these figures.

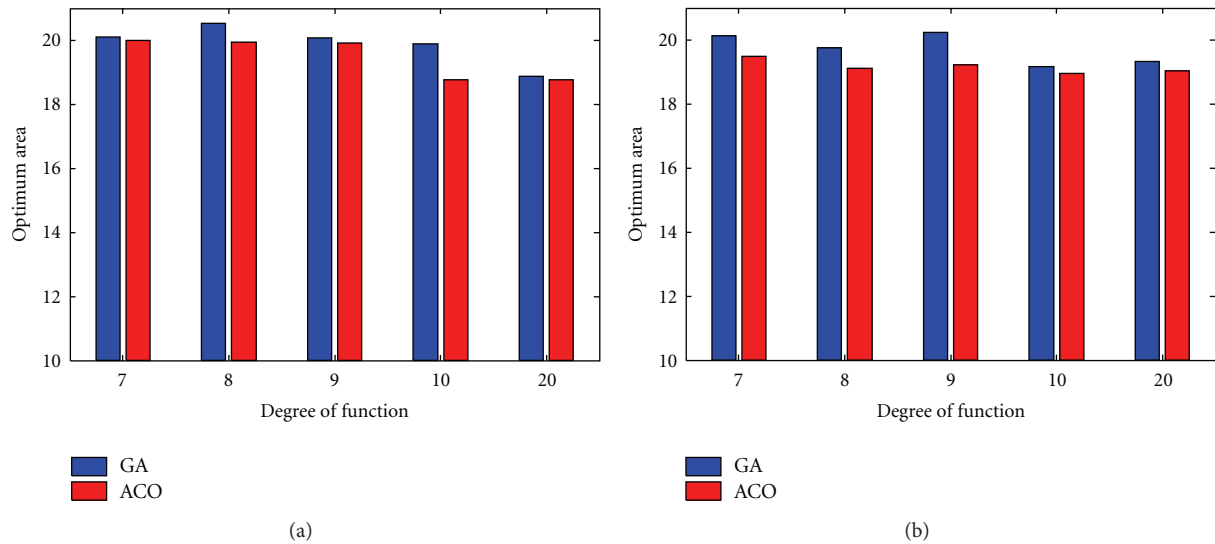


FIGURE 5: Comparison of final optimum results obtained by ACO and GA; (a) type I and (b) type II.

A comparison of final optimum results is performed as shown in Figure 4. The profile of type II (without vertical wall) is known as the best results when the degree of the function is set to 20. Another important result is that the differences between the functions with order 10 and 20 are small, and therefore, due to the existence of more variables for the function with degree 20, one may be satisfied to use a function with order of 10. Also, Figure 5 compares the final results obtained by the ACO and GA. The differences between the final results obtained by the ACO and GA are small; however, almost in all cases, the ACO can find better results.

## 5. Concluding Remarks

The choice of the profile aims at accommodating the performance requirements of the tunnel. Optimum cross section tries to minimize displacements as well as costs for excavation and lining. For the first time, this paper utilizes ant colony optimization (ACO) to determine optimum cross section of tunnels. ACO, a metaheuristic method, is inspired from natural phenomena which do not require an explicit relationship between the objective function and constraints, and it is not necessary for a given function to be derivable. The proposed method is tested on a numerical example. A section without vertical wall is found as the best design when the degree of the function is set to 20. The investigation shows that using a function with order 10 can reduce the computational costs while the final results do not change considerable. The result comparisons with genetic algorithm prove the robustness of the proposed method.

## Acknowledgment

This work was supported by “Rahsazi va Omran Iran Construction Company”. The details of the case study are provided by this company and hereby the author is thankful for the supports.

## References

- [1] P. Lu, S. Chen, and Y. Zheng, “Artificial intelligence in civil engineering,” *Mathematical Problems in Engineering*, vol. 2013, Article ID 145974, 20 pages, 2013.
- [2] A. Kaveh and S. Talatahari, “An improved ant colony optimization for the design of planar steel frames,” *Engineering Structures*, vol. 32, no. 3, pp. 864–873, 2010.
- [3] S. Chen, Y. Zheng, C. Cattani, and W. Wang, “Modeling of biological intelligence for SCM system optimization,” *Computational and Mathematical Methods in Medicine*, vol. 2012, Article ID 769702, 10 pages, 2012.
- [4] A. Kaveh and S. Talatahari, “Particle swarm optimizer, ant colony strategy and harmony search scheme hybridized for optimization of truss structures,” *Computers and Structures*, vol. 87, no. 5–6, pp. 267–283, 2009.
- [5] A. Kaveh and S. Talatahari, “A hybrid charged system search and particle swarm optimization algorithm for optimal design of structures,” *Structural Engineering and Mechanics*, vol. 42, no. 6, pp. 783–797, 2012.
- [6] S. Talatahari, A. Kaveh, and R. Sheikholeslami, “Engineering design optimization using chaotic enhanced charged system search algorithms,” *Acta Mechanica*, vol. 223, no. 10, pp. 2269–2285, 2012.
- [7] S. Gholizadeh and F. Fattahi, “Design optimization of tall steel buildings by a modified particle swarm algorithm,” *The Structural Design of Tall and Special Buildings*, 2012.
- [8] S. Gholizadeh and A. Barzegar, “Shape optimization of structures for frequency constraints by sequential harmony search algorithm,” *Engineering Optimization*, 2012.
- [9] H. R. Maier, A. R. Simpson, A. C. Zecchin et al., “Ant colony optimization for design of water distribution systems,” *Journal of Water Resources Planning and Management*, vol. 129, no. 3, pp. 200–209, 2003.
- [10] V. Nourani, S. Talatahari, P. Monadjemi, and S. Shahrifar, “Application of ant colony optimization to optimal design of open channels,” *Journal of Hydraulic Research*, vol. 47, no. 5, pp. 656–665, 2009.

- [11] K. C. Abbaspour, R. Schulin, and M. T. van Genuchten, "Estimating unsaturated soil hydraulic parameters using ant colony optimization," *Advances in Water Resources*, vol. 24, no. 8, pp. 827–841, 2001.
- [12] Y. Li and A. B. Chan Hilton, "Reducing spatial sampling in long-term groundwater monitoring using ant colony optimization," *International Journal of Computational Intelligence Research*, vol. 1, no. 1, pp. 19–28, 2006.
- [13] D. Kolymbas, *Tunelling and Tunnel Mechanics*, Springer, Berlin, Germany, 2005.
- [14] S. Chen, Y. Wang, and C. Cattani, "Key issues in modeling of complex 3D structures from video sequences," *Mathematical Problems in Engineering*, vol. 2012, Article ID 856523, 17 pages, 2012.
- [15] S. Chen, W. Huang, C. Cattani, and G. Altieri, "Traffic dynamics on complex networks: a survey," *Mathematical Problems in Engineering*, vol. 2012, Article ID 732698, 23 pages, 2012.
- [16] C. Cattani, S. Chen, and G. Aldashev, "Information and modeling in complexity," *Mathematical Problems in Engineering*, vol. 2012, Article ID 868413, 4 pages, 2012.
- [17] S. C. Lim, C. H. Eab, K. H. Mak, M. Li, and S. Y. Chen, "Solving linear coupled fractional differential equations by direct operational method and some applications," *Mathematical Problems in Engineering*, vol. 2012, Article ID 653939, 28 pages, 2012.
- [18] S. Talatahari, R. Sheikholeslami, M. Shadfaran, and M. Porbaba, "Charged system search algorithm for optimum design of gravity retaining walls subject to seismic loading," *Mathematical Problems in Engineering*, vol. 2012, Article ID 301628, 10 pages, 2012.
- [19] M. Dorigo and T. Stützle, *Ant Colony Optimization*, The MIT Press, Cambridge, Mass, USA, 2004.

## Research Article

# Wind Speed Forecasting by Wavelet Neural Networks: A Comparative Study

**Chuanan Yao, Xiankun Gao, and Yongchang Yu**

*College of Mechanical and Electrical Engineering, Henan Agricultural University, Zhengzhou 450002, China*

Correspondence should be addressed to Yongchang Yu; [hnyych@163.com](mailto:hnyych@163.com)

Received 30 October 2012; Revised 29 December 2012; Accepted 30 December 2012

Academic Editor: Sheng-yong Chen

Copyright © 2013 Chuanan Yao et al. This is an open access article distributed under the Creative Commons Attribution License, which permits unrestricted use, distribution, and reproduction in any medium, provided the original work is properly cited.

Due to the environmental degradation and depletion of conventional energy, much attention has been devoted to wind energy in many countries. The intermittent nature of wind power has had a great impact on power grid security. Accurate forecasting of wind speed plays a vital role in power system stability. This paper presents a comparison of three wavelet neural networks for short-term forecasting of wind speed. The first two combined models are two types of basic combinations of wavelet transform and neural network, namely, compact wavelet neural network (CWNN) and loose wavelet neural network (LWNN) in this study, and the third model is a new hybrid method based on the CWNN and LWNN models. The efficiency of the combined models has been evaluated by using actual wind speed from two test stations in North China. The results show that the forecasting performances of the CWNN and LWNN models are unstable and are affected by the test stations selected; the third model is far more accurate than the other forecasting models in spite of the drawback of lower computational efficiency.

## 1. Introduction

Utilization of renewable energy has been paid increasing attention to around the world. Wind energy is one of the most promising energy resources, and wind power generation has been growing rapidly in many countries [1–3]. Wind power generation has rapidly developed over the last decade and global wind power installations reached 240 GW in 2011, accounting for about 5% of global power installed capacity; global wind power generation will increase to about 450 GW by the year 2020 [4]. However, the randomness of wind in speed and direction leads to the fluctuation of wind power. The large-scale wind power generation integrated in electrical power systems may cause some problems, including power quality, stability, and especially power dispatching [5]. The accurate forecasting of wind speed has an important effect on solving the instability of wind power generation and increasing wind power penetration [6].

Recently, some researchers have proposed a number of methods to forecast wind speed and wind power, which can be classified as physical methods, spatial correlation methods, conventional statistical methods (i.e., persistence

method, ARMA), and artificial intelligence methods [7–14]. In the last two decades, artificial intelligence methods, including artificial neural network (ANN) [15–18], fuzzy logic, support vector machine [19, 20], are applied widely in energy engineering area [21, 22]. Among the methods, ANN is one of the most widely used models and a promising technology in wind speed forecast [3, 15–18].

However, ANN methods have limitations with nonstationary data, which may not be able to handle nonstationary data if the preprocessing of the input data is not done [23]. Wind speed is influenced by many factors, and its change displays a strong stochastic and intermittent feature. A single forecasting model cannot fully approximate the characteristics of wind speed.

Wavelet transform has been applied to a number of disciplines outside of the power system, and it has been found to be very effective to analyze nonstationary time series [24]. Wavelet transform not only has the multiresolution characteristics but also can capture the local feature of signal in both time and frequency domains [25]. The wavelet-transformed data can improve the ability of a forecasting

model by capturing useful information on various resolution levels.

Recently, some hybrid prediction techniques using the combination of wavelet transform and ANN have been developed for wind speed prediction. There are two types of basic combination forms based on wavelet transform and ANN. The first combination method uses discrete wavelet transform (DWT) as a preprocessing tool to decompose the original time series signal into some subsequences with different frequency bands. Then ANN models are used as forecasting modules to predict these subsequences, respectively. The combination method, namely, loose wavelet neural network (LWNN) in this study has been applied in energy and power systems [26, 27]. The second combination method is similar to back propagation neural networks (BPNN) and uses a kind of wavelet basis function to replace sigmoidal activation function of the hidden layer nodes of BPNN. This combination network is presented firstly by Zhang and Benveniste [28], namely, compact wavelet neural network (CWNN) in this study. At present, this method has been widely applied to various fields [29, 30]. Other combination methods are rarely reported in the literature [31–35].

In this study, we are interested in combined models based on the wavelet transform and neural network for wind speed forecasting. This paper presents three types of short-term wind speed forecasting models, including the preceding two wavelet neural networks (CWNN and LWNN). The third model is a new hybrid method based on a combination of the preceding two types of wavelet neural networks. The aim of this paper is to investigate the three models and compare the forecasting performance for wind speed by using the actual wind speed data in two different wind farms.

The remainder parts of the paper are organized as follows. In Section 2, three models based on the combination of wavelet and neural network are outlined. In Section 3, the model parameters are described, and some evaluating indexes used in this study are presented. In Section 4, obtained numerical results and discussion from these methods are presented. In Section 5, some relevant conclusions about the performance achieved by comparing CWNN, LWNN, and LCWNN models are provided.

## 2. Three Types of Wavelet Neural Network Models

**2.1. The CWNN Model.** The architecture of the CWNN model is based on the topology of BPNN. In this method, a kind of continuous wavelet basis function (i.e., Morlet wavelet or Mexican hat wavelet) is employed to replace sigmoidal activation function of the hidden layer nodes, and the scaling and shifting parameters of wavelet basis functions are used to replace the corresponding connection weights and thresholds from the input to the hidden layer. Wavelet function is a local function and influences the output of the hidden layer only in some local range [36]. The CWNN method may solve the conventional problems of poor convergence or trapping in local optima encountered in BPNN. The structure of the CWNN model is shown in Figure 1(a).

In Figure 1(a),  $x_1, x_2, \dots, x_k$  and  $y_1, y_2, \dots, y_m$  are the input and the output variables of the model, respectively;  $\omega_{ij}$  is the weight for the connection between the  $i$ th node of the input layer and the  $j$ th node of the hidden layer;  $\omega_{jk}$  is the weight for the connection between the  $j$ th node of the hidden layer and the  $k$ th node of the output layer. The output of each hidden layer neuron is calculated with the following formula:

$$h(j) = \psi_j \left( \frac{\sum_{i=1}^k \omega_{ij} x_i - b_j}{a_j} \right), \quad j = 1, 2, \dots, l, \quad (1)$$

where  $h(j)$  is the output of the  $j$ th node in the hidden layer;  $\psi_j$  denotes wavelet basis function of the  $j$ th node in the hidden layer;  $a_j$  and  $b_j$  are the scaling and shifting parameters of wavelet function;  $l$  defines the number of hidden layer nodes.

The output of the network is given by

$$y_k = \sum_{i=1}^l \omega_{ik} h(i), \quad k = 1, 2, \dots, m, \quad (2)$$

where  $\omega_{ik}$  is the weight for the connection between the hidden and the output layer.  $h(i)$  is the output of the  $i$ th node in hidden layer.  $m$  is the number of the output layer nodes.

Similar to the training algorithm of BPNN, the model adopts gradient descent rule to correct the connection weights and the parameters of wavelet basis function.

**2.2. The LWNN and LCWNN Models.** Both of the LWNN and LCWNN models consist of two parts: the preprocessing module based on discrete wavelet transform and the prediction module based on neural network.

Figures 1(b) and 1(c) show the architecture of the LWNN and LCWNN models, respectively. Their structures are similar. In the preprocessing modules, both models take discrete wavelet transform as preprocessing tools to decompose original wind speed time series  $x(n)$  into a set of wavelet coefficients, then reconstruct these coefficients into the time subseries. In the prediction modules, both models take neural networks as forecasting methods to predict the subseries. However, the difference between the two prediction modules is that the LWNN model uses the conversational BP neural networks to forecast the decomposed subseries, and the LCWNN model uses the CWNN model to predict them. In Figures 1(b) and 1(c),  $ca_j, cd_j, cd_{j-1}, \dots, cd_1$  ( $j$  is the scaling factor) are wavelet coefficients and  $a_j(n), d_j(n), d_{j-1}(n), \dots, d_1(n)$  are the reconstructed time subseries.  $ca_j$  and  $a_i(n)$  denote low-frequency component or approximation of original wind speed signal;  $d_j(n), d_{j-1}(n), \dots, d_1(n)$  and  $d_i(n)$  represent high-frequency components or details of original wind speed signal.

The modeling steps of the two methods are described as follows:

- (1) Use discrete wavelet transform to decompose original time series  $x(n)$  into a set of wavelet coefficients at scaling factor  $j$ , including low-frequency coefficients,  $j$  high-frequency coefficients, and then separately reconstruct these coefficient series into a set of time subseries that is equal to the length of original wind speed time series.

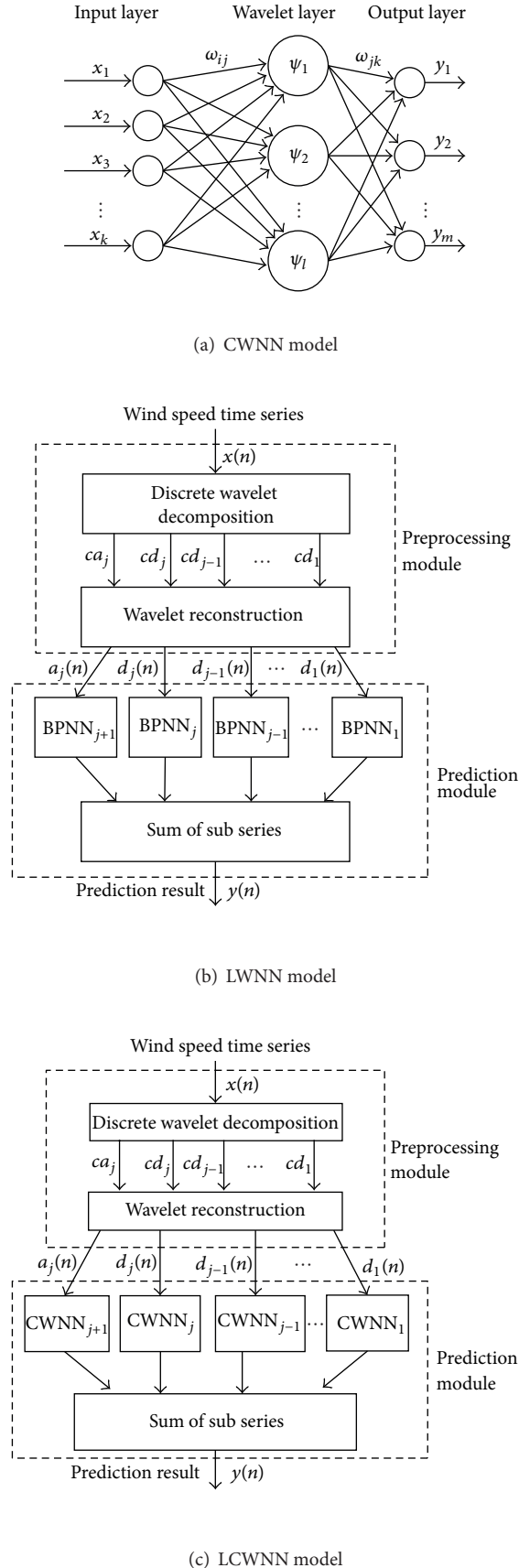


FIGURE 1: Structures of the three types of wavelet neural network models.

(2) Establish the BPNN and CWNN prediction models for these subseries, respectively, and make the short-term prediction for each subseries.

(3) Calculate the sum of forecasting results of all subseries to obtain the final forecasting for original time series.

### 3. Wind Speed Prediction Based on the Three Models

**3.1. Wind Speed Data.** Two stations (test station 1 and test station 2) located in Inner Mongolia Autonomous Region of China are used in this study. The hourly wind speed data are recorded from two wind farms in March 2010. Monitors on site sampled the wind speed data for every five-minute interval, which are collected 12 times in an hour. These measured data have been averaged to obtain the hourly mean wind speed (720 samplings). These samplings are divided into two groups. The first group of the samplings (1st–600th) is used for training and establishing models, and the second group of the samplings (601st–720th) is used for testing the validity of the prediction models.

**3.2. Forecasting Model Parameters.** For purpose of analyzing and assessing the forecasting performances of the combined models, two sets of wind speed data in two test stations are input into CWNN, LWNN, LCWNN, and the conventional BPNN models, respectively.

Wavelet transform is used in the LCWNN model as well as the CWNN and LWNN models. In the LWNN and LCWNN models, their preprocessing modules both apply discrete wavelet transform, and the wind speed series of test station 1 is decomposed discretely using db4 (Daubechies wavelet family) at scaling factor 3, respectively; the wind speed series in test station 2 is decomposed discretely using db3 at scaling factor 2, respectively.

In the forecasting modules of CWNN and LCWNN for every test station, the transfer functions both apply continuous Morlet mother wavelet function. The neurons in the input and the hidden layer in the forecasting modules are chosen by trial and error. The model parameters of the three wavelet neural networks and BP network with a single algorithm are shown in Table 1.

**3.3. Evaluation Criteria.** To compare the efficiency of the three wavelet neural networks for the prediction of wind speed, some error criteria are employed in this study. The mean absolute error (MAE), the root mean squared error (RMSE), and the mean absolute percentage error (MAPE) are defined as follows:

$$\text{MAE} = \frac{1}{n} \sum_{i=1}^n |\hat{y}_i - y_i|,$$

$$\text{RMSE} = \sqrt{\frac{1}{n} \sum_{i=1}^n (\hat{y}_i - y_i)^2}, \quad (3)$$

$$\text{MAPE} = \frac{100}{n} \sum_{i=1}^n \left| \frac{\hat{y}_i - y_i}{y_i} \right|,$$

TABLE 1: Model parameters of the three wavelet neural networks and BP networks.

Test station	Model	Wavelet preprocessing module			Neural network prediction module		
		Wavelet function	Decomposition coefficients	Structure of network	Transfer function of hidden layer	Transfer function of output layer	Training algorithm
Test station 1	BPNN			4-12-1*	tansig	purelin	trainlm
	CWNN			4-9-1	Morlet	purelin	trainlm
				$ca_3$ : 3-11-1	tansig	purelin	trainlm
				$cd_3$ : 4-7-1	tansig	purelin	trainlm
	LWNN	db4	$ca_3, cd_3, cd_2, cd_1$	$cd_2$ : 4-12-1	tansig	purelin	trainlm
				$cd_1$ : 4-12-1	tansig	purelin	trainlm
				$ca_3$ : 3-9-1	tansig	purelin	trainlm
				$cd_3$ : 4-7-1	tansig	purelin	trainlm
	LCWNN	db4	$ca_3, cd_3, cd_2, cd_1$	$cd_2$ : 4-7-1	tansig	purelin	trainlm
				$cd_1$ : 4-12-1	tansig	purelin	trainlm
Test station 2	BPNN			4-11-1	tansig	purelin	trainlm
	CWNN			3-8-1	Morlet	purelin	trainlm
				$ca_2$ : 3-8-1	tansig	purelin	trainlm
				$cd_2$ : 4-7-1	tansig	purelin	trainlm
	LWNN	db3	$ca_2, cd_2, cd_1$	$cd_1$ : 4-12-1	tansig	purelin	trainlm
				$ca_2$ : 3-9-1	tansig	purelin	trainlm
				$cd_2$ : 3-10-1	tansig	purelin	trainlm
				$cd_1$ : 4-11-1	tansig	purelin	trainlm
	LCWNN	db3	$ca_2, cd_2, cd_1$				

\*  $m-n-p$  denotes structure pattern of neural network.  $m, n, p$  are the numbers of the input, the hidden, and the output layer nodes, respectively.

TABLE 2: MAE, RMSE, and MAPE by deferent models for test station 1.

Model	MAE (m/s)	RMSE (m/s)	MAPE (%)	Average computation time (s)
Persistence	1.279	1.432	36.65	0.12
BPNN	1.186	1.338	30.19	3.36
CWNN	1.015	1.296	29.44	5.73
LWNN	0.475	0.522	13.17	9.69
LCWNN	0.426	0.468	11.82	19.74

TABLE 3: MAE, RMSE, and MAPE by deferent models for test station 2.

Model	MAE (m/s)	RMSE (m/s)	MAPE (%)	Average computation time (s)
Persistence	1.382	1.593	16.71	0.10
BPNN	1.343	1.584	16.26	3.49
CWNN	0.879	0.984	10.65	6.26
LWNN	0.808	0.958	9.78	11.70
LCWNN	0.549	0.621	6.64	22.35

where  $n$  is the number of testing wind speed values;  $y_i$  and  $\hat{y}_i$  are the actual and predicted wind speed at time  $i$ , respectively.

#### 4. Comparative Analysis

In the study, the persistence method and the conventional BPNN model are adopted as the benchmark for testing the performances of the three wavelet neural networks. These models are used for forecasting wind speed in two wind farms. Figure 2 and Tables 2 and 3 are the forecasting results for these prediction models.

Figures 2(a) and 2(b) show the forecasting results of wind speed made in two test stations, respectively. The subfigures, respectively, show the measured and the forecasted wind speed values obtained by the persistence method, BPNN, CWNN, LWNN, and LCNN.

Tables 2 and 3 give the comparative MAE, RMSE and MAPE error results obtained by the three types of wavelet network models (CWNN, LWNN and LCWNN) along with the persistence method and BPNN according to the error criteria in (3). The computation time of each algorithm is also shown in Tables 2 and 3.

Table 2 presents the results in test station 1. It can be seen that the MSE, RMSE, and MAPE values for the three combination wavelet neural network models are all smaller than those obtained by the persistence method and BPNN. For example, the MSE values for the CWNN, LWNN, and LCWNN are 1.015 m/s, 0.475 m/s, and 0.426 m/s, respectively, which are reduced by 20.6%, 62.9%, and 66.7% compared with those of the persistence method, and 14.4%, 59.9%, and 64.1% compared with those of BPNN. Among the three combination models, the LCWNN method presents better forecasting accuracy. The MAE, RMSE, and MAPE values

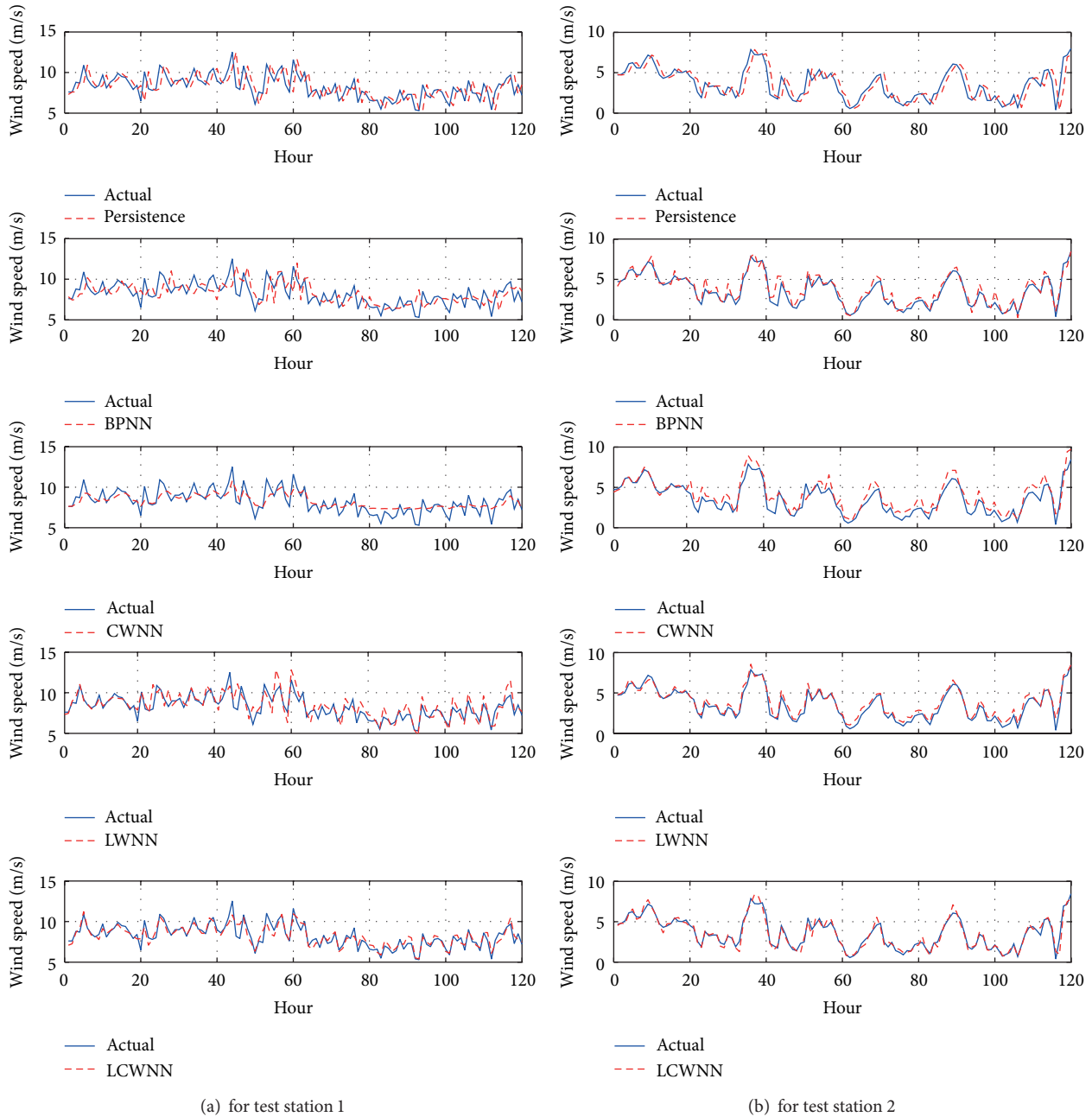


FIGURE 2: Forecasting results of wind speed series made by different models.

of the LCWNN model are 0.426 m/s, 0.468 m/s, and 11.82%, respectively. Improvements in the errors of the LCWNN model as against the CWNN model are 49.7%, 63.9%, and 59.9%. But the errors of the LWNN model are close to those of the LCWNN model.

Table 3 also lists the simulation results where these forecasting models are applied in test station 2. Table 3 shows that the prediction accuracy of the three wavelet neural network models also outperforms that of the persistence method and BPNN. But for the wavelet neural network models, the prediction accuracy of CWNN are close to that of LWNN, and both are much lower than that of the LCWNN method.

From Tables 2 and 3, the error values of the LCWNN model are the smallest in two test stations. In test station 1, the error values of CWNN are worse than those of LWNN; whereas in test station 2, the comparison between CWNN and LWNN shows that the two models yield similar results, and it is difficult to definitively conclude which model is better.

Besides, it can also be observed that the prediction performance of the persistence method is the weakest compared with the other four models based on neural networks. The persistence method assumes the current measured value as the prediction value of the next wind speed, and its

forecasting accuracy depends on the similarity of adjacent wind speed data. Some research shows the models based on neural networks generally outperform the persistence method [18].

Additionally, simulation results also exhibit that the prediction performance of BPNN model is weaker than the other three models based on the combination of wavelet transform and neural network, which can be explained by the fact that BP algorithm is not a global optimization method and easy to fall into local optimum, and its approximation and generalization abilities rely on the learning sample selected. The prediction accuracy can be improved by CWNN, LWNN, and LCWNN approaches because the wavelet transform can produce a good local representation of wind speed signals in both time and frequency domains. However, the prediction accuracy by CWNN and LWNN is unstable, easily influenced by geographical conditions, and the LCWNN model based on the combination of CWNN and LWNN can capture the complex features of wind speed and overcome the instability occurred in CWNN and LWNN models.

Unfortunately, the wavelet neural network methods spend more computation time than the persistence method and BPNN. Among the combined methods, the computational efficiency of the LWNN and the LCWNN methods is lower than CWNN and BPNN, because the prediction modules of the two methods both consist of several other models (i.e., BPNN and CWNN) in Figure 1. As shown in Tables 2 and 3, the average computation time of LCWNN is much longer than the other models using MATLAB on a PC with 2 GB of RAM and a 2.8 GHz based processor.

## 5. Conclusions

In this paper, three types of forecasting methods for wind speed based on the combinations of wavelet transform and neural networks were proposed. These combined methods were investigated by using two sets of wind speed data from different test stations in North China and compared with the persistence method and the conventional single BPNN. Due to the ability of wavelet transform for revealing the local characteristics of nonlinear time series and of neural network for self-learning and nonlinear approximation properties, the three wavelet neural network models have better forecasting accuracy than the persistence method and BPNN. The comparative result of different wavelet neural networks shows that the CWNN and the LCNN methods are unstable, easily influenced by different wind data sets; the LCWNN method combines the advantages of the CWNN and the LCWW models, and can reduce the prediction errors and improve the uncertainty. However, the operation time of the LCWNN method is much longer than other models because its prediction module consists of several CWNN models. In spite of its lower computational efficiency, it can be recommended that the LCWNN model could be a robust method for wind speed forecasting.

## Acknowledgments

The research was supported in part by Science and Technology Development entitled “Research on remote monitoring technology of hybrid wind-photovoltaic system” from the Department of Science and Technology in Henan province of China (Grant no. 122102210128) and the Key Laboratory of Zhengzhou for agricultural testing technology and instrumentation (Grant no. 121PYFZX184).

## References

- [1] O. Carranza, E. Figueres, G. Garcerá, and L. G. Gonzalez, “Comparative study of speed estimators with highly noisy measurement signals for Wind Energy Generation Systems,” *Applied Energy*, vol. 88, no. 3, pp. 805–813, 2011.
- [2] J. Zhao, X. Li, J. Hao, and J. Lu, “Reactive power control of wind farm made up with doubly fed induction generators in distribution system,” *Electric Power Systems Research*, vol. 80, no. 6, pp. 698–706, 2010.
- [3] L. Ma, S. Luan, C. Jiang, H. Liu, and Y. Zhang, “A review on the forecasting of wind speed and generated power,” *Renewable and Sustainable Energy Reviews*, vol. 13, no. 4, pp. 915–920, 2009.
- [4] J. Li, *China Wind Power Outlook 2012*, China Environmental Science Press, Beijing, China, 2012.
- [5] E. Cadenas and W. Rivera, “Wind speed forecasting in three different regions of Mexico, using a hybrid ARIMA-ANN model,” *Renewable Energy*, vol. 35, no. 12, pp. 2732–2738, 2010.
- [6] L. Cao and R. Li, “Short-term wind speed forecasting model for wind farm based on wavelet decomposition,” in *Proceedings of the 3rd International Conference on Deregulation and Restructuring and Power Technologies (DRPT '08)*, pp. 2525–2529, April 2008.
- [7] S. Y. Chen, C. Y. Yao, G. Xiao, Y. S. Ying, and W. L. Wang, “Fault detection and prediction of clocks and timers based on computer audition and probabilistic neural networks,” *Lecture Notes on Computer Science*, vol. 3512, pp. 952–959, 2005.
- [8] S. Castellucci and M. Carlini, “Modelling and simulation for energy production parametric dependence in greenhouses,” *Mathematical Problems in Engineering*, vol. 2010, Article ID 590943, 28 pages, 2010.
- [9] H. Liu, H. Q. Tian, C. Chen, and Y. F. Li, “A hybrid statistical method to predict wind speed and wind power,” *Renewable Energy*, vol. 35, no. 8, pp. 1857–1861, 2010.
- [10] L. Landberg, “Short-term prediction of the power production from wind farms,” *Journal of Wind Engineering and Industrial Aerodynamics*, vol. 80, no. 1-2, pp. 207–220, 1999.
- [11] I. J. Ramirez-Rosado, L. A. Fernandez-Jimenez, C. Monteiro, J. Sousa, and R. Bessa, “Comparison of two new short-term wind-power forecasting systems,” *Renewable Energy*, vol. 34, no. 7, pp. 1848–1854, 2009.
- [12] S. Chen, Y. Zheng, C. Cattani, and W. Wang, “Modeling of biological intelligence for SCM system optimization,” *Computational and Mathematical Methods in Medicine*, vol. 2012, Article ID 769702, 10 pages, 2012.
- [13] C. Cattani, “Shannon wavelets for the solution of integrodifferential equations,” *Mathematical Problems in Engineering*, vol. 2012, Article ID 408418, 22 pages, 2010.
- [14] Y. K. Wu and J. S. Hong, “A literature review of wind forecasting technology in the world,” in *Proceedings of the IEEE Lausanne PowerTech*, pp. 504–509, July 2007.

- [15] M. Bilgili, B. Sahin, and A. Yasar, "Application of artificial neural networks for the wind speed prediction of target station using reference stations data," *Renewable Energy*, vol. 32, no. 14, pp. 2350–2360, 2007.
- [16] G. Li and J. Shi, "On comparing three artificial neural networks for wind speed forecasting," *Applied Energy*, vol. 87, no. 7, pp. 2313–2320, 2010.
- [17] M. Monfared, H. Rastegar, and H. M. Kojabadi, "A new strategy for wind speed forecasting using artificial intelligent methods," *Renewable Energy*, vol. 34, no. 3, pp. 845–848, 2009.
- [18] G. Li, J. Shi, and J. Zhou, "Bayesian adaptive combination of short-term wind speed forecasts from neural network models," *Renewable Energy*, vol. 36, no. 1, pp. 352–359, 2011.
- [19] M. A. Mohandes, T. O. Halawani, S. Rehman, and A. A. Hussain, "Support vector machines for wind speed prediction," *Renewable Energy*, vol. 29, no. 6, pp. 939–947, 2004.
- [20] J. Zhou, J. Shi, and G. Li, "Fine tuning support vector machines for short-term wind speed forecasting," *Energy Conversion and Management*, vol. 52, no. 4, pp. 1990–1998, 2011.
- [21] H. Bouzgou and N. Benoudjit, "Multiple architecture system for wind speed prediction," *Applied Energy*, vol. 88, no. 7, pp. 2463–2471, 2011.
- [22] S. A. P. Kani and M. M. Ardehali, "Very short-term wind speed prediction: a new artificial neural network-Markov chain model," *Energy Conversion and Management*, vol. 52, no. 1, pp. 738–745, 2011.
- [23] J. Adamowski and K. Sun, "Development of a coupled wavelet transform and neural network method for flow forecasting of non-perennial rivers in semi-arid watersheds," *Journal of Hydrology*, vol. 390, no. 1-2, pp. 85–91, 2010.
- [24] J. Eynard, S. Grieu, and M. Polit, "Wavelet-based multi-resolution analysis and artificial neural networks for forecasting temperature and thermal power consumption," *Engineering Applications of Artificial Intelligence*, vol. 24, no. 3, pp. 501–516, 2011.
- [25] N. Amjady and F. Keynia, "Short-term load forecasting of power systems by combination of wavelet transform and neuro-evolutionary algorithm," *Energy*, vol. 34, no. 1, pp. 46–57, 2009.
- [26] J. P. S. Catalão, H. M. I. Pousinho, and V. M. F. Mendes, "Short-term wind power forecasting in Portugal by neural networks and wavelet transform," *Renewable Energy*, vol. 36, no. 4, pp. 1245–1251, 2011.
- [27] S. J. Yao, Y. H. Song, L. Z. Zhang, and X. Y. Cheng, "Wavelet transform and neural networks for short-term electrical load forecasting," *Energy Conversion and Management*, vol. 41, no. 18, pp. 1975–1988, 2000.
- [28] Q. Zhang and A. Benveniste, "Wavelet networks," *IEEE Transactions on Neural Networks*, vol. 3, no. 6, pp. 889–898, 1992.
- [29] A. Mellit, M. Benganem, and S. A. Kalogirou, "An adaptive wavelet-network model for forecasting daily total solar radiation," *Applied Energy*, vol. 83, no. 7, pp. 705–722, 2006.
- [30] Y. Jin, G. Chen, and H. Liu, "Fault diagnosis of analog circuit based on wavelet neural network," *Chinese Journal of Scientific Instrument*, vol. 28, no. 9, pp. 1600–1604, 2007 (Chinese).
- [31] C. Cattani, S. Chen, and G. Aldashev, "Information and modeling in complexity," *Mathematical Problems in Engineering*, vol. 2012, Article ID 868413, 4 pages, 2012.
- [32] S. Y. Chen, "Kalman filter for robot vision: a survey," *IEEE Transactions on Industrial Electronics*, vol. 59, no. 11, pp. 4409–4420, 2012.
- [33] M. Li, S. C. Lim, and S. Chen, "Exact solution of impulse response to a class of fractional oscillators and its stability," *Mathematical Problems in Engineering*, vol. 2011, Article ID 657839, 9 pages, 2011.
- [34] S. Y. Chen, H. Tong, and C. Cattani, "Markov models for image labeling," *Mathematical Problems in Engineering*, vol. 2012, Article ID 814356, 18 pages, 2012.
- [35] W. Huang and S. Chen, "Epidemic metapopulation model with traffic routing in scale-free networks," *Journal of Statistical Mechanics*, vol. 2011, no. 12, Article ID P12004, 19 pages, 2011.
- [36] A. Mellit, "Artificial Intelligence technique for modeling and forecasting of solar radiation data: a review," *International Journal of Artificial Intelligence and Soft Computing*, vol. 1, no. 1, pp. 52–76, 2008.

## Review Article

# Bio-Inspired Optimization of Sustainable Energy Systems: A Review

Yu-Jun Zheng,<sup>1</sup> Sheng-Yong Chen,<sup>1</sup> Yao Lin,<sup>2</sup> and Wan-Liang Wang<sup>1</sup>

<sup>1</sup> College of Computer Science & Technology, Zhejiang University of Technology, Hangzhou 310023, China

<sup>2</sup> College of Life Sciences, Fujian Normal University, Fuzhou, Fujian 350108, China

Correspondence should be addressed to Sheng-Yong Chen; sy@ieee.org

Received 12 December 2012; Accepted 17 January 2013

Academic Editor: Maurizio Carlini

Copyright © 2013 Yu-Jun Zheng et al. This is an open access article distributed under the Creative Commons Attribution License, which permits unrestricted use, distribution, and reproduction in any medium, provided the original work is properly cited.

Sustainable energy development always involves complex optimization problems of design, planning, and control, which are often computationally difficult for conventional optimization methods. Fortunately, the continuous advances in artificial intelligence have resulted in an increasing number of heuristic optimization methods for effectively handling those complicated problems. Particularly, algorithms that are inspired by the principles of natural biological evolution and/or collective behavior of social colonies have shown a promising performance and are becoming more and more popular nowadays. In this paper we summarize the recent advances in bio-inspired optimization methods, including artificial neural networks, evolutionary algorithms, swarm intelligence, and their hybridizations, which are applied to the field of sustainable energy development. Literature reviewed in this paper shows the current state of the art and discusses the potential future research trends.

## 1. Introduction

The demand for energy supply is increasing rapidly in recent years and will probably continue to grow in the future. The realization that fossil fuel resources are becoming scarce and that climate change is related to carbon emissions has stimulated interest in sustainable energy development [1]. In general, sustainable energy development strategies involve three major technological changes: energy savings on the demand side, efficiency improvements in the energy production, and replacement of fossil fuels by various sources of renewable energy [2]. In particular, due to its multifold advantages including inexhaustibility, safety, decrease in external energy dependence, decrease in impact of electricity production and transformation, increase in the level of services for the rural population, and so forth [3], renewable energy is now considered an important resource around the world and regarded as a key component in obtaining a sustainable development of our society.

The implementation of sustainable energy development strategies involves a wide range of design, planning, and control optimization problems. Various conventional optimization methods, such as linear programming [4–6], integer

programming [7, 8], mixed integer linear programming [9–12], nonlinear programming [13–16], dynamic programming (DP) [17–20], constrained programming [21, 22], and so forth, have been applied for solving these problems. Nevertheless, current optimization problems in sustainable energy systems become more and more complex, especially when they include the integration of renewable sources in coherent energy systems. This is because most of such problems are nonlinear, nonconvex, with multiple local optima, and included in the category of NP-hard problems [23]. In consequence, those conventional methods might need exponential computation time in the worst case to obtain the optimum, which leads to computation time that is too high for practical purposes [24]. In recent years, modern heuristic optimization techniques, which are stochastic search methods inspired by the concepts and principles of artificial intelligence, have gained popularity in the optimization of sustainable energy systems.

In this paper, we give an overview of the latest research advances in bio-inspired solution methods for sustainable energy development. We particularly focus on the bio-inspired optimization algorithms that have been applied to the design, planning, and control problems in the field of

renewable and sustainable energy systems. We roughly group those methods into three categories, which are artificial neural networks (ANNs), evolutionary algorithms (EAs), and swarm intelligence. Besides, we also describe the recent work about the hybridization of individual methods. These heuristic methods usually do not require deep mathematical knowledge and have been demonstrated to be quite useful and efficient in optimization search for complex optimization problems in science and engineering. We believe that this paper can help researchers to gain knowledge about the major developments emerged throughout the years and find valuable approaches that can be applied in the practice of implementing sustainable energy systems.

The rest of the paper is synthesized as follows: Section 2 reviews the application of ANNs in sustainable energy development, Section 3 summarizes the work about EAs applied to different types of optimization problems in energy, Section 4 presents the recent advances in swarm-based methods used in the field, Section 5 introduces the hybrid techniques combining two or more of above methods, and Section 6 concludes with discussion.

## 2. Artificial Neural Networks

An ANN is a collection of neuron-like processing units with weighted connections between the units, which is inspired by our present understanding of biological nervous systems. Roughly speaking, ANNs use processing elements connected by links of variable weights to form a black box representation of systems [25]. ANNs can be trained by adjusting the weights so as to be able to predict or classify new patterns, and they provide some of the human characteristics of problem solving that are difficult to simulate using other computational technologies. Advantages of ANN include their high tolerance of noisy data, their ability to process patterns on which they have not been trained, as well as that they can be used without much preliminary knowledge about the problem domain. However, ANNs typically involve long training times and have been criticized for their poor interpretability [26].

ANNs are popular for prediction and forecasting nonlinear physical series (such as wind [27] and water level [28]) which are beyond the capability of linear predictors such as autoregressive (AR), moving average (MA), and autoregressive moving average (ARMA), [29–31]. Since 1990s, various studies have been reported on the applications of ANN in predicting electric loads and energy demands. An early work of Kawashima [32] developed an ANN backpropagation model with three-phase annealing for the first building energy prediction competition held by the American Society of Heating, Refrigerating- and Air-Conditioning Engineers in 1993. Islam et al. [33] proposed an ANN-based weather-load and weather-energy models, where a set of weather and other variables are identified for both models together with their correlations and contribution to the forecasted variables. They applied the models to historical energy, load, and weather data available for the Muscat power system from 1986 to 1990, and the forecast results for 1991–1992 show that monthly electric energy and load can be predicted within

a maximum error of 6% and 10%. Al-Shehri [34] used an ANN model for forecasting the residential electrical energy in the Eastern Province of Saudi Arabia, the forecasting result of which is shown to be closer to the real data than that predicted by the polynomial fit model. Azadeh et al. [35] developed a simulated-based ANN and applied it in forecasting monthly electrical energy consumption in Iran from March 1994 to February 2005 (131 months), and the result shows that the ANN model always provides the best solutions and estimation in comparison with other models such as time series.

ANNs have also been applied in midterm and long-term energy forecasting in different industrial sectors, areas, and countries and demonstrated their superiorities in comparison with conventional prediction models [36–41]. In [42] Ermis et al. presented an ANN model which is trained based on world energy consumption data from 1965 to 2004 and applied for forecasting world green energy consumption to the year 2050. It is estimated that world green energy and natural gas consumption will continue increasing after 2050, while world oil and coal consumption are expected to remain relatively stable after 2025 and 2045, respectively.

In recent years, ANN-based models have also been widely used in design and implementation of different kinds of renewable energy systems. For example, in the design of solar energy systems the estimation and calculation of radiation data are very important. Bosch et al. [43] presented an ANN approach for calculating solar radiation levels over complex mountain terrains using data from only one radiometric station. Cao and Lin [44] proposed a diagonal recurrent wavelet neural network which uses historical information of cloud cover to sample data sets for network training and applied their approach in hourly irradiance forecasting in Shanghai, China. Zervas et al. [45] developed an ANN-based prediction model of global solar irradiance distribution on horizontal surfaces, which has been applied to the meteorological database of NTUA, Zografou Campus, Athens.

In the same manner, the prediction of water level is fundamental for ocean energy generation. Huang et al. [46] developed an ANN for water level predictions, which has been applied to coastal inlets taking into account long-term water level observations. Kazeminezhad et al. [47] studied an ANN-based fuzzy inference system for predicting wave parameters, with an application to the data set comprising of fetch-limited wave data and over water wind data gathered from deep-water location in Lake Ontario.

The performance of photovoltaic system heavily depends on the meteorological conditions, and sizing represents an important part of photovoltaic systems design, that is, the optimal selection of the number of solar, cell panels, the size of the storage battery, and the size of wind generator to be used for certain hybrid applications [48]. ANNs have the capability to model complex, nonlinear processes without having to assume the form of the relationship between input and output variables, and thus ANN-based models, including adaptive ANN [49, 50], recurrent ANN [51], radial basis function network (RBFN) [52], have been successfully applied for sizing of photovoltaic systems.

### 3. Evolutionary Algorithms

Evolutionary algorithms (EAs) are stochastic search methods inspired by the principles of natural biological evolution for computationally difficult problems. They are very suitable for complex engineering optimization problems which may be multimodal, nondifferentiable, or discontinuous and thus cannot be solved by conventional gradient-based methods. In general, an EA simultaneously evolves a population of possible solutions and also returns a population of solutions. Typical EAs include genetic algorithms (GAs) [53], evolutionary programming (EP) [54], evolution strategies (ES) [55], differential evolution (DE) [56], and biogeography-based optimization (BBO) [57]. The advantages of EAs include their relative simplicity of implementation, inherent parallel architecture, and scalability to high-dimensional solution spaces.

Moreover, in real-world applications there are a large number of multiobjective optimization problems, that is, problems requiring the simultaneous optimization of several objectives which are often conflicted. For most of such problems, there is no single optimal solution and thus a solution method should search for a set of nondominated (Pareto optimal) solutions, that is, all the solutions such that there exists no other individual better in all the objectives. EAs are capable of finding several members of the Pareto optimal set in a single run of the algorithm, instead of having to perform a series of separate runs as in the case of the traditional mathematical programming techniques [58] and thus are very suitable for tackling with complex multiobjective optimization problems.

*3.1. Genetic Algorithms.* Genetic algorithms (GAs) are of the famous evolutionary algorithms which simulate the Darwinian principle of natural selection and the survival of the fittest in optimization [53]. A GA typically works with a fixed-size population of solutions and uses three genetic operations, namely selection, crossover, and mutation, to modify the solutions chosen from the current generation and select the most appropriate offspring to pass on to the next generations.

A number of researches have been reported on the application of GA in the optimal design and operation of sustainable energy systems. For wind energy systems, Li et al. [59] used a multilevel GA to solve the optimal design problem of integrating the number of actuators, the configuration of the actuators, and the active control algorithms in buildings excited by strong wind force. Li et al. [60] employed a GA to optimize the ranges of gearbox ratios and power ratings of multihybrid permanent-magnet wind generator systems. Grady et al. [61] used a GA to determine the optimal placement of wind turbines for maximum production capacity while limiting the number of turbines installed and the acreage of land occupied by each wind farm. Emami and Noghreh [62] proposed a GA with a new coding and a new objective function with adjustable coefficients for the similar problem, and their algorithm shows better performance on the optimal control of the cost, power, and efficiency of the wind farm. For solar energy systems, Varun and Siddhartha [63] proposed a GA to optimize system parameters in order

to maximize the thermal performance of flat plate solar air heaters. Zagrouba et al. [64] adapted a GA to identify the electrical parameters of photovoltaic solar cells and modules to determine the maximum power point from the illuminated current-voltage characteristic. GAs have also been used in geothermal systems [65] and hybrid photovoltaic systems [66–70].

*3.2. Evolutionary Programming and Evolution Strategies.* Evolutionary Programming (EP) was devised in order to evolve finite state machines for the prediction of events on the basis of former observations and has been demonstrated useful for searching the optimum of nonlinear functions [71]. Cau and Kaye [72] proposed a constructive EP approach to minimize the cost of operating a power system with multiple distributed energy storage resources. Their approach combines DP and EP by evolving piecewise linear convex cost-to-go functions and thus decomposes the multistage scheduling problem into smaller one-stage sub-problems which are easy to cope with. Fong et al. [73] developed a simulation-EP coupling method to solve the discrete, nonlinear, and highly constrained optimization problems related to energy management of heating, ventilating, and air-conditioning (HVAC) systems. The application of the method to a local HVAC installation project achieved a saving potential of about 7% as compared to the existing operational settings, without any extra cost. In [74] MacGill presented a dual EP approach integrating with software agents for power system resources to coevolve optimal operational behaviors over repeated power system simulations. The proposed tool was successfully applied to a real-world problem exploring the potential operational synergies between significant PV penetrations and distributed energy storage options including controllable loads.

Evolution strategies (ES) are a class of general optimization methods which evolve a population of solutions by means of variation and selection. Original ES uses a mutation operator that produces a single descendent from a given ancestor, denominated ES-(1 + 1), and was progressively generalized to ES-( $\mu + \lambda$ ), that is, several ancestors ( $\mu > 1$ ) and descendents ( $\lambda > 1$ ) in each generation [75]. In [76] Chang used an ES approach to solve optimal chiller loading problem, which takes the chilled water supply temperature as the variable to be determined for the decoupled air-conditioning system. The result shows, the approach outperforms both the Lagrangian method and the GA method. Considering the optimal selection and sizing of distributed energy resources which can be formulated as a nonlinear mixed-integer minimization problem, Logenthiran et al. [77] used ES for the minimization of capital and annual operational cost of DER under a variety of system and unit constraints. Their method was applied to design integrated microgrids for an intelligent energy distribution system project.

*3.3. Differential Evolution.* Differential evolution (DE) approach combines simple arithmetic operators with the classical operators of crossover, mutation, and selection to evolve a randomly generated starting population to a final solution. It is similar to a ( $\mu + \lambda$ ) ES, but in DE

the mutation is not done via some separately defined probability density function [78]. Chakraborty et al. [79] presented a fuzzy DE method for solving thermal unit commitment problem integrated with solar energy system, where the solar radiation, forecasted load demand and associated constraints are formulated as fuzzy sets considering the error. Slimani and Bouktir [80] developed a DE method to solve the optimal power flow problem, whose objective function is the minimization of the cost of the thermal and the wind generators with different sizes. The method decomposes the optimization constraints of the power system into active constraints manipulated directly by DE, and passive constraints maintained in their soft limits using a conventional constraint load flow.

dos Santos Coelho et al. [81] developed a cultural DE algorithm for optimizing the economic dispatch of electrical energy using thermal generators and validated their approach on a test system consisting of 13 thermal generators whose nonsmooth fuel cost function takes into account the valve-point loading effects. Suzuki et al. [82] studied a large-scale mixed-integer nonlinear problem for generating optimal operational planning for energy plants and developed an  $\epsilon$  constrained DE algorithm to effectively solve the problem without much parameters tuning effort. Hejazi et al. [83] developed a DE algorithm for optimal allocation of energy and spinning reserve, taking all security and power systems constraints in steady state and system credible contingencies into consideration. Lee et al. [84] conducted a comparative study of DE, GA, PSO, and LP methods for solving the optimal chiller loading problem for reducing energy consumption, and the result shows that the DE algorithm achieves the best result. Peng et al. [85] considered a problem in the design of the Earth-Moon low-energy transfer to find the patch point of the unstable manifold of the Lyapunov orbit around Sun-Earth L2 and the stable manifold of the Lyapunov orbit around Earth-Moon L2. They designed an improved differential evolution algorithm which incorporates the uniform design technology and the self-adaptive parameter control method into standard differential evolution to accelerate its convergence speed and improve the stability, and thus effectively solve the problem.

**3.4. Multiobjective Evolutionary Algorithms.** Multiobjective evolutionary algorithms (MOEAs) have received much interest in recent years. A number of metaheuristic algorithms, such as the nondominated sorting genetic algorithm NSGA [86] and the NSGA-II [87], the strength Pareto evolutionary algorithm (SPEA) [88] and the SPEA2 [89], the Pareto archived evolution strategy (PAES) [90], the Pareto differential evolution algorithm (PDE) [91], the nondominated sorting differential evolution (NSDE) [92], and so forth have gained great success in solving multiobjective optimization problems [93].

Benini and Toffolo [94] presented an MOEA for the design of stall-regulated horizontal-axis wind turbines, the aim of which is to achieve the best trade-off performance between the total energy production per square meter of wind park and cost. Their method can optimize the geometrical parameters of the rotor configuration of wind turbines,

achieving the best trade-off performance between the two objectives. Zhao et al. [95] employed a GA whose input parameters are the main components of a wind farm and key technical specifications and whose output is an optimal electrical system design of the wind farm which is optimized in terms of both production cost and system reliability. Kusiak et al. [96] proposed an MOEA for evaluating wind turbine performance, where the objectives include the maximization of the wind power output and the minimization of the vibration of the drive train and of the tower. In [97] Kusiak and Song used the MOEA for optimizing wind turbine placement based on wind distribution, including the selection of the best turbine combination from a given list of available turbines.

Bernal-Aguistin et al. [98] applied the SPEA to the design of a photovoltaic-wind-diesel system, where the objectives include the minimization of both the total cost throughout the useful life of the installation and the pollutant emissions. They later applied the algorithm to an extension of the problem, which adds an objective of the unmet load in the system [99]. Ould Bilal [100] proposed a multiobjective GA for minimizing the annualized cost system and the loss of power supply probability of a hybrid solar-wind-battery system. Montoya et al. [101] combined PAES with simulated annealing (SA) and tabu search (TS) to minimize voltage deviations and power losses in power networks. Thiaux et al. [102] applied NSGA-II to optimize stand-alone photovoltaic systems by reducing the gross energy requirement and minimizing the storage capacity. In [103] Rao and Peng considered a multiobjective optimal model of dispatch of energy-saving and emission reduction generation in the power system and developed a multiobjective DE algorithm with niche strategy for improving the crowing mechanism in the process of Pareto nondominated sorting operation. The experiment shows that their method can achieve better result than NSGA-II and NSDE.

## 4. Swarm Intelligence

The expression “swarm intelligence” was originally used in the context of cellular robotic systems to describe the self-organization of simple mechanical agents through nearest-neighbor interaction [104]. Bonabeau et al. [105] extended the definition to include “any attempt to design algorithms or distributed problem-solving devices inspired by the collective behavior of social insect colonies and other animal societies.” Since the 1990s, a number of swarm-based algorithms, including particle swarm optimization (PSO) [106], ant colony optimization (ACO) [107], artificial bee algorithms [108, 109], artificial immune systems (AIS) [110] have been proposed for difficult optimization problems especially with large continuous or combinatorial search spaces.

**4.1. Particle Swarm Optimization.** PSO is another population-based global optimization technique that enables a number of individual solutions, called particles, to move through a hyperdimensional search space to search for the optimum. Each particle has a position vector and a velocity vector, which are adjusted at iterations by learning from a local best found by the particle itself and a current global

best found by the whole swarm. Empirical studies have shown that PSO has a high efficiency in convergence to desirable optima and performs better than GA and other EAs on many problems [111].

AlRashidi and EL-Naggar [112] employed a PSO algorithm for estimating annual peak load forecasting in an electrical power system, the aim of which is to minimize the error associated with the estimated model parameters. Their approach was validated on actual recorded data from Kuwaiti and Egyptian networks. Niknam and Firouzi [113] developed a PSO algorithm combined with simplex search, for estimating load and renewable energy source output on the power systems, and their comparative experiment show that the PSO performs better than several EAs and other swarm-based algorithms.

Amjady and Soleymanpour [114] developed a modified adaptive PSO for daily hydrothermal generation scheduling, which is a complicated nonlinear, nonconvex, and nonsmooth optimization problem with discontinuous solution space. As some other adaptive PSOs [115, 116], their method dynamically changes the inertia weight and acceleration coefficients of the algorithm to increase activities of particles to explore broad space. Lee [117] applied PSO to solve short-term hydroelectric generation scheduling of a power system with wind turbine generators. Kongnam and Nuchprayoon [118] used PSO for the control problem of a wind turbine, which involves the determination of rotor speed and tip-speed ratio to maximize power and energy capture from the wind. Khanmohammadi et al. [119] developed a method based on PSO and Nelder-Mead algorithms for determining the optimal unit commitment (startups and shutdowns scheduling) of hydropower plants. López et al. [120] presented a binary PSO-based method to accomplish optimal location of biomass-fuelled systems for distributed power generation with forest residues as biomass source, and the results outperformed those obtained by a GA when maximizing a profitability index taking into account technical constraints. In [121] the authors also applied a PSO algorithm for the optimal location and supply area for biomass-based power plants. There are also a number of researches reported on the application of PSO in the design and control of hybrid photovoltaic systems [122–126].

Economic dispatch problems, the main aim of which is to schedule the committed generating units output so as to meet the required load demand at minimum cost satisfying all unit and system operational constraints, typically have nonlinear, nonconvex type objective function with intense equality and inequality constraints. Mahor et al. [127] presented a yearly (2003–2008) review of work of application of PSO to solve the various economic dispatch problems. The algorithms include linearly varying inertia weight PSO [128, 129], PSO with constriction factor and inertia weight [130, 131], PSO with linearly varying inertia weight with constriction factor [132], chaotic PSO [133–135], and multiobjective PSO [136–139]. It was suggested that PSO algorithms (in particular those with time varying control parameters) can give an improved results within less computational time in comparison to conventional methods, but still further improvements in PSO

algorithms are required, especially for real-time scheduling problems.

*4.2. Ant Colony Optimization.* Ant colony optimization (ACO) algorithms mimic the behavior of real ants living in colonies that communicate with each other using pheromones in order to accomplish complex tasks such as establishing a shortest path from the nest to food sources [107]. Li et al. [140] applied an ACO algorithm to the optimal design of solar energy dynamic power system in space station, with the aim to minimize the launching mass of the system subject to a set of constraints on parameters including pressure, temperature, compression coefficient, numbers and diameter of heat exchangers, height of recycling refrigerant, and so forth. Considering the optimal sizing of the design of standalone hybrid wind/photovoltaic power systems, Xu et al. [141] used ACO to minimize the total capital cost, subject to the constraint of the loss of power supply probability calculated by simulation. Foong et al. [142] considered a power plant maintenance scheduling optimization formulation incorporating the options of shortening the maintenance duration and/or deferring maintenance tasks in the search for practical maintenance schedules and developed an improve ACO algorithm for solving the problem. Warner and Vogel [143] considered planning of an energy supply network by simultaneously choosing the plants and the optimal network and implemented an ACO algorithm for the problem. See et al. [144] used ACO for determining optimal parameter values to the control model of energy extraction and thus improving the performance of wave energy converters as well as their long-term economic value.

Toksari [145] proposed an ACO electricity energy estimation model for forecasting electricity energy generation and demand, taking population, gross domestic product (GDP), import and export into consideration. He found that the model with quadratic equations can provide better fit solution due to the fluctuations of the economic indicators. The proposed model was applied to indicate Turkey's net electricity energy generation and demand until 2025. Baskan et al. [146] used ACO for estimating the transport energy demand of Turkey using gross domestic product, population, and vehicle-km. It is also expected that the work will be helpful in developing highly applicable and productive planning for transport energy policies.

*4.3. Artificial Bee Algorithms.* Artificial bee algorithms simulate the intelligent foraging behavior of a honeybee swarm. Two most popular algorithms are the artificial bee colony (ABC) algorithm and the honey bee mating optimization (HBMO) algorithm [147]. Niknam et al. [148] presented a multiobjective HBMO algorithm for the siting and sizing of renewable electricity generators, in order to optimize the placement of renewable electricity generators by considering objective functions including losses, costs of electrical generation, and voltage deviation. In [149] Niknam et al. also proposed an improve a HBMO algorithm for economic dispatch in power systems, with the aim to get maximum usable power using minimum resources. Abu-Mouti and El-Hawary [150] considered a dynamic economic dispatch problem, whose

aim is to determine the optimal power outputs of online generating units in order to meet the load demand subject to satisfying various operational constraints over finite dispatch periods, and they applied an ABC algorithm to solve the problem.

Vera et al. [151] proposed a binary honey bee foraging (HBF) swarm approach for searching the optimal location, biomass supply area, and power plant size that offer the best profitability for investor. Experimental results show that the HBF approach method outperforms PSO and GA. Hong [152] presented an electric load forecasting model based on a chaotic ABC algorithm combined with the seasonal recurrent support vector regression model, and the experiments indicated that the model can provide a promising forecasting performance for electric load.

**4.4. Artificial Immune System (AIS).** Inspired by the theoretical immunology, observed immune functions, principles, and models, AIS stimulates the adaptive immune system of a living creature to unravel the various complexities in real-world engineering optimization problems. Abdul Rahman et al. [153] developed an AIS algorithm for the economic dispatch problem, which uses the total generation cost as the objective function. Through genetic evolution, the antibodies with high affinity measure are produced and become the solution, and the algorithm converges within an acceptable execution time and highly optimal solution for economic dispatch with minimum generation cost. Coelho and Mariani [154] coped with the problem by using a chaotic artificial immune network approach, which has been demonstrated by the experiments to be an effective alternative to schedule the committed generating unit outputs to meet the required load demand at minimum operating cost while satisfying system constraints. Recently, Aرسالani and Seddighizadeh [155] used an AIS algorithm to minimize the deviation of bus voltage from its nominal value as well as the loss of energy in a power system. The main advantage of the algorithm is that it prevents many times repetition of similar solutions, and the result shows that the algorithm can achieve a solution that meets a level of preferences better than that required although the threshold is determined by means of fuzzy logic to reflect the imprecise nature of optimization objectives.

## 5. Hybrid Methods

By exploiting the advantages and disadvantages of two or more solution methods, we have a chance to obtain a powerful approach that is much more competitive than any individual method. Research and development on hybrid bio-inspired methods in sustainable energy systems have grown dramatically since the late 1990s.

Mellit and Kalogirou [156] studied the combination of GA and ANN for optimal sizing of stand-alone photovoltaic systems. Firstly the GA was used to optimize the sizing parameters of sites, and then the ANN was used to predict the optimal parameters in remote areas. Mellit later developed a hybrid model combining adaptive-network-based fuzzy inference system (ANFIS) and GA and demonstrated that

the model with ANFIS presents more accurate results [157]. Chang and Ko [158] designed a hybrid heuristic method which combines PSO with nonlinear time-varying evolution and ANN in order to determine the tilt angle of photovoltaic modules with the aim of maximizing the electrical energy output of the modules.

Li et al. [159] proposed a method combining AIS and PSO, for optimal load distribution among cascade hydropower stations. Their hybrid method involves the immune information processing mechanism into PSO and thus improves the ability to find the globally excellent result and the convergence speed with its special concentration selection mechanism and immune vaccination. Yang et al. [160] combined GA and ABC into a bee evolutionary genetic algorithm (BEGA), which has characteristics of higher precision and faster convergence rate and has been effectively applied to a problem of minimizing the energy consumption of central air-conditioning system without lowering the degree of comfort. The test on a common load distribution case shows that the hybrid method can achieve an energy-saving rate at 25.1%.

Kiran et al. [161] proposed a hybrid method of PSO and ACO for estimating energy demand, PSO for solving continuous optimization part and ACO for discrete part. The experiments demonstrated that the hybrid method outperforms both the individual PSO and ACO. In [162] Ghanbari et al. combined GA and ACO to model and simulate fluctuations of energy demand under the influence of related factors. Firstly the GA is used for generating data base of the expert system, and then the ACO is used for learning linguistic fuzzy rules such that degree of cooperation between data base and rule base increases. Results showed that the method can provide more accurate-stable results than ANFIS- and ANN-based approaches.

## 6. Discussion and Conclusion

We have summarized the recent research advances in bio-inspired solutions applied to the design, control, and implementation of sustainable energy systems. Typical illustrations are addressed for ANNs, EAs, swarm-based algorithms, and their hybridizations. Representative works are summarized to help readers have a general overview of the state-of-the-art and easily refer suitable methods in practical solutions.

The first finding of this paper is that the number of research papers on bioinspired optimization algorithms on sustainable energy problems has increased dramatically since 1990s. A large percent of early work was GA related. However, in recent years, DE has become more popular in the category of EAs, and swarm-based methods have gained more and more attentions of the researchers and practitioners. In the last three years, we found that PSO algorithms have become one of the most widely used methods in the field of renewable and sustainable energy development.

In general, none of the individual methods could perform better than all the other methods on all kinds of problems, suggesting that customized methods need to be carefully chosen or designed according to the respective problem. But researchers and practitioners can learn from the experiences

of early researchers. For example, on most problems of unit sizing of stand-alone hybrid energy systems, PSO typically outperforms GAs [163], mainly because PSO algorithms are more suitable for high-dimensional optimization problems, and improved versions of PSO are less sensitive to multiple local optima than GAs.

With the increasing importance and complexity of energy systems, we are facing the challenges to promote the performance, reliability, and scalability of solution methods [164, 165]. In consequence, it can be anticipated that future research will continuously put great emphasis on the hybridization of bio-inspired methods. In addition, more and more real-world problems in sustainable energy consider more than one objective. It can be expected that multiobjective bio-inspired optimization algorithms and parallel processing will be promising research areas in this field [166]. Moreover, current studies on multiobjective algorithms combining more than one metaheuristics are still rare, and we think that this can be a valuable direction for the researchers.

Today's new computational paradigms, such as quantum computing [167], DNA computing [168], and fractal computing [169–172], provide valuable inspiration for creating new heuristics for extremely difficult problems. Thus, the extensions of current bio-inspired methods based on these new paradigms are expected to achieve dramatic improvement on computational performance. For example, quantum-inspired EAs are regarded as one of the three main research areas related to the complex interaction between quantum computing and EAs [173]. In the aspect of quantum computing, if applying ANNs, it is worth considering time series models in that aspect as that discussed by Bakhoun and Toma [174, 175]. We believe that the fruits of these researches are continuously becoming new technological solutions to new open problems, and the full potential is far from being reached.

## Acknowledgments

This work was supported by the National Natural Science Foundation of China (61105073, 61173096, and 61103140), Doctoral Fund of Ministry of Education of China (20113317110001), and Zhejiang Provincial Natural Science Foundation (R1110679).

## References

- [1] E. Vine, "Breaking down the silos: the integration of energy efficiency, renewable energy, demand response and climate change," *Energy Efficiency*, vol. 1, no. 1, pp. 49–63, 2008.
- [2] H. Lund, "Renewable energy strategies for sustainable development," *Energy*, vol. 32, no. 6, pp. 912–919, 2007.
- [3] A. Hepbasli, "A key review on exergetic analysis and assessment of renewable energy resources for a sustainable future," *Renewable and Sustainable Energy Reviews*, vol. 12, no. 3, pp. 593–661, 2008.
- [4] R. Chedid and Y. Saliba, "Optimization and control of autonomous renewable energy systems," *International Journal of Energy Research*, vol. 20, no. 7, pp. 609–624, 1996.
- [5] S. Iniyar and K. Sumathy, "The application of a Delphi technique in the linear programming optimization of future renewable energy options for India," *Biomass and Bioenergy*, vol. 24, no. 1, pp. 39–50, 2003.
- [6] G. Privitera, A. R. Day, G. Dhesi, and D. Long, "Optimising the installation costs of renewable energy technologies in buildings: a linear programming approach," *Energy and Buildings*, vol. 43, no. 4, pp. 838–843, 2011.
- [7] M. Gong, "Optimization of industrial energy systems by incorporating feedback loops into the MIND method," *Energy*, vol. 28, no. 15, pp. 1655–1669, 2003.
- [8] P. Liu, D. I. Gerogiorgis, and E. N. Pistikopoulos, "Modeling and optimization of polygeneration energy systems," *Catalysis Today*, vol. 127, no. 1–4, pp. 347–359, 2007.
- [9] T. Ikegami, Y. Iwafune, and K. Ogimoto, "Development of the optimum operation scheduling model of domestic electric appliances for the supply-demand adjustment in a power system," *IEEE Transactions on Power and Energy*, vol. 130, no. 10, pp. 877–887, 2010.
- [10] B. Wille-Hausmann, T. Erge, and C. Wittwer, "Decentralised optimisation of cogeneration in virtual power plants," *Solar Energy*, vol. 84, no. 4, pp. 604–611, 2010.
- [11] H. Morais, P. Kádár, P. Faria, Z. A. Vale, and H. M. Khodr, "Optimal scheduling of a renewable micro-grid in an isolated load area using mixed-integer linear programming," *Renewable Energy*, vol. 35, no. 1, pp. 151–156, 2010.
- [12] S. Ruangpattana, D. Klabjan, J. Arinez, and S. Biller, "Optimization of on-site renewable energy generation for industrial sites," in *Proceedings of IEEE/PES Power Systems Conference and Exposition (PSCE '11)*, March 2011.
- [13] C. A. Babu and S. Ashok, "Optimal utilization of renewable energy-based IPPs for industrial load management," *Renewable Energy*, vol. 34, no. 11, pp. 2455–2460, 2009.
- [14] Z. Kravanja, "Mathematical programming approach to sustainable system synthesis," *Chemical Engineering Transactions*, vol. 21, pp. 481–486, 2010.
- [15] A. Borghetti, M. Bosetti, S. Grillo et al., "Short-term scheduling and control of active distribution systems with high penetration of renewable resources," *IEEE Systems Journal*, vol. 4, no. 3, pp. 313–322, 2010.
- [16] A. Vergnano, C. Thorstenson, B. Lennartson et al., "Modeling and optimization of energy consumption in cooperative multi-robot systems," *IEEE Transactions on Automation Science and Engineering*, vol. 9, no. 2, pp. 423–428, 2012.
- [17] E. D. Castronuovo and J. A. P. Lopes, "Optimal operation and hydro storage sizing of a wind-hydro power plant," *International Journal of Electrical Power and Energy System*, vol. 26, no. 10, pp. 771–778, 2004.
- [18] N. Löhdorf and S. Minner, "Optimal day-ahead trading and storage of renewable energies—an approximate dynamic programming approach," *Energy Systems*, vol. 1, no. 1, pp. 61–77, 2010.
- [19] V. Marano, G. Rizzo, and F. A. Tiano, "Application of dynamic programming to the optimal management of a hybrid power plant with wind turbines, photovoltaic panels and compressed air energy storage," *Applied Energy*, vol. 97, pp. 849–859, 2012.
- [20] A. Sinha and P. Chaporkar, "Optimal power allocation for a renewable energy source," in *Proceedings of National Conference on Communications*, 2012.
- [21] Y. P. Cai, G. H. Huang, Z. F. Yang, Q. G. Lin, and Q. Tan, "Community-scale renewable energy systems planning under uncertainty—an interval chance-constrained programming approach," *Renewable and Sustainable Energy Reviews*, vol. 13, no. 4, pp. 721–735, 2009.

- [22] S. Tomasin and T. Erseghe, "Constrained optimization of local sources generation in smart grids by SDP approximation," in *Proceedings of IEEE International Symposium on Power Line Communications and Its Applications (ISPLC '11)*, pp. 187–192, April 2011.
- [23] M. R. Garey and D. S. Johnson, *Computers and Intractability: A Guide to the Theory of NP-Completeness*, A Series of Books in the Mathematical Sciences, W. H. Freeman, San Francisco, Calif, USA, 1979.
- [24] R. Baños, F. Manzano-Agugliaro, F. G. Montoya, C. Gil, A. Alcayde, and J. Gómez, "Optimization methods applied to renewable and sustainable energy: a review," *Renewable and Sustainable Energy Reviews*, vol. 15, no. 4, pp. 1753–1766, 2011.
- [25] K. Chau, "A review on the integration of artificial intelligence into coastal modeling," *Journal of Environmental Management*, vol. 80, no. 1, pp. 47–57, 2006.
- [26] J. Han, M. Kamber, and J. Pei, *Data Mining: Concepts and Techniques*, Morgan Kaufmann, Waltham, Mass, USA, 3rd edition, 2012.
- [27] M. Li, S. C. Lim, and W. Zhao, "Cauchy-Matern model of sea surface wind speed at the Lake Worth, Florida," *Mathematical Problems in Engineering*, vol. 2012, Article ID 843676, 10 pages, 2012.
- [28] M. Li, Y. Q. Chen, J.-Y. Li, and W. Zhao, "Hölder scales of sea level," *Mathematical Problems in Engineering*, vol. 2012, Article ID 863707, 22 pages, 2012.
- [29] J. Makhoul, "Linear prediction: a tutorial review," *Proceedings of the IEEE*, vol. 63, no. 4, pp. 561–580, 1975.
- [30] B. S. Atal, "The history of linear prediction," *IEEE Signal Processing Magazine*, vol. 23, no. 2, pp. 154–161, 2006.
- [31] M. Li, W. Zhao, and B. Chen, "Heavy-tailed prediction error: a difficulty in predicting biomedical signals of  $1/f$  noise type," *Computational and Mathematical Methods in Medicine*, vol. 2012, Article ID 291510, 5 pages, 2012.
- [32] M. Kawashima, "Artificial neural network backpropagation model with three-phase annealing developed for the building energy predictor shootout," *ASHRAE Transactions*, vol. 100, no. 2, pp. 1096–1103, 1994.
- [33] S. M. Islam, S. M. Al-Alawi, and K. A. Ellithy, "Forecasting monthly electric load and energy for a fast growing utility using an artificial neural network," *Electric Power Systems Research*, vol. 34, no. 1, pp. 1–9, 1995.
- [34] A. Al-Shehri, "Artificial neural network for forecasting residential electrical energy," *International Journal of Energy Research*, vol. 23, no. 8, pp. 649–659, 1999.
- [35] A. Azadeh, S. F. Ghaderi, and S. Sohrabkhani, "A simulated-based neural network algorithm for forecasting electrical energy consumption in Iran," *Energy Policy*, vol. 36, no. 7, pp. 2637–2644, 2008.
- [36] G. J. Tsekouras, N. D. Hatzigiorgiou, and E. N. Dialynas, "An optimized adaptive neural network for annual midterm energy forecasting," *IEEE Transactions on Power Systems*, vol. 21, no. 1, pp. 385–391, 2006.
- [37] A. Sözen, M. A. Akçayol, and E. Arcaklioğlu, "Forecasting net energy consumption using artificial neural network," *Energy Sources, Part B*, vol. 1, no. 2, pp. 147–155, 2006.
- [38] A. Azadeh, S. F. Ghaderi, and S. Sohrabkhani, "Annual electricity consumption forecasting by neural network in high energy consuming industrial sectors," *Energy Conversion and Management*, vol. 49, no. 8, pp. 2272–2278, 2008.
- [39] A. H. Neto and F. A. S. Fiorelli, "Comparison between detailed model simulation and artificial neural network for forecasting building energy consumption," *Energy and Buildings*, vol. 40, no. 12, pp. 2169–2176, 2008.
- [40] R. Yokoyama, T. Wakui, and R. Satake, "Prediction of energy demands using neural network with model identification by global optimization," *Energy Conversion and Management*, vol. 50, no. 2, pp. 319–327, 2009.
- [41] Z. W. Geem and W. E. Roper, "Energy demand estimation of South Korea using artificial neural network," *Energy Policy*, vol. 37, no. 10, pp. 4049–4054, 2009.
- [42] K. Ermis, A. Midilli, I. Dincer, and M. A. Rosen, "Artificial neural network analysis of world green energy use," *Energy Policy*, vol. 35, no. 3, pp. 1731–1743, 2007.
- [43] J. L. Bosch, G. López, and F. J. Batlles, "Daily solar irradiation estimation over a mountainous area using artificial neural networks," *Renewable Energy*, vol. 33, no. 7, pp. 1622–1628, 2008.
- [44] J. Cao and X. Lin, "Application of the diagonal recurrent wavelet neural network to solar irradiation forecast assisted with fuzzy technique," *Engineering Applications of Artificial Intelligence*, vol. 21, no. 8, pp. 1255–1263, 2008.
- [45] P. L. Zervas, H. Sarimveis, J. A. Palyvos, and N. C. G. Markatos, "Prediction of daily global solar irradiance on horizontal surfaces based on neural-network techniques," *Renewable Energy*, vol. 33, no. 8, pp. 1796–1803, 2008.
- [46] W. Huang, C. Murray, N. Kraus, and J. Rosati, "Development of a regional neural network for coastal water level predictions," *Ocean Engineering*, vol. 30, no. 17, pp. 2275–2295, 2003.
- [47] M. H. Kazeminezhad, A. Etemad-Shahidi, and S. J. Mousavi, "Application of fuzzy inference system in the prediction of wave parameters," *Ocean Engineering*, vol. 32, no. 14–15, pp. 1709–1725, 2005.
- [48] A. Mellit, S. A. Kalogirou, L. Hontoria, and S. Shaari, "Artificial intelligence techniques for sizing photovoltaic systems: a review," *Renewable and Sustainable Energy Reviews*, vol. 13, no. 2, pp. 406–419, 2009.
- [49] A. Mellit, M. Benghaneim, A. H. Arab, and A. Guessoum, "Modelling of sizing the photovoltaic system parameters using artificial neural network," in *Proceedings of IEEE Conference on Control Applications*, vol. 1, pp. 353–357, June 2003.
- [50] A. Mellit, M. Benghaneim, A. H. Arab, and A. Guessoum, "An adaptive artificial neural network model for sizing stand-alone photovoltaic systems: application for isolated sites in Algeria," *Renewable Energy*, vol. 30, no. 10, pp. 1501–1524, 2005.
- [51] L. Hontoria, J. Aguilera, and P. Zufiria, "A new approach for sizing stand alone photovoltaic systems based in neural networks," *Solar Energy*, vol. 78, no. 2, pp. 313–319, 2005.
- [52] A. Mellit, M. Benghaneim, A. Hadj Arab, and A. Guessoum, "Identification and modeling of the optimal sizing combination of stand-alone photovoltaic systems using the radial basis function networks," in *Proceedings of the World Renewable Energy Congress VIII (WREC '04)*, Denver, Colo, USA, 2004.
- [53] J. H. Holland, *Adaptation in Natural and Artificial Systems*, University of Michigan Press, Ann Arbor, Mich, USA, 1975.
- [54] D. B. Fogel, "Introduction to simulated evolutionary optimization," *IEEE Transactions on Neural Networks*, vol. 5, no. 1, pp. 3–14, 1994.
- [55] I. Rechenberg, *Evolutions Strategies: Optimierung Technischer Systemenach Prinzipien der Biologischen Evolution*, Frommberg-Holzboog, Stuttgart, Germany, 1973.

- [56] R. Storn and K. Price, "Differential evolution—a simple and efficient heuristic for global optimization over continuous spaces," *Journal of Global Optimization*, vol. 11, no. 4, pp. 341–359, 1997.
- [57] D. Simon, "Biogeography-based optimization," *IEEE Transactions on Evolutionary Computation*, vol. 12, no. 6, pp. 702–713, 2008.
- [58] K. Miettinen, *Nonlinear Multiobjective Optimization*, International Series in Operations Research & Management Science, 12, Kluwer Academic Publishers, Boston, Mass, USA, 1999.
- [59] Q. S. Li, D. K. Liu, J. Q. Fang, and C. M. Tam, "Multi-level optimal design of buildings with active control under winds using genetic algorithms," *Journal of Wind Engineering and Industrial Aerodynamics*, vol. 86, no. 1, pp. 65–86, 2000.
- [60] H. Li, Z. Chen, and H. Polinder, "Optimization of multibrid permanent-magnet wind generator systems," *IEEE Transactions on Energy Conversion*, vol. 24, no. 1, pp. 82–92, 2009.
- [61] S. A. Grady, M. Y. Hussaini, and M. M. Abdullah, "Placement of wind turbines using genetic algorithms," *Renewable Energy*, vol. 30, no. 2, pp. 259–270, 2005.
- [62] A. Emami and P. Noghreh, "New approach on optimization in placement of wind turbines within wind farm by genetic algorithms," *Renewable Energy*, vol. 35, no. 7, pp. 1559–1564, 2010.
- [63] Varun and Siddhartha, "Thermal performance optimization of a flat plate solar air heater using genetic algorithm," *Applied Energy*, vol. 87, no. 5, pp. 1793–1799, 2010.
- [64] M. Zagrouba, A. Sellami, M. Bouaicha, and M. Ksouri, "Identification of PV solar cells and modules parameters using the genetic algorithms: application to maximum power extraction," *Solar Energy*, vol. 84, no. 5, pp. 860–866, 2010.
- [65] K. Tselepidou and K. L. Katsifarakis, "Optimization of the exploitation system of a low enthalpy geothermal aquifer with zones of different transmissivities and temperatures," *Renewable Energy*, vol. 35, no. 7, pp. 1408–1413, 2010.
- [66] S. H. El-Hefnawi, "Photovoltaic diesel-generator hybrid power system sizing," *Renewable Energy*, vol. 13, no. 1, pp. 33–40, 1998.
- [67] R. Dufo-López and J. L. Bernal-Agustín, "Design and control strategies of PV-diesel systems using genetic algorithms," *Solar Energy*, vol. 79, no. 1, pp. 33–46, 2005.
- [68] E. Koutroulis, D. Kolokotsa, A. Potirakis, and K. Kalaitzakis, "Methodology for optimal sizing of stand-alone photovoltaic/wind-generator systems using genetic algorithms," *Solar Energy*, vol. 80, no. 9, pp. 1072–1088, 2006.
- [69] R. Dufo-López, J. L. Bernal-Agustín, and J. Contreras, "Optimization of control strategies for stand-alone renewable energy systems with hydrogen storage," *Renewable Energy*, vol. 32, no. 7, pp. 1102–1126, 2007.
- [70] T. Senjyu, D. Hayashi, A. Yona, N. Urasaki, and T. Funabashi, "Optimal configuration of power generating systems in isolated island with renewable energy," *Renewable Energy*, vol. 32, no. 11, pp. 1917–1933, 2007.
- [71] D. Fogel and K. Chellapilla, "Revisiting evolutionary programming," in *Applications and Science of Computational Intelligence*, Proceedings of SPIE, pp. 2–11, Orlando, Fla, USA, 1998.
- [72] T. D. H. Cau and R. J. Kaye, "Multiple distributed energy storage scheduling using constructive evolutionary programming," in *Proceedings of the 22nd IEEE International Conference on Power Industry Computer Applications*, pp. 402–407, May 2001.
- [73] K. F. Fong, V. I. Hanby, and T. T. Chow, "HVAC system optimization for energy management by evolutionary programming," *Energy and Buildings*, vol. 38, no. 3, pp. 220–231, 2006.
- [74] I. F. MacGill, "An evolutionary programming tool for assessing the operational value of distributed energy resources within restructured electricity industries," in *Proceedings of the Australasian Universities Power Engineering (AUPEC '07)*, pp. 1–6, Australasian Universities, December 2007.
- [75] S. Chen, Y. Zheng, C. Cattani, and W. Wang, "Modeling of biological intelligence for SCM system optimization," *Computational and Mathematical Methods in Medicine*, vol. 2012, Article ID 769702, 10 pages, 2012.
- [76] Y. C. Chang, "Optimal chiller loading by evolution strategy for saving energy," *Energy and Buildings*, vol. 39, no. 4, pp. 437–444, 2007.
- [77] T. Logenthiran, D. Srinivasan, A. M. Khambadkone, and T. Sundar Raj, "Optimal sizing of distributed energy resources for integrated microgrids using evolutionary strategy," in *Proceedings of IEEE Congress on Evolutionary Computation*, pp. 1–8, 2012.
- [78] M. A. Falcone, H. S. Lopes, and L. dos Santos Coelho, "Supply chain optimisation using evolutionary algorithms," *International Journal of Computer Applications in Technology*, vol. 31, no. 3-4, pp. 158–167, 2008.
- [79] S. Chakraborty, T. Senjyu, A. Yona, A. Y. Saber, and T. Funabashi, "Fuzzy unit commitment strategy integrated with solar energy system using a modified differential evolution approach," in *Proceedings of Asia and Pacific Conference & Exposition on Transmission & Distribution*, pp. 1–4, October 2009.
- [80] L. Slimani and T. Bouktir, "Application of differential evolution algorithm to optimal power flow with high wind energy penetration," *Acta Electrotehnica*, vol. 53, no. 1, pp. 59–68, 2012.
- [81] L. dos Santos Coelho, A. D. V. De Almeida, and V. C. Mariani, "Cultural differential evolution approach to optimize the economic dispatch of electrical energy using thermal generators," in *Proceedings of the 13th IEEE International Conference on Emerging Technologies and Factory Automation (ETFA '08)*, pp. 1378–1383, September 2008.
- [82] R. Suzuki, F. Kawai, S. Kitagawa et al., "The  $\epsilon$  constrained differential evolution approach for optimal operational planning of energy plants," in *Proceedings of IEEE Congress on Evolutionary Computation (CEC '10)*, July 2010.
- [83] H. A. Hejazi, H. R. Mohabati, S. H. Hosseinian, and M. Abedi, "Differential evolution algorithm for security-constrained energy and reserve optimization considering credible contingencies," *IEEE Transactions on Power Systems*, vol. 26, no. 3, pp. 1145–1155, 2011.
- [84] W. S. Lee, Y. T. Chen, and Y. Kao, "Optimal chiller loading by differential evolution algorithm for reducing energy consumption," *Energy and Buildings*, vol. 43, no. 2-3, pp. 599–604, 2011.
- [85] L. Peng, Y. Wang, G. Dai, Y. Chang, and F. Chen, "Optimization of the Earth-Moon low energy transfer with differential evolution based on uniform design," in *Proceedings of IEEE Congress on Evolutionary Computation (CEC '10)*, July 2010.
- [86] N. Srinivas and K. Deb, "Multiobjective optimization using nondominated sorting in genetic algorithms," *Evolutionary Computing*, vol. 2, pp. 221–248, 1994.
- [87] K. Deb, A. Pratap, S. Agarwal, and T. Meyarivan, "A fast and elitist multiobjective genetic algorithm: NSGA-II," *IEEE Transactions on Evolutionary Computation*, vol. 6, no. 2, pp. 182–197, 2002.
- [88] E. Zitzler and L. Thiele, "Multiobjective evolutionary algorithms: a comparative case study and the strength Pareto

- approach," *IEEE Transactions on Evolutionary Computation*, vol. 3, no. 4, pp. 257–271, 1999.
- [89] E. Zitzler, M. Laumanns, and L. Thiele, "SPEA2: improving the strength Pareto evolutionary algorithm," in *Evolutionary Methods for Design, Optimization and Control with Applications to Industrial Problems*, K. Giannakoglou, D. Tsahalis, J. Periaux, P. Papailou, and T. Fogarty, Eds., Athens, Greece, 2001.
- [90] J. D. Knowles and D. W. Corne, "M-PAES: a memetic algorithm for multiobjective optimization," in *Proceedings of the Congress on Evolutionary Computation (CEC '00)*, vol. 1, pp. 325–332, July 2000.
- [91] H. A. Abbass, R. Sarker, and C. Newton, "PDE: a pareto-frontier differential evolution approach for multi-objective optimization problems," in *Proceedings of IEEE Congress on Evolutionary Computation*, vol. 2, pp. 971–978, May 2001.
- [92] R. Angira and B. V. Babu, "Non-dominated sorting differential evolution (NSDE): an extension of differential evolution for multi-objective optimization," in *Proceedings of 2nd Indian International Conference on Artificial Intelligence*, 2005.
- [93] Y. J. Zheng, Q. Song, and S. Y. Chen, "Multiobjective fireworks optimization for variable-rate fertilization in oil crop production," *Applied Soft Computing*. In press.
- [94] E. Benini and A. Toffolo, "Optimal design of horizontal-axis wind turbines using blade-element theory and evolutionary computation," *Journal of Solar Energy Engineering*, vol. 124, no. 4, pp. 357–363, 2002.
- [95] M. Zhao, Z. Chen, and F. Blaabjerg, "Optimisation of electrical system for offshore wind farms via genetic algorithm," *IET Renewable Power Generation*, vol. 3, no. 2, pp. 205–216, 2009.
- [96] A. Kusiak, Z. Zhang, and M. Li, "Optimization of wind turbine performance with data-driven models," *IEEE Transactions on Sustainable Energy*, vol. 1, no. 2, pp. 66–76, 2010.
- [97] A. Kusiak and Z. Song, "Design of wind farm layout for maximum wind energy capture," *Renewable Energy*, vol. 35, no. 3, pp. 685–694, 2010.
- [98] J. L. Bernal-Agustín, R. Dufo-López, and D. M. Rivas-Ascaso, "Design of isolated hybrid systems minimizing costs and pollutant emissions," *Renewable Energy*, vol. 31, no. 14, pp. 2227–2244, 2006.
- [99] R. Dufo-López and J. L. Bernal-Agustín, "Multi-objective design of PV-wind-diesel-hydrogen-battery systems," *Renewable Energy*, vol. 33, no. 12, pp. 2559–2572, 2008.
- [100] B. Ould Bilal, V. Sambou, P. A. Ndiaye, C. M. F. Kébé, and M. Ndong, "Optimal design of a hybrid solar-wind-battery system using the minimization of the annualized cost system and the minimization of the loss of power supply probability (LPSP)," *Renewable Energy*, vol. 35, no. 10, pp. 2388–2390, 2010.
- [101] F. G. Montoya, R. Banos, C. Gil, A. Espin, A. Alcayde, and J. Gomez, "Minimization of voltage deviation and power losses in power networks using Pareto optimization methods," *Engineering Applications of Artificial Intelligence*, vol. 23, pp. 695–703, 2010.
- [102] Y. Thiaux, J. Seigneurbieux, B. Multon, and H. Ben Ahmed, "Load profile impact on the gross energy requirement of stand-alone photovoltaic systems," *Renewable Energy*, vol. 35, no. 3, pp. 602–613, 2010.
- [103] P. Rao and C. H. Peng, "A research on power dispatch of energy-saving and emission-reduction generation based on the improved differential evolution algorithm," *Journal of East China Jiaotong University*, vol. 5, pp. 48–52, 2010.
- [104] P. Tarasewich and P. R. McMullen, "Swarm intelligence powers in numbers," *Communications of the ACM*, vol. 45, no. 8, pp. 62–67, 2002.
- [105] E. Bonabeau, M. Dorigo, and G. Theraulaz, *Swarm Intelligence: From Natural to Artificial Systems*, Oxford University Press, New York, NY, USA, 1999.
- [106] J. Kennedy and R. Eberhart, "Particle swarm optimization," in *Proceedings of the IEEE International Conference on Neural Networks*, pp. 1942–1948, Perth, Australia, December 1995.
- [107] A. Colorni, M. Dorigo, and V. Maniezzo, "Distributed optimization by ant colonies," in *Proceedings of European Conference on Artificial Life*, pp. 134–142, Paris, France, 1991.
- [108] X. S. Yang, "Engineering optimizations via nature-inspired virtual bee algorithms," in *Proceedings of the 1st International Work-Conference on the Interplay Between Natural and Artificial Computation (IWINAC '05)*, vol. 3562 of *Lecture Notes in Computer Science*, pp. 317–323, Springer, Las Palmas, Spain, June 2005.
- [109] D. Karaboga and B. Basturk, "A powerful and efficient algorithm for numerical function optimization: artificial bee colony (ABC) algorithm," *Journal of Global Optimization*, vol. 39, no. 3, pp. 459–471, 2007.
- [110] J. D. Farmer, N. H. Packard, and A. S. Perelson, "The immune system, adaptation, and machine learning," *Physica D*, vol. 22, no. 1–3, pp. 187–204, 1986.
- [111] J. Kennedy, "Bare bones particle swarms," in *Proceedings of IEEE Swarm Intelligence Symposium*, pp. 120–127, IEEE Press, 2003.
- [112] M. R. AlRashidi and K. M. EL-Naggar, "Long term electric load forecasting based on particle swarm optimization," *Applied Energy*, vol. 87, no. 1, pp. 320–326, 2010.
- [113] T. Niknam and B. B. Firouzi, "A practical algorithm for distribution state estimation including renewable energy sources," *Renewable Energy*, vol. 34, no. 11, pp. 2309–2316, 2009.
- [114] N. Amjady and H. R. Soleymanpour, "Daily Hydrothermal Generation Scheduling by a new Modified Adaptive Particle Swarm Optimization technique," *Electric Power Systems Research*, vol. 80, no. 6, pp. 723–732, 2010.
- [115] Z. H. Zhan, J. Zhang, Y. Li, and H. S. H. Chung, "Adaptive particle swarm optimization," *IEEE Transactions on Systems, Man, and Cybernetics, Part B*, vol. 39, no. 6, pp. 1362–1381, 2009.
- [116] Y.-J. Zheng, H.-F. Ling, and Q. Guan, "Adaptive parameters for a modified comprehensive learning particle swarm optimizer," *Mathematical Problems in Engineering*, vol. 2013, 11 pages, 2013.
- [117] T. Y. Lee, "Short term hydroelectric power system scheduling with wind turbine generators using the multi-pass iteration particle swarm optimization approach," *Energy Conversion and Management*, vol. 49, no. 4, pp. 751–760, 2008.
- [118] C. Kongnam and S. Nuchprayoon, "A particle swarm optimization for wind energy control problem," *Renewable Energy*, vol. 35, no. 11, pp. 2431–2438, 2010.
- [119] S. Khanmohammadi, M. Amiri, and M. T. Haque, "A new three-stage method for solving unit commitment problem," *Energy*, vol. 35, no. 7, pp. 3072–3080, 2010.
- [120] P. R. López, F. Jurado, N. Ruiz-Reyes, S. García Galán, and M. Gómez, "Particle swarm optimization for biomass-fuelled systems with technical constraints," *Engineering Applications of Artificial Intelligence*, vol. 21, no. 8, pp. 1389–1396, 2008.
- [121] P. R. Lopez, S. G. Galan, N. Ruiz-Reyes, and F. Jurado, "A method for particle swarm optimization and its application in location of biomass power plants," *International Journal of Green Energy*, vol. 5, no. 3, pp. 199–211, 2008.

- [122] T. Y. Lee and C. L. Chen, "Wind-photovoltaic capacity coordination for a time-of-use rate industrial user," *IET Renewable Power Generation*, vol. 3, no. 2, pp. 152–167, 2009.
- [123] A. K. Kaviani, G. H. Riahy, and S. M. Kouhsari, "Optimal design of a reliable hydrogen-based stand-alone wind/PV generating system, considering component outages," *Renewable Energy*, vol. 34, no. 11, pp. 2380–2390, 2009.
- [124] A. Kornelakis and E. Koutroulis, "Methodology for the design optimisation and the economic analysis of grid-connected photovoltaic systems," *IET Renewable Power Generation*, vol. 3, no. 4, pp. 476–492, 2009.
- [125] A. Kornelakis and Y. Marinakis, "Contribution for optimal sizing of grid-connected PV-systems using PSO," *Renewable Energy*, vol. 35, no. 6, pp. 1333–1341, 2010.
- [126] S. M. Hakimi and S. M. Moghaddas-Tafreshi, "Optimal sizing of a stand-alone hybrid power system via particle swarm optimization for Kahnouj area in south-east of Iran," *Renewable Energy*, vol. 34, no. 7, pp. 1855–1862, 2009.
- [127] A. Mahor, V. Prasad, and S. Rangnekar, "Economic dispatch using particle swarm optimization: a review," *Renewable and Sustainable Energy Reviews*, vol. 13, no. 8, pp. 2134–2141, 2009.
- [128] Z. L. Gaing, "Particle swarm optimization to solving the economic dispatch considering the generator constraints," *IEEE Transactions on Power Systems*, vol. 18, no. 3, pp. 1187–1195, 2003.
- [129] D. N. Jeyakumar, T. Jayabarathi, and T. Raghunathan, "Particle swarm optimization for various types of economic dispatch problems," *International Journal of Electrical Power & Energy Systems*, vol. 28, no. 1, pp. 36–42, 2006.
- [130] L. Wang and C. Singh, "Reserve-constrained multiarea environmental/economic dispatch based on particle swarm optimization with local search," *Engineering Applications of Artificial Intelligence*, vol. 22, no. 2, pp. 298–307, 2009.
- [131] K. K. Mandal, M. Basu, and N. Chakraborty, "Particle swarm optimization technique based short-term hydrothermal scheduling," *Applied Soft Computing Journal*, vol. 8, no. 4, pp. 1392–1399, 2008.
- [132] R. Chakrabarti, P. K. Chattopadhyay, M. Basu, and C. K. Panigrahi, "Particle swarm optimization technique for dynamic economic dispatch," *Journal of the Institution of Engineers*, vol. 87, pp. 48–54, 2006.
- [133] J. B. Park, Y. W. Jeong, H. H. Kim, and J. R. Shin, "An improved particle swarm optimization for economic load dispatch with valve point effect," *International Journal of Innovations in Energy Systems and Power*, vol. 1, no. 1, 2006.
- [134] L. dos Santos Coelho and V. C. Mariani, "Economic dispatch optimization using hybrid chaotic particle swarm optimizer," in *Proceedings of IEEE International Conference on Systems, Man, and Cybernetics (SMC '07)*, pp. 1963–1968, October 2007.
- [135] J. Cai, X. Ma, L. Li, and P. Haipeng, "Chaotic particle swarm optimization for economic dispatch considering the generator constraints," *Energy Conversion and Management*, vol. 48, no. 2, pp. 645–653, 2007.
- [136] A. I. S. Kumar, K. Dhanushkodi, J. J. Kumar, and C. K. C. Paul, "Particle swarm optimization solution to emission and economic dispatch problem," in *Proceedings of IEEE Conference on Convergent Technologies for the Asia-Pacific Region (TENCON '03)*, vol. 1, pp. 435–439, October 2003.
- [137] B. Zhao, C. Guo, and Y. Cao, "Dynamic economic dispatch in electricity market using particle swarm optimization algorithm," in *Proceedings of 5th World Congress on Intelligent Control and Automation (WCICA '04)*, pp. 5050–5054, June 2004.
- [138] M. A. Abido, "Multiobjective particle swarm for environmental/economic dispatch problem," in *Proceedings of the 8th International Power Engineering Conference (IPEC '07)*, pp. 1385–1390, December 2007.
- [139] M. A. Alrashidi and M. E. Hawary, "Impact of loading conditions on the emission economic dispatch," in *Proceedings of World Academy of Science and Engineering and Technology*, pp. 148–151, 2008.
- [140] Z. Li, X. P. Chang, and J. H. Qin, "Application of ant colony algorithms to optimization design of solar energy dynamic power system in space station," *Proceedings of the Chinese Society of Electrical Engineering*, vol. 25, pp. 294–298, 2005.
- [141] D. Xu, L. Kang, and B. Cao, "Graph-based ant system for optimal sizing of standalone hybrid wind/PV power systems," in *Computational Intelligence*, vol. 4114 of *Lecture Notes in Computer Science*, pp. 1136–1146, Springer, 2006.
- [142] W. K. Foong, H. R. Maier, and A. R. Simpson, "Power plant maintenance scheduling using ant colony optimization: an improved formulation," *Engineering Optimization*, vol. 40, no. 4, pp. 309–329, 2008.
- [143] L. Warner and U. Vogel, "Optimization of energy supply networks using ant colony optimization," in *Proceedings of 22th International Conference on Informatics for Environmental Protection*, pp. 327–334, 2008.
- [144] P. C. See, V. C. Tai, and M. Molinas, "Ant colony optimization applied to control of ocean wave energy converters," *Energy Procedia*, vol. 20, pp. 148–155, 2012.
- [145] M. D. Toksari, "Estimating the net electricity energy generation and demand using the ant colony optimization approach: case of Turkey," *Energy Policy*, vol. 37, no. 3, pp. 1181–1187, 2009.
- [146] O. Baskan, S. Haldenbilen, H. Ceylan, and H. Ceylan, "Estimating transport energy demand using ant colony optimization," *Energy Sources, Part B*, vol. 7, no. 2, pp. 188–199, 2012.
- [147] A. Afshar, O. Bozorg Haddad, M. A. Mariño, and B. J. Adams, "Honey-bee mating optimization (HBMO) algorithm for optimal reservoir operation," *Journal of the Franklin Institute*, vol. 344, no. 5, pp. 452–462, 2007.
- [148] T. Niknam, S. I. Taheri, J. Aghaei, S. Tabatabaei, and M. Nayyeripour, "A modified honey bee mating optimization algorithm for multiobjective placement of renewable energy resources," *Applied Energy*, vol. 88, no. 12, pp. 4817–4830, 2011.
- [149] T. Niknam, H. D. Mojarrad, H. Z. Meymand, and B. B. Firouzi, "A new honey bee mating optimization algorithm for non-smooth economic dispatch," *Energy*, vol. 36, no. 2, pp. 896–908, 2011.
- [150] F. S. Abu-Mouti and M. E. El-Hawary, "Optimal dynamic economic dispatch including renewable energy source using artificial bee colony algorithm," in *Proceedings of IEEE Systems Conference*, 2012.
- [151] D. Vera, J. Carabias, F. Jurado, and N. Ruiz-Reyes, "A Honey Bee Foraging approach for optimal location of a biomass power plant," *Applied Energy*, vol. 87, no. 7, pp. 2119–2127, 2010.
- [152] W. C. Hong, "Electric load forecasting by seasonal recurrent SVR (support vector regression) with chaotic artificial bee colony algorithm," *Energy*, vol. 36, no. 9, pp. 5568–5578, 2011.
- [153] T. K. Abdul Rahman, Z. M. Yasin, and W. N. W. Abdullah, "Artificial-immune-based for solving economic dispatch in power system," in *Proceedings of National Power and Energy Conference (PECon '04)*, pp. 31–35, November 2004.
- [154] L. D. S. Coelho and V. C. Mariani, "Chaotic artificial immune approach applied to economic dispatch of electric energy using

- thermal units,” *Chaos, Solitons & Fractals*, vol. 40, no. 5, pp. 2376–2383, 2009.
- [155] P. Arsalani and M. Seddighzadeh, “Minimizing the loss of energy in transmission systems with capacitor placement using an immune algorithm and fuzzy logic,” in *Proceedings of 2nd Conference on Energy Management and Conservation*, 2012.
- [156] A. Mellit and S. A. Kalogirou, “Application of neural networks and genetic algorithms for predicting the optimal sizing coefficient of photovoltaic supply (PVS) systems,” in *Proceedings of the World Renewable Energy Congress IX and Exhibition*, 2006.
- [157] A. Mellit, “ANFIS-based genetic algorithm for predicting the optimal sizing coefficient of photovoltaic supply (PVS) systems,” in *Proceedings of 3rd International Conference on Thermal Engineering: Theory and Applications*, pp. 96–102, 2007.
- [158] Y. P. Chang and C. N. Ko, “A PSO method with nonlinear time-varying evolution based on neural network for design of optimal harmonic filters,” *Expert Systems with Applications*, vol. 36, no. 3, pp. 6809–6816, 2009.
- [159] A. Li, L. Wang, J. Li, and C. Ji, “Application of immune algorithm-based particle swarm optimization for optimized load distribution among cascade hydropower stations,” *Computers and Mathematics with Applications*, vol. 57, no. 11-12, pp. 1785–1791, 2009.
- [160] Z. X. Yang, X. F. Yue, and L. Wang, “Study on the energy consumption optimization in a central air-conditioning system based on bee evolutionary genetic algorithm method,” *Building Science*, vol. 27, no. 6, pp. 78–82, 2011.
- [161] M. S. Kiran, E. Özceylan, M. Gündüz, and T. Paksoy, “A novel hybrid approach based on particle swarm optimization and ant colony algorithm to forecast energy demand of Turkey,” *Energy Conversion and Management*, vol. 53, no. 1, pp. 75–83, 2012.
- [162] A. Ghanbari, M. Kazemi, F. Mehmanpazir, and M. M. Nakhostin, “A cooperative ant colony optimization-genetic algorithm approach for construction of energy demand forecasting knowledge-based expert systems,” *Knowledge-Based Systems*, vol. 39, pp. 194–206, 2013.
- [163] B. Tudu, S. Majumder, K. K. Mandal, and N. Chakraborty, “Comparative performance study of genetic algorithm and particle swarm optimization applied on off-grid renewable hybrid energy system,” in *Swarm, Evolutionary, and Memetic Computing*, vol. 7076 of *Lecture Notes in Computer Science*, pp. 151–158, Springer, 2011.
- [164] M. Carlini and S. Castellucci, “Modelling and simulation for energy production parametric dependence in greenhouses,” *Mathematical Problems in Engineering*, vol. 2010, Article ID 590943, 28 pages, 2010.
- [165] M. Carlini, S. Castellucci, M. Guerrieri, and T. Honorati, “Stability and control for energy production parametric dependence,” *Mathematical Problems in Engineering*, vol. 2010, Article ID 842380, 21 pages, 2010.
- [166] M. Fadaee and A. M. Radzi, “Multi-objective optimization of a stand-alone hybrid renewable energy system by using evolutionary algorithms: a review,” *Renewable and Sustainable Energy Reviews*, vol. 16, no. 5, pp. 3364–3369, 2012.
- [167] J. Gruska, *Quantum Computing*, Advanced Topics in Computer Science Series, McGraw-Hill, New York, NY, USA, 1999.
- [168] G. Păun, G. Rozenberg, and A. Salomaa, *DNA Computing: New Computing Paradigms*, Texts in Theoretical Computer Science. An EATCS Series, Springer, Berlin, Germany, 1998.
- [169] M. Joyeux, S. Buyukdagli, and M. Sanrey, “ $1/f$  fluctuations of DNA temperature at thermal denaturation,” *Physical Review E*, vol. 75, no. 6, Article ID 061914, 9 pages, 2007.
- [170] A. Castro, M. A. L. Marques, D. Varsano, F. Sottile, and A. Rubio, “The challenge of predicting optical properties of biomolecules: what can we learn from time-dependent density-functional theory?” *Comptes Rendus Physique*, vol. 10, no. 6, pp. 469–490, 2009.
- [171] C. Cattani, E. Laserra, and I. Bochicchio, “Simplicial approach to fractal structures,” *Mathematical Problems in Engineering*, vol. 2012, Article ID 958101, 21 pages, 2012.
- [172] C. Cattani, “On the existence of wavelet symmetries in archaea DNA,” *Computational and Mathematical Methods in Medicine*, Article ID 673934, 21 pages, 2012.
- [173] G. Zhang, “Quantum-inspired evolutionary algorithms: a survey and empirical study,” *Journal of Heuristics*, vol. 17, no. 3, pp. 303–351, 2011.
- [174] E. G. Bakhoum and C. Toma, “Dynamical aspects of macroscopic and quantum transitions due to coherence function and time series events,” *Mathematical Problems in Engineering*, vol. 2010, Article ID 428903, 13 pages, 2010.
- [175] E. G. Bakhoum and C. Toma, “Mathematical transform of traveling-wave equations and phase aspects of quantum interaction,” *Mathematical Problems in Engineering*, vol. 2010, Article ID 695208, 15 pages, 2010.

## Research Article

# Cauchy-Matern Model of Sea Surface Wind Speed at the Lake Worth, Florida

Ming Li,<sup>1</sup> S. C. Lim,<sup>2</sup> and Wei Zhao<sup>3</sup>

<sup>1</sup> School of Information Science & Technology, East China Normal University, Shanghai 200241, China

<sup>2</sup> Faculty of Engineering, Multimedia University, 63100 Cyberjaya, Selangor, Malaysia

<sup>3</sup> Department of Computer and Information Science, University of Macau, Avenida Padre Tomas Pereira, Taipa, Macau, China

Correspondence should be addressed to Ming Li, ming\_lihk@yahoo.com

Received 4 November 2012; Accepted 5 December 2012

Academic Editor: Sheng-yong Chen

Copyright © 2012 Ming Li et al. This is an open access article distributed under the Creative Commons Attribution License, which permits unrestricted use, distribution, and reproduction in any medium, provided the original work is properly cited.

We study the Cauchy-Matern (CM) process with long-range dependence (LRD). The closed form of its power spectrum density (PSD) function is given. We apply it to model the autocovariance function (ACF) and the PSD of the sea surface wind speed (wind speed for short) observed in the Lake Worth, Florida, over the 1984–2006 period. The present results exhibit that the wind speed at the Lake Worth over 1984–2006 is of LRD. The present results exhibit that the CM process may yet be a novel model to fit the wind speed there.

## 1. Introduction

Stochastic processes with LRD gain applications in many fields of science and technologies ranging from hydrology to network traffic; see, for example, Mandelbrot [1], Beran [2], and references therein. The fractional Gaussian noise (fGn) introduced by Mandelbrot and van Ness [3] is a widely used model in this field. However, there are other models; see, for example, Lawrance and Kottegoda [4], Kaplan and Kuo [5], Martin and Walker [6], Granger and Ding [7], Beran [8], Yazici and Kashyap [9], Li et al. [10], and Chiles and Delfiner [11], in addition to fGn. In this paper, we focus on the correlation model that was first introduced by Matérn [12]. Later, it was discussed by Yaglom [13] and Chiles and Delfiner applied it to the geo-statistics [11]. Since it is in the Cauchy class, we call a process that obeys that correlation model as the Cauchy-Matern process (CM process for short).

This paper is organized as follows. We will dissertate the CM process and give its closed form of PSD in Section 2. Its application to wind speed is explained in Section 3 and discussions in Section 4, which is followed by conclusions.

## 2. CM Process

Let  $X(t)$  be a random function with zero mean for  $-\infty < t < \infty$ . Denote by  $p_{\text{Cauchy}}(x)$  the probability density function (pdf) of the Cauchy distribution in the form

$$p_{\text{Cauchy}}(x) = \frac{b}{\pi \left[ (x - m)^2 + b^2 \right]}, \quad (2.1)$$

where  $b$  is the half width at half maximum and  $m$  is the statistical median [14, 15]. The term ‘‘Cauchy process’’ conventionally implies that the pdf of  $X(t)$  obeys (2.1); see, for example, Bertoin [16], or its variations; see, for example, Zanzotto [17], Garbaczewski and Olkiewicz [18].

Let  $C(\tau) = E[X(t)X(t + \tau)]$  be the ACF of  $X(t)$ , where  $\tau$  is the time lag. Then, another meaning of the Cauchy process is the ACF of  $X(t)$  being in the form, see Yaglom [13, page 365] or Chilès and Delfiner [11, page 86],

$$C(\tau) = \left( 1 + |\tau|^2 \right)^{-1}, \quad \tau \in \mathbb{R}. \quad (2.2)$$

Obviously, the two are different in meaning. Our research utilizes the term in the sense of (2.2).

Matern generalized the ACF of the ordinary Cauchy model (2.2) to the following:

$$C(\tau) = \left( 1 + \frac{|\tau|^2}{a^2} \right)^{-b_1}, \quad \tau \in \mathbb{R}, \quad a > 0, \quad b_1 > 0. \quad (2.3)$$

Therefore, considering that Matern is a scientist in geosciences, we call a process  $X(t)$  that follows (2.3) the CM process.

Note that Matern did introduce the parameter  $a$  described in (2.3). However, it may be unnecessary because  $\tau$  is a real number. Thus, for the purpose of simplicity, we let  $a = 1$  and  $b_1 = b/2$ . In this way, (2.3) becomes the form

$$C(\tau) = \left( 1 + |\tau|^2 \right)^{-b/2}, \quad \tau \in \mathbb{R}, \quad b > 0. \quad (2.4)$$

The correlation model Matern discussed is of short-range dependence (SRD). In this research, we generalize it such that the LRD condition of  $X(t)$  can be considered when  $0 < b < 1$  in (2.4). Following the tradition in fractal time series, we let  $b/2 = 1 - H$  for  $0.5 < H < 1$ , where  $H$  is the Hurst parameter. Therefore, we may rewrite (2.4) by

$$C(\tau) = \left( 1 + |\tau|^2 \right)^{H-1}. \quad (2.5)$$

The SRD condition of the CM process is described by  $b > 1$ , which implies  $0 < H < 0.5$ .

Because  $C(\tau)$  is nonintegrable for  $0 < b < 1$ , the Fourier transform of  $C(\tau)$  denoted by  $S(\omega)$  does not exist in the domain of ordinary functions for  $0 < b < 1$ . This reminds

us that PSD of the CM process with LRD should be treated as a generalized function over the Schwartz space of test functions. In the domain of generalized functions (see [19, §2.5, Chapter 2]), the PSD of the CM process is given by

$$S(\omega) = \int_{-\infty}^{\infty} (1 + |\tau|^2)^{-b/2} e^{-j\omega\tau} d\tau = \frac{2^{(1-b)/2}}{\sqrt{\pi}\Gamma(b/2)} |\omega|^{1/2(b-1)} K_{1/2(b-1)}(|\omega|), \quad (2.6)$$

where  $K_\nu(\cdot)$  is the modified Bessel function of the second kind (Gradshteyn and Ryzhik [20]), which is expressed by

$$K_\nu(z) = \frac{\Gamma(\nu + 1/2)(2z)^\nu}{\sqrt{\pi}} \int_0^\infty \frac{\cos t dt}{(t^2 + z^2)^{\nu+1/2}}. \quad (2.7)$$

In the case of LRD, that is,  $0 < b < 1$ , one can infer that  $S(\omega) \sim 1/\omega$  for  $\omega \rightarrow 0$ ; see the details in Li and Zhao [15] for this inference. Thus, in order to plot the PSD of the CM process, we need regularizing  $S(\omega)$  such that the regularized PSD is finite for  $\omega \rightarrow 0$ . The regularization can be done in the following way. Denote by  $S_0(\omega)$  the regularized PSD. Then,

$$S_0(\omega) = \frac{S(\omega)}{\lim_{\omega \rightarrow 0} S(\omega)}. \quad (2.8)$$

The above implies that  $S_0(0) = 1$ . The plots below for PSD are in the sense of regularized PSD. Figures 1(a) and 1(b) indicate  $C(\tau)$  and  $S_0(\omega)$  for three values of  $H$ , respectively.

It is noted that the CM process is non-Markovian since its correlation  $C(t_1, t_2)$  does not satisfy the triangular relation given by

$$C(t_1, t_3) = \frac{C(t_1, t_2)C(t_2, t_3)}{C(t_2, t_2)}, \quad t_1 < t_2 < t_3, \quad (2.9)$$

which is a necessary condition for a Gaussian process to be Markovian; see Todorovic [21] for details. In fact, up to a multiplicative constant, the Ornstein-Uhlenbeck process is the only stationary Gaussian Markov process (Lim and Muniandy [22], Wolpert and Taqqu [23]).

The CM process is not self-similar but its Lamperti transformation is self-similar. For a stationary process  $X(t)$ , if  $\lambda > 0$ , the Lamperti transform of  $X(t)$  is given by

$$Y(t) = t^\lambda X(\ln t), \quad \text{for } t > 0, \quad Y(0) = 0. \quad (2.10)$$

Then,  $Y(t)$  is a  $\lambda$  self-similar process (Lamperti [24], Flandrin et al. [25]). Applying the Lamperti transformation to the CM process  $X(t)$  results in the covariance given by

$$E[Y(t)Y(s)] = (ts)^\lambda \left[ 1 + \left| \frac{\ln t}{s} \right|^2 \right]^{-b/2}, \quad t, s > 0. \quad (2.11)$$

The above exhibits that  $Y(t)$  is a Gaussian nonstationary process with the self-similarity index  $\lambda$ .

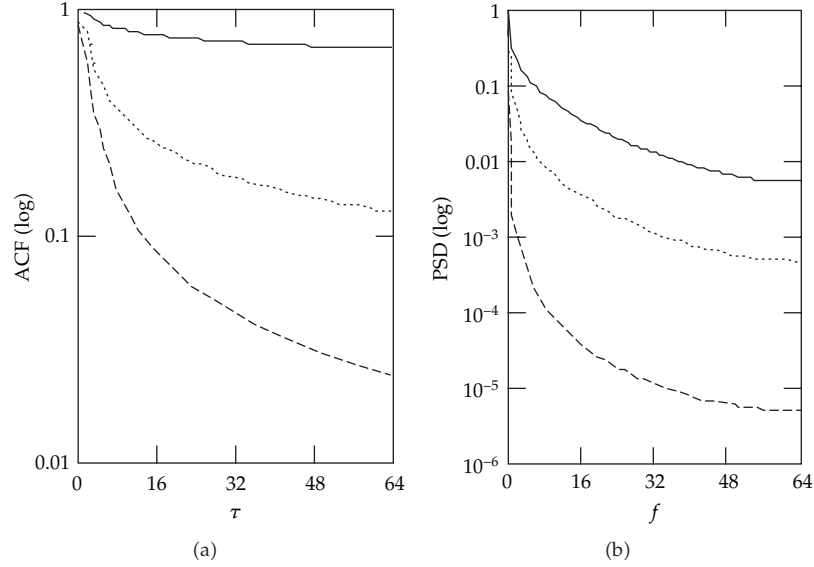


**Figure 1:** (a) ACF of CM process. Solid line for  $H = 0.95$ , dot line for  $H = 0.75$ , and dash line for  $H = 0.55$ . (b) Regularized PSD of CM process. Solid line for  $H = 0.55$ , dot line for  $H = 0.75$ , and dash line for  $H = 0.95$ .

### 3. Application of the CM Model to a Set of Wind Speed Data

Wind speed plays a role in several areas of science and engineering, such as ocean physics, ocean engineering, wind engineering, and meteorology; see, for example, Massel [26], Li [27]. In this section, we shall apply the CM process to the ACF and the PSD of the wind speed (m/s) observed at the Station LKWF1 (Lake Worth, Florida) [28]. The data are available from the category of Standard Meteorological [29]. They were averaged over an eight-minute period for buoys and a two-minute period for land stations (Gilhousen [30, 31]).

Denote the data series by  $x_{\text{yyyy}}(t)$ , where yyyy stands for the index of year. Denote  $C_{\text{yyyy}}(k)$  ( $k = 0, 1, \dots$ ) and  $S_{\text{yyyy}}(f)$  as the measured ACF and the measured PSD in the year of yyyy, respectively. For instance,  $x_{2003}(t)$  and  $S_{2003}(f)$  represent the measured time series and the measured PSD at the station LKMF1 in 2003, respectively.

Note that the measured ACF and PSD are estimates of the true ACF and PSD. Therefore, a PSD or ACF estimation of wind speed should be reliable and traceable. For that reason, we estimated the ACFs and the PSDs with the recognized instrument Solartron 1200 Real Time Signal Processor [32]. Practically, an ACF or PSD is estimated on a block-by-block basis by averaging PSD (or ACF) estimates of blocks of data with a certain window weight function for the sake of variance reduction (Mitra and Kaiser [33]). Let  $B$  be the block size and  $M$  be the average count, respectively. We sectioned the data in the nonoverlapping case. On Solartron 1200 Real Time Signal Processor, a Hanning widow was set.  $M$  is selected such that  $0 < [L - (B \times M)] < B$ , where  $L$  is the total length of  $x_{\text{yyyy}}(t)$ . Table 1 lists the measured data and the settings for the PSD (or ACF) estimation, where  $B = 128$ .

The key parameter in the CM model is  $H$ . The literature regarding  $H$  estimation is affluent. Commonly used estimators of  $H$  are  $R/S$  analysis, maximum likelihood method, variogram-based methods, box-counting, detrended fluctuation analysis, spectrum regression, and correlation regression; see, for example, [1, 2, 34–36]. In this paper, we use the

**Table 1:** Measured data at LKWF1, the settings for signal processing, and the modeling results.

Series	Record date and time	$L$	$M$	$b$	$H$	MSE
$x_{1984}(t)$	19:00, 20 Jul–23:00, 31 Dec. 1984	3175	24	0.262	0.869	$9.861 \times 10^{-4}$
$x_{1985}(t)$	0:00, 1 Jan.–23:00, 31 Dec. 1985	7848	61	0.342	0.829	$8.353 \times 10^{-4}$
$x_{1986}(t)$	0:00, 1 Jan.–23:00, 31 Dec. 1986	8376	65	0.320	0.840	$7.509 \times 10^{-4}$
$x_{1987}(t)$	0:00, 1 Jan.–23:00, 31 Dec. 1987	8682	67	0.361	0.819	$1.170 \times 10^{-4}$
$x_{1988}(t)$	1:00, 1 Jan.–23:00, 31 Dec. 1988	8598	67	0.338	0.831	$9.666 \times 10^{-4}$
$x_{1989}(t)$	0:00, 1 Jan.–23:00, 31 Dec. 1989	8694	67	0.330	0.850	$8.300 \times 10^{-4}$
$x_{1990}(t)$	0:00, 1 Jan.–23:00, 31 Dec. 1990	8604	67	0.300	0.850	$7.778 \times 10^{-4}$
$x_{1991}(t)$	0:00, 1 Jan.–18:00, 31 Oct. 1990	7273	56	0.304	0.848	$6.964 \times 10^{-4}$
$x_{1993}(t)$	11:00, 20 Dec.–23:00, 31 Dec. 1993	277	2	0.276	0.862	$1.952 \times 10^{-3}$
$x_{1994}(t)$	0:00, 1 Jan.–18:00, 31 Oct. 1994	8571	66	0.332	0.834	$7.433 \times 10^{-4}$
$x_{1995}(t)$	0:00, 1 Jan.–18:00, 31 Oct. 1995	8503	66	0.302	0.849	$6.950 \times 10^{-4}$
$x_{1996}(t)$	0:00, 1 Jan.–23:00, 31 Dec. 1996	8112	63	0.299	0.850	$6.459 \times 10^{-4}$
$x_{1997}(t)$	0:00, 1 Jan.–23:00, 31 Dec. 1997	8184	63	0.318	0.841	$6.242 \times 10^{-4}$
$x_{1998}(t)$	0:00, 1 Jan.–23:00, 31 Dec. 1998	8784	68	0.326	0.837	$8.667 \times 10^{-4}$
$x_{1999}(t)$	0:00, 1 Jan.–23:00, 31 Dec. 1999	8760	68	0.310	0.845	$6.162 \times 10^{-4}$
$x_{2000}(t)$	0:00, 1 Jan.–17:00, 26 Feb. 2000	8072	63	0.311	0.844	$6.643 \times 10^{-4}$
$x_{2001}(t)$	17:00, 8 Aug.–23:00, 31 Dec. 2001	8760	68	0.310	0.845	$8.636 \times 10^{-4}$
$x_{2002}(t)$	0:00, 1 Jan.–23:00, 31 Dec. 2002	8760	68	0.293	0.853	$7.555 \times 10^{-4}$
$x_{2003}(t)$	0:00, 1 Jan.–23:00, 31 Dec. 2003	8650	67	0.300	0.850	$9.175 \times 10^{-4}$
$x_{2004}(t)$	0:00, 1 Jan.–14:00, 5 Oct. 2004	6650	52	0.330	0.835	$8.911 \times 10^{-4}$
$x_{2006}(t)$	0:00, 31 May–23:00, 31 Dec. 2006	5149	40	0.353	0.824	$1.169 \times 10^{-4}$

regression method to estimate  $H$ . The following uses the PSD regression to estimate  $H$  that is equivalent to the ACF regression owing to the Wiener-Khinchin theorem.

After obtaining a measured PSD  $S_{yyyy}(f)$ , we input it into a PC to do the data fitting with the theoretic PSD  $S_0(f)$  by using the least square fitting. Denote the cost function by

$$J(b) = \frac{2}{B} \sum_k [S_0(f) - S_{yyyy}(f)]^2, \quad (3.1)$$

where  $S_{yyyy}(f)$  is in the normalized case. The derivative of  $J$  with respect to  $b$ , which will be zero when  $J$  is minimum, yields the estimate  $b$  or equivalently the  $H$  estimate, which is the solution of  $dJ/db = 0$ .

Figures 2(a) and 2(b) indicate 2 series  $x_{1990}(t)$  and  $x_{2004}(t)$  at the station LKWF1, respectively. Each starts from the first data point to the 256th one, that is, about the first 10 days of data. The data fitting between the measured PSD and the theoretical one for each series is demonstrated in Figures 3(a) and 3(b). By the least square fitting, we have the estimated  $H$  values 0.850, 0.835 for  $x_{1990}(t)$ ,  $x_{2004}(t)$ , respectively (Table 1). The MSEs for the data fitting of the most series are in the order of magnitude of  $10^{-4}$  except that  $x_{1993}(t)$  has the MSE in the order of magnitude of  $10^{-3}$ , likely due to the too short series (Table 1). Figures 3(c) and 3(d) illustrate the data fitting for  $C_{1990}(k)$  and  $C_{2004}(k)$ , respectively. Hence, from the modeling results, we experimentally infer that the CM model well fits the wind speed observed. The  $H$  estimates for all series are summarized in Table 1, exhibiting the LRD property of wind speed due to  $0.5 < H < 1$ .

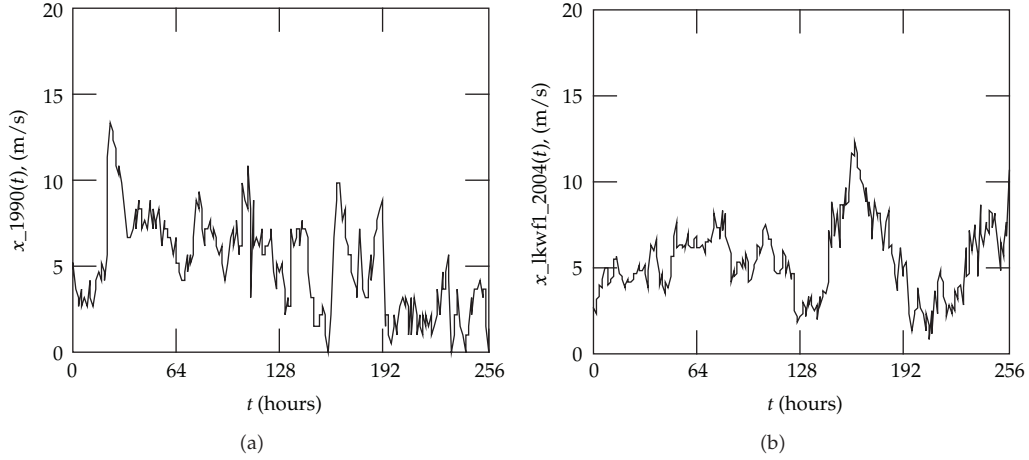


Figure 2: Measured data at LKWF1. (a)  $x_{1990}(t)$ . (b)  $x_{2004}(t)$ .

#### 4. Discussions

In order to exhibit that the present CM process is a novel model of wind speed, we brief some results with respect to several models of wind speed, which are used in wind engineering.

In the aspect of PSD of wind speed, Davenport [37] proposed a well-known form of the normalized PSD given by

$$\frac{f S_{\text{Dav}}(f)}{u_f^2} = 4 \frac{u^2}{(1 + u^2)^{4/3}}, \quad u = \frac{1200n}{z}, \quad (4.1)$$

where  $f$  is the frequency (Hz),  $u_f$  friction velocity ( $\text{ms}^{-1}$ ), and  $n$  is the normalized frequency ( $fz/U$  (10 m)), where  $U$  (10 m) is the mean wind speed ( $\text{ms}^{-1}$ ) measured at height 10 m,  $U(z)$  mean wind speed ( $\text{ms}^{-1}$ ) measured at height  $z$ . Kaimal et al. [38] introduced the following PSD:

$$\frac{f S_{\text{Kai}}(f)}{u_f^2} = \frac{100n}{(0.44 + 33n)^{5/3}}. \quad (4.2)$$

Antoniou et al. [39] discussed the one expressed by

$$\frac{f S_{\text{Ant}}(f)}{u_f^2} = \frac{18n}{(0.44 + 5n)^{5/3}}. \quad (4.3)$$

For this class of spectra, Hiriart et al. [40] gave a general form written by

$$\frac{f S_{\text{Hir}}(f)}{u_f^2} = \frac{4n^2}{(1 + n^2)^{2\gamma}}, \quad \gamma > 0, \quad (4.4)$$

which generalized the Davenport PSD form by using the spectral index  $\gamma$ .

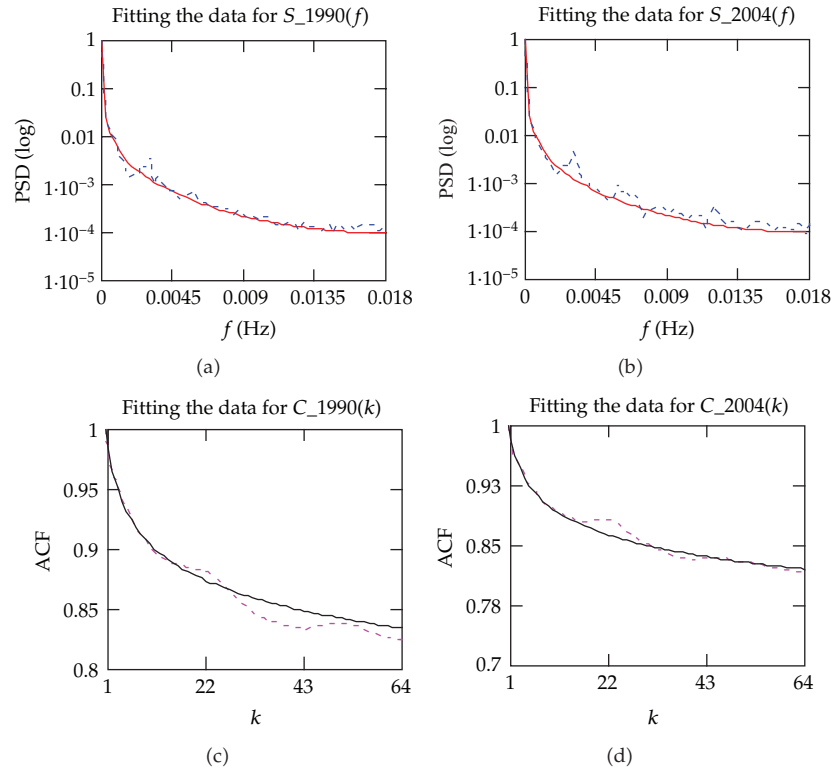


**Figure 3:** Modeling demonstrations. Solid line: theoretic PSD/ACF. Dot line: measured PSD/ACF. (a) Fitting the data for  $S_{1990}(f)$ . (b) Fitting the data for  $S_{2004}(f)$ . (c) Fitting the data for  $C_{1990}(k)$ . (d) Fitting the data for  $C_{2004}(k)$ .

The spectra mentioned above, including the Hojstrup-type PSD [41], are finite near the origin. Therefore, the inverse Fourier transforms of those PSDs are summable [42]. Hence, they are PSDs of processes with SRD. Though the models discussed in [37–41] are of SRD, the slow-decayed ACF of wind speed (slower than an exponential-type function) was noticed as can be seen from Brett and Tuller [43, abstract section] that is actually the  $1/f$  noise behavior of a time series [42]. Recently, fractal descriptions of wind speed were reported (Kavasseri and Nagarajan [44, 45], Santhanam and Kantz [46]). Nevertheless, the closed form of either ACF or PSD of wind speed in the LRD case is rarely seen, to the best of our knowledge. Consequently, different from the models commonly used in the field, the present CM model provides a closed form of either ACF or PSD of wind speed with LRD.

The CM model (2.4) differs from those, that is, (4.1)–(4.4), conventionally used in wind engineering. However, it must be noting that our research used the data measured above sea surface while others, we mean those discussed in [37–40], utilized data recorded above ground. For instance, the data Davenport utilized were measured using cup anemometers mounted at 12.2 m, 64 m, and 153 m on a radio mast [37, page 195]. Kaimal et al. studied the data measured on a 32 m tower [38, page 563], and Hiriart et al. investigated the data for the purpose of selecting the site of the new Mexican Optical-Infrared Telescope (TIM) installed at the Sierra of San Pedro Martir [40, page 213]. One thing worth keeping in mind is that the present model in this paper never implies that one model may be superior to another. More precisely, we consider that a model may be site dependent.

Note that the CM process is LRD. Thus, its PSD follows power law; see (2.6). In fact, any random functions that are LRD have power-law-type PSDs [15]. From that point of view, consequently, one thing in common for different models described by say (2.6), (4.1)–(4.4) is that their PSDs all follow power laws, which implies that all may be explained from the point of view of fractal time series [42, 47].

The main point in this paper is to exhibit the possible LRD property of sea surface wind speed in addition to its CM model. The research is a beginning in this regard. The other properties of sea surface wind speed, such as fractal structure, periodicity, probability distributions, and complex dynamics [48–60], remain to be studied from that point of view in the future.

## 5. Conclusions

We have studied the Cauchy-Matern process with LRD. The closed form of its PSD has been obtained. We also consider its application to wind speed modeling in the Lake Worth, Florida. The modeling results are satisfactory, suggesting a new model of wind speed. Though the climatologic study of wind speed is in general site dependent, one thing in common for different models appears that PSDs of the different models all are of power-law type.

## Acknowledgments

This work was supported in part by the 973 Plan under the Project Grant no. 2011CB302800, and by the National Natural Science Foundation of China under the Project Grant nos. 61272402, 61070214, and 60873264. S. C. Lim would like to thank the Malaysian Ministry of Science, Technology and Innovation for the support under its Brain Gain Malaysia (Back to Lab) Program. The National Data Buoy Center is highly appreciated for their measurements of wind speed data, which make our research possible.

## References

- [1] B. B. Mandelbrot, *Gaussian Self-Affinity and Fractals*, Springer, 2001.
- [2] J. Beran, *Statistics for Long-Memory Processes*, Chapman & Hall, 1994.
- [3] B. B. Mandelbrot and J. W. van Ness, "Fractional Brownian motions, fractional noises and applications," *SIAM Review*, vol. 10, no. 4, pp. 422–437, 1968.
- [4] A. J. Lawrance and N. T. Kottegoda, "Stochastic modelling of riverflow time series," *Journal of the Royal Statistical Society A*, vol. 140, no. 1, pp. 1–47, 1977.
- [5] L. M. Kaplan and C.-C. J. Kuo, "Extending self-similarity for fractional Brownian motion," *IEEE Transactions on Signal Processing*, vol. 42, no. 12, pp. 3526–3530, 1994.
- [6] R. J. Martin and A. M. Walker, "A power-law model and other models for long-range dependence," *Journal of Applied Probability*, vol. 34, no. 3, pp. 657–670, 1997.
- [7] C. W. J. Granger and Z. Ding, "Varieties of long memory models," *Journal of Econometrics*, vol. 73, no. 1, pp. 61–77, 1996.
- [8] J. Beran, "Fitting long-memory models by generalized linear regression," *Biometrika*, vol. 80, no. 4, pp. 817–822, 1993.
- [9] B. Yazici and R. L. Kashyap, "A class of second-order stationary self-similar processes for  $1/f$  phenomena," *IEEE Transactions on Signal Processing*, vol. 45, no. 2, pp. 396–410, 1997.
- [10] M. Li, W. Jia, and W. Zhao, "Correlation form of timestamp increment sequences of self-similar traffic on Ethernet," *Electronics Letters*, vol. 36, no. 19, pp. 1668–1669, 2000.
- [11] J.-P. Chilès and P. Delfiner, *Geostatistics, Modeling Spatial Uncertainty*, John Wiley & Sons, 1999.
- [12] B. Matérn, *Spatial Variation*, vol. 36 of *Lecture Notes in Statistics*, Springer, 2nd edition, 1980.
- [13] A. M. Yaglom, *Correlation Theory of Stationary and Related Random Functions*, vol. 1 of *Basic Results*, Springer, New York, NY, USA, 1987.

- [14] G. A. Korn and T. M. Korn, *Mathematical Handbook For Scientists and Engineers*, McGraw-Hill, 1961.
- [15] M. Li and W. Zhao, "On  $1/f$  noise," *Mathematical Problems in Engineering*, vol. 2012, Article ID 673648, 23 pages, 2012.
- [16] J. Bertoin, "The convex minorant of the cauchy process," *Electronic Communications in Probability*, vol. 5, pp. 51–55, 2000.
- [17] P. A. Zanzotto, "On stochastic differential equations driven by a cauchy process and other stable Lévy motions," *The Annals of Probability*, vol. 30, no. 2, pp. 802–825, 2002.
- [18] P. Garbaczewski and R. Olkiewicz, "Ornstein-Uhlenbeck-Cauchy process," *Journal of Mathematical Physics*, vol. 41, no. 10, pp. 6843–6860, 2000.
- [19] I. M. Gelfand and K. Vilenkin, *Generalized Functions*, vol. 1, Academic Press, New York, NY, USA, 1964.
- [20] I. S. Gradshteyn and I. M. Ryzhik, *Table of Integrals, Series, and Products*, Elsevier, Singapore, 7th edition, 2007, Edited by: A. Jeffrey and D. Zwillinger.
- [21] P. Todorovic, *An Introduction to Stochastic Processes and Their Applications*, Springer, New York, NY, USA, 1992.
- [22] S. C. Lim and S. V. Muniandy, "Generalized Ornstein-Uhlenbeck processes and associated self-similar processes," *Journal of Physics A*, vol. 36, no. 14, pp. 3961–3982, 2003.
- [23] R. L. Wolpert and M. S. Taqqu, "Fractional Ornstein-Uhlenbeck Lévy processes and the Telecom process: upstairs and downstairs," *Signal Processing*, vol. 85, no. 8, pp. 1523–1545, 2005.
- [24] J. W. Lamperti, "Semi-stable stochastic processes," *Transactions of the American Mathematical Society*, vol. 104, no. 1, pp. 62–78, 1962.
- [25] P. Flandrin, P. Borgnat, and P.-O. Amblard, *From Stationarity to Self-Similarity, and Back: Variations on the Lamperti Transformation*, vol. 621, Springer, 2003, Edited by: G. Ra-ganjaran and M. Ding.
- [26] S. R. Massel, *Ocean Surface Waves: Their Physics and Prediction*, World Scientific, 1997.
- [27] M. Li, "A method for requiring block size for spectrum measurement of ocean surface waves," *IEEE Transactions on Instrumentation and Measurement*, vol. 55, no. 6, pp. 2207–2215, 2006.
- [28] [http://www.ndbc.noaa.gov/station\\_page.php?station=lkwf1](http://www.ndbc.noaa.gov/station_page.php?station=lkwf1).
- [29] [http://www.ndbc.noaa.gov/historical\\_data.shtml](http://www.ndbc.noaa.gov/historical_data.shtml).
- [30] D. B. Gilhousen, "A field evaluation of NDBC moored buoy winds," *Journal of Atmospheric and Oceanic Technology*, vol. 4, no. 1, pp. 94–104, 1987.
- [31] <http://www.ndbc.noaa.gov/wndav.shtml>.
- [32] Schlumberger Electronics Ltd, *1200 Real Time Signal Processor Operating Manual*, London, UK, 1983.
- [33] S. K. Mitra and J. F. Kaiser, *Handbook For Digital Signal Processing*, John Wiley & Sons, 1993.
- [34] M. Li, "Modeling autocorrelation functions of long-range dependent teletraffic series based on optimal approximation in Hilbert space—a further study," *Applied Mathematical Modelling*, vol. 31, no. 3, pp. 625–631, 2007.
- [35] J. W. Kantelhardt, E. Koscielny-Bunde, H. H. A. Rego, S. Havlin, and A. Bunde, "Detecting long-range correlations with detrended fluctuation analysis," *Physica A*, vol. 295, no. 3-4, pp. 441–454, 2001.
- [36] M. S. Taqqu, V. Teverovsky, and W. Willinger, "Estimators for long-range dependence: an empirical study," *Fractals*, vol. 3, no. 4, pp. 785–798, 1995.
- [37] A. G. Davenport, "The spectrum of horizontal gustiness near the ground in high winds," *Quarterly Journal of the Royal Meteorological Society*, vol. 87, no. 372, pp. 194–211, 1961.
- [38] J. C. Kaimal, J. C. Wyngaard, Y. Izumi, and O. R. Coté, "Spectral characteristics of surface-layer turbulence," *Quarterly Journal of the Royal Meteorological Society*, vol. 98, no. 417, pp. 563–589, 1972.
- [39] I. Antoniou, D. Asimakopoulos, A. Fragoulis, A. Kotronaros, D. P. Lalas, and I. Panourgias, "Turbulence measurements on top of a steep hill," *Journal of Wind Engineering and Industrial Aerodynamics*, vol. 39, no. 1–3, pp. 343–355, 1992.
- [40] D. Hiriart, J. L. Ochoa, and B. García, "Wind power spectrum measured at the San Pedro Mártir Sierra," *Revista Mexicana de Astronomia y Astrofisica*, vol. 37, no. 2, pp. 213–220, 2001.
- [41] J. Hojstrup, S. E. Larsen, and P. H. Madsen, "Power spectra of horizontal wind components in the neutral atmospheric boundary layer," in *Proceedings of the 9th Symposium of Turbulence and Diffusion*, N. O. Jensen, L. Kristiansen, and S. E. Larsen, Eds., pp. 305–308, American Meteorology Society, 1990.
- [42] M. de O. Santos, T. Stosic, and B. D. Stosic, "Long-term correlations in hourly wind speed records in Pernambuco, Brazil," *Physica A*, vol. 391, no. 4, pp. 1546–1552, 2012.
- [43] A. C. Brett and S. E. Tuller, "The autocorrelation of hourly wind speed observations," *Journal of Applied Meteorology*, vol. 30, no. 6, pp. 823–833, 1991.
- [44] R. G. Kavasseri and R. Nagarajan, "A multifractal description of wind speed records," *Chaos, Solitons & Fractals*, vol. 24, no. 1, pp. 165–173, 2005.

- [45] R. G. Kavasseri and R. Nagarajan, "A qualitative description of boundary layer wind speed records," *Fluctuation & Noise Letters*, vol. 6, no. 2, pp. L201–L213, 2006.
- [46] M. S. Santhanam and H. Kantz, "Long-range correlations and rare events in boundary layer wind fields," *Physica A*, vol. 345, no. 3-4, pp. 713–721, 2005.
- [47] M. Li, Y.-Q. Chen, J.-Y. Li, and W. Zhao, "Hölder scales of sea level," *Mathematical Problems in Engineering*, vol. 2012, Article ID 863707, 22 pages, 2012.
- [48] C. Cattani, E. Laserra, and I. Bochicchio, "Simplicial approach to fractal structures," *Mathematical Problems in Engineering*, vol. 2012, Article ID 958101, 21 pages, 2012.
- [49] C. Cattani, "Fractals and hidden symmetries in DNA," *Mathematical Problems in Engineering*, vol. 2010, Article ID 507056, 31 pages, 2010.
- [50] X. A. Yin, X. H. Yang, and Z. F. Yang, "Using the R/S method to determine the periodicity of time series," *Chaos, Solitons & Fractals*, vol. 39, no. 2, pp. 731–745, 2009.
- [51] X.-H. Yang and Y.-Q. Li, "DNA optimization threshold autoregressive prediction model and its application in ice condition time series," *Mathematical Problems in Engineering*, vol. 2012, Article ID 191902, 10 pages, 2012.
- [52] C. Toma, "Advanced signal processing and command synthesis for memory-limited complex systems," *Mathematical Problems in Engineering*, vol. 2012, Article ID 927821, 13 pages, 2012.
- [53] E. G. Bakhoun and C. Toma, "Specific mathematical aspects of dynamics generated by coherence functions," *Mathematical Problems in Engineering*, vol. 2011, Article ID 436198, 10 pages, 2011.
- [54] E. G. Bakhoun and C. Toma, "Mathematical transform of traveling-wave equations and phase aspects of quantum interaction," *Mathematical Problems in Engineering*, vol. 2010, Article ID 695208, 15 pages, 2010.
- [55] R. S. A. R. Abdullah, M. F. A. Rasid, and M. K. Mohamed, "Improvement in detection with forward scattering radar," *Science China Information Sciences*, vol. 54, no. 12, pp. 2660–2672, 2011.
- [56] T. J. Koo, R. Q. Li, M. M. Quottrup, C. A. Clifton, R. Izadi-Zamanabadi, and T. Bak, "A framework for multi-robot motion planning from temporal logic specifications," *Science China Information Sciences*, vol. 55, no. 7, pp. 1675–1692, 2012.
- [57] C. Z. Fan, Y. H. Liu, B. Q. Song, and D. X. Zhou, "Dynamic visual servoing of a small scale autonomous helicopter in uncalibrated environments," *Science China Information Sciences*, vol. 54, no. 9, pp. 1855–1867, 2011.
- [58] J. Gavalda, J. Massons, J. Camps, and F. Díaz, "Statistical and spectral analysis of the wind regime in the area of Catalonia," *Theoretical and Applied Climatology*, vol. 46, no. 2-3, pp. 143–152, 1992.
- [59] E. G. Pavia and J. J. O'Brien, "Weibull statistics of wind speed over the ocean," *Journal of Climate and Applied Meteorology*, vol. 25, no. 10, pp. 1324–1332, 1986.
- [60] P. Sorensen, A. D. Hansen, and P. A. C. Rosas, "Wind models for simulation of power fluctuations from wind farms," *Journal of Wind Engineering and Industrial Aerodynamics*, vol. 90, no. 12–15, pp. 1381–1402, 2002.

## Research Article

# Hölder Scales of Sea Level

Ming Li,<sup>1,2</sup> YangQuan Chen,<sup>3</sup> Jia-Yue Li,<sup>4</sup> and Wei Zhao<sup>1</sup>

<sup>1</sup> Department of Computer and Information Science, University of Macau, Avenida Padre Tomas Pereira, Taipa, Macau, Macau

<sup>2</sup> School of Information Science and Technology, East China Normal University, Shanghai 200241, China

<sup>3</sup> School of Engineering, University of California, Merced, CA 95343, USA

<sup>4</sup> College of Resources and Environmental Science, East China Normal University, Shanghai 200241, China

Correspondence should be addressed to Ming Li, ming.lihk@yahoo.com

Received 2 November 2012; Accepted 21 November 2012

Academic Editor: Sheng-yong Chen

Copyright © 2012 Ming Li et al. This is an open access article distributed under the Creative Commons Attribution License, which permits unrestricted use, distribution, and reproduction in any medium, provided the original work is properly cited.

The statistics of sea level is essential in the field of geosciences, ranging from ocean dynamics to climates. The fractal properties of sea level, such as long-range dependence (LRD) or long memory,  $1/f$  noise behavior, and self-similarity (SS), are known. However, the description of its multiscale behavior as well as local roughness with the Hölder exponent  $h(t)$  from a view of multifractional Brownian motion (mBm) is rarely reported, to the best of our knowledge. In this research, we will exhibit that there is the multiscale property of sea level based on  $h(t)$ s of sea level data recorded by the National Data Buoy Center (NDBC) at six stations in the Florida and Eastern Gulf of Mexico. The contributions of this paper are twofold as follows. (i) Hölder exponent of sea level may not change with time considerably at small time scale, for example, daily time scale, but it varies significantly at large time scale, such as at monthly time scale. (ii) The dispersion of the Hölder exponents of sea level may be different at different stations. This implies that the Hölder roughness of sea level may be spatial dependent.

## 1. Introduction

The study of sea level fluctuations plays a role in geosciences [1–3]. There are two categories of time scales of sea level. One is for yearly data with time scales in one yr, or 10 yr, or more; see, for example, [4–16]. The other is about data with time scales hourly, daily, weekly, or monthly; see, for example, [17–39]. The former generally relates to the study of trend of relative mean sea level with respect to global and Earth or planetary changes, for example, in the field of climates, while the latter is usually associated with the research of local dynamics of sea level in the aspects of navigations, coastal engineering, tide power production, ship design, and so forth. Our research uses the hourly sea level data recorded by NDBC [40].

Since the pioneering work of Hurst on time series with long-range dependence (LRD) is observed in the Nile Basin [41], the LRD property of time series in geosciences has been

widely observed; see, for example, [42–59]. By LRD, one means that the covariance function  $C(\tau)$  of time series  $x(t)$  decays so slowly such that

$$\int_0^{\infty} C(\tau) d\tau = \infty, \quad (1.1)$$

where  $\tau$  is time lag and  $C(\tau) = E[x(t + \tau)x(t)]$ . Therefore, LRD is a global property of time series [60–66].

In addition to LRD, there is another essential property of processes in geosciences, called self-similarity (SS); see, for example, [67–84]. By SS, we mean that a random function  $x(t)$  satisfies the property given by

$$x(t) \triangleq a^H x(at), \quad \forall a > 0, t > 0, \quad (1.2)$$

where  $\triangleq$  is the equality in distribution,  $H \in (0, 1)$  is the Hurst parameter that measures SS, and  $a$  is a scale [61, 83–86]. Note that the term SS implies the roughness or irregularity of a random function [86]. If  $x(t)$  satisfies (1.2), it is globally self-similar. That is, its irregularity characterized by  $H$  keeps the same for all  $t > 0$  [87], corresponding the case of monofractal [88, 89].

Since the global SS implies the same value of  $H$  for all  $t$ , it may be too restrictive to describe real data in engineering and sciences to use a monofractal model. Therefore, multifractal models are desired in various fields of sciences and engineering; see, for example, [85–92] and references therein, including those in geosciences; see, for example, [93–110], just citing a few. From a view of multifractal, a random function that is not self-similar may be of local self-similarity (LSS).

There are several ways of describing multifractality of a random function based on various definitions of dimensions, such as the Minkowski dimension, the Rényi dimension, the Hausdorff dimension, the packing dimension, the box-counting dimension, and the correlation dimension [86, 89, 90, 111–114]. In this paper, we adopt the Hölder exponent  $0 < h(t) < 1$  in multifractional Brownian motion (mBm) introduced by Peltier and Levy-Vehel [115]. Taking into account  $h(t)$  in mBm, therefore, one may use the following:

$$x(t) \triangleq a^{h(t)} x(at), \quad \forall a > 0, t > 0, \quad (1.3)$$

to characterize the LSS property of a locally self-similar random function  $x(t)$  on a point-by-point basis. We call the LSS or local roughness characterized by  $h(t)$  the Hölder roughness in this paper. The applications of  $h(t)$  attract increasing interests of researchers in sciences and technologies, ranging from teletraffic to geophysics; see, for example, [116–134], simply mentioning a few.

This paper aims at investigating the Hölder multiscales (Hölder scales for short) of sea level. By Hölder scales, we mean the time scales described by the Hölder exponents in mBm. The contributions of this paper are in two aspects. On the one hand, we will reveal that variations of  $h(t)$  of sea level may be indistinctively at small time scale, for example, daily time scale, but  $h(t)$  of sea level varies significantly at large time scale, such as at monthly time scale. On the other hand, we will exhibit that the dispersion of the Hölder exponents of sea level may usually be spatial dependent.

**Table 1:** Measured data at LKWF1.

Series name	Record date and time	$L$ (record length)
$x_{\text{lkwf1}_{1996}}(t)$	0:00, 1 Jan.–23:00, 31 Dec. 1996	8208
$x_{\text{lkwf1}_{1997}}(t)$	0:00, 1 Jan.–23:00, 31 Dec. 1997	7776
$x_{\text{lkwf1}_{1998}}(t)$	0:00, 1 Jan.–23:00, 31 Dec. 1998	8736
$x_{\text{lkwf1}_{1999}}(t)$	0:00, 1 Jan.–23:00, 31 Dec. 1999	8760
$x_{\text{lkwf1}_{2000}}(t)$	0:00, 1 Jan.–17:00, 26 Feb. 2000	1362
$x_{\text{lkwf1}_{2001}}(t)$	17:00, 8 Aug.–23:00, 31 Dec. 2001	2972
$x_{\text{lkwf1}_{2002}}(t)$	0:00, 1 Jan.–23:00, 31 Dec. 2002	8740
$x_{\text{lkwf1}_{2003}}(t)$	0:00, 1 Jan.–23:00, 31 Dec. 2003	8582
$x_{\text{lkwf1}_{2004}}(t)$	0:00, 1 Jan.–14:00, 5 Oct. 2004	6655

The remaining paper is organized as follows. Data used in this research are briefed in Section 2. The method for describing the Hölder exponent in mBm is explained in Section 3. Results of data processing and discussions are given in Section 4, which is followed by conclusions.

## 2. Data

NDBC is a part of the US National Weather Service (NWS) [135]. It provides scientists with data for their scientific research, including significant wave height and water level [136]. We use the data measured at stations named LKWF1, LONF1, SAUF1, SMKUF1, SPGF1, and VENF1, respectively. In terms of the names of measurement stations, LKWF1 implies the station at Lake Worth, FL [137]; the station LONF1 is the one at Long Key, FL [138]; the station SAUF1 is at St. Augustine, FL [139]; SMKUF1 is the station at Sombrero Key, FL [140]; SPGF1 is at Settlement Point, GBI [141]; and VENF1 is at Venice, FL [142]. They are located in the Florida and Eastern Gulf of Mexico. The data are under the directory of Water Level, which are publicly accessible [143], referring Gilhousen [144] as an instance of research using the data by NDBC.

All data were hourly recorded with ten separate devices indexed by  $TGn$  ( $n = 01, 02, \dots, 10$ ). Without losing generality, this research utilizes the data from the device  $TG01$ . Denote the data series by  $x_{s\_yyyy}(t)$ , where  $s$  is the name of the measurement station and  $yyyy$  stands for the index of year. Denote by  $h_{s\_yyyy}(t)$  its corresponding  $h(t)$  at the station  $s$  in the year of  $yyyy$ . For example,  $x_{\text{lkwf1}_{2002}}(t)$  and  $h_{\text{lkwf1}_{2002}}(t)$ , respectively, represent the measured sea level time series and its  $h(t)$  at the station LKWF1 in 2002.

If the recorded data are labeled by 99, they are taken as outliers, which are not involved in the computations. In this case, they are replaced with the mean of that series. NDBC suggests that 10 ft should be subtracted from every level series  $x_{s\_yyyy}(t)$  [145]. By taking into account this suggestion in the computation of  $h(t)$ , we modify  $x_{s\_yyyy}(t)$  by subtracting 10 ft and denote  $y_{s\_yyyy}(t)$  modified data of sea level. That is,

$$y_{s\_yyyy}(t) = x_{s\_yyyy}(t) - 10. \quad (2.1)$$

Tables 1, 2, 3, 4, 5 and 6 list those data.

**Table 2:** Measured data at LONF1.

Series name	Record date and time	<i>L</i> (record length)
<i>x_lonf1_1998(t)</i>	0:00, 3 Nov.–23:00, 31 Dec. 1998	1416
<i>x_lonf1_1999(t)</i>	0:00, 1 Jan.–21:00, 31 Dec. 1999	8757
<i>x_lonf1_2000(t)</i>	0:00, 1 Jan.–23:00, 31 Dec. 2000	8484
<i>x_lonf1_2001(t)</i>	0:00, 1 Jan.–23:00, 31 Dec. 2001	8760
<i>x_lonf1_2002(t)</i>	0:00, 1 Jan.–23:00, 31 Dec. 2002	8760
<i>x_lonf1_2003(t)</i>	0:00, 1 Jan.–23:00, 31 Dec. 2003	8697
<i>x_lonf1_2004(t)</i>	0:00, 1 Jan.–23:00, 31 Dec. 2004	8758
<i>x_lonf1_2005(t)</i>	0:00, 1 Jan.–23:00, 31 Dec. 2005	8750
<i>x_lonf1_2006(t)</i>	0:00, 1 Jan.–23:00, 31 Dec. 2006	8735
<i>x_lonf1_2007(t)</i>	0:00, 1 Jan.–23:00, 31 Dec. 2007	8692
<i>x_lonf1_2008(t)</i>	0:00, 1 Jan.–21:00, 19 Jan. 2008	444

**Table 3:** Measured data at SAUF1.

Series name	Record date and time	<i>L</i> (record length)
<i>x_sauf1_1996(t)</i>	0:00, 1 Jan.–14:00, 10 Aug. 1996	5511
<i>x_sauf1_1997(t)</i>	0:00, 25 Feb.–23:00, 31 Dec. 1997	6240
<i>x_sauf1_1998(t)</i>	0:00, 1 Jan.–23:00, 31 Dec. 1998	8736
<i>x_sauf1_1999(t)</i>	0:00, 1 Jan.–23:00, 31 Dec. 1999	8136
<i>x_sauf1_2000(t)</i>	0:00, 1 Jan.–23:00, 31 Dec. 2000	8715
<i>x_sauf1_2001(t)</i>	0:00, 1 Jan.–21:00, 31 Dec. 2001	8758
<i>x_sauf1_2002(t)</i>	20:00, 6 Feb.–23:00, 20 Aug. 2002	4684

**Table 4:** Measured data at SMKF1.

Series name	Record date and time	<i>L</i> (record length)
<i>x_smkf1_1998(t)</i>	0:00, 3 Nov.–23:00, 31 Dec. 1998	1416
<i>x_smkf1_1999(t)</i>	0:00, 1 Jan.–23:00, 31 Dec. 1999	7775
<i>x_smkf1_2000(t)</i>	0:00, 1 Aug.–23:00, 31 Dec. 2000	3542
<i>x_smkf1_2001(t)</i>	0:00, 1 Jan.–23:00, 31 Dec. 2001	5776
<i>x_smkf1_2002(t)</i>	0:00, 1 Jan.–23:00, 31 Dec. 2002	8742
<i>x_smkf1_2003(t)</i>	0:00, 1 Jan.–23:00, 31 Dec. 2003	5851
<i>x_smkf1_2004(t)</i>	0:00, 1 Jan.–23:00, 31 Dec. 2004	8439
<i>x_smkf1_2005(t)</i>	0:00, 1 Jan.–23:00, 31 Dec. 2005	8667
<i>x_smkf1_2006(t)</i>	0:00, 1 Jan.–23:00, 31 Dec. 2006	8623
<i>x_smkf1_2007(t)</i>	0:00, 1 Jan.–23:00, 31 Dec. 2007	8702
<i>x_smkf1_2008(t)</i>	0:00, 1 Jan.–23:00, 31 Dec. 2008	8679
<i>x_smkf1_2009(t)</i>	0:00, 1 Jan.–23:00, 31 Dec. 2009	8109
<i>x_smkf1_2010(t)</i>	0:00, 1 Jan.–23:00, 31 July 2010	5074
<i>x_smkf1_2011(t)</i>	0:00, 1 Jan.–23:00, 31 Dec. 2011	8759

**Table 5:** Measured data at SPGF1.

Series name	Record date and time	<i>L</i> (record length)
<i>x_spgf1_1996(t)</i>	0:00, 1 Jan.–23:00, 15 Dec. 1996	8616
<i>x_spg1_1997(t)</i>	0:00, 6 Mar.–23:00, 15 Dec. 1997	7080
<i>x_spg1_1998(t)</i>	0:00, 1 Jan.–23:00, 7 Jan. 1998	168

**Table 6:** Measured data at VENF1.

Series name	Record date and time	L (record length)
$x_{\text{venf1}_2002}(t)$	0:00, 1 Oct.–23:00, 31 Dec. 2002	2208
$x_{\text{ven1}_2003}(t)$	0:00, 1 Jan.–23:00, 31 Dec. 2003	8760
$x_{\text{ven1}_2004}(t)$	0:00, 1 Jan.–16:00, 7 Jan. 2004	634
$x_{\text{ven1}_2006}(t)$	14:00, 22 July–23:00, 31 Dec. 2006	3882
$x_{\text{ven1}_2007}(t)$	0:00, 1 Jan.–23:00, 31 Dec. 2007	8663
$x_{\text{ven1}_2008}(t)$	0:00, 1 Jan.–23:00, 31 Oct. 2008	7189

### 3. Methodology

Let  $B(t)$  be the standard Brownian motion. Then,  $B(t)$  satisfies the following properties.

- (i) The increments  $B(\tau + t) - B(t)$  are Gaussian.
- (ii)  $E[B(\tau + t) - B(t)] = 0$  and

$$\text{Var}[B(t + \tau) - B(t)] = \sigma^2 \tau, \quad (3.1)$$

where  $\sigma^2 = E\{[B(t + 1) - B(t)]^2\} = E\{[B(1) - B(0)]^2\} = E\{[B(1)]^2\}$ .

- (iii) In nonoverlapping intervals  $[t_1, t_2]$  and  $[t_3, t_4]$ , the increments  $B(t_4) - B(t_3)$  and  $B(t_2) - B(t_1)$  are independent.
- (iv)  $B(0) = 0$  and  $B(t)$  is continuous at  $t = 0$ .

Kolmogorov introduced a class of random functions the covariance function of which is now recognized as the one of fractional Brownian motion (fBm) [146, Theorem 6]. Note that, for a random function  $x(t)$ , the function  $f(\tau)$  expressed by

$$f(\tau) = \text{Var}[x(t + \tau) - x(t)] = E\{[x(t + \tau) - x(t)]^2\} \quad (3.2)$$

is termed serial variation function; see, for example, Matérn [147, page 51]. It is usually called variogram in geosciences [148–157]. In the field of fluid mechanics, it is named structure function [158–161]. Yaglom derived fBm based on the theory of structure functions [162]. In this paper, we use the fBm introduced by Bandelbrot and van Ness based on fractional calculus [163].

It is well known that  $B(t)$  is nondifferentiable in the domain of ordinary functions [164–166]. In the domain of generalized functions, however, it is differentiable [167, 168].

Denote the fBm by  $B_H(t)$ . Based on the Weyl's fractional derivative or integral [163], it is expressed by

$$B_H(t) - B_H(0) = \frac{1}{\Gamma(H + 1/2)} \left\{ \int_{-\infty}^0 [(t - u)^{H-0.5} - (-u)^{H-0.5}] dB(u) + \int_0^t (t - u)^{H-0.5} dB(u) \right\}. \quad (3.3)$$

If the first item on the right hand of (3.3) is taken as the zero-input response of the system that generates  $B_H(t)$  for  $t > 0$ , we may regard the fBm as the convolution of the impulse function  $t^{H-1/2}/\Gamma(H+1/2)$  and  $dB(t)/dt$  [169]. Therefore, (3.3) may be rewritten by

$$B_H(t) - B_H(0) = B^0(u) + \frac{t^{H-0.5}}{\Gamma(H+1/2)} * \frac{dB(t)}{dt}, \quad (3.4)$$

where  $*$  is the operator of convolution and

$$B^0(u) = \frac{1}{\Gamma(H+1/2)} \int_{-\infty}^0 \left[ (t-u)^{H-0.5} - (-u)^{H-0.5} \right] dB(t). \quad (3.5)$$

It may be interesting to note that  $t^{H-1/2}/\Gamma(H+1/2)$  is a special case of the operators of fractional order discussed by Mikusinski [170, Equation (59.1)].

The function  $B_H(t)$  has the following properties.

- (i)  $B_H(0) = 0$ .
- (ii) The increments  $B_H(t+t_0) - B_H(t_0)$  are Gaussian.
- (iii) Its structure function is given by

$$\text{Var}[B_H(t+\tau) - B_H(t)] = \sigma^2 \tau^{2H}, \quad (3.6)$$

where  $\sigma^2 = E\{[B_H(t+1) - B_H(t)]^2\} = E\{[B_H(1) - B_H(0)]^2\} = E\{[B_H(1)]^2\}$ .

In addition, it satisfies the self-similarity expressed by (1.2), which implies that  $B_H(t)$  is globally self-similar. Consequently, there is a limitation that its self-similarity or roughness keeps the same for all  $t > 0$ . To release such a limitation, one may adopt the tool of the mBm equipped with the Hölder exponent  $h(t)$ ; see, for example, [115, 119, 133]. In fact, the mBm is a generalization of fBm by replacing the Hurst parameter  $H$  in (3.3) with a continuous function  $h(t)$  that satisfies  $H : [0, \infty) \rightarrow (0, 1)$ ; see [87, 115–134, 171–182]. Denote the mBm by  $X(t)$ . Then,

$$X(t) = \frac{1}{\Gamma(h(t)+1/2)} \left\{ \begin{array}{l} \int_{-\infty}^0 \left[ (t-u)^{h(t)-0.5} - (-u)^{h(t)-0.5} \right] dB(u) \\ + \int_0^t (t-u)^{h(t)-0.5} dB(u) \end{array} \right\}. \quad (3.7)$$

Considering the local growth of the increment process of  $X(t)$ , one may write a sequence given by

$$S_k(j) = \frac{m}{N-1} \sum_{j=0}^{j+k} \left| X(i+1) - X(i) \right|, \quad 1 < k < N, \quad (3.8)$$

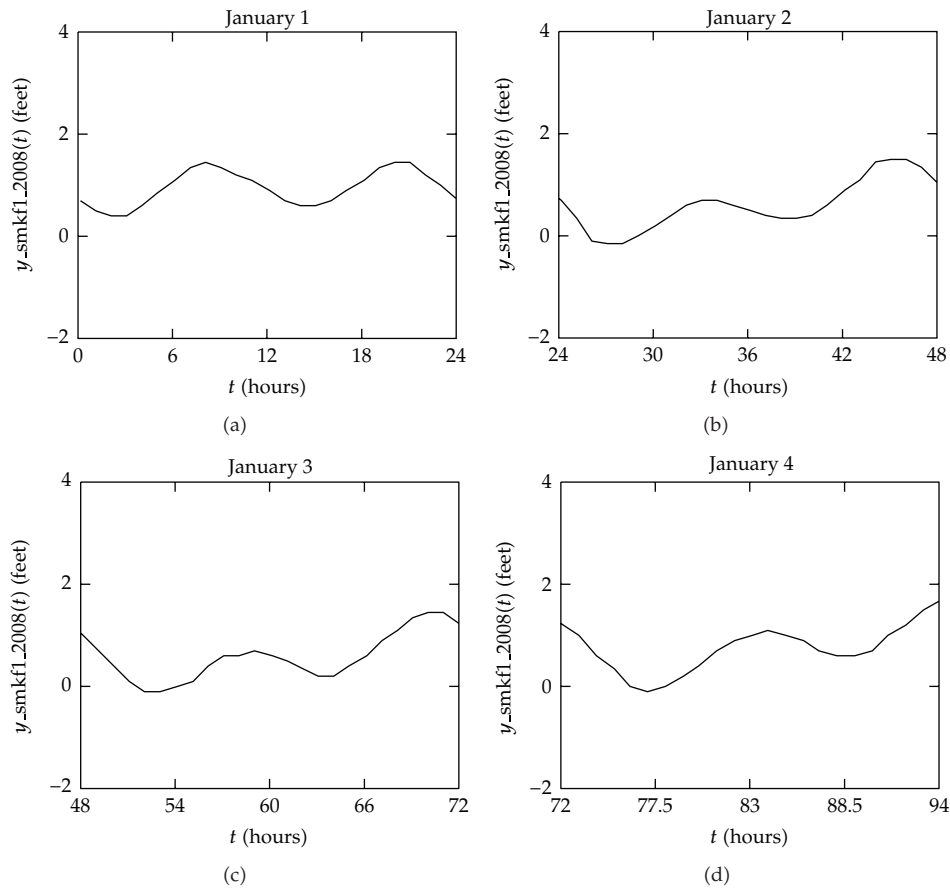


**Figure 1:** Daily sea level at the station SMKUF1 from January 1 to Jan. 4 in 2008. (a).  $x\_smkf1\_2008(t)$  on Jan. 1, 2008. (b).  $x\_smkf1\_2008(t)$  on Jan. 2, 2008. (c).  $x\_smkf1\_2008(t)$  on Jan. 3, 2008. (d).  $x\_smkf1\_2008(t)$  on Jan. 4, 2008.

where  $m$  is the largest integer not exceeding  $N/k$ . Then,  $h(t)$  at point  $t = j/(N - 1)$  is given by

$$h(t) = -\frac{\log\left(\sqrt{\pi/2}S_k(j)\right)}{\log(N - 1)}. \quad (3.9)$$

The above is the expression of applying mBm to investigate  $h(t)$  of sea level time series, which measures the Hölder roughness of sea level on a point-by-point basis.

#### 4. Observations and Discussions

We demonstrate  $h(t)$ s of sea level series  $x\_smkf1\_2008(t)$  at the time scales of day, week, and month, respectively.

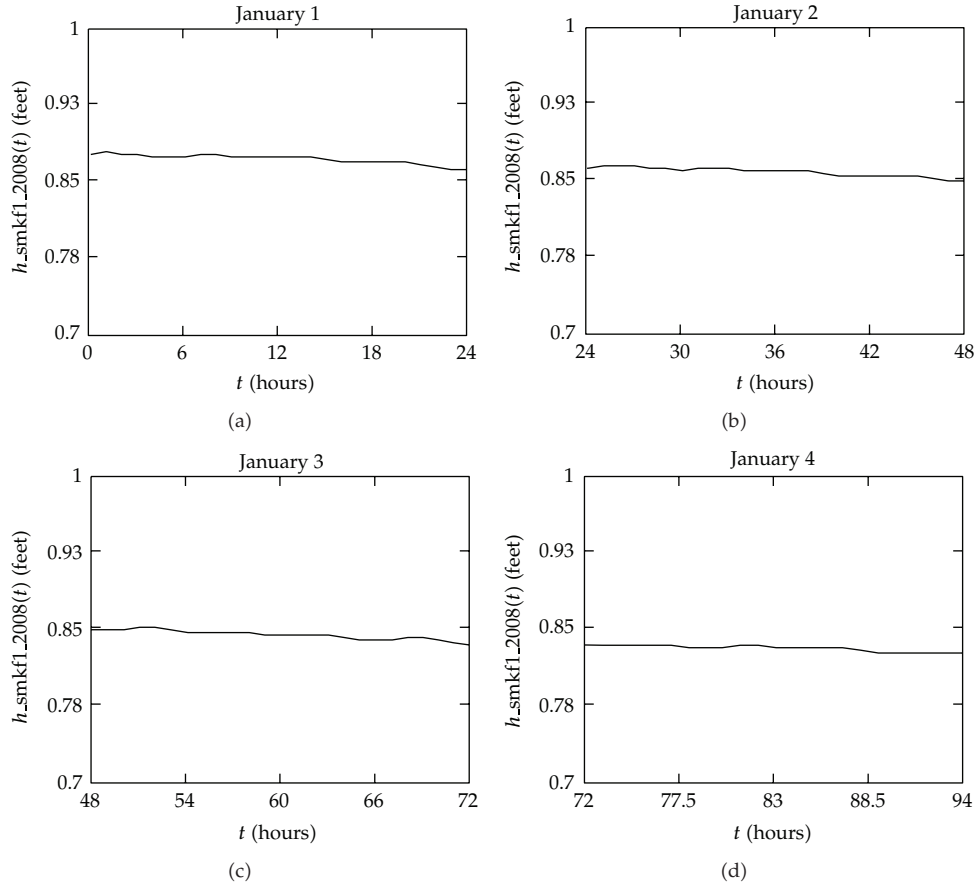


**Figure 2:** Hölder exponents of daily sea level at the station SMKUF1 from Jan. 1 to Jan. 4 in 2008. (a).  $h_{\text{smkf1\_2008}}(t)$  on Jan. 1, 2008. (b).  $h_{\text{smkf1\_2008}}(t)$  on Jan. 2, 2008. (c).  $h_{\text{smkf1\_2008}}(t)$  on Jan. 3, 2008. (d).  $h_{\text{smkf1\_2008}}(t)$  on Jan. 4, 2008.

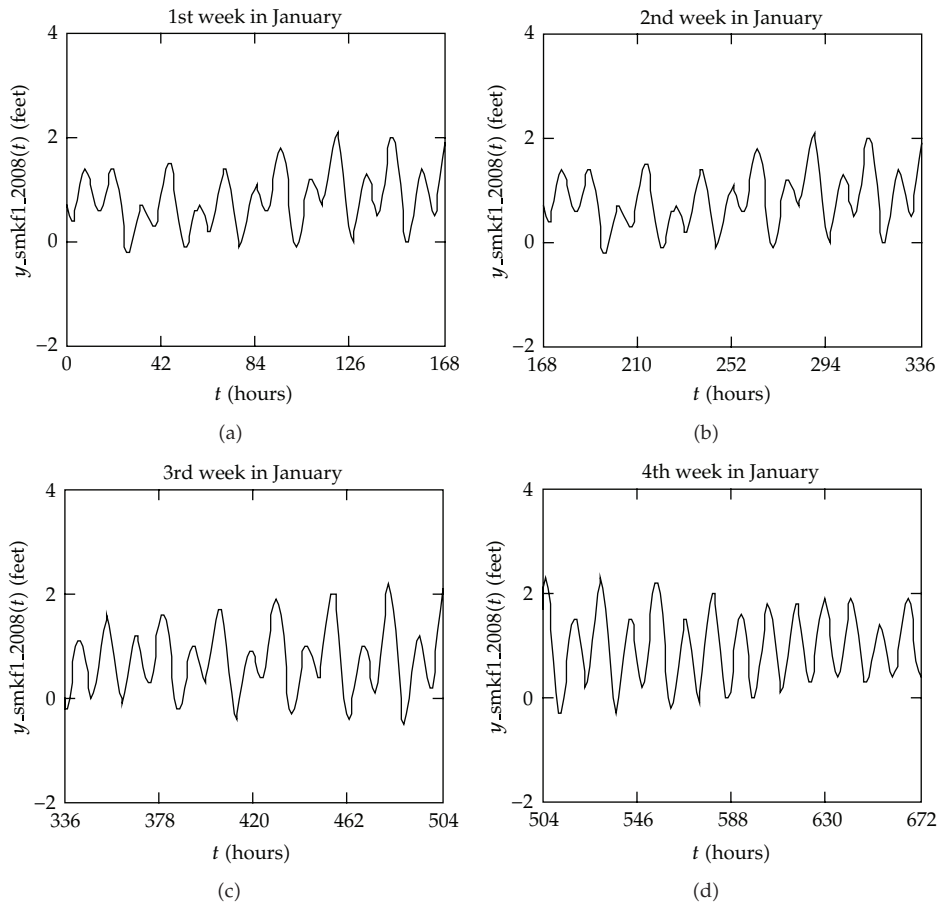
#### 4.1. Hölder Roughness at Daily Time Scale

Figure 1 indicates 4 daily series of sea level at the station SMKUF1 from Jan. 1 to Jan. 4 in 2008. Figure 2 demonstrates their corresponding Hölder exponents. From Figure 2, we see that  $4h(t)$ s of daily series of sea level vary with time insignificantly. Therefore, we obtain the remark below.

*Remark 4.1.* The Hölder exponents of sea level at the daily time scale, that is, 24 hours, may not vary significantly. This may imply that  $h(t) \approx h(t + \tau)$  if  $\tau \leq 24$  hours.

#### 4.2. Hölder Roughness at Weekly Time Scale

Four weekly series of sea level at the station SMKUF1 in Jan. 2008 are shown in Figure 3. Their corresponding Hölder exponents are plotted in Figure 4. They appear monotonically increase, see Figures 4(b) and 4(d), or decrease, see Figures 4(a) and 4(c). In general, they imply the following remark.



**Figure 3:** Weekly sea level at the station SMKUF1 on January 2008. (a).  $x_{\text{smkf1\_2008}}(t)$  in the 1st week in Jan. 2008. (b).  $x_{\text{smkf1\_2008}}(t)$  in the 2nd week in Jan. 2008. (c).  $x_{\text{smkf1\_2008}}(t)$  in the 3rd week on January 2008. (d).  $x_{\text{smkf1\_2008}}(t)$  in the 4th week in Jan. 2008.

*Remark 4.2.* The Hölder exponents of sea level at the weekly time scale, that is, 168 hours, may not vary considerably enough.

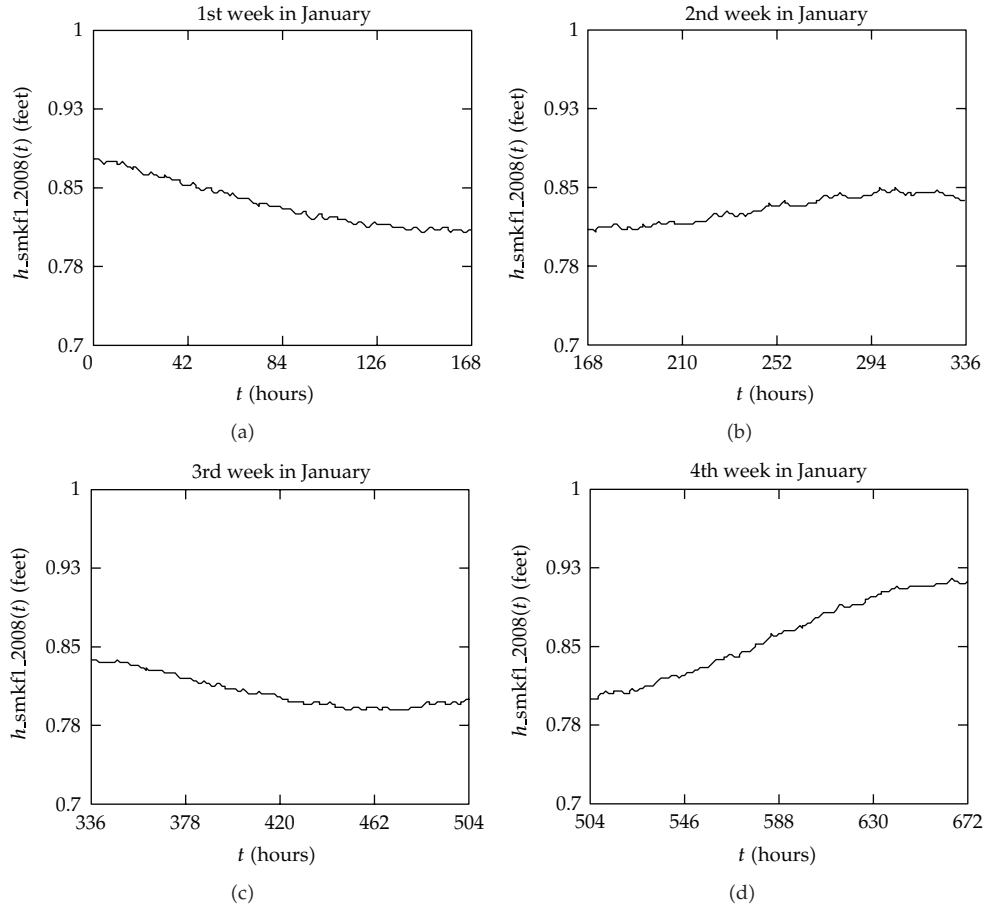
### 4.3. Hölder Roughness at Monthly Time Scale

Figure 5 illustrates 4 monthly series of sea level at the station SMKUF1 in 2008. Their corresponding Hölder exponents are indicated in Figure 6. From Figure 6, we see the following.

*Remark 4.3.* The Hölder exponents of sea level at the monthly time scale vary with time significantly.

### 4.4. Variation of Hölder Roughness at Large Time Scale

We now investigate the Hölder exponents of sea level at large time scale. By large time scale, we mean that the scale is around month or larger. Figure 7(a) indicates the sea level series



**Figure 4:** Hölder exponents of weekly sea level at the station SMKUF1 in January 2008. (a).  $h\_smkf1\_2008(t)$  in the 1st week on January 2008. (b).  $h\_smkf1\_2008(t)$  in the 2nd week in Jan. 2008. (c).  $h\_smkf1\_2008(t)$  in the 3rd week in Jan. 2008. (d).  $h\_smkf1\_2008(t)$  in the 4th week in Jan. 2008.

$x\_smkf1\_2008(t)$ , Figure 7(b) shows its Hölder exponent, and Figure 7(c) the histogram of its Hölder exponent.

One thing worth noting is that variances of Hölder exponents of sea level at different stations may be considerably different. For instance,

$$\begin{aligned} \text{Var}[h\_smkf1\_2008(t)] &= 1.203 \times 10^{-3}, \\ \text{Var}[h\_lonf112005(t)] &= 6.425 \times 10^{-4}. \end{aligned} \tag{4.1}$$

The above implies that the variance of  $h\_smkf1\_2008(t)$  is larger than that of  $h\_lonf112005(t)$  in one magnitude of order. Consequently, comes the following remark.

*Remark 4.4.* The variances of the Hölder exponents of sea level at different observation stations may be considerably different.

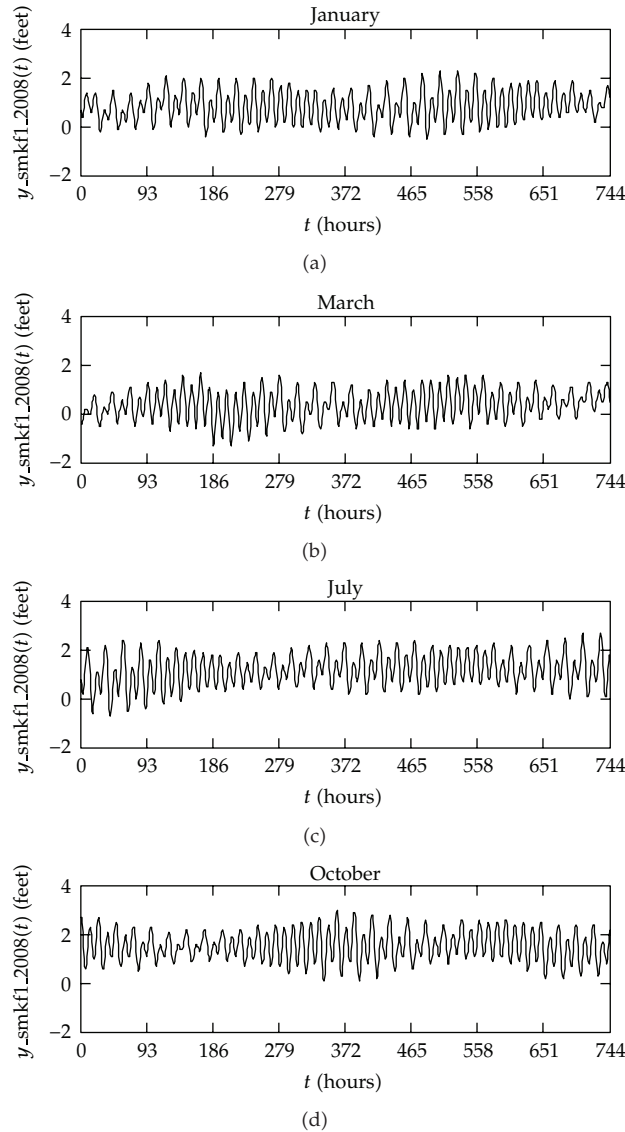


**Figure 5:** Monthly sea level at the station SMKUF1 in 2008. (a).  $x_{\text{smkf1\_2008}}(t)$  on January 2008. (b).  $x_{\text{smkf1\_2008}}(t)$  in March 2008. (c).  $x_{\text{smkf1\_2008}}(t)$  on July 2008. (d).  $x_{\text{smkf1\_2008}}(t)$  on October 2008.

We summarize the variances of the Hölder exponents of test data in Tables 7, 8, 9, 10, 11 and 12.

#### 4.5. Discussions

Generally, the Hölder exponents of sea level series are time varying. They are considerably at large time scales but insignificantly at small time scales. In addition, their variations are in general spatial dependent as the Tables 7–12 exhibit. For instance, in 2002,  $\text{Var}[h(t)]$  varies, in the form of magnitude of order, from  $10^{-3}$  to  $10^{-4}$  at different stations. This motivates us to

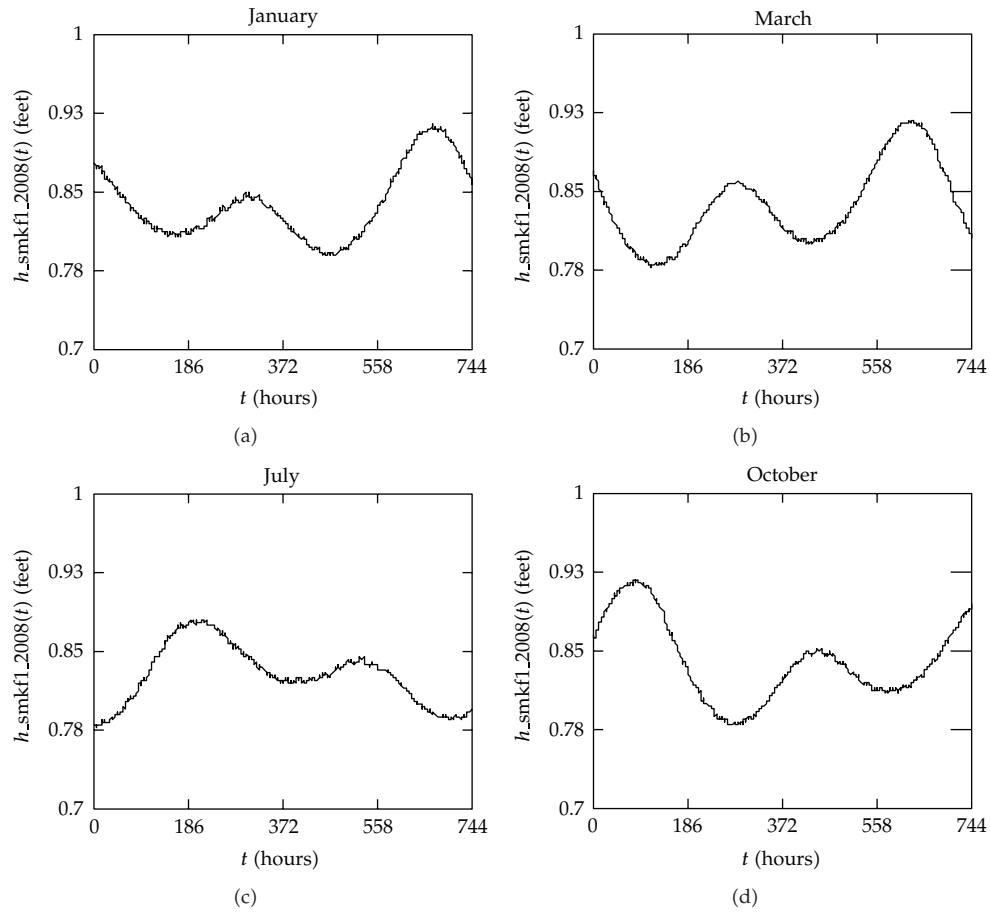


**Figure 6:** Hölder exponents of month sea level at the station SMKUF1 in 2008. (a).  $h\_smkf1\_2008(t)$  on Jan. 2008. (b).  $h\_smkf1\_2008(t)$  on March 2008. (c).  $h\_smkf1\_2008(t)$  in July 2008. (d).  $h\_smkf1\_2008(t)$  in October 2008.

take the spatial-time modeling of Hölder roughness of sea level as our possible future work. Finally, we note that the meaning of the term of local roughness of a random function is the same as that of local self-similarity [60, 65, 86]. Thus, according to (1.2), Remarks 4.1–4.3 exhibit the self-similarity of sea level at small and large time scales, respectively.

## 5. Conclusions

We have presented our results in the Hölder exponents of sea level in the Florida and Eastern Gulf of Mexico. The present results reveal an interesting phenomenon of time scales of sea level. To be precise, the Hölder exponents of sea level may not vary considerably at small time scales, such as daily time scale, but vary with time significantly at large time scale, such as monthly time scale. Moreover, our research exhibits that variations of the Hölder exponents of sea levels may be spatial dependent. Though the research is with the data in Florida and Eastern Gulf of Mexico, the results may be useful for further exploring general properties of the Hölder scales and roughness of sea level.

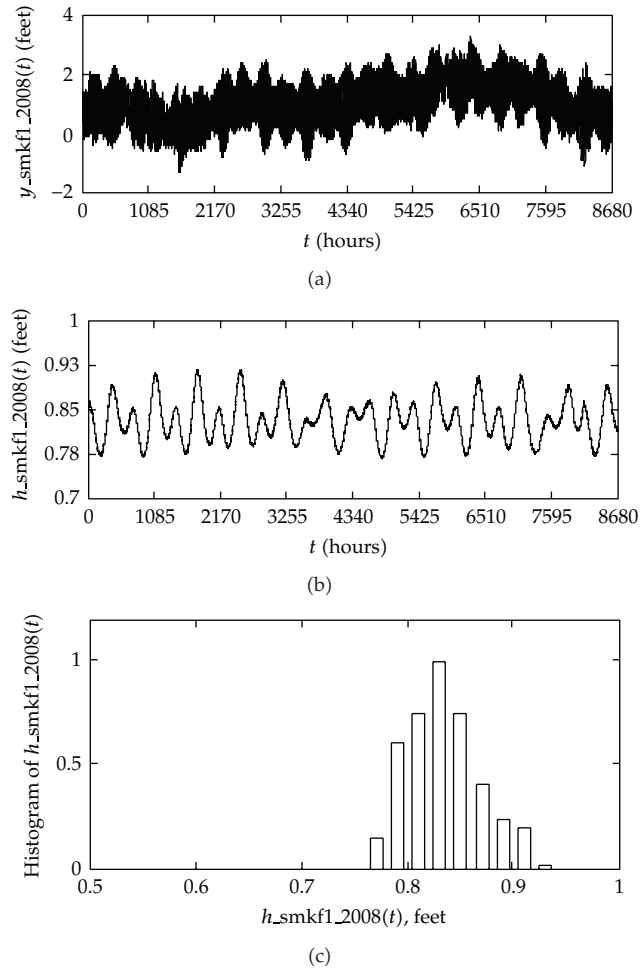


**Figure 7:** Illustrations of  $h_{\_smkf1\_2008}(t)$  and its Hölder exponent. (a).  $x_{\_smkf1\_2008}(t)$ . (b) Hölder exponent  $h_{\_smkf1\_2008}(t)$ . (c). Histogram of  $h_{\_smkf1\_2008}(t)$ .

**Table 7:** Variances of the Hölder exponents at LKWF1.

Series name	Var[ $h(t)$ ]
$x_{\_lkwf1\_1996}(t)$	$1.217 \times 10^{-3}$
$x_{\_lkwf1\_1997}(t)$	$1.006 \times 10^{-3}$
$x_{\_lkwf1\_1998}(t)$	$9.499 \times 10^{-4}$
$x_{\_lkwf1\_1999}(t)$	$1.164 \times 10^{-3}$
$x_{\_lkwf1\_2000}(t)$	$5.901 \times 10^{-4}$
$x_{\_lkwf1\_2001}(t)$	$1.169 \times 10^{-3}$
$x_{\_lkwf1\_2002}(t)$	$8.939 \times 10^{-4}$
$x_{\_lkwf1\_2003}(t)$	$9.710 \times 10^{-4}$
$x_{\_lkwf1\_2004}(t)$	$9.361 \times 10^{-4}$

**Table 8:** Variances of the Hölder exponents at LONF1.

Series name	Var[ $h(t)$ ]
$h_{\text{lonf1}}_{1998}(t)$	$3.978 \times 10^{-3}$
$h_{\text{lonf1}}_{1999}(t)$	$4.123 \times 10^{-4}$
$h_{\text{lonf1}}_{2000}(t)$	$1.570 \times 10^{-3}$
$h_{\text{lonf1}}_{2001}(t)$	$1.135 \times 10^{-3}$
$h_{\text{lonf1}}_{2002}(t)$	$1.407 \times 10^{-3}$
$h_{\text{lonf1}}_{2003}(t)$	$2.359 \times 10^{-3}$
$h_{\text{lonf1}}_{2004}(t)$	$9.493 \times 10^{-4}$
$h_{\text{lonf1}}_{2005}(t)$	$6.425 \times 10^{-4}$
$h_{\text{lonf1}}_{2006}(t)$	$1.245 \times 10^{-3}$
$h_{\text{lonf1}}_{2007}(t)$	$2.142 \times 10^{-3}$
$h_{\text{lonf1}}_{2008}(t)$	$8.245 \times 10^{-5}$

**Table 9:** Variances of the Hölder exponents at SAUF1.

Series name	Var[ $h(t)$ ]
$x_{\text{sauf1}}_{1996}(t)$	$1.083 \times 10^{-3}$
$x_{\text{sauf1}}_{1997}(t)$	$1.355 \times 10^{-3}$
$x_{\text{sauf1}}_{1998}(t)$	$8.766 \times 10^{-4}$
$x_{\text{sauf1}}_{1999}(t)$	$1.324 \times 10^{-3}$
$x_{\text{sauf1}}_{2000}(t)$	$7.272 \times 10^{-4}$
$x_{\text{sauf1}}_{2001}(t)$	$6.961 \times 10^{-4}$
$x_{\text{sauf1}}_{2002}(t)$	$3.992 \times 10^{-3}$

**Table 10:** Variances of the Hölder exponents at SMKf1.

Series name	Var[ $h(t)$ ]
$x_{\text{smkf1}}_{1998}(t)$	$9.501 \times 10^{-4}$
$x_{\text{smkf1}}_{1999}(t)$	$1.144 \times 10^{-3}$
$x_{\text{smkf1}}_{2000}(t)$	$1.310 \times 10^{-3}$
$x_{\text{smkf1}}_{2001}(t)$	$1.520 \times 10^{-3}$
$x_{\text{smkf1}}_{2002}(t)$	$1.181 \times 10^{-3}$
$x_{\text{smkf1}}_{2003}(t)$	$1.176 \times 10^{-3}$
$x_{\text{smkf1}}_{2004}(t)$	$1.243 \times 10^{-3}$
$x_{\text{smkf1}}_{2005}(t)$	$1.210 \times 10^{-3}$
$h_{\text{smkf1}}_{2006}(t)$	$1.101 \times 10^{-3}$
$h_{\text{smkf1}}_{2007}(t)$	$1.164 \times 10^{-3}$
$h_{\text{smkf1}}_{2008}(t)$	$1.203 \times 10^{-3}$
$h_{\text{smkf1}}_{2009}(t)$	$1.242 \times 10^{-3}$
$h_{\text{smkf1}}_{2010}(t)$	$1.084 \times 10^{-3}$
$h_{\text{smkf1}}_{2011}(t)$	$1.176 \times 10^{-3}$

**Table 11:** Variances of the Hölder exponents at SPGF1.

Series name	Var[ $h(t)$ ]
$x_{\text{spgf1}}_{1996}(t)$	$1.018 \times 10^{-3}$
$x_{\text{spgf1}}_{1997}(t)$	$8.803 \times 10^{-4}$
$x_{\text{spgf1}}_{1998}(t)$	$2.659 \times 10^{-4}$

**Table 12:** Variances of the Hölder exponents at VENF1.

Series name	Var[ $h(t)$ ]
$x_{\text{venf1\_2002}}(t)$	$1.069 \times 10^{-3}$
$x_{\text{venf1\_2003}}(t)$	$1.271 \times 10^{-3}$
$x_{\text{venf1\_2004}}(t)$	$8.863 \times 10^{-4}$
$x_{\text{venf1\_2006}}(t)$	$2.268 \times 10^{-3}$
$x_{\text{venf1\_2007}}(t)$	$2.454 \times 10^{-3}$
$x_{\text{venf1\_2008}}(t)$	$2.930 \times 10^{-3}$

## Acknowledgments

This work was supported in part by the 973 Plan under the Project no. 2011CB302800, and the National Natural Science Foundation of China under the project Grants nos. 61272402, 61070214, and 60873264. The National Data Buoy Center is highly appreciated for its measured data that makes our research possible.

## References

- [1] Geophysics Study Committee and National Research Council, *Sea-Level Change*, National Academic Press, 1990.
- [2] Committee on Engineering Implications of Changes in Relative Mean Sea Level, Marine Board, and National Research Council, *Responding To Changes in Sea Level: Engineering Implications*, National Academic Press, 1987.
- [3] V. Gornitz, S. Couch, and E. K. Hartig, "Impacts of sea level rise in the New York City metropolitan area," *Global and Planetary Change*, vol. 32, no. 1, pp. 61–88, 2001.
- [4] S. Jevrejeva, J. C. Moore, and A. Grinsted, "Sea level projections to AD2500 with a new generation of climate change scenarios," *Global and Planetary Changes*, vol. 80-81, pp. 14–20, 2012.
- [5] M. Becker, B. Meyssignac, C. Letetrel, W. Llovel, A. Cazenave, and T. Delcroix, "Sea level variations at tropical Pacific islands since 1950," *Global and Planetary Change*, vol. 80-81, pp. 85–98, 2012.
- [6] B. Meyssignac and A. Cazenave, "Sea level: a review of present-day and recent-past changes and variability," *Journal of Geodynamics*, vol. 58, pp. 96–109, 2012.
- [7] A. J. Long, S. A. Woodroffe, G. A. Milne, C. L. Bryant, M. J. R. Simpson, and L. M. Wake, "Relative sea-level change in Greenland during the last 700 yrs and ice sheet response to the Little Ice Age," *Earth and Planetary Science Letters*, vol. 315-316, pp. 76–85, 2012.
- [8] M. Eliot, "Sea level variability influencing coastal flooding in the Swan River region, Western Australia," *Continental Shelf Research*, vol. 33, pp. 14–28, 2012.
- [9] N. N. Warner and P. E. Tissot, "Storm flooding sensitivity to sea level rise for Galveston Bay, Texas," *Ocean Engineering*, vol. 44, pp. 23–32, 2012.
- [10] A. Ozyavas and S. D. Khan, "The driving forces behind the Caspian Sea mean water level oscillations," *Environmental Earth Sciences*, vol. 65, no. 6, pp. 1821–1830, 2012.
- [11] J. Hinkel, S. Brown, L. Exner, R. J. Nicholls, A. T. Vafeidis, and A. S. Kebede, "Sea-level rise impacts on Africa and the effects of mitigation and adaptation: an application of DIVA," *Regional Environmental Change*, vol. 12, no. 1, pp. 207–224, 2012.
- [12] E. Gasson, M. Siddall, D. J. Lunt, O. J. L. Rackham, C. H. Lear, and D. Pollard, "Exploring uncertainties in the relationship between temperature, ice volume, and sea level over the past 50 million years," *Reviews of Geophysics*, vol. 50, no. 1, Article ID RG1005, 2012.
- [13] G. Wopelmann and M. Marcos, "Coastal sea level rise in southern Europe and the nonclimate contribution of vertical land motion," *Journal of Geophysical Research*, vol. 117, no. 1, Article ID C01007, 2012.

- [14] J. M. Gregory, J. A. Church, G. J. Boer et al., "Comparison of results from several AOGCMs for global and regional sea-level change 1900–2100," *Climate Dynamics*, vol. 18, no. 3-4, pp. 223–240, 2001.
- [15] F. Albrecht, T. Wahl, J. Jensen, and R. Weisse, "Determining sea level change in the German Bight," *Ocean Dynamics*, vol. 61, no. 12, pp. 2037–2050, 2011.
- [16] R. D. Ray and B. C. Douglas, "Experiments in reconstructing twentieth-century sea levels," *Progress in Oceanography*, vol. 91, no. 4, pp. 496–515, 2011.
- [17] N. F. Barber and F. Ursell, "The generation and propagation of ocean waves and swell," *Philosophical Transactions A*, vol. 240, no. 824, pp. 527–560, 1948.
- [18] E. M. Bitner-Gregersen and S. Gran, "Local properties of sea waves derived from a wave record," *Applied Ocean Research*, vol. 5, no. 4, pp. 210–214, 1983.
- [19] A. Veltcheva, P. Cavaco, and C. G. Soares, "Comparison of methods for calculation of the wave envelope," *Ocean Engineering*, vol. 30, no. 7, pp. 937–948, 2003.
- [20] C. G. Soares and Z. Cherneva, "Spectrogram analysis of the time-frequency characteristics of ocean wind waves," *Ocean Engineering*, vol. 32, no. 14-15, pp. 1643–1663, 2005.
- [21] H. B. Bluestein, "A review of ground-based, mobile, W-band Doppler-radar observations of tornadoes and dust devils," *Dynamics of Atmospheres and Oceans*, vol. 40, no. 3, pp. 163–188, 2005.
- [22] A. Baxevani, I. Rychlik, and R. J. Wilson, "A new method for modelling the space variability of significant wave height," *Extremes*, vol. 8, no. 4, pp. 267–294, 2005.
- [23] L. C. Breaker, "Nonlinear aspects of sea surface temperature in Monterey Bay," *Progress in Oceanography*, vol. 69, no. 1, pp. 61–89, 2006.
- [24] J. Gower, C. Hu, G. Borstad, and S. King, "Ocean color satellites show extensive lines of floating sargassum in the gulf of Mexico," *IEEE Transactions on Geoscience and Remote Sensing*, vol. 44, no. 12, pp. 3619–3625, 2006.
- [25] R. Schumann, H. Baudler, Å. Glass, K. Dümcke, and U. Karsten, "Long-term observations on salinity dynamics in a tideless shallow coastal lagoon of the Southern Baltic Sea coast and their biological relevance," *Journal of Marine Systems*, vol. 60, no. 3-4, pp. 330–344, 2006.
- [26] A. Sarkar, J. Kshatriya, and K. Satheesan, "Auto-correlation analysis of wave heights in the Bay of Bengal," *Journal of Earth System Science*, vol. 115, no. 2, pp. 235–237, 2006.
- [27] S. Caires, V. R. Swail, and X. L. Wang, "Projection and analysis of extreme wave climate," *Journal of Climate*, vol. 19, no. 21, pp. 5581–5605, 2006.
- [28] T. L. Walton Jr., "Projected sea level rise in Florida," *Ocean Engineering*, vol. 34, no. 13, pp. 1832–1840, 2007.
- [29] P. A. Pirazzoli and A. Tomasin, "Estimation of return periods for extreme sea levels: a simplified empirical correction of the joint probabilities method with examples from the French Atlantic coast and three ports in the southwest of the UK," *Ocean Dynamics*, vol. 57, no. 2, pp. 91–107, 2007.
- [30] R. J. Romanowicz, P. C. Young, K. J. Beven, and F. Pappenberger, "A data based mechanistic approach to nonlinear flood routing and adaptive flood level forecasting," *Advances in Water Resources*, vol. 31, no. 8, pp. 1048–1056, 2008.
- [31] S. Castanedo, F. J. Mendez, R. Medina, and A. J. Abascal, "Long-term tidal level distribution using a wave-by-wave approach," *Advances in Water Resources*, vol. 30, no. 11, pp. 2271–2282, 2007.
- [32] R. Kalra and M. C. Deo, "Derivation of coastal wind and wave parameters from offshore measurements of TOPEX satellite using ANN," *Coastal Engineering*, vol. 54, no. 3, pp. 187–196, 2007.
- [33] P. K. Tonnon, L. C. van Rijn, and D. J. R. Walstra, "The morphodynamic modelling of tidal sand waves on the shoreface," *Coastal Engineering*, vol. 54, no. 4, pp. 279–296, 2007.
- [34] H. Bazargan, H. Bahai, and A. Aminzadeh-Gohari, "Calculating the return value using a mathematical model of significant wave height," *Journal of Marine Science and Technology*, vol. 12, no. 1, pp. 34–42, 2007.
- [35] K. Günaydin, "The estimation of monthly mean significant wave heights by using artificial neural network and regression methods," *Ocean Engineering*, vol. 35, no. 14-15, pp. 1406–1415, 2008.
- [36] J. W. Kang, S.-R. Moon, S.-J. Park, and K.-H. Lee, "Analyzing sea level rise and tide characteristics change driven by coastal construction at Mokpo Coastal Zone in Korea," *Ocean Engineering*, vol. 36, no. 6-7, pp. 415–425, 2009.
- [37] T. Ito, M. Okubo, and T. Sagiya, "High resolution mapping of Earth tide response based on GPS data in Japan," *Journal of Geodynamics*, vol. 48, no. 3–5, pp. 253–259, 2009.

- [38] Y. Lin, R. J. Greatbatch, and J. Sheng, "The influence of Gulf of Mexico loop current intrusion on the transport of the Florida Current," *Ocean Dynamics*, vol. 60, no. 5, pp. 1075–1084, 2010.
- [39] P. Xiao, Z. Yu, and C. S. Li, "Compressive sensing SAR range compression with chirp scaling principle," *Science China Information Sciences*, vol. 54, no. 1, pp. 2292–2300, 2012.
- [40] [http://www.ndbc.noaa.gov/historical\\_data.shtml](http://www.ndbc.noaa.gov/historical_data.shtml).
- [41] H. E. Hurst, "Long-term storage capacity of reservoirs," *Transactions of the American Society of Civil Engineers*, vol. 116, pp. 770–799, 1951.
- [42] B. B. Mandelbrot and J. R. Wallis, "Robustness of the rescaled range R/S in the measurement of noncyclic long run statistical dependence," *Water Resources Research*, vol. 5, no. 5, pp. 967–988, 1969.
- [43] B. B. Mandelbrot and J. R. Wallis, "Some long-run properties of geophysical records," *Water Resources Research*, vol. 5, no. 2, pp. 967–988, 1969.
- [44] W. Rea, M. Reale, J. Brown, and L. Oxley, "Long memory or shifting means in geophysical time series?" *Mathematics and Computers in Simulation*, vol. 81, no. 7, pp. 1441–1453, 2011.
- [45] J. D. Pelletier and D. L. Turcotte, "Long-range persistence in climatological and hydrological time series: analysis, modeling and application to drought hazard assessment," *Journal of Hydrology*, vol. 203, no. 1–4, pp. 198–208, 1997.
- [46] Q. Shao and M. Li, "A new trend analysis for seasonal time series with consideration of data dependence," *Journal of Hydrology*, vol. 396, no. 1–2, pp. 104–112, 2011.
- [47] B. M. Dolgonosov, K. A. Korchagin, and N. V. Kirpichnikova, "Modeling of annual oscillations and 1/f-noise of daily river discharges," *Journal of Hydrology*, vol. 357, no. 3–4, pp. 174–187, 2008.
- [48] V. Ganti, K. M. Straub, E. Foufoula-Georgiou, and C. Paola, "Space-time dynamics of depositional systems: experimental evidence and theoretical modeling of heavy-tailed statistics," *Journal of Geophysical Research F*, vol. 116, no. 2, Article ID F02011, 2011.
- [49] J. Alvarez-Ramirez, J. Alvarez, L. Dagdug, E. Rodriguez, and J. C. Echeverria, "Long-term memory dynamics of continental and oceanic monthly temperatures in the recent 125 years," *Physica A*, vol. 387, no. 14, pp. 3629–3640, 2008.
- [50] A. Berrones, "Persistence in a simple model for the Earth's atmosphere temperature fluctuations," *Fluctuation and Noise Letters*, vol. 5, no. 3, pp. L365–L374, 2005.
- [51] J. Haslett and A. E. Raftery, "Space-time modelling with long-memory dependence: assessing Ireland's wind power resource," *Journal of the Royal Statistical Society C*, vol. 38, no. 1, pp. 1–50, 1989.
- [52] K. Fraedrich, U. Luksch, and R. Blender, "1/f model for long-time memory of the ocean surface temperature," *Physical Review E*, vol. 70, no. 3, Article ID 037301, 4 pages, 2004.
- [53] M. S. Santhanam and H. Kantz, "Long-range correlations and rare events in boundary layer wind fields," *Physica A*, vol. 345, no. 3–4, pp. 713–721, 2005.
- [54] J.-C. Bouette, J.-F. Chassagneux, D. Sibai, R. Terron, and A. Charpentier, "Wind in Ireland: long memory or seasonal effect?" *Stochastic Environmental Research and Risk Assessment*, vol. 20, no. 3, pp. 141–151, 2006.
- [55] R. A. Monetti, S. Havlin, and A. Bunde, "Long-term persistence in the sea surface temperature fluctuations," *Physica A*, vol. 320, pp. 581–589, 2003.
- [56] R. Blender, K. Fraedrich, and F. Sienz, "Extreme event return times in long-term memory processes near 1/f," *Nonlinear Processes in Geophysics*, vol. 15, no. 4, pp. 557–565, 2008.
- [57] T. S. Prass, J. M. Bravo, R. T. Clarke, W. Collischonn, and S. R. C. Lopes, "Comparison of forecasts of mean monthly water level in the Paraguay River, Brazil, from two fractionally differenced models," *Water Resources Research*, vol. 48, no. 5, Article ID W05502, 13 pages, 2012.
- [58] S. M. Barbosa, M. J. Fernandes, and M. E. Silva, "Long-range dependence in North Atlantic sea level," *Physica A*, vol. 371, no. 2, pp. 725–731, 2006.
- [59] M. Li, C. Cattani, and S. Y. Chen, "Viewing sea level by a one-dimensional random function with long memory," *Mathematical Problems in Engineering*, vol. 2011, Article ID 654284, 13 pages, 2011.
- [60] B. B. Mandelbrot, *The Fractal Geometry of Nature*, W. H. Freeman, New York, NY, USA, 1982.
- [61] R. J. Adler, R. E. Feldman, and M. S. Taqqu, Eds., *A Practical Guide To Heavy Tails: Statistical Techniques and Applications*, Birkhäuser, Boston, Mass, USA, 1998.
- [62] P. Abry, P. Borgnat, F. Ricciato, A. Scherrer, and D. Veitch, "Revisiting an old friend: on the observability of the relation between long range dependence and heavy tail," *Telecommunication Systems*, vol. 43, no. 3–4, pp. 147–165, 2010.
- [63] T. Gneiting and M. Schlather, "Stochastic models that separate fractal dimension and the hurst effect," *SIAM Review*, vol. 46, no. 2, pp. 269–282, 2004.

- [64] M. Li, "Generation of teletraffic of generalized Cauchy type," *Physica Scripta*, vol. 81, no. 2, Article ID 025007, 10 pages, 2010.
- [65] S. C. Lim and M. Li, "A generalized Cauchy process and its application to relaxation phenomena," *Journal of Physics A*, vol. 39, no. 12, pp. 2935–2951, 2006.
- [66] S. V. Muniandy and J. Stanslas, "Modelling of chromatin morphologies in breast cancer cells undergoing apoptosis using generalized Cauchy field," *Computerized Medical Imaging and Graphics*, vol. 32, no. 7, pp. 631–637, 2008.
- [67] D. Ceresetti, G. Molinié, and J.-D. Creutin, "Scaling properties of heavy rainfall at short duration: a regional analysis," *Water Resources Research*, vol. 46, no. 9, Article ID W09531, 12 pages, 2010.
- [68] M. Radziejewski and Z. W. Kundzewicz, "Fractal analysis of flow of the river Warta," *Journal of Hydrology*, vol. 200, no. 1–4, pp. 280–294, 1997.
- [69] S. Hirabayashi and T. Sato, "Scaling of mixing parameters in stationary, homogeneous, and stratified turbulence," *Journal of Geophysical Research C*, vol. 115, no. 9, Article ID C09023, 9 pages, 2010.
- [70] R. Mantilla, B. M. Troutman, and V. K. Gupta, "Testing statistical self-similarity in the topology of river networks," *Journal of Geophysical Research F*, vol. 115, no. 3, Article ID F03038, 12 pages, 2010.
- [71] A. A. Suleymanov, A. A. Abbasov, and A. J. Ismaylov, "Fractal analysis of time series in oil and gas production," *Chaos, Solitons & Fractals*, vol. 41, no. 5, pp. 2474–2483, 2009.
- [72] S. Rehman and A. H. Siddiqi, "Wavelet based hurst exponent and fractal dimensional analysis of Saudi climatic dynamics," *Chaos, Solitons & Fractals*, vol. 40, no. 3, pp. 1081–1090, 2009.
- [73] R. Zuo, Q. Cheng, Q. Xia, and F. P. Agterberg, "Application of fractal models to distinguish between different mineral phases," *Mathematical Geosciences*, vol. 41, no. 1, pp. 71–80, 2009.
- [74] R. C. García, A. S. Galán, J. R. Castrejón Pita, and A. A. C. Pita, "The fractal dimension of an oil spray," *Fractals*, vol. 11, no. 2, pp. 155–161, 2003.
- [75] S. Benmehdi, N. Makarava, N. Benhamidouche, and M. Holschneider, "Bayesian estimation of the self-similarity exponent of the Nile River fluctuation," *Nonlinear Processes in Geophysics*, vol. 18, no. 3, pp. 441–446, 2011.
- [76] S. I. Badulin, A. N. Pushkarev, D. Resio, and V. E. Zakharov, "Self-similarity of wind-driven seas," *Nonlinear Processes in Geophysics*, vol. 12, no. 6, pp. 891–945, 2005.
- [77] V. Carbone, P. Veltri, and R. Bruno, "Solar wind low-frequency magnetohydrodynamic turbulence: extended self-similarity and scaling laws," *Nonlinear Processes in Geophysics*, vol. 3, no. 4, pp. 247–261, 1996.
- [78] T. B. Sangoyomi, U. Lall, and H. D. I. Abarbanel, "Nonlinear dynamics of the Great Salt Lake: dimension estimation," *Water Resources Research*, vol. 32, no. 1, pp. 149–159, 1996.
- [79] M. Ozger, "Scaling characteristics of ocean wave height time series," *Physica A*, vol. 390, no. 6, pp. 981–989, 2011.
- [80] A. Chmel, V. N. Smirnov, and M. P. Astakhov, "The Arctic sea-ice cover: fractal space-time domain," *Physica A*, vol. 357, no. 3–4, pp. 556–564, 2005.
- [81] F. Berizzi, G. Bertini, M. Martorella, and M. Bertacca, "Two-dimensional variation algorithm for fractal analysis of sea SAR images," *IEEE Transactions on Geoscience and Remote Sensing*, vol. 44, no. 9, pp. 2361–2373, 2006.
- [82] K. Fraedrich and R. Blender, "Scaling of atmosphere and ocean temperature correlations in observations and climate models," *Physical Review Letters*, vol. 90, no. 10, Article ID 108501, 4 pages, 2003.
- [83] T. Xu, I. D. Moore, and J. C. Gallant, "Fractals, fractal dimensions and landscapes—a review," *Geomorphology*, vol. 8, no. 4, pp. 245–262, 1993.
- [84] G. Korvin, *Fractal Models in the Earth Science*, Elsevier, 1992.
- [85] J. Levy-Vehel, E. Lutton, and C. Tricot, Eds., *Fractals in Engineering*, Springer, 1997.
- [86] B. B. Mandelbrot, *Gaussian Self-Affinity and Fractals*, Springer, 2001.
- [87] S. C. Lim and S. V. Muniandy, "On some possible generalizations of fractional Brownian motion," *Physics Letters A*, vol. 266, no. 2–3, pp. 140–145, 2000.
- [88] H. E. Stanley, L. A. N. Amaral, A. L. Goldberger, S. Havlin, P. C. Ivanov, and C.-K. Peng, "Statistical physics and physiology: monofractal and multifractal approaches," *Physica A*, vol. 270, no. 1–2, pp. 309–324, 1999.
- [89] B. B. Mandelbrot, *Multifractals and 1/f Noise*, Springer, 1998.
- [90] D. Harte, *Multifractals: Theory and Applications*, Chapman & Hall, 2001.

- [91] D. L. Turcotte, *Fractals and Chaos in Geology and Geophysics*, Cambridge University Press, Cambridge, UK, 2nd edition, 1997.
- [92] J. Lévy-Véhel and E. Lutton, Eds., *Fractals in Engineering: New Trends in Theory and Applications*, Springer, 2005.
- [93] S. Gaci, N. Zaourar, L. Briquieu, and M. Hamoudi, "Regularity analysis of airborne natural Gamma ray data measured in the Hoggar area (Algeria)," in *Advances in Data, Methods, Models and Their Applications in Geoscience*, D. Chen, Ed., pp. 93–108, InTech, 2011.
- [94] S. Gaci and N. Zaourar, "Two-dimensional multifractional Brownian motion-based investigation of heterogeneities from a core image," in *Advances in Data, Methods, Models and Their Applications in Geoscience*, D. Chen, Ed., pp. 109–124, InTech, 2011.
- [95] P. Afzal, A. Z. Zarifi, and A. B. Yasrebi, "Identification of uranium targets based on airborne radiometric data analysis by using multifractal modeling, Tark and Avanligh 1:50 000 sheets, NW Iran," *Nonlinear Processes in Geophysics*, vol. 19, no. 2, pp. 283–289, 2012.
- [96] M. S. Jouini, S. Vega, and E. A. Mokhtar, "Multiscale characterization of pore spaces using multifractals analysis of scanning electronic microscopy images of carbonates," *Nonlinear Processes in Geophysics*, vol. 18, no. 6, pp. 941–953, 2011.
- [97] S. S. Teotia and D. Kumar, "Role of multifractal analysis in understanding the preparation zone for large size earthquake in the North-Western Himalaya region," *Nonlinear Processes in Geophysics*, vol. 18, no. 1, pp. 111–118, 2011.
- [98] F. Serinaldi, "Multifractality, imperfect scaling and hydrological properties of rainfall time series simulated by continuous universal multifractal and discrete random cascade models," *Nonlinear Processes in Geophysics*, vol. 17, no. 6, pp. 697–714, 2010.
- [99] W. M. Macek, "Multifractality and intermittency in the solar wind," *Nonlinear Processes in Geophysics*, vol. 14, no. 6, pp. 695–700, 2007.
- [100] S. I. Badulin, A. N. Pushkarev, D. Resio, and V. E. Zakharov, "Self-similarity of wind-driven seas," *Nonlinear Processes in Geophysics*, vol. 12, no. 6, pp. 891–945, 2005.
- [101] Y. Ida, M. Hayakawa, A. Adalev, and K. Gotoh, "Multifractal analysis for the ULF geomagnetic data during the 1993 Guam earthquake," *Nonlinear Processes in Geophysics*, vol. 12, no. 2, pp. 157–162, 2005.
- [102] L. Seuront, F. Schmitt, D. Shertzer, Y. Lagadette, and S. Lovejoy, "Multifractal intermittency of Eulerian and Lagrangian turbulence of ocean temperature and plankton fields," *Nonlinear Processes in Geophysics*, vol. 3, no. 4, pp. 236–246, 1996.
- [103] M. Arias, P. Gumiel, D. J. Sanderson, and A. Martin-Izard, "A multifractal simulation model for the distribution of VMS deposits in the Spanish segment of the Iberian Pyrite Belt," *Computers & Geosciences*, vol. 37, no. 12, pp. 1917–1927, 2011.
- [104] J. Paz-Ferreiro, E. V. Vázquez, and J. G. V. Miranda, "Assessing soil particle-size distribution on experimental plots with similar texture under different management systems using multifractal parameters," *Geoderma*, vol. 160, no. 1, pp. 47–56, 2010.
- [105] P. C. Chu, "Multi-fractal thermal characteristics of the southwestern GIN sea upper layer," *Chaos, Solitons & Fractals*, vol. 19, no. 2, pp. 275–284, 2004.
- [106] N. Su, Z.-G. Yu, V. Anh, and K. Bajracharya, "Fractal tidal waves in coastal aquifers induced both anthropogenically and naturally," *Environmental Modelling & Software*, vol. 19, no. 12, pp. 1125–1130, 2004.
- [107] X. S. Liang and A. R. Robinson, "Localized multiscale energy and vorticity analysis. I. Fundamentals," *Dynamics of Atmospheres and Oceans*, vol. 38, no. 3-4, pp. 195–230, 2005.
- [108] J. D. Pelletier, "Natural variability of atmospheric temperatures and geomagnetic intensity over a wide range of time scales," *Proceedings of the National Academy of Sciences of the United States of America*, vol. 99, supplement 1, pp. 2546–2553, 2002.
- [109] K. Daoudi and J. Lévy-Véhel, "Signal representation and segmentation based on multifractal stationarity," *Signal Processing*, vol. 82, no. 12, pp. 2015–2024, 2002.
- [110] T. Bedford, "Hölder exponents and box dimension for self-affine fractal functions," *Constructive Approximation*, vol. 5, no. 1, pp. 33–48, 1989.
- [111] K. J. Falconer, *Fractal Geometry, Mathematical Foundations and Applications*, John Wiley & Sons, 2003.
- [112] J. W. Kantelhardt, S. A. Zschiegner, E. Koscielny-Bunde, S. Havlin, A. Bunde, and H. E. Stanley, "Multifractal detrended fluctuation analysis of nonstationary time series," *Physica A*, vol. 316, no. 1–4, pp. 87–114, 2002.

- [113] K. Daoudi, J. Lévy-Véhel, and Y. Meyer, "Construction of continuous functions with prescribed local regularity," *Constructive Approximation*, vol. 14, no. 3, pp. 349–385, 1998.
- [114] B. J. West, "Fractal physiology and the fractional calculus: a perspective," *Frontiers in Fractal Physiology*, vol. 1, article 12, 2010.
- [115] R. F. Peltier and J. Levy-Vehel, *Multifractional Brownian Motion: Definition and Preliminaries Results*, 1995, INRIA RR, 2645.
- [116] A. Ayache, S. Cohen, and J. Levy Vehel, "Covariance structure of Multifractional Brownian motion, with application to long range dependence," in *Proceedings of the IEEE International Conference on Acoustics, Speech, and Signal Processing (ICASSP '00)*, pp. 3810–3813, June 2000.
- [117] A. Ayache, "The generalized multifractional field: a nice tool for the study of the generalized multifractional brownian motion," *Journal of Fourier Analysis and Applications*, vol. 8, no. 6, pp. 581–601, 2002.
- [118] A. Ayache and J. Levy-Vehel, "The generalized multifractional Brownian motion," *Statistical Inference For Stochastic Processes*, vol. 3, no. 1-2, pp. 7–18, 2000.
- [119] R. L. Guevel and J. Levy-Vehel, *Incremental Moments and Hölderexponents of Multifractional Multistable Processes*, INRIA, 2010.
- [120] K. J. Falconer, R. Le Guével, and J. Lévy-Véhel, "Localizable moving average symmetric stable and multistable processes," *Stochastic Models*, vol. 25, no. 4, pp. 648–672, 2009.
- [121] K. J. Falconer and J. Lévy Véhel, "Multifractional, multistable, and other processes with prescribed local form," *Journal of Theoretical Probability*, vol. 22, no. 2, pp. 375–401, 2009.
- [122] K. J. Falconer, "The local structure of random processes," *Journal of the London Mathematical Society A*, vol. 67, no. 3, pp. 657–672, 2003.
- [123] K. Dębicki and P. Kisowski, "Asymptotics of supremum distribution of  $\alpha$  (t)-locally stationary Gaussian processes," *Stochastic Processes and Their Applications*, vol. 118, no. 11, pp. 2022–2037, 2008.
- [124] C. Cattani, G. Pierro, and G. Altieri, "Entropy and multifractality for the myeloma multiple TET 2 gene," *Mathematical Problems in Engineering*, vol. 2012, Article ID 193761, 14 pages, 2012.
- [125] S. V. Muniandy, S. C. Lim, and R. Murugan, "Inhomogeneous scaling behaviors in Malaysian foreign currency exchange rates," *Physica A*, vol. 301, no. 1–4, pp. 407–428, 2001.
- [126] P. Shang, Y. Lu, and S. Kama, "The application of Hölder exponent to traffic congestion warning," *Physica A*, vol. 370, no. 2, pp. 769–776, 2006.
- [127] T. Jin and H. Zhang, "Statistical approach to weak signal detection and estimation using Duffing chaotic oscillators," *Science China Information Sciences*, vol. 54, no. 11, pp. 2324–2337, 2011.
- [128] M. Li, W. Zhao, and S. Y. Chen, "MBm-based scalings of traffic propagated in internet," *Mathematical Problems in Engineering*, vol. 2011, Article ID 389803, 21 pages, 2011.
- [129] H. Sheng, Y.-Q. Chen, and T.-S. Qiu, "Heavy-tailed distribution and local long memory in time series of molecular motion on the cell membrane," *Fluctuation and Noise Letters*, vol. 10, no. 1, pp. 93–119, 2011.
- [130] H. Sheng, H. Sun, Y.-Q. Chen, and T.-S. Qiu, "Synthesis of multifractional Gaussian noises based on variable-order fractional operators," *Signal Processing*, vol. 91, no. 7, pp. 1645–1650, 2011.
- [131] H. Sheng, Y. Q. Chen, and T. S. Qiu, *Fractional Processes and Fractional Order Signal Processing*, Springer, 2012.
- [132] J. F. Muzy, E. Bacry, and A. Arneodo, "Multifractal formalism for fractal signals: the structure-function approach versus the wavelet-transform modulus-maxima method," *Physical Review E*, vol. 47, no. 2, pp. 875–884, 1993.
- [133] O. Barrière and J. Lévy-Véhel, "Local Hölder regularity-based modeling of RR intervals," INRIA-00539046, Version 1, 2010.
- [134] S. Gaci, N. Zaourar, M. Hamoudi, and M. Holschneider, "Local regularity analysis of strata heterogeneities from sonic logs," *Nonlinear Processes in Geophysics*, vol. 17, no. 5, pp. 455–466, 2010.
- [135] <http://www.ndbc.noaa.gov/index.shtml>.
- [136] [http://www.ndbc.noaa.gov/historical\\_data.shtml](http://www.ndbc.noaa.gov/historical_data.shtml).
- [137] [http://www.ndbc.noaa.gov/station\\_page.php?station=lkwf1](http://www.ndbc.noaa.gov/station_page.php?station=lkwf1).
- [138] [http://www.ndbc.noaa.gov/station\\_page.php?station=lonf1](http://www.ndbc.noaa.gov/station_page.php?station=lonf1).
- [139] [http://www.ndbc.noaa.gov/station\\_page.php?station=sauf1](http://www.ndbc.noaa.gov/station_page.php?station=sauf1).
- [140] [http://www.ndbc.noaa.gov/station\\_page.php?station=smkf1](http://www.ndbc.noaa.gov/station_page.php?station=smkf1).
- [141] [http://www.ndbc.noaa.gov/station\\_page.php?station=spgf1](http://www.ndbc.noaa.gov/station_page.php?station=spgf1).

- [142] [http://www.ndbc.noaa.gov/station\\_page.php?station=venf1](http://www.ndbc.noaa.gov/station_page.php?station=venf1).
- [143] [http://www.ndbc.noaa.gov/historical\\_data.shtml#wlevel](http://www.ndbc.noaa.gov/historical_data.shtml#wlevel).
- [144] D. B. Gilhousen, "A field evaluation of NDBC moored buoy winds," *Journal of Atmospheric and Oceanic Technology*, vol. 4, no. 1, pp. 94–104, 1987.
- [145] <http://www.ndbc.noaa.gov/measdes.shtml#wlevel>.
- [146] A. N. Kolmogorov, "Wiensche Spiralen und einige andere interessante Kurven im Hilbertschen Raum," *Comptes Rendus de l'Académie des Sciences de l'URSS*, vol. 26, no. 2, pp. 115–118, 1940.
- [147] B. Matérn, *Spatial Variation*, Springer, 2nd edition, 1986.
- [148] J.-P. Chiles and P. Delfiner, *Geostatistics, Modeling Spatial Uncertainty*, Wiley, New York, NY, USA, 1999.
- [149] R. Webster and M. A. Oliver, *Geostatistics For Environmental Scientists*, Wiley, Chichester, UK, 2007.
- [150] H. Wackernagel, *Multivariate Geostatistics: An Introduction With Applications*, Springer, Dordrecht, The Netherlands, 2005.
- [151] O. Schabenberger and C. A. Gotway, *Statistical Methods For Spatial Data Analysis*, Chapman & Hall, CRC, Boca Raton, Fla, USA, 2005.
- [152] B. D. Ripley, *Spatial Statistics*, Wiley-Interscience, Hoboken, NJ, USA, 2004.
- [153] M. Schlather and T. Gneiting, "Local approximation of variograms by covariance functions," *Statistics & Probability Letters*, vol. 76, no. 12, pp. 1303–1304, 2006.
- [154] B. Minasny and A. B. McBratney, "The Matérn function as a general model for soil variograms," *Geoderma*, vol. 128, no. 3–4, pp. 192–207, 2005.
- [155] D. J. Gorsich and M. G. Genton, "Variogram model selection via nonparametric derivative estimation," *Mathematical Geology*, vol. 32, no. 3, pp. 249–270, 2000.
- [156] M. G. Genton, "The correlation structure of Matheron's classical variogram estimator under elliptically contoured distributions," *Mathematical Geology*, vol. 32, no. 1, pp. 127–137, 2000.
- [157] D. Marcotte, "Fast variogram computation with FFT," *Computers & Geosciences*, vol. 22, no. 10, pp. 1175–1186, 1996.
- [158] A. S. Monin and A. M. Yaglom, *Statistical Fluid Mechanics: Mechanics of Turbulence*, vol. 2, The MIT Press, Cambridge, Mass, USA, 1971.
- [159] E. I. Kaganov and A. M. Yaglom, "Errors in wind-speed measurements by rotation anemometers," *Boundary-Layer Meteorology*, vol. 10, no. 1, pp. 15–34, 1976.
- [160] E. O. Schulz-DuBois and I. Rehberg, "Structure function in lieu of correlation function," *Applied Physics*, vol. 24, no. 4, pp. 323–329, 1981.
- [161] Z. Warhaft, "Turbulence in nature and in the laboratory," *Proceedings of the National Academy of Sciences of the United States of America*, vol. 99, 1, pp. 2481–2486, 2002.
- [162] A. M. Yaglom, *Correlation Theory of Stationary and Related Random Functions, Vol. I: Basic Results*, Springer, 1987.
- [163] B. B. Bandelbrot and J. W. van Ness, "Fractional Brownian motions, fractional noises and applications," *SIAM Review*, vol. 10, no. 4, pp. 422–437, 1968.
- [164] T. Hida, *Brownian Motion*, Springer, 1980.
- [165] N. C. Nigam, *Introduction To Random Vibrations*, The MIT Press, 1983.
- [166] A. Papoulis, *Probability, Random Variables, and Stochastic Processes*, McGraw-Hill, 2nd edition, 1984.
- [167] I. M. Gelfand and K. Vilenkin, *Generalized Functions*, vol. 1, Academic Press, New York, NY, USA, 1964.
- [168] F. Biagini, Y. Hu, B. Øksendal, and T. Zhang, *Stochastic Calculus For Fractional Brownian Motion and Applications*, Springer, 2008.
- [169] M. Li, "Fractal time series—a tutorial review," *Mathematical Problems in Engineering*, vol. 2010, Article ID 157264, 26 pages, 2010.
- [170] J. Mikusinski, *Operational Calculus*, Pergamon Press, 1959.
- [171] A. Ayache, S. Jaffard, and M. S. Taqqu, "Wavelet construction of generalized multifractional processes," *Revista Matemática Iberoamericana*, vol. 23, no. 1, pp. 327–370, 2007.
- [172] A. Ayache and J. L. Véhel, "On the identification of the pointwise Hölder exponent of the generalized multifractional Brownian motion," *Stochastic Processes and their Applications*, vol. 111, no. 1, pp. 119–156, 2004.
- [173] P. R. Bertrand, A. Hamdouni, and S. Khadhraoui, "Modelling NASDAQ series by sparse multifractional Brownian motion," *Methodology and Computing in Applied Probability*, vol. 14, no. 1, pp. 107–124, 2012.
- [174] Z. Lin and J. Zheng, "Some properties of a multifractional Brownian motion," *Statistics and Probability Letters*, vol. 77, no. 7, pp. 687–692, 2007.

- [175] S. C. Lim and L. P. Teo, "Weyl and Riemann-Liouville multifractional Ornstein-Uhlenbeck processes," *Journal of Physics A*, vol. 40, no. 23, pp. 6035–6060, 2007.
- [176] S. V. Muniandy and S. C. Lim, "Modeling of locally self-similar processes using multifractional Brownian motion of Riemann-Liouville type," *Physical Review E*, vol. 63, no. 4, 7 pages, 2001.
- [177] S. C. Lim, "Fractional Brownian motion and multifractional Brownian motion of Riemann-Liouville type," *Journal of Physics A*, vol. 34, no. 7, pp. 1301–1310, 2001.
- [178] S. A. Stoev and M. S. Taqqu, "How rich is the class of multifractional Brownian motions?" *Stochastic Processes and Their Applications*, vol. 116, no. 2, pp. 200–221, 2006.
- [179] J.-F. Coeurjolly, "Identification of multifractional Brownian motion," *Bernoulli*, vol. 11, no. 6, pp. 987–1008, 2005.
- [180] S. Stoev and M. S. Taqqu, "Path properties of the linear multifractional stable motion," *Fractals*, vol. 13, no. 2, pp. 157–178, 2005.
- [181] A. Benassi, S. Cohen, and J. Istas, "Identifying the multifractional function of a Gaussian process," *Statistics and Probability Letters*, vol. 39, no. 4, pp. 337–345, 1998.
- [182] R. Navarro Jr., R. Tamangan, N. Guba-Natan, E. Ramos, and A. D. Guzman, "The identification of long memory process in the Asean-4 stock markets by fractional and multifractional Brownian motion," *The Philippine Statistician*, vol. 55, no. 1-2, pp. 65–83, 2006.

## Research Article

# Energy Dependent Divisible Load Theory for Wireless Sensor Network Workload Allocation

Haiyan Shi,<sup>1,2</sup> Wanliang Wang,<sup>1</sup> and Ngaiming Kwok<sup>3</sup>

<sup>1</sup> College of Computer Science, Zhejiang University of Technology, Hangzhou 310023, China

<sup>2</sup> School of Computer Science and Technology, Shaoxing University, Shaoxing 312000, China

<sup>3</sup> School of Mechanical and Manufacturing Engineering, The University of New South Wales, Sydney 2052, Australia

Correspondence should be addressed to Haiyan Shi, shi\_haiyan@163.com

Received 31 October 2012; Accepted 4 December 2012

Academic Editor: Sheng-yong Chen

Copyright © 2012 Haiyan Shi et al. This is an open access article distributed under the Creative Commons Attribution License, which permits unrestricted use, distribution, and reproduction in any medium, provided the original work is properly cited.

The wireless sensor network (WSN), consisting of a large number of microsensors with wireless communication abilities, has become an indispensable tool for use in monitoring and surveillance applications. Despite its advantages in deployment flexibility and fault tolerance, the WSN is vulnerable to failures due to the depletion of limited onboard battery energy. A major portion of energy consumption is caused by the transmission of sensed results to the master processor. The amount of energy used, in fact, is related to both the duration of sensing and data transmission. Hence, in order to extend the operation lifespan of the WSN, a proper allocation of sensing workload among the sensors is necessary. An assignment scheme is here formulated on the basis of the divisible load theory, namely, the energy dependent divisible load theory (EDDLT) for sensing workload allocations. In particular, the amount of residual energies onboard sensors are considered while deciding the workload assigned to each sensor. Sensors with smaller amount of residual energy are assigned lighter workloads, thus, allowing for a reduced energy consumption and the sensor lifespan is extended. Simulation studies are conducted and results have illustrated the effectiveness of the proposed workload allocation method.

## 1. Introduction

Sensors are devices that are frequently used in surveillance applications including industrial plant conditions, highway traffics, building security, and environment monitoring. When sensors are wire connected, their deployments or relocations may be severely hindered [1–3]. With advancements in sensing, electronics, and radio technologies, sensors equipped with computation and communication capabilities have become available. A wireless sensor network (WSN) can then be formed to perform an assigned surveillance task independently

[4] or in a collaborative manner [5]. Usually, each sensor in a WSN collects sensing data and then sends the result to a central processor for further analysis. In order to maximize the data transfer efficiency, careful transmission routing designs are required [6]. On the other hand, wireless sensors are embedded with only onboard batteries as the sole power source. Because the deployment of wireless sensors is mostly carried out in an ad hoc manner, it may be difficult to gain access to their locations and makes battery replacements difficult. Hence, it is very desirable that the rate of battery energy consumption could be carefully managed [7]. Otherwise, some form of energy harvesting [8] is needed to ensure that the sensor can operate in an extended duration. Such approach, however, is complicated and may increase the cost in setting up the WSN. Alternatively, approaches to prolong the operation duration by choosing data transmission routes [9] can be properly determined to reduce battery energy consumption.

In addition to properly determine the data transmission route, it is also possible to reduce sensor energy consumption by dividing the sensing workload appropriately among elements in the WSN [10]. This approach is frequently developed by making use of the divisible load theory (DLT) [11]. In the theory, it is assumed that the computation or sensing workload can be arbitrarily divided into portions [12] so that the time to complete the task could be minimized. The DLT has been applied in computation load sharing among distributed processors [13] because of its tractability in closed-form solutions. This theory is also generic enough that it has been used in load scheduling for a variety of network architectures such as systems having time-varying computation speeds [14]. The DLT was employed in a bus network of processors [15] while the cost of computation was optimized. Furthermore, DLT can also be applied in the scheduling of loads on a star and tree network [16] where the theory was used to assign loads to processors in multirounds.

For wireless sensor networks, scheduling is concerned with proper assignments of the sensing and result reporting workloads [17] corresponding to the computation and communication phases in distributed networks. For example, in [18], several sensing and reporting strategies were studied and their performances were evaluated by the use of DLT. These strategies include simultaneous sensing start and sequential report, simultaneous sensing start and simultaneous report termination, concurrent sensing, and reporting. Each strategy is adopted on the basis of the network architecture whether coprocessors or multichannel communication is available. Although the DLT can be applied for wireless sensor network workload scheduling, the operation of a WSN is quite different from that of computer networks. Specifically, sensors engaged in the WSN operate only from onboard battery energies and the amount of such energy is always limited.

Energy consumption is a prominent issue that network designers have to take into consideration [19] even for distributed computer networks. Because of the need for WSNs to transmit the sensed data to a master processor, a majority of energy would be consumed therein. Therefore, in order to mitigate the adverse effect of energy depletion on network lifetime, sensors are formed into clusters depending on their physical location vicinity [20]. Clustering itself is a challenging task for deterministic approaches that designer may employ soft computing techniques to design clusters [21–27]. A further development, the low-energy adaptive clustering hierarchy (LEACH) protocol was reported in [28] that sensor clusters are formed according to the sensor locations with the objective to minimize the overall energy consumed by the sensors in the network. An alternative scheme was presented [29] where the sensor network lifetime was extended by dynamically adjusting the transmission routes. Furthermore, the minimization of total energy consumed along a sensor data reporting route was considered [30] for multihop transmission. Moreover, an attempt was made to employ

a spanning tree [31] representation of the sensed data reporting route which resulted in the reduction of sensor energy consumption.

Issues on sensor energy consumption are receiving a considerable amount of recent research attention. Its reduction to prolong network lifetime has also been tackled from diversified perspectives. For example, sensor clusters were formed and the cluster head, responsible to process or retransmit the sensed data, was elected in accordance with the ratio of residual energies of neighboring sensors [32]. By building on the cluster structure, hierarchies of sensor clusters were constructed to carry out a sensing task in a coordinated manner [33] in order to minimize the energy used in radio transmission. Moreover, a challenging design case [34], where network communication resources such as sensing and transmission speed were not known, was approached using an adaptive strategy to allocate sensing workloads.

In the reported works, attempts to extend network lifetime were made by using the proper workload allocation strategy or the transmission routing optimization strategy in order to minimize energy consumption. However, it has not been studied in detail how workload division can effectively increase the WSN operation duration. Here, the divisible load theory is adopted for WSN workload assignment. The modification on DLT makes use of the ratio of the initial to residual sensor energies when the workload allocated to an individual sensor is determined. By adopting this design philosophy, sensors having a lesser amount of remaining energy will be given a smaller portion of sensing workload and provides a reduction on its energy consumption. The overall result is that the energy depletion time of each sensor is prolonged; hence, the whole wireless sensor network can operate for an extended duration.

The rest of the paper is organized as follows. In Section 2, the WSN structure is firstly presented and the application of DLT is described. In Section 3, the energy consumption profile is formulated and the development of the proposed energy dependent divisible load theory is given. Simulations to verify the proposed method are described and results are presented in Section 4. Finally, a conclusion is drawn in Section 5.

## **2. Wireless Sensor Network Workload Allocation**

Sensors in the network consume battery energy in their electronic circuits when carrying out sensing and radio transmission [35]. In practice, the amount of energy used is proportional to the duration that these activities are being conducted. In order to reduce the rate of energy consumption, it is desirable that sensing and reporting operations can be completed in the shortest time. It is also assumed that, in terms of some demanded sensing precision that leads to a certain quantity of measured data required, the sensing workload can be divided among sensors in the network. To this end, the divisible load theory is applied to derive a set of optimal workloads in the sense of minimum sensing completion time and minimum sensor energy consumption. In the following, the WSN architecture adopted in the current work is presented and the enhancement of DLT in determining workloads is illustrated.

### **2.1. Wireless Sensor Network Architecture**

Let the wireless sensor network contains  $N$  sensors clustered in a star topology [16], see Figure 1. Sensors  $S_i$ ,  $i = 1, \dots, N$ , are responsible to measure the environment and report

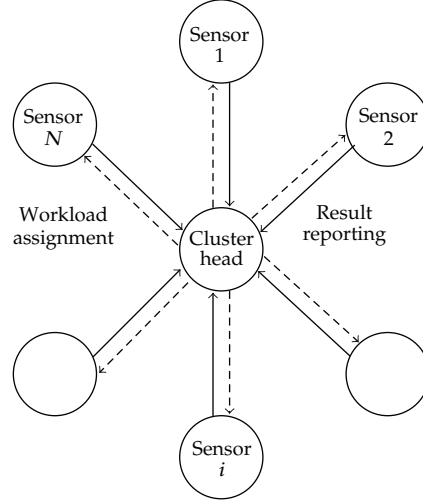


Figure 1: Star network architecture.

the results via wireless communication to the cluster head CH. The cluster head relays workload assignments from the master processor to sensors, performs data aggregation and transmits them back to the master processor for analysis [18]. On the other hand, the CH does not take measurements nor reports its own data. It is also assumed that the network operates on a single two-way channel but radio communication is only permitted for one-direction transmission from a sole originator at any time. Thus, workload assignments are transmitted from the CH to sensors sequentially. Furthermore, sensors report the sensed results to the CH via the same radio channel also in the sequential transmission mode. Each sensor receives the workload assignment from the CH but measurement is allowed to commence only after the last sensor has received its workload allocation command. The sensor then carries out sensing the environment and reports the results when the measurement is completed. The time and amount of result data to be sent to the CH is proportional to the workload assigned. Moreover, it is assumed that the duration of reporting is a scaled portion of the sensing time. All sensor characteristics including energy consumption rate, sensing, and reporting rates all remain constant during the course of a sensing task. However, the residual battery onboard the sensor diminishes in proportional to the amount of sensing workload carried out as well as the distance between the CH and the sensor.

## 2.2. Application of Divisible Load Theory

Based on the aforementioned wireless sensor network architecture, a timing diagram could then be drawn and is depicted in Figure 2. It can be seen that the time for workload assignment  $T_{as}$  is equal for all sensors and measurement starts simultaneously for all sensors at time  $T_0$ . The sensing time for sensor  $S_i$  is given by

$$T_{ms,i} = \alpha_i \gamma_i T_{ms}, \quad (2.1)$$

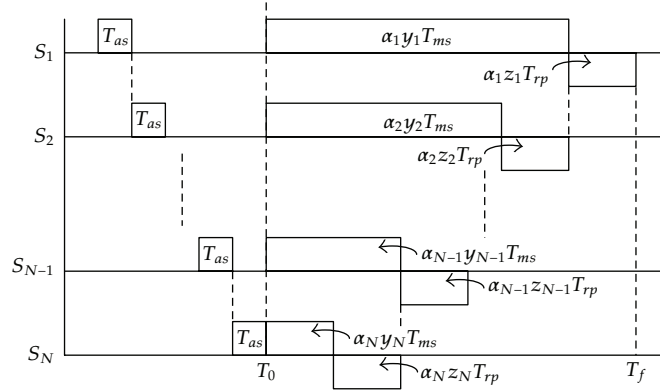


Figure 2: Sensing and result reporting schedule.

where  $\alpha_i$  is the portion of assigned sensing workload,  $y_i$  is a design coefficient to modify  $\alpha_i$ , and  $T_{ms}$  is the sensor measurement time determined by the sensor circuitry. When sensing is completed, the sensor sends the result to the CH in time

$$T_{rp,i} = \alpha_i z_i T_{rp}, \quad (2.2)$$

where  $z_i$  is also a design parameter that modifies the radio transmission duration,  $T_{rp}$  is the time used for result reporting. The overall time that sensor  $S_i$  used for the portion of assigned workload is

$$T_{S_i} = \alpha_i y_i T_{ms} + \alpha_i z_i T_{rp}. \quad (2.3)$$

Since the communication channel allows only one originator to transmit, the strategy adopted here is to align the sensing time of sensor  $S_{i-1}$  to that of the overall sensing and reporting time of sensor  $S_i$ . Thus

$$\alpha_{i-1} y_{i-1} T_{ms} = \alpha_i y_i T_{ms} + \alpha_i z_i T_{rp}. \quad (2.4)$$

This equation can be written as

$$\alpha_i = s_i \alpha_{i-1}, \quad i = 2, \dots, N, \quad (2.5)$$

where

$$s_i = \frac{y_{i-1} T_{ms}}{y_i T_{ms} + z_i T_{rp}}. \quad (2.6)$$

The portion of workload coefficients  $\alpha_i$  can then be obtained recursively from the following set of equations, namely,

$$\begin{aligned}
 \alpha_2 &= s_2 \alpha_1 \\
 \alpha_3 &= s_3 \alpha_2 = s_3 s_2 \alpha_1 \\
 &\vdots \\
 \alpha_N &= s_N \alpha_{N-1} = s_N s_{N-1} \cdots s_2 \alpha_1.
 \end{aligned} \tag{2.7}$$

In general, we have

$$\alpha_i = \alpha_1 \prod_{j=2}^i s_j. \tag{2.8}$$

Furthermore, when the sensing workload is normalized to unity, that is

$$\sum_{i=1}^N \alpha_i = 1, \tag{2.9}$$

then the first workload assignment  $\alpha_1$  can be obtained from separating  $\alpha_1$  from all other workload assignment coefficients in (2.8), then

$$\alpha_1 = \frac{1}{1 + \sum_{i=2}^N \prod_{j=2}^i s_j} \tag{2.10}$$

and the other assignments,  $\alpha_2, \dots, \alpha_N$ , can be found from invoking (2.7) recursively.

### 3. Energy Dependent Workload Allocation

The assignment of proper workload to individual sensors, according to the divisible load theory, enables the measurement task to be completed in the shortest time. However, in wireless sensor networks, it is required to consider the energy consumed by each sensor in order to maintain the network in operation for an extended period. Sensors at longer distance to the cluster head may have their onboard battery energy depleted early due to the need to transmit at higher radio power. In order to compromise the task completion time and the lifespan of the whole network, workload assignments should be designed by taking the available or residual energy of sensors into consideration. First, a profile of sensor energy consumption is sketched below, then the incorporation of energy dependence into the divisible load theory is proposed.

### 3.1. Residual Energy Profile

Consider that the master processor requires a set of  $B$  bytes of data to interpret the environment being monitored. This amount of data is the quantity of report produced by all sensors and takes a total of  $T_{rp} = 8 \times B\tau_b$  seconds to complete, where  $\tau_b$  is the time to transmit 1 bit of data. Furthermore, the time to generate the result data is directly proportional to the amount of data, that is,  $T_{ms} = kT_{rp}$ , where  $k > 0$ , in general, is the scale factor representing the data compression process and depends on the sensor design. Also assume the current drained to sense a bit of data be  $I$ , then the energy consumed per bit in sensing is  $E_s = VI\tau_b$ .

Each sensor is initially installed with a battery onboard as the energy source [36]. Let the normal battery voltage be  $V$  volt and the battery capacity is  $A$  ampere-hour. Therefore, the initial energy carried by the sensor is

$$\bar{E}_0 = VA \times 60^2. \quad (3.1)$$

Further assume that when the network is deployed for the first time and sensor locations are to be determined, for example, using directional antenna [37]. Throughout this localization phase, some energy  $\eta_1\bar{E}_0$  would be consumed. Moreover, sensors may also form into clusters [28] and a further amount of energy  $\eta_2\bar{E}_0$  is consumed. Thus, the onboard energy of a sensor before any measurement is made becomes

$$E_{0,i} = (1 - \eta_1 - \eta_2)\bar{E}_0, \quad (3.2)$$

where  $\eta_1 \in [0.00 \ 0.02]$  and  $\eta_2 \in [0.00 \ 0.03]$  are random numbers representing the initial portion of energy usage.

For a sensor  $S_i$  assigned with workload fraction  $\alpha_i$ , the sensing time is  $T_{ms,i} = \alpha_i T_{ms}$ . During this period, an equivalent number of data bits that consume energy are  $B_{ms,i} = T_{ms,i}/\tau_b$  and the energy consumed is  $E_{ms,i} = B_{ms,i}E_s$ . For sensed data reporting, the report time is  $T_{rp,i} = \alpha_i T_{rp}$ , and the number of bits reported is  $B_{rp,i} = T_{rp,i}/\tau_b$ .

In addition, assume that the transmit power can be adjusted according to the distance  $d$  between the sensor and the cluster head [38]. The energy consumed in transmitting the result to the cluster head is

$$E_{rp,i} = B_{rp,i} \left( 1046 \times 10^{-9} + 22.2 \times 10^{-12} d^2 \right). \quad (3.3)$$

The residual energy remained on the sensor, after the  $t$ th sensing and reporting round, is hence equal to

$$E_{t,i} = E_{t-1,i} - E_{ms,i} - E_{rp,i}, \quad \text{for } t = 1, 2, \dots. \quad (3.4)$$

### 3.2. Proposed Workload Allocation Scheme

An examination of the energy consumption profile reveals that energy consumed in a sensor depends both on the time used in sensing and the distance between the sensor and the cluster head. However, the distance is fixed once the sensor is deployed and cannot be altered. On the contrary, the time used in sensing and result reporting can be properly determined in

order to reduce energy usage. The philosophy adopted is that a lighter workload would be assigned to a sensor which a lesser amount of residual energy has remained onboard.

Recall the time  $T_{S_i}$  that a sensor used for measuring and result reporting, as given by (2.3) and repeated here,

$$T_{S_i} = \alpha_i y_i T_{ms} + \alpha_i z_i T_{rp}. \quad (3.5)$$

Without loss of generality, we make the timing scale factors equal,  $y_i = z_i$ . Furthermore, by making use of the fact that the amount of data reported by a sensor is proportional to its sensing time,  $T_{ms} = kT_{rp}$ , then

$$T_{S_i} = \alpha_i y_i (1 + k) T_{rp}. \quad (3.6)$$

Now, put the coefficient  $y_i$  as a function of the ratio of the initial energy  $E_{0,i}$  to the instantaneous onboard energy  $E_{t,i}$ , that is

$$y_i = \frac{E_{0,i}}{E_{t,i} + \epsilon}, \quad (3.7)$$

where  $\epsilon$  is a small positive constant to prevent division by zero.

Consider the recursive equations in calculating the workload allocation  $\alpha_i$ , (2.5), substitute the above assumptions and the energy dependence, we have

$$\begin{aligned} s_i &= \frac{y_{i-1} k T_{rp}}{y_i k T_{rp} + y_i T_{rp}} \\ &= \frac{k y_{i-1}}{(1+k) y_i} \\ &\approx \frac{k E_{0,i} / E_{t,i-1}}{(1+k) E_{0,i} / E_{t,i}} \\ &\approx \frac{k E_{t,i}}{(1+k) E_{t,i-1}}. \end{aligned} \quad (3.8)$$

Furthermore, the workload ratio for two consecutive sensors is

$$\alpha_i = s_i \alpha_{i-1}, \quad (3.9)$$

and substitute (3.8), then

$$\frac{\alpha_i}{\alpha_{i-1}} = \frac{k E_{t,i}}{(1+k) E_{t,i-1}}. \quad (3.10)$$

It can be observed that workloads assigned are now made proportional to the residual energy remained onboard the sensor together with the constant system dependent scaling

**Table 1:** Simulation parameters.

Parameter description	Value
Number of simulation runs for each SDLT and EDDLT case	100
Area of square environment monitored	$50 \times 50$ m
Number of sensors ( $N$ )	30
Data required by master processor ( $B$ )	$2 \times 10^6$ bytes
Time to transmit 1 bit ( $\tau_b$ )	$64 \times 10^{-6}$ sec
Ratio of sensing/reporting durations ( $k$ )	8
Average battery voltage ( $V$ )	3 V
Battery capacity ( $A$ )	0.5 Ah
Current drain per bit ( $I$ )	$0.3 \times 10^{-3}$ A/bit

factor  $k/(1+k)$ . Hence, sensors with a lesser amount of residual energy will receive a lesser amount of workload consequently reduces its energy consumption and prolongs its operation lifetime. Furthermore, when the factor  $k$  is large, the workload becomes largely dependent on the residual energies.

## 4. Simulation

Simulations are conducted to verify the effectiveness of the proposed energy dependent divisible load theory when it is applied in the workload allocation of a wireless sensor network. Two test cases are studied including the standard DLT (SDLT) approach and the energy dependent DLT (EDDLT) approach. It is assumed that sensors are deployed randomly over an area that is to be monitored. Because of the randomness in initial sensor deployments, the effectiveness will be assessed by a large number of repetitive tests. Statistics are collected on the sensing rounds that the first sensor energy depletes, the sensing rounds that the last sensor depleted its energy, and distribution of residual energies when the first sensor depletes its energy. The simulations conducted are based on the system and sensor parameters given in Table 1.

### 4.1. History of Energy Depletion

In the simulations for SDLT and EDDLT approaches, sensors are deployed randomly over a square sensing area as shown in Figures 3(a) and 4(a), respectively, at the first sensing round. In the figures, a red square is used to represent the cluster head. Sensors are indicated as black dots while their initial energies are denoted by circles whose diameters are proportional to the onboard energy. The instances that the first sensor depletes its energy for the SDLT and EDDLT cases are depicted in Figures 3(b) and 4(b). Since the sensors are deployed randomly and their positions relative to the cluster head would affect the energy consumption, numerical values given here are regarded as typical sample values only.

It can be seen that in the SDLT approach, at a small number of sensing rounds at 1900, other sensors still maintain relative large amount of remaining energies. On the other hand, in the EDDLT case, when the first sensor depletes its energy, energies on other sensors are also depleted to a large extend. In addition, the sensing round at 6244 that the first sensor depletes its energy is much more than that in the SDLT case. Figures 3(c) and 4(c) illustrate the instance

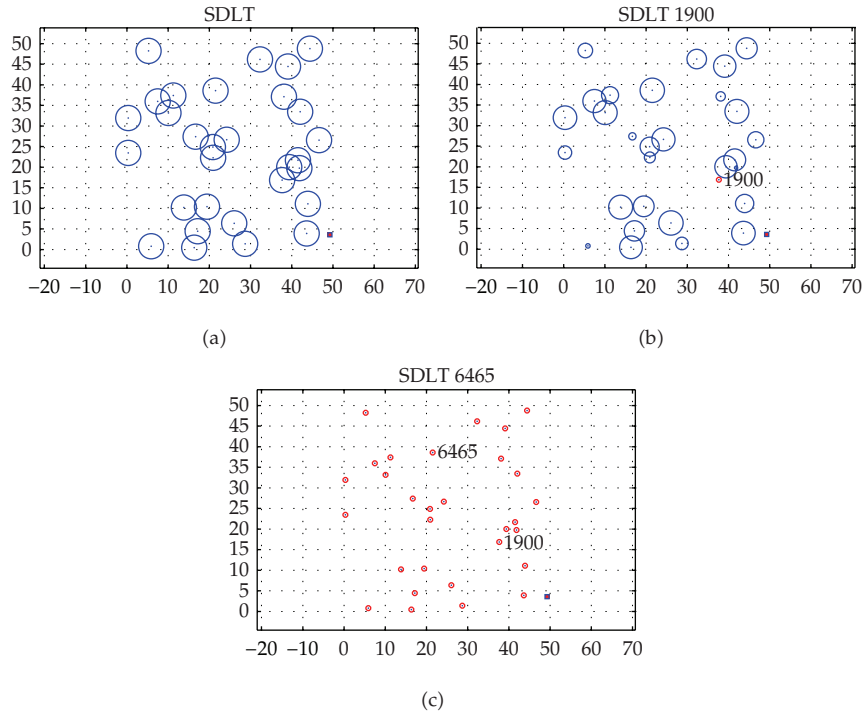


**Figure 3:** Sensor energy evolution in standard DLT (SDLT) workload allocation. (a) initial energy onboard sensors, (b) instance when first sensor depleted, (c) instance when last sensor depleted.

when the last sensor depletes its energy. The sensing round conducted in the SDLT case is 6465 while that in the EDDLTL case is 6469. These sensing rounds are approximately the same as expected. It is because the total amount energies inherent in the system and the amount of resultant sensed data are the same.

#### 4.2. History of Life Sensors in Operation

Graphical plots depicting the histories of the number of life sensors remaining in operation, for the SDLT and EDDLTL cases, are given in Figures 5(a) and 5(b). It can be observed that the first sensor depletes much earlier in the SDLT case as compared with the EDDLTL case. Furthermore, the figures also illustrate that the overall system failure times are approximately the same in these two cases. Contradictorily, the slope of sensor death in the EDDLTL case is much steeper than the SDLT case. This observation reflects the fact that the EDDLTL approach is effective in prolonging the overall operation of the wireless sensor network.

#### 4.3. Distribution of Energy Onboard Sensors

The plots of the distribution of energies onboard sensors, when the first sensor depletes, are shown in Figures 6(a) and 6(b). The graph of energy onboard sensors in the SDLT case shows that many sensors still carry substantial amount of energies when the first sensor depletes. This observation indicates that the SDLT strategy for workload allocation is not effective to

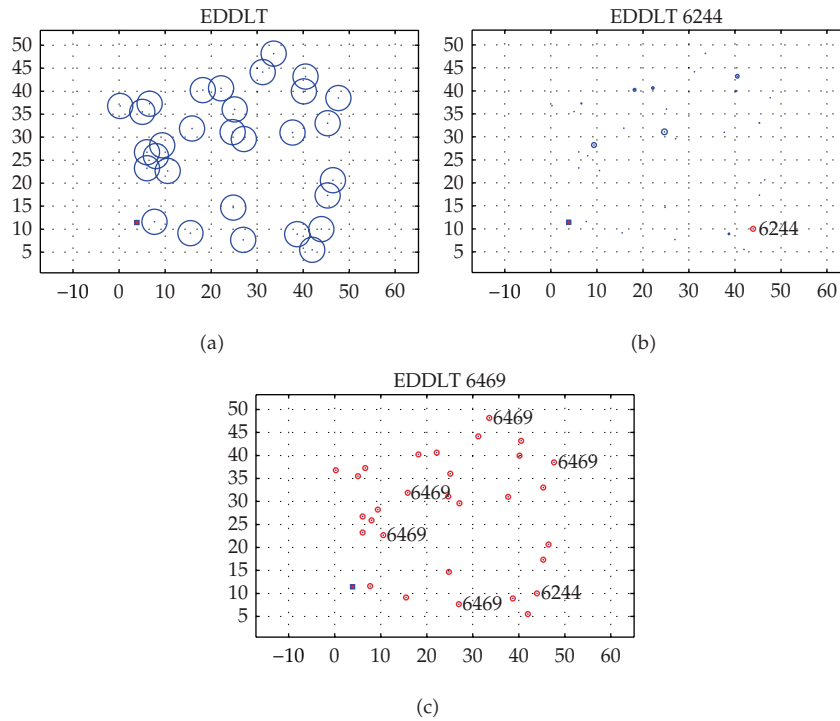


**Figure 4:** Sensor energy evolution in energy dependent DLT (EDDLT) workload allocation. (a) initial energy onboard sensors, (b) instance when first sensor depleted, (c) instance when last sensor depleted.

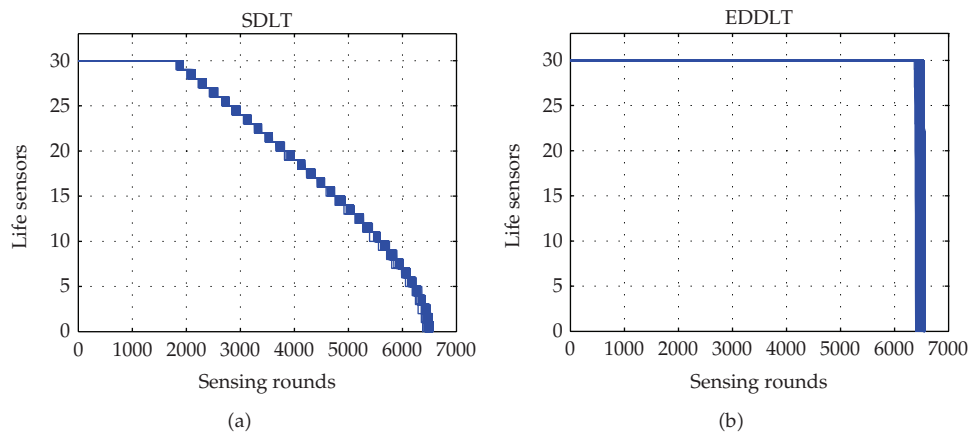


**Figure 5:** History of number of life sensors. (a) SDLT case, (b) EDDLTL case.

maintain the whole WSN to operation at full capacity. On the other hand, in the EDDLTL case, most sensors have used up their energies at later sensing rounds when the first sensor depletes. This reflects the fact that in a large portion of the sensing period, most sensors are in operation and a better monitoring of the environment is made.

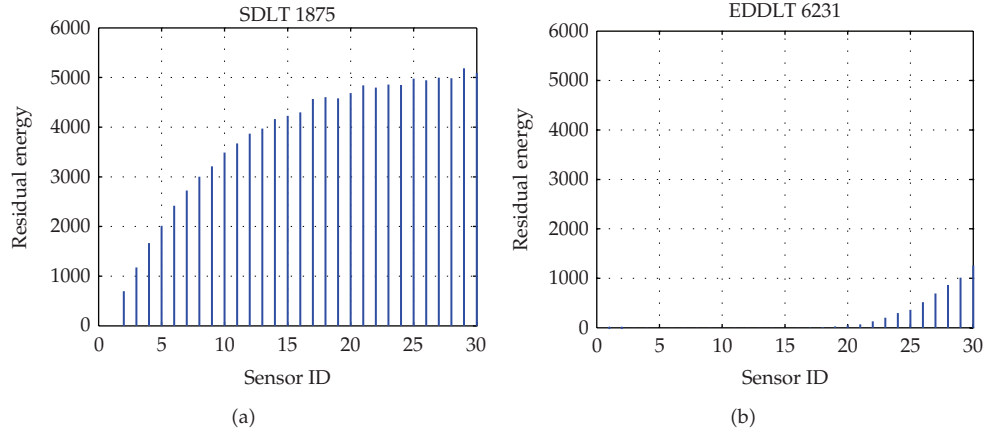


Figure 6: Distribution of energy onboard sensors. (a) SDLT case, (b) EDDL case.

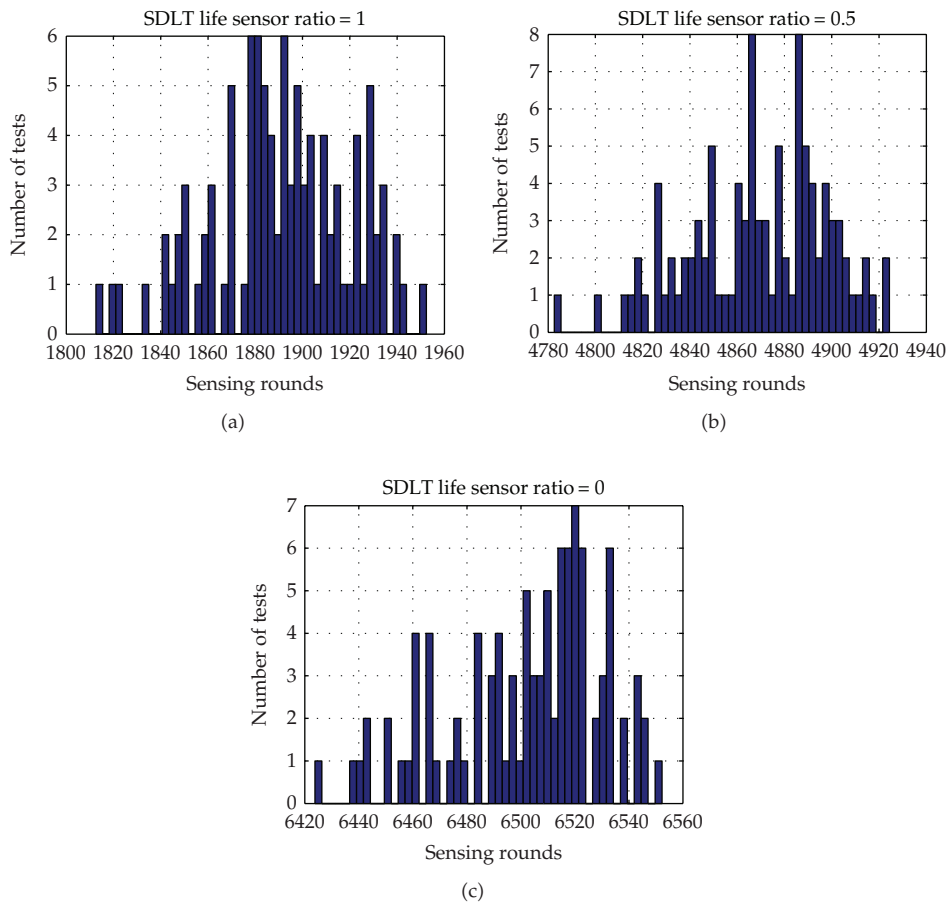
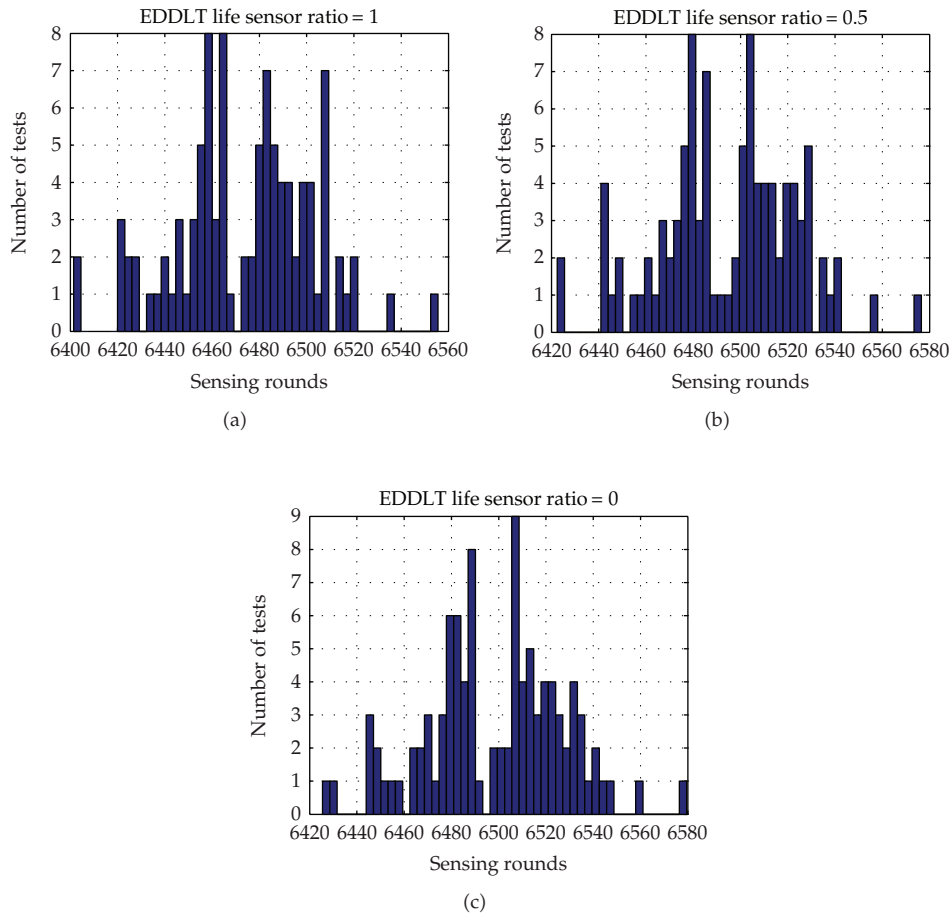


Figure 7: Statistics of test runs - SDLT case. (a) first sensor depletes, (b) 50% sensors remain life, (c) last sensor depletes.



**Figure 8:** Statistics of test runs - EDDLTL case. (a) first sensor depletes, (b) 50% sensors remain life, (c) last sensor depletes.

#### 4.4. Network Performance Statistics

Since the initial random deployment of sensors critically affects the network performance, its characterization is here based on the statistics from a repetition of 100 simulations. Figures 7 and 8 show, from simulation results from the SDLT and EDDLTL cases, the distribution of first sensor depletion, the instance of 50% sensors remain life in the sensing round when all sensors consumed their energies. The distributions demonstrate that the number of sensing rounds approximately obeys normal distributions in both the SDLT and EDDLTL cases, thus, providing statistical evidences on the validity of the results. As it is suggested from other performance measures presented above, the sensing rounds that the first sensor depletes in the EDDLTL cases are much later than that of the SDLT cases. Figure 9 further compares the statistics of the ratio of the number of sensors remaining life throughout the sensing task duration. The SDLT case is given in dotted lines with the mean value and  $\pm 3\sigma$  deviations from the mean. It is seen that the EDDLTL approach has enabled the network to operate with the full number of sensors at sensing rounds much later than the SDLT case.

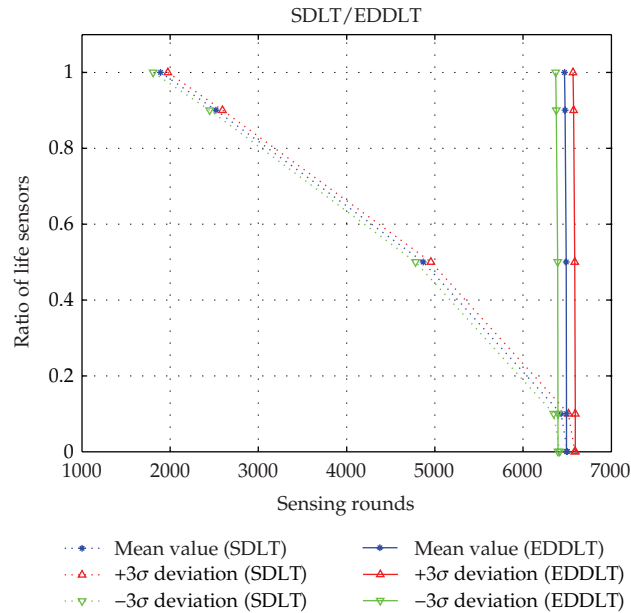


**Figure 9:** Comparison of ratio of life sensors between standard and energy dependent DLT for workload allocation.

## 5. Conclusion

This paper has presented a study on the wireless sensor network workload allocation scheme. An energy dependent divisible load theory (EDDLT) based approach is developed. In the proposed approach, the residual energies of sensors are considered while assigning the workload to each sensor. Sensors with smaller residual energy are assigned lighter workload. With this strategy, the number of sensing rounds that the first sensor depletes is increased as compared to the standard divisible load theory approach. Experiments are included to illustrate the effectiveness of the EDDLTL method in extending the lifespan of the wireless sensor network.

## Acknowledgments

This work was supported by the National Natural Science Foundation of China (Grant nos. 61070043, 60573123), Zhejiang Provincial Key Disciplines on Information Processing & Automation Technology (20110815), and Zhejiang Education Department (Y201122434).

## References

- [1] C. Cattani, S. Chen, and G. Aldashev, "Information and modeling in complexity," *Mathematical Problems in Engineering*, vol. 2012, Article ID 868413, 3 pages, 2012.
- [2] S. Y. Chen, H. Tong, Z. Wang, S. Liu, M. Li, and B. Zhang, "Improved generalized belief propagation for vision processing," *Mathematical Problems in Engineering*, vol. 2012, Article ID 416963, 12 pages, 2011.

- [3] S. Wen, W. Zheng, J. Zhu, X. Li, and S. Chen, "Elman fuzzy adaptive control for obstacle avoidance of mobile robots using hybrid force/position incorporation," *IEEE Transactions on Systems, Man and Cybernetics C*, vol. 42, no. 4, pp. 603–608, 2012.
- [4] J. Yick, B. Mukherjee, and D. Ghosal, "Wireless sensor network survey," *Computer Networks*, vol. 52, no. 12, pp. 2292–2330, 2008.
- [5] H. Y. Shi, W. L. Wang, N. M. Kwok, and S. Y. Chen, "Game theory for wireless sensor networks: a survey," *Sensors*, vol. 12, no. 7, pp. 9055–9097, 2012.
- [6] K. Akkaya and M. Younis, "A survey on routing protocols for wireless sensor networks," *Ad Hoc Networks*, vol. 3, no. 3, pp. 325–349, 2005.
- [7] G. Anastasi, M. Conti, M. Di Francesco, and A. Passarella, "Energy conservation in wireless sensor networks: a survey," *Ad Hoc Networks*, vol. 7, no. 3, pp. 537–568, 2009.
- [8] A. Kansal and M. B. Srivastava, "An Environmental Energy Harvesting Framework for Sensor Networks," in *Proceedings of the International Symposium on Low Power Electronics and Design (ISLPED '03)*, pp. 481–486, August 2003.
- [9] C. K. Toh, "Maximum battery life routing to support ubiquitous mobile computing in wireless ad hoc networks," *IEEE Communications Magazine*, vol. 39, no. 6, pp. 138–147, 2001.
- [10] H. Y. Shi, N. M. Kwok, and W. L. Wang, "Mechanism penalty for task scheduling in wireless sensor networks," *Advances in Information Sciences and Service Sciences*, vol. 4, no. 11, pp. 233–242, 2012.
- [11] T. G. Robertazzi, "Ten reasons to use divisible load theory," *Computer*, vol. 36, no. 5, pp. 63–68, 2003.
- [12] J. Błażewicz, M. Drozdowski, and M. Markiewicz, "Divisible task scheduling—concept and verification," *Parallel Computing*, vol. 25, no. 1, pp. 87–98, 1999.
- [13] V. Bharadwaj, D. Ghose, and T. G. Robertazzi, "Divisible load theory: a new paradigm for load scheduling in distributed systems," *Cluster Computing*, vol. 6, pp. 7–17, 2003.
- [14] J. Sohn and T. G. Robertazzi, "Optimal time-varying load sharing for divisible loads," *IEEE Transactions on Aerospace and Electronic Systems*, vol. 34, no. 3, pp. 907–923, 1998.
- [15] J. Sohn, T. G. Robertazzi, and S. Luryi, "Optimizing computing costs using divisible load analysis," *IEEE Transactions on Parallel and Distributed Systems*, vol. 9, no. 3, pp. 225–234, 1998.
- [16] O. Beaumont, H. Casanova, A. Legrand, Y. Robert, and Y. Yang, "Scheduling divisible loads on star and tree networks: results and open problems," *IEEE Transactions on Parallel and Distributed Systems*, vol. 16, no. 3, pp. 207–218, 2005.
- [17] C. F. Gamboa and T. G. Robertazzi, "Efficient scheduling for sensing and data reporting in wireless sensor networks," in *Proceedings of the 40th Annual Conference on Information Sciences and Systems (CISS '06)*, pp. 171–176, March 2006.
- [18] M. Moges and T. G. Robertazzi, "Wireless sensor networks: scheduling for measurement and data reporting," *IEEE Transactions on Aerospace and Electronic Systems*, vol. 42, no. 1, pp. 327–340, 2006.
- [19] M. Drozdowski, "Energy considerations for divisible load processing," in *Proceedings of the 8th International Conference on Parallel Processing and Applied Mathematics (PPAM '09)*, Lecture Notes in Computer Science, pp. 92–101, 2009.
- [20] W. R. Heinzelman, A. Chandrakasan, and H. Balakrishnan, "Energy-efficient communication protocol for wireless microsensor networks," in *Proceedings of the 33rd Annual Hawaii International Conference on System Sciences (HICSS '00)*, p. 223, January 2000.
- [21] J. S. Lee and W. L. Cheng, "Fuzzy-logic-based clustering approach for wireless sensor networks using energy prediction," *IEEE Sensors Journal*, vol. 12, no. 9, pp. 2891–2896, 2012.
- [22] J. Xue, M. Li, W. Zhao, and S. Chen, "Bound maxima as a traffic feature under DDOS flood attacks," *Mathematical Problems in Engineering*, vol. 2012, Article ID 419319, 20 pages, 2012.
- [23] S. Castellucci and M. Carlini, "Modelling and simulation for energy production parametric dependence in greenhouses," *Mathematical Problems in Engineering*, vol. 2010, Article ID 590943, 28 pages, 2010.
- [24] S. C. Lim, C. H. Eab, K. H. Mak, M. Li, and S. Y. Chen, "Solving linear coupled fractional differential equations by direct operational method and some applications," *Mathematical Problems in Engineering*, vol. 2012, Article ID 653939, 28 pages, 2012.
- [25] S. Chen, W. Huang, C. Cattani, and G. Altieri, "Traffic dynamics on complex networks: a survey," *Mathematical Problems in Engineering*, vol. 2012, Article ID 732698, 23 pages, 2012.
- [26] M. Li, S. C. Lim, and S. Chen, "Exact solution of impulse response to a class of fractional oscillators and its stability," *Mathematical Problems in Engineering*, vol. 2011, Article ID 657839, 9 pages, 2011.
- [27] S. Castellucci, M. Carlini, M. Guerrieri, and T. Honorati, "Stability and control for energy production parametric dependence," *Mathematical Problems in Engineering*, vol. 2010, Article ID 842380, 21 pages, 2010.

- [28] W. B. Heinzelman, A. P. Chandrakasan, and H. Balakrishnan, "An application-specific protocol architecture for wireless microsensor networks," *IEEE Transactions on Wireless Communications*, vol. 1, no. 4, pp. 660–670, 2002.
- [29] M. Younis, M. Youssef, and K. Arisha, "Energy-aware management for cluster-based sensor networks," *Computer Networks*, vol. 43, no. 5, pp. 649–668, 2003.
- [30] S. Fedor and M. Collier, "On the problem of energy efficiency of multi-hop vs one-hop routing in Wireless Sensor Networks," in *Proceedings of the 21st International Conference on Advanced Information Networking and Applications Workshops/Symposia (AINAW '07)*, pp. 380–385, May 2007.
- [31] S. Hussain and O. Islam, "An energy efficient spanning tree based multi-hop routing in wireless sensor networks," in *Proceedings of IEEE Wireless Communications and Networking Conference (WCNC '07)*, pp. 4386–4391, March 2007.
- [32] J. Yu, Y. Qi, G. Wang, Q. Guo, and X. Gu, "An energy-aware distributed unequal clustering protocol for wireless sensor networks," *International Journal of Distributed Sensor Networks*, vol. 2011, Article ID 202145, 8 pages, 2011.
- [33] X. L. Li and J. N. Cao, "Coordinated workload scheduling in hierarchical sensor networks for data fusion applications," *Journal of Computer Science and Technology*, vol. 23, no. 3, pp. 355–364, 2008.
- [34] D. Ghose, H. J. Kim, and T. H. Kim, "Adaptive divisible load scheduling strategies for workstation clusters with unknown network resources," *IEEE Transactions on Parallel and Distributed Systems*, vol. 16, no. 10, pp. 897–907, 2005.
- [35] R. Min, M. Bhardwaj, S. H. Cho et al., "Architecture for a power-aware distributed microsensor node," in *Proceedings of the Workshop on Signal Processing Systems (SIPS '00)*, pp. 581–590, October 2000.
- [36] O. Younis and S. Fahmy, "An experimental study of routing and data aggregation in sensor networks," in *Proceedings of the 2nd IEEE International Conference on Mobile Ad-hoc and Sensor Systems (MASS '05)*, pp. 50–57, November 2005.
- [37] C. H. Ou, "A localization scheme for wireless sensor networks using mobile anchors with directional antennas," *IEEE Sensors Journal*, vol. 11, no. 7, pp. 1607–1616, 2011.
- [38] G. Hou and K. W. Tang, "Evaluation of LEACH protocol subject to different traffic models," in *Proceedings of the 1st International Conference on Next Generation Network*, pp. 281–283, 2006.

*Research Article*

# **The Semitransparent Photovoltaic Films for Mediterranean Greenhouse: A New Sustainable Technology**

**Alvaro Marucci,<sup>1</sup> Danilo Monarca,<sup>1</sup> Massimo Cecchini,<sup>1</sup>  
Andrea Colantoni,<sup>1</sup> Alberto Manzo,<sup>2</sup> and Andrea Cappuccini<sup>1</sup>**

<sup>1</sup> *Department of Agriculture, Forests, Nature and Energy (DAFNE), University of Tuscia, 01100 Viterbo, Italy*

<sup>2</sup> *SACO VI Office-Nursery Gardening, Ministry of Agricultural, Food and Forestry Policies (IMAFFP), Via XX Settembre, 20, 00187 Rome, Italy*

Correspondence should be addressed to Alvaro Marucci, marucci@unitus.it

Received 16 October 2012; Accepted 8 November 2012

Academic Editor: Massimo Scalia

Copyright © 2012 Alvaro Marucci et al. This is an open access article distributed under the Creative Commons Attribution License, which permits unrestricted use, distribution, and reproduction in any medium, provided the original work is properly cited.

Mediterranean countries offer very favorable climatic conditions for growing plants in a protected environment: as a matter of fact, the high solar radiation allows the use of greenhouses with simple structures, covered with plastic film and without fixed installations for winter heating. They are called “Mediterranean greenhouses” and are totally different from those in Central and Northern Europe. In the photovoltaic greenhouses, the cover on the pitch facing south is usually replaced by very opaque panels. However, this solution compromises the possibility to grow plants in covered and protected environments since solar radiation availability is limited and strongly nonuniform. In order to overcome this problem, semitransparent photovoltaic materials can be used to let the solar energy, necessary for plant growth, pass into the green house. The aim of this research is to analyze the radiometric properties of innovative semitransparent flexible photovoltaic materials in order to evaluate their performances in comparison with materials commonly used in the coverage of the greenhouses. Particular attention is paid to the transmittance of these materials in the visible range and in the long wave infrared for the achievement of greenhouse effect.

## **1. Introduction**

Recently, the use of greenhouse surface has increasingly spread worldwide.

Spain is in the first place in Europe with 50,000 hectares; there are 60,000 hectares in Japan and in China it is estimated that from 350,000 to 700,000 hectares are destined to protected crops. The phenomenon is developing not only in countries with temperate climate,

but also in tropical and subtropical areas in Latin America, Africa, Asia, and around the Mediterranean basin.

In Europe, greenhouse design and construction are governed by the Standard EN 13031-1:2001 where the following definition is given: "Greenhouse is structure used for the cultivation and/or protection of plants and crops that exploits the transmission of solar radiation under controlled conditions to improve the environment of growth, with dimensions that allow people to work inside."

The greenhouse can be seen as a solar collector which exploits the radiation coming from the sun to create optimal conditions for plant growth and development.

The solar radiation inside the greenhouse depends on

- (i) incident radiation on the ground;
- (ii) shape and orientation of the greenhouse;
- (iii) type of structure;
- (v) transmittance, absorption, and reflection of the covering material;
- (vi) size and position of the opaque structure;
- (vii) dust on the cover;
- (viii) cover condensation.

Covering material is the most important feature among the above-mentioned parameters since its own characteristics influence the microclimate in the confined environment.

Greenhouse cover, structural elements, soil, and crop contribute to the solar radiation absorption, and consequently, to the generation of sensible or latent heat [1].

Glass, semirigid plastics and plastic films are the most widely used greenhouse covering materials. They protect crop from adverse weather conditions and influence the greenhouse microclimate modifying the growing conditions of crops in comparison with the open-field climatic conditions.

Covering materials modify greenhouse microclimate due to their transmissivity to solar radiation in the visible range and in the long infrared radiation.

The spectral distribution of solar radiation at the earth's surface must be taken into account as a weighting function to calculate radiometric coefficients of covering materials. About 50% of the total energy is emitted in the near infrared radiation (NIR) range (700–2,500 [nm]) and nearly 40% in the PAR range (400–700 [nm]), where the solar radiation has a maximum at a wavelength of approximately 500 [nm] [2].

The transmissivity coefficient in the solar wavelength range, from 300 [nm] to 2,500 [nm], represents the fraction of the overall solar radiation passing through the covering material. The transmissivity coefficient in the PAR range expresses the quantity of solar PAR radiation transmitted by the covering material and strongly influences crop growth and yield.

Long wave infrared radiation energy losses from protected environments depend on the transmissivity of the covering material in the wavelength values higher than 3000 [nm]. However, at ambient temperature the bodies have the maximum energy emission in the range 7,500–12,500 [nm] [3].

The air temperature inside greenhouse is significantly influenced by the emissivity of the covering material which is a measure of the thermal radiative energy emitted in the long infrared radiation: if the covering material has high emissivity, high energy losses occur from the protected environment.

**Table 1:** Transmissivity coefficients of different greenhouse covering materials.

Transmissivity coefficients, %	Glass	LDPE	EVA	ETFE
	4 mm	0.180 mm	0.180 mm	0.100 mm
$\tau_{SR}$	80.4	88.6	89.1	93.1
$\tau_{PAR}$	87.5	91.0	89.7	92.4
$\tau_{LWIR}$	0.00	53.7	25.9	10.9

SR: solar radiation; PAR: photosynthetically active radiation; LWIR: long wave infrared [4].

Thus, the radiometric properties of the greenhouse cover play an important role in reducing energy consumption [4]. Sustainability of greenhouse industry can be increased with innovative covering materials aimed at obtaining energy savings in greenhouse heating and cooling together with profitable yield. Moreover, covering materials—able to modify the spectral distribution of the solar radiation—can be used to influence plant growth in place of agrochemicals. In the latest decades research has been addressed to improve the radiometric properties of glasses and, more recently, of plastic films that are the most widespread greenhouse covering materials [4].

Plastic films are very different from glass, are characterized by low cost, and require a lighter support frame. Furthermore, they have good thermo-optical and mechanical properties, good chemical resistance, and considerable opposition to microbial degradation.

In the last decades of the past century different kinds of plastic films for greenhouses were made by different raw materials and additives.

- (i) LDPE (low-density polyethylene) is the most used covering material and has good mechanical and radiometric properties. In the wavelength range 200–2,500 [nm] the total transmissivity of the LDPE film is similar to that of glass. On the other hand, the LDPE has high value of the transmissivity in the long wave infrared radiation.
- (ii) EVA (Ethylene vinyl acetate) is the copolymer of ethylene and vinyl acetate, is characterized by lower transmissivity in long wave infrared radiation, and allows to reduce the thermal infrared losses.
- (iii) ETFE (ethylene-tetrafluoroethylene copolymers): these innovative recently developed films are characterized by very good radiometric properties (high transmissivity in the solar range and low transmissivity in the long wave infrared radiation). ETFE films costs are higher than LDPE and EVA films but they last longer (also 15 years).

Table 1 shows the values of average transmittance of the covering materials for the above-described greenhouse. While transmittance of plastic films is nearly 10% higher than that of glass, the infrared transmittance of the LDPE exceeds 50% with negative consequences on greenhouse effect, EVA is strongly better reaching about 25% and ETFE is close to 10%. There are few differences of transmittance of the materials considered in the PAR.

Energy production from renewable sources, the diversification of the productive activities, and the development of photovoltaic technology and integrated systems have led to the development of solar greenhouses [5].

Currently, the research is directed to the creation of semi-transparent photovoltaic films. This need stems from the following fact: in some periods of the year, Mediterranean areas are characterised by strong surplus of solar radiation if compared with needs. As a consequence, passive (such as shading nets and thermal shields) or dynamic (natural or

forced ventilation, spraying or evaporation of water, etc.) protections are required; otherwise suspending farming becomes mandatory.

This has led to exploit the surplus of solar energy to produce electricity to be used in different ways, for example, for cooling systems and/or for direct sale to the distribution companies, and so forth.

A significant problem has to be considered: the traditional photovoltaic silicon-based panels are not transparent and do not let the solar radiation penetrate inside the greenhouse. Thus, plants, cultivation becomes problematic and it is difficult to create greenhouse effect necessary to develop the microclimatic conditions for crops.

In order to solve this problem, researchers are developing panels with partially transparent materials in flexible sheets or semitransparent rigid panels that allow the passage of sunlight necessary for the plants, cultivation in protected environments.

A research has been carried out in an area with a strong vocation for greenhouse crops, that is, the Agro Pontino, in order to obtain useful information on the possibility of using the structures of the greenhouses—meant for horticultural production—to support semitransparent photovoltaic covers. This research has tried to identify available solar energy surplus for its conversion into electrical energy and simultaneously satisfying the needs of the crop in terms of solar energy.

It was found that within the greenhouse—not only in summer, but also in other periods of the year—excess solar energy obliges the farmer to control the internal microclimate systems to prevent damage to the crops. Such systems often become burdensome and complex since high solar radiation is related to high values of air temperature. These excesses could then be used to produce electricity by photovoltaic cells with the advantage of producing energy and saving up for cooling in the protected area.

The research showed that the foot, outside the greenhouse, with cultivations (eggplant) can reach peak daily average of about  $15 \text{ MJ m}^{-2} \text{ d}^{-1}$ . These peaks remain almost constant in clear sky days during summer.

On cloudy days, of course, these peaks undergo a sharp drop down to about  $5 \text{ MJ m}^{-2} \text{ d}^{-1}$ , only for the summer months and in the absence of crops.

Moreover, during the months of April and October, a modest surplus occurs (about  $2.5 \text{ MJ m}^{-2} \text{ d}^{-1}$ ) at the transplant eggplant (two cycles per year). Taking into account that the surveyed area can be considered clear more than 70% of the days during summer, solar energy is available for a bit more than 4 months per year and can be transformed using photovoltaic technology.

Once magnitude and temporal distribution of energy surplus are defined; photovoltaic roofs have to be identified. Rigid and opaque panels (the well-known and common silicon solar panels) are not recommended. The solution may be found in the use of flexible photovoltaic and semi-transparent sheets. These being flexible have the ability to be rolled up and, therefore, could be stretched during periods of surplus of the day quite easily as if they were shading nets.

These semitransparent sheets must ensure that the inside of the greenhouse reaches a rate of solar radiation necessary for plants and to create the greenhouse effect. In this way it will be possible to combine the use of the greenhouse for agricultural production and the production of electricity by means of photovoltaic cells.

In order to achieve this goal, the radiometric characterization of these new semitransparent photovoltaic films is needed.

In spectral analysis some wavelengths result more important than others. Variations of blue (B, 400–500 [nm]), red (R, 650–670 [nm]), and far-red (FR, 720–740 [nm]) radiation,

in the protected environment affect the plant photomorphogenesis. Infact, the phytochrome response is characterized in terms of the R/FR ratio [6–11].

Significant increases of the growth and of the elongation of shoots were pointed out in peach and cherry trees grown under a photoselective film that reduced the R/FR ratio to 0.93, from the value 1.15, which was recorded in open field at the University of Bari [4].

Tests carried out on ornamental plants showed that the increase of the R/FR ratio has a dwarfing effect on the plant growth [9].

The purpose of this work is to characterize the semitransparent photovoltaic flexible film innovative from a radiometric point of view.

## 2. Preliminary Remarks

### 2.1. Solar Radiation

The sun emits as a black body at 5700 [°K]. According to the Wien's law, the maximum of the emission is at a wavelength  $\lambda$ :

$$\lambda_{\max} = \frac{2885000}{T} = 506 \text{ [nm]}. \quad (2.1)$$

The spectrum of solar radiation is between 290 and 3000 [nm]: ultraviolet (290–380 [nm]), visible (380–760 [nm]), and near wave infrared (760–3000 [nm]).

The incident radiation on the ground, with clear skies, can be calculated with the following relations:

$$R_b = \text{direct radiation at ground} = R_e \tau_b \cos \theta_Z \text{ [W m}^{-2}\text{]};$$

$$R_d = \text{diffuse radiation at ground} = R_e \tau_d \cos \theta_Z \text{ [W m}^{-2}\text{]};$$

$$R_g = \text{global radiation at ground} = R_b + R_d \text{ [W m}^{-2}\text{]};$$

where

$$R_e = \text{outer radiation} = 1367 (1 + 0.033 \cos(360/365n)) \text{ [W m}^{-2}\text{]};$$

$$n = \text{Julian day};$$

$$\cos \theta_Z = \text{cosine zenith angle} = \sin \phi \sin \delta + \cos \phi \cos \delta \cos \omega;$$

$$\phi = \text{local latitude [}^\circ\text{]};$$

$$\delta = \text{Inclination of the sun} = 23.45 \text{ sen}[(360/365)(284 + n)] \text{ [}^\circ\text{]};$$

$$\omega = \text{hour angle} = (360/24)(12 - h) \text{ [}^\circ\text{]};$$

$$h = \text{hour days [h]};$$

$$A = \text{altitude [km]};$$

$$\tau_b = \text{transmissivity of the atmosphere to the direct radiation} = A_0 + A_1 \times e^{-k/\cos \theta_Z};$$

$$\tau_d = \text{transmissivity of the atmosphere to the diffuse radiation} = 0.271 - 0.294\tau_b;$$

$$A_0 = [0.4237 - 0.00821(6 - A)^2][1 + 0.03 \text{ sen}(\pi((91 + n)/182))];$$

$$A_1 = [0.5055 + 0.00595(6.5 - A)^2][1 + 0.01 \text{ sen}(\pi((91 + n)/182))];$$

$$K = [0.2711 + 0.01858(2.5 - A)^2][1.01 - 0.01 \text{ sen}(\pi((91 + n)/182))].$$

If the surface is inclined, there will be two angles:

$Z$  = inclination of the surface normal with respect to zenith;

$\psi$  = angle between the horizontal projection of the surface normal and the south.

The angle between the direction of the sun and the normal surface is

$$\begin{aligned} \cos I = \text{sen}\lambda \text{sen}\delta \cos Z - \cos\lambda \text{sen}\delta \text{sen}Z \cos\psi + \cos\lambda \cos\delta \cos\omega \cos Z \\ + \text{sen}\lambda \cos\delta \cos\omega \text{sen}Z \cos\psi + \cos\delta \text{sen}\omega \text{sen}Z \text{sen}\psi. \end{aligned} \quad (2.2)$$

The components of radiation are

$R_{bI}$  = direct radiation on inclined surface =  $R_e \tau_b \cos I$ ;

$R_{dI}$  = diffuse radiation on inclined surface =  $R_e \tau_d \cos I$ .

The solar radiation that enters the greenhouse is obtained from the previous considering the transmittance of the covering material which varies with the angle of incidence.

In order to calculate this parameter, the following model can be considered.

## 2.2. Transmittance of the Cover

$S$  is the thickness of the cover,  $n$  the refractive index, and  $k$  the coefficient of absorption.

$$\text{By the relation: } \frac{n_1}{n_2} = \frac{\text{sen}\theta_r}{\text{sen}\theta_i}, \quad (2.3)$$

being the refractive index of air close to 1, with  $n_2 = n$  (refractive index of the second), it has

$$\begin{aligned} \theta_r = \text{refraction angle} &= \arcsen\left(\frac{\text{sen}\theta_i}{n}\right), \\ \text{Surface reflectance (normal component)} &= r_{\perp} = \frac{\text{sen}^2(\theta_r - \theta_i)}{\text{sen}^2(\theta_r + \theta_i)}, \\ \text{Surface reflectance (parallel component)} &= r_{\parallel} = \frac{\tan^2(\theta_r - \theta_i)}{\tan^2(\theta_r + \theta_i)}, \end{aligned} \quad (2.4)$$

$$\text{Total surface reflectance} = r = \frac{I_r}{I_i} = \frac{1}{2}(r_{\perp} + r_{\parallel}).$$

The transmittance value of the perpendicular component considering the only loss by reflection is

$$\tau_{\perp} = (1 - r_{\perp})^2 \sum_{n=0}^{\infty} r_{\perp}^{2n} = \frac{(1 - r_{\perp})^2}{(1 - r_{\perp}^2)} = \frac{1 - r_{\perp}}{1 + r_{\perp}}. \quad (2.5)$$

Similarly, the parallel component of transmittance, considering only losses by reflection, will be

$$\tau_{\parallel} = \frac{1 - r_{\parallel}}{1 + r_{\parallel}}. \quad (2.6)$$

Global transmittance considering only losses by reflection is

$$\tau_r = \frac{1}{2} \left[ \frac{1 - r_{\perp}}{1 + r_{\perp}} + \frac{1 - r_{\parallel}}{1 + r_{\parallel}} \right]. \quad (2.7)$$

Global transmittance considering only losses by absorption is

$$\tau_a = e^{-K \cdot s / \cos \theta_r}. \quad (2.8)$$

The transmittance, reflectance, and absorbance of a single covering, considering the losses by reflection and absorption, can be determined:

$$\tau_{\parallel} = \frac{\tau_a (1 - r_{\parallel})^2}{1 - (r_{\parallel} \tau_a)^2} = \tau_a \cdot \frac{1 - r_{\parallel}}{1 + r_{\parallel}} \cdot \frac{1 - r_{\parallel}^2}{1 - (r_{\parallel} \tau_a)^2} \cong \tau_a \cdot \frac{1 - r_{\parallel}}{1 + r_{\parallel}}. \quad (2.9)$$

Similarly,

$$\tau_{\perp} \cong \tau_a \cdot \frac{1 - r_{\perp}}{1 + r_{\perp}}. \quad (2.10)$$

Whence,

$$\begin{aligned} \tau &= \frac{1}{2} (\tau_{\parallel} + \tau_{\perp}) \cong \frac{1}{2} \left( \tau_a \cdot \frac{1 - r_{\parallel}}{1 + r_{\parallel}} + \tau_a \cdot \frac{1 - r_{\perp}}{1 + r_{\perp}} \right), \\ \tau &\cong \tau_a \cdot \frac{1}{2} \left( \frac{1 - r_{\parallel}}{1 + r_{\parallel}} + \frac{1 - r_{\perp}}{1 + r_{\perp}} \right) \cong \tau_a \cdot \tau_r. \end{aligned} \quad (2.11)$$

Therefore, the global transmittance considering both the absorption losses both the reflection losses is equal to

$$\tau \cong \tau_a \cdot \tau_r. \quad (2.12)$$

The reflectance of the cover will be

$$\rho_{\parallel} = r_{\parallel} + \frac{(1 - r_{\parallel})^2 \tau_a^2 r_{\parallel}}{1 - (r_{\parallel} \tau_a)^2} = r_{\parallel} (1 + \tau_a \tau_{\parallel}). \quad (2.13)$$

Similarly,

$$\rho_{\perp} = r_{\perp}(1 + \tau_a \tau_{\perp}). \quad (2.14)$$

Whence,

$$\rho = \frac{1}{2}(\rho_{\parallel} + \rho_{\perp}). \quad (2.15)$$

The absorbance is

$$\alpha_{\parallel} = (1 - \tau_a) \left( \frac{1 - r_{\parallel}}{1 - r_{\parallel} \tau_a} \right). \quad (2.16)$$

Similarly,

$$\alpha_{\perp} = (1 - \tau_a) \left( \frac{1 - r_{\perp}}{1 - r_{\perp} \tau_a} \right). \quad (2.17)$$

Whence,

$$\alpha = \frac{1}{2}(\alpha_{\parallel} + \alpha_{\perp}). \quad (2.18)$$

The transmittance of the diffuse radiation is assumed to be equal to the transmittance to direct radiation with  $I = 60^\circ$ .

### **2.3. Energy Flows in Mediterranean Greenhouse (Tunnel)**

The energy balance equation per unit area for Mediterranean greenhouse (tunnel) is (Figure 1)

$$R_i + R_{ac} = RT_{g,sky} + RT_{g,atm} + RT_{p,sky} + RT_{p,atm} + RT_{c,sky} + RT_{c,atm} + T_c + V + \Delta E_g + S_g, \quad (2.19)$$

where

$$T = KS(T_i - T_e), \quad (2.20)$$

$K$  is the thermal transmittance [ $\text{W m}^{-2} \text{K}^{-1}$ ];  $S$  is the wall surface [ $\text{m}^2$ ];  $T_i$  is the internal temperature [ $^\circ\text{C}$ ];  $T_e$  is the external temperature [ $^\circ\text{C}$ ];

$$E_v = V(H_i - H_e); \quad (2.21)$$

$E_v$  is the energy lost for ventilation [ $\text{KJ h}^{-1}$ ];  $V$  is the flow rate of ventilation [ $\text{KgDryAir h}^{-1}$ ];  $H_i$  is the internal air enthalpy [ $\text{KJ KgDryAir}^{-1}$ ];  $H_e$  is the external air enthalpy [ $\text{KJ KgDryAir}^{-1}$ ].

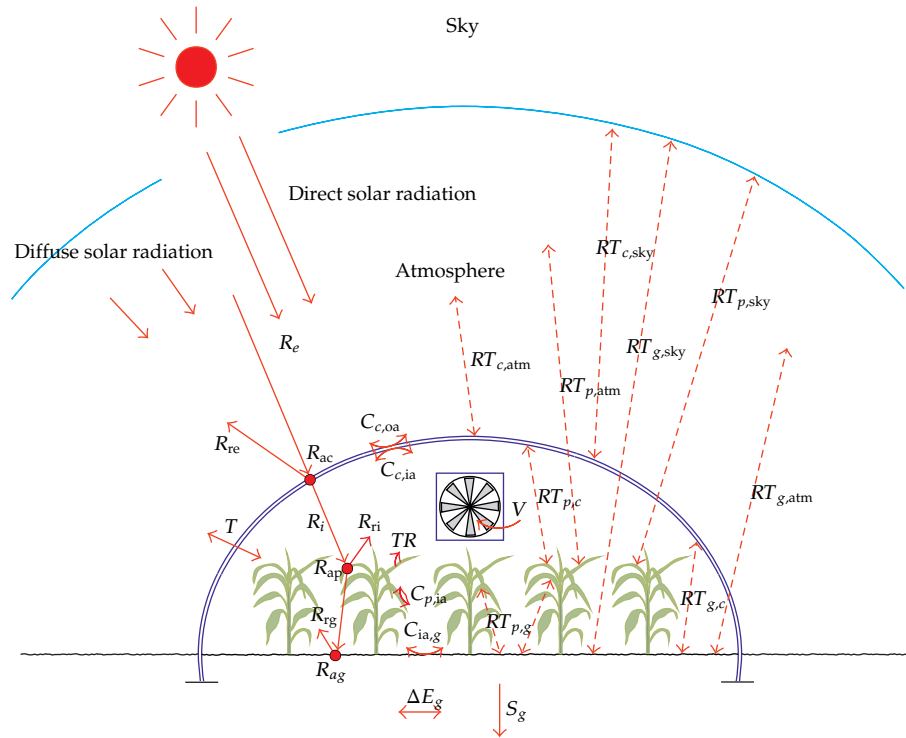


Figure 1: Energy flows in Mediterranean greenhouse.

The enthalpy  $H$  [KJ KgDryAir<sup>-1</sup>] of a Kg of air, at temperature  $t$  [°C] and with a water content, in the form of water, equal to  $x$  [Kg KgDryAir<sup>-1</sup>] is obtained from

$$H = 1.005t + x(2499.5 + 2.005t), \quad (2.22)$$

where  $x$  [Kg KgDryAir<sup>-1</sup>] represents the water vapor contained in the air and can be determined through the psychrometric diagram or by the following formula:

$$x = 0.6215 \frac{p_{\text{H}_2\text{O}}}{p - p_{\text{H}_2\text{O}}}, \quad (2.23)$$

where  $p = 1.013$  [Kg cm<sup>-2</sup>] is the atmospheric pressure;  $p_{\text{H}_2\text{O}}$  is the vapor pressure of the air, expressed in Kg cm<sup>-2</sup> at the temperature  $T$  [°K] and at relative humidity UR [%];

$$p_{\text{H}_2\text{O}} = 1.41 \times 10^{10} e^{(-3928.5/(T-41.5))} \times \text{UR} \text{ [Pa];}$$

$$RT_{12} = \sum_{\lambda=2.5\mu\text{m}}^{\lambda=20\mu\text{m}} \varepsilon_{12}(\lambda) \times \tau_a(\lambda) \times \frac{C_1}{\lambda^5} \times \left[ \frac{1}{e^{C_2/(\lambda \times T_1)} - 1} - \frac{1}{e^{C_2/(\lambda \times T_2)} - 1} \right] \times \Delta\lambda; \quad (2.24)$$

$RT_{12}$  is the radiated radiation [W m<sup>-2</sup>];  $\lambda$  is the wavelength [ $\mu\text{m}$ ];  $T$  is the absolute temperature [°K];  $C_1 = 3.7410^8$  [W  $\mu\text{m}^4$  m<sup>-2</sup>];  $C_2 = 14385$  [K· $\mu\text{m}$ ].  $\tau_{a(\lambda)}$  is the transmittance

of the atmosphere at the wavelength  $\lambda$ ;  $\varepsilon_{(\lambda)}$  is the monochromatic emissivity of the object at the wavelength  $\lambda$  [12–14].

### 3. Materials and Methods

In order to exploit the above-described mathematical models, it is important to know the transmittance of the covering material in the wavelengths of the visible and long wave infrared. Using these parameters it is possible to evaluate the efficiency of the covering material for the purposes of the greenhouse effect in the structures for protected crops. In this paper we analyze the spectrum of an innovative photovoltaic film created as part of the research project “ECOFLECS” by the Research Unit of Tor Vergata (Rome) for its efficiency in the greenhouse cover.

The film was made in PVB, laminating material that covers the modules at sandwich, plastic substrates PET/ITO, conducting polymer Pedot-PSS. 6 arrays of 8 modules each were realized. The thickness of the flexible film is about 0.5 mm. The single module has the following sizes: 220 mm  $\times$  220 mm. These modules can be assembled to obtain large surfaces necessary for the covering of greenhouses. The remarkable flexibility allows the photovoltaic film to fit even to curved surfaces of the tunnels and greenhouses tunnel.

IR measurements were performed with a Perkin Elmer Paragon 1000 instrument with Detector MCT (mercury telluride and cadmium); UV-VIS measurements were performed with a Lambda 9, Perkin Elmer, with photomultiplier highly sensitive at VIS and NIR.

In both cases, the optical filter was set equal to 2 [nm], while the sweep was 120 [nm/min].

### 4. Results and Discussion

Three samples of semi-transparent films (innovative solutions and still in the experimental phase) were analysed in the spectrophotometer. Diagrams with the average values of the measurements are shown in Figure 2.

Figure 2 shows the trend of the transmittance of the photovoltaic film in relation with the solar spectrum. It seems clear that the transmittance is very low in the first part of the visible, is maintained below 10% up to 395 [nm], about 38–40% between 400 and 520 [nm], increases almost linearly up to 650 [nm] where it reaches 68%, and remains almost constant up to 760 [nm].

The average transmittance determined as the arithmetic average is 56.9% but in this way does not take into account the variation of the flow of solar energy as a function of wavelength (solar spectral irradiance at sea level).

More precisely, the determination of the average transmittance with the weighted average using the flow of solar radiation at different wavelengths is

$$\tau_m = \frac{\sum_{\lambda=380}^{760} (\tau_{\lambda} \cdot SR_{\lambda})}{\sum_{\lambda=380}^{760} SR_{\lambda}}, \quad (4.1)$$

where  $SR_{\lambda}$  is the solar radiation at sea level [ $W m^{-2} nm^{-1}$ ] and  $\tau_{\lambda}$  is the photovoltaic film transmissivity [%]. In this way the average transmittance of the photovoltaic film in the range 380–760 [nm] is equal to 49.5%, value less than that obtained by measuring with a

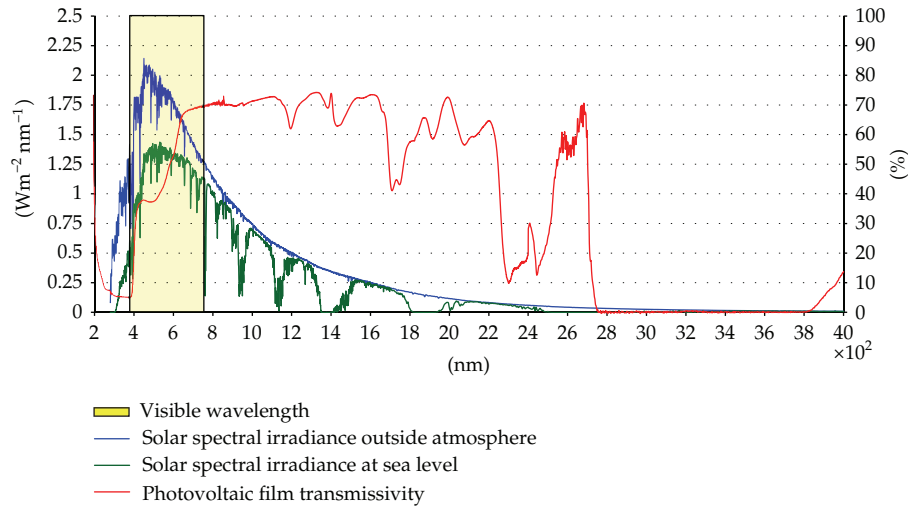


Figure 2: Solar spectral irradiance outside atmosphere and at sea level and photovoltaic film transmissivity in the wavelength range 200–4000 [nm].

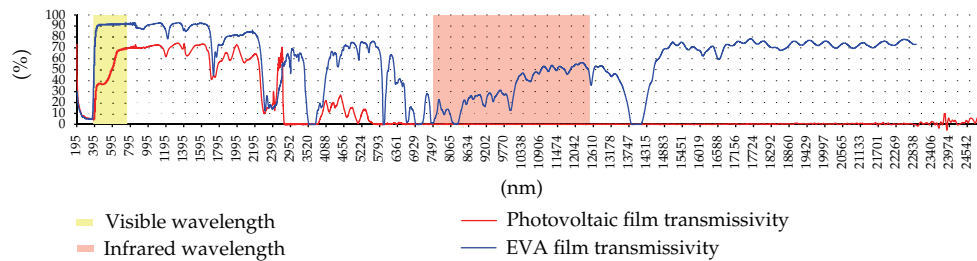


Figure 3: Photovoltaic film transmissivity and EVA film transmissivity in the wavelength range 195–25000 [nm].

pyranometer solar radiation above and below the photovoltaic film in the range of 300–1100 [nm] but comparable to it because in the near infrared the energy is lower in respect to visible.

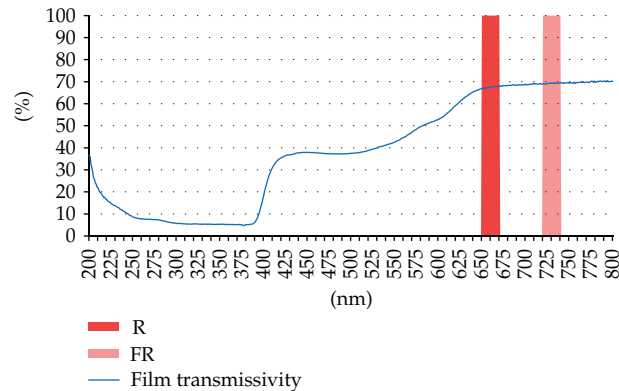
For the photovoltaic effect the useful wavelength is between 400 and 1100 [nm], and then the low transmittance before 650 [nm] is advantageous for the production of electricity.

Figure 3 shows the transmissivity of the photovoltaic films and that of the EVA films which are very common in the greenhouse covering. Furthermore, the wavelengths of visible (380–760 [nm]) and long wave infrared (7500–12500 [nm]) were also highlighted since they are important for the purposes of the greenhouse effect.

The indoor greenhouse air temperature rises with the decrease of the long wave infrared transmissivity coefficient of the greenhouse covering material.

High transmissivity in the visible and low transmissivity in long wave infrared are essential to a good greenhouse effect.

The transmissivity in the visible of photovoltaic films, as reported above, is very low up to 650 [nm]. As a matter of fact, the average value in the visible is less than 50% while that



**Figure 4:** Total transmissivity of the photovoltaic film with red (R, 650–670 [nm]) and far-red (FR, 720–740 [nm]) wavelengths in the range 200–800 [nm].

of the EVA film is of about 90%, much higher value. If the photovoltaic film loses a lot in the visible, it gains a lot in the far infrared: its transmittance is practically null in this range of wavelengths that, as it is known, is the interval where it is greater than the energy emitted by radiation from the bodies (Planck's law). Thus, from our point of view, it seems reasonable to assume an overall efficiency of the photovoltaic film in the greenhouse effect similar to that of traditional EVA films.

Figure 4 shows the transmissivity of the photovoltaic film in the range 200–800 [nm], pointing out the values of the red (R, 650–670 [nm]) and far-red (FR, 720–740 [nm]) wavelengths. The ratio between these values is important for the purposes of plants, accretion. The calculated ratio is 0.97 for this PV films: this value should encourage increases of the growth and the elongation of shoots.

In relation to the reflectivity and the absorbance this film gives priority to absorbance because absorbed energy is used for the production of electricity with an efficiency that in the current state does not exceed 10%.

## 5. Conclusions

In this paper, the spectrum of an innovative photovoltaic film has been analysed in order to evaluate its efficiency in the greenhouse cover.

Spectral analysis showed that the transmittance of the photovoltaic film is very low in the first part of the visible in relation with the transmittance of the traditional EVA film commonly used for covering greenhouses. This is advantageous for electricity generation, but at the same time is in contrast with the production of plant material since this portion of the spectrum is useful for photosynthesis (PAR).

The transmittance of the photovoltaic film in the range of the infrared long is null, and therefore much lower than that related to the EVA films with considerable advantages for the purposes of achieving the greenhouse effect.

According to this analysis, in the greenhouse effect it is possible to assume an overall efficiency of the photovoltaic film similar to that of the traditional EVA films.

## Nomenclature

### Alphabetic Symbols

- $R$ : Global solar radiation [ $\text{MJ m}^{-2} \text{d}^{-1}$ ]  
 $RT$ : Energy lost by radiation [ $\text{MJ m}^{-2} \text{d}^{-1}$ ]  
 $C$ : Energy exchanged by convection [ $\text{MJ m}^{-2} \text{d}^{-1}$ ]  
 $T$ : Energy lost by transmission [ $\text{MJ m}^{-2} \text{d}^{-1}$ ]  
 $V$ : Energy lost by ventilation [ $\text{MJ m}^{-2} \text{d}^{-1}$ ]  
 $TR$ : Plant transpiration [ $\text{MJ m}^{-2} \text{d}^{-1}$ ]  
 $S$ : Energy transferred by conduction in the deep layers [ $\text{MJ m}^{-2} \text{d}^{-1}$ ]  
 $E$ : Thermal storage [ $\text{MJ m}^{-2} \text{d}^{-1}$ ].

### Subscripts

- $e$ : External  
 $re$ : Reflected external  
 $ac$ : Absorbed by the cover  
 $i$ : Internal  
 $ri$ : Reflected internal  
 $ap$ : Absorbed by the plants  
 $rg$ : Reflected from the ground  
 $ag$ : Absorbed by the soil  
 $c$ : Covering film  
 $p$ : Plants  
 $g$ : Ground  
 $ia$ : Indoor air  
 $oa$ : Outdoor air  
 $atm$ : Atmosphere  
 $sky$ : Vault of heaven.

## References

- [1] A. Mistriotis, C. Arcidiacono, P. Picuno, G. P. A. Bot, and G. Scarascia-Mugnozza, "Computational analysis of ventilation in greenhouses at zero- and low-wind-speeds," *Agricultural and Forest Meteorology*, vol. 88, no. 1-4, pp. 121-135, 1997.
- [2] J. A. Duffie and W. A. Beckman, *Solar Engineering of Thermal Processes*, John Wiley & Sons, New York, NY, USA, 1991.
- [3] R. Siegel and J. R. Howell, *Thermal Radiation Heat Transfer*, McGraw-Hill, New York, NY, USA, 1972.
- [4] G. Vox, M. Teitel, A. Pardossi, A. Minuto, F. Tinivella, and E. Schettini, *Chapter 1: Sustainable Greenhouse Systems, Sustainable Agriculture: Technology, Planning and Management*, Nova Science Publishers, New York, NY, USA, 2010.
- [5] M. Carlini, T. Honorati, and S. Castellucci, "Photovoltaic greenhouses: comparison of optical and thermal behaviour for energy savings," *Mathematical Problems in Engineering*, vol. 2012, Article ID 743764, 10 pages, 2012.
- [6] C. Kittas and A. Bailie, "Determination of the spectral properties of several greenhouse cover materials and evaluation of specific parameters related to plant response," *Journal of Agricultural Engineering Research*, vol. 71, no. 2, pp. 193-202, 1998.

- [7] C. Kittas, A. Baille, and P. Giaglaras, "Influence of covering material and shading on the spectral distribution of light in greenhouses," *Journal of Agricultural Engineering Research*, vol. 73, no. 4, pp. 341–351, 1999.
- [8] K. Murakami, H. Cui, M. Kiyota, Y. Takemura, R. Oi, and I. Aiga, "Covering materials to control plant growth by modifying the spectral balance of daylight," *Plasticulture*, vol. 110, no. 2, pp. 2–14, 1996.
- [9] H. Smith, "Light quality, photoperception, and plant strategy," *Annual Review of Plant Physiology*, vol. 33, pp. 481–518, 1982.
- [10] M. Oren-Shamir, E. E. Gussakovsky, E. Shpiegel et al., "Coloured shade nets can improve the yield and quality of green decorative branches of *Pittosporum variegatum*," *Journal of Horticultural Science and Biotechnology*, vol. 76, no. 3, pp. 353–361, 2001.
- [11] M. Takaichi, H. Shimaji, and T. Higashide, "Effect of red/far-red photon flux ratio of solar radiation on growth of fruit vegetable seedlings," *Acta Horticulturae*, vol. 514, pp. 147–156, 2000.
- [12] E. Campiglia, G. Colla, R. Mancinelli, Y. Roupael, and A. Marucci, "Energy balance of intensive vegetable cropping systems in central Italy," *Acta Horticulturae*, vol. 747, pp. 185–191, 2007.
- [13] A. Marucci, E. Campiglia, G. Colla, and B. Pagniello, "Environmental impact of fertilization and pesticide application in vegetable cropping systems under greenhouse and open field conditions," *Journal of Food, Agriculture and Environment*, vol. 9, no. 3-4, pp. 840–846, 2011.
- [14] A. Marucci and B. Pagniello, "Simulation of the growth and the production of the tomato in typical greenhouses of the Mediterranean environment," *Journal of Food, Agriculture and Environment*, vol. 9, no. 3-4, pp. 407–411, 2011.

## *Research Article*

# **Modeling Small Scale Solar Powered ORC Unit for Standalone Application**

**Enrico Bocci,<sup>1</sup> Mauro Villarini,<sup>2</sup> Luca Bove,<sup>2</sup>  
Stefano Esposto,<sup>3</sup> and Valerio Gasperini<sup>3</sup>**

<sup>1</sup> *Università degli Studi Guglielmo Marconi, Via Plinio 44, 00193 Roma, Italy*

<sup>2</sup> *Università degli Studi della Tuscia, Via S.M.in Gradi n.4, 01100 Viterbo, Italy*

<sup>3</sup> *Energetca s.r.l., Via della Polveriera 14, 00184 Roma, Italy*

Correspondence should be addressed to Enrico Bocci, e.bocci@unimarconi.it

Received 17 October 2012; Accepted 15 November 2012

Academic Editor: Maurizio Carlini

Copyright © 2012 Enrico Bocci et al. This is an open access article distributed under the Creative Commons Attribution License, which permits unrestricted use, distribution, and reproduction in any medium, provided the original work is properly cited.

When the electricity from the grid is not available, the generation of electricity in remote areas is an essential challenge to satisfy important needs. In many developing countries the power generation from Diesel engines is the applied technical solution. However the cost and supply of fuel make a strong dependency of the communities on the external support. Alternatives to fuel combustion can be found in photovoltaic generators, and, with suitable conditions, small wind turbines or microhydroplants. The aim of the paper is to simulate the power generation of a generating unit using the Rankine Cycle and using refrigerant R245fa as a working fluid. The generation unit has thermal solar panels as heat source and photovoltaic modules for the needs of the auxiliary items (pumps, electronics, etc.). The paper illustrates the modeling of the system using TRNSYS platform, highlighting standard and "ad hoc" developed components as well as the global system efficiency. In the future the results of the simulation will be compared with the data collected from the 3 kW prototype under construction in the Tuscia University in Italy.

## **1. Introduction**

Solar energy is available everywhere and completely renewable. In remote locations, the conversion of solar energy in electricity could be an important option to enhance the development of rural communities. The low energy density and the fluctuations of the source availability are the main obstacles in the solar energy applications. The photovoltaic module is a commercial technology to convert solar energy directly in electricity, but the low efficiency conversion and above all the need of batteries for storage purpose limit the application in developing countries. As a matter of fact, storage of electricity with batteries requires skilled

maintenance and it is not easily achievable in remote locations. The technological option analyzed in this paper is the conversion of solar energy through solar collectors and storage as hot water in an insulated tank. This tank is the hot source of an Organic Rankine Cycle system with electricity output. The appropriate design of all the components involved is important to achieve high efficiency and continuous electricity production. Thus, an efficient mathematical model that describes systems performances, environmental interaction, and development is needed [1]. The modeling with TRNSYS supports the analysis allowing the user to interact with the numerous parameters involved and obtaining different scenarios and results [2–4]. The aim of the present work is developing an important tool for guiding the assembling of a prototype of a solar energy/ORC compact electricity generator with 3 kW as power output.

The first important choice is individuating the working fluid in the ORC system [5, 6]. Among the liquids for the Organic Rankine Cycle R245fa is an interesting fluid. It is a nonchlorinated hydrofluorocarbon, non-Ozone depleting liquid with a low global warming potential [7]. In the mathematical model R245fa has been used, individuating all the necessary thermodynamic properties for the simulation of the Rankine Cycle. Data from the NIST Chemistry WebBook has been used in the simulation [8].

## 2. Mathematical Model of the Working Fluid

The working fluids that are suitable for low temperature ORCs are well known in the literature [5]. The choice of the fluid depends on the following main factors [9]:

- (i) the critical point of the working fluid (in this case of small solar power plant the maximum temperature can be within 100 and 200°C);
- (ii) the specific volume ratio over the expander must be low in order to reduce the size, and, thus, the cost (in general the higher the critical temperature, the higher the specific volume ratio over the expander);
- (iii) the working fluid should have a null Ozone Depleting Potential (Montreal Protocol and, for EC, Regulation 2037/2000);
- (iv) the fluid must fulfill other conditions such a toxicity, cost, and flammability;
- (v) if scroll compressors is used for the expander the temperature must be below 150°C because refrigeration compressors are not designed for temperatures higher than 150°C.

We have chosen the fluid R245fa, because of the following:

- (i) its critical temperature is greater than 150°C (temperature that can be reached in a boiler feed by vacuum solar panels);
- (ii) it shows very advantageous swept volumes no toxicity and low cost;
- (iii) it has a null Ozone Depleting Potential;
- (iv) it is the fluid most often used in small ORC applications [10].

The data from the NIST Chemistry WebBook indicates the thermodynamic properties of the fluid chosen, R245fa, varying according to the different working conditions. Thus it is necessary to develop a mathematical model of the fluid in order to have the thermodynamic properties of the fluid inside the global power plant simulation. The model developed is based on the following assumptions.

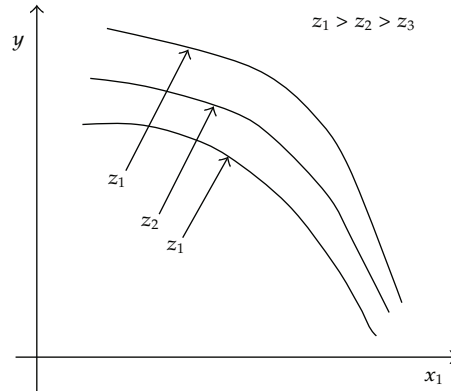


**Figure 1:** The function  $y(x)$  considering  $z$  as parameter.

Assuming that a single thermodynamic property is individuated by the values of two other properties:

$$y = f(x, z) \quad (2.1)$$

and considering  $z$  as parameter, it is possible to show the function  $y$  in an  $x, y$  Cartesian graph, as shown in Figure 1.

Having the different values of  $x, y$  of the two properties for each  $z$  (the source is the NIST Chemistry WebBook), we can interpolate using software like Matlab and obtaining polynomials (the following example is a second grade polynomial):

$$y = c_1x^2 + b_1x + a_1 \quad (z = z_1). \quad (2.2)$$

The same can be done for the other values of the parameter  $z$ :

$$y = c_2x^2 + b_2x + a_2 \quad (z = z_2), \quad (2.3)$$

$$y = c_3x^2 + b_3x + a_3 \quad (z = z_3).$$

The constants  $a, b$ , and  $c$  can be also interpolated related to the different values of the parameter  $z$ :

$$\begin{aligned} a_n &= A_0 + A_1z + A_2z^2, \\ b_n &= B_0 + B_1z + B_2z^2, \\ c_n &= C_0 + C_1z + C_2z^2. \end{aligned} \quad (2.4)$$

Equation (2.1) is therefore

$$y = (A_0 + A_1z + A_2z^2) + (B_0 + B_1z + B_2z^2)x + (C_0 + C_1z + C_2z^2)x^2. \quad (2.5)$$

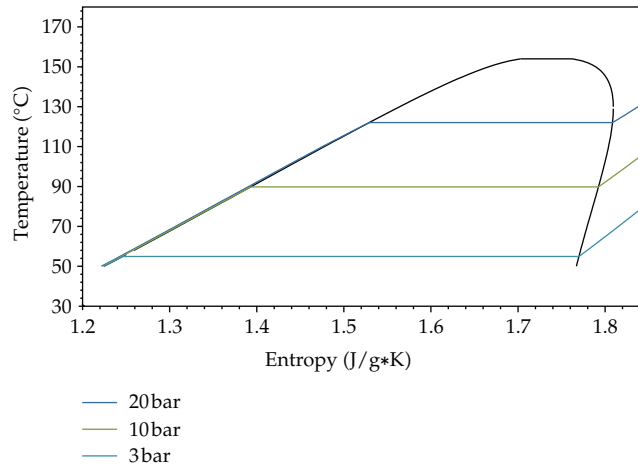


Figure 2:  $T$ - $S$  diagram of the working fluid.

In the mathematical model, the pressure of the fluid is the parameter and the other properties are interpolated using the NIST database. Figure 2 shows different cycles of the working fluid R245fa in the  $T$ - $S$  diagram.

### 3. TRNSYS 16 Simulation

TRNSYS 16 is a powerful software using Fortran subroutines and able to simulate energy patterns with time dependent inputs. Therefore it is possible to include the fluctuant and variable sun irradiation as input and to monitor the energy fluxes linked to it. Each Fortran subroutine, linked together in the TRNSYS environment, represents a component of the system, and a mathematical model simulates his functions having inputs, outputs, variable with time, and parameters, constant for all the duration of the simulation. The TRNSYS library has a wide set of already tested subroutines “type” for the simulation of solar collectors, thermal storage, and piping. The subroutine for the simulation of the Organic Rankine Cycle has been developed to include this component in the simulation.

The graphic environment of Studio has been used to run the TRNSYS simulation. The system simulated is composed by the following components.

#### *Irradiation (Solar Energy Source)*

A standard type 109 has been chosen to give the necessary irradiation values. The simulation reads the weather data from the chosen geographic location. In this case Orte is the location where the prototype will be assembled and installed. Because TRNSYS dataset does not have the Orte data, the Rome data has been chosen. Rome is near to Orte so solar irradiation is similar. Moreover the authors are inserting Orte data in TRNSYS dataset and this will be used in the future publication which compares the simulation with the experimental data available from the prototype under construction in Orte.

### *Solar Collector and Storage Tank*

The vacuum solar collectors type with CPC technology to enhance the diffuse radiation absorption has been chosen, in particular the SKY 21 CPC 58 made by Kloben. Thus the type 71 and the Kloben data of the SKY 21 collector have been used in the simulation. In particular the SKY 21 has an efficiency of 0.718, a first order coefficient of  $0.974 \text{ W/m}^2 \text{ K}$ , a second order coefficient of  $0.005 \text{ W/m}^2 \text{ K}^2$ , and a collector area of  $3.75 \text{ m}^2$ . A collector slope of  $45^\circ$  has been chosen in order to maximize the winter power, like usually in Italy [11, 12]. We use only one collector in order to test the simulation with the minimum module of collector. The water heated by the solar collector is pumped to a storage tank only if the temperature of the tank is lower than the outlet solar collector temperature, avoiding heat losses during night or cloudy days.

### *Storage Tank and ORC Unit*

A suitable heat storage system is required to maximize the productivity of the solar plant and to provide solar heat at the desired rate regardless the instantaneous solar radiation availability and the thermal needs [13–15]. The overall aim of this basic component is the same for the high temperature concentrated solar power systems and for the small scale solar system with the difference that the second one has to directly face the user energy needs. The storage tank is simulated with the type 4a, a standard stratified tank, with loss coefficient of  $0.0833 \text{ W/m}^2 \text{ K}$ . The ORC unit, being not in standard TRNSYS components, has been developed like a user type with the mathematical model showed in the next paragraph. The hot fluid from the upper part of the storage tank is pumped to the evaporator of the ORC unit only if the temperature is higher than the working ORC fluid evaporation temperature. The working fluid (R245fa) is then cooled down by a cold source.

### *Photovoltaic Modules*

The photovoltaic modules are part of the simulation to supply energy to the ORC unit in the start-up phase. A standard PV type, the 194b, has been chosen with standard PV values (panel slope  $30^\circ$ ) [16].

Figure 3 shows the global power plant scheme in the TRNSYS environment.

## **4. The ORC Type: Mathematical Model**

The Fortran subroutine simulating the Organic Rankine Cycle unit has been developed using the R245fa as working fluid in the equation of state present in the algorithm. Using Matlab, it was possible to interpolate the NIST Chemistry data to obtain second/third grade polynomial equations among the thermodynamic properties [5].

The expander type has not been specified, thus an efficiency  $\eta$  has been generally indicated to calculate the work. The outlet enthalpy after the expander is calculated using the following equation:

$$h_2 = h_1 - \eta(h_1 - h_{2s}). \quad (4.1)$$

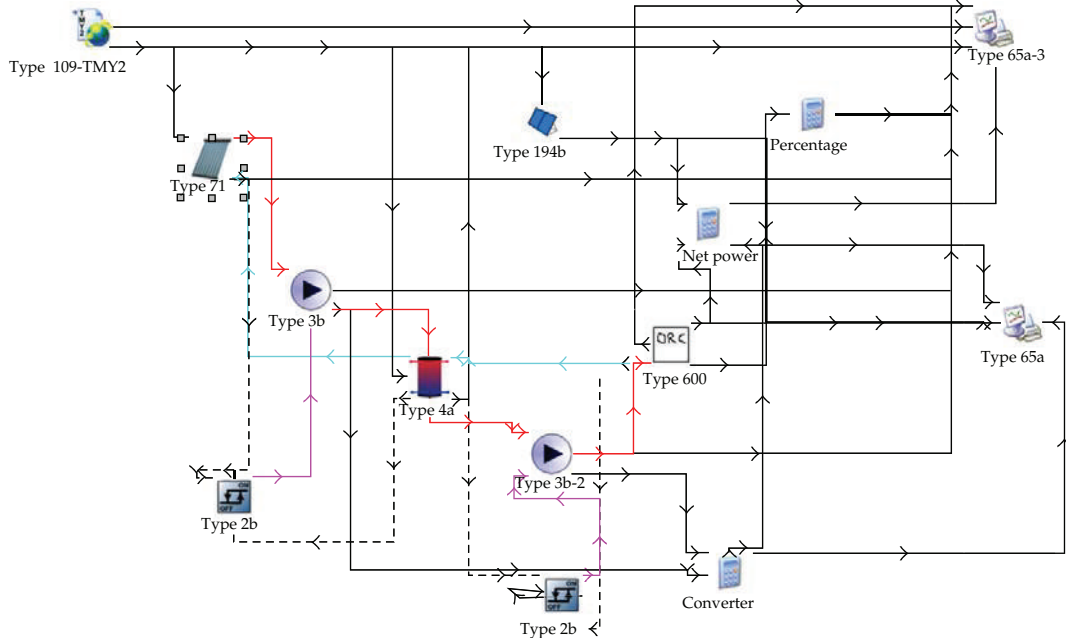


Figure 3: Global power plant scheme.

The evaporator and the condenser have been modeled using the NTU efficiency method. One has

$$\varepsilon = \frac{1 - e^{-NTU(1-C_r)}}{1 - C_r e^{-NTU(1-C_r)}}. \quad (4.2)$$

NTU is the Number of Transfer Unit and  $C_r$  is the ratio between the lower and higher capacity of the two fluids participating in the heat transfer, in our case water and R245fa.

## 5. Results

Following are the main assumptions for the simulation:

- (i) working fluid: R245fa,
- (ii) expander efficiency: 0.7,
- (iii) evaporation pressure: 20 bar,
- (iv) evaporation temperature: 150°C,
- (v) condensation pressure: 3 bar,
- (vi) pump efficiency: 0.5,
- (vii) storage tank volume: 0.1 m<sup>3</sup>.

The results show efficiency for the ORC in the range 4.6%–5.3%, according to the existing references for similar systems [9, 17]. Indeed Quoilin et al. [9] have shown that, with

real expander efficiency curves, an overall electrical efficiency between 6.9% and 7.9% can be reached. These efficiencies are higher than the ones calculated here because the greater expansion considered. In this paper the minimum expander temperature was limited to about 100°C (condensation pressure of 3 bar versus 1 bar of [9]) in order to have residual heat at temperature as high as the inlet temperature of different machines (e.g., absorbers for cold generation). Moreover Quoilin et al. [9] efficiency is a steady-state efficiency at a nominal working point, while the calculated efficiency of the TRNSYS simulation is linked to a dynamic model.

In more detail Quoilin et al. [9] argue that only three working fluids, R245fa, Solkatherm (SES36), and n-pentane, are suitable for ORCs at evaporation temperature of about 150°C. But if the Solkatherm is the fluid showing the highest efficiency of 7.9%, it is also the one requiring the biggest expander, while n-Pentane requires recuperator area very high due to the low density and the very high pressure drops in the low-pressure vapor [9]. Thus the best working fluid for Quoilin et al. [9] is the R245fa also if it shows an overall efficiency of 6.9%.

In general the global efficiency depends on the efficiency of the solar collector and the ORC systems. The evacuated tube collectors solar systems have higher efficiency than the plate technology systems (normally 70% versus 55%) and higher collection temperatures. The higher collection temperatures give higher ORC efficiency (normally the ORC efficiency is about 10% for a maximum temperature cycle of 100°C, [5, 18]). Thus the global system is efficient if the solar collectors have high efficiency and are able to generate high boiler temperature values (i.e., 150°C) and if the expander efficiency is high (from at least 60 to 80%) and the consumptions (pumps, fans, etc.) are low. As a consequence, analyzing, for example, the heat transfer fluid flow rate, it must be not so high in order to avoid very high fluid pumping consumption but not so low in order to avoid low heat transfer coefficient in the collector (e.g., optimum heat transfer fluid flow rate of 1.2 kg/s corresponding to a temperature glide of 15 K [9]). Finally the part-load conditions, necessary to increase the annual production, have to be reduced to the minimum in order to avoid high global efficiency loss.

Figure 4 shows the behavior of the outlet solar collector temperature (solar irradiation, measured in W on the right) and of the power output (power, measured in W on the left) during about ten days during the summer (when there is the maximum solar irradiation in Italy). The figure shows how the power output from the ORC is linked to the solar energy availability; when there is sufficient solar energy (e.g., the storage reaches the evaporation temperature of the working fluid) the power is generated; the power is generated also after the solar energy availability, that is, until the temperature of the storage is over the evaporation temperature of the working fluid.

## 6. Conclusions

Small-scale solar Organic Cycles are well adapted for remote off-grid areas. Compared to the main competitive technology, the PV collector, Solar ORCs have an advantage of being manufacturable locally. They are also more flexible and allow the production of hot water as a by-product [9]. With little commercial experience to draw on, realistic costs estimates for solar thermal power plants are extremely difficult to make; however, it is expected that cost reduction will result from technical and commercial progress. At the moment the overall plant costs for a 3 kW production (and thus 30–60 kW of solar thermal with a useful heat

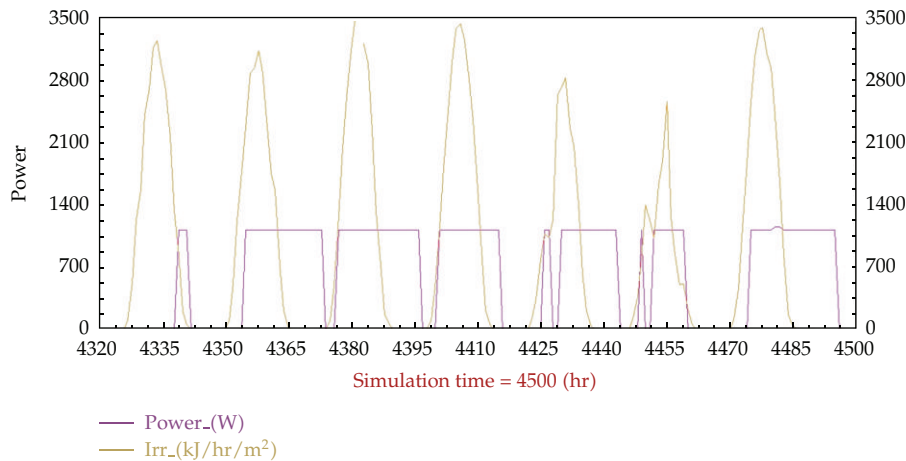


**Figure 4:** Solar energy and power output.

power of 15–30 kW) are about 40.000 euro; thus the investment is not profitable. This is common for new power plants like other small scale power plants analyzed by the authors [19–21]. But the system can be economically feasible with higher size of the plant, higher degree of storage, and low cost of land or with, as expected, a reduced components cost because of an industrial production of the components and the advance of the technologies involved. Indeed, as the size of the solar thermal plant increases and the number of daily operating hours increases (i.e., from kW to MW and from 1500 to 5000 operating hours), the investment becomes more attractive [22]. Furthermore, one of the most important reasons of the remarkable difference of costs between small scale solar thermodynamic and photovoltaic lies in the lack of incentives for the first application. In fact, up to now the incentives apparatus have almost uniquely accompanied the large scale solar power systems [23].

This work focused on the simulation of the power generation of a solar thermal ORC using refrigerant R245fa as a working fluid. An efficiency of about 5%, even with residual heat at temperature of about 100°C and the use of a dynamic model, was calculated. Further studies will include analysis of different size of solar collector plant and storage tank in a 1-year simulation and a comparison of the simulation results with the first experimental data of the plant under construction in Orte (Italy).

### Conflict of Interests

The authors certify that there is no conflicts of interest with any financial organization regarding the material discussed in the paper. The company ENERTECNA is partner of CIRDER (Tuscia University Department), coordinator of the National project STS. In particular S. Esposto and V. Gasperini have started this collaboration for the project purpose in July 2011.

### Acknowledgment

The authors acknowledge the financial support of Italian Contract SEC-DEC-2011-0000564 (regarding the research project STS, Solar Trigenation System) by the Italian Ministry

for the Environment, Land and Sea (Ministero dell'Ambiente e della Tutela del Territorio e del Mare).

## References

- [1] C. Cattani, S. Chen, and G. Aldashev, "Information and modeling in complexity," *Mathematical Problems in Engineering, AID*, vol. 2012, Article ID 868413, 4 pages, 2012.
- [2] M. Carlini, S. Castellucci, M. Guerrieri, and T. Honorati, "Stability and control for energy production parametric dependence," *Mathematical Problems in Engineering*, vol. 2010, Article ID 842380, 21 pages, 2010.
- [3] M. Carlini and S. Castellucci, "Modelling and simulation for energy production parametric dependence in greenhouses," *Mathematical Problems in Engineering*, vol. 2010, Article ID 590943, 28 pages, 2010.
- [4] M. Carlini, M. Villarini, S. Esposto, and M. Bernardi, "Performance analysis of greenhouses with integrated photovoltaic modules," *Lecture Notes in Computer Science*, vol. 6017, no. 2, pp. 206–214, 2010.
- [5] B. Saleh, G. Koglbauer, M. Wendland, and J. Fischer, "Working fluids for low-temperature organic Rankine cycles," *Energy*, vol. 32, no. 7, pp. 1210–1221, 2007.
- [6] U. Drescher and D. Brüggemann, "Fluid selection for the Organic Rankine Cycle (ORC) in biomass power and heat plants," *Applied Thermal Engineering*, vol. 27, no. 1, pp. 223–228, 2007.
- [7] A. Boretti, "Recovery of exhaust and coolant heat with R245fa organic Rankine cycles in a hybrid passenger car with a naturally aspirated gasoline engine," *Applied Thermal Engineering*, vol. 36, pp. 73–77, 2012.
- [8] <http://webbook.nist.gov/chemistry/fluid/>.
- [9] S. Quoilin, M. Orosz, H. Hemond, and V. Lemort, "Performance and design optimization of a low-cost solar organic Rankine cycle for remote power generation," *Solar Energy*, vol. 85, no. 5, pp. 955–966, 2011.
- [10] A. M. Delgado-Torres and L. García-Rodríguez, "Analysis and optimization of the low-temperature solar organic Rankine cycle (ORC)," *Energy Conversion and Management*, vol. 51, no. 12, pp. 2846–2856, 2010.
- [11] M. Villarini, D. Germanò, F. Fontana, and M. Limiti, *I Sistemi SoLari Termici Per La Climatizzazione (SoLar Thermal Cooling and Heating pLants Design)*, Maggioli Editore, 2010.
- [12] M. Gasparro, D. Germanò, and M. Villarini, *Principi Di Progettazione Degli Impianti Solari Termici (Solar Thermal Plants Design)*, Maggioli Editore, Rimini, Italy, 2011.
- [13] V. Piemonte, M. De Falco, P. Tarquini, and A. Giaconia, "Life cycle assessment of a high temperature molten salt concentrated solar power plant," *Computer Aided Chemical Engineering*, vol. 28, pp. 1063–1068, 2010.
- [14] C. J. Winter, R. L. Sizmann, and L. L. Vant-Hull, *Solar Power Plants*, Springer, New York, NY, USA, 1991.
- [15] M. Carlini, S. Castellucci, E. Allegrini, and A. Tucci, "Down-hole heat exchangers: modelling of a low-enthalpy geothermal system for district heating," *Mathematical Problems in Engineering*, vol. 2012, Article ID 845192, 11 pages, 2012.
- [16] M. Carlini, T. Honorati, and S. Castellucci, "Photovoltaic greenhouses: comparison of optical and thermal behaviour for energy savings," *Mathematical Problems in Engineering*, vol. 2012, Article ID 743764, 10 pages, 2012.
- [17] J. P. Roy, M. K. Mishra, and A. Misra, "Performance analysis of an Organic Rankine Cycle with superheating under different heat source temperature conditions," *Applied Energy*, vol. 88, no. 9, pp. 2995–3004, 2011.
- [18] E. Bocci, A. Di Carlo, and D. Marcelo, "Power plant perspectives for sugarcane mills," *Energy*, vol. 34, no. 5, pp. 689–698, 2009.
- [19] F. Orecchini, E. Bocci, and A. Di Carlo, "Process simulation of a neutral emission plant using chestnut's coppice gasification and molten carbonate fuel cells," *Journal of Fuel Cell Science and Technology*, vol. 5, no. 2, Article ID 021015, 9 pages, 2008.
- [20] E. Bocci, F. Zuccari, and A. Dell'Era, "Renewable and hydrogen energy integrated house," *International Journal of Hydrogen Energy*, vol. 36, no. 13, pp. 7963–7968, 2011.
- [21] A. Di Carlo, E. Bocci, and V. Naso, "Process simulation of a SOFC and double bubbling fluidized bed gasifier power plant, International," *Journal of Hydrogen Energy*. In press.

- [22] A. Poullikkas, "Economic analysis of power generation from parabolic trough solar thermal plants for the Mediterranean region-A case study for the island of Cyprus," *Renewable and Sustainable Energy Reviews*, vol. 13, pp. 2474–2484, 2009.
- [23] M. Villarini, M. Limiti, and R. Impero Abenavoli, "Overview and comparison of global concentrating solar power incentives schemes by means of computational models," *Computational Science and Its Applications*, vol. 6785, pp. 258–269, 2011.

## Research Article

# Agent-Based Modeling and Genetic Algorithm Simulation for the Climate Game Problem

Zheng Wang<sup>1</sup> and Jingling Zhang<sup>2</sup>

<sup>1</sup> The College Computer Engineering, Zhejiang Institute of Mechanical and Electrical Engineering, Hangzhou 310053, China

<sup>2</sup> Computer Science and Technology College, Zhejiang University of Technology, Hangzhou 310014, China

Correspondence should be addressed to Zheng Wang, 527494328@qq.com

Received 17 August 2012; Accepted 7 October 2012

Academic Editor: Sheng-yong Chen

Copyright © 2012 Z. Wang and J. Zhang. This is an open access article distributed under the Creative Commons Attribution License, which permits unrestricted use, distribution, and reproduction in any medium, provided the original work is properly cited.

The cooperative game of global temperature lacks automaticity and emotional jamming. To solve this issue, an agent-based modelling method is developed based on Milinski's noncooperative game experiments. In addition, genetic algorithm is used to improve the investment strategy of each agent. Simulations are carried out by designing different coding schemes, mutation schemes, and fitness functions. It is demonstrated that the method can achieve maximum benefits under the premise of the agent non-cooperative game through encouraging optimal individuals. The results provide a sound basis for developing tools and methods to support the simulation of climate game strategy that involves multiple stakeholders.

## 1. Introduction

Climate change is a global issue that is addressed by taking into account various factors in society. Aiming at a complex social game issue, a large number of participants should make effort to prevent global climate variation. Global climate cooperation is proved to be very necessary in the climate game [1]. A comprehensive research of climate game is a challenging topic.

Global greenhouse gas (GHG) emissions have been growing greatly [2, 3]. Humankind is facing a dramatic change of living conditions on the earth when the already-rising global temperature passes a certain threshold [4–8]. To reduce the risk of dangerous climate change, it needs to take the main GHG emissions countries into a "climate coalition," which provides climate ambitious emission reduction at the least cost [9]. At the same time, the broad alliance may reflect strongly to realize the incentive to "free ride" [10]. Therefore, GHG emission is not a problem for a single country. In other words, no country can solve the global climate change problem by acting alone. States have to cooperate in order to address the threat of climate change.

Although there are a few game-theoretical works on climate change, in general the social dilemma situations and the public goods game are perfectly fine models for the problem too. And these games have a very rich history as agent-based simulations. The most famous mathematical metaphor for a social dilemma denotes the prisoner's dilemma [11, 12]. Other well-studied models include public goods games [13, 14], which essentially represent a generalization of the pairwise prisoner's dilemma to interactions in groups of arbitrary size [15, 16]. Foremost, there is the issue of reward and punishment, which has recently been studied a lot in order to understand how these two basic social forces may avert the dilemma [17–20]. Then there are also works concerning the critical mass, conditional strategies, population density, heterogeneity, and interdependent networks in social dilemmas. These subjects have been studied extensively in the very recent past, and their implications for the resolution of social dilemmas such as the climate change dilemma as agent-based models are very significant [21–25]. Most recently, the shift to agent-based modeling has also been highlighted for human bargaining [26], which is obviously of relevance for the climate change dilemma as their players (countries, nations) have to agree on a certain policy that they will then carry out.

In essence, global climate game is the process of competition between the participants with different game strategies [27–31]. They must balance the relationship between economic development and environmental protection by finding the Nash equilibrium between these two interests. In other words, only in content with optimality condition and Nash equilibrium of the dual requirement, the climate cooperation will be the most stable and efficiency international cooperation.

Climate protection programs that appeal to a human sense of fairness, that is, each player contributes a "fair share" to the collective goal, are more likely to avoid irrational self-detrimental behavior [32]. Milinski et al. [33] proposed the collective-risk social dilemma as a framework for investigating the inherent problems of avoiding dangerous climate change, and performed simulation to study the game. According to Milinski's experiment, students invest anonymously, with each student being informed of the cumulative investment sum after each round. Under such circumstance, the trade-off between personal benefits and group interests provides a basis for each student to make its investment scheme. Moreover, students can learn from a successful scheme to make better decisions in the next round. However, this strategy, in which computer runs the dice program, is a kind of the random investment strategy. A stochastic process is one whose behavior is nondeterministic, and subsequent of investment is determined by a random element. Therefore, it is more difficult to obtain the optimal investment strategy.

All those works can be linked to the voluntary contribution games with punishment possibility. The final step of the complex game process should be built by several models, algorithms, and different experiments application in order to make it clear and systematic. This is also the next stage of this work.

The aim of this paper focuses on developing evolutionary model and simulation strategy to improve Milinski's investment strategy. The investment strategy using genetic algorithm (GA) of agent-based modeling is established based on the noncooperative game experiments in [33]. Firstly, used agents represent climate game players to develop the game modeling. Then, we use GA for investment strategy simulation. The GA investment strategy is specifically designed to support the study of multiparticipant climate change game using computational modeling, simulation, programming, and running. GA is a population-based biomimetic evolutionary method to solve various complex decision-making problems [34–36]. This heuristic is routinely used to generate useful solutions for optimization and search

problems. In this work, the climate game problem is regarded as an optimization problem, and thus, optimal investment scheme for each agent will be obtained through GA.

## 2. Agent-Based Modeling of the Climate Game Problem

Climate change is a classic instance of complex, bottom-up, and multiagent human behavior. Using game theory to research on global climate change is an effective way for climate cooperation. Each agent represents a student or a commonwealth of them. The essence of climate game is the process of competition between the agents' strategies. Each agent must balance between economic development and environmental protection, trying to find the Nash equilibrium between these two interests.

In [33], thirty groups of six agents took part in a climate game where each agent needs to build a data account to store its amount of investment. At the beginning, the initial balance of each agent's account is €40. Subsequently, each agent must invest €2 in each round of game, and all six agents must invest an average of €120 in 10 rounds. Only in this way, it can be possible to ensure that the finally total investment is more than or equal to €120. At the same time, each agent in each round is required to invest only €0, €2, or €4. Therefore, this section will discuss the strategy of the random selection of €0, €2, or €4 in each investment, that is, it chooses a value with a certain probability.

According to Milinski's experiment, half of the groups succeed in reaching the target sum, whereas the others only marginally fail. When the risk of loss was only as high as the necessary average investment or even lower, the groups generally failed to reach the target sum. It was shown that the investment sum of about half of the agents was not less than €120, and in the most reasonable way, each agent invested €2 at each round in average. Therefore, the possibility of investing €2 was twice that of investing other numbers. It can be seen on this basis that the probability of providing €2 is 0.5, \$0 with the probability 0.25, and \$4 with the probability 0.25.

## 3. Genetic Algorithm for the Climate Game Problem

To improve investment strategy, an evolutionary strategy based on GA is proposed in this paper. Specifically, the focus is on agent's decision-making process through simulation experiment. A GA-based model for the climate game problem is developed, and its details are described as follows.

- (i) Each player is viewed as an autonomous agent.
- (ii) Each agent establishes and maintains a database.
- (iii) Each agent's investment sum in all 10 rounds will be stored in the database.
- (iv) The contribution of each agent is determined by the GA-based strategy.
- (v) Individual code: each agent's investment in 10 rounds and each agent's investment sequence as an individual of GA.
- (vi) Integer code: 0, 2, 4. For example, the first agent in 10 rounds can be encoded as 2222222222.

The main program based on GA is illustrated in Figure 1. In the figure,  $p = 0.9$  means that an agent has a probability of 90% to lose all savings if the target sum €120 is not reached.

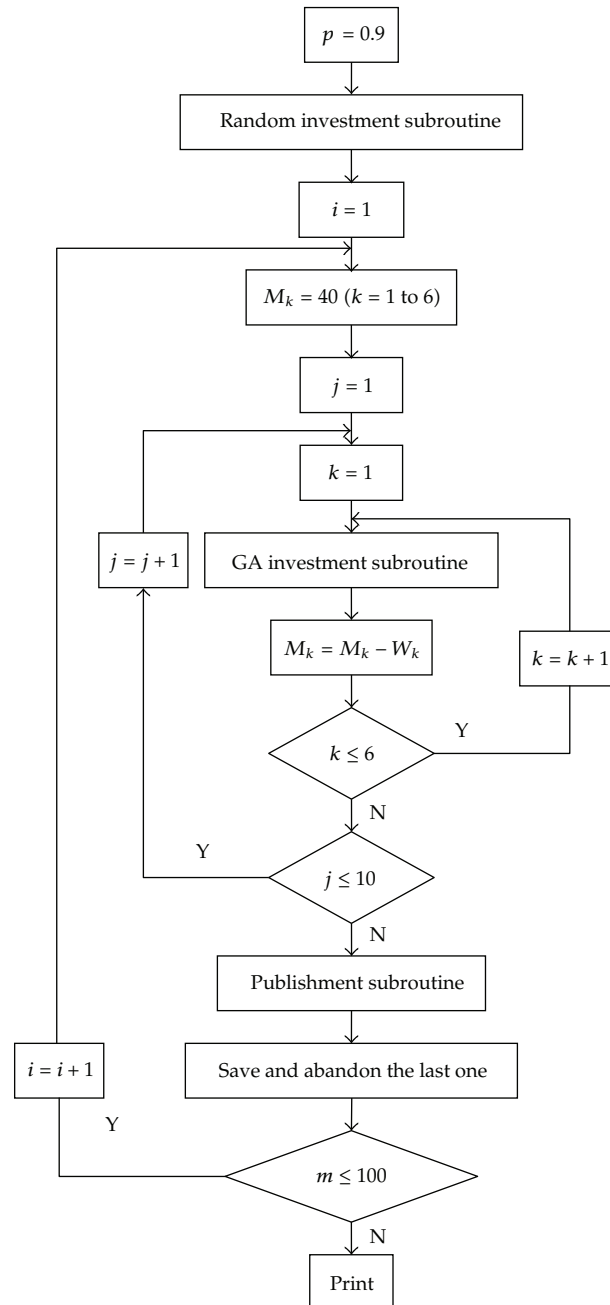


**Figure 1:** The main program based on GA.

The meaning of  $p = 0.5$  and  $p = 0.1$  is that the probabilities of losing all their money are 50% and 10%, respectively, if €120 is not reached.

The meanings of other marks are explained as follows:

- (i)  $W_k$  represents the investment amount of the  $k$ th agent;
- (ii)  $M_k$  represents the total remaining saving in the account of the  $k$ th agent;

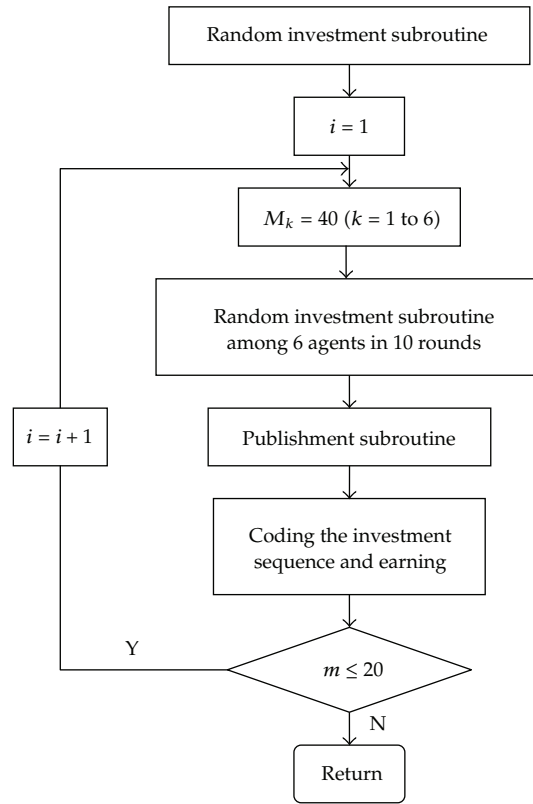


Figure 2: Random investment subroutine.

(iii)  $M_m$  represents the total remaining saving in the account of the  $m$ th agent;

(iv)  $r, R$  are the random variables;

(v)  $p$  represents the punishment probability;

(vi)  $i, j, m, \text{ and } k$ , are the loop variables.

In initialization, we set the population size as 20 and randomly generate 20 individuals as the initial population to represent 20 investment schemes. In order to contrast, we save the generated 20 investment schemes into the corresponding records in the database established.

### 3.1. Random Investment

The random investment subroutine is shown in Figure 2 where each agent is provided €40 at the beginning. After that, the random subroutine will run to simulate the investment activities of the six agents for 10 rounds, then transfer the generated data to the punishment subprogram. The investment results and the incomes of each agent will be stored in the database at last.

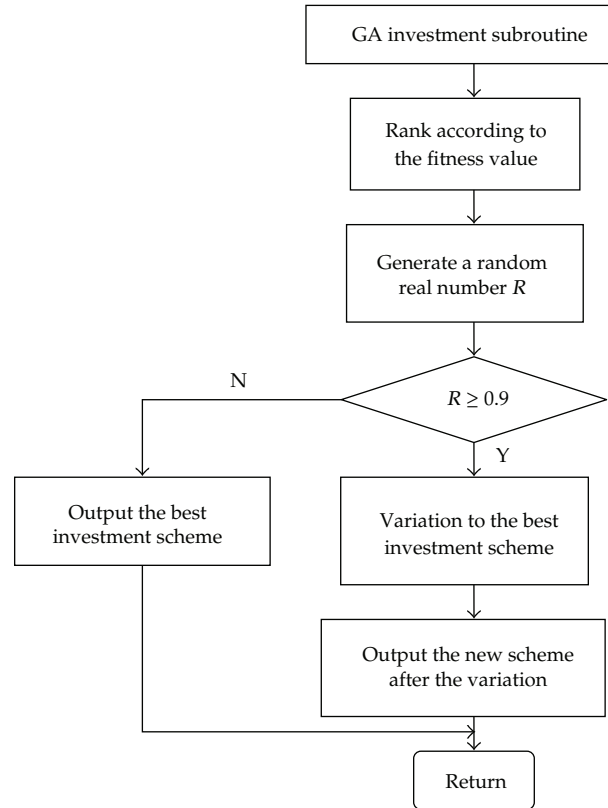


Figure 3: GA investment subroutine.

### 3.2. GA Investment

By running the GA investment subroutine for each agent, a new investment scheme can be generated, from which the total amount of money can be obtained. Then, the personal benefit for each agent after experiencing the risk of losing all the remaining money can be calculated. The investment scheme for each agent, the total amount of money that each agent invested, and the cumulative investment sum among all these agents will be saved into the database. As such, there are 21 records of investment in the database.

Figure 3 is the process of the simple GA investment subroutine.  $R$  is a randomly generated real number, and the condition  $R \geq 0.9$  implies that the mutation probability of variation is 0.1. The process is explained as follows.

*Step 1.* Rank the fitness values of the investment schemes (which are decoded as individuals in GA) in descending order.

*Step 2.* If the random number  $R \geq 0.9$ , the best individual would mutate using single-point mutation; otherwise, go to Step 3.

*Step 3.* If the random number  $R < 0.9$ , there is no mutation in the game. The best individual is selected as the new one directly.

*Step 4.* When iteration  $> 100$ , end the execution; otherwise, return.

### 3.2.1. Individual Representation

As discussed earlier in this paper, a database is established for each agent to save its investment record (which includes its investment quota and its remaining money in each round). In this case, the cumulative investment sums for  $k$  agents can be obtained. For instance, if the investment record of the  $k$ th agent during 10 rounds is 2220044220, which means that the agent invests €2 in the first three rounds, €0 in the fourth and fifth rounds, and so on. We can get that the total amount of money invested by the  $k$ th agent throughout 10 rounds reaches €18. If the cumulative investment sum among  $k$  agents during 10 rounds is €110, and the  $k$ th agent is chosen to be punished since the target sum (€120) has not been achieved, the  $k$ th agent will lose its remaining €22. In this way, we put data 2220044220, 22, and 110 in the database for the  $k$ th agent.

The integer coding method is used in GA, with each individual representing the investment quotas in 10 rounds for each agent. An individual can be 2220044220 for the  $k$ th agent in the example mentioned in the last paragraph.

### 3.2.2. Fitness Function

Individuals in GA are evaluated via the fitness function. Since the goal is to achieve the maximization of personal benefits and cumulating the investment sum, the fitness function is designed as follows:

$$f(i) = \alpha M_{ki} + (1 - \alpha) \sum_{k=1}^6 W_k. \quad (3.1)$$

In the equation,  $k$  refers to the agent index, and  $i$  refers to the investment scheme index.  $f(i)$  denotes the fitness value of the  $i$ th scheme for the  $k$ th agent,  $M_{ki}$  refers to the remaining saving of the  $k$ th agent via its  $i$ th scheme, that is, profits after the punishment which is 90% probability to punish if the target sum has not been reached, and  $\sum_{k=1}^6 W_k$  means the cumulative investment sum from all agents involved. The weighting coefficient  $\alpha \in [0, 1]$  reflects the balance between individual benefits and cumulative investment sum.

All the investment schemes are ranked in descending order in terms of fitness value. Consequently, the best investment scheme with the largest fitness value can be obtained, and it can be directly established as the designated scheme for the next game or established after an appropriate adjustment.

### 3.2.3. Mutation

In the GA investment subroutine, mutation is performed for the adjustment of the best investment scheme with a probability of 0.9. Specifically, a real number  $R$  (within  $[0, 1]$ ) is randomly generated. If  $R < 0.9$ , the best investment scheme is directly established as the designated scheme for the next game; otherwise, perform the mutation.

Site-based mutation method is adopted, which can be described as follows: randomly select a gene from the individual and replace it with randomly generated numbers 0, 2, or 4, and a new scheme is obtained. The mutation probability can be 0.1 or other values between (0,1). Through the GA investment subroutine, an agent can get a recommended option as a reference scheme.

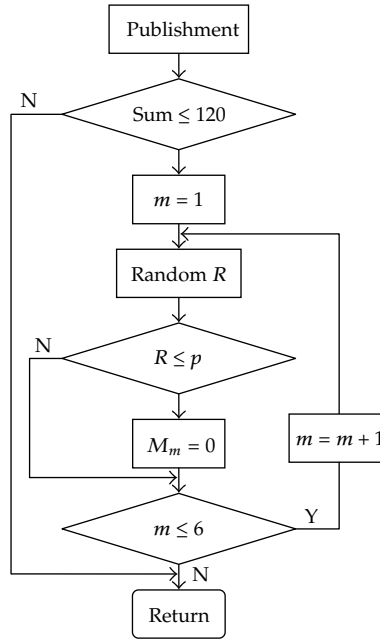


Figure 4: Punishment subroutine.

### 3.3. Punishment

According to [28], the subroutine of random investment with punishment is shown in Figure 4. After 10 rounds, if an agent's investment sum achieves or exceeds €120, it will obtain the surplus in its account. Otherwise, it will enter the punishment subroutine. The routine will punish all agents through throwing dice, leading to that all agents have 90%, 50%, or 10% probabilities to lose their surpluses. This case will be discussed as follows.

In the punishment subroutine, for every agent, the computer produces a random number  $R$ , and if  $R$  is greater than  $p$  ( $p = 0.9, 0.5, \text{ or } 0.1$ ), the step  $M_m = 0$  will be skipped, and the surplus money in the account will be saved. Otherwise, all surplus money in the account will be confiscated.

### 3.4. Fitness Calculation and Sorting

This stage involves calculating the fitness value of 21 individuals in the database, ranking these individuals in terms of fitness value and abandoning the one with the minimum fitness value. So there are still 20 records of investment in the database. Then it moves to the next round, until the given number of games (i.e., 100) is completed.

## 4. Simulations and Results

The results of the simulation include three parts. First, we obtained variation curves of the total remaining savings in all six agents' accounts under different losing probability  $p$  and weighting coefficient  $\alpha$ . Then we also obtained variation curves of cumulative investment sum under varying  $p$  and  $\alpha$ , and finally, we identified the relationship between the variables and the parameters.

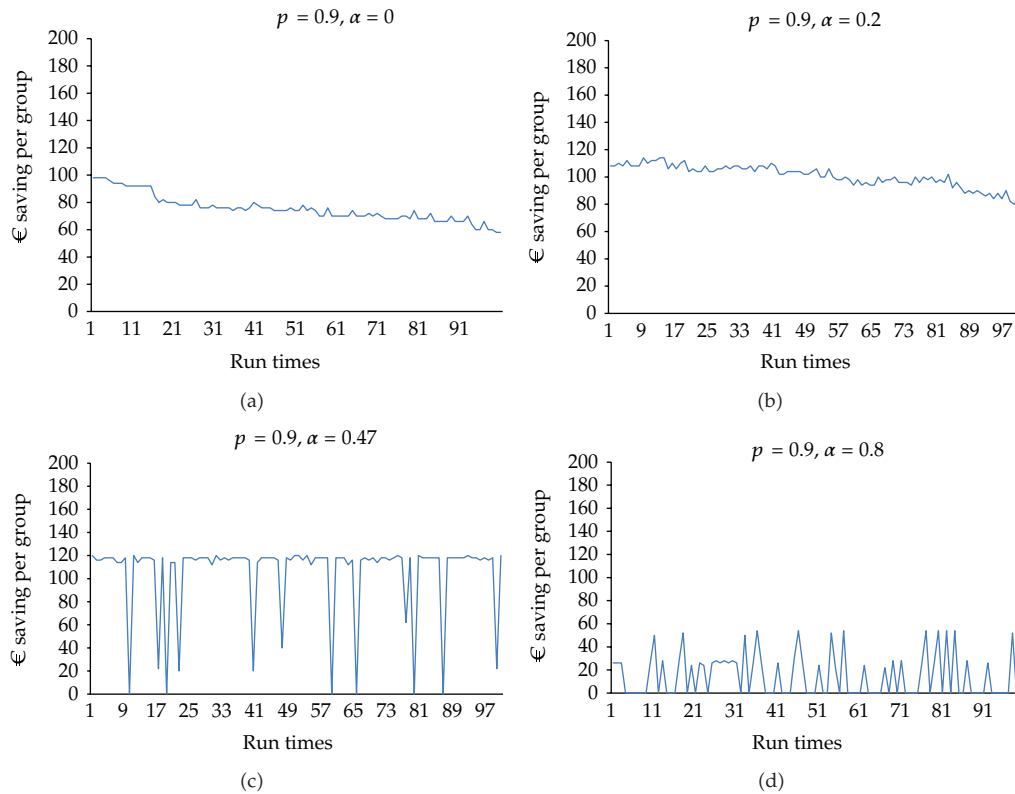


**Figure 5:** (a) The total remaining saving when  $p = 0.9$  and  $\alpha = 0$ . (b) The total remaining saving when  $p = 0.9$  and  $\alpha = 0.2$ . (c) The total remaining saving when  $p = 0.9$  and  $\alpha = 0.47$ . (d) The total remaining saving when  $p = 0.9$  and  $\alpha = 0.8$ .

#### 4.1. Parameter Set 1

We first carry out the experiments to study the total remaining savings and the cumulative investment sum with  $p = 0.9$  and varying  $\alpha$ . By implementing the experiment with different values of the parameters, variation curves of total remaining savings in all six agents' accounts are shown in Figures 5(a)–5(d), where  $p$  denotes the punishment probability if the target sum is not reached, and  $\alpha$  refers to the weighting coefficient in the equation.

There are two observations from the above figures under the 90% treatment: (1) the total remaining savings for all the six agents in a group decrease in response to the growth of the weighting coefficient  $\alpha$ ; (2) the total remaining savings remain as €120 when  $\alpha = 0.47$ . Consequently, the total remaining savings increase when coefficient  $\alpha$  declines, showing a bias towards the group interests. On the other hand, personal benefits are more inclined to be accomplished, and the total remaining savings decrease when a higher value of  $\alpha$  is used. The group interests and personal benefits are well balanced when  $\alpha = 0.47$ , where the total remaining saving remains as €120 and the Nash equilibrium is achieved. Variation curves of the cumulative investment sum among all the six agents in a group under different values of  $\alpha$  in the 90% treatment are illustrated in Figure 6.

Two observations can be obtained from Figure 6: (1) the cumulative investment sum among all the six agents in a group decreases in response to the growth of the weighting coefficient  $\alpha$ ; (2) the cumulative investment sum remains as €120 when  $\alpha = 0.47$ . The results

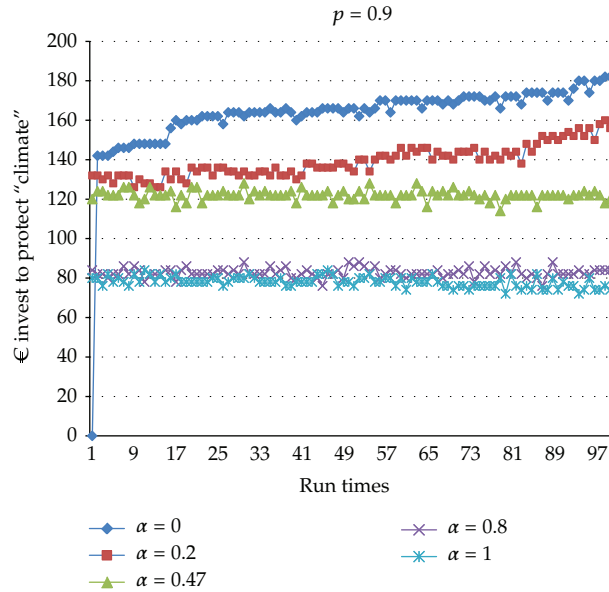


Figure 6: The cumulative investment sum under different  $\alpha$ .

indicate that the fitness function designed in (3.1) inclines toward the group interests, and that the cumulative investment sum increases as  $\alpha$  decreases. The results also show a bias towards personal benefits, and the cumulative investment sum decreases when a higher value of  $\alpha$  is used. When  $\alpha = 0.47$ , the group interests and personal benefits are both well taken care of, and the cumulative investment sum is about €120.

Although the experiment is in the 90% treatment (i.e.,  $p = 0.9$ ), the above conclusions are also applicable for cases in the 50% treatment (i.e.,  $p = 0.5$ ) and 10% treatment (i.e.,  $p = 0.1$ ).

#### 4.2. Parameter Set 2

We then carry out the experiments to study the total remaining savings and the cumulative investment sum with  $p = 0.5$  and varying  $\alpha$ . If the target sum €120 is not reached, an agent will risk losing all their remaining money with a probability of either 0.9, 0.5, or 0.1. Results on the total remaining saving among all the 6 agents in a group under different values of  $\alpha$  in the 50% treatment (i.e.,  $p = 0.5$ ) are drawn through our experiment, as shown in Figures 7(a)–7(c). Those on the cumulative investment sum are illustrated in Figure 8.

#### 4.3. Parameter Set 3

We further carry out the experiments to study the total remaining savings and the cumulative investment sum with  $p = 0.1$  and varying  $\alpha$ . Results on the total remaining savings and the cumulative investment sum among all the six agents in a group under different values of  $\alpha$  in the 10% treatment (i.e.,  $p = 0.1$ ) are shown in Figures 9(a)–9(c) and Figure 10, respectively.

It can be concluded that the cumulative investment sum goes down, and that the total remaining saving increases when loss probability increases. This indicates that a country

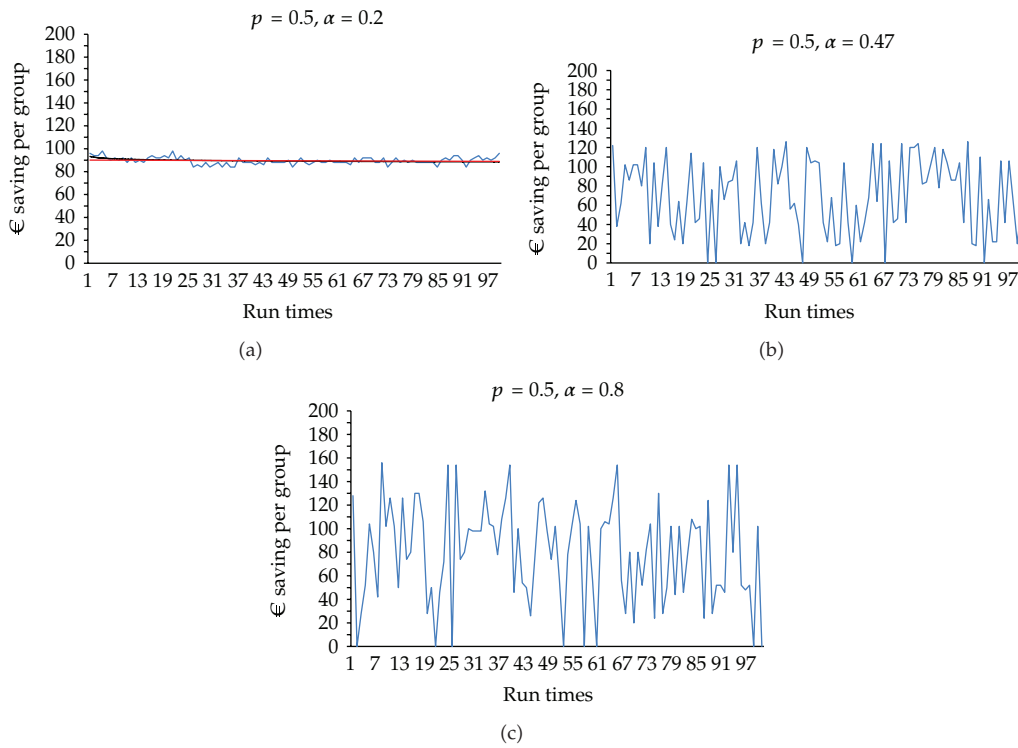


**Figure 7:** (a) The total remaining saving in the 50% treatment when  $\alpha = 0.2$ . (b) The total remaining saving in the 50% treatment when  $\alpha = 0.47$ . (c) The total remaining saving in the 50% treatment when  $\alpha = 0.8$ .

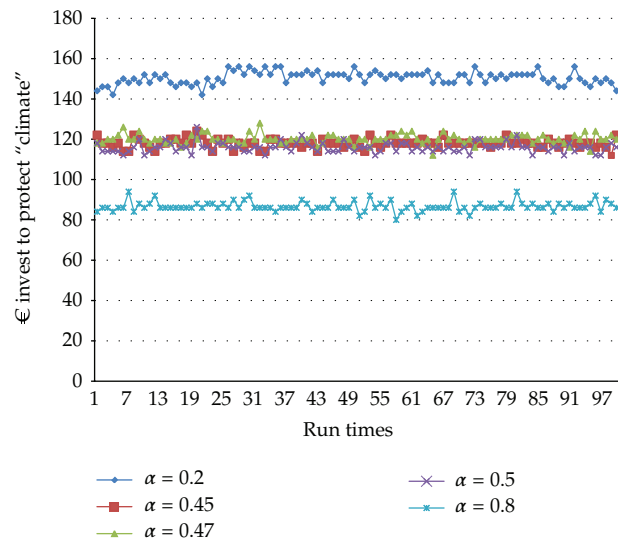


**Figure 8:** The cumulative investment sum in the 50% treatment.

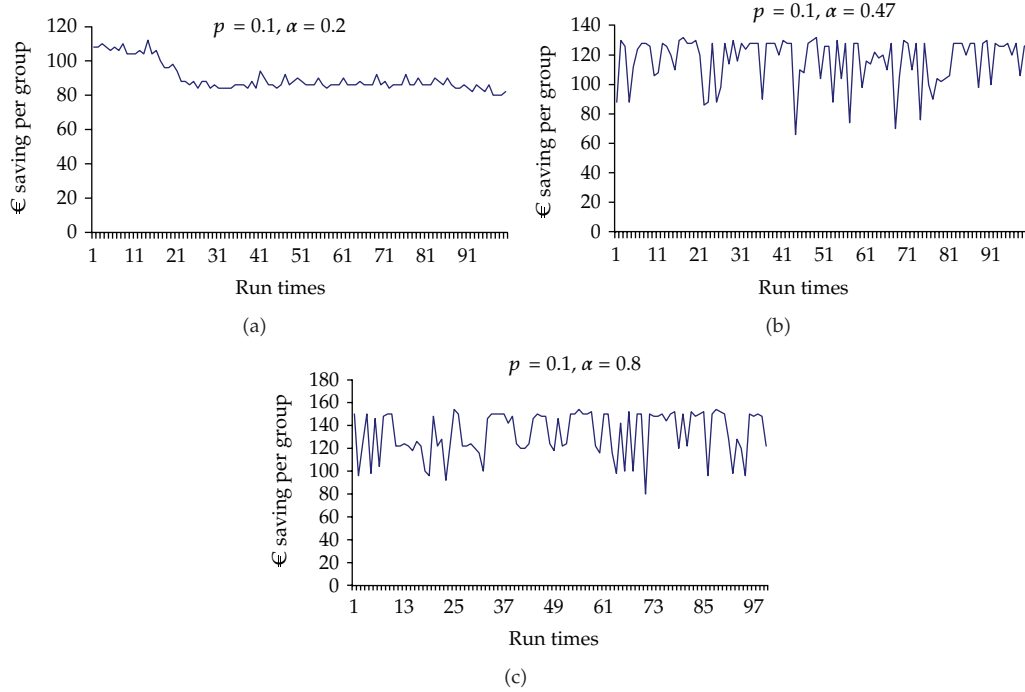


**Figure 9:** (a) The total remaining saving in the 10% treatment when  $\alpha = 0.2$ . (b) The total remaining saving in the 10% treatment when  $\alpha = 0.47$ . (c) The total remaining saving in the 10% treatment when  $\alpha = 0.8$ .

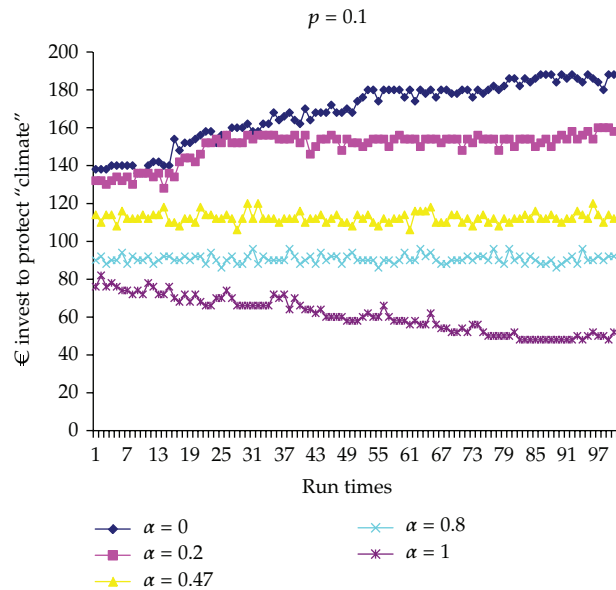


**Figure 10:** The cumulative investment sum in the 10% treatment.

needs to invest more for recovery if dangerous climate change occurs and causes great damage.

## 5. Conclusion

An agent-based evolutionary model and a GA-based solution strategy are proposed in this paper. Based on the principle of maximizing individual and collective interests, linear weighting is used for the GA fitness function, and a coding and mutation operator is designed for GA evolutionary optimization strategies. The simulation experiments with groups of six agents show that it can achieve maximum benefits under the premise of the agent noncooperative game through encouraging optimal individuals. The results provide a solid basis for studying climate game strategy using multiagent modelling and simulation. This approach also has the potential to simulate the experiment that contains a large amount of data.

## Acknowledgments

This work is supported in part by the National Natural Science Foundation of China (no. 60970021) and the Department of Education Foundation of Zhejiang Province (no. Y201225032). The authors are grateful to Dr. Hywel Williams who gave much advice to them concerning this paper at the University of East Anglia.

## References

- [1] D. G. Rand, A. Dreber, T. Ellingsen, D. Fudenberg, and M. A. Nowak, "Positive interactions promote public cooperation," *Science*, vol. 325, no. 5945, pp. 1272–1275, 2009.
- [2] T. Barker, I. Bashmakov, and L. Bernstein, "Summary for policymakers," in *The 9th Session of Working Group III of the IPCC*, 2007.
- [3] H. Rowlands, *The Climate Challenge Game: How Might Computer Games be Used to Communicate the Issues of Climate Change?* [Ph.D. thesis], University of Oxford, 2006.
- [4] C. Cattani, R. Badea, S. Chen, and M. Crisan, "Biomedical signal processing and modeling complexity of living systems," *Computational and Mathematical Methods in Medicine*. In press.
- [5] S. Chen, J. Zhang, H. Zhang, N. M. Kwok, and Y. F. Li, "Intelligent lighting control for vision-based robotic manipulation," *IEEE Transactions on Industrial Electronics*, vol. 59, no. 8, pp. 3254–3263, 2012.
- [6] M. Carlini, S. Castellucci, M. Guerrieri, and T. Honorati, "Stability and control for energy production parametric dependence," *Mathematical Problems in Engineering*, vol. 2010, Article ID 842380, 21 pages, 2010.
- [7] T. Pfeiffer and M. A. Nowak, "Climate change: all in the game," *Nature*, vol. 441, no. 7093, pp. 583–584, 2006.
- [8] S. H. Schneider, "What is "dangerous" climate change?" *Nature*, vol. 411, no. 6833, pp. 17–19, 2001.
- [9] M. Milinski, D. Semmann, H. J. Krambeck, and J. Marotzke, "Stabilizing the Earth's climate is not a losing game: supporting evidence from public goods experiments," *Proceedings of the National Academy of Sciences of the United States of America*, vol. 103, no. 11, pp. 3994–3998, 2006.
- [10] M. Inman, *The Climate Change Game*, *Nature Reports Climate Change*, Macmillan, 2009.
- [11] R. Axelrod, "Effective choice in the prisoner's dilemma," *Journal of Conflict Resolution*, vol. 24, no. 1, pp. 3–25, 1980.
- [12] R. Axelrod and W. D. Hamilton, "The evolution of cooperation," *Science*, vol. 211, no. 4489, pp. 1390–1396, 1981.
- [13] M. Bagnoli and M. McKee, "Voluntary contribution games: efficient private provision of public goods," *Economic Inquiry*, vol. 29, no. 2, pp. 351–366, 1991.
- [14] A. Dannenberg, T. Riechmann, B. Sturm, and C. Vogt, "Inequity Aversion and Individual Behavior in Public Good Games: An Experimental Investigation," ZEW—Centre for European Economic Research Discussion Paper No. 07-034, 2007.

- [15] C. Hauert and G. Szabó, "Prisoner's dilemma and public goods games in different geometries: compulsory versus voluntary interactions," *Complexity*, vol. 8, no. 4, pp. 31–38, 2003.
- [16] M. Doebeli and C. Hauert, "Models of cooperation based on the Prisoner's Dilemma and the Snowdrift game," *Ecology Letters*, vol. 8, no. 7, pp. 748–766, 2005.
- [17] D. Helbing, A. Szolnoki, M. Perc, and G. Szabó, "Punish, but not too hard: how costly punishment spreads in the spatial public goods game," *New Journal of Physics*, vol. 12, Article ID 083005, 2010.
- [18] D. Helbing, A. Szolnoki, M. Perc, and G. Szabó, "Defector-accelerated cooperativeness and punishment in public goods games with mutations," *Physical Review E*, vol. 81, no. 5, Article ID 057104, 2010.
- [19] M. Perc and A. Szolnoki, "Self-organization of punishment in structured populations," *New Journal of Physics*, vol. 14, Article ID 043013, 2012.
- [20] A. Szolnoki, G. Szabó, and M. Perc, "Phase diagrams for the spatial public goods game with pool punishment," *Physical Review E*, vol. 83, no. 3, Article ID 036101, 2011.
- [21] A. Szolnoki and M. Perc, "Conditional strategies and the evolution of cooperation in spatial public goods games," *Physical Review E*, vol. 85, Article ID 026104, 2012.
- [22] Z. Wang, A. Szolnoki, and M. Perc, "If players are sparse social dilemmas are too: importance of percolation for evolution of cooperation," *Scientific Reports*, vol. 2, p. 369, 2012.
- [23] M. Perc and Z. Wang, "Heterogeneous aspirations promote cooperation in the prisoner's dilemma game," *PLoS ONE*, vol. 5, no. 12, Article ID e15117, 2010.
- [24] A. Szolnoki and M. Perc, "Impact of critical mass on the evolution of cooperation in spatial public goods games," *Physical Review E*, vol. 81, no. 5, Article ID 057101, 2010.
- [25] Z. Wang, A. Szolnoki, and M. Perc, "Evolution of public cooperation on interdependent networks: the impact of biased utility functions," *Europhysics Letters*, vol. 97, Article ID 48001, 2012.
- [26] A. Szolnoki, M. Perc, and G. Szabó, "Defense mechanisms of empathetic players in the spatial ultimatum game," *Physical Review Letters*, vol. 109, no. 7, 2012.
- [27] H. Shi, W. Wang, N. M. Kwok, and S. Y. Chen, "Game theory for wireless sensor networks: a survey," *Sensors*, vol. 12, no. 7, pp. 9055–9097, 2012.
- [28] C. Cattani, S. Chen, and G. Aldashev, "Information and modeling in complexity," *Mathematical Problems in Engineering*, vol. 2012, Article ID 868413, 4 pages, 2012.
- [29] Y. Zheng, H. Shi, and S. Chen, "Fuzzy combinatorial optimization with multiple ranking criteria: a staged tabu search framework," *Pacific Journal of Optimization*, vol. 8, no. 3, pp. 457–472, 2012.
- [30] S. C. Lim, C. H. Eab, K. H. Mak, M. Li, and S. Y. Chen, "Solving linear coupled fractional differential equations by direct operational method and some applications," *Mathematical Problems in Engineering*, vol. 2012, Article ID 653939, 28 pages, 2012.
- [31] S. Chen and Z. Wang, "Acceleration strategies in generalized belief propagation," *IEEE Transactions on Industrial Informatics*, vol. 8, no. 1, pp. 41–48, 2012.
- [32] E. Fehr and K. M. Schmidt, "A theory of fairness, competition, and cooperation," *Quarterly Journal of Economics*, vol. 114, no. 3, pp. 817–868, 1999.
- [33] M. Milinski, R. D. Sommerfeld, H. J. Krambeck, F. A. Reed, and J. Marotzke, "The collective-risk social dilemma and the prevention of simulated dangerous climate change," *Proceedings of the National Academy of Sciences of the United States of America*, vol. 105, no. 7, pp. 2291–2294, 2008.
- [34] S. Y. Chen and Y. F. Li, "Automatic sensor placement for model-based robot vision," *IEEE Transactions on Systems, Man, and Cybernetics Part B*, vol. 34, no. 1, pp. 393–408, 2004.
- [35] S. Chen, H. Tong, Z. Wang, S. Liu, M. Li, and B. Zhang, "Improved generalized belief propagation for vision processing," *Mathematical Problems in Engineering*, vol. 2011, Article ID 416963, 12 pages, 2011.
- [36] D. E. Goldberg, *Genetic Algorithms in Search, Optimization and Machine Learning*, Addison-Wesley Longman, Boston, Mass, USA, 1989.

*Research Article*

# **Photovoltaic Pumps: Technical and Practical Aspects for Applications in Agriculture**

**A. Petroselli,<sup>1</sup> P. Biondi,<sup>1</sup> A. Colantoni,<sup>1</sup> D. Monarca,<sup>2</sup>  
M. Cecchini,<sup>2</sup> A. Marucci,<sup>2</sup> and Cividino Sirio<sup>2</sup>**

<sup>1</sup> *Department of Agriculture, Forests, Nature and Energy (DAFNE), University of Tuscia,  
Via S. Camillo de Lellis, 01100 Viterbo, Italy*

<sup>2</sup> *Department of Agrarian and Environment Science, University of Udine, Via delle Scienze 208,  
33100 Udine, Italy*

Correspondence should be addressed to A. Colantoni, colantoni@unitus.it

Received 22 August 2012; Accepted 23 September 2012

Academic Editor: Massimo Scalia

Copyright © 2012 A. Petroselli et al. This is an open access article distributed under the Creative Commons Attribution License, which permits unrestricted use, distribution, and reproduction in any medium, provided the original work is properly cited.

The paper deals with a series of tests conducted on a PV-DC pump in Viterbo (42°24' North, 12°06' East). The tests lasted from January 2003 up to November 2004 and involved measurements of solar radiation, on both a horizontal surface and the tilted module surface, flow rates, volumes, and total dynamic heads. In total, up to 3000 data were collected every day whose analysis allowed us to find empirical relationships among system efficiencies, solar radiations, and total dynamic heads. In the second part of the paper we develop a simple method that allows both the assessment of performances of the whole system when installed in a different site from that in which the tests were performed and the optimal inclination angle of the panel to be determined in relation to annual or seasonal use (see irrigation).

## **1. Introduction**

Solar photovoltaic (PV) systems have shown their potential in rural electrification projects around the world, especially concerning Solar Home Systems. With continuing price decreases of PV systems, other applications are becoming economically attractive, and growing experience is gained with the use of PV in such areas as social and communal services, agriculture and other productive activities, which can have a significant impact on rural development. There is still a lack of information, however, on the potential and limitations of such PV applications. Rural energy is generally recognized as an important element of rural socioeconomic development, not as an end in itself, but through the demand for the services made possible through energy inputs, such as potable water pumping

and extension of the day by lighting and cooking. As a general trend, an increasing energy demand—both in quantity and quality—is highly correlated with socioeconomic development.

This study is focused on solar photovoltaic (PV) systems, which can fulfil only a part of rural energy needs. As has been noted before, most PV programmes have given attention to the so called “Solar Home Systems” as the most proven of PV applications. With continuing advances in PV technology, decreasing prices and growing experience in the organizational aspects of introducing this new technology, many other applications of PV have shown their potential. This promises to open the door for a greater contribution of PV systems to rural development [1].

Our department took on two research problems:

- (i) to test the field performances of a commercialized solar pump that is sold with a photovoltaic panel,
- (ii) to estimate, once the system’s operational characteristics were defined, what performances could be expected when the same complex would be located in such African countries as Ghana, Benin, and Burkina Faso.

These were the cues to set up a test bed for this type of equipment and to try to deepen our knowledge regarding a subject that is not without interest, also from an economic point of view. At present, the lack of electricity and high gas-oil costs (where and when available) are opening vast markets for these pumps in many developing countries, both Asian and African (particularly sub-Saharan).

The reasons for this increasing use are manifold, among them: easy and rapid installation, low and rare maintenance, the long service life of these types of photovoltaic panels, and the great increase in their efficiency [2, 3], with a vertiginous rapid descent of the panels’ costs that in the last decade of the last century decreased—at equal power output—to 1/4 of their initial value [4-6].

Hence, there is a growing interest in this type of machinery and the promotion of their diffusion, especially in third world countries, by individual western countries like Germany and other northern European countries [7-10], as well by the UE, FAO, UNESCO, and the previously cited World Bank.

Nevertheless, they are not many works in the literature which deal specifically with tests run on photovoltaic pumps. In fact, with few exceptions (e.g., [11, 12]), the tests that exist concern either the solar panel and its performance or—as in the case of the advertising material supplied by the manufacturers—the solar pump for which it is provided, without many details, only the total head-flow rate curves obtained by coupling the pump to the electric network instead of to the photovoltaic panel [13, 14].

The tests conducted by *Argaw*—that, unlike the others, consider the whole panel/pump complex—were performed on community plants (in Brazil) and, therefore, were subject to a series of conditions that limited the possibility of the researchers to vary the operating conditions of the system (e.g., discharge and/or total head).

In this regard, a test bed was set up in the Hydraulic Laboratory of our department that essentially consists of a closed hydraulic circuit, complete with valves and measuring instruments (flow rates, total heads, and volumes), and that is equipped with the measuring instrumentation for photoelectric parameters (solar radiation, both on the horizontal plane and on the panel, intensity, and voltage of the electricity inside and outside the panel).

The present work is organised in two parts:

- (i) the first contains a description of the experimental equipment and a discussion of the results obtained by a long series of tests that lasted for about two years;
- (ii) the second is essentially theoretical and aimed at defining: first, a methodology that allows a technician to easily and reliably estimate the performances of the panel/pump system (the one we experienced or another whose operational characteristics are known), taking into consideration its installation in places different from Viterbo (42°24' North; 12°06' East) where the tests were performed; second, the optimum spatial position to be assigned to the panel depending on the use, annual, or seasonal (irrigation), required of the pump.

This work ends with a practical application that shows what results are to be expected in the case of installation of the experimented system in one of the African countries mentioned above.

## **2. Layout of the Experimental Installation and Measurement Techniques**

### **2.1. Experimental Installation**

The whole panel/pump system was installed in the experimental field of our department, which is situated within the Faculty of Agriculture. The pump—a “SOLAFLUX” made by FLUXINOS in Grosseto, central Italy—is a submerged piston pump of low power and fed by direct current (tension 20–70 V; intensity 1–4 Å.). Among the various models of pumps, we gave preference to the lower total head type, for which the manufacturer specifies the maximum available total head in 5.0 bars.

The photovoltaic panel, supplied by the same company, was produced by HELIOS TECHNOLOGY; it has a surface  $S$  of 2.8 m<sup>2</sup> and was mounted, on the supplier's instructions, with its surface directed south (azimuth = 180°) and inclination  $\beta$  directed to the horizontal plane (in other terms,  $\beta$  is the angle between the normal line to the panel surface and the vertical line of the site) equal to the latitude  $\varphi$  of Viterbo (42°24').

Panel performances were recorded by means of the followings tools, all having a current exit from 4 to 20 mA for connection to the datalogger (see below) used for data management and memorization:

- (i) 2 silicon pyranometers: the first one in a horizontal plane for measuring global solar radiation  $R_h$  on the horizontal plane and the second one, lined up with the panel, for measuring global radiation  $R_\beta$  on the panel itself; the radiations measured were those with wavelengths between 0.3 and 2  $\mu\text{m}$ ;
- (ii) 2 platinum thermometers: the first one for measuring standard atmosphere temperature (therefore placed, according to the law, inside a special ventilated protection) and the second one for measuring panel temperature, and therefore glued to panel's back side;
- (iii) 1 voltmeter and 1 ammeter, both with a precision of 0.1% for measuring, respectively, current voltage (up to 100 V) and intensity (up to 10 A) that, on leaving the panel, feed the pump.

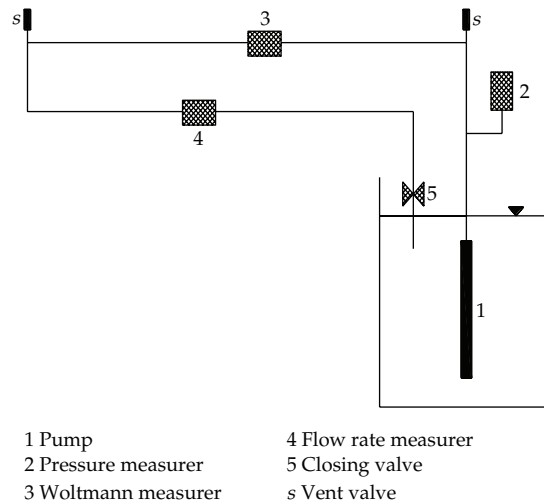


Figure 1: Hydraulic layout.

The hydraulic scheme is shown in Figure 1. The pump was connected to a plastic pipe (PEAD,  $\Phi 25$  mm; PFA 16 bars) that started from a plastic tank and then returned to the same tank; the following tools, all with a current exit from 4 to 20 mA, were inserted on the pipe for the connection to the datalogger:

- (i) 1 GEMS piezoelectric pressure transducer, with  $\pm 0.25\%$  precision, set immediately after the pump, to measure pressures up to 10 bars (operating temperatures  $-25/+85^\circ\text{C}$ );
- (ii) 1 electromagnetic flow measurer (operating temperatures  $-20 +150^\circ\text{C}$ , PN 40 bars), equipped with a signal converter (accuracy 0.5%), for connection to the datalogger; it allowed the measurement of the instant flow rates and even total volumes.

A “Woltmann” type volumetric measurer, for checking the data recorded with the electromagnetic flow measurer described above, completed the equipment.

The experimental data, recorded by the datalogger, were transmitted to our department by GSM modem. The datalogger used had 12 analogical and 2 digital channels and the capability of memorizing up to 62,000 data. It was set in a closed container with an emergency battery system and the equipment necessary to transfer the data. The datalogger, pyranometers, thermometers, voltmeter, and ammeter alimentations were fed by a small 20 W photovoltaic panel.

Measurements were recorded by the instruments every 5 seconds and then averaged over a time arc of 2 minutes for a variable daily duration dependant on the insolation hours of the period considered, that is, (in our tests) 12 hours (from 6.00 am to 6.00 pm) for the winter months and 16 hours (from 5.00 am to 9.00 pm) for the others.

The tests carried out can be divided into two series:

- (i) in the first series, tests were conducted by modifying—within the total head limits foreseen by the manufacturer—the relationships between flow rate  $Q$  and total head  $H$  that characterized the hydraulic circuit. This was achieved by manually varying the opening degree of the closing valve, as shown in the scheme of Figure 1, after

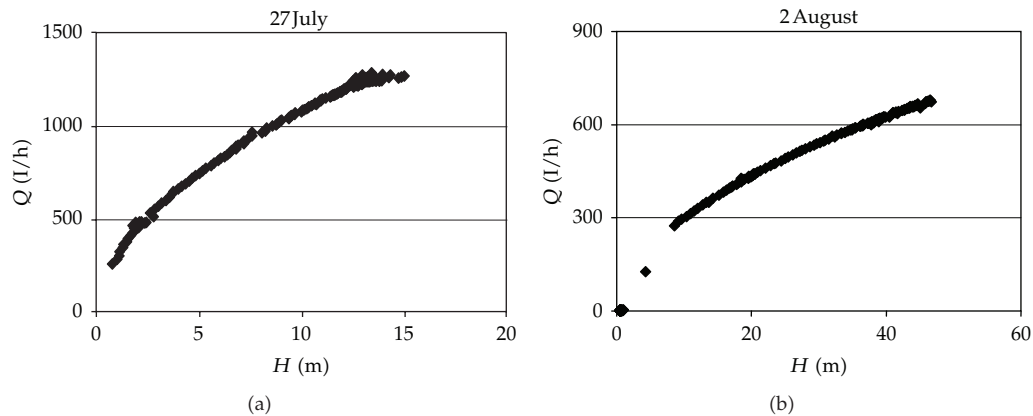


Figure 2: Daily  $H$ - $Q$  relationships.

sunset when the pump was at rest. For every day, therefore, we have a unique relationship between among  $Q$  and  $H$ ; some examples are in Figure 2;

- (ii) the second series was obtained by modifying the hydraulic scheme with the insertion of a sustaining valve into the pipe that was able to assure a constant total head—fixed by the operator—at the pump exit although the flow rate was variable. This change was implemented for a double purpose to test the reliability of the system under conditions of operation similar to real ones, to avoid the introduction—as in the first test series—of an averaged value of the total head into the formulas that concern the daily performances evaluation.

In this work we refer mostly to this second series of tests. The results obtained with the first series of tests that have been the subject of a previous publication [15] will be briefly summarized in the following section.

## 2.2. First Tests Results and Data Processing

As a premise, it should be noted that the performances of these types of pumps are influenced negatively by the presence of cloudiness, especially if intermittent. That is because the pump is forced to continuously “stop and go” with consequent dispersion of the experimental data and, what is more important, with consequent diminution of efficiency, given the system’s response time, both electric (condensers) and mechanic.

This is clearly visible in Figure 3 where two diagrams are shown: one (June, 20th) relative to a cloudless day, the other (June, 29th) relative to a cloudy day. The following can be seen in every diagram: in abscissas, time and minutes of the measurement (hhmm); in ordinates, the values of the radiation  $R_\beta$  ( $W\ m^{-2}$ ) incident on the panel plane and of the flow rate  $Q$  (L/h).

The results obtained with the first series of test will be synthesized below.

As usual, the panel/pump system’s efficiency is defined as the ratio between useful power and absorbed power; in the latter case, to obtain this we must calculate the incident radiation that is given by  $R_\beta$  ( $W\ m^{-2}$ ) times the panel surface  $S$  ( $m^2$ ).

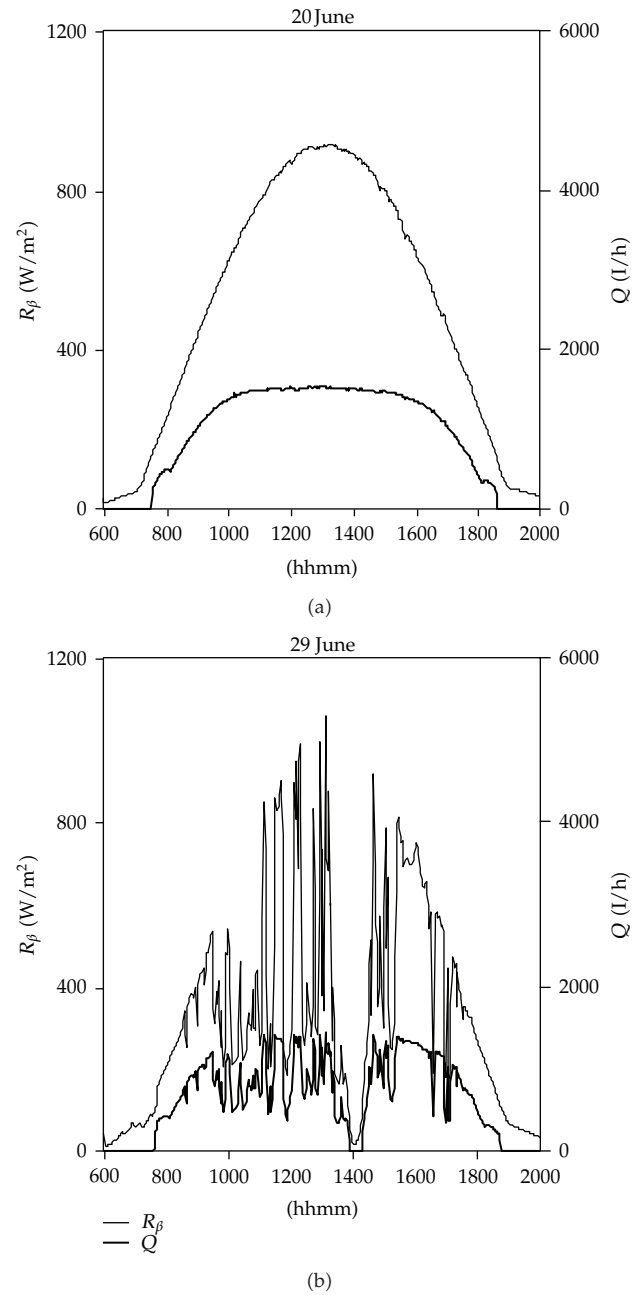


**Figure 3:** Examples of daily radiation and flow rates.

Being  $Q$  in L/h and  $S = 2 \text{ m}^2$ , in the formulas we have the theoretical expression:

$$\eta = 9.81 \left( \frac{(Q/3600)H}{R_\beta S} \right) = 9.73 \cdot 10^{-4} \frac{QH}{R_\beta}. \quad (2.1)$$

Introducing the measured values (16,000 for every considered greatness) of  $Q$ ,  $H$ , and  $R_\beta$  into (2.1), many values of the output can be calculated. The empirical relationship obtained by regression analysis of  $\eta$ ,  $H$ , and  $R_\beta$  is

$$\eta = 0.0047 \frac{H^{0,577}}{R_\beta^{0,02}} \quad (2.2)$$

with  $R^2 = 0.934$ .

Using the same data, it is also possible, always through regression, to obtain the empirical relationship that exists among  $Q$ ,  $H$ , and  $R_\beta$ :

$$Q = 4.92 \frac{R_\beta^{0,98}}{H^{0,42}} \quad (2.3)$$

with  $R^2$  equal to 0.89.

The two previous expressions were obtained independently; nevertheless, it is important, as a proof of the validity of the results obtained, that (2.3) can be obtained by replacing in (2.2) the expression of  $\eta$  as given by (2.1).

Concerning daily performances, if  $H_m$  is the daily average of total head, we calculated through summations of  $Q \cdot \Delta T$  and  $R_\beta \cdot \Delta T$  extended to the day duration ( $T$  in hours), respectively, daily pumped volumes  $w$  ( $\text{m}^3 \text{day}^{-1}$ ) and global energy  $E_\beta$  incident daily on the panel unity area ( $\text{Wh m}^{-2} \text{day}^{-1}$ ). The analysis of regression led to the following empirical expression:

$$w = 0.0033 \frac{E_\beta^{1,27}}{H_m^{0,44}} \quad (2.4)$$

with  $R^2 = 0.976$ .

As  $H$  varies continuously during the day (Figure 2), when we try to pass from instantaneous values to daily values—as in the case of the evaluation of the daily lifted volumes  $w$ —we are forced to introduce an averaged value  $H_m$  of  $H$ , (2.4), which could arouse perplexities regarding the possibility of the practical use of the same (2.4).

Hence, as previously stated, the hydraulic circuit was modified by introducing an automatic pressure regulation valve able to assure a constant total head at the pump exit equal to that established by the operator.

Therefore, we began a second series of test whose results are shown in the following paragraph.

### **2.3. Second Tests Results and Data Processing**

This second and conclusive test series lasted from June to November 2004; the results were basically identical to those previously described since there were no substantial changes. Indeed, we modified, again with the pump at rest, the opening degree of the sustaining pressure valve which allowed the total head to be kept constant for several consecutive days. On the other hand, the solar incidental radiation changed—that is, the power input—affecting

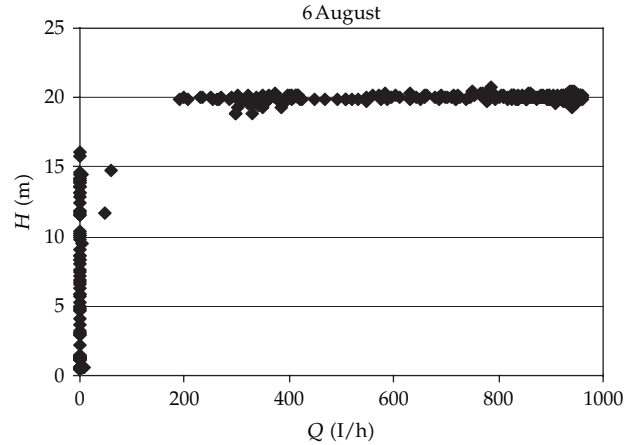


**Figure 4:** Example of  $(H; Q)$  daily data with the automatic sustaining valve.

the flow rate. Typically, the behaviour of the automatic valve was more than satisfactory, even if it required continuous surveillance. Indeed—probably due to resonance phenomena—sometimes when the pump started, the whole system became unstable; usually, but not always, the problem resolved itself after few seconds; otherwise, the test had to be ended.

The field of total heads investigated varied from a 7 to 50 meter water column.

As an example, the relationship between  $Q$  and  $H$  for August, 6th, is visible in Figure 4.

As you can see, total head remained virtually constant throughout the day, if we exclude the points on the left of the figure which are characterized by almost null discharges. The explanation of this phenomenon must be sought in two possible reasons:

- (i) the first, already present in the preliminary tests, requires that there is an incidental radiation threshold  $R_\beta$  greater than  $100\text{--}150\text{ W/m}^2$  for the whole system to be functioning. This is particularly evident in Figure 3, in which the lower  $Q$  curves begin later and end before of above  $R_\beta$  curves;
- (ii) the second, peculiar to this second series of test, is connected with the previously described instabilities that raise the value limit of  $R_\beta$  up to around  $200\text{--}250\text{ W m}^{-2}$ , over which the experimental data become reliable.

Regarding the elaborations that follow reference will be made only to the measurements obtained with  $R_\beta > 250\text{ W m}^{-2}$ . In doing so there was obviously some data manipulation, in particular concerning general daily evaluations, but, to our mind, this is virtually of no importance for the reasons that follow:

- (i) in the field  $R_\beta \leq 250\text{ W m}^{-2}$  values fall lower, and, therefore, there are less-significant values of  $Q$  (and of course, of  $R_\beta$ );
- (ii) in the absence of clouds, modest values of  $R_\beta$  occur only in the morning and in the evening and, therefore, for a small part of the daily time of the pump's functioning.

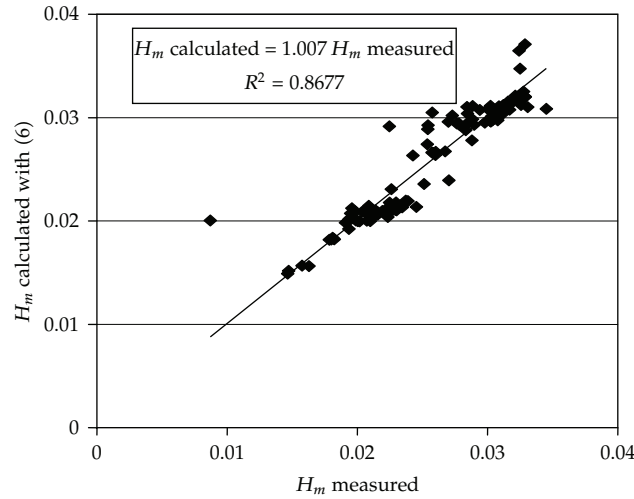


**Figure 5:** Comparison between measured efficiencies and those calculated with (2.6).

To obtain a theoretical expression for daily efficiency,  $\eta_m$  is defined as the ratio between the pump's average power output and the panel's average power input; proceeding as in (2.1), we have

$$\eta_m = 9.73 \cdot 10^{-4} \frac{Q_m H}{R_{\beta,m}}, \quad (2.5)$$

where  $Q_m$  is the average daily flow rate,  $R_{\beta,m}$  is the average daily panel radiation, and  $H$  is total head (that was kept constant during the entire day for the tests of this series).

Once calculated, though (2.5) represents the experimental values of efficiency, from the regression of  $\eta_m$  on  $H$  and  $R_{\beta,m}$  we obtained an expression analogous to (2.2) but with the exponent of  $R_{\beta,m}$  so small that it was almost equal to zero. Therefore, for practical purposes, this parameter is irrelevant, and the expression can be written as

$$\eta_m = 0.0048 \sqrt{H}. \quad (2.6)$$

In Figure 5, the values of  $\eta_m$  are reported, calculated by means of (2.6) versus the  $\eta_m$  measured values; as can be seen, (2.6) succeeds in interpreting the experimental data in a satisfactory way. Especially since it gives results that are practically identical to (2.2) which was obtained starting from instantaneous values of the parameters involved. In fact, if considering only the daily average data, we calculate the efficiency with both the formulas obtaining the relationship

$$\eta = 1.02 \eta_m \quad (2.7)$$

with  $R^2 = 0.98$ .

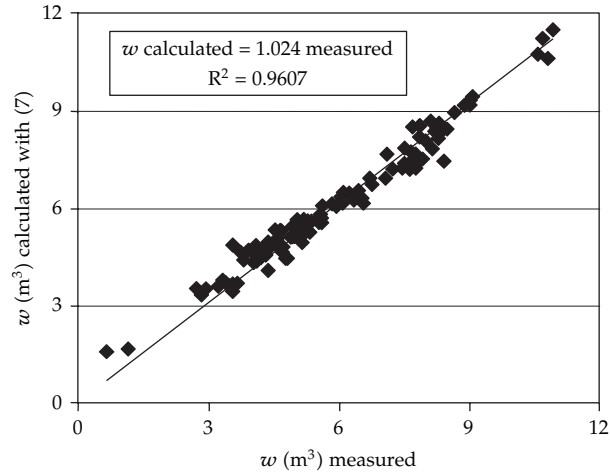


**Figure 6:** Comparison between measured volumes and those calculated with (2.8).

Considering now the daily lifted volumes,  $w$ , the relationship that best interprets the experimental data is

$$w = 0.0049 \frac{E_{\beta}}{\sqrt{H}}, \quad (2.8)$$

where, as always,  $E_{\beta}$  is the global daily energy incident on panel unit area obtained, as previously stated, from summations of  $R_{\beta} \cdot \Delta T$  (obviously, between  $E_{\beta}$  and  $R_{\beta,m}$  there is the relation:  $E_{\beta} = T \cdot R_{\beta,m}$ ) values extended to  $T$ .

In Figure 6, that has no need of any comments, the  $w$  values are shown calculated with (2.8) versus those measured.

Even in this case, (2.8) would have been directly derived from (2.5). In effect, replacing (2.5) with (2.6) we have

$$Q_m = 4.95 \frac{R_{\beta,m}}{\sqrt{H}} \quad (2.9)$$

from which (2.8) is immediately obtained if we multiply both the members for  $T$ —day duration by hours—and if we remember that  $w$  is in  $\text{m}^3$  while the product  $Q_m \cdot T$  is in litres.

Before proceeding further, a brief comment, throughout the whole trial period taken into account, the values of  $E_{\beta}$  ranged between  $1,500$  and  $7,500 \text{ Wh m}^{-2} \text{ day}^{-1}$ . This means that with, for example,  $H = 30 \text{ m}$ , the tested pump (that of those produced by the supplier company can be classified as of medium power) would be able to raise from  $1.5$  to  $6 \text{ m}^3 \text{ day}^{-1}$ . This performance—not exceptional if compared with traditional pumps—is mainly caused by efficiencies  $\eta_m$  of the whole panel/pump complex that, in line with those of similar installations [12], are around 2-3%. In particular, according to our measurements, this fact is mainly due to the panel and, to a lesser extent, to the electric feeding circuit that, in our tests, was able to feed the pump with electric power equal to 6-7% of the incidental solar power.

### 3. Operation Forecasts and Performances Optimization

Regarding forecasts, the problem can be posed in these terms: knowing operating characteristics of the whole panel/pump system—those of the one we tested or others of different manufacturers—assesses its performance when it is installed in locations different from where tested. In concrete, we have to estimate, the total head  $H$  being fixed, the volumes and/or the averages discharges lifted up daily or monthly or yearly (even the possibility of estimating “instantaneous” flow rates could exist. But it would be necessary to obtain hourly distribution of solar radiation  $R_\beta$ , starting from values of  $E_\beta$ , which would implicate the use of rather complex procedures to achieve an estimation that would usually be of limited practical interest). To this end, in order to use relations such as (2.8) and (2.9), the values of  $E_\beta$ , incidental energy on panel, or of  $R_{\beta,m}$ , average radiation on the same panel, must be known, being climatological parameters that are variable from day to day and from place to place.

#### 3.1. Theory

Some databases currently exist that give the values, averaged over long series of years, of global energy  $E_h$  that reaches the unit area of a horizontal surface for various places in the world. In this paper we will refer mainly to ESRA [16] commissioned by the European Commission and edited by a team of universities and organizations of our continent. The years of observation are ten in number; the countries considered are those with latitudes  $\varphi$  between  $30^\circ$  (Morocco, Tunisia, and Middle-east) and  $60^\circ$  (Baltic countries). The parameters considered are numerous (the CD-ROM that accompanies the two-volume text contains, in addition to the measured data, those derived from them (yearly and monthly averages, e.g.) that proved to be very useful to verify our elaborations.) (temperature, pressure, rainfall, etc.); among the ones that concern us are the daily values of energy  $E_h$  and of brightness index  $K_t$  that depends on the presence of clouds and that will be defined later.

In Italy, the Central Bureau of Agricultural Ecology (UCEA) operates a database commissioned by the Ministry of Agriculture that, among other things, provides daily values of  $E_h$  for thirty national locations.

In any case, if we do not use software programs to estimate  $w$  or  $Q$ , that is, in order to use (2.8) or (2.9), it is necessary to obtain the values of  $E_\beta$  or  $R_{\beta,m}$  from the  $E_h$  values. The procedure to be followed, which is quite long, is shown below and is furnished with diagrams and tips to make it easier and also to allow us to make choices that are more appropriate in relation to the optimal photovoltaic panel inclination.

In general,  $E_h$  is the sum of three components:

$$E_h = E_{h,d} + E_{h,r} + E_{h,df}, \quad (3.1)$$

where  $E_{h,d}$  is the direct radiation energy incident on a horizontal unit area with a precise incidence angle;  $E_{h,r}$  is the reflected radiation energy on the same unit area that comes from the ground and land objects;  $E_{h,df}$  is the diffuse radiation energy on the same unit area that comes reflected from the sky and clouds, after reflection and dispersion in the atmosphere.

In any case, if we are not in the presence of snowy mantles (very reflecting), generally  $E_{h,r}$  is very small compared to the other two terms; furthermore, it depends on local situations

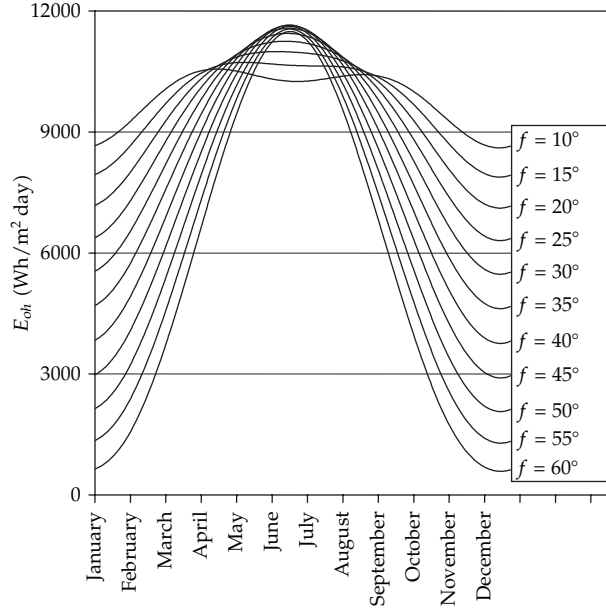


Figure 7:  $E_{oh}$  annual trend.

that are evidently not possible to take into account. Therefore in our elaborations, we make reference to the simplified relationship:

$$E_h = E_{h,d} + E_{h,df}. \quad (3.2)$$

As known, with the purpose to optimize performances, photovoltaic panels are not horizontally disposed, and thus, as previously mentioned, we are forced to deduce the  $E_\beta$  values by starting from the corresponding  $E_h$  ones. In fact, the procedure to follow is rather laborious because the two components that form  $E_h$  by (3.2) vary according to laws when  $\beta$  varies, and, therefore, we need to decompose  $E_h$  into  $E_{h,d}$  and  $E_{h,df}$ ; separately calculate the  $E_{\beta,d}$  and  $E_{\beta,df}$  values that these two parameters assume on the panel plane, and, finally, by the sum of these two, come to  $E_\beta$ .

The proportions between the two components, from which  $E_h$  is constituted by (3.2), exclusively depend on cloudiness and, therefore, on the so-called brightness coefficient:

$$K_t = \frac{E_h}{E_{oh}}, \quad (3.3)$$

where  $E_{oh}$  is the maximum global radiation available. This represents the theoretical limit of  $E_h$  in ideal atmospheric conditions and depends only on spatial latitude  $\varphi$  and on time, that is, on angle  $\delta$  (declination) which, in the moment, the sunrays form with the equatorial plane.

Following the procedure recommended by the ESRA, we calculated and reported in Figure 7 the annual trend of  $E_{oh}$  for different latitudes (one curve for each). As visible in the same figure, as  $\varphi$  decreases, passing from  $60^\circ$  in Finland to  $10^\circ$ – $15^\circ$  in African countries,

the diagram tends to flatten so that, for practical purposes, for  $\varphi < 10^\circ$ ,  $E_{oh}$  can be assumed constant and equal to  $10 \text{ kWh m}^{-2} \text{ day}^{-1}$ .

By (3.3), knowing  $E_h$  from the database and  $E_{oh}$  determined by the graphic of Figure 7, it is possible to obtain  $K_t$  and, consequently, the value of  $E_{h,df}/E_h$  by means of the following relations:

$$\frac{E_{h,df}}{E_h} = 0.14 \quad (3.4')$$

if  $K_t > 0.75$ ;

$$\frac{E_{h,df}}{E_h} = 1 - 0.273K_t + 2.45K_t^2 - 11.95K_t^3 + 9.39K_t^4 \quad (3.4'')$$

if  $K_t \leq 0.75$ .

By calculating  $E_{h,df}$  with the previous relations, by (3.2), it is possible to determine direct radiation  $E_{h,d}$ .

The next step is to transform  $E_{h,d}$  and  $E_{h,df}$  values into those of  $E_{\beta,d}$  and  $E_{\beta,df}$  that the two energies, respectively, direct and diffused, assume on the unity area and on an angle  $\beta$  with respect to the horizon. The formulas to be used, in the case of a panel oriented, as always, south for the northern and vice versa for the southern hemisphere, are

$$\frac{E_{\beta,d}}{E_{h,d}} = \frac{\cos(\varphi \mp \beta) \cos \delta \cdot \text{sen } \omega_s + \omega_s \text{sen } (\varphi \mp \beta) \text{sen } \delta}{\cos \varphi \cdot \cos \delta \cdot \text{sen } \omega_s + \omega_s \cdot \text{sen } \varphi \cdot \text{sen } \delta}, \quad (3.5')$$

$$\frac{E_{\beta,df}}{E_{h,df}} = \frac{1 + \cos \beta}{2}. \quad (3.5'')$$

Referring to (3.5'), it must be noted that a minus sign for the northern hemisphere and a plus sign for the other must be used; furthermore, in addition to the symbols already known,  $\omega_s$  appears, which is function of  $\delta$  and  $\varphi$ .

To simplify the calculations, even in this case, it was possible to develop graphs (Figure 8) that, for the values assigned to  $K_t$ , allow the daily values of  $E_\beta/E_h = (E_{\beta,d} + E_{\beta,df})/E_h$  to be estimated for several latitudes. To draw them, in this last equation we had to replace the expressions of  $E_{\beta,d}$  and of  $E_{\beta,df}$  obtained from (3.5') and (3.5'') in the numerator; use (3.2) and (3.4') and (3.4'') to write  $E_{h,d}$  and  $E_{h,df}$  as functions of  $E_h$ ; reduce the parameters expressing  $\beta$  as function of  $\varphi$ . As will be explained in the next section, this last relationship was obtained by determining mathematically the optimal value  $\beta^*$  of  $\beta$  that, for a given  $\varphi$ , is able to maximize the total energy reaching the panel. In doing so, two possible uses of the pump were taken into account: annual, which, of course, is the most usual, and seasonal, which is in connection with irrigation that lasts from May to September in our climate.

### 3.2. Best Panel Tilting

Obviously, the best panel position would be, in principle, that for which every day the sun's rays are at astronomical noon, exactly perpendicular to the panel itself, which implies a daily update of its inclination  $\beta$ . If the values of  $\beta$ , in function of the different days of the year,

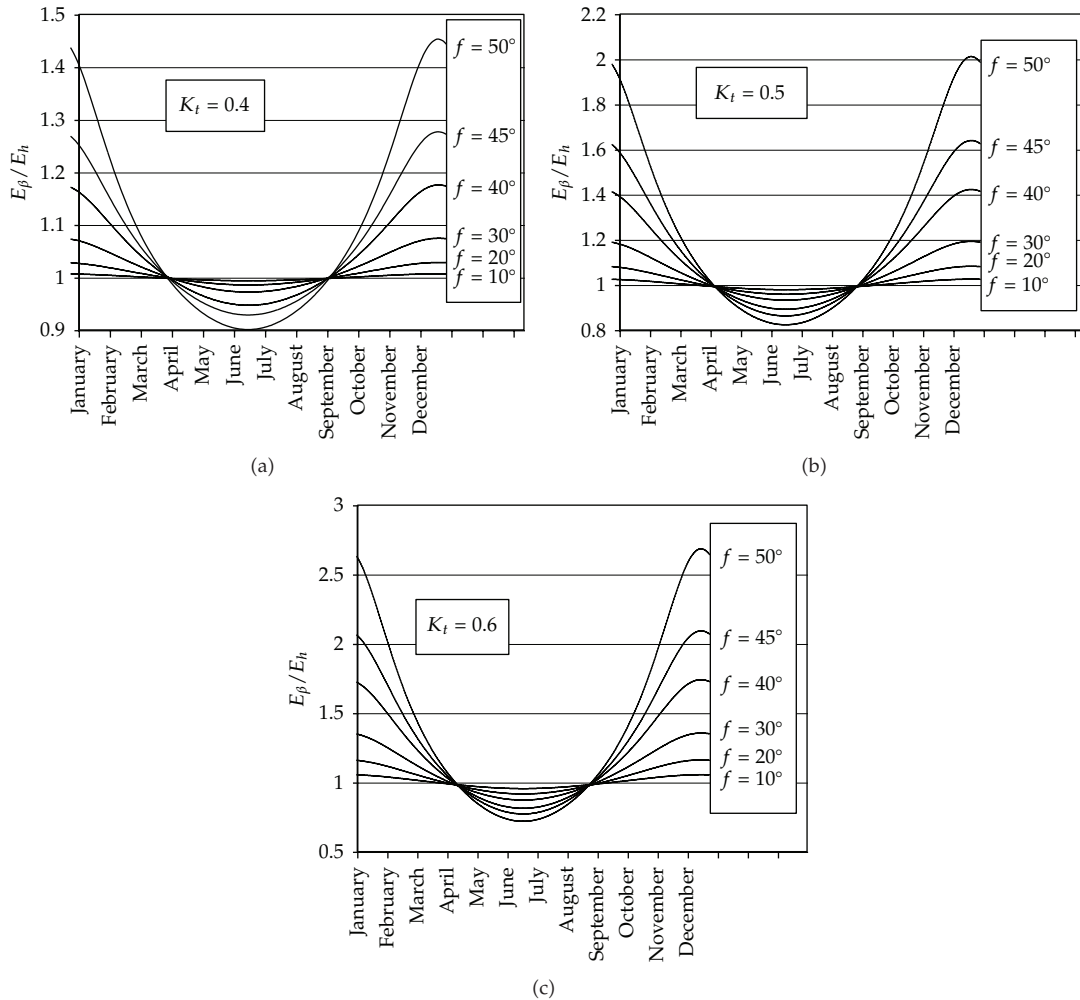


**Figure 8:** Annual trend of  $E_\beta/E_h$  ratio.

are plotted in a graph, we obtain, for a fixed latitude, a sinusoidal curve that is symmetric around its lowest point—which is the summer solstice in mid-June—with a maximum at the winter solstice in mid-December. For instance for a latitude like that of Viterbo ( $\varphi = 42^\circ$ , approximately)  $\beta$  would rise from  $17^\circ$  at the winter solstice to  $63^\circ$  at the summer solstice.

Indeed, if you do not use the solar tracking that has been mentioned in a previous note, to give the panel constant inclination, it is usual to refer to a kind of average value choosing  $\beta = \varphi$ , which implies that the condition of perpendicularity of the sunrays is exactly verified only in correspondence to the two equinoctial astronomical noons.

This practical rule is common and is very simple, yet it implies that the energy that annually reaches the panel is not the maximum possible but is lower by about 4–5% in the case of annual utilization and, on the basis of our evaluations, to a greater extent in the case of seasonal use (irrigation) of the pump.

Therefore, even if it is known that the influence of  $\beta$  is rather modest, we checked whether there are equally easy alternative rules to optimize the position of the panel in both utilization cases.

To this end, in the sum  $E_\beta = E_{\beta,d} + E_{\beta,df}$ , we replaced the expressions of  $E_{\beta,d}$  and  $E_{\beta,df}$ , obtainable by (3.5') and (3.5''), and tried to find mathematically the inclination values  $\beta_a^*$  and  $\beta_s^*$  able to maximize the integrals of  $E_\beta$  extended to the entire year or to the months from May to September, respectively.

Assuming that  $K_{t,a}$  is the annual average value of  $K_t$ , for annual use we obtained the relationship

$$\beta_a^* = 0.01 \cdot \varphi^2 + 0.4 \cdot \varphi \quad (3.6)$$

that is valid for  $0.4 < K_{t,a} < 0.6$  which, in any case, is the range where the values of  $K_{t,a}$  usually fall. In fact, from the data reported by the ESRA—and also from another database found on the web (*So.Da, Joint Research Centre*)— $K_{t,a}$  varies between 0.39–0.42 for northern countries and 0.53–0.60 for Mediterranean countries (Morocco, the Middle-East, etc.) and north Africa.

With the exception of the equatorial areas, where it is worthwhile to keep the panel horizontal or nearly so, from (3.6) we can deduce that a practical rule is *to adopt an inclination equal to  $\varphi$  minus  $6^\circ$ – $7^\circ$ , for latitudes between  $10^\circ$  and  $55^\circ$ .*

Greater advantages, of 10–12% (even of 17% for northern-Europe) and also greater corrections to the rule that would require  $\beta = \varphi$ , occur when we consider a primarily seasonal pump utilization. In effect, if we consider the countries for which we have an irrigation season covering the months from May to September—and therefore those between  $30^\circ$  of latitude of the African Mediterranean countries and  $53^\circ$  of the northern Germany—following the previously described procedure we obtained the empirical relationship:

$$\beta_s^* = 0.52 \cdot \varphi - 13.2 \quad (3.6')$$

which is valid, like (3.6), for  $0.4 \leq K_{t,s} \leq 0.6$ . As for  $K_{t,a}$ , even the usual values of  $K_{t,s}$  are within these limits. In effect, from the dataset of the ESRA, we can see that  $K_{t,s}$  is only 12–13% greater than correspondent  $K_{t,a}$ .

From (3.6'), we can deduce that in practice we can *obtain the optimal panel inclination by subtracting  $13^\circ$  from half the latitude value*. This implies very low  $\beta_s^*$  values, from  $2^\circ$  to  $14^\circ$  for latitudes  $30^\circ \leq \varphi \leq 53^\circ$ , and in particular, for Italian countries ( $37^\circ \leq \varphi \leq 46^\circ$ ), an almost horizontal panel disposition ( $\beta_s^* = 4^\circ$ – $10^\circ$ ).

One last note. In the case of a utilization primarily finalized, but not exclusively, for agricultural uses, it would be worthwhile to increase the panel inclination at the end of the irrigation season. It is a very simple operation that, with the help of an inclinometer, can be performed in few minutes and that involves an increase in energy  $E_\beta$  reaching the panel in the remaining months of the year by some percentages points (from October to April). In such a case, our elaborations, carried out with the same previously adopted procedure, show that angle  $\beta$  should be raised to a value *equal to latitude  $\varphi$  plus  $6^\circ$ – $8^\circ$*  at the end of the irrigation season.

All the aforementioned conclusions have been verified through simulations. In particular, reference has been made to the ESRA CD-ROM, for locations and for the years (from 1981 to 1990) of its database, furnishes the values of  $E_\beta$  related to the various months,

**Table 1:** Average value simulations for Tamalè.

Month	$E_h$	$R_{h,m}$	$E_\beta$	$R_{\beta,m}$	$w$	$Q_m$
Jan	5766	501	5905	513	5.28	464
Feb	5994	512	6090	520	5.45	470
Mar	5917	495	5946	497	5.32	449
Apr	5624	460	5590	457	5.00	413
May	5433	436	5357	430	4.79	389
Jun	4640	369	4556	363	4.08	328
Jul	3900	312	3838	307	3.43	277
Aug	3623	294	3591	291	3.21	263
Sep	4003	332	4003	332	3.58	300
Oct	5352	453	5411	458	4.84	414
Nov	5771	499	5897	510	5.28	461
Dec	5686	497	5840	510	5.22	461

for each  $\beta$  value assigned; this allows us to proceed by trials to the determination of the  $\beta$  value that maximizes the sum of  $E_\beta$  extended to the period May–September.

Analogous checks have been performed for (3.5') and (3.5'') even if the presence of some sites on the web which give the value of  $\beta_a^*$  must be cited. Of particular interest—see bibliography—are the European Commission Joint Research Centre and the So.Da. Project websites.

#### 4. A Case Study

As a practical application of our work and in response to a specific request from the firm, we have estimated the performances of a pump of the type that we tested in view of its installation in the Tamalè area (central Ghana;  $\varphi = 9^\circ 41'$ ) assuming the total head being  $H = 30$  m.

From the So.Da. Project website, monthly mean values of  $K_t$  were derived for the years from 1997 to 2004; they ranged from about 0.40 in the summer months to 0.63–0.65 in the period from November to February, with an average annual  $K_{t,a}$  value = 0.54.

An inclination  $\beta_a^* = 5^\circ$  was assigned to the panel according to (3.6), and in Table 1 the following are reported:

- (i) in the first and second column the monthly average values of  $E_h$  and  $R_{h,m}$ , respectively;
- (ii) in columns three and four, the corresponding values of  $E_\beta$  and  $R_{\beta,m}$ , found—for  $\varphi \approx 10^\circ$  and  $K_t \equiv K_{t,a} \approx 0.5$ —by means of the graph in Figure 8;
- (iii) in the last two columns, the monthly average values of  $w$  and  $Q$  estimated, respectively, by (2.8) and (2.9).

The same procedure is to be followed, obviously, in the case we wish to expand the estimates, going beyond the simple monthly averages. For example, with reference to the month of January, we found that, over the arc of the years of observation, the daily values of  $R_{\beta,m}$  ranged between 439 and 544  $\text{W m}^{-2}$  so, by (2.9), they led to values of average daily flow rates of between 396 and 491  $\text{L h}^{-1}$ . These  $Q_m$  would correspond to possible peaks of maximum discharge of the order of 1200–1300  $\text{L h}^{-1}$  in the hottest hours if we consider that,

on cloudless days, the hourly distribution of the solar radiation presents peaks of about 2.5–3 times the average value.

## 5. Conclusions

Thanks to an opportunity offered to us by company we became interested in photovoltaic pumps and, in particular, in the development of a “test bench” that could test the performances of a whole panel/pump complex. It is not, to our knowledge, a kind of installation that is frequently created because even if it is quite easy to find information on photovoltaic panel and pump performances produced by different companies, these data are obtained from tests that were performed on the two components separately, that is, the panel only or solely the pump, and not with the whole complex consisting of both. The results are quite misleading because the companies test their pumps inside establishments, coupling them to the electric network and not to a photovoltaic panel. The reasons for this state of things are probably many; among them there are certainly economic reasons related to both the costs of instruments and, above all, the necessarily long duration of the tests.

Our tests have clarified the operating characteristics of the panel/pump system in the sense that they allowed us to find relationships that link flow rates and daily pumped volumes to the total head and to the radiation incident on the panel. These results, however, depending on solar radiation, have only a local validity in that they are useful only for latitudes equal to those of Viterbo (42°24' North) and on a panel inclination equal to that latitude, as the general routine.

Therefore, we have developed—providing also a practical application—a simple methodology that can allow

- (1) reliable assessment of the performances of the panel/pump complex tested in Viterbo or of another complex whose operating characteristics are known and that is called upon to operate in areas of different geographic coordinates;
- (2) a more informed choice of the panel inclination that maximizes the energy incident, both in the case of annual operation of the pump or in the case of such predominantly seasonal usage as irrigation, for example.

Regarding the panel/pump system we have tested: on the one hand, it proved to be reliable during the whole long period of our tests, and, on the other, it also highlighted the limitations typical of all these kinds of devices [12] that use photovoltaic energy.

Efficiencies equal to 2–3% are certainly not thrilling; nevertheless, they are not so small that an installation of this type is not able to satisfy modest demands, both in western countries and, above all—as in the case study related to Ghana—in those third world countries where there are often no alternatives.

Of course, despite the progress in recent times, a great deal of work has to be done; just think that the main reason for this state of affairs lies in the efficiency of the panel whose value is currently about 10–12%. But this is precisely the reason that leads to hope in the future; PV technology is relatively new and, therefore, as such, is an evolving area in which further progress can be made (in 1980, the average efficiency of the panels was approximately 3%). The cost, even in terms of human lives, of traditional energy sources such as oil has reached such levels that it is reasonable to expect that, even due to the recent pushing exerted by the United States of President Obama, also the EU will develop an even stronger interest in this area which could lead to an increased flow of resources, both human and financial.

## Symbols

For all the parameters we adopted international system units, or ones accepted by it (like bar), with the exception of flow rates  $Q$  expressed, for obviously practical reasons, in liters per hour.

- $E_{0h}$ : Maximum specific energy (referred to unit area) of daily global radiation incident on the horizontal plane, expressed in  $\text{Wh m}^{-2} \text{day}^{-1}$
- $E_h$ : Specific energy (referred to unit area) of daily global radiation incident on the horizontal plane, expressed in  $\text{Wh m}^{-2} \text{day}^{-1}$
- $E_{h,d}$ : Specific energy (referred to unit area) of daily direct radiation incident on the horizontal plane, expressed in  $\text{Wh m}^{-2} \text{day}^{-1}$
- $E_{h,df}$ : Specific energy (referred to unit area) of daily diffuse radiation incident on the horizontal plane, expressed in  $\text{Wh m}^{-2} \text{day}^{-1}$
- $E_{h,r}$ : Specific energy (referred to unit area) of daily reflected radiation incident on the horizontal plane, expressed in  $\text{Wh m}^{-2} \text{day}^{-1}$
- $E_\beta$ : Specific energy (referred to unit area) of daily global radiation incident on the panel plane, expressed in  $\text{Wh m}^{-2} \text{day}^{-1}$
- $E_{\beta,d}$ : Specific energy (referred to unit area) of daily direct radiation incident on the panel plane, expressed in  $\text{Wh m}^{-2} \text{day}^{-1}$
- $E_{\beta,df}$ : Specific energy (referred to unit area) of daily diffuse radiation incident on the panel plane, expressed in  $\text{Wh m}^{-2} \text{day}^{-1}$
- $H$ : Total head pump (m)
- $H_m$ : Average daily total head pump (m)
- $K_t$ : Brightness index, adimensional
- $K_{t,a}$ : Average yearly brightness index
- $K_{t,s}$ : Average seasonal brightness index
- $Q$ : Flow rate ( $\text{L h}^{-1}$ )
- $Q_m$ : Average daily flow rate ( $\text{L h}^{-1}$ )
- $R_h$ : Global radiation incident on the horizontal plane ( $\text{W m}^{-2}$ )
- $R_{h,m}$ : Average daily global radiation incident on the horizontal plane ( $\text{W m}^{-2}$ )
- $R_\beta$ : Global radiation incident on the panel plane ( $\text{W m}^{-2}$ )
- $R_{\beta,m}$ : Average daily global radiation incident on the panel plane ( $\text{W m}^{-2}$ )
- $R^2$ : Correlation coefficient
- $S$ : Panel surface ( $\text{m}^2$ )
- $T$ : Time duration (hours)
- $w$ : Volume daily pumped, expressed in  $\text{m}^3 \text{day}^{-1}$
- $\beta$ : Panel tilt angle; that is, the angle between the normal line to the surface of the panel and the vertical line of the site ( $^\circ$ )
- $\beta^*$ : Best panel tilt angle ( $^\circ$ )
- $\beta_a^*$ : Best panel tilt angle in the case of annual use ( $^\circ$ )
- $\beta_s^*$ : Best panel tilt angle in the case of seasonal use ( $^\circ$ )
- $\delta$ : Declination angle ( $^\circ$ )
- $\eta$ : Panel/pump complex efficiency
- $\eta_m$ : Average daily panel/pump system efficiency

$\Phi$ : Latitude ( $^{\circ}$ )

$\omega_s$ : Examination site hourly angle at sunset  
or sunrise.

## Authors' Contribution

The author's contributions to this paper can be considered equal.

## References

- [1] M. Carlini and S. Castellucci, "Modelling and simulation for energy production parametric dependence in greenhouses," *Mathematical Problems in Engineering*, vol. 2010, Article ID 590943, 28 pages, 2010.
- [2] G. R. Whitfield, R. W. Bentley, and J. D. Burton, "Increasing the cost-effectiveness of small solar photovoltaic pumping systems," *Renewable Energy*, vol. 6, no. 5-6, pp. 483-486, 1995.
- [3] G. R. Whitfield, R. W. Bentley, J. D. Burton, and F. Ibanez, "Increasing the performance of small solar photovoltaic water pumping systems," in *Proceedings of the International Solar Energy Society (ISES '95)*, World Solar Congress, Harare, Zimbabwe, 1995.
- [4] I. de Villiers, "Ensuring a bright future for solar powered water pumps," *World Pumps*, no. 389, pp. 29-32, 1999.
- [5] World Bank Group, *Solar Electricity—Rural and Renewable Energy*, 2000, <http://www.worldbank.org/fpd/energy/subenergy/solar.pv.htm>.
- [6] A. Derrick, *Testing and Cost Reduction of Photovoltaic Water Pumping Systems*, Contract number: AVI-CT94-0~04, IT Power Ltd, United Kingdom, 1997.
- [7] S. S. R. Prasad, "Management of solar photovoltaic water pumping systems in India," *Solar Energy Society of India Journal*, vol. 1, pp. 13-123, 1991.
- [8] M. A. R. Sarkar, Z. Mahud, and A. M. A. Huq, "Solar P-V submersible water pumping for small scale use in Bangladesh," in *Proceedings of the Renewable Energy Technology for Rural Development Meeting (RETRUD '98)*, Kathmandu, Nepal, 1998.
- [9] G. R. Whitfield and L. J. Xiao, "A solar PV water pumping system for Chinese villages," in *Proceedings of the 2nd World Renewable Energy Conference*, 1992.
- [10] P. J. M. Mushamba, *The Photovoltaic (PVP) Water Pumping Programme in Zimbabwe*, World-wide Information system for Renewable Energy (WIRE), 1998.
- [11] R. Saravanan, G. Karthikeyan, R. Sethumadhavan, S. Renganarayanan, and A. N. Rao, "Performance evaluation of solar photovoltaic water pumping system," in *Proceedings of the International Conference on Role of Renewable Energy Technology for Rural Development*, Kathmandu, Nepal, October 1998.
- [12] N. Argaw, *Evaluation of real application experiences with PVP systems [M.S. thesis]*, Oldenburg University, Oldenburg, Germany, 2000.
- [13] J. A. Duffie and W. A. Beckman, *Solar Engineering of Thermal Processes*, John Wiley & Sons, New York, NY, USA, 1991.
- [14] D. L. Larson and S. Al Rawahy, "Development of a small solar thermal mechanical pumping system," in *Proceedings of the of American Society of Agricultural and Biological Engineers Annual Meeting*, 2002, Paper number 024184.
- [15] A. Petroselli, M. Pica, and P. Biondi, "Prove su una pompa ad energia fotovoltaica: primi risultati," *Rivista Di Ingegneria Agraria*, no. 1, pp. 83-92, 2005.
- [16] J. J. Greif and K. Scharmer, *The European Solar Radiation Atlas*, vol. 1, 2, Ecole Des Mines de Paris Les Presses, Paris, France, 2000.

## *Research Article*

# **Robust Nash Dynamic Game Strategy for User Cooperation Energy Efficiency in Wireless Cellular Networks**

**Shuhuan Wen,<sup>1</sup> Baozhu Hu,<sup>1</sup> Ahmad B. Rad,<sup>2</sup> Xinbin Li,<sup>1</sup> Huibin Lu,<sup>3,4</sup> and Jianhua Zhang<sup>5</sup>**

<sup>1</sup> Key Laboratory of Industrial Computer Control Engineering of Hebei, Qinhuangdao, Hebei 066004, China

<sup>2</sup> School of Engineering Science, Simon Fraser University, 250-13450 102 Avenue, Surrey, BC, Canada V3T 0A3

<sup>3</sup> College of Information Science and Engineering, Yanshan University, Hebei, Qinhuangdao, China

<sup>4</sup> The Key Laboratory for Special Fiber and Fiber Sensor of Hebei Province, Yanshan University, Hebei, Qinhuangdao 066004, China

<sup>5</sup> College of Computer Science and Technology, Zhejiang University of Technology, Hangzhou 310023, China

Correspondence should be addressed to Ahmad B. Rad, arad@sfu.ca

Received 2 October 2012; Accepted 25 October 2012

Academic Editor: Sheng-yong Chen

Copyright © 2012 Shuhuan Wen et al. This is an open access article distributed under the Creative Commons Attribution License, which permits unrestricted use, distribution, and reproduction in any medium, provided the original work is properly cited.

Recently, there is an emerging trend of addressing “energy efficiency” aspect of wireless communications. It has been shown that cooperating users relay each other’s information to improve data rates. The energy is limited in the wireless cellular network, but the mobile users refuse to relay. This paper presents an approach that encourages user cooperation in order to improve the energy efficiency. The game theory is an efficient method to solve such conflicts. We present a cellular framework in which two mobile users, who desire to communicate with a common base station, may cooperate via decode-and-forward relaying. In the case of imperfect information assumption, cooperative Nash dynamic game is used between the two users’ cooperation to tackle the decision making problems: whether to cooperate and how to cooperate in wireless networks. The scheme based on “cooperative game theory” can achieve general pareto-optimal performance for cooperative games, and thus, maximize the entire system payoff while maintaining fairness.

## **1. Introduction**

The continuously growing demand for ubiquitous wireless access leads to the rapid development of the wireless cellular networks during the last decade. Such tremendous growth in wireless industry has made it become one of the leading sources of the world energy consumption, and it is expected to grow dramatically in the future. The electricity

bill has become a significant portion of the operational expenditure of operators [1]. Rapidly rising energy costs and increasingly rigid environmental standards have led to an emerging trend of addressing “energy efficiency” aspect of wireless communication technologies.

In a typical wireless cellular network, user cooperation can increase the users’ data rates [2–5]. It has been shown that cooperating users relay each other’s information to improve the data rates [6]. One user’s rate increases only when another user expends relay energy on its behalf. The energy is limited in the wireless cellular network but mobile users refuse to relay, which renders user cooperation (ostensibly) unappealing. But it is very important that user cooperation is advantageous from the perspective of energy efficiency. We need an approach that encourages user cooperation in order to improve their energy efficiency. The game theory is an efficient method to solve such conflicting problems [7]. It was introduced by von Neumann and Morgenstern [8]. In [9], a cooperative Nash game is used between the two users’ cooperation to improve the bits-per-energy efficiency, but it assumed global channel state information, which is often difficult to obtain in practice. Each player is given a utility function (the reward or penalty it receives) of its own strategy and the strategies are played by all the other players (or a subset of them). In the general approach, the game and the strategies are discrete, and therefore, matrices with strategies and payoffs (the rewards or penalties) may be assembled. The players should make decision when each player has not a small number of strategies. To tackle the decision-making problems on whether to cooperate and how to cooperate in wireless networks, a differential game was introduced by Isaacs [10]. Many research works based on game theory have been published [11]. Cooperative games hold out the promise of socially optimal and group efficient solutions to problems involving strategic actions. Formulation of the optimal player’s behavior is a fundamental element in this theory. The schemes based on “cooperative game theory” can achieve the general pareto-optimal performance for cooperative games and, thus, maximize the entire system payoff while maintaining fairness [12].

Generally, when solving a game theoretically, one also assumes that one agent (or player) has access to the states of the other players involved in the game at all times as well as their cost functions [13, 14]. This is called the perfect information assumption. In fact, it is impossible to realize that each player knows the decision making of all the others. Little attention has been paid to how a player may learn to play the game. So in this paper, we adopt dynamic game, which investigates how decision making takes place over time [15]. Robust Nash Equilibria is derived based on the Robust Maximum Principle [16]. This extension of the traditional Maximum Principle [17], allows us to deal with systems that can be interpreted, to be presented as a family of ordinary differential equations, each of which corresponds to a different scenario or possible dynamics. But there are always uncertainties in the game. The main drawback of this last approach ignores uncertainties. Therefore, in the situation when there are any unmeasured uncertainties, another design concept must be developed.

Generally, imperfect channel state information has significant impacts on the performance of not only cellular networks, but also wireless networks. Many works also assume global channel state information, which is often difficult to obtain in practice. Moreover, since the channel state information in cellular networks is often limited, we introduce the possibility of channel prediction. We study an efficient solution, which is AR-model-based prediction method, to take the prediction for the channel information states. AR-model-based prediction method has good suitability and robustness that utilizes fast tracking of channel coefficients, which demonstrates for realistic channel conditions.

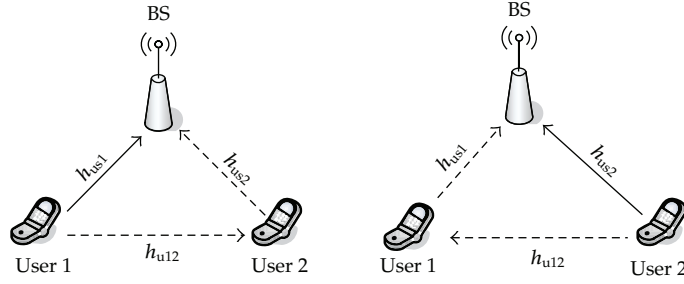


**Figure 1:** Transmission schedule. During odd time blocks, user 1 acts as source and user 2 acts as relay, and vice versa for even time blocks.

## 2. System Models

### 2.1. Transmission Model

In cellular networks, we consider that two mobile users communicate with a common base-station (BS). We assume a simple uplink scenario in Figure 1. User 1 transmits its data to the BS during the odd time blocks, while user 2 transmits its data during the even time blocks. The idle user can choose to act as a relay for the active user in order to help to increase the active users' rate. The received signals at the relay and destination then [9]

$$\begin{aligned}
 y_1 &= h_{u21}(k)x_2 + \xi_1(k) \quad (\text{even } k), \\
 y_2 &= h_{u12}(k)x_1 + \xi_2(k) \quad (\text{odd } k), \\
 y_3 &= h_{us1}(k)x_1 + h_{us2}(k)x_2 + \xi_3(k),
 \end{aligned} \tag{2.1}$$

where  $x_1, x_2$  are transmission or relay symbols, and  $\xi$  is additive white Gaussian noise.

### 2.2. Channel Prediction Model

We consider a simple uplink transmission scenario from users to the BS in the cellular networks, as depicted in Figure 1. We assume that the BSs map a set of messages onto a set of sequences, which are precoded and transmitted symbol-wise over the channel. The transmission in each single channel access at sample time slot  $k$  can be stated as

$$y(k) = H(k)x(k) + z(k), \tag{2.2}$$

where  $y(k)$  is the received signals,  $H(k)$  denotes the time-varying channel coefficient,  $x(k)$  is the symbols connected to the messages to be transmitted in channel access  $k$ , and  $z(k)$  is the additive noise at the receiver side, also assumed to be zero-mean Gaussian.

In the AR-model-based algorithm, the prediction of the channel state in time slot  $k$ , the value of channel state  $H(k)$  is given by [18]

$$\widehat{H}(k) = \sum_{j=1}^J d_j(k)H(k-j) + e(k), \tag{2.3}$$

where  $J$  is the AR-model order, and  $H(k-1)\cdots H(k-j)\cdots H(k-J)$  are  $J$  previous channel samples, and  $e(k)$  is a complex white Gaussian noise signal. The AR-model-based prediction methods are also often referred to as linear predictors (LPs). The knowledge of the identifying is needed for the computation of the AR coefficients  $d_j(k)$  in (2.3). Because the channel coefficients are unknown and slowly time-variant in practice, it has to be estimated from noise-corrupted channel observations. Efficient adaptive filtering techniques, such as recursive least squares estimate (RLSE), were used to track the changes of predictor coefficients  $d_j(k)$  in (2.3).

The prediction error, which is defined as the difference between the predicted value  $\widehat{H}(k)$  and the actual value  $H(k)$ , is employed as a performance measure [19–21]. The prediction error can be normalized with the respect to the root mean squared value (RMS) of the considered fading process [22]. The prediction error analysis of  $M$  consecutive predictions can be done by using the variance defined as follows:

$$\gamma^2(k) = \frac{1}{M} \sum_{m=0}^{M-1} \left( H(k-m) - \widehat{H}(k-m) \right)^2. \quad (2.4)$$

In this paper, we use RLSE due to its superior performance in accommodating time-varying system conditions, which results in an efficient method for time-varying radio channels [23].

### 2.3. Bits-per-Energy Efficiency

One common method to measure energy efficiency is to use bits per Joule [24]. Strict maximization of energy efficiency, then, is not typically useful in practice when users have target rates to meet or delay constraints to satisfy [9]. However, the channel prediction in Section 3 is used to sidestep this obstacle. The total energy expenditure is proportional to the sum of the power allocations in the previous time blocks. So, the total bits-per-energy efficiency for each user is proportional to [9]

$$e_i(p_{r1}, p_{r2}) = \frac{E_h[r_i(p_{rj}(h))]}{1 + E_h[p_{ri}(h)]}, \quad (2.5)$$

for  $i \neq j$ , where  $p_{r1}$ ,  $p_{r2}$  are the power allocated by user1 and user2 while acting as the relay.  $r_i(\cdot)$  is the achievable rate, whose expression follows [9]

$$r_i(k) = \min\{\max\{I(x_i; x_j | x_j), I(x_i; x_3)\}, I(x_i, x_j; y_3)\}, \quad (2.6)$$

where  $x_i, y_i$  are jointly Gaussian, and the mutual information terms depend on the channel gains and the source and relay powers at time slot  $k$ .

## 3. Theoretic Formulation of Discrete Dynamic Game

A game consists of three objects: a set of players, a set of strategies which those players can enact, and a set of cost functions denoting the payoff each player derives from the strategies

enacted [9]. We assume our scenario as a game in which each mobile user is a player whose strategies are the relay power allocations  $p_{ri}$  and whose cost functions are the bits-per-energy efficiencies  $e_i p_{ri}$ .

### 3.1. Noncooperative Games

In order to compare the energy efficiency of noncooperative and cooperative users, the energy efficiency expression of noncooperative users is given. The classic solution concept for a noncooperative game is the Nash equilibrium (NE). The payoff of every noncooperative user is [9]

$$e_i^{\text{NE}} = E_h \left[ \log_2 \left( 1 + |h_{i3}|^2 \right) \right], \quad (3.1)$$

where  $E(\cdot)$  is the expectation.

The noncooperative game is a strategy that the selfish users simply select their strategies and never interact again. They improve their payoff by lowering their relay power. While in fact, users can obtain higher payoff by cooperation.

### 3.2. Nash Equilibrium Dynamic Game

Recently, the game theory of user cooperation has been studied in the literature. However neither of these works considers the energy efficiency. In [9], the paper studies energy efficiency of user cooperation, but it ignores the process of decision making. The results of these works assume perfect situation in which each player knows the decision making of all the others. In fact, it is impossible to implement.

In this paper we consider the linear discrete-time dynamic game model with uncertainties:

$$x(k+1) = Ax(k) + bu(k) + Dg(x, k), \quad (3.2)$$

where  $A, B$  are the known game constant matrices,  $x(k)$  is the state vector of the game,  $u(k)$  is the control strategies of each user,  $D$  is the constant matrix, and  $g(x, k)$  is the unknown noises or disturbances part. Each vector belongs to an appropriate dimensional Euclidean space.

If the game under study is (as it is for this paper) between only two players, the system dynamics (3.2) may be written as

$$x_i(k+1) = Ax_i(k) + bu_i(k) + Dg_i(x, k), \quad (3.3)$$

where  $i = 1, 2$  denotes the two users.

With this linear discrete-time system, we associate a quadratic performance index

$$\begin{aligned} J(u_1(k), u_2(k)) &= \sum_{k=1}^K \left\{ |x_i(k+1)|_{Q(k+1)}^2 + |u_i(k)|^2 \right\} \\ &= \|x_i\|_Q^2 + \|u_i\|^2, \end{aligned} \quad (3.4)$$

where  $Q(k+1) \geq 0$ ,  $|\cdot|_Q$  denotes an appropriate Euclidean (semi-) norm weighted by a nonnegative definite matrix  $Q$ ,  $\|\cdot\|$  denotes a corresponding  $l^2$  norm.

Then we give the Nash Equilibrium strategies of the two users. The payoff, now represented as  $L(u_1(k), u_2(k))$ , is given in the form

$$L(u_1(k), u_2(k)) = J(u_1(k), u_2(k)) + |x_i|_Q^2. \quad (3.5)$$

In this case it is also assumed that the users who use strategy  $u_1(k), u_2(k)$  want to maximize the payoff  $L(\cdot)$ . Therefore, the objective of the game is to find a saddle-point solution  $u_1^*(k), u_2^*(k)$  to satisfy the Nash-equilibrium condition

$$L(u_1^*(k), u_2(k)) \leq L(u_1^*(k), u_2^*(k)) \leq L(u_1(k), u_2^*(k)), \quad (3.6)$$

$u_1^*(k), u_2^*(k)$  is known as a feedback saddle-point solution, then  $u_1^*(k), u_2^*(k)$  is characterized as the point on the Pareto boundary that satisfies (3.6), symmetry between players, and independence to irrelevant alternatives. The control strategies of the users in a cooperative game are their relay power allocations and the cost functions are their bits-per-energy efficiencies.

#### 4. Simulation Results and Discussions

In this section, we use computer simulations to evaluate the performance of the proposed scheme and the influence of uncertainties. The results of numerical experiments are shown to see the payoff of the cooperation users. The energy efficiency of every user increases when the proposed scheme is used. We compare the proposed scheme with the noncooperation game scheme, which is a single-stage noncooperative game. The solution to a game depends on the particular game theoretic frame work employed. We consider a simple case that the selfish players select strategies in order to maximize individual energy efficiency in spite of the payoff of other players. The players never interact again. Then another user cooperation scheme which does not use dynamic game and assumes perfect channel state information [9] is compared with the proposed scheme.

Figure 2 shows the coefficients in the AR-model-based channel prediction algorithm of one wireless channel,  $d_1$  and  $d_2$ , which are defined in (2.3). As we can see from the figure, the AR-model coefficients vary with simulation time due to the time-varying wireless channel. The recursive least square estimate (RLSE) algorithm presented in Section 3 can accommodate the time-varying wireless channel conditions to make accurate channel predictions.

The performance of the channel prediction algorithm can be measured by using the error variance, which is defined in (2.4). Figure 3 shows the error variance in the AR-model-based channel prediction algorithm. In Figure 3, we can observe that, when the simulation time increases, the error variance decreases, meaning that the channel prediction becomes more accurate. In addition, we can see that the variance drops below 1 quickly in the simulation, which means that the prediction algorithm is sufficiently accurate.

Because there is time-varying external disturbance and uncertainties in the cellular network, the cooperation of users should consider the effect of them for energy efficiency. It is assumed that the external disturbance is given by  $w_d(k+1) = 0.95w_d(k)$  with  $w_d(0) = 1$ .

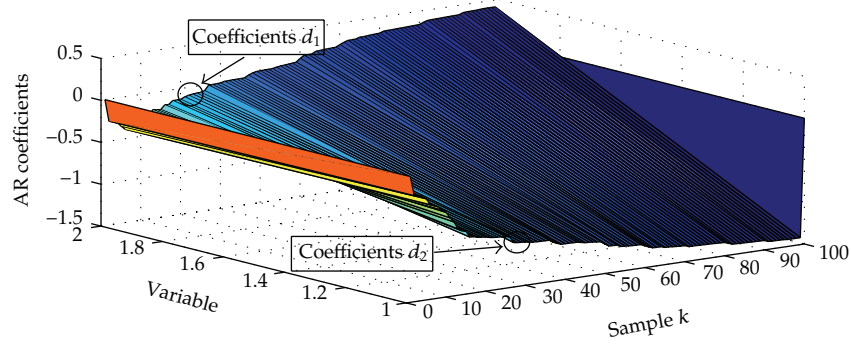


Figure 2: The coefficients in the AR-model-based channel prediction algorithm.

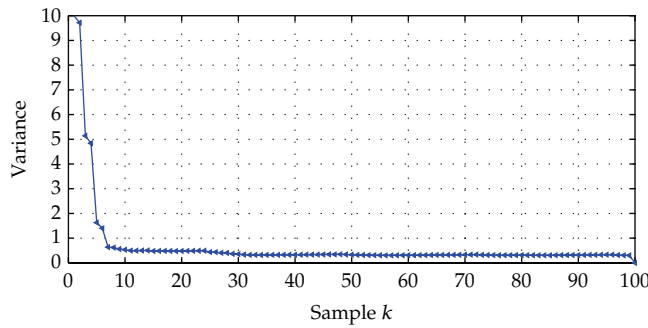


Figure 3: The error variance in the AR-model-based channel prediction algorithm.

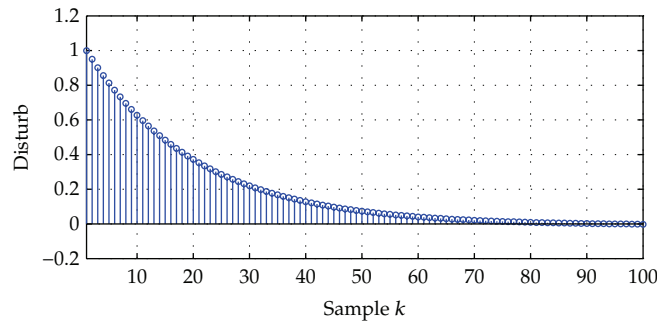


Figure 4: Time-varying external disturbance.

Figure 4 shows the plot of the time-varying external disturbance. It is also assumed that there is an unknown uncertainty which is time-varying in the range  $|v_{un}(k)| \leq 1$ . The time-varying uncertainty  $v_{un}(k)$  is randomly generated as shown in Figure 5.

Figure 6 depicts the variation bit per Joule efficiency of the user cooperation in the uplink scenario. The result indicates that the cooperation of the users is helpful to increase the energy efficiency. We set the expected interuser gains to set user 2's expected gain  $E\|h_{23}^2\| = 10$  dB and make  $E\|h_{13}^2\|$  dB vary between  $-5$  dB and  $20$  dB in order to compare with [9]. This range allows us to see the cooperation performance of the proposed scheme when users' channel conditions are asymmetric, which gives us a reasonable result. Figure 6 shows that

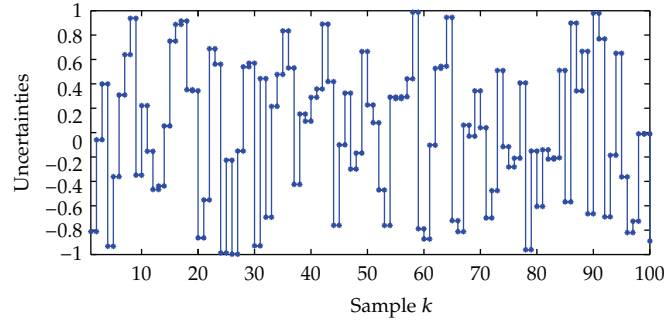


Figure 5: Time-varying external disturbance.

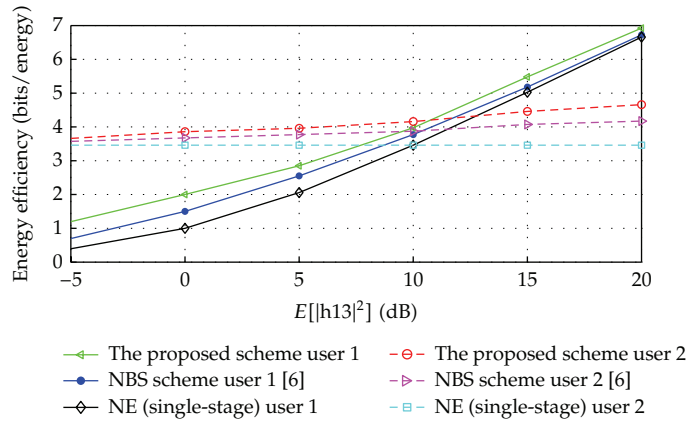


Figure 6: The energy efficiency of different schemes.

each user's bit per Joule efficiency by using the proposed scheme is the largest, and the [9] is the second. The bit per Joule efficiency of the users without cooperation is the smallest. This shows it can benefit from the cooperation for selfish users by using the proposed scheme.

## 5. Conclusion

In wireless cellular networks, it is very important to increase the energy efficiency of the radio access networks to meet the challenges raised by the high demands of traffic and energy consumption. In this paper, we proposed a dynamic game based on the control-theoretical approach to study the energy efficiency issues in cooperative wireless cellular networks with cellular communications. In addition, we use a predictor in our control-theoretical approach to supervise the data of imperfect channel state information. Simulation results have been presented to show the effectiveness of the proposed scheme.

Mutiuser cooperation case is considered in the future work. We also consider heterogeneous cellular networks with femtocells, which is another promising technique to increase the indoor network coverage and capacity for the growing demands of cellular services, and it has been integrated in current and future radio access networks. In addition, intercell interference will be considered in our control-theoretical framework.

## Acknowledgment

This paper is supported by National Natural Science Foundation of China under Grant (Contract no. 61172095).

## References

- [1] E. Oh, B. Krishnamachari, X. Liu, and Z. Niu, "Toward dynamic energy-efficient operation of cellular network infrastructure," *IEEE Communications Magazine*, vol. 49, no. 6, pp. 56–61, 2011.
- [2] M. Li, W. Zhao, and S. Y. Chen, "MBM-based scalings of traffic propagated in internet," *Mathematical Problems in Engineering*, vol. 2011, Article ID 389803, 21 pages, 2011.
- [3] S. Chen, W. Huang, C. Cattani, and G. Altieri, "Traffic dynamics on complex networks: a survey," *Mathematical Problems in Engineering*, vol. 2012, Article ID 732698, 23 pages, 2012.
- [4] W. Huang and S. Y. Chen, "Epidemic metapopulation model with traffic routing in scale-free networks," *Journal of Statistical Mechanics: Theory and Experiment*, vol. 2011, no. 12, Article ID P12004, 19 pages, 2011.
- [5] A. Sendonaris, E. Erkip, and B. Aazhang, "User cooperation diversity, part i: system description," *IEEE Transactions on Communications*, vol. 51, no. 11, pp. 1927–1938, 2003.
- [6] Z. Zhang, J. Shi, H-H. Chen, M. Guizani, and P. Qiu, "A cooperation strategy based on nash bargaining solution in cooperative relay networks," *IEEE Transactions on Vehicular Technology*, vol. 57, no. 4, pp. 2570–2577, 2008.
- [7] M. R. B. Myerson, *Game Theory: Analysis of Conflict*, Harvard University Press, Cambridge, Mass, USA, 1991.
- [8] J. von Neumann and O. Morgenstern, *Theory of Games and Economic Behavior*, Princeton University Press, Princeton, NJ, USA, 1947.
- [9] M. Nokleby and B. Aazhang, "User cooperation for energy-efficient cellular communications," in *Proceedings of the IEEE International Conference on Communications (ICC '10)*, May 2010.
- [10] R. Isaacs, *Differential Games: A Mathematical Theory with Applications to Warfare and Pursuit*, Wiley, New York, NY, USA, 1965.
- [11] N. Shastry and R. S. Adve, "Stimulating cooperative diversity in wireless ad hoc networks through pricing," in *Proceedings of the IEEE International Conference on Communications (ICC '06)*, pp. 3747–3752, July 2006.
- [12] Z. Han, T. Himsoon, W. P. Siriwongpairat, and K. J. R. Liu, "Energy-efficient cooperative transmission over multiuser OFDM networks: who helps whom and how to cooperate," in *Proceedings of the IEEE Wireless Communications and Networking Conference (WCNC '05)*, pp. 1030–1035, March 2005.
- [13] H. Shi, W. Wang, N. M. Kwok, and S. Y. Chen, "Game theory for wireless sensor networks: a survey," *Sensors*, vol. 12, no. 7, pp. 9055–9097, 2012.
- [14] C. Cattani, S. Chen, and G. Aldashev, "Information and modeling in complexity," *Mathematical Problems in Engineering*, vol. 2012, Article ID 868413, 4 pages, 2012.
- [15] D. W. K. Yeung and L. A. Petrosyan, *Cooperative Stochastic Differential Games*, Springer, New York, NY, USA, 2006.
- [16] A. S. Poznyak, T. E. Duncan, B. Pasik-Duncan, and V. G. Boltyanski, "Robust maximum principle for multi-model LQ-problem," *International Journal of Control*, vol. 75, no. 15, pp. 1170–1177, 2002.
- [17] L. S. Pontryagin, V. G. Boltyanskii, R. V. Gamkrelidze, and E. F. Mishchenko, *The Mathematical Theory of Optimal Processes*, Interscience Publishers, New York, NY, USA, 1962.
- [18] A. Duel-Hallen, "Fading channel prediction for mobile radio adaptive transmission systems," *Proceedings of the IEEE*, vol. 95, no. 12, pp. 2299–2313, 2007.
- [19] M. Li, S. C. Lim, and S. Chen, "Exact solution of impulse response to a class of fractional oscillators and its stability," *Mathematical Problems in Engineering*, vol. 2011, Article ID 657839, 9 pages, 2011.
- [20] S. Chen, Y. Wang, and C. Cattani, "Key issues in modeling of complex 3D structures from video sequences," *Mathematical Problems in Engineering*, vol. 2012, Article ID 856523, 17 pages, 2012.
- [21] X.-H. Yang, B. Wang, S.-Y. Chen, and W.-L. Wang, "Epidemic dynamics behavior in some bus transport networks: statistical mechanics and its applications," *Physica A*, vol. 391, no. 3, pp. 917–924, 2012.
- [22] J. Hwang, J. Winters, and F. Golnaraghi, "Sinusoidal modeling and prediction of fast fading processes," in *Proceedings of the IEEE Globecom '98*, November 1998.

- [23] S. Haykin, *Adaptive Filter Theory*, Prentice-Hall, Englewood Cliffs, NJ, USA, 1999.
- [24] G. Miao, N. Himayat, and G. Y. Li, "Energy-efficient link adaptation in frequency-selective channels," *IEEE Transactions on Communications*, vol. 58, no. 2, pp. 545–554, 2010.

*Research Article*

# **Energy Characterization and Gasification of Biomass Derived by Hazelnut Cultivation: Analysis of Produced Syngas by Gas Chromatography**

**D. Monarca,<sup>1</sup> A. Colantoni,<sup>1</sup> M. Cecchini,<sup>1</sup> L. Longo,<sup>1</sup>  
L. Vecchione,<sup>1</sup> M. Carlini,<sup>1</sup> and A. Manzo<sup>2</sup>**

<sup>1</sup> *Department of Agriculture, Forest, Nature and Energy (DAFNE), University of Tuscia,  
Via S. Camillo de Lellis snc, 01100 Viterbo, Italy*

<sup>2</sup> *Ministry of Agriculture, Food and Forestry, Via XX Settembre 20, 00100 Rome, Italy*

Correspondence should be addressed to A. Colantoni, colantoni@unitus.it

Received 22 August 2012; Accepted 21 September 2012

Academic Editor: Nataliya Krasnogorskaya

Copyright © 2012 D. Monarca et al. This is an open access article distributed under the Creative Commons Attribution License, which permits unrestricted use, distribution, and reproduction in any medium, provided the original work is properly cited.

Modern agriculture is an extremely energy intensive process. However, high agricultural productivities and the growth of green revolution has been possible only by large amount of energy inputs, especially those coming from fossil fuels. These energy resources have not been able to provide an economically viable solution for agricultural applications. Biomass energy-based systems had been extensively used for transportation and on farm systems during World War II: the most common and reliable solution was wood or biomass gasification. The latter means incomplete combustion of biomass resulting in production of combustible gases which mostly consist of carbon monoxide (CO), hydrogen (H<sub>2</sub>) and traces of methane (CH<sub>4</sub>). This mixture is called syngas, which can be successfully used to run internal combustion engines (both compression and spark ignition) or as substitute for furnace oil in direct heat applications. The aim of the present paper is to help the experimentation of innovative plants for electric power production using agro-forest biomass derived by hazelnut cultivations. An additional purpose is to point out a connection among the chemical and physical properties of the outgoing syngas by biomass characterization and gas-chromatography analysis.

## **1. Introduction**

The global environment conditions are badly influenced by the exploitation and the extreme utilization of typical energetic sources, which is mainly due to industrialized countries and exponential population growth. Industrialization leads to atmospheric emissions of pollutants and greenhouse gases, whose carbon dioxide (CO<sub>2</sub>) is considered as the most

important. Even if it is not toxic, CO<sub>2</sub> is extremely dangerous because it may cause global overheating and climate change. This work is based on the idea of energetically independent agroforest farms, able to generate electric power using renewable sources as agroforest biomass from agricultural discards [1, 2].

If we consider this idea applied on a large scale, we could create an agroenergetic ecodistrict. This concept would have potential benefits for environment, such as reduction of CO<sub>2</sub> emissions, and also for farmers, because they could sell the electric power and receive green certificates. The aim of the present work is to help the experimentation of innovative plants for electric power production using agroforest biomass. An additional purpose is to point out a connection among the chemical and physical properties of the outgoing syngas by biomass characterization and gas chromatography analysis.

## 2. Material and Methods

The tests were carried out using hazelnut (*Corylus avellana* L.) shells by farms located in the area of Lake of Vico, in the province of Viterbo (Latium region). The gasification reactor is a small plant: its capacity reaches 30 kWe and 60 kWt which are the appropriate values for small local farms. The used biomass and the outgoing syngas were analyzed in laboratory in order to assess the potential energy of the residual biomass in relation to that of the produced syngas. This is to evaluate the effectiveness of the gasification process. The purpose of this study is to obtain a gas which can be successfully used in internal combustion engines in cogeneration. According to that, specific cleaning systems are located at the end of the gasification process in order to make it suitable for the oxidation step in internal combustion engines. Moreover, they avoid any possible damage to the mechanical parts of the gasifier and reduce harmful emissions for environment and human beings. It should be underlined that the most significant problems in the usage of syngas are associated with the presence of particulate, sulfur compounds, and nitrogen [3, 4].

### 2.1. Gasification Processes

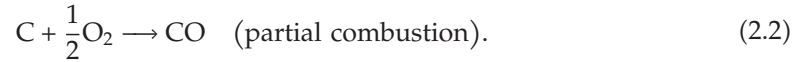
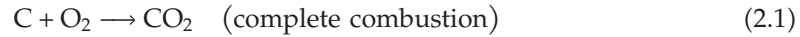
The "gasification" is the use of heat to transform solid biomass or other carbonaceous solids into a synthetic "natural gas like" flammable fuel. Gasification can convert nearly any dry organic matter into a clean burning, carbon neutral fuel that can replace fossil fuels in many cases. Furthermore, gasification will transform common "waste" into a flexible gaseous fuel which can be successfully used to run internal combustion engine, cooking stove, furnace, or flamethrower. This does not depend on the initial biomass (wood chips, walnut shells, construction debris, or agricultural waste).

Thus, gasification is a partial combustion of solid fuel (biomass): temperatures close to 1000°C are required. The reactor is called "gasifier." The combustion products, coming from complete combustion of biomass, generally contain nitrose, water vapor, carbon dioxide, and surplus of oxygen. However, when gasification is characterized by solid fuel surplus (incomplete combustion), the products of combustion are combustible gases, such as carbon monoxide (CO), hydrogen (H<sub>2</sub>), traces of methane and unhelpful products (i.e., tar and char).

The main reactions take place in combustion and reduction zone [5, 6].

*Combustion Zone (Exothermic Reactions)*

The combustion products of solid fuel are usually carbon, hydrogen, and oxygen. When complete combustion occurs, carbon dioxide is obtained from hydrogen, usually as steam. The main reactions, therefore, are

*Reaction Zone*

The products of partial combustion (water, carbon monoxide, and uncombusted partially cracked pyrolysis) now pass through a red-hot charcoal bed where the following reduction reactions take place:



As residence time of biomass, temperature, and pressure of the process increase, higher fuel conversion occurs. Temperature rises leading to more endothermic reactions and, as a consequence, CO and H<sub>2</sub>. High pressure values help those reactions aimed at reducing the number of moles and at producing CO<sub>2</sub>, CH<sub>4</sub>, and H<sub>2</sub>O. The content of CO and H<sub>2</sub> is regulated through incoming water as shown in reaction 2.3 called "water gas shift." Humidity content influences the ratio between CO and H<sub>2</sub> and, at the same time, is the most important tool to reduce temperature [7, 8].

**2.2. The Downdraft Gasifier Prototype**

The experimental gasifier is a fixed cocurrent bed, fed with hazelnut shells (Figure 1). The developed prototype is a small sized plant. The electrical capacity is 30 kW and the thermal power reaches 60 kW. The internal structure is made of stainless steel 304.

The outline of the gasifier (Figure 2) consists of a loading hopper in which hazelnut shells are stored. The hopper (1) is connected to the gasification reactor by means of a cochlea with horizontal axis (2) which allows the biomass to enter the upper part of the reactor (4) and separates the input zone from the combustion air (5). Air enters the reactor from the opening in (3). The biomass conversion into gaseous phase, with the consequent production of ashes, takes place during the descent inside the bed. The obtained syngas comes out from



**Figure 1:** Biomass used in the process.

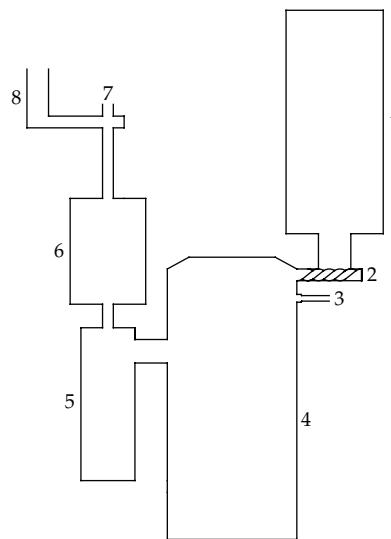


**Figure 2:** Gasification system layout.

the bottom part of the reactor. Moreover, in order to remove the coarse particulate, it passes first through a cyclone and a cooling air system (3) and then in a filter. The latter step is to clean TAR and smaller sized particles. The gas, leaving the filter, is mixed with air (7) and combusted in torch (8).

Figure 3 shows the detailed layout of the gasification reactor used for the experiments. It is interesting to note that the internal structure is characterized by a narrowing or “throat” where the highest process temperatures occur. They are aimed at TAR thermal cracking which is contained in vapor and comes from pyrolysis in the upper parts. In the part below the throat, reduction reactions occur and lead to the production of the greatest interesting molecular species:  $H_2$  and CO.

The gasification test starts with the aid of an initial pilot flame, necessary to allow the achievement of the thermal conditions required for self-maintenance of the gasification process (Figure 4).

SKC-1 L *Tedlar bags* black layered (Figure 5) have been used depending on the biomass quality to analyze the chemical and physical properties of the syngas. The latter has been



Figure 3: Reactor gasifier layout (Render).



Figure 4: Start phase of the test.

analyzed by gas chromatography in order to point out the main chemical components according to the type of biomass used during the process.

The experiment was carried out under established thermodynamic conditions, necessary for the startup and the maintenance of the gasification process (Figure 6). In more detail, temperature values were detected with the aim of maintaining the process in the suitable range for the optimal biomass conversion into synthesis gas. After adding the biomass into the reactor, the combustion process starts by entering the necessary air and using a pilot flame required for the achievement of process temperatures. Once the thermodynamic conditions—required for the self-maintenance of the thermochemical process—are reached, the test continues without the help of the pilot flame or other external heating sources but only by the introduction of hazelnut shells and combustion air. From this moment on, the sampling gas started. During the gasification test, temperatures between 900 and 1000°C are reached inside the reactor with pressure values close to 0.025 bar.

### ***2.3. Energy Characterization of Biomass: Analysis in Laboratory***

The laboratory tests were carried out at CIRDER (Energy Biomass Certification Laboratory) of the University of Tuscia in Viterbo. Sampling of hazelnut shells, coming from a hazelnut orchard in Caprarola, was carried out according to ISO 14778.



Figure 5: Tedlar bags, before the sampling.

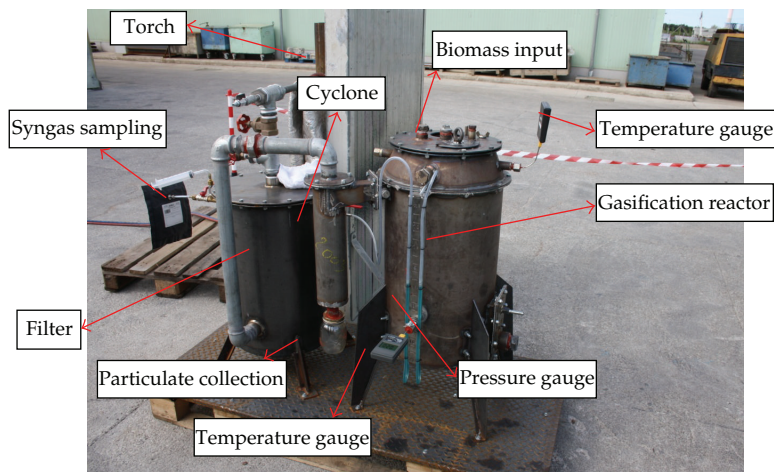


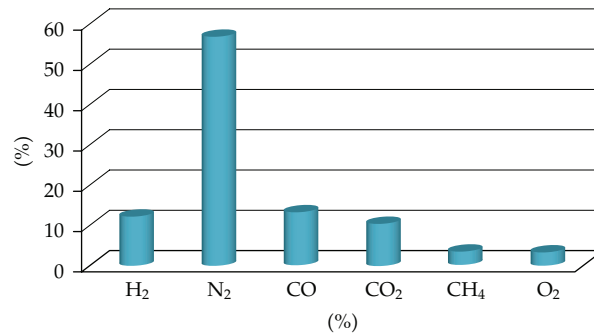
Figure 6: Gasification system.

Table 1: Characterization of hazelnut shells.

Parameter	Value	Unit of measurement
Moisture content	6.4	% on dry basis
Lower calorific value	18.83	MJ/kg on dry basis
Carbon content	51.14	% by mass
Hydrogen content	5.7	% by mass
Nitrogen content	0.42	% by mass
Ash content	1.71	% by mass

Table 2: Syngas composition.

Test number	H <sub>2</sub> [%]	N <sub>2</sub> [%]	CO [%]	CO <sub>2</sub> [%]	CH <sub>4</sub> [%]	O <sub>2</sub> [%]
1	12.00	57.00	13.00	10.00	3.17	3.09
2	11.83	56.12	12.50	9.97	3.11	2.86
3	11.78	56.53	13.00	10.00	3.12	2.82
4	11.73	56.45	12.80	9.98	3.30	2.78
5	11.81	56.43	12.98	10.2	3.24	2.74
6	11.69	56.48	12.96	10.1	3.19	2.74



**Figure 7:** Average composition of the syngas.

The preparation of biomass samples was carried out following ISO 14780 and analysis lead to the determination of moisture content on a dry basis complying with the ISO 14774-1, ash content following ISO 14775, lower calorific value on a dry basis according to ISO 14918 and mass content of carbon, hydrogen, and nitrogen as ISO 15104 established.

The results of analysis—carried out on the hazelnut shells used as biomass in the gasification experiment—are shown in Table 1.

#### **2.4. Syngas Analysis**

The outgoing gas from the experimental gasifier was analyzed by the gas chromatograph CP-4900 Micro GC Varian in order to estimate the molecular species of gaseous mixture. The syngas is collected in pockets of *tedlar* through donor sites located along the duct between the filter and the air premixing zone for combustion in torch. Once the bags are filled, the placing of the gas inside the gas chromatography is carried out through the use of a latex tube which acts as a connecting element between the valve of the bag and the analysis tool.

### **3. Results and Discussion**

The analysis of the synthesis gas has allowed determination of the molecular species present in the gaseous mixture obtained as the result of hazelnut shells gasification inside the experimental gasifier presented in this paper. The gas chromatography results are shown in Table 2.

Figure 7 shows the average composition of the molecular species present in the gaseous mixture.

H<sub>2</sub> and CO<sub>2</sub> have been the main components of the syngas produced by the gasification process (Figure 8). Moreover, comparing the results with literature data, it can be seen that the highest values were obtained in the gasification of hazelnut shells, except for CO<sub>2</sub>. This difference could be due to size, homogeneity, and a better calorific value, which is the main factor for thermochemical processes like gasification.

Literature fixes the syngas quality on the basis of the oxidant agents; keeping the same oxidant agents, highest values of the syngas components have been founded than the ones previously stated (Figure 8 and Table 3).

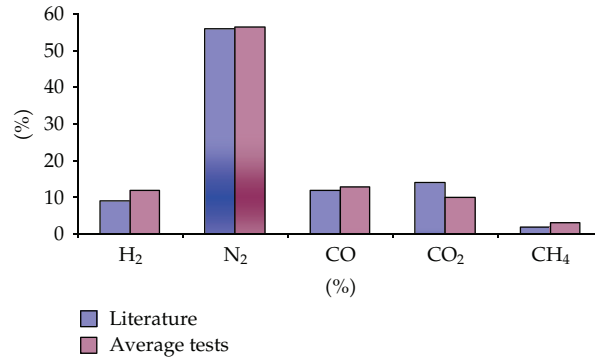


Figure 8: Comparison between literature data and tests average.

Table 3: Syngas quality on the basis of oxidant agents (ISES Italia, 2005) [4].

%	Air	Oxygen	Water vapour
CO	12–15	30–37	32–41
CO <sub>2</sub>	14–17	25–29	17–19
H <sub>2</sub>	9–10	30–34	24–26
CH <sub>4</sub>	2–4	4–6	12.4
N <sub>2</sub>	56–59	2–5	2.5

In particular tests showed a proportional increase of H<sub>2</sub> (2.8%), CO (0.87%), and CH<sub>4</sub> (around 1.1%) and a proportional decrease of CO<sub>2</sub> and N<sub>2</sub>. Generally, the results show that the produced syngas is relatively rich in carbon dioxide, methane, and hydrogen and also contains a large amount of nitrogen.

The carbon dioxide resulting from partial combustion process takes place simultaneously with biomass gasification. The prototype worked properly producing good quality syngas. However, it should be noted that it could be improved, providing a better automation and electronic system. This is to ensure technical and economical sustainability. Further researches will be carried out in the future.

### Authors' Contribution

The authors' contribution to this paper can be considered equal.

### Acknowledgment

The authors would like to thank Mrs. Elena Allegrini, Ph.D. student at the Department of Agriculture, Forest, Nature and Energy (DAFNE), University of Tuscia, for her support and help in drafting the present paper.

## References

- [1] D. Monarca, M. Carlini, M. Cecchini, and A. Colantoni, "Gasification of agroforestry biomasses by means of a multi-reactor gasifier for electric power production: experimental tests and syngas analysis," *Annual Review of Agricultural Engineering*, vol. 7, no. 1, pp. 57–64, 2009.
- [2] D. Monarca, M. Cecchini, A. Colantoni, and A. Marucci, "Feasibility of the electric energy production through gasification processes of biomass: technical and economic aspects," in *Proceedings of the Computational Science and its Applications (ICCSA '11)*, vol. 4 of *Lecture Notes in Computer Science*, pp. 307–315, Springer, Santander, Spain, June 2011.
- [3] G. Bruni, R. Solimene, A. Marzocchella et al., "Self-segregation of high-volatile fuel particles during devolatilization in a fluidized bed reactor," *Powder Technology*, vol. 128, no. 1, pp. 11–21, 2002.
- [4] A. Çağlar and A. Demirbaş, "Hydrogen rich gas mixture from olive husk via pyrolysis," *Energy Conversion and Management*, vol. 43, no. 1, pp. 109–117, 2002.
- [5] S. T. Chaudhari, S. K. Bej, N. N. Bakhshi, and A. K. Dalai, "Steam gasification of biomass-derived char for the production of carbon monoxide-rich synthesis gas," *Energy and Fuels*, vol. 15, no. 3, pp. 736–742, 2001.
- [6] P. Morf, P. Hasler, and T. Nussbaumer, "Mechanisms and kinetics of homogeneous secondary reactions of tar from continuous pyrolysis of wood chips," *Fuel*, vol. 81, no. 7, pp. 843–853, 2002.
- [7] P. McKendry, "Energy production from biomass—part 3—: gasification technologies," *Bioresource Technology*, vol. 83, no. 1, pp. 55–63, 2002.
- [8] T. A. Milne and R. J. Evans, "Biomass gasifier "Tars": their nature, formation, and conversion," Tech. Rep. NREL/TP-570-25357, NREL, Golden, Colo, USA, 1998.